Fall 9-5-2018

Radiation Effects in Metal Oxides and Carbides

Benjamin Jackson Cowen
University of New Mexico

Benjamin Jackson Cowen

Candidate

Nuclear Engineering

Department

This dissertation is approved, and it is acceptable in quality and form for publication:

Approved by the Dissertation Committee:

Mohamed El-Genk, Chairperson

Anil Prinja

Osman Anderoglu

Yu-Lin Shen

RADIATION EFFECTS IN METAL OXIDES AND CARBIDES

by

BENJAMIN JACKSON COWEN

B.S. Mathematics, North Carolina State University
M.S. Nuclear Engineering, University of New Mexico

DISSERTATION

Submitted in Partial Fulfillment of the
Requirements for the Degree of

Doctor of Philosophy
Engineering

The University of New Mexico
Albuquerque, New Mexico

December, 2018

ACKNOWLEDGEMENTS

This research is partially funded by the University of New Mexico's Institute for Space and Nuclear Power Studies, a U.S. NRC Graduate Fellowship Grant # NRC-38-09-931 to the University of New Mexico, the New Mexico Space Grant Consortium, and a Center for Integrated Nanotechnologies Proposal (CINT).

In order to carry out the large-scale simulations carried out in this work, this research made use of the resources of the High Performance Computing Center at Idaho National Laboratory, which is supported by the Office of Nuclear Energy of the U.S. Department of Energy and the Nuclear Science User Facilities under Contract No. DEAC0705ID14517. I would also like to thank the UNM Center for Advanced Research Computing, supported in part by the National Science Foundation, for providing the high performance computing and large-scale storage used in this work.

I extend my appreciation to the CINT thin film deposition laboratory at Los Alamos National Laboratory and the *in situ* ion beam irradiation (I^3TEM) facility at the Ion Beam Laboratory at Sandia National Laboratories. I appreciate the valuable support and guidance by Kevin Baldwin, Dr. Khalid Hattar, Dr. Samuel Briggs, and Dr. Caitlin Taylor, for their help with the experiments that I carried out.

I would like to acknowledge my advisor Distinguished and Regents' Professor Mohamed S. El-Genk, for his guidance and support in completing this degree, and appreciate the long meetings, advice, and mentoring he has provided throughout the degree program.

I am grateful to the other members of my dissertation committee, Dr. Anil Prinja, Dr. Osman Anderoglu, and Dr. Yu-Lin Shen for their time and guidance spent on helping me to obtain this degree. I would also like to thank my fellow graduate students at the University of New Mexico's Institute for Space and Nuclear Power Studies, Timothy Schreiner, Luis Palomino, Arthur Suszko, Denise Haskins, Mahyar Pourghasemi, and Khaled Talaat, for their help and support.

Lastly, I would like to thank my wife, Marcia Cowen, for her support and patience during this long journey. I would also like to thank my son, Graham Cowen, for bringing so much joy to my life during this time.

Radiation Effects in Metal Oxides and Carbides

by

Benjamin Cowen

B.S. Mathematics (2012)

M.S. Nuclear Engineering (2015)

PhD Engineering (2018)

ABSTRACT

MD simulations of SiO_2, TiO_2, Cr_2O_3, Al_2O_3, MgO, and SiC, are performed to: (a) calculate TDE probability distributions and dependence on crystallographic direction, and (b) determine the number and types of defects formed with low- and high-energy PKAs and projectiles. In addition, a qualitative comparison of the MD simulation results of radiation damage in TiO_2, MgO, and crystalline and amorphous SiC thin films are compared with those of *in situ* TEM ion beam irradiation experiments at the Sandia National Laboratories' I^3TEM facility.

The TDE probability distributions show strong anisotropy and those with 50% probability agree well with the reported experimental values. Results show that MgO and TiO_2 are the most radiation hard of all metal oxides investigated and that the lost long-range order in TiO_2 during the ballistic phase of interaction by a 46 keV Ti projectile, reemerges as most of the produced defects anneal within tens of picoseconds.

The MD simulations of Si PKAs of up to 100 keV in 3C-SiC shows only dispersed subcascades forming. The sizes of defect clusters in 3C-SiC are in general agreement with the *in situ* TEM irradiation experiments using a 1.7 MeV Au^{3+} ion beam. The defect structures show contrast changes ranging from 9.1 to 83.5 nm^2, which is in general agreement with the MD simulation values ranging from 5 to 76 nm^2. SiC amorphization is not observed in the MD simulations. The stored potential energy due to defect production in 3C-SiC is ~10% of the 10-100 keV Si PKAs in the MD simulations, and indistinguishable in a-SiC.

Simulations using single and multiple Au projectiles show that the extent of the defect cascades strongly depend on the number of projectiles and that defect structures are in

general agreement with those induced by single 1.7 MeV Au^{3+} ion strikes in the *in situ* TEM experiments. The MD simulations with 10, 20-keV projectiles in MgO produces a void of 102,500 vacancies during the ballistic phase, decreasing to 5,000 vacancies after annealing. Simulated SAED patterns and RDFs show local amorphization of MgO at the peak of the ballistic phase, which partially recrystallizes during the annealing phase.

Table of Contents

List of Figures

List of Tables

Nomenclature

Abs.	Absorption
ADOPT	Advanced Doped Pellet Technology
ATF	Accident Tolerant Fuel
atm	atmosphere
BKS	Potential by van Beest, Kramer, and van Santen
CARC	Center for Advanced Research Computing
CINT	Center for Integrated Nanotechnologies
COMB	Charge-Optimized Many Body
CVD	Chemical Vapor Deposition
D_{ij}	Parameter
DP	Detachment Points
dpa	Displacements per atom
ϵ_0	Electrical permittivity of vacuum
e	Electron charge
E_d	Energy required to permanently displace the PKA (eV)
E_{FP}	Energy required to create a stable Frenkel pair (eV)
E_{ij}	Potential energy between atoms “i” and “j”
E_{PKA}	Energy of the primary knock-on atom
EPR	Electron Paramagnetic Resonance (eV)
F_{ij}	Parameter
FWHM	Full-Width Half-Maximum
GPa	GigaPascals
GPU	Graphics Processing Unit
I^3TEM	In Situ Ion Irradiation Transmission Electron Microscope
INL	Idaho National Laboratory
IVEM	Intermediate Voltage Electron Microscope
ISNPS	Institute for Space and Nuclear Power Studies
LAMMPS	Large-scale Atomic/Molecular Massively Parallel Simulator
LANL	Los Alamos National Laboratory
KP	Kinchin-Pease

LOCA	Loss-of-coolant accident
LANL	Los Alamos National Laboratory
MD	Molecular Dynamics
mDCG	Potential by Demiralp, Cagin, and Goddard
NMSGC	New Mexico Space Grant Consortium
N_{ou}	Number of over- or under-coordinated defects
NPT	Isothermal-Isobaric Ensemble
NRC	Nuclear Regulatory Commission
NRT	Norgett-Robinson-Torrens
NVE	Microcanonical Ensemble
NVT	Canonical Ensemble
0^{I}	Under-coordinated oxygen
0^{III}	Over-coordinated oxygen
OVITO	Open Visualization Tool
PCI	Pellet-Cladding Interaction
P_{damp}	Pressure Damping Parameter
PKA	Primary Knock-on Atom
PNNL	Pacific Northwest National Laboratory
PPPM	Particle-Particle Particle-Mesh
Prob.	Probability
PWR	Pressurized Water Reactor
q_i	Charge of atom “i”
q_j	Charge of atom “j”
r_{ij}	Distance between atoms “i” and “j”
SAED	Selected Area Electron Diffraction
SNL	Sandia National Laboratories
Si^{III}	Under-coordinated silicon atom
Si^{V}	Over-coordinated silicon atom
SNL	Sandia National Laboratories
$S(r_{ij})$	Switching function
SRIM	Stopping and Ranges of Ions in Matter

T_{damp}	Temperature Damping Parameter
TDE	Threshold Displacement Energy
TEM	Transmission Electron Microscopy
TDSE	Time-dependent Schrödinger equation
TRIM	Transport of Ions in Matter
TRISO	Tristructural-Isotropic
TS	Potential by Tangney & Scandolo
ZBL	Ziegler-Biersack-Littmark
Z_i	Nuclear charge of atom “i”
Z_j	Nuclear charge of atom “j”

1. INTRODUCTION

Innovative nuclear reactor designs and technologies have been developed for decades to improve the safety, reliability, and economy of the conventional UO_2+Zircaloy fuel materials. This focused effort has led to steady improvements in the fuel system of UO_2 fuel pellets and Zircaloy claddings, providing extensive operation and experimental databases for these materials. Properties of interest include high thermal conductivity, good mechanical properties, low swelling and fission gas release, and safety in design-basis and beyond design-basis accident scenarios.[1-3] However, on March 11th, 2011, a magnitude 9.0 earthquake struck off the coast of Japan, triggering a tsunami that destroyed the external power supply and the onsite power source at the Fukushima Daichii Nuclear Power Station in Japan. After the turbine-driven pumps stopped working, the water in the vessels of the four boiling water reactors at the site, and used fuel storage pool, evaporated or leaked, leaving the fuel uncovered. Subsequently, the fuel rods heated up to 2300°C. The high-temperature steam environment led to the physical and chemical degradation of the fuel rods. At temperatures above 1200°C, oxidation of the Zircaloy cladding becomes self-catalytic, producing high levels of hydrogen.[4] By escaping through uncontrolled leakage pathways, the hydrogen reacted violently with the oxygen in the air and the in-vessel steam, leading to the discharge of radioactive fission products into the atmosphere.[5,6]

The Fukushima Daiichi nuclear reactor accident emphasized some undesirable performance characteristics of the current fleet of deployed nuclear reactors in design-basis and severe accident scenarios. This has led to an international effort to develop next generation nuclear reactor designs such as sodium-cooled fast reactors, molten-salt reactors, supercritical water or CO_2 cooled reactors, and very high temperature gas cooled reactors. These next-generation nuclear reactor designs will require advanced materials with demonstrated performance in harsh environments of high temperature and irradiation.[5,7-10] One of the primary campaigns focused on the development of a new class of materials that withstand these environments, is accident-tolerant fuel (ATF) systems.

1.1 Accident Tolerant Fuel Systems (ATFs)

ATFs are being developed to: (a) delay incipient UO_2 fuel melting, (b) retain fuel-rod like geometry, (c) delay cladding oxidation and thus, the production of hydrogen, and (d) reduce

self-ignition of hydrogen in loss-of-coolant accidents (LOCAs) in pressurized water reactors (PWRs). The ATF materials should allow for backwards compatibility to existing reactors, have minimal impact on the fuel cycle and reactor operations, and provide improved safety in design-basis and beyond-design basis accident scenarios.

Cladding materials being considered in ATFs include SiC/SiC composites, FeCrAl, and Zircaloy with various coatings, such as SiC, TiO_2, and Al_2O_3. Fuel materials being considered include U-Mo, the micro-encapsulated fuel pellet, which consists of TRISO fuel particles, with an outer shell comprised of SiC, to act as a barrier to fission products, and uranium nitride, silicide, mixed nitride–silicide, and uranium dioxide with additives (< 0.1 vol.%) of dispersed oxide nanoparticles.[5,11,12] Recently, Cr_2O_3 and Al_2O_3 nanoparticles have been shown to improve the performance, and increase the mechanical strength, radiation tolerance, and the creep resistance of the UO_2 fuel.[13] Other oxides, such as SiO_2 and TiO_2, have also been shown to potentially reduce Zircaloy cladding strain during reactor operation.[12] The effects of Cr_2O_3, Al_2O_3, SiO_2, and MgO nanoparticles on increasing the retention of fission gases in nuclear fuel matrices have been investigated.[14] The SiO_2 nanoparticles yield an order of magnitude smaller diffusion coefficient for Xenon than in the un-doped UO_2 fuel over a range of temperatures. On the other hand, MgO and Al_2O_3 had no effect on the diffusion coefficient of the fission gases.

1.2 Advanced Doped Pellet Technology

Another promising fuel concept that has been developed by Westinghouse, Sweden,[15] over the last several decades is the Advanced Doped Pellet Technology (ADOPT) fuel. This technology uses UO_2 with small amounts of Cr_2O_3 and Al_2O_3 oxide nanoparticles (Fig. 1.1), making it possible to use larger UO_2 grains without compromising the structural strength of the fuel pellets.[5,13,16-19] In fact, with the addition of these oxide nanoparticles, UO_2 fuel pellets with 40-45 μm size grains retain structural strength, in contrast to 15-20 μm in conventional UO_2 fuel, increasing fission gas retention and decreasing fuel swelling. The larger grain delays the arrival of the intragranular voids of fission gases to the grain boundary, and the oxide nanoparticles pin dislocations and intragranular voids, and trap radiation defects. The net outcome is improvements in the fuel's mechanical strength, creep resistance and radiation tolerance, and increased fuel burnup attainable. Other oxides, such as SiO_2, MgO, and TiO_2 may have similar effects.

Out of all the materials investigated for both ATFs and ADOPT fuel, one recurring theme is the use of metal oxides, whether in the form of additives to UO_2, or coatings of Zircaloy cladding to reduce oxidation. Alternative cladding materials under strong consideration are crystalline and amorphous SiC. However, the irradiation of these materials causes irradiation-induced displacements, leading to permanent structural changes, and altered material properties. These structural changes originate from produced point defects, which can cluster to form larger-scale defects such as dislocations and voids, which ultimately lead to fuel swelling, thus limiting the burnup of the reactor. For these reasons, there is a need to carry out an extensive investigation of irradiation effects in the ceramic materials of interests, to understand their morphology in high-irradiation environments.

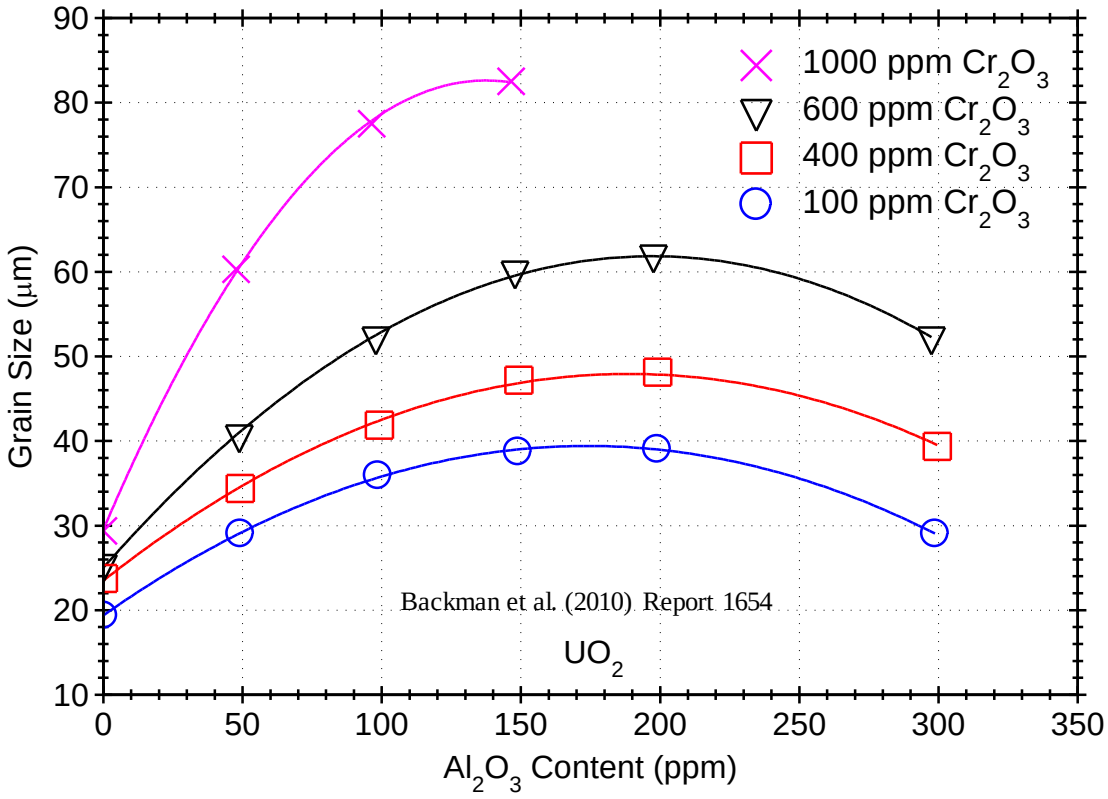

Figure 1.1: Effect of Cr_2O_3 and Al_2O_3 nanoparticles on increasing grain size of the ADOPT UO_2 fuel during sintering.

1.3 Other Applications

Metal oxides are also being considered for next-generation nuclear reactor designs including high temperature gas cooled reactors, sodium cooled fast reactors, and molten salt cooled reactors, where the materials are needed to withstand high irradiation and reactive

environments.[5,9,11,20-24] Metal oxides, such as Al_2O_3, Cr_2O_3, Y_2O_3, and MgO, in the form of additives, nanoparticles, or coatings, have been used to increase the strength and the radiation hardness of these materials.[5,11-13,25,26]

Ceramics have also been used extensively in the semiconductor industry in various applications including thin films. For example, TiO_2 is often used as a switching material, due to its high compatibility with Si-based semiconductors,[27] and the Si/SiO_2 interface is encountered in the manufacturing of semiconductor transistors.[28,29] The O/SiO_2 interface is encountered in the dry-etching of silica surfaces, and in space and aerospace crafts exposed to atomic oxygen.[30,31] Because of its wide band-gap, Cr_2O_3 is commonly used in electronic and optical devices, and is a necessary component in corrosion-resistant nanocrystalline ceramics.[32] The highly textured MgO films have also been used in semiconductor industry as a buffer between ferroelectric films and semiconductor substrates.[33]

Silicon carbide (SiC) is a high temperature material that is of interest in many applications. Examples include the development of strong spacecraft structures, structural and fuel cladding materials for current and next-generation nuclear power reactors,[34,35] development of radiation-hardened electronics,[36,37] and uses in the plasma-facing blankets for protecting structural materials in proposed nuclear fusion reactor designs.[38,39] Pure SiC and SiC fiber-reinforced composites are favored for uses in space, aerospace and terrestrial applications because of their light weight, low activation under neutron irradiation, good thermal and mechanical properties, and chemical stability in high temperature and oxidizing environments.[38] More information can be found about ATFs and ADOPT fuel in Appendices A-C.

In summary, metal oxides and carbides are widely used in many industries as thin films, coatings, nano-particles, etc., and some may be exposed to irradiation or used in radiation detectors.[12,33,40-42] Therefore, it is desirable to investigate radiation effects in these materials. Understanding radiation damage in these materials at the atomic and nano scale is essential for the development of multi-scale predictive models for advancing nuclear science and engineering applications.

1.4 Investigating Radiation Damage

Computational models to estimate displaced atoms in irradiated materials include the Kinchin-Pease (KP) and Norgett-Robinson-Torrens (NRT). They use the threshold

displacement energy (TDE) as an input. However, determining representative TDEs is challenging, particularly for polyatomic materials in which interaction sequences of different atom types occur, depending on the type and initial direction of the primary knock-on atom (PKA). The Stopping and Ranges of Ions in Matter (SRIM)[43] code, based on a Monte-Carlo binary collision approximation, is widely used for calculating the average displacements per atom (dpa), a standard unit for quantifying the radiation-induced damage in materials. While these computational options are adequate for approximating displacement damage, mechanistic insight needs to be gained in terms of Frenkel pair formation, diffusion, and annihilation in crystalline materials, as well as the defect clustering and the crystalline-to-amorphous phase transitions.

Recent advances in computational hardware have allowed molecular dynamics (MD) simulations to become a useful tool for investigating irradiation effects in materials at the nano-scale.[44-51] They use Newton's equations of motion and an interatomic potential to model atom-atom interactions. The selected potential is usually fitted to experimental or high-level *ab initio* simulation results.[52,53] MD simulations have been extensively used to predict the TDE values and probability distributions[8,54-67] and the evolution of the damage cascade,[44,48,49,68-71] and investigate the behavior and migration of individual defects and clusters in various materials.[72-74] MD simulations model the evolution of radiation damage cascades on time scales of tens to hundreds of picoseconds, with attosecond resolution. Until recently, MD simulations of radiation damage by high energy PKAs has been primarily of metals, due to the computational robustness of the potentials used. However, the advances in computational hardware and the improved algorithms made it possible to investigate the progression of the radiation damage cascades with high-energy PKAs in ceramics.[44,45,48,51,68,75]

Another state-of-the-art technique used for investigating irradiation effects is *in situ* transmission electron microscopy (TEM), which can provide millisecond resolution of defect clustering and amorphization. Despite the significantly longer time scale compared to that of the MD simulations, the experiments provide real time observation of the ions strikes, and potential radiation damage information. At the *in situ* ion beam irradiation facility (I^3TEM) at Sandia National Laboratories (SNL), the high energy of the ions in the irradiation experiments is selected to produce high cascade damage in the tilted (30^o) thin film

specimens, without affecting composition since the vast majority of ions pass through the thin specimens. The ion flux and TEM imaging conditions can be optimized to facilitate direct real-time observation of single strikes. A limitation of the TEM is the low spatial and temporal resolutions, for identifying point defects and small defect clusters. The spatial resolution of a few nanometers and the temporal resolution of milliseconds (ms) are much higher than in MD simulations (angstroms and attoseconds).

While the MD simulations results of irradiation-induced defects at the atomistic scale could not substitute for those of the ion beam irradiation results at the macroscale, together they can enhance the broad understanding of radiation effects in materials. The use of both techniques should be an effective tool-set for understanding and characterizing the effects of radiation in materials and the resulting changes in microstructure.

1.5 Research Objectives

The objectives of this dissertation research are to use MD simulations to characterize radiation damage in ceramic materials of interest to the Department of Energy (DOE) ATFs and advanced ADOPT fuel, and make qualitative comparisons to experimental results. The materials investigated are: SiO_2, TiO_2, MgO, Cr_2O_3, Al_2O_3, and SiC (amorphous and crystalline). The specific foci of the proposed research are:

a) Review and identify interatomic potentials suitable for modeling ceramics, based on computational cost, accuracy of the results compared to experiments, and transferability.

b) Calculate TDE probability distributions for SiO_2, TiO_2, Cr_2O_3, Al_2O_3, MgO, and SiC, and determine the TDE dependence on crystallographic direction, with PKAs from both anion and cation sublattices, and identify the sublattice in which different types of defects form.

c) Determine the number and types of defects formed with low- and high-energy PKAs, to develop correlations and characterize the material response to irradiation.

d) Deposit thin films of TiO_2, MgO, and amorphous SiC for performing *in situ* experiments using ion beams at the I^3TEM facility,[76] at Sandia National Laboratories.

e) Perform qualitative comparison of the MD simulation results with the *in situ* TEM ion beam irradiation experiments for TiO_2, MgO, and both crystalline and amorphous SiC.

The Dissertation is structured as follows (2) the following section provides background on the

The Dissertation is structured as follows. Chapter 2 provides the background on the various computational methods and experimental techniques used for investigating irradiation effects in materials. Prior work of investigating irradiation effects in metal oxides and carbides is presented and discussed. Chapter 3 presents the results of interatomic potential validation with regards to accuracy, transferability, and computational cost. Both pair potentials and many-body potentials are investigated over the range of the phase diagram of the materials. Chapter 4 presents and discusses the threshold displacement energy in the metal oxides and carbides of interest, including the directional dependence and probability distributions for displacements. Results from this study are compared to experimental results, when available, and could be used as input into binary collision approximation codes, such as SRIM. Chapter 5 presents the MD simulation results of bulk radiation damage in SiO_2 and TiO_2 up to 2 and 10 keV, respectively. Defect production is quantified in terms of Frenkel pairs, coordination analysis, cascade morphology, and changes in crystallinity. Chapter 6 presents the comparison of MD simulation results with those obtained using *in situ* TEM ion beam irradiation in TiO_2, MgO, and crystalline and amorphous SiC thin films. The MD simulation results and experimental results together provide a complementary perspective of radiation effects, and could be used to develop multi-scale models for predicting irradiation effects in materials. Chapter 7 presents the key summary and conclusions from this dissertation research, and recommends further research to build off of the work presented herein.

2 BACKGROUND

This section provides background information on the different ways for measuring and detecting radiation damage, as well as prior work of investigating irradiation effects in the ceramics of interest.

2.1 Measuring and Detecting Radiation Damage

Several different computational methods and experimental techniques are used for detecting and measuring radiation damage in materials. One method to investigate irradiation effects of materials is using computer models or simulations. The latter can vary from a simple binary collision approximation to solving the complex time-dependent Schrödinger equation (TDSE). Advantages and limitations of the different models and simulations of radiation damage are reviewed next.

2.1.1 SRIM/TRIM, KP, and NRT Models

The models of Stopping and Ranges of Ions in Materials (SRIM)/TRIM, Kinchin-Pease, and Norgett-Robinson-Torrens (NRT) are widely used to predict irradiation effects in materials. The modified Kinchin-Pease model is simply expressed as:

$$N_d = \begin{cases} 0 & E_v < E_d \\ 1 & E_d \leq E_v < 2E_d/0.8 \\ 0.8E_v/2E_d & E_v > 2E_d/0.8 \end{cases} \quad \text{Eq. 2.1}$$

where E_v is the energy going into the nuclear collisions, and E_d is the TDE. These types of models are computationally efficient, because estimating the number of displacements can be carried out just by simply knowing the TDE of the material. However, TDE values are not always agreed upon throughout the literature, are direction-dependent, and can vary significantly, especially for polyatomic materials which can have oxygen-metal, oxygen-oxygen, and metal-metal collisions.

SRIM has an easy-to-use interface with parameters loaded or available for all elements. and gives rough approximations of the irradiation-induced displacements. The displacements per atom (dpa) can be calculated in order to determine the dose of ion beam irradiation experiments. However, SRIM is limited to only modeling amorphous materials, and does not account for thermal recombination, or defect clustering in the form of voids and dislocations. In SRIM, the TDE is used as an input, and is obtained from either experiments or computer simulations. In order to gain more mechanistic insight into defect production, clustering,

amorphization, and recombination, which would take place in nuclear reactors, a more sophisticated model needs to be used, which is discussed next.

2.1.2 Molecular Dynamics

MD simulations are an effective tool for characterizing atom-atom interactions and determining mechanical, chemical, and thermal properties by averaging the results over simulation times of 10s to 100s of picoseconds. Recent advances in materials science at the nano- and micro-scales, including methods for atoms self-assembly, have inspired interest in simulating atomic interactions for designing and engineering new materials and composites with superior performance and characteristics.[77,78] The ability to successfully simulate atomic interactions, and extract the material properties at the nano- and micro-scale and relate them to the bulk material properties offers unlimited opportunities for developing new materials and modifying material properties through the manipulation of atoms. MD simulations have created an opportunity for investigating material properties at the atomic scale and relate them to those at the macro-scale. This has been accompished through the continuing leaps in computing capabilities at progressively lower costs.[79,80]

Simulating atom-atom interactions using improved algorithms is at the forefront of computational materials science. MD simulations have been used in a myriad of investigations in many fields, including physics, chemistry, biology, engineering, aerospace, bioengineering, pollution, drug delivery, etc. Specific examples are materials self-assembly, interactions of proteins and ligands, selection of additives for improving the mechanical and surface properties, and radiation hardening of materials for uses in space, medical, diagnostics, drug delivery, and nuclear reactors.[77,78,81,82]

In computational materials science, there are two distinct methods for describing atom-atom interactions, namely: (a) Ab Initio Molecular Dynamics (AIMD), and (b) Classical Mechanics. Both methods model the time evolution of the atom-atom interactions and can extract the dynamic, thermodynamic, and structural properties of the materials. The AIMD simulation method models atom-atom interactions by performing "on-the-fly" electronic structure calculations to calculate the forces acting on the nuclei and the atom trajectories. The electronic structure calculations originate from the TDSE, which cannot be solved analytically, except for the simplest of systems.[83] Since AIMD cannot be used to investigate large-scale defect cascades, it is not a focus of this dissertation research. However, many of

the interatomic potentials used in MD simulations are developed from the AIMD method, in addition to experiment results. For this reason, a further review of AIMD is provided in Appendix D.

Classical MD simulations typically consist of a data file of the initial coordinates of the atoms of interest, and an interatomic potential or force field for characterizing the atom-atom interactions. The accuracy of the simulation results depends on the approximations used in calculating the trajectories of the atoms. The trajectories are generated by numerically integrating Newton's equations of motion, and using a numerical method such as the velocity-Verlet algorithm.

In the late 1950s, Alder and Wainwright,[84,85] pioneers in the field of MD, have studied the interaction of hard spheres. However, it was not until 1964 that the first potential to produce realistic results was used to model liquid argon.[86] Still, the first credible simulation that accurately reproduced the water properties took place in 1974.[87] The early successes of MD simulations have inspired the development of an exhaustive list of pair and many-body potentials, with terms to account for the various interactions, such as those due to van der Waals, Coulomb, bond, bend, and dihedral angle.[88] The different ways for expressing the atom-atom interactions resulted in a diverse list of potentials. For instance, incorporating the Coulomb interactions with fixed charges is typically associated with solvers such as Ewald[89] or particle-particle particle-mesh (PPPM).[90] However, some have used dynamic charges, which often incorporate the electronegativity equilibration (QEq) scheme (or a derivative) developed by Rappé & Goddard,[91] to calculate the self-charges on the atoms. Still, others have elected to neglect the Coulomb interactions altogether in the simulations that do not require them for decreasing the computation times of the simulations. Choosing between a pair-potential and a many-body potential, and the manner of accounting for the Coulomb interactions, is often a compromise between accuracy, transferability, and computational cost.

A shortcoming of MD simulations is the limited transferability to various regions of the phase diagram for a given material. The reason for this is that the potentials are typically not fitted to the experimental data in all these regions. Additionally, MD simulations do not accurately model the changes in the chemical bonding due to neglecting the effects of quantum chemical electronic polarization. When the materials undergo transformations to

other polymorphs, the empirically derived potentials may not perform well. In order to overcome this challenge, some potential employ the QEq[91] empirical scheme, which allows for charge transfer. Another limitation of MD simulations is the high computational cost of incorporating several materials into a single model or including many-body effects.

Classical MD simulations can be used to investigate radiation damage cascades that form at picosecond time scales not possible with experiments, and could be used to determine different types of defects produced in a material under irradiation, such as point, line, and planar defects. Additionally, MD can be used to determine the TDE for use in the models based off of the binary collision approximation, discussed in the previous section. For these reasons, MD simulations have been recognized as an effective tool with inherent limitations, to characterize irradiation effects, such as the types of defects, and TDE probability distributions at time scales not possible with experiments.

Such short time scales in MD simulations, compared to seconds in experiments, limit a quantitative comparison of the MD simulations and experiments. Furthermore, in the experiments with ion beam irradiation, it is impossible to determine a single value or a probability distribution of TDEs, possible with MD simulations. Typical limitations of MD simulations are: computationally expensive, the difficulty in relating nano-scale properties to the macro-scale, the methods used to describe atom-atom interactions are based on interatomic potentials, fitted to certain regions of the phase diagram, and the inability to quantitatively compare the results with experiments. Further discussion of MD is provided in Appendix D.

2.1.3 Experimental Approach

Throughout the last several decades, several experimental methods have been developed to detect and characterize induced radiation damage in materials. These include optical spectroscopy,[92-95] electron paramagnetic resonance (EPR),[96,97] and transmission electron microscopy (TEM).[98-101] These techniques are discussed in Appendix E. Due to the presence of a band gap in ceramics, paramagnetic defects can be investigated with optical spectroscopy and EPR. Advantages of these methods include the ability to perform investigations at various temperatures, ion beam energies, and orientations, and the absence of theoretical models that may be ineffective at describing material properties. However, it can be difficult to identify the induced damage unless defects occur on both the anion and the

cation sublattices. Additionally, experiments can be time-consuming and expensive to carry out, making MD simulations a practical alternative, despite inherent limitations.

Of all of the experimental techniques used for observing radiation damage in materials, TEM is proving itself to be the gold standard by providing comprehensive data on the different types of defects in the material. Contrast mechanisms are utilized such as bright-field and dark-field images, which take advantage of the changes in diffraction due to the local defect strain field.[102] *In situ* ion beam irradiation experiments help identify the extent of damage, and even identify types of defects, such as dislocation loops, stacking fault tetrahedra, cavities, voids, and bubbles. While using TEM can provide unique insight into irradiation, there are limitations. For instance, the thin films used might not represent bulk material properties accurately, since the surface area to volume ratio is much higher than in bulk materials. Additionally, with TEM, it is challenging to identify point defects, as resolution is usually on the order of several nanometers. For instance, Liu *et al*.[103] irradiated SiC with 1 MeV Kr at 800 °C and found that 2/3 of the defect clusters which were less than 1 nm in diameter were observable using advanced scanning transmission electron microscopy (STEM), but not TEM. Still, not even STEM can be used to identify the number and types of defects that form both during the ballistic phase and the residuals. One recurring theme among experimental results is the inability to obtain resolution on the scale of the angstrom. However, by pushing the limitations on the computational end by increasing the system size and carrying out the radiation damage simulations for hundreds of picoseconds, and performing *in situ* ion beam irradiation tests with resolution on the order of several nanometers, it is possible to begin bridging the two worlds.

2.2 Prior Work in Characterization of Irradiation Effects in Oxides and Carbides

The following sections review prior experimental and computational work to determine the irradiation effects in the oxides and carbides of interest for this dissertation research. The most fundamental quantity that largely governs the effects of irradiation is the TDE, and has been investigated for many different materials. However, most studies report single values for a few crystallographic directions. Additionally, the effects of irradiation under high energy PKAs is limited, and is also discussed in the following sections.

2.2.1 Threshold Displacement Energy

Arnold[104] has experimentally determined the TDE for slow-growth quartz through the development of absorption bands (C bands) in near ultraviolet under electron bombardment. Arnold[104] investigated the optical density per unit path length versus the effective electron energy in SiO_2. This was compared with the calculated total cross sections for oxygen and silicon atoms, normalized to unity at 1.85 MeV. They were unable to identify the atom species that were displaced at PKA energies of 50±5 eV, but speculated that it was probably the oxygen atoms, since they require only two bonds to be broken. On the other hand, the silicon atoms require four bonds to be broken. In this study,[104] and studies like it, the PKA initial direction was not reported, making it difficult to determine if the TDE of 50 eV is an averaged value of over all directions, or only representative of a few directions.

Often times, as in the study of the TDE in SiO_2 by Arnold,[104] the experimental and computational estimates of the TDEs for the various oxides are reported as single values, with no or little information on the applicable crystallographic direction. Thus, reported results cannot truly assess the directional dependence of the TDE values, by accounting for all types of collisions, including low-index, high-index, and collisions between all atom types. Additionally, the definition used to determine the TDE varies from one study to another. This can occur due to fundamental differences in the perceived definition of the TDE. The three commonly used definitions of the TDE are: (1) the minimum energy to permanently displace the primary knock-on atom (PKA) from its original lattice site (E_d), (2) the minimum energy to permanently displace an atom (not necessarily the PKA), and (3) the minimum energy to create a stable Frenkel pair (E_{FP}). The first definition assumes that a PKA displacement is always associated with the formation of a stable Frenkel pair, which is not always the case.[55]

Table 2.1: Listing of the TDE values for the oxygen and silicon atoms in SiO_2.

Method	Direction	Temp (K)	E_d (O)	E_d (Si)	Reference
MD	-	0	28.9	70.5	Wang et al.[51]
Optical Abs.	-	77	50	-	Arnold[104]

The first definition is often used, such as in SRIM, to assess radiation damage in amorphous materials, in which the production of Frenkel pairs is meaningless, due to the absence of crystalline structure. However, it is unclear if PKA displacement always leads to Frenkel pair formation in the ceramic materials of interest. The production of a stable Frenkel pair is the most useful definition to use in terms of understanding permanent radiation effects. The accumulation of vacancies, interstitials, and antisites into defect clusters ultimately leads to larger-scale defects such as dislocation loops and voids, which can alter material properties and cause swelling. An extensive search of the literature showed various TDEs for the ceramics of interest, and are shown in Tables 2.1-2.5.

Table 2.2: Listing of the TDE values for the oxygen and magnesium atoms in MgO.

Method	Direction	Temp (K)	E_d (O)	E_d (Mg)	Reference
MD	[121]	10	67±3	-	Park et al.[58]
	[131]	10	67±3	90±2	
	[135]	10	73±3	-	
	[171]	10	>150	-	
	[100]	10	-	136±2	
	[120]	10	-	153±2	
	[001]	0	160	125	Sonada et al.[105]
	[011]	0	200	200	
	-	0	52	57	Kittiratanawasin et al.[106]
Luminescence	-	-	55	52	Caulfield et al.[107]
	-	298	49±2	38±2	Grant et al.[108]
TEM (loops)	[001]	298	97±2	64±2	Sharp & Rumsby[109]
	[001]	298	44±3	60±2	Pells[110]
	[011]	298	64±3	60±2	
	[111]	298	46±3	60±2	
	-	-	30±8	-	Satoh et al.[111]
Optical Abs.	[001]	78	60	-	Chen et al.[112]

Due to the sensitive nature of the TDE to the definition, crystallographic direction, sublattice of the material, and experimental technique or computational method used, the TDE values reported throughout the literature can vary significantly, making it difficult to determine the appropriate one. A compilation of many of these studies have been previously highlighted in two reviews.[8,113]

From the various TDE values in these tables, it is clear that there is not a single TDE value for a specific material which can be agreed upon in the literature. However, codes such as SRIM require the TDE as input in order to estimate the dose of ion beam irradiation experiments. Thus, there is a need to investigate the TDE in many different crystallographic directions, and identify the types of defects produced. Additionally, since the TDE value depends on the type and energy of the PKAs, a probability distribution, rather than a single value, would be more realistic and useful for capturing the stochastic nature of radiation effects in materials.

Table 2.3: Listing of the TDE values for the oxygen and aluminum atoms in Al_2O_3.

Method	Direction	Temp (K)	E_d (O)	E_d (Al)	Reference
Luminescence	-	-	51		Caulfield et al.[107]
TEM (loops)	[0001]	-	50	<30	Barnard[114]
TEM (loops)	[0001]	-	53	<32	Das[115]
TEM (loops)	$[11\bar{2}0]$	-	41	<24	
Optical Abs.	[0001]	-	79	24	Agnew[116]
Optic. Abs. TEM	[0001]	-	75	18	Pells & Phillips[117]
Optic. Abs.	[0001]	-	76	18	Pells & Stathopoulos[118]
	-	-	<70		Compton & Arnold[119]
	-	-	<52		Townsend[92]
Computational	$[10\bar{1}0]$	-	54.3	27.7	Williford et al.[120]

Table 2.4: Listing of the TDE values for the oxygen and titanium atoms in TiO_2.

Method	Direction	Temp (K)	E_d (O)	E_d (Ti)	Reference
Optical Abs.	[100]	673 - 773	-	52	Buck et al.[121]
	[111]	673 - 773	-	50	
	[001]	673 - 773	-	47	
TRCS		1673 - 1773		39±4	
MD – 0% Prob.	-	-	19.4	69.1	Robinson et al.[55]
MD – 10% Prob.	[001]	160	65±5	70±5	Thomas et al.[60]
	[100]	160	30±5	110±5	
	[110]	160	55±5	95±5	
	[101]	160	30±5	105±5	
	[111]	160	35±5	115±5	
	Wt. Avg.	160	40±5	105±5	
MD – 50% Prob.	[001]	160	85±5	80±5	Thomas et al.[60]
	[100]	160	50±5	115±5	
	[110]	160	60±5	100±5	
	[101]	160	60±5	140±5	
	[111]	160	70±5	160±6	
	Wt. Avg.	160	65±5	130±5	

2.2.2 Radiation Damage Cascades

Radiation damage in metals has been investigated extensively with interatomic potentials such as the embedded atom method (EAM)[122,123] and the modified embedded atom method (MEAM).[124-127] High energy radiation damage cascades, from a few keV, up to several hundreds of keV, have been studied.[128-132] However, MD simulations of high-energy radiation damage in oxides and carbides is limited, and the interatomic potentials that describe the atom-atom interactions are more computationally expensive and harder to develop. The next sections highlight further motivations for investigating the materials of

interest, and prior work done in investigating irradiation effects in those materials using MD simulations.

2.2.2.1 **SiO_2**

Silica is used in many industrial and engineering applications, including micro/nano-electronics,[41,133,134] photonics,[135] solar-energy,[136] space power and electronics,[137] super high performance concrete,[138,139] and accident-tolerant fuel systems (ATFs) for next generation nuclear reactors.[5,12,14,140] However, some of these, as well as other engineering and industrial applications, require assessing the radiation tolerance of silica or quartz (SiO_2). The production of radiation-induced point defects in quartz has been investigated for applications such as quantum computing, radiation dosimetry, radiation-hard electronics, advanced instrumentations for space exploration, etc. However, despite the extensive usage of SiO_2 in different fields that would expose it to radiation damage, a general consensus has not emerged on the amount and types of the irradiation produced defects with different PKAs at low and high energies.[141]

The most widely investigated irradiation effects in silica are the production of point defects and the changes in material properties. The production of oxygen-deficient point defects (E'-centers) in crystalline and amorphous silica was first identified by Weeks,[142] using electron paramagnetic resonance (EPR) spectroscopy. The E_1'-centers in α-quartz are formed when oxygen vacancies lead to a locally trapped electron (hole).[143] These paramagnetic defects that include vacancies and impurities[144] are not considered the primary point defect under ion implantation.[145,146] The production of vacancies and impurities are considered by many to be the primary induced defects in irradiated α-quartz, and have been the subject of several reviews.[147-149]

Despite the extensive studies on the subject, further investigations to characterize and quantify point defect production in α-quartz, including low PKA energies (< a few keV) are needed. Cowen & El-Genk[54] have used a BKS-ZBL force field successfully, for short (5.5 Å) and long (15 Å) cutoffs, to calculate the TDE probability distributions for oxygen and silicon atoms, up to 150 eV.[32] MD simulations of characterizing irradiation effects in α-quartz have focused on estimating the threshold displacement energies (TDEs) of oxygen and silicon atoms and the production of point defects.[51,54] Wang et al.[51] reported single TDE values for the oxygen and silicon atoms of 28.9 and 70.5 eV, respectively. Additionally, they used a

BKS-ZBL force field with a short cutoff of 5.5 Å and the coordination analysis to estimate the production of under and over-coordinated defects in α-quartz with PKA energies up to 900 eV. Their results showed that after annealing, oxygen vacancies constituted a small fraction of the total defects produced.[51] They also suggested that oxygen vacancies typically anneal to Si^{V}, creating edge-shared tetrahedral.[33] This process results in two or more O^{III} defects forming instead of an oxygen vacancy (2 Si^{III}). Unfortunately, coordination analysis could not be used to estimate the production of point defects when compared to the perfect crystal lattice, for which the Wigner-Seitz (WS) defect analysis is used for characterizing the production of point defects such as vacancies, interstitials, and antisites. However, once the material is disordered, it is difficult to compare lattice sites to the original configuration. Although neither analysis methods give a full account of the nature and type of point defects produced, together they provide comprehensive and complementary information. Therefore, there is a need to use both methods to investigate irradiation effects in α-quartz.

In addition to the method of analysis, the choice of interatomic potential and the cutoff affects the estimates of the amount and the type of defects produced.[54] The short and long potential cutoffs of 5.5 and 15 Å, model the atom-atom interactions somewhat differently. The short cutoff, which allows atoms to only "see" nearby atoms, has regularly been used for modeling amorphous silica with the BKS potential.[150-152] Wang et al.[51] have used the short cutoff in their MD simulations to allow the transition of α-quartz to amorphous silica under irradiation. However, a short potential cutoff tends to under-predict the density of α-quartz at equilibrium conditions, ~2.38 g/cm^3, as opposed to 2.60 g/cm^3, using a long cutoff of 15 Å, which is much closer to the experimental value of 2.646 g/cm^3.[153] On the other hand, the long cutoff does not readily allow for the formation of amorphous silica using standard melt and quench methods. Consequently, MD simulations with a long cutoff, suitable for crystalline silica, might yield different estimates of defects production than with a short cutoff.[51]

For these reasons, there is a need to investigate the formation of defects in SiO_2, including vacancies, interstitials, antisites, and over- and under-coordinated defects during both the thermal spike and annealing phases. Additionally, annealing efficiencies would be useful to determine the ability of the crystal lattice to rebuild itself amongst the disorder in the system.

2.2.2.2 **SiC**

Silicon carbide (SiC) is a high temperature material that is of interest in many applications. Examples include the development of spacecraft structures, current and generations III+ and IV nuclear power reactors,[34,35] development of radiation-hard electronics,[36,37] and in the forward-facing blankets of fusion reactors.[38,39] The SiC fiber-reinforced composites and SiC are favored for use in space, aerospace and terrestrial applications because of their light weight, low activation under neutron irradiation, good thermal and mechanical properties, and chemical stability in high temperature and oxidizing environment.[38] Therefore, it is also important to understand and assess the radiation damage in SiC to develop predictive models for estimating irradiation effects.

Several potentials have been developed to model SiC,[64-66,154-160] but the generally accepted one for modeling irradiation effects in 3C-SiC is the Tersoff+ZBL potential.[64] Despite the fact that it overestimates the carbon interstitial migration energy, compared to density functional theory (DFT) results, it can provide a fairly accurate representation of radiation effects in SiC. The Tersoff+ZBL potential has recently been used to simulate the production of defect cascades and estimate TDEs for 3C-SiC.[64,65,75,154,155,161-163] The TDEs for both C and Si PKAs in SiC are highly anisotropic,[67,157] which makes it difficult to choose a single value as input into SRIM. Recent studies[60,67,164] have shown that TDEs that correspond to 50% probability for displacement closely match the reported experiment values, and thus are suitable for SRIM calculations.

Investigation of radiation damage in ceramics using MD simulations is typically limited to PKAs with energies up to a few or tens of keV.[44,45,48,75,165] However, several studies have used MD simulations to investigate radiation effects in 3C-SiC with high-energy PKAs, sometimes up to 50 keV.[75,162,163,165-167] One study[168] used MD simulations to investigate radiation damage with 10 keV Si and Au^{2+} projectiles, and compared the results to those of *in situ* TEM experiments in the 3.4 MeV tandem accelerator facility at the Pacific Northwest National Laboratory (PNNL). A higher disordering occurred using the Au^{2+}, rather than the Si projectiles, and the Au projectiles were more likely to cause amorphization and larger defect clusters.

Some other studies have investigated defect production and clustering with up to 50 keV PKAs.[75,165,167,169] However, the cutoff to identify the defect clusters varied between studies.

For example, Gao *et al.*[167] used the first nearest neighbor, Liu *et al.*[165] used the second nearest neighbor, and Samolyuk *et al.*[75] used the lattice parameter. Defect clustering was not significant in any of these studies, as the largest clusters did not exceed tens of defects. Liu *et al.*[165] showed that the clusters had from 30-100% carbon vacancies, and 60-100% carbon interstitials. Gao *et al.*[167] showed that the largest cluster did not exceed 4 interstitials, due to the short lifetime of the thermal spike phase which prevented short-range diffusion and clustering.

The results from all three studies[31,59,61] showed that PKAs of 50 keV produced dispersed sub-cascades, and the defects were spread out across the entire simulation domain. While PKA energies of 50 keV are higher than most energies investigated in ceramics, this is possible by using the Tersoff potential which neglect Coulomb interactions. Still, it would be useful to determine and compare the results for PKAs with energies up to 100 keV. In metals, clustered interstitials are thermally stable and can be absorbed in grain boundaries and dislocations.[129] The absence of this type of defect production in 3C-SiC could affect the evolution of the cascade over longer time-scales. Investigating the clustering of defects produced in SiC with high energy PKAs, up to 100 keV, would help identify potential causes of amorphization. Prior work has shown that crystalline SiC at 300 K would amorphize at a high enough dose.[170-172] Thus, it is desirable to compare irradiation effects in the crystalline and amorphous phases of SiC.

Since the amorphous phase has no grain boundaries, corrosion is not an issue and it could be more radiation-hard than the crystalline phase. One way to test this hypothesis is to estimate and compare the amount of energy stored in the material by the produced defects. In 3C-SiC, the change in the potential energy of the atoms are likely caused by the radiation-produced vacancies, interstitials, and antisites. These point defects and defect clusters would increase the stored energy, which is released upon heating.[173] In a-SiC, the production of point defects is not as readily attainable as in crystalline SiC. However, the resulting changes in the ring-structure, coordination, and potential crystallization could store some energy.

2.2.2.3 **MgO**

Previous studies have investigated irradiation effects in MgO using MD simulations. Uberuagu et al.[45,46] investigated defect mobility in MgO generated by PKAs of up to 5 keV. The production of point defects and small defect clusters as a result of the radiation damage

cascades was observed. They also showed that while vacancies were immobile at room temperature, interstitials diffused and either clustered with other interstitials or recombined with the produced vacancies. Some of the defect interstitial clusters were hypothesized to be stable over time frames of years.

In order to bypass the computationally expensive ballistic phase of radiation damage, another approach was developed to investigate defect annealing on both sublattices in MgO, by inserting Frenkel pairs in a previously equilibrated system.[174] This allows for creating systems much richer in defect concentrations by not having to model a high-energy PKA or projectile capable of producing such large defect clusters. This method was used to identify defect structures that had not yet been reported with conventional MD simulations. Despite the fact that the large produced defect clusters were generated by unconventional means, the fact that the smaller defect clusters and point defects recombine suggest these types of defects are the ones that are stable and ultimately effect the long-term stability of the material under irradiation.

2.2.2.4 **TiO_2**

Many industrial and space applications apply TiO_2 coatings to alter the superhydrophobic and superhydrophillic properties of fabrics and metallic surfaces exposed to ultraviolet light[175] and space energetic particles and atoms. Potential applications include satellites and spacecraft surfaces, photocatalysis for water decontamination,[176-180] blanket materials in fusion reactors,[181-184] and advanced cladding in nuclear reactors. The TiO_2 coating potentially increases creep resistance, irradiation tolerance, and mechanical strength of metallic substrates.[13] In some applications, TiO_2 coating exposed to irradiation by neutrons, ions and/or high energy particles would experience the formation of vacancies, interstitials, antisites, and large clusters of defects, such as voids. These defects can alter the mechanical properties and may cause embrittlement and amorphization. Thus, it is desirable to investigate irradiation damage and characterize defect production in TiO_2 for potential uses in harsh environments.

Some of the reported results of MD simulations, include TDE estimates[55,164,8] and defects production near grain boundaries,[49] and potential amorphization[48,68] in TiO_2. However, no studies have investigated the effects of the PKA type and temperature, on defect production and potential amorphization in TiO_2 with PKA energies up to 10 keV. Radiation damage in

materials is highly stochastic in nature. Therefore, performing MD simulations of multiple cascades would be needed to obtain statistically significant results. Among the important parameters that affect the results are the PKA type and energy, and the temperature of the target material. In addition, understanding and characterizing point defects production are important to quantifying radiation damage, and the effect on the electrical, mechanical, and thermal properties of materials. Recently, a study[173] has discussed potential energy storage in the produced point defects, which requires a specific activation energy for recombination. Raising the material temperature allows some defects to overcome the recombination barrier and release energy to its surroundings. Thus, determining the amount of stored energy due to defect production in materials as a function of temperature would be useful.

2.2.2.5 **Various Materials**

Some studies have investigated radiation damage with high energy PKAs in some oxides, using ~8000 computing cores, but focused on providing qualitative descriptions of their resistance to amorphization, rather than a quantitative correlation for predicting bulk radiation damage.[48,68] Their results indicate that SiO_2 is more prone to amorphization under irradiation than Al_2O_3 and TiO_2. While this study[68] reported the total number of defects for a single cascade, it did not indicate the types of defects that formed, and whether the formation of voids would form in the material under irradiation. From these simulations, it is clear that MD is a useful tool for characterizing radiation effects and can capture details in a very short timescale, not possible with experiments. However, there is little information regarding the production of different types of defects in oxides and carbides at high PKA and projectile energies. Therefore, there is a need to carry out simulations of large-scale radiation damage cascades, and determine the number and types of defects produced as a function of the PKA energy, defect clustering, annihilation, and changes in crystallinity.

2.2.3 Experiments

Several experimental techniques have been developed to investigate radiation damage in materials. These include optical absorption,[92,104,112,116,118,119,121] luminescence,[107,108] and *in situ*[185-188] and *ex situ*[189] transmission electron microscopy (TEM). Since this dissertation research compares TEM observations with MD simulations, this section reports observations from prior TEM ion beam irradiation experiments. Additionally, while several studies throughout the literate have reported ion beam irradiation effects, most are not *in situ*, and

thus contrast changes from single ion strikes cannot be obtained. This section reports on some of the different studies that investigated ion beam irradiation effects in TiO_2, MgO, and SiC.

Radiation effects in SiC have previously been investigated using in-pile neutron irradiation tests[11,21] and electron and ion beam irradiation experiments with both *in situ* and *ex situ* transmission electron microscopy (TEM).[171,172,190-195] Many of the ion beam irradiation experiments employed different ion species, different temperatures, and varying microstructures, resulting in an assortment of data points without a cohesive narrative to describe irradiation effects in SiC. In fact, the reported values of the dose for the amorphization of SiC at 300 K vary by more than an order of magnitude.[171,190]

Jamison *et al.*[172] compiled much of the published information and, in addition to carrying out their own extensive ion beam irradiation tests, have been able to explain some of the differences in the reported radiation effects in SiC across different studies. They showed that several seeming contradictions in the literature, such as dose-to-amorphization and whether nc-SiC is more or less radiation resistant than μc-SiC, could be attributed to many experimental factors. Examples include differences in the irradiating ion species, the microstructure (such as grain texture, refinement, and presence of stacking faults), and the method of observation (*in situ* vs. *ex situ* TEM).[172] This extensive review of published data[9] shows that predicting consistent effects of irradiation in SiC is challenging, which makes the development of comprehensive predictive models difficult.

Liu *et al.*[103] have irradiated SiC with a 1 MeV Kr ion beam at 800 °C and found that 2/3 of the produced defect clusters were less than 1 nm in diameter. These clusters were observable using advanced scanning transmission electron microscopy (STEM). Their cluster dynamics (CD) simulations, based on prior models of point defect production, clustering, and annihilation, were unable to reproduce the defect density distribution observed in their experiments. They were, however, able to improve the agreement between the predictions of the CD models and the experimental results by accounting for other phenomena, such as irradiation-induced mobility of clusters, intra-cascade cluster production, and the differences in morphologies of various defect clusters.

Another study by Katoh *et al.*[196] can only account for 10-45% of macroscopically measured swelling based on the produced defect clusters and loops visible with TEM.

However, a full account of the swelling is not attainable using TEM because many of the defects are too small to observe due to resolution limitations. The remainder of the produced defects is assumed to be small interstitial clusters, since vacancies in SiC are immobile until the temperature reaches ≈1273-1473 K.[22,197] Even with STEM, the exact nature of the irradiation produced defects is impossible to determine. Thus, using computational models in conjunction with experiments would help assess radiation effects at time scales and resolution not possible with TEM.

Radiation effects in TiO_2 and MgO have not been as extensively investigated as SiC. Prior work has shown that TiO_2 rutile amorphizes when exposed to 360 keV Xe^{2+} at a fluence of $5x10^{15}$ ions/cm^2, which corresponds to a dose of ≈10 dpa for the peak damage.[198] Other TEM studies[101,188] of ion beam irradiation have also shown that at 300 K, amorphization in TiO_2 rutile forms with 1 MeV Kr^{2+} at a fluence of $2.5x10^{15}$ ions/cm^2 and 360 keV Xe^{2+} at a fluence of $8x10^{15}$ ions/cm^2. Since several studies have confirmed that amorphization will occur at 300 K, it would be useful to understand the mechanisms that cause this structural change. While TiO_2 has been shown to amorphize at room temperature, MgO has been shown to be much tougher to cause amorphization, even at doses as high as 70 dpa.[199,200] MgO samples that were irradiated at 430 K were shown to swell by 2.8% and caused the formation of dislocation loops, but not amorphization.[201] While there are other studies that investigate radiation effects in MgO, most are not *in situ*, precluding the ability to observe contrast changes from single ion strikes.

3 INTERATOMIC POTENTIAL VALIDATION

This section first presents the results of an extensive review of the literature for interatomic potentials for modeling SiO_2. Investigated are no-charge, fixed-charge, and variable-charge potentials, for modeling equations of state, radial and bond-angle distribution functions, lattice constants, and phase transitions.

3.1 Potentials for modeling SiO_2

For silica, the Si-O bonds can be characterized as both covalent and ionic. The ionicity is due to the electronegative atoms, whereas the covalency is developed through bond-angles. It has been shown that the contributions of the electronegativity are an order of magnitude higher than those of the short-range forces, such as bond-angles.[202] Therefore, it is imperative that the potentials for MD simulations include the Coulomb forces in order to provide an accurate description of silica. Owing to the complex nature of the covalent/ionic Si-O bond, and the many polymorphs that can form (Fig. 3.1), several potentials have been developed in an attempt to provide a sound physics model.[203]

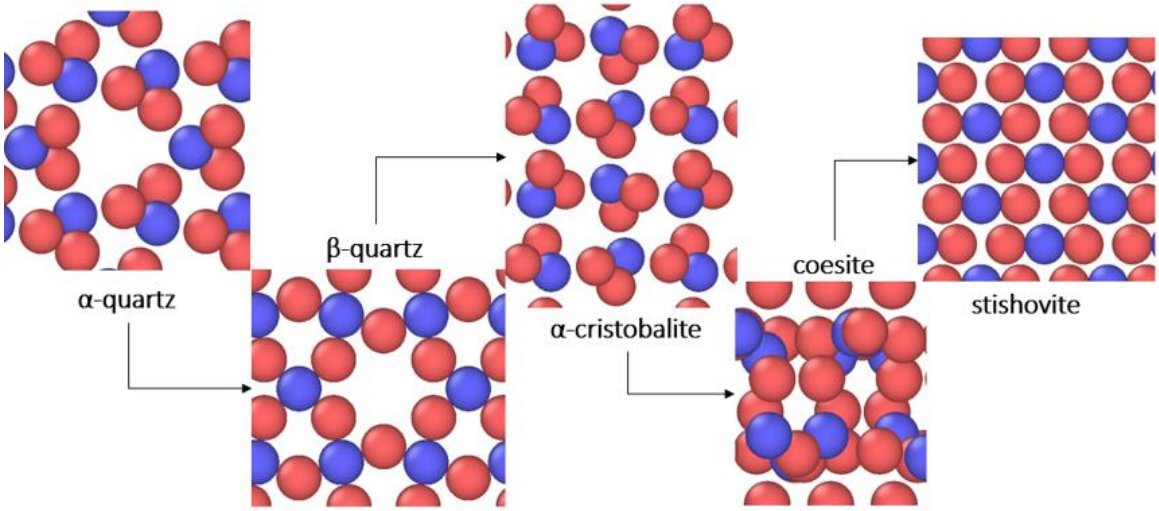

Figure 3.1*:* Crystalline phases of silica investigated using various interatomic potentials.

Fig. 3.2 provides a timeline of introducing the potentials commonly used in MD simulations of crystalline silica.[204-227] Fig. 3.3 presents a hierarchy chart of the potentials and where each was originated;[204-225,228-234] The potentials indicated in bold in this figure do not explicitly model silica, but were stepping-stones to introducing potentials that do. However, the potentials in bold boxes in Fig. 3.3 are those reviewed herein for the MD simulations of crystalline silica, and the calculated results are compared in terms of the computational time,

accuracy, and transferability. As indicated in Fig. 3.3, there are five major roots of the methods of characterizing atom-atom interactions leading to the introduction of potentials that model crystalline silica.

To assess the ability of a given potential for modeling crystalline silica, it is useful to review the underlying physics of the various terms included. Some potentials do not incorporate the necessary physics to model certain material properties. Potentials generally include various contributions of one-body, two-body, three-body, etc., as follows:

$$E(1,\dots,N) = \sum_{i} v_1(i) + \sum_{\substack{i,j \\ i<j}} v_2(i,j) + \sum_{\substack{i,j,k \\ i<j<k}} v_3(i,j,k) + \cdots + v_N(1,\dots,N) \qquad \text{Eq. 3.1}$$

Many potentials neglect the first order term that describes external forces, such as from a container wall. The choice of using a simple two-body potential (pair-potential) or including many-body effects, can impact the accuracy of the results and the computational time.

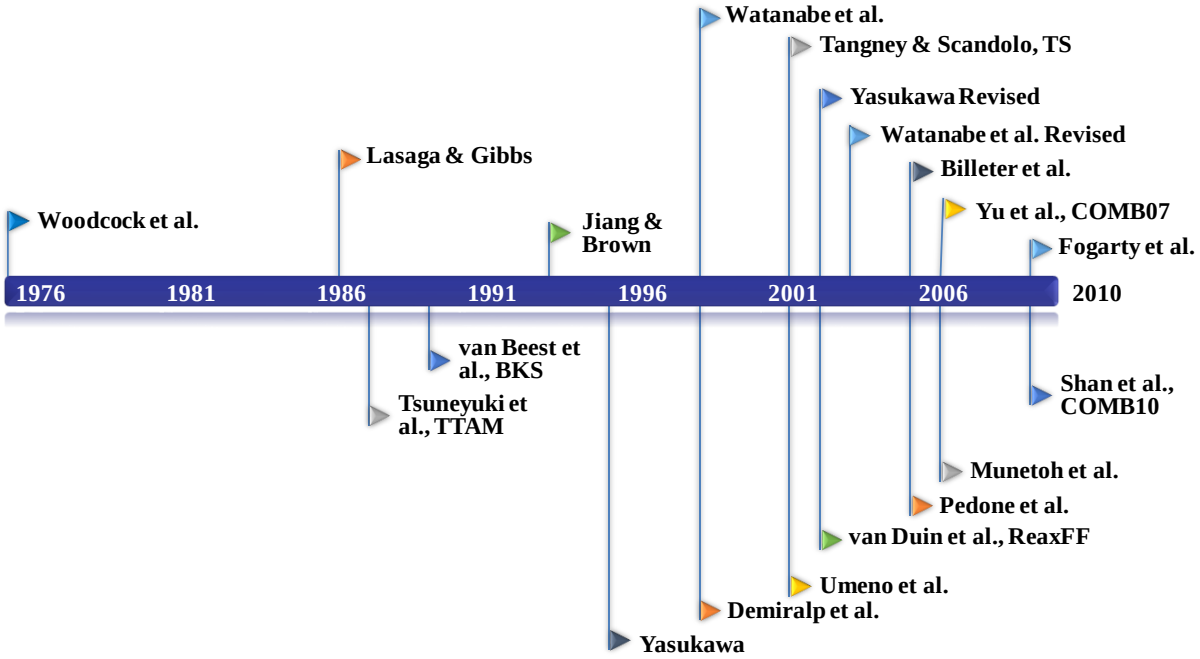

Figure 3.2: Timeline since 1987 of the MD simulation potentials for explicitly modeling silica.

The three-body Tersoff[228] root potential (Fig. 3.3) models atom-atom interactions by characterizing the strength of the bonds using the coordination number of the atoms. It is parameterized for silicon, but has inspired many bond-order, variable-charge

potentials,[209,214,220,221] no-charge potentials[213,218,219] and a fixed-charge potential,[225] that were used to model silica. The Stillinger-Weber[231] root potential (Fig. 3.3) characterizes the atom energies from the sum of two-body and three-body interactions. The two-body term is solely a function of distance, and the three-body term incorporates the rotational and translational symmetry. This root potential is also originally designed for modeling silicon. However, Watanabe et al.[210,216] have made slight modifications and parameterized it for silica.

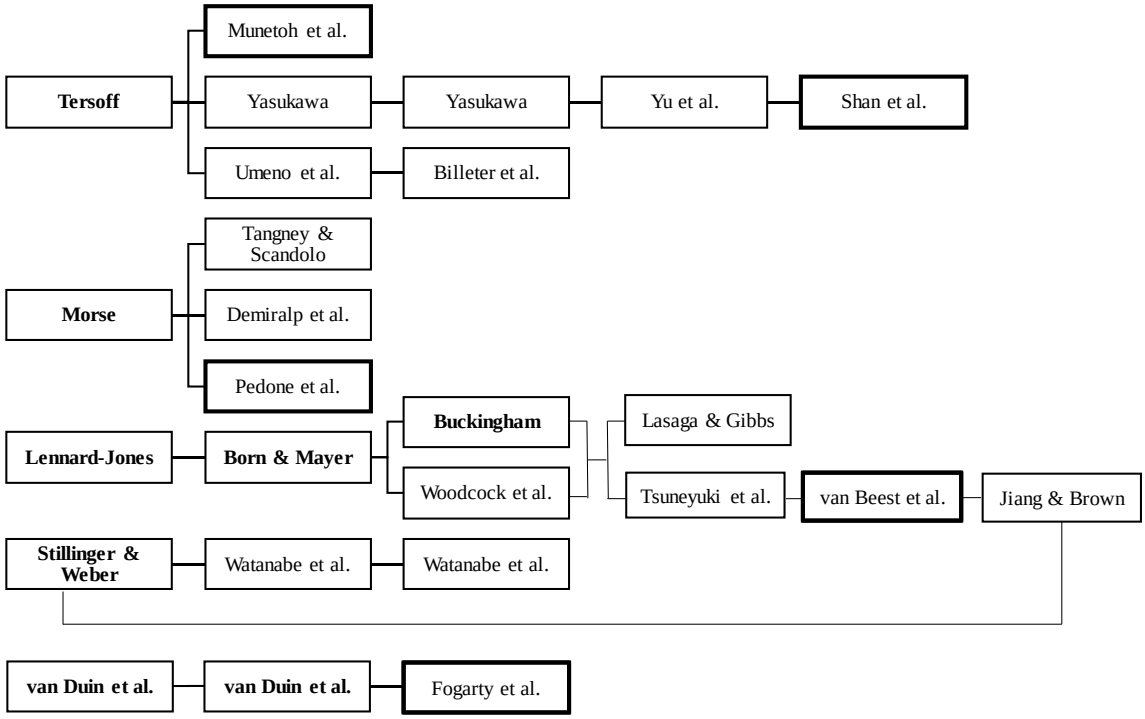

Figure 3.3*:* Hierarchy of potentials' development of potentials for modeling crystalline silica. Potentials in bold do not explicitly model silica, but have led to potentials that do. Potentials in bold boxes are investigated in this paper for computational efficiency, accuracy, and transferability.

The Morse[229] root potential (Fig. 3.3) has led to the introduction of the highly transferable and fixed-charge Morse-stretch potential by Pedone et al.[217] It can model several metallic oxides, while keeping the oxygen-oxygen parameter constant. This root potential has inspired other Morse-stretch potentials by Demiralp et al.[211] and Tangney & Scandolo.[212] These use the approaches by Rappé & Goddard[91] and Rowley et al.[235] to account for the effects of the charge-transfer and polarization, respectively.

The Lennard-Jones[230] root potential (Fig. 3.3), similar to that of Morse, expresses the atom-atom interactions using pair-potentials, albeit with different terms. However, this root

potential[230] has led to the development of the fixed-charge, Born-Mayer-Huggins (BMH) potentials by Tsuneyuki et al.[206] and van Beest et al.,[207] that are widely used today. Carré re-parameterized the BKS potential to more accurately model amorphous silica. A hybrid potential by Jiang & Brown[208] utilized the potential forms of van Beest et al.,[207] and Stillinger & Weber.[231] Fueston & Garofalini[224] used a hybrid potential that incorporates the BMH and another potential form, similar to that of Stillinger & Weber.[231]

The ReaxFF[232] bond-order, reactive root potential (similar to COMB), determines the atoms' self-charge from the local bonding environments. Both the ReaxFF and COMB potentials, with striking similarities, are powerful for modeling complex chemical behavior. A notable difference is that the ReaxFF models silica as a primarily covalent material, while the COMB potential describes silica in terms of ionic charges. It is likely at some point that these two potentials could merge into an even more powerful and transferable form, paving the way for the introduction of the next generation of bond-order potentials.[236]

Owing to the high band-gap of quartz, and its chemically homogenous environment, there is no justification to include charge-transfer, unless when modeling a complex reactive process or an interface of quartz with another material. Yu et al.[225] stipulated that variable-charge can be neglected when modeling silica, dismissing the COMB and ReaxFF potentials. The Munetoh potential neglects the Coulomb interactions, which is prohibitive for ionic crystals. The displacement of a single atom could create forces far away, resulting in unphysical effects. Despite this oversimplification, the authors of the Munetoh potential stipulated that the potential is still able to capture the structural and dynamical properties of silica. However, this potential may be unsuitable for MD simulations of crystalline silica. For instance, the calculated lattice parameters for several of the silica polymorphs have a margin of error much greater that those seen with other potentials such as the BKS potential. Some recent studies indicate that the Munetoh potential is appropriate for systems involving amorphous silica.[237-239] This work will investigate the ability of the Munetoh potential for modeling crystalline silica, despite the exclusion of Coulomb interactions. The potentials first presented for modeling crystalline are BKS, Pedone, Munetoh, TTAM, and CHIK.

The Tersoff[228] potential, originally fitted for modeling silicon, is re-parameterized by Munetoh et al,[219] which incorporates the dependence of the bond order but neglects the Coulomb interactions, as:

$$E_{ij} = \frac{1}{2}\{f_{ij}^{c}(r_{ij})[f_{ij}^{R}(r_{ij}) + b_{ij}f_{ij}^{A}(r_{ij})]\} \quad \text{Eq. 3.2}$$

The BKS,[207] TTAM,[206] and CHIK[223] potentials, which take on the Buckingham form with an additional term to account for the Coulomb interactions, are expressed as:

$$E_{ij} = \frac{q_i q_j}{r_{ij}} + A_{ij}\exp\left(\frac{-r_{ij}}{\rho_{ij}}\right) - \frac{C_{ij}}{r_{ij}^{6}} \quad \text{Eq. 3.3}$$

Note that the CHIK potential includes an additional repulsive term for high-pressure and temperature simulations, expressed as:

$$\mu_{\alpha\beta}^{cor}(r) = \frac{D_{\alpha\beta}}{r^{24}} \quad \text{Eq. 3.4}$$

The Pedone et al.[217] potential, parameterized for several metal oxides, enhances the Morse-stretch potential for increased accuracy by the addition of a Columbic term, and transferability by the addition of a repulsive term. This potential is expressed as:

$$E_{ij} = \frac{q_i q_j}{r_{ij}} + D_{ij}\left\{\left[1 - e^{-\alpha_{ij}(r_{ij}-r_o)}\right]^2 - 1\right\} + \frac{F_{ij}}{r_{ij}^{12}} \quad \text{Eq. 3.5}$$

Several published reviews have analyzed various potentials for modeling many phases of silica. Schaible[203] reviewed the empirical MD force fields for modeling silicon and silica. Schaible[203] described several potentials for modeling both crystalline and amorphous silica, and suggested future work on handling the silicon-silica interface. Since then, the COMB and ReaxFF potential have been developed, which can accurately model this interface. Schaible's[203] review indicated the ability of the classical MD potentials, such as TTAM, for modeling the α-β transition in quartz, while excluding dielectric polarization.[240] This has been challenged by others investigating this transition.[241] A further review of many different potential forms is in Appendix D.

Herzbach et al.[241] have studied the structural, thermo-mechanical, and dynamic properties of silica with the BKS,[207] TS,[212] and a modified DCG potential[211] (mDCG). They investigated if potentials such as TS and mDCG could remedy some of the shortcomings of the BKS potential with regards to modeling the c/a in the α-β transition of quartz, the phononic density of states, the instabilities in cristobalite and tridymite, and the stishovite I-II transition. They found no significant improvements using the mDCG potential. The

polarizable TS potential provided a more accurate representation of silica with respect to the aforementioned properties. However, they[241] noted that the TS potential only outperforms the BKS potential for four-coordinated polymorphs.

Lacks and Gordon[242] have studied the pressure-induced phase transitions in quartz and stishovite with the BKS, TTAM, a polarization-included electron gas (PEG) model, and an electron gas model.[243-245] They showed that the PEG model produced more accurate results for the quartz and stishovite properties than the other potentials. In addition, the polarization of the oxygen ion yielded a bulk modulus and the calculated phase transitions at pressures more comparable to the experimental results.

Another extensive review by Soules et al.[246] has investigated the ability of various potentials to model amorphous silica. The potentials reviewed were the BKS,[207] CHIK,[223] the potential by Takada et al.,[226] an extension of the DCG potential, and the potential by Soules et al.[247] As the BKS and CHIK potentials diverge at small distances, they added a repulsive term that prevents the fusing of atoms. They found that the BKS and CHIK potentials produced accurate liquid properties, but at much higher temperatures than the experimental results. Additionally, they indicated that although the softer force fields, such as that by Takada et al.,[226] accurately predicted the melting point of β-cristobalite, they failed to fit the experimental values at low thermal expansion and densification. They proposed the development of a hybrid force field to capture the properties of silica at low and high temperatures and pressures.

Tse & Klug[248] carried out a comprehensive analysis of the BKS potential and its ability to reproduce the experimental values for the structural properties, and the pressure-volume relationships for α-quartz, cristobalite, and stishovite. Their results showed that the equations of state for the three polymorphs were well reproduced; however, the dynamical properties, such as the density of states, were only in fair agreement with experimental results. They went on to suggest that the BKS potential be re-parameterized to amend some of the weaknesses found; however, they noted that this would be difficult to do due to the potential's highly correlated parameters.

An interesting aspect to all of these reviews is the inclusion of the BKS potential in all their analyses. The BKS potential has been extensively used throughout the years due to its simplicity, yet ability to model silica. In addition to the BKS potential, the next section also

examines the Munetoh and Pedone potentials, as well as the CHIK and TTAM potentials to a lesser degree. The calculated results using these potentials are compared to those of previous work by Herzbach et al.[241] for modeling silica and to experimental results.

3.1.1 Fixed-Charge and No-Charge Potentials

The following section reviews many of the developed potentials for MD simulations of silica including those by van Beest et al.,[207] Pedone et al.,[217] Munetoh et al.,[219] Tsuneyuki et al.,[206] and Carré et al.[223] These potentials will hereon be referred to as BKS,[207] Pedone,[217] Munetoh,[219] TTAM,[206] and CHIK,[223] respectively. It is important to note that the Pedone potential models a whole class of oxides and thus its transferability to modeling more complex materials is one of its key advantages, compared to other potentials. The TTAM potential, a precursor to BKS, is not extensively reviewed. Additionally, the CHIK potential, primary fitted for modeling amorphous silica, is excluded from some of the calculations in this paper.

3.1.1.1 **Methodology**

To quantify the computational time for quartz with the different potentials, MD simulations are conducted for 100 time steps and systems of 1,296, 10,368, and 82,944 atoms, using the Large-scale Atomic/Molecular Massively Parallel Simulator (LAMMPS),[249] an open-source classical molecular dynamics code distributed by Sandia National Laboratories. The computer hardware for these simulations consists of a dual CPU with 2 12-core AMD Opteron 6344 2.6 GHz processors with 16 gigabytes of DDR3 memory. The computational time is determined by averaging the running time of three identical simulations, running on 1, 2, 4, 8, 12, 16, 20, and 24 cores. It is important to note that the computational time will vary, depending on the computer hardware, the MD code used, and the input arguments. Many potentials require a solver in order to calculate the long-range Coulomb interactions. As previously mentioned, the Ewald[89] and PPPM[90] solvers are among the most popular; however, it has been reported that PPPM is faster than the Ewald solver for system sizes of more than 50 atoms.[250] Since the systems modeled in this work comprise a greater number of atoms, the PPPM solver is used in the present MD simulations for calculating the long-range Coulomb interactions in the fixed-charge potentials,[206,207,217,223] with a relative error of 1.0e-6.

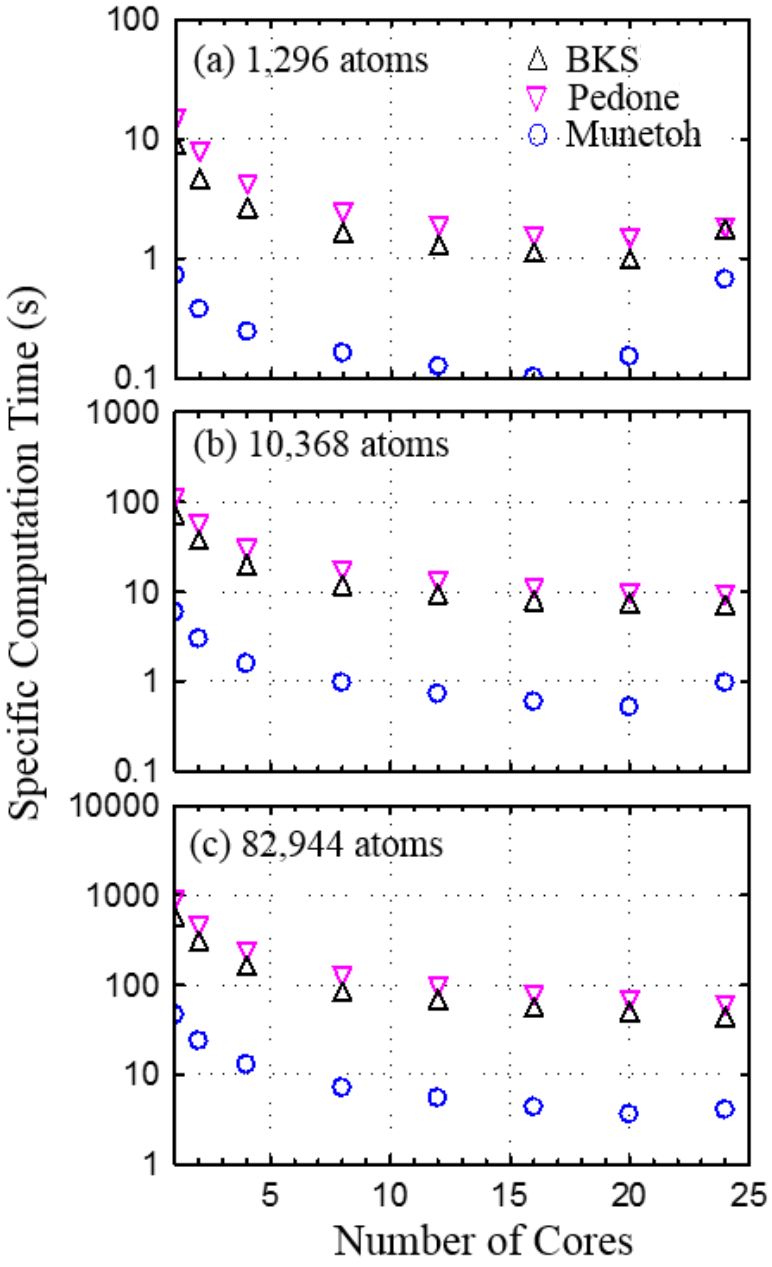

Figure 3.4: Comparison of computation time for simulating silica using different potentials and different numbers of cores and atoms.

The computation time to complete the MD simulations with the BKS potential is shorter than with the Pedone potential, for a given number of computation cores and system sizes. The longer computation time using the Pedone potential is because it incorporates two expensive exponential terms, whereas the BKS has only one exponential term (Fig. 3.4). Highly parallelized MD codes, such as LAMMPS,[249] make it possible to use more complex

and computationally intensive potentials, especially as the system size increases. However, depending on the potential selected and the system size, running on less cores may sometimes be faster. The parallelizability of the Munetoh potential for the system of 82,944 atoms, decreases when using 24 cores, but is enhanced on 20 cores. This indicates that 20 cores is the most optimal for this potential (for the computer hardware, inputs and MD program used). The decreased parallelizability is likely because the increased communication time with increasing the number of cores from 20 to 24, is larger than the time savings of distributing the atoms over more cores. Thus, depending on the choices of the system size and potential, carrying out the MD simulations with fewer cores may prove to be more efficient.

The transition of crystalline silica into different polymorphs depends on temperature and pressure. MD simulations of crystalline materials with several different polymorphs, such as silica, are a challenge to model. This is because potentials are fitted to a region of the phase diagram to reproduce the materials properties for a specific phase. Attempting to model the material properties outside of the potentials' fitting region can produce unphysical results. Thus, careful attention is required to ensure that the simulation results are physically correct and accurate. Using different potentials to model the same material at different conditions could be very cumbersome, which is deriving the ongoing effort to create transferable potentials. MD simulations with highly transferable potentials are beneficial over a large range of operating conditions. In order to assess the ability of the various potentials to model quartz, cristobalite, coesite, and stishovite, the results of the MD simulations of the lattice constants, density, and radial and bond-angle distribution functions at 300 K and 1 atm, are compared to experimental measurements.[153,251-253]

In the performed MD simulations, each polymorph undergoes energy minimization based on the Polak-Ribiere[254,255] version of the conjugate gradient (CG) algorithm. In a given iteration, this algorithm combines the force gradient with that calculated in the previous iteration to compute a new search direction that is perpendicular to the previous search direction, and is restarted once progress stops.[256] The used stopping tolerance for energy minimization is 1.0e-15.The systems are then equilibrated for 1,000 ps, before collecting data over the following 200 ps. All collected data is then averaged to obtain the values of the material properties. To ensure convergence of the equilibrated systems, the relative potential

energy, density, and volume of coesite are shown in Fig. 3.5 up to 20 ps during equilibration. The value of each property is divided by the value after 1,000 ps to determine how quickly convergence is reached. Fig. 3.5b shows that all 5 of the investigated potentials fully converge within less than 10 ps, well before the total time of 1,000 ps.

3.1.1.2 **Results**

The following sections present and discuss the accuracy and transferability of the BKS, Pedone, Munetoh, TTAM, and CHIK potentials for modeling various polymorphs and phase transitions of SiO_2.

3.1.1.2.1 Quartz

The low-energy polymorph, α-quartz, is one of the most common materials on the planet. It is commonly found as an aggregate in various types of rock in the earth's crust,[257,258] and draws technological importance because of the interesting optical and piezoelectric properties.[259-261] For this reason, the quartz polymorph is extensively studied in this section.

Munetoh et al.[219] have reported that the energy minimization of α-quartz produces a density of 2.4209 g/cm^3, which is well below the experimental value (Table 3.1). The performed MD simulations with the Munetoh potential use a short cutoff, and gives an energy-minimized density of 2.43 g/cm^3, which is very close to that reported by Munetoh et al.[219] However, the MD simulations using the Munetoh potential show that a transformation occurs in α-quartz upon equilibration after about 16 ps, which is unphysical. Because the density reported at 300 K and 1 atm is higher than that reported at 0 K and 0 atm, equilibrating quartz at 300 K increases the bond fluctuations that exclude atom pairs separated by ~2.8 Å in the force calculations. When the time step in the MD simulation is changed from 1.0 fs to 0.2 fs, the results are not statistically different. The results suggest that the Munetoh potential is not the best force field for modeling α-quartz at room temperature.

Table 3.1: Listing of the calculated structural properties of α-quartz using different potentials and reported experimental results.

Property	Exp.[153]	BKS[207]	Pedone[217]	TTAM[206]	CHIK[223]	Munetoh[219]
a (Å)	4.916	4.94	4.95	5.02	5.05	5.08
c (Å)	5.405	5.45	5.45	5.55	5.52	5.44
Density (g/cm^3)	2.646	2.60	2.59	2.47	2.45	2.46

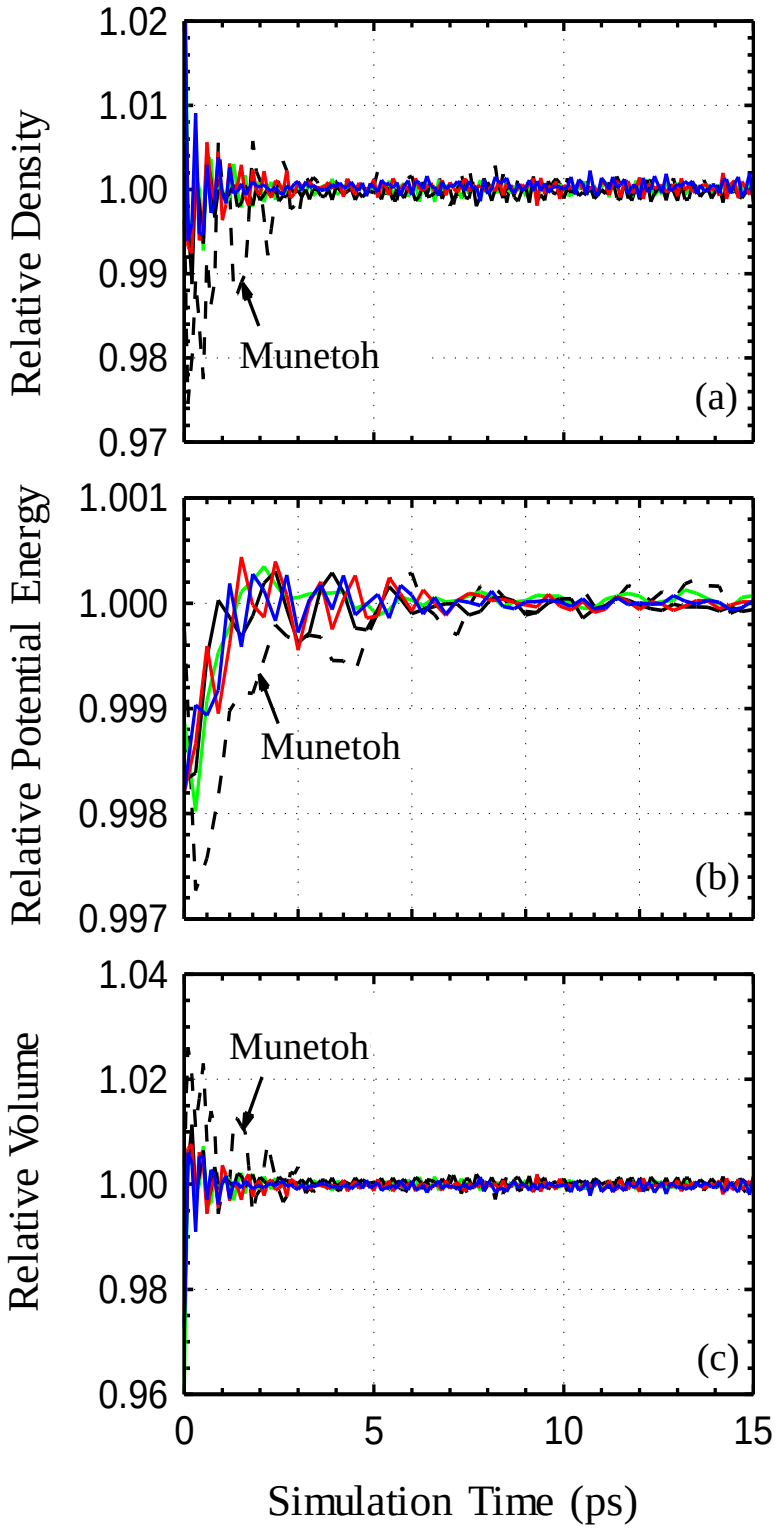

Figure 3.5: Convergent time for the performed MD simulations of the properties of coesite using different potentials: (a) density, (b) potential energy, and (c) volume.

Table 3.1 lists the calculated structural properties of α-quartz using different potentials, compared to experimental values. The calculated density of α-quartz using the BKS potential is 2.6 g/cm^3, compared to 2.54 g/cm^3 reported by Tse and Klug.[248] The calculated lattice constants and density of α-quartz with the BKS potential, while varying the cutoffs, are listed in Table 3.2. For α-quartz, the calculated properties are in better agreement with experimental values at higher cutoffs. The calculations converge at 15 Å, thus little would be gained from increasing the cutoff past this point.

The calculated pair distribution functions using different potentials are compared in Fig. 3.6a-c. These figures also show the experimental results for a perfect α-quartz crystal. If the potentials are completely accurate, the peaks of the distribution functions should match up with the dashed lines representing the experimental values. Simulation results with peaks closer to the experimental value indicate the ability of the used potentials to reproduce the structural order of α-quartz.

Table 3.2: Listing of the calculated structural properties of α-quartz using the BKS potential with varying cutoff values and reported experimental results.

Parameter/ Property	Exp.[153]	BKS[207]					
Cutoff (Å)	N/A	8	10	12	15	18	20
a (Å)	4.916	4.99	4.96	4.95	4.94	4.94	4.94
c (Å)	5.405	5.49	5.47	5.45	5.45	5.45	5.45
Density (g/cm^3)	2.646	2.53	2.57	2.59	2.60	2.60	2.60

The peak in Fig. 3.6a are representative of the O-Si bond-lengths of quartz. Note that the figure shows two different Si-O bond lengths.[203] The results with the BKS and Pedone potentials are ~1% lower than experimental values, while the calculated O-Si pair distribution with the Munetoh potential is ~2% higher than the experimental values. The TTAM potential reveals similar results as with the Munetoh potential, despite including the Coulomb interactions.

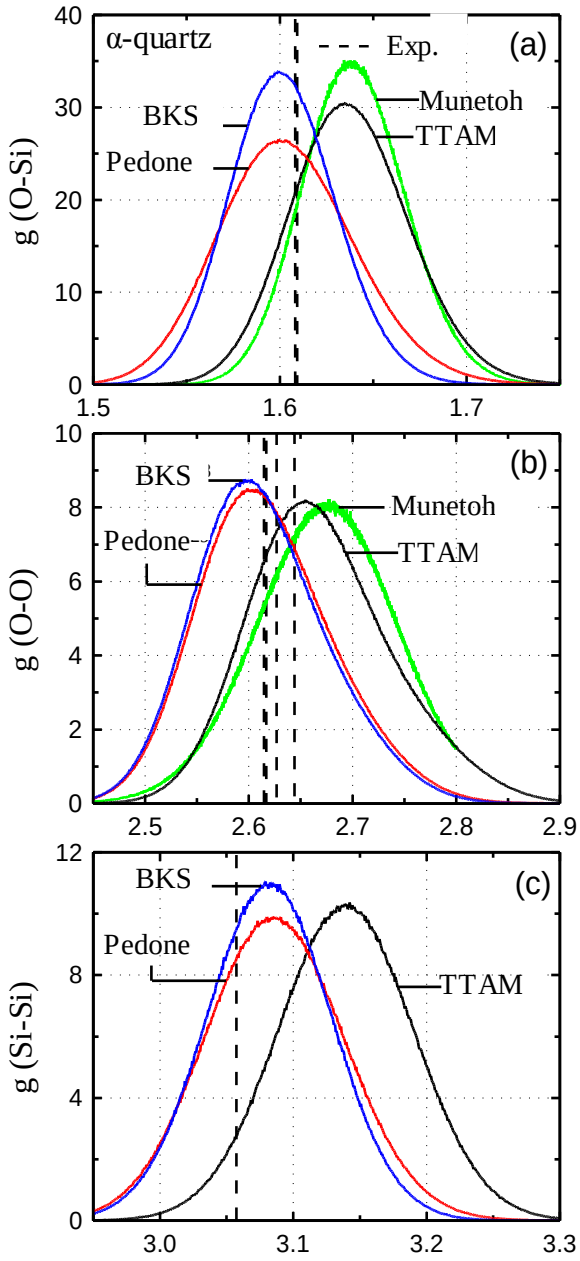

Figure 3.6: Comparison of the pair distribution functions for α-quartz at ambient conditions (300 K and 1 atm), in MD simulations with different potentials to experimental results.

The O-O peak in Fig. 3.6b makes it easy to discern the short cutoff of the Munetoh potential as the distribution is cut short at 2.8 Å. The calculations with the Munetoh potential completely miss the closest Si-Si bonds at approximately 3.2 Å (Fig. 3.6c). The simulation results with the BKS and Pedone potentials reveal good structural agreement of both the O-O and Si-Si experimental pairs, with values to within ~1%. Unlike the BKS and Pedone

potentials, the TTAM potential does not accurately reporoduce the experimental O-O and Si-Si pair distribution functions.

The calculated O-Si-O and Si-O-Si bond-angle distribution functions for α-quartz at 300 K and 1 atm with various potentials are shown in Fig. 3.7. MD simulation results show that the potentials all soundly reproduce the O-Si-O bond angle distribution (Fig. 3.7). However, the results of the Si-O-Si bond angle distributions are more divergent. The simulations with the different potentials all overestimate the experimental results by several degrees (Fig. 3.7). The results with the Munetoh potential indicate a higher peak, and those with the fixed-charge potentials show a distribution that is broader.

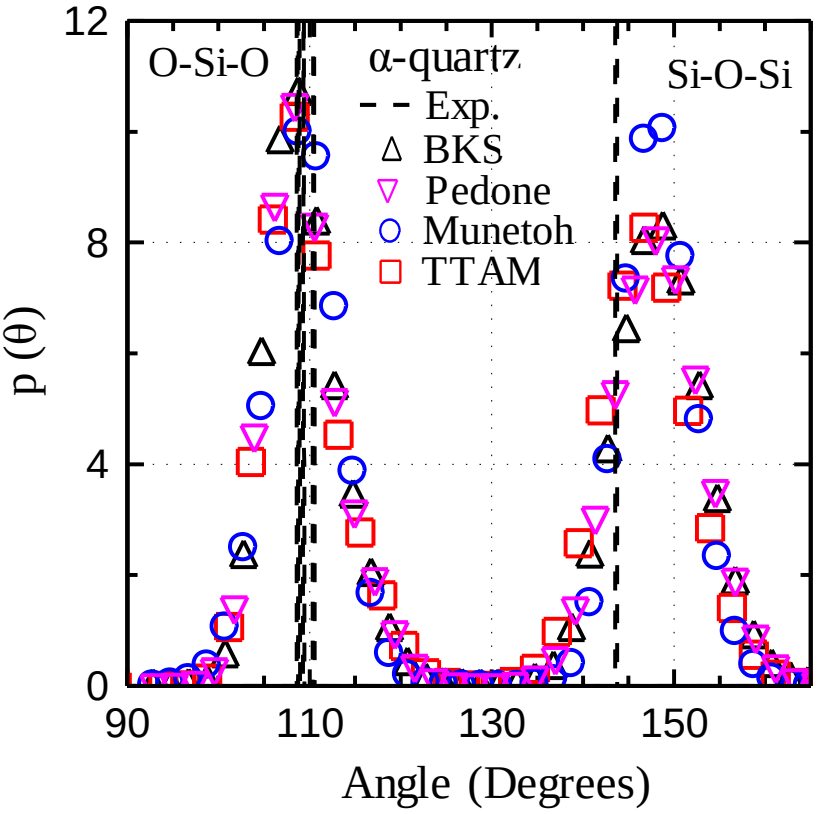

Figure 3.7: Comparison of calculated O-Si-O and Si-O-Si bond angle distribution functions for α-quartz at 300 K and 1 atm using different potentials to experimental results.

3.1.1.2.2 α-β Transition

One of the most highly studied and investigated transitions of crystalline silica is the α-β transition for quartz. The α-quartz, with trigonal symmetry, can have two different orientations, depending on the sign of the tilt factor. These orientations correspond to space

groups $P3_121$ (right-handed) and $P3_221$ (left-handed). Similarly, β-quartz, with hexagonal symmetry, can have orientations that correspond to $P6_222$ (right-handed) and $P6_422$ (left-handed). The α-quartz undergoes a reversible crystal structure transformation into β-quartz at ~846 K.[262] This used to be considered an order-to-disorder transition,[240] but recent evidence indicates that it is a displacement phase transition.[263] It has also been shown that the β-quartz can undergo a structural transformation into α-quartz by rotating the SiO_4 tetrahedra (Fig. 3.8). Despite the extensive studies in the last century, the nature of the α-β transition is still not entirely clear. Tsuneyuki et al.[240] argued that the dielectric polarization of electrons is not needed to model this transition because it is not ferroelectric. Additionally, they stipulated that since the α-β transition temperature (846 K) is much higher than the Debye temperature (470 K), using classical MD simulations is acceptable.

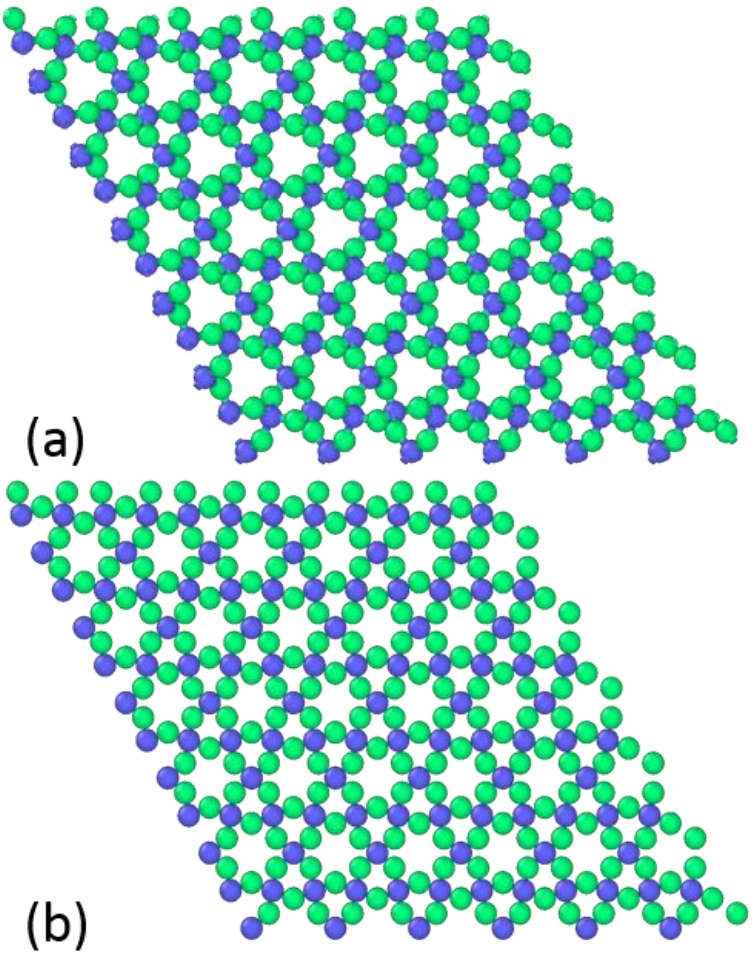

Figure 3.8: Comparison of the obtained structure from experimental results for (a) α-quartz and (b) β quartz.

Recently, there have been attempts to characterize the α-β transition for quartz at the atomic scale using MD simulations.[241,263-265] Herzbach et al.[241] have studied the α-β transition using the TS,[212], BKS,[207] and DCG[211] potentials. They modified the DCG potential, hereon referred to as mDCG, and showed that the original fluctuating charge model was flawed. In the simulations with the BKS, TS, and mDCG potentials, the predicted temperature of the α-β transition was found to be 740 K, 712 K, and 581 K, respectively. The simulation with the BKS potential slightly overestimated the volume of the quartz, while the results with the TS potential accurately match the experimental results. These results suggest that the TS polarizable force field more accurately models the four-coordinated polymorphs than the BKS potential.

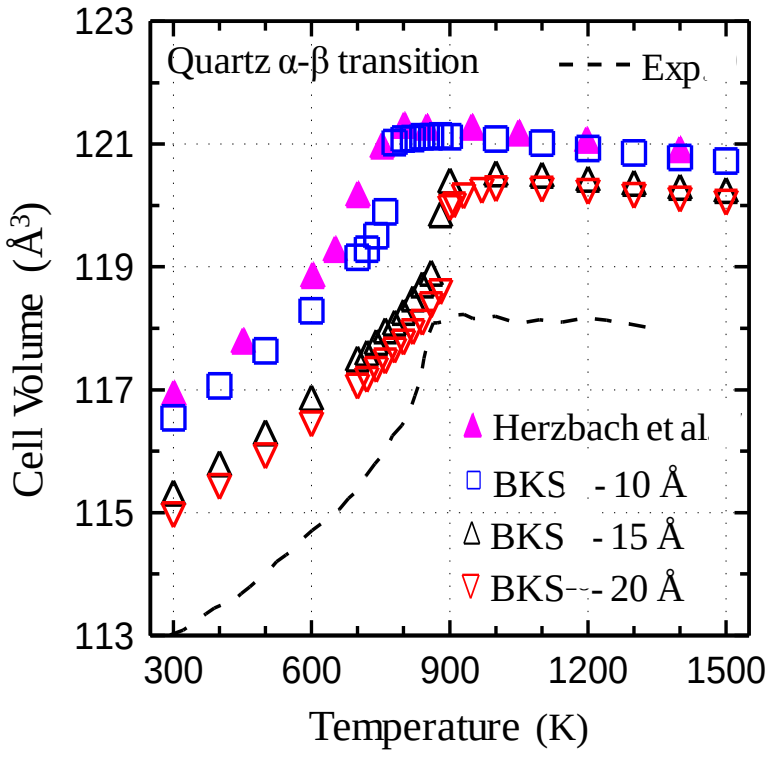

Figure 3.9: Comparison of the calculated cell volume using the BKS potential and different cutoff distances with the results by Herzbach et al.[241] and experimental measurements.

In an attempt to reproduce the results by Herzbach et al.[241] with the BKS potential (as well as to implement other potentials), MD simulations which employ the NPT ensemble are performed to characterize the α-β transition. In the simulations with the BKS and Pedone potentials, the temperature increased in increments of 100 K during the heating periods from

300 – 700 K and from 900 – 1,500 K. In the intermediate temperature range of 700 – 900 K (the range in which the α-β transition occurs), the temperature increased in smaller increments of 10 K. The heating time between temperature changes is constant at 10 ps. Following each heating increment, the system is allowed to equilibrate at the final temperature before collecting data. The equilibration and data collection times are each 70 ps.

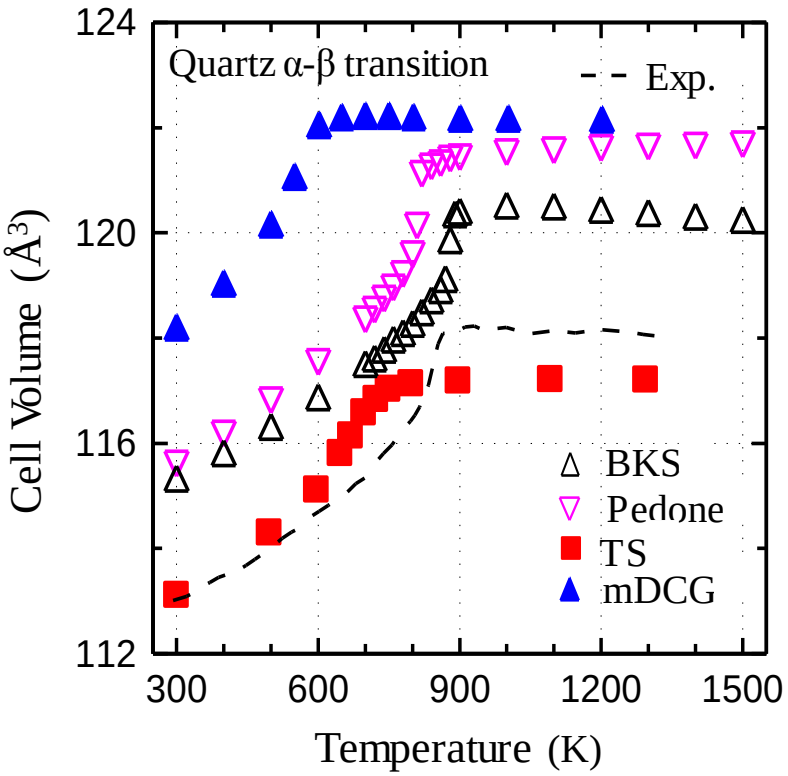

Figure 3.10: Comparison of the calculated cell volume expansion over the α-β transition of quartz using different potentials to experimental measurements.

Fig. 3.9 shows that the cutoff distance of the BKS potential can influence the accuracy of predicting the α-β transition. A cutoff distance of 10 Å reproduces the BKS potential results by Herzbach et al,[241] but higher cutoffs of 15 and 20 Å are in better agreement with experimental results.

Fig. 3.10 compares the cell volume expansion as calculated using different potentials, and their ability to accurately reproduce the nature of the α-β transition. The qualitative trend of this transition is modeled more appropriately with the BKS than the TS potential in the work by Herzbach et al.[241] This can be difficult to discern from Fig. 3.10 because the BKS

potential overestimates the initial volume of quartz, because this potential at 0 K is fitted to the experimental data at 300 K.

Fig. 3.11 shows that the BKS potential is in better agreement with experimental results for predicting the relative cell volume expansion, than all other potentials. The relative cell volume expansion with the BKS potential is nearly identical to experimental results,[262] suggesting that despite overestimating the volume of quartz, the BKS potential accurately expresses the change in cell volume expansion at the α-β transition. Thus, the results in Fig. 3.11 suggest that the calculations with the TS potential do not necessarily outperform those with the BKS potential for all four-coordinated silica polymorphs.

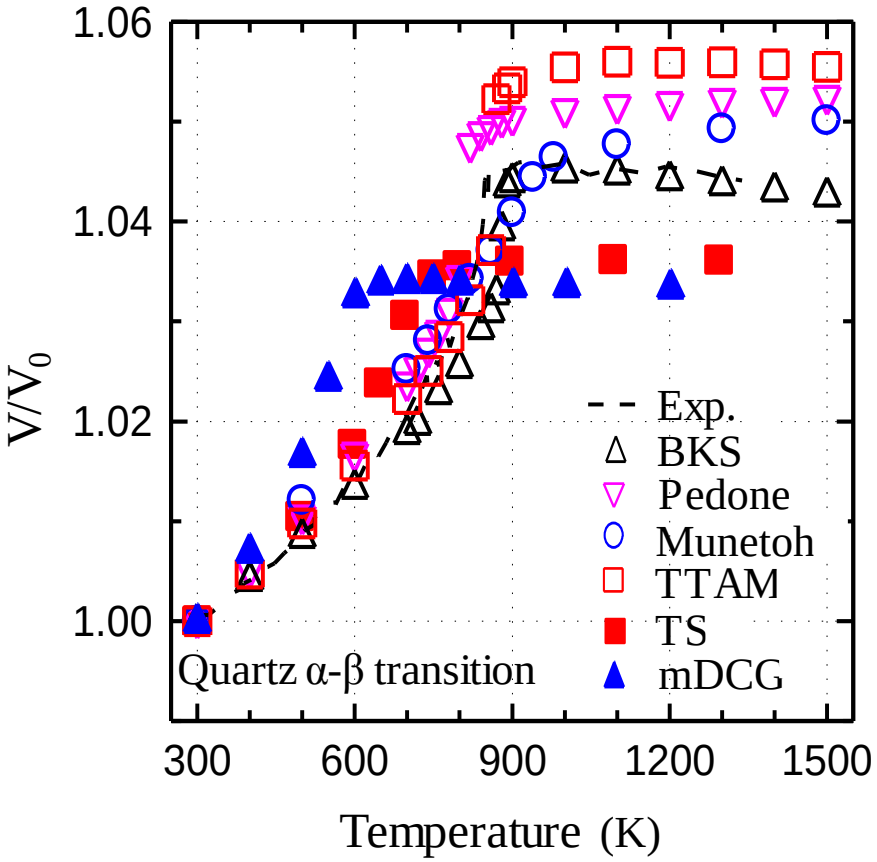

Figure 3.11: Comparison of the calculated relative cell volume expansion over the α-β transition of quartz using different potentials with experimental measurements.

Fig. 3.11 shows that MD simulations that employ the Pedone potential consistently over-predict the cell volume expansion, while those with the mDCG and TS potentials under-predict it. The results with the TTAM potential are in agreement with experimental results up until the α-β transition, for which the relative cell volume expansion is overestimated. The

simulations that employ the Munetoh potential show a structural transformation that is likely not associated with a sudden jump in volume, as would be expected with the proper rotation of the SiO_4 tetrahedra.

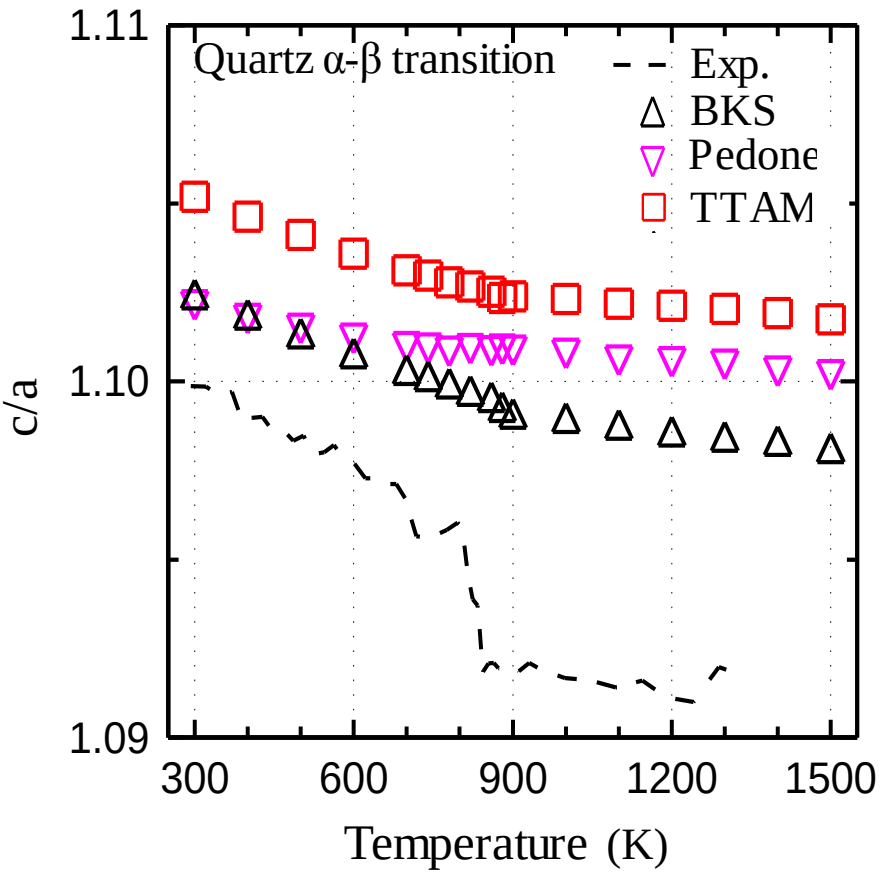

Figure 3.12: Comparison of the calculated c/a ratio over the α-β transition of quartz using different potentials with experimental measurements.

Herzbach et al.[241] noted that prior simulations with the BKS[207] and TTAM[206] potentials failed to reproduce the c/a ratio at the α-β transition in quartz. At the transition location, experimental results[262] show a discontinuity and a sharp change in the slope, not predicted by the MD simulations with either the BKS or TTAM potentials. They investigated how well the reproduce this event. They carried out MD simulations with the mDCG and TS potential and showed that the mDCG potential produced a very slight change in the slope, while the TS potential predicted a c/a ratio that was in agreement with experimental results. Fig. 3.12 shows that there is a slight change in the slope at the α-β transition using the BKS and TTAM

potentials, only for high cutoff, long simulation time, and small temperature intervals. The results with the Pedone potential do not show a change in slope at the α-β transition, but the Munetoh potential shows a slope change that is the opposite of experimental results (not shown in Fig. 3.12). The c/a ratio produced by the simulations with the TS potential is best agreement with experimental results, and can be found elsewhere.[241]

3.1.1.2.3 Quartz I-II Transition

This section presents the results of the equation of state for the α-quartz under pressure at 300 K. Prior MD simulations have investigated the structural transformations of quartz at high pressures.[241,266-268] Herzbach et al.[241] and Campana et al.[267] have studied the irreversibility of the pressure-induced quartz I-II transition. Simulations are carried out to calculate the location of the quartz I-II transition with the various potentials considered in this work. The results of the quartz I-II transition using the TS potential and the *ab initio* calculations are included from the work by Herzbach et al.[241] and Campana et al.,[267] respectively. Experimental measurements are obtained from the work by Hazen et al.[269]

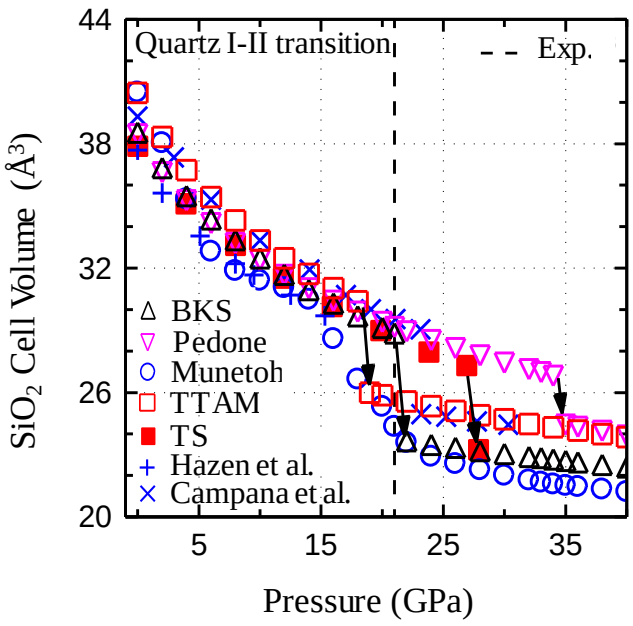

Figure 3.13: Comparison of the calculated equation of state for quartz as a function of pressure at 300 K, using different potentials, to experimental results.

Fig. 3.13 compares the modeled equations of state for the quartz I-II transition by MD simulations using different potentials at 300 K, with experimental results. The dashed line in

Fig. 13 corresponds to a phase-change seen by Kingma.[270] The transition has been shown experimentally to occur at ~21 GPa,[270] however, the experimental results did not show the transition as a function of cell volume. Table 3.3 lists the calculated location of the quartz I-II transition by the simulations with the different potentials. The results with the BKS potential most precisely reproduce the location of the quartz I-II transition, occurring between 21-22 GPa. The MD simulations with the TTAM potential only slightly underestimate (18-19 GPa) the transition location that corresponds well with the quartz I and quartz II phases from *ab initio* results.[267] The Pedone potential does a poor job of capturing the location of this transition, calculating a much higher value of 34-35 GPa. It is difficult to discern an obvious transition location based on the simulations results with the Munetoh potential. The nature of the irreversibility of this transition is not reviewed herein, but can be found elsewhere.[241,267]

Badro et al.[268] have showed that the BKS potential supports a five-coordinated environment as opposed to the normally occurring four-coordinated environment under high pressure. The five-coordinated polymorph is also supported by *ab initio* results.[271] The present work confirms the five-coordinated environment at high pressures, following the quartz I-II transition.

Table 3.3: Listing of the calculated quartz I-II transition location (GPa) using different potentials, compared with experimental measurements.

Property	Exp.[270]	BKS[207]	Pedone[217]	Munetoh[219]	TTAM[206]	TS
Quartz I-II Transition Location (GPa)	21	21-22	34-35	-	18-19	27

The analysis of quartz with the selected potentials reveals that the BKS potential more accurately reproduces the calculated relative cell volume expansion of quartz compared to the polarizable TS force field which underestimates the α-β transition by ~1% . On the other hand, Herzbach et al.[241] showed that the TS potential outperforms all of the other potentials investigated in accurately calculating the c/a ratio, and matching the experimental results of the cell volume expansion. The BKS potential reproduces the quartz I-II transition at 21 GPa under anisotropic pressure, whereas the other potentials either under-predict (TTAM) or over-predict this transition (TS, Pedone).

3.1.1.2.4 Cristobalite

Cristobalite exists in two primary phases, α-cristobalite and β-cristobalite. The low-temperature α-phase maintains a tetragonal lattice, whereas the high-temperature β-phase is face-centered cubic with diamond-like symmetry.[203] The transition location between the two phases occurs around 540 K, but is subject to chemical impurities and stacking faults.[272,273] Cristobalite, a low-density silica polymorph, is similar to quartz and composed of corner-bonded tetrahedra. This four-coordinated polymorph is stable at ambient pressures above 1743 K. At lower temperatures, cristobalite is metastable due to the large activation barrier, and thus experiences a slower transition to quartz and/or tridymite.[273,274]

Table 3.4: Listing of the structural properties of α-cristobalite using different potentials and reported experimental results.

Property	Exp.[251]	BKS[207]	Pedone[217]	TTAM[206]	CHIK[223]	Munetoh[219]
a (Å)	4.978	4.92	4.94	5.00	5.01	5.14
c (Å)	6.948	6.60	6.67	6.72	6.65	7.04
Density (g/cm^3)	2.318	2.50	2.45	2.37	2.40	2.15

Table 3.5: Listing of the structural properties of α-cristobalite using the BKS potential with varying cutoff values and reported experimental results.

Parameter/Property	Exp.[251]	BKS[207]		
Cutoff (Å)	N/A	8	10	15
a (Å)	4.978	4.99	4.94	4.92
c (Å)	6.948	6.77	6.65	6.60
Density (g/cm^3)	2.318	2.37	2.46	2.50

Table 3.4 lists the calculated structural properties of α-cristobalite using different potentials, as well as the experimental results. The results of the MD simulations using the Pedone, TTAM, and CHIK potentials are all somewhat close to the experimental values, reproducing the density to within 6%. The BKS potential calculates a density with the highest error, ~8%, making it prudent to determine the effect the cutoff might have on the accuracy of the results. The results in Table 3.5 reveal that a higher cutoff value actually

impairs the accuracy of the BKS potential for modeling α-cristobalite. In fact, after the adjusted cutoff, the BKS potential outperforms those of other potentials for calculating the lattice constants and density. It appears that the inclusion of all forces past 8 Å negatively impacts the results, despite the limited force contribution at these distances. At higher cutoffs, the polymorph finds a denser state at about 2.5 g/cm^3.

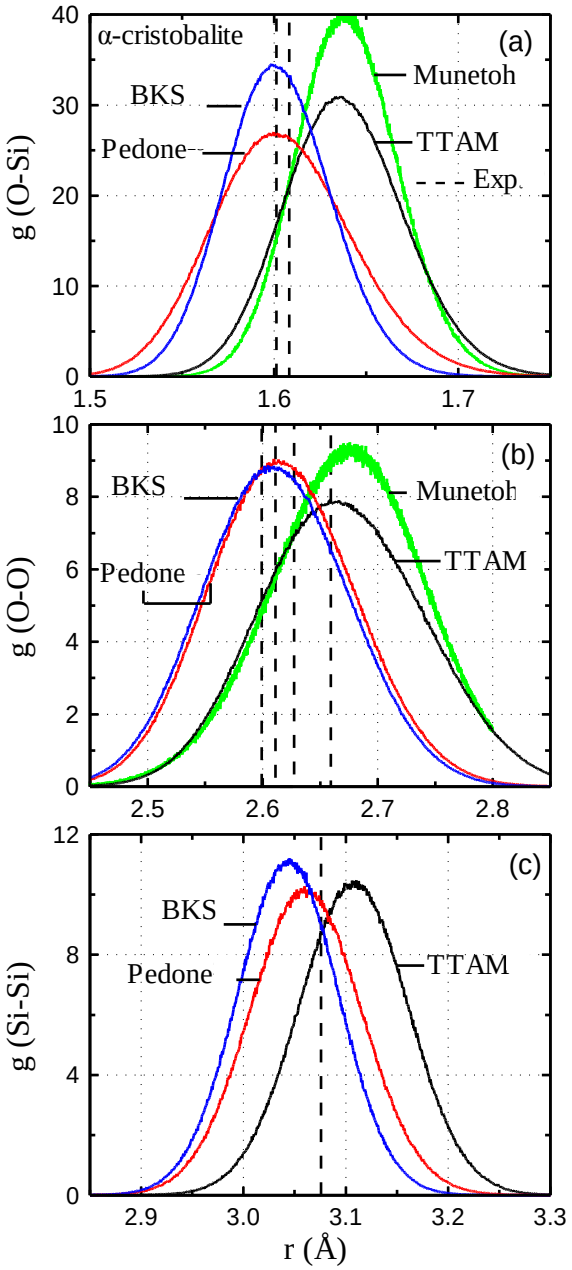

Figure 3.14: Comparison of the calculated pair distribution functions for α-cristobalite at ambient conditions (300 K and 1 atm), using different potentials, to experimental results.

Fig. 3.14a-c compares the calculated results of the partial pair distribution functions for modeling α-cristobalite using various potentials with the experimental values. Results show that the BKS and Pedone potentials are the most accurate, with the most probable O-Si bond length to within 1% of experimental values. In fact, the O-Si bond lengths are captured quite well with both potentials, in contrast to the Munetoh and TTAM potentials that over-predict the distribution by ~2.5%. The O-O pair distribution functions are more widely distributed, as the experimental results show. All four potentials investigated appear to be moderately centered on these lines, while the BKS and Pedone potentials appear to be the most promising. The Si-Si bonds are under-predicted and over-predicted (~1.5%) by the BKS and TTAM potentials, respectively, compared to the experimental results The Pedone potential reproduces the experimental Si-Si bond length almost perfectly, with the most probable Si-Si bond length nearly identical to experimental values.

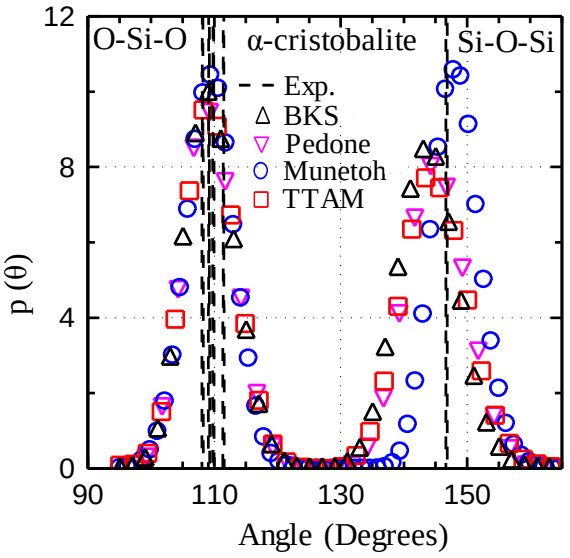

Figure 3.15: Comparison of the calculated O-Si-O and Si-O-Si bond angle distribution functions of α-cristobalite at 300 K and 1 atm, using different potentials, to experimental results.

The O-Si-O and Si-O-Si bond-angle distribution functions for α-cristobalite at ambient conditions are also investigated. Unlike quartz, the O-Si-O distribution for α-cristobalite is actually comprised of four distinct angles that are a few degrees apart. Fig. 3.15 shows that all four potentials investigated accurately capture the O-Si-O bond-angle distributions, with little difference between them. The simulations with the Munetoh potential are the most

accurate for modeling the Si-O-Si bond-angle distributions, compared to the fixed-charge potentials.

3.1.1.2.5 Coesite

Coesite, a high-pressure monoclinic polymorph of silica, is the densest four-coordinated phase (one silicon atom surrounded by four oxygen atoms).[275] Coesite was first synthesized in the laboratory,[276] but has since been found as a result of high-pressure events such as meteor craters.[277]

Table 3.6: Listing of the structural properties of coesite using different potentials and reported experimental results.

Property	Exp.[252]	BKS[207]	Pedone[217]	TTAM[206]	CHIK[223]	Munetoh[219]
a (Å)	7.136	7.14	7.13	7.26	7.27	7.35
b (Å)	12.369	12.46	12.48	12.73	12.62	12.31
c (Å)	7.174	7.20	7.21	7.36	7.29	7.12
Density (g/cm^3)	2.921	2.86	2.86	2.70	2.75	2.78

The results of the calculated lattice constants and density of coesite using different potentials are presented in Table 3.6. The results in this table show that the values calculated using the BKS and Pedone potentials are very similar, and accurate when compared to experimental data. The calculated density with the BKS and Pedone potential of 2.86 g/cm^3 within 2% of the experimental value, 2.921 g/cm^3. The calculations with the TTAM, CHIK, and Munetoh potentials predict lower densities, between 2.7 and 2.78 g/cm^3. It is interesting to note that although the Munetoh potential neglects the Coulomb interactions, results are comparable to those with the TTAM and CHIK potentials, both including Coulomb forces. This indicates that the BKS parameters are more precise than TTAM and CHIK, compared to experimental measurements, despite the fact that they use the same functional form.

Fig. 3.16a-c present the calculated pair distribution functions for coesite and compares the MD results using the different potentials to experimental results. It is more difficult to arrive at a conclusion regarding the accuracy, as the O-Si, O-O, and Si-Si bond lengths are much more variable. Results with the BKS and Pedone potentials match each other quite well, but different from those using the TTAM and Munetoh potentials.

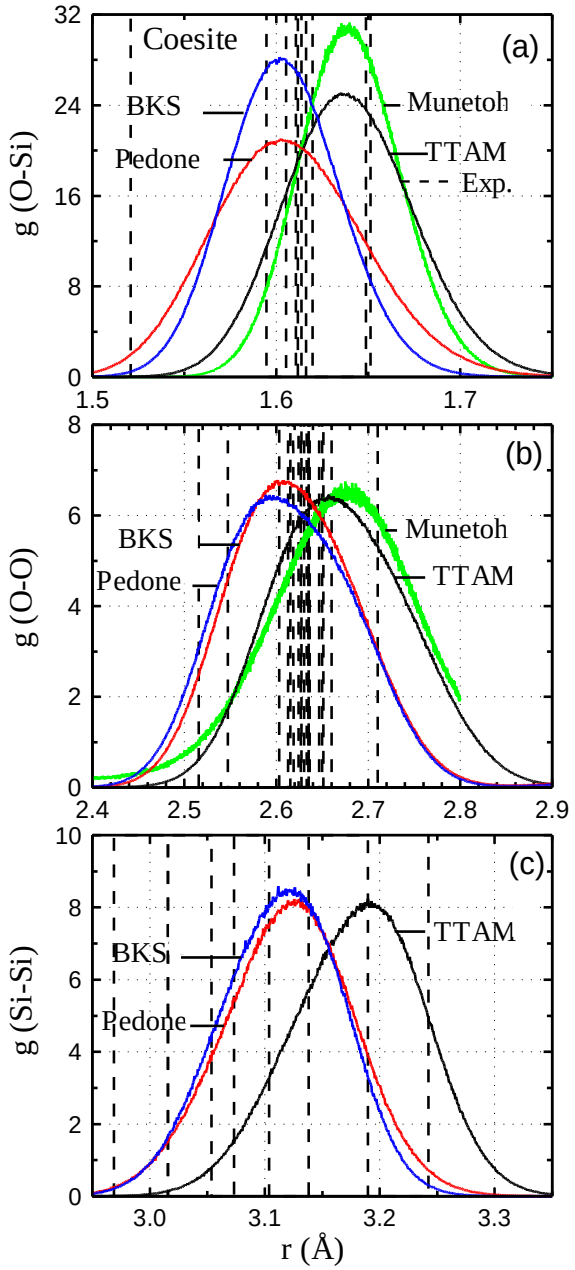

Figure 3.16: Comparison of the calculated pair distribution functions for coesite at ambient conditions (300 K and 1 atm), with different potentials, to experimental results.

3.1.1.2.6 Stishovite

The stishovite, a high-pressure rutile-type polymorph of silica, can be found in meteor impacts and in the Earth's mantle.[278-280] Stishovite contains edge and corner-sharing SiO_6 octahedra, which provides stronger covalent bonds than found in the four-coordinated polymorphs. The six-coordinated polymorph is thus a stringent test of the transferability of

the potentials. It is interesting to study how various potentials would adapt to the change in the bonding environment.

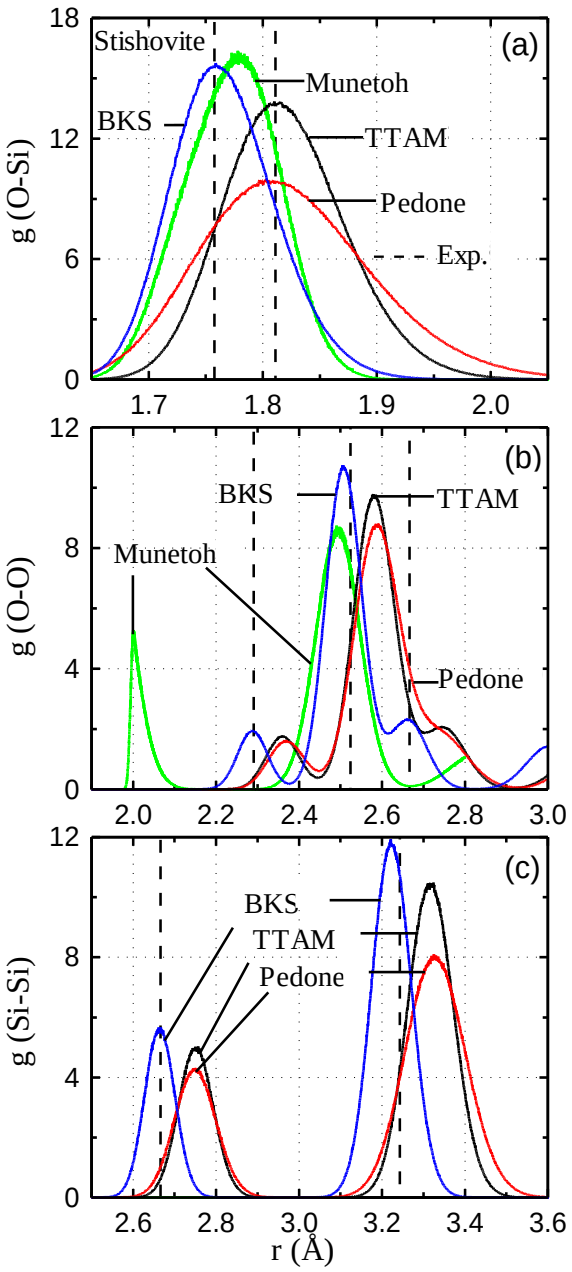

Figure 3.17: Comparison of the calculated pair distribution functions for stishovite at ambient conditions (300 K and 1 atm), with different potentials, to experimental results.

Table 3.7 presents the calculated structural properties of stishovite in MD simulations using different potentials. It also compares the calculations with experimental results. Despite the significant change in bonding environment, many of the potentials investigated

reasonably model the high-pressure polymorph, stishovite. The results using the BKS and CHIK potentials are the most accurate, with the calculated density by both to within ~1.3% from the experimental values. As the CHIK potential is fitted for amorphous silica, it comes as no surprise that stishovite, which as McQueen et al.[279] argued, would be hard to discern the differences between the vitreous and crystalline form at short-order, is produced the most accurately of the polymorphs investigated. The Munetoh potential is reasonably accurate, with the calculated density within ~4% of the experimental values. The results with the Pedone and TTAM potentials are the least accurate, within ~8% of the experimental values.

Fig. 3.17a-c presents the calculated pair distribution functions of stishovite at ambient conditions, using the various potentials investigated in this paper. The figure also shows the experimental O-Si bond lengths. The results using the BKS potential model the shorter bond length more accurately, whereas the TTAM and Pedone potentials predict the longer bond-length more accurately. The results using the Munetoh potential lies in between, showing no bias towards one bond-length or the other. The first three O-O peaks, within a few angstroms of each other, are included. The BKS potential accurately predicts all three peaks, whereas the TTAM and Pedone potentials only reasonably predict this distribution, to within ~4% of the experimental values. The results using the Munetoh potential show a large variance, with the predicted first peak at ~2.0 angstroms, within ~13% of the experimental O-O peak.[253] Finally, the results of the Si-Si pair distribution once again reveal that the BKS potential is the most accurate, within ~1% of experimental values, while TTAM and Pedone both over-estimate the Si-Si bond-lengths by ~4.5%.

Table 3.7: Listing of the structural properties of stishovite using different potentials and reported experimental results.

Property	Exp.[253]	BKS[207]	Pedone[217]	TTAM[206]	CHIK[223]	Munetoh[219]
a (Å)	4.180	4.15	4.29	4.27	4.19	3.89
c (Å)	2.666	2.66	2.75	2.75	2.68	2.96
Density (g/cm^3)	4.283	4.34	3.94	3.97	4.23	4.47

Fig. 3.18 presents the calculated equation of state for stishovite under pressure, using different potentials, and the experimental data. Experimental data of Tsuchida et al.[280] and

Ross et al.[281] are included in this figure to quantify the accuracy of the calculations. The Pedone and Munetoh potentials, respectively, overestimate and underestimate the equation of state of the SiO_2 cell volume for stishovite under pressure by ~5%. The BKS and TS potentials both accurately predict the equation of state under anisotropic pressure, with respect to cell volume, up to approximately 90 GPa. With respect to relative cell volume, the results using the BKS decrease at a slower rate than those using the TS potential. Fig. 3.19 compares the calculated values of the relative cell volume expansion using the different potentials with experimental results. The BKS potential performs better than the other potentials for modeling the relative cell volume under pressure. The TS and Pedone potentials, with almost identical results, underestimate the equation of state by about 3% above 20 GPa. The MD simulation results with the Munetoh potential underestimate the equation of state with respect to relative cell volume expansion by ~4%.

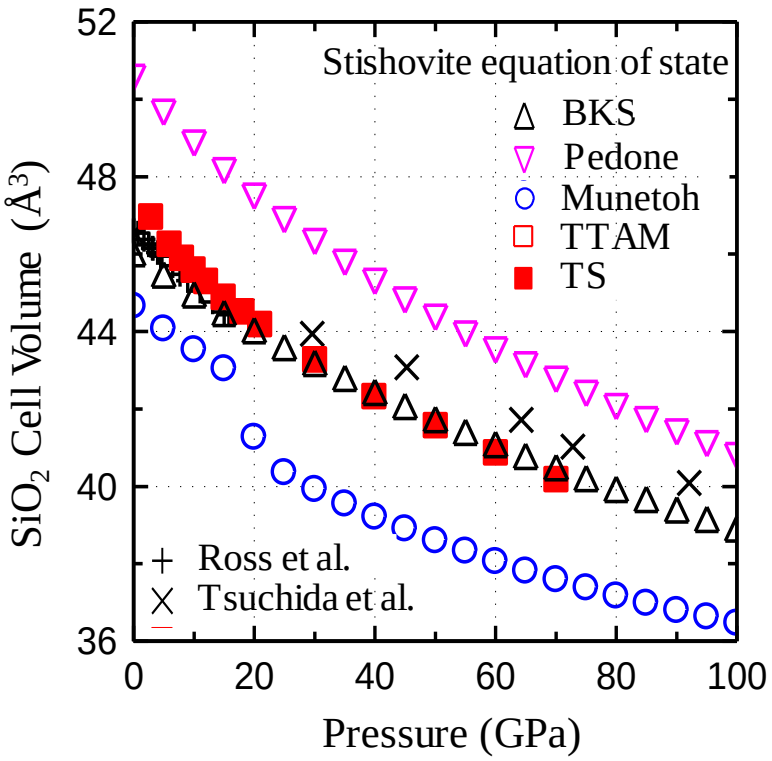

Figure 3.18: Comparison of the calculated equation of state with respect to the volume of stishovite, as a function of pressure at 300 K, using different potentials, to experimental results.

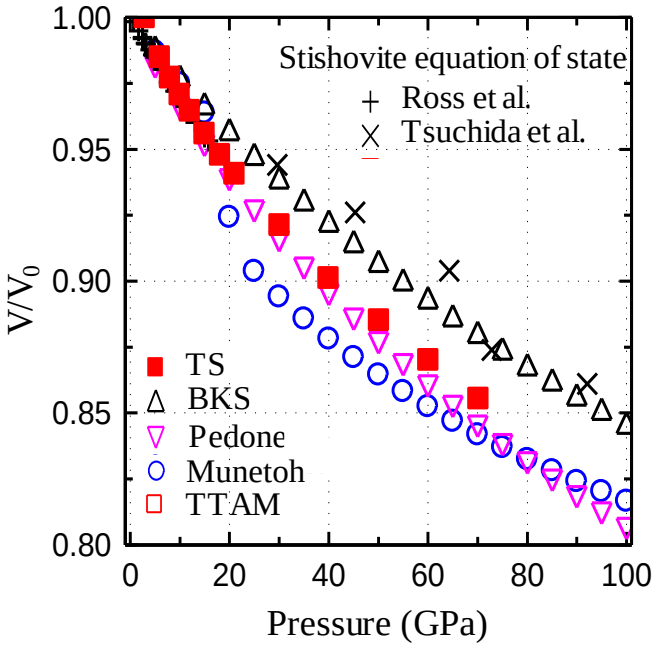

Figure 3.19: Comparison of the calculated relative cell volume of stishovite at 300 K as a function of pressure, using different potentials, to experimental results.

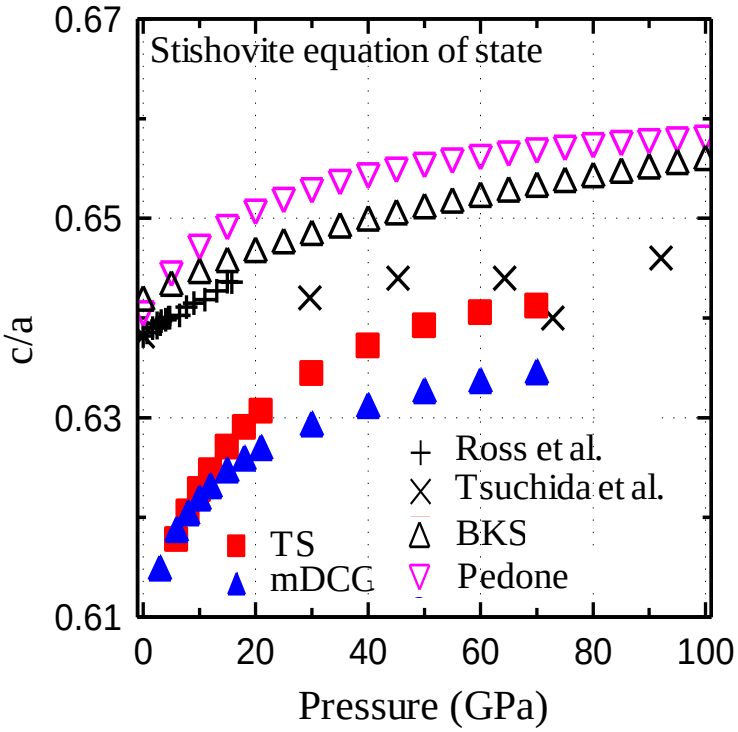

Figure 3.20: Comparison of the calculated equation of state with respect to the c/a ratio of stishovite, as a function of pressure at 300 K to experimental results.

All of the potentials considered herein do not accurately model the c/a ratio in stishovite as a function of pressure (Fig. 3.20). However, the two most accurate are the BKS and TS potentials. The results using the Pedone potential are similar to those of the BKS potential, but ~7% higher. The mDCG potential, as reviewed by Herzbach et al.,[241] produces similar, but slightly lower results to those using the TS potential. The BKS accurately models the c/a ratio below 20 GPa. Above this pressure, the calculated results for the c/a ratio diverge from the experimental data and become closer to the predictions by the TS potential.

The analysis of the six-coordinated polymorph, stishovite, is a good test of the transferability of the different potentials. The BKS and TS potentials accurately reproduce the experimental equations of state under pressure. The polarizable TS potential certainly has some benefits that the others do not due to the inclusion of polarization. However, the exclusion of dielectric polarization in the BKS potential yields good results as well.

3.1.1.3 **Highlights and Concluding Remarks**

Reviewed are four fixed-charge and one no-charge potentials for MD simulations of crystalline silica. The results are compared in terms of the computational time, accuracy compared to experimental values, and transferability to different bonding environments. The simulation results of the four polymorphs of silica using the BKS, Pedone, Munetoh, TTAM, and CHIK potentials are compared to the reported experimental values of the structural properties, phase transitions, and equations of state.

The simulations with the Munetoh potential are computationally the least expensive, but are not accurate for all polymorphs investigated. The results could not produce the nature of the α-β and I-II phase transitions in quartz, and the equation of state for stishovite. Additionally, some of the calculated structural properties at equilibrium conditions, differ from experimental values by more than 10%.

The MD simulations with the BKS potential are the most accurate. The calculated structural properties, phase transitions, and equations of state are within ~2% of experimental values, except for cristobalite, where the comparison of the calculated results compared to experimental values are improved using shorter cutoffs. The accuracy of the BKS potential, over the range of the phase diagram of crystalline silica confirmed a high transferability in modeling various bonding environments. The simulation results with the TTAM potential are

not as accurate as with the BKS potential. Since both potentials are of the same functional form, they require the same computational resources.

The MD simulations with the CHIK potential, also of the same functional form as BKS, with an additional repulsive term, calculate most structural properties of crystalline silica to within ~8% of experimental values, except for stishovite, the structural properties are within ~1.3% of the experimental values. The transferability of the CHIK potential is restricted primarily to vitreous silica and to polymorphs that appear vitreous at short order, such as stishovite.

The results of MD simulations with the Pedone potential are within ~5% of experimental values, except for the high-pressure polymorph, stishovite, in which the calculations overestimate the structural properties and equation of state by ~8%, and the quartz I-II phase transition by ~60%. This potential is more computationally expensive than those of the Buckingham form (BKS, TTAM, and CHIK) for all system sizes investigated, and is not as accurate, but is still acceptable for MD simulations of crystalline silica. The next section investigates more sophisticated potential models, which incorporate many-body effects as well as variable-charge. However, the inclusion of these additional terms does affect the computational cost.

3.1.2 Bond-order variable-charge potentials

The objectives of this study are to investigate the accuracy and transferability of COMB10,[221] ReaxFF$^{H_2O}_{SiO}$,[222] and ReaxFF$^{GSI}_{SiO}$[282] for calculating the material properties of crystalline silica, including the lattice constants, density, radial and bond-angle distribution functions, and quartz α-β phase transition. The transferability of these force fields is examined by comparing simulation results with the experimental data of the various silica polymorphs; namely, quartz, cristobalite, coesite, and stishovite.

3.1.2.1 **Methodology**

The crystallographic information files (CIF) for all four polymorphs of silica were obtained from the Crystallography Open Database.[283-285] The silica polymorphs are replicated in all three spatial dimensions using symmetry operations to create a supercell. The MD simulations with COMB10, ReaxFF$^{H_2O}_{SiO}$, and ReaxFF$^{GSI}_{SiO}$, are carried out using LAMMPS,[249] with a time step of 0.2 fs. Aktulga et al.[286] implemented the ReaxFF parameterization into LAMMPS.

The performed MD simulations track the positions and velocities of the atoms by time-integrating the Nose-Hoover style, non-Hamiltonian equations of motion, specifically by sampling from the isothermal-isobaric (NPT) ensemble.[249] The QEq[91] scheme is used to calculate the charge of each atom, based on the local bonding environment. The MD simulations of quartz, cristobalite, coesite, and stishovite used 5184, 768, 768, and 864 atoms, respectively. The energy minimization is carried out using the Polak-Ribiere version of the conjugate gradient (CG) algorithm,[287] as discussed by Cowen & El-Genk.[53] The simulated systems are equilibrated for 100 ps and the results of the lattice constants, the average charge, and density, are collected over the following 100 ps. The range of charges are obtained by finding the minimum and maximum charges of the atoms following data collection.

The COMB10[221] and ReaxFF[222,282] force fields are expressed somewhat differently. The COMB10[221] force field is given as:

$$E_T = E^{self} + E^{Coul} + E^{vdW} + E^{bond} + E^{others} \qquad \text{Eq. 3.6}$$

The ReaxFF[222,282] is expressed as:

$$E_T = E^{self} + E^{Coul} + E^{vdW} + E^{bond} + E^{angle} + E^{torsion} + E^{conjugation} + E^{H-bond} + E^{lone-pair} + E^{over} + E^{under} + E^{others} \qquad \text{Eq. 3.7}$$

The first four terms in Eq. 3.7 are basically the same for the COMB10[221] force field, Eq. 3.6. Other terms: $E^{angle}, E^{torsion}, E^{over}, E^{under}, E^{conjugation}$ in Eq. 3.7 are incorporated implicitly in the E^{bond} term of the COMB10 force field, Eq. 3.6. The E^{self} term represents the energy difference in the various states of the atom charges, while E^{others} consists of several terms that correct for allene-type terminal triple bond, and C_2 species.[236] For more details on the physics of the various terms in Eq. 3.6 and Eq. 3.7, the reader is referred to the original papers on the BOVC force fields.[221,222,282]

The results in Figure 3.22 show that while the Munetoh, BKS, and Pedone potentials can generally be used for MD simulations on an average workstation and produce results within a reasonable timeframe, the COMB10 and ReaxFF potentials require far more computing resources.

Table 3.8: Comparison of the computational time (in seconds) of the MD simulations of quartz with various potentials for 100 time steps and 82,944 atoms, versus the number of cores.

(a) 1,296 Atoms								
No. of Cores	Munetoh	BKS	Pedone	Pedone NRC	COMB10 – 1	COMB 10 – 10	ReaxFF – 1	ReaxFF – 10
1	0.72 (1)*	8.7 (1)*	15 (1)*	12 (1)*	33 (1)*	16.6 (1)*	41 (1)*	37 (1)*
2	0.37 (0.51)	4.5 (0.52)	8.1 (0.54)	5.8 (0.48)	16.7 (0.51)	8.9 (0.54)	25.9 (0.63)	24 (0.65)
4	0.24 (0.33)	2.5 (0.29)	4.3 (0.29)	3.2 (0.27)	9 (0.27)	4.5 (0.27)	17.8 (0.43)	16.5 (0.45)
8	0.16 (0.22)	1.6 (0.18)	2.5 (0.17)	2.1 (0.18)	5.1 (0.15)	2.6 (0.16)	14.1 (0.34)	13.2 (0.36)
12	0.12 (0.17)	1.2 (0.14)	2 (0.13)	1.6 (0.13)	3.9 (0.12)	2 (0.12)	13.8 (0.34)	12.6 (0.34)
16	0.1 (0.14)	1.1 (0.13)	1.6 (0.11)	1.4 (0.12)	3.2 (0.1)	1.6 (0.1)	13.9 (0.34)	13.3 (**0.36**)
20	0.15 (**0.21**)	0.94 (0.11)	1.5 (0.1)	1.4 (0.12)	2.7 (0.08)	1.5 (0.09)	14.5 (**0.35**)	13.8 (**0.37**)
24	0.67 (**0.93**)	1.7 (**0.2**)	1.9 (**0.13**)	1.8 (**0.15**)	3.2 (**0.1**)	1.8 (**0.11**)	15.1 (**0.37**)	14 (**0.38**)
(b) 10,368 Atoms								
No. of Cores	Munetoh	BKS	Pedone	Pedone NRC	COMB10 – 1	COMB 10 – 10	ReaxFF – 1	ReaxFF – 10
1	5.9 (1)	67 (1)	116 (1)	89 (1)	263 (1)	134 (1)	240 (1)	203 (1)
2	3 (0.51)	35 (0.52)	59 (0.51)	46 (0.52)	134 (0.51)	69 (0.51)	140 (0.58)	119 (0.59)
4	1.6 (0.27)	19 (0.28)	32 (0.28)	25 (0.28)	68 (0.26)	36 (0.27)	82 (0.34)	72 (0.35)
8	1 (0.17)	11 (0.16)	18 (0.16)	15 (0.17)	36 (0.14)	20 (0.15)	52 (0.22)	44 (0.22)
12	0.7 (0.12)	9 (0.13)	14 (0.12)	11 (0.12)	26 (0.1)	14 (0.1)	43 (0.18)	37 (0.18)
16	0.6 (0.1)	7.4 (0.11)	12 (0.1)	9 (0.1)	21 (0.08)	11 (0.08)	40 (0.17)	36 (0.18)
20	0.5 (0.08)	7.1 (0.11)	10 (0.09)	8.1 (0.091)	18 (0.07)	10 (0.07)	39 (0.16)	35 (0.17)
24	1 (**0.17**)	6.7 (0.1)	10 (0.09)	8.4 (**0.094**)	16 (0.06)	9 (0.07)	36 (0.15)	33 (0.16)
(c) 82,944 Atoms								
No. of Cores	Munetoh	BKS	Pedone	Pedone NRC	COMB10 – 1	COMB 10 – 10	ReaxFF – 1	ReaxFF – 10
1	46.4 (1)	539 (1)	932 (1)	717 (1)	1984 (1)	1031 (1)	1696 (1)	1404 (1)
2	24 (0.52)	288	477 (0.51)	377	988 (0.5)	522	928	771

		(0.53)		(0.53)		(0.51)	(0.55)	(0.55)
4	13 (0.28)	157 (0.29)	249 (0.27)	195 (0.27)	499 (0.25)	275 (0.27)	497 (0.29)	419 (0.3)
8	7.2 (0.16)	80 (0.15)	133 (0.14)	102 (0.14)	267 (0.13)	145 (0.14)	280 (0.17)	243 (0.17)
12	5.5 (0.12)	65 (0.12)	103 (0.11)	81 (0.11)	200 (0.1)	108 (0.1)	223 (0.13)	187 (0.13)
16	4.3 (0.09)	53 (0.1)	83 (0.09)	66 (0.09)	158 (0.08)	85 (0.08)	191 (0.11)	162 (0.12)
20	3.6 (0.08)	47 (0.09)	72 (0.08)	58 (0.08)	133 (0.07)	71 (0.07)	176 (0.1)	146 (0.1)
24	4 (**0.09**)	42 (0.08)	63 (0.07)	51 (0.07)	112 (0.06)	61 (0.06)	159 (0.09)	134 (0.1)

*Numbers in parenthesis indicate the relative values compared to those for a single core.

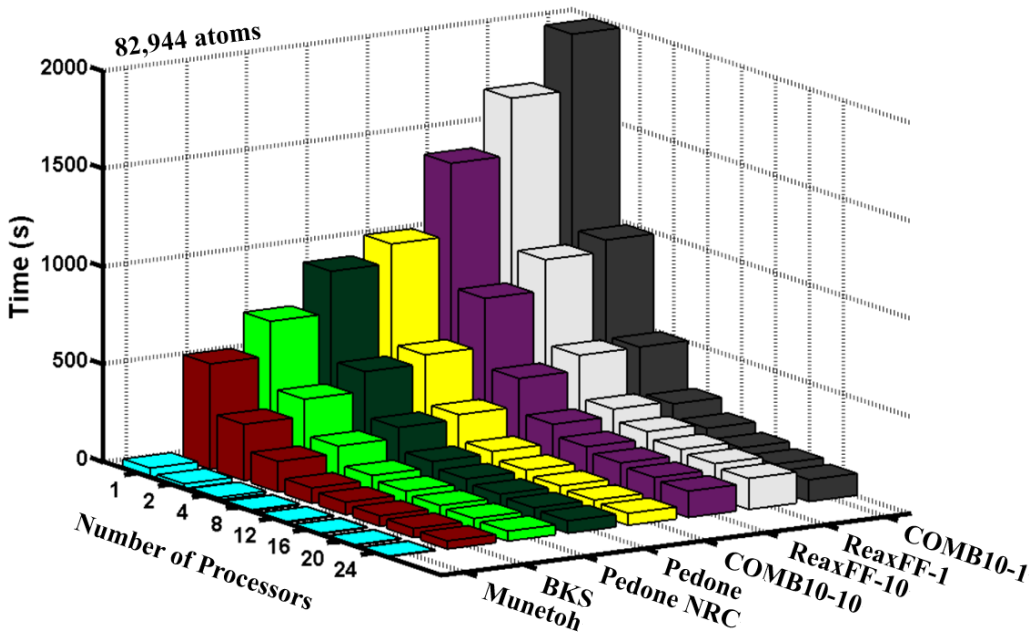

Figure. 3.21: Comparison of the computational times for the MD simulations of quartz for 100 time steps with 82,944 atoms, versus the number of cores.

The parallelizability of the potentials for MD simulations is also important for determining how the computational cost scales with the number of atoms (Table 3.8). The relative parallelizability can also be quantified by normalizing the simulation times listed in Table 3.8 using different cores to those of the simulations running on a single core.

As indicated in bold in Table 3.8, it is sometimes more efficient to run with 16 or 20 cores than with 24 cores, depending on the potential used in the simulations. The Munetoh

potential is an excellent example of this. Since this potential is inexpensive to begin with, the added communication time with increasing the number of cores from 20 to 24 is larger than the saved time distributing atoms among cores. The BKS and Pedone potentials follow a similar pattern, but are more parallelizable that the Munetoh potential (Table 3.8).

The results in Table 3.8 confirm that the simulations with the COMB10 potential are the most parallelizable, and those with the ReaxFF are the least parallelizable. While both are variable-charge potentials, the simulations with the COMB10 potential perform much better on multiple cores. It is important to note that "perform better" in this case, does not imply faster, but that the speed-up gained running the MD simulations on multiple cores is higher than on less cores. The time to complete the MD simulations with a given potential increases exponentially with decreasing the number of cores and/or increasing the total number of atoms (Table 3.8 and Figure 3.21).

For MD simulations on an average workstation with a single core, it is wise to avoid the reactive, bond-order potentials altogether. They would not produce results within a reasonable timeframe. Instead, consider using a two-body potential with fixed charges, or a many-body potential without charges. These potentials would produce results in a more reasonable timeframe (Table 3.8). Of course, it is important to remember that using an expensive potential that produces meaningful results is better than a less expensive potential that produces unreliable results. For example, modeling a complex reactive process with a non-reactive potential will not generate reliable results.

In the performed MD simulations of the α-β transition for quartz using COMB10-1, ReaxFF$^{H_2O}_{SiO}$-1, and ReaxFF$^{H_2O}_{SiO}$-10, the temperature in the ranges of 300 - 700 K and 900 - 1500 K is increased in increments of 100 K. In the intermediate range of 700 - 900 K, the temperature increased in small increments of 10 K. The COMB10-10 force field required a slightly different approach, because the initial simulations predicted a structural transformation outside the 700 - 900 K range. Thus, the range for using the 10 K increments is shifted to higher temperatures to accurately capture the quartz α-β transition. In the simulations with the COMB10-10 force field, the temperature in the ranges of 300 - 1100 K and 1400 - 1500 K is increased in increments of 100 K. Increments of 10 K are used in the intermediate range of 1100 - 1400 K. The used heating time between temperatures is 1.0 ps, whereas equilibration times of 1, 2, 4, 8, and 16 ps and equal times for data collection are

used. For example, a 16-ps of data collection time followed a 16-ps equilibration time is used at each temperature.

3.1.2.2 **Results**

This section compares the calculated properties of the crystalline silica polymorphs of quartz, cristobalite, coesite, and stishovite, using MD simulations with COMB10, ReaxFF$^{H_2O}_{SiO}$, and ReaxFF$^{GSI}_{SiO}$, with experimental results. These material properties are the lattice constants, density, and the pair and bond-angle distribution functions. The presented results demonstrate the effect of changing the frequency of updating the atom charges every time step, and every 10-time steps on the calculated materials properties. Only the MD simulations with the COMB10 and ReaxFF$^{H_2O}_{SiO}$ force fields are investigated for predicting the quartz α-β transition.

3.1.2.2.1 Quartz

Quartz, the most abundant and stable SiO_2 polymorph at ambient conditions, is used in many applications due to its superior optical and piezoelectric properties and the formation of SiO_2 at the SiO_2/Si interface.[259-261] Table 3.9 compares the calculated properties (standard deviation shown in parenthesis) and the atom charges for α-quartz, using MD simulations with the BOVC force fields to experimental values. The simulations results with the ReaxFF$^{GSI}_{SiO}$-1 accurately predict the lattice constants and density of α-quartz, to within ~2.1% of experimental values. The calculated material properties in the simulations with the ReaxFF$^{H_2O}_{SiO}$-1 are within ~3.6%, and those with COMB10 are within ~7.3%, of the experimental values. In the MD simulations of α-quartz with the COMB10 force field, the charge-equilibration frequency negligibly affects the results. In the simulations with the ReaxFF$^{H_2O}_{SiO}$, there is a larger disparity in the results, predicting α-quartz densities of 2.55 g/cm^3 and 2.60 g/cm^3 with a charge equilibration frequency of every time step and every 10-time steps, respectively.

Fig. 3.22 compares the calculated pair distribution functions for α-quartz at ambient conditions, in the MD simulations with the COMB10-1, COMB10-10, ReaxFF$^{H_2O}_{SiO}$-1, and ReaxFF$^{H_2O}_{SiO}$-10 force fields, with experimental values. The pair distribution functions are important for showing the structural order of crystalline materials. There are differences in the calculated distributions with updating the atom charges every time step and every 10-time

steps. The distribution functions' curves, produced by evaluating the atom charges every time step are smoother and more accurate, compared to experimental values. The most accurate curves for the O-Si and O-O pairs are those calculated in the simulations with the COMB10-1 force field. They are accurate to within ~1% of the experimental results. The simulation results with ReaxFF$^{H_2O}_{SiO}$-1 for the Si-Si pairs are the most accurate; they are within ~1% of experimental values.

Table 3.9: Comparison of calculated properties (standard deviation shown in parenthesis) and atom charges for α-quartz, using MD simulations with the BOVC force fields to experimental values.

Parameter	Experimental/Force Field					
	Exp.[153]	**COMB10-1**	**COMB10-10**	**ReaxFF$^{H_2O}_{SiO}$-1**	**ReaxFF$^{H_2O}_{SiO}$-10**	**ReaxFF$^{GSI}_{SiO}$-1**
a (**Å**)	4.916	4.79 (4e-3)	4.79 (3e-3)	4.95 (3e-3)	4.93 (1e-2)	4.95 (3e-3)
c (**Å**)	5.405	5.30 (6e-3)	5.28 (5e-3)	5.52 (3e-3)	5.48 (3-e2)	5.46 (3e-3)
ρ (g/cm^3)	2.646	2.84 (3e-3)	2.85 (2e-3)	2.55 (1e-3)	2.60 (3e-3)	2.59 (1e-3)
q_{avg} (O)	-	-1.45 (1e-4)	-1.45 (5e-5)	-0.81 (2e-3)	-0.81 (1e-3)	-0.46 (9e-4)
q_{avg} (Si)	-	2.91 (3e-4)	2.91 (1e-4)	1.62 (4e-3)	1.62 (4e-3)	0.92 (2e-3)
q_{range} (O)	-	-1.38 to -1.54	-1.39 to -1.53	-0.69 to -0.91	-0.69 to -0.91	-0.41 to -0.50
q_{range} (Si)	-	2.88 – 2.93	2.89 – 2.92	1.40 – 1.80	1.58 – 1.64	0.88 – 0.96

The MD simulations with the COMB10 force field underestimate the Si-Si distribution by ~3%, and that with the ReaxFF$^{H_2O}_{SiO}$ underestimate both the O-Si and O-O pairs by ~3%, compared to the experimental values of the pair distribution functions (Fig. 3.22). For an accurate characterization, Table 3.10 lists the ranges of the calculated bond-lengths at the base and half-width, the average values of the bond-lengths, and the bond-lengths at the peaks of the pair distribution functions.

Fig. 3.23 compares the calculated O-Si-O and Si-O-Si bond-angle distribution (BAD) functions for α-quartz at ambient conditions, using MD simulations with the COMB10-1, COMB10-10, ReaxFF$^{H_2O}_{SiO}$-1, and ReaxFF$^{H_2O}_{SiO}$-10 to the experimental values. The results with all BOVC force fields predict the O-Si-O BAD to within 1% of the experimental values.

However, there are slight kinks in the calculated curves with ReaxFF$^{H_2O}_{SiO}$-10, which disappear when updating the atom charges every time step.

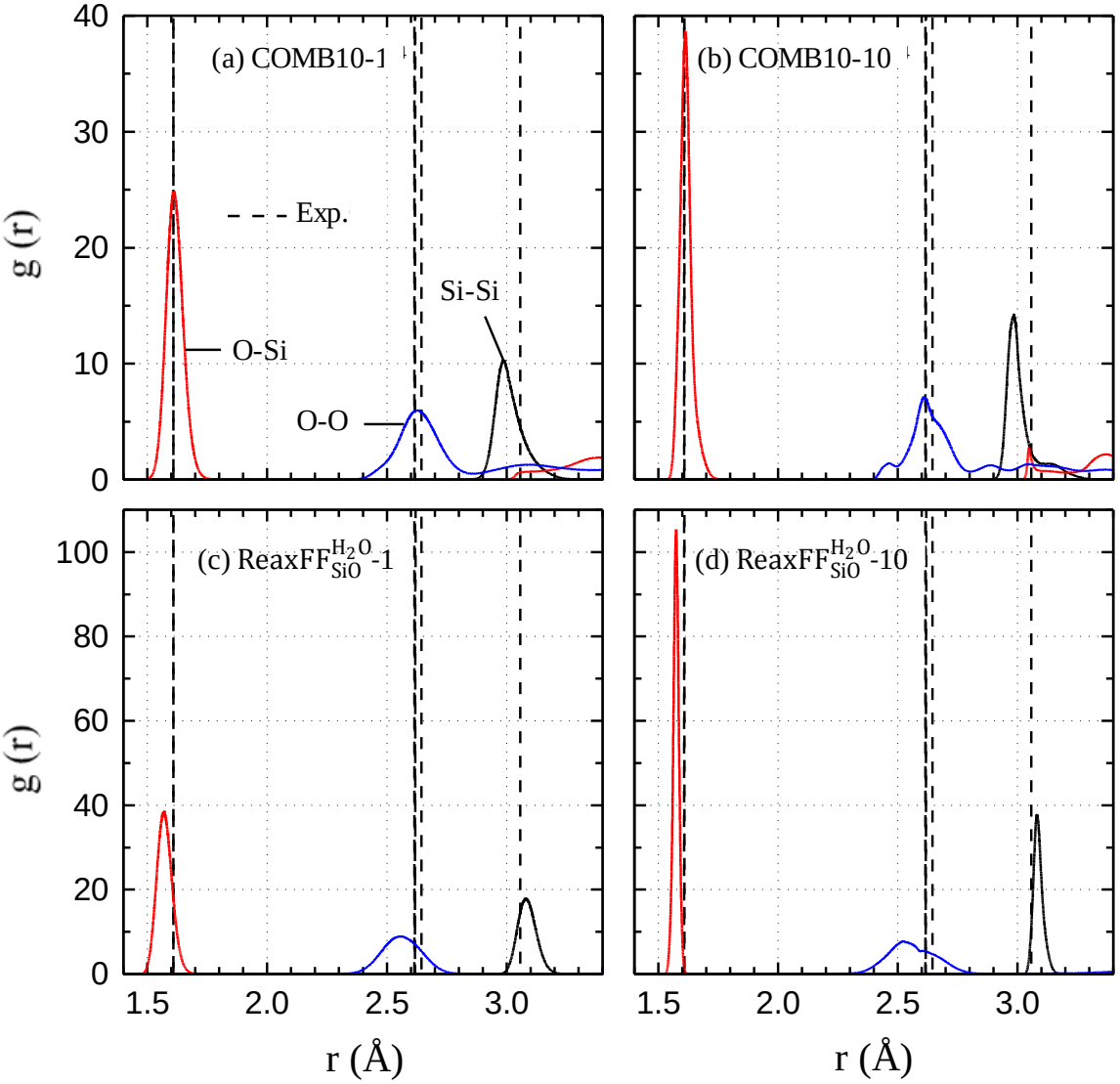

Figure 3.22: Comparison of the predictions of the pair distribution functions for α-quartz at ambient conditions (300 K and 1 atm), in MD simulations with COMB10 and $ReaxFF^{H_2O}_{SiO}$, to experimental results.

The MD simulations with the COMB10 force field underestimate the experimental results of the Si-O-Si BAD by ~4%, while the simulations with ReaxFF$^{H_2O}_{SiO}$ over-predict the experimental results by as much as ~10% (Fig. 3.23). For judicious comparison to experimental results, Table 3.10 lists the ranges of the calculated bond-angles at the base and half-width, the average values of the bond-angles, and the bond-angles at the peaks of the

BAD functions. The results in this table show close agreements with the experimental values of the average bond angles.

Table 3.10: Comparison of the bond-lengths at the 1st peak of the pair distribution function, and the bond-angles for α-quartz, using MD simulations with the BOVC force fields, to experimental values.

Force Field	**Atom Pairs**	**Bond lengths for 1st Peak in RDF (Å)**				
		Min-Max @ Base	**Min-Max @ Half-Width**	**@ Peak**	**Average Value**	
					Calculated	**Exp.[153]**
COMB10-1	O-Si	1.46 – 1.86	1.57 – 1.64	1.61	1.62	1.61
	O-O	2.29 – 2.87	2.54 – 2.72	2.63	2.63	2.61 - 2.64
	Si-Si	2.76 – 3.41	2.95 – 3.05	2.98	3.01	3.06
COMB10-10	O-Si	1.51 – 1.80	1.59-1.64	1.61	1.62	1.61
	O-O	2.33 – 2.82	2.56 – 2.70	2.61	2.62	2.61 - 2.64
	Si-Si	2.85 – 3.38	2.95 – 3.02	2.99	3.02	3.06
$ReaxFF_{SiO}^{H_2O}$-1	O-Si	1.46 – 1.78	1.53 – 1.61	1.57	1.57	1.61
	O-O	2.19 – 2.94	2.47 – 2.66	2.55	2.56	2.61 - 2.64
	Si-Si	2.94 – 3.31	3.04 – 3.13	3.08	3.09	3.06
$ReaxFF_{SiO}^{H_2O}$-10	O-Si	1.52 – 1.65	1.56 – 1.59	1.57	1.57	1.61
	O-O	2.16 – 2.90	2.44 – 2.67	2.52	2.57	2.61 - 2.64
	Si-Si	3.02 – 3.23	3.06 – 3.10	3.08	3.09	3.06
	Interface	**Bond Angles (°)**				
COMB10-1	O-Si-O	89.9 – 130.5	103.6 – 115.2	108.9	109.3	109.5
	Si-O-Si	99.2 – 153.5	133.6 – 141.5	136.7	137.7	143.7
COMB10-10	O-Si-O	94.4 – 128.5	104.4 – 115.1	108.7	109.3	109.5
	Si-O-Si	128.6 – 155.3	134.1 – 140.1	137.2	138.0	143.7
$ReaxFF_{SiO}^{H_2O}$-1	O-Si-O	91.2 – 132.6	103.6 – 114.6	108.3	109.4	109.5
	Si-O-Si	137.5 – 179.6	151.9 – 163.5	156.6	158.0	143.7
$ReaxFF_{SiO}^{H_2O}$-10	O-Si-O	89.6 – 134.2	102.6 – 115.5	107.0	109.3	109.5
	Si-O-Si	146.6 – 172.0	154.2 – 160.8	157.0	157.7	143.7

The equilibration frequency of the atom charges clearly affects the simulations results, as demonstrated in Figs. 3.22 and 3.23. In addition to not conserving energy, when updating the atom charges each 10 time steps, the peaks of the calculated pair and bond-angle distribution functions are not smooth, unlike those with updating the atom charges each time step.

Notwithstanding that, the average values are still remarkably close to the experimental results for both charge-equilibration frequencies. At ambient conditions, the impact of the charge-equilibration frequency on the MD simulation results is small; however, predicting the complex phase transition is a challenge.

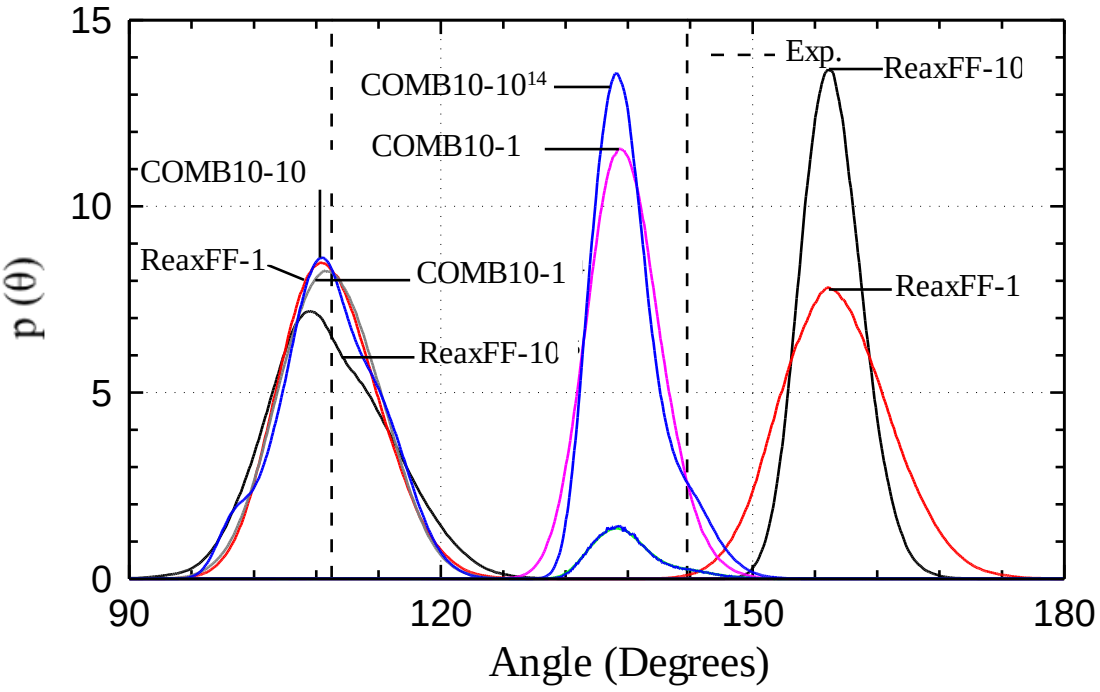

Figure 3.23: Comparison of the predictions of the BAD functions for α-quartz at ambient conditions (300 K and 1 atm), in MD simulations with COMB10 and $ReaxFF_{SiO}^{H_2O}$, to experimental results.

3.1.2.2.2 α - β Transition

The α-β phase transition for quartz has been shown experimentally to occur at 846 K.[262] A good test of the transferability of a force field in MD simulations is to characterize this transition. This section compares the calculated cell volume and c/a ratio at the α-β transition in MD simulations with the different BOVC force fields, as a function of temperature, to reported experimental values.

Fig. 3.24a shows that in the performed MD simulations with the COMB10-1 force field for durations of 1, 2, and 4 ps, the calculated cell volume steadily increases with increasing temperature, with no structural transformation. The simulation results with the COMB10-1 force field and with equilibration and data collection times of 8 ps and 16 ps show a sharp drop in the calculated cell volume at the α-β transition. Conversely, the experimental results

indicate a plateau in the cell volume expansion at the α-β transition, due to the rotation of the SiO_4 tetrahedra.

The MD simulations with the COMB10-10 force field (Fig. 3.24b) and different equilibration times reveal a structural transformation, but at a much higher temperature than predicted with the COMB10-1 potential. As with the COMB10-1 potential, the not fully converged results show a continuous decrease in the cell volume at the α-β transition, rather than reaching a plateau, as indicated experimentally (Fig. 3.24b).

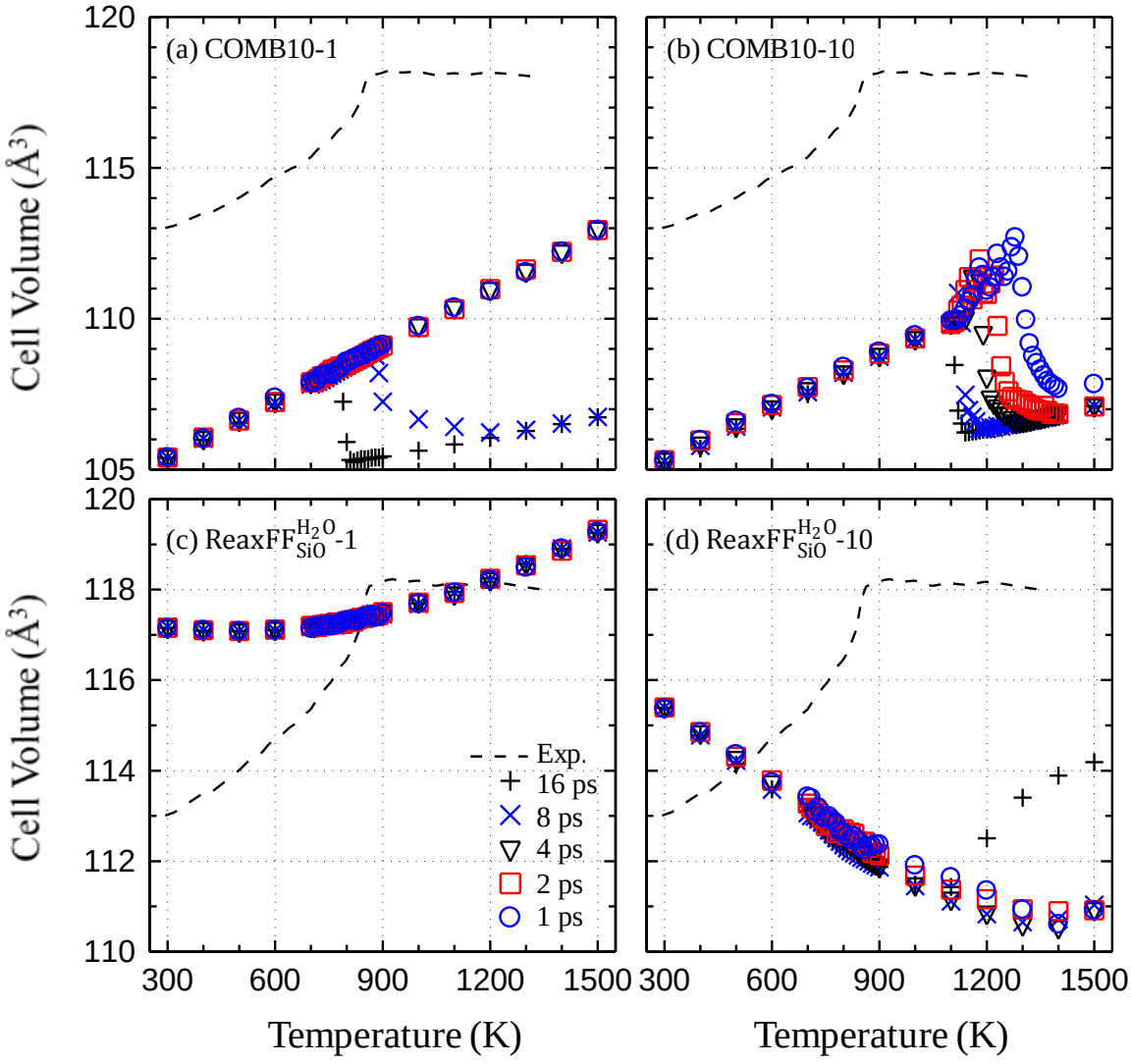

Figure 3.24: Comparison of the calculated cell volume expansion over the α-β transition of quartz, in MD simulations with COMB10 and $ReaxFF_{SiO}^{H_2O}$, to experimental results.

The MD simulation results with the ReaxFF$^{H_2O}_{SiO}$-1 converged for all cases (Fig. 3.24c). However, a plateau is not predicted over the entire temperature range (300 - 1500 K) of interest, indicating the inability of the ReaxFF$^{H_2O}_{SiO}$-1 to model the α-β transition for quartz. Only the simulation results of the cell volume expansion using the ReaxFF$^{H_2O}_{SiO}$-10, with 16 ps of equilibration and data collection time, predict a structural transformation. However, the transformation does not predict the experimentally measured plateau at the α-β transition (Fig. 3.24d).

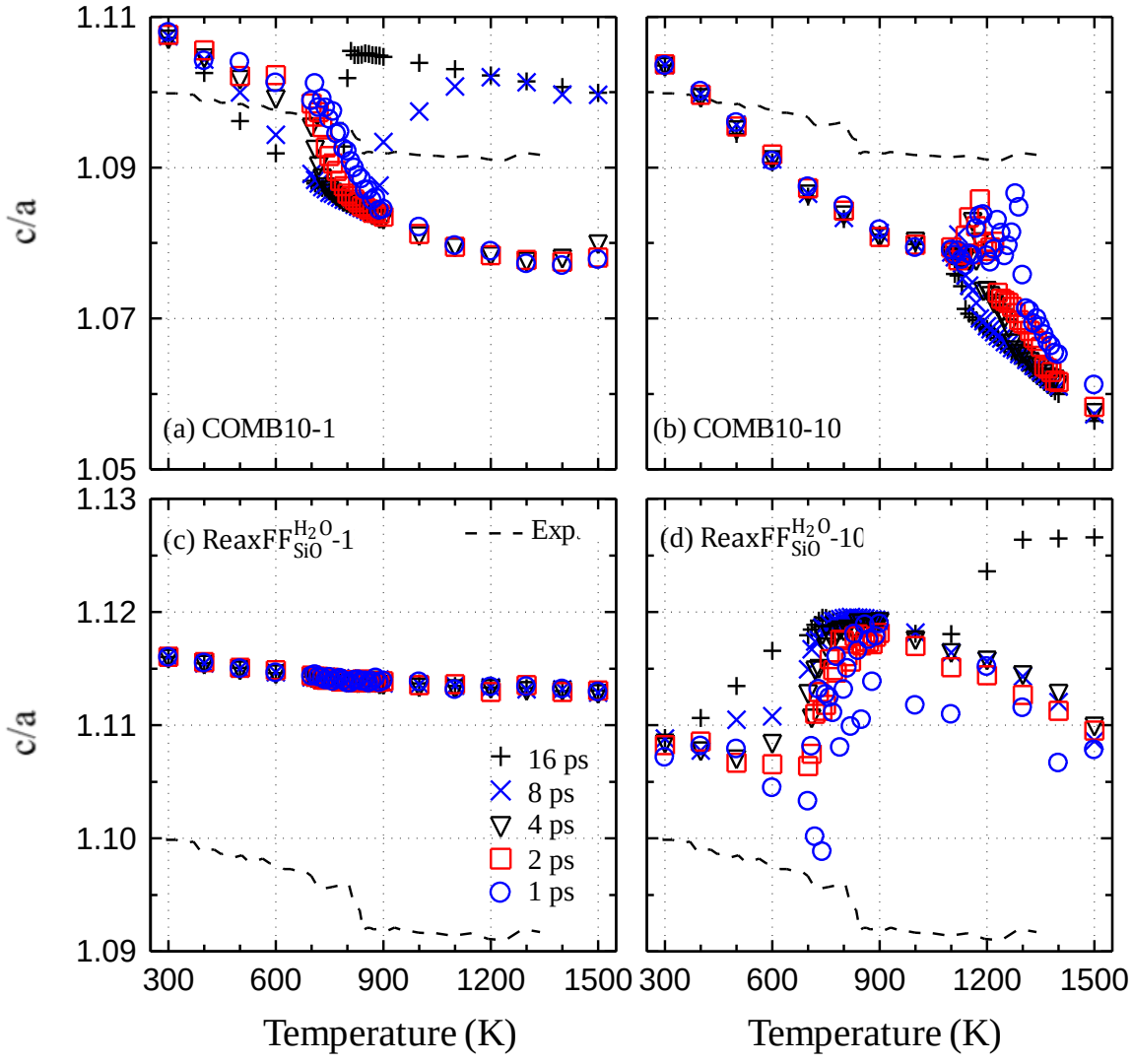

Figure 3.25: Comparison of the calculated c/a ratio over the α-β transition of quartz, in MD simulations with COMB10 and $ReaxFF^{H_2O}_{SiO}$, to experimental results.

The simulations with the BOVC force fields and with updating the atom charges every 10 time steps give drastically different results than when updating the charges every time step. Indeed, the period of the vibrational modes for the high frequency asymmetric Si-O bond stretching is approximately an order of magnitude larger than the 2 fs time interval for the lower charge-equilibration frequency.[288] However, the charge-equilibration frequency is uncoupled to the vibrational modes. Thus, in the MD simulations with the force fields of COMB and ReaxFF, the atom charges need to be updated every time step in order to find the local energy minima. As indicated earlier, updating the atom charges less frequently no longer conserves energy.

At ambient conditions, the effect of the charge-equilibration frequency on the calculated results is small, but more pronounced over the quartz α-β transition, as the results using charge-equilibration frequencies of each time step and each 10 time steps diverge. Therefore, for the complex α-β structural phase transition, it is important to update atom charges as often as possible to compensate for the change in the bonding environment. Perhaps there is a more optimal value between the two investigated in this work, namely each time step and 10-time steps. Even when the atom charges are updated every time step, the MD simulations results with the COMB10 and the ReaxFF$^{H_2O}_{SiO}$ inaccurately predict the quartz α-β transition.

The c/a ratio at the α-β transition for quartz is difficult to model and has eluded many force fields. Herzbach et al.[241] indicated that the polarizable TS[212] is the only force field, among those they investigated, that is capable of modeling the sudden drop in c/a ratio at the α-β transition for quartz. The present MD simulation results with the COMB10-1 and COMB10-10 force fields inaccurately predict the c/a ratio at the α-β transition (Fig. 3.25). At the α-β transition, the calculated c/a ratio experiences a sudden increase, rather than a decrease, as obtained experimentally. The performed simulations with the ReaxFF$^{H_2O}_{SiO}$-10 show a similar increase in the c/a ratio near the α-β transition. The ReaxFF$^{H_2O}_{SiO}$-1 is the only force field that does not show any structural transformation in the calculated c/a ratio.

3.1.2.2.3 Cristobalite

Similar to quartz, cristobalite is formed at higher pressures, and is a four-coordinated polymorph. However, the density is lower, comparable to that of amorphous silica. Based on the previous results showing that evaluating the atom charges every 10 time steps is not quite accurate and does not conserve energy (Figs. 3.22-3.25), the results of the performed MD

simulations discussed in remainder of this paper, are with updating the atom charges every time step.

In Table 3.11, the calculated structural properties and charges of the oxygen and silicon atoms of α-cristobalite, in MD simulations with the three BOVC force fields investigated in this work, are compared to experimental values. Despite the fact that α-quartz and α-cristobalite have similar crystal structures, with the silicon atoms tetrahedrally coordinated, the results of the MD simulations with the COMB10 force field of the material properties are not as accurate for this polymorph, as they are for α-quartz (Table 3.11). Despite the extensive simulations with different time steps, frequencies of updating the atom charges of the atoms, equilibration and data collection times, and number of atoms, the calculated results for this polymorph are significantly different from those previously reported with the COMB10 force field.[221] Energy minimization of the force field produces results consistent with the experimental values, but equilibration at ambient conditions produces a ~21% higher density.

Table 3.11: Comparison of calculated properties (standard deviation shown in parenthesis) and atom charges for α-cristobalite in MD simulations with the BOVC force fields, to experimental values.

Parameter	Experimental / Force Field			
	Exp.[251]	**COMB10**[221]	**ReaxFF$^{H_2O}_{SiO}$**[222]	**ReaxFF$^{GSI}_{SiO}$**[282]
a (Å)	4.978	4.81 (1e-2)	5.03 (7e-3)	5.04 (9e-3)
c (Å)	6.948	6.13 (1e-2)	7.11 (1e-2)	7.12 (1e-2)
ρ (g/cm^3)	2.318	2.81 (7e-3)	2.22 (3e-3)	2.20 (4e-3)
q_{avg} (O)	-	-1.45 (1e-4)	-0.87 (4e-3)	-0.47 (1e-3)
q_{avg} (Si)	-	2.90 (3e-4)	1.73 (7e-3)	0.94 (3e-3)
q_{range} (O)	-	-1.39 to -1.51	-0.76 to -0.97	-0.43 to -0.51
q_{range} (Si)	-	2.88 – 2.92	1.58 – 1.90	0.90 – 0.98

The calculated density in this work for the α-cristobalite of 2.81 g/cm^3 is similar to that calculated for α-quartz of 2.84 g/cm^3. Thus, it is unclear how reported work[221] could have predicted values closer to experimental results. The calculated properties for α-cristobalite in

the performed MD simulations with both ReaxFF$^{H_2O}_{SiO}$ and ReaxFF$^{GSI}_{SiO}$ are within ~3% and 5% of the lattice constants and density, respectively, compared to experimental values (Table 3.11). These results demonstrate the transferability of these force fields to the α-cristobalite bonding environment.

3.1.2.2.4 Coesite

Coesite is another four-coordinated silica polymorph, which forms at high pressures due to events such as meteor impacts.[277] The bonding environment is thus much different from those for quartz and cristobalite. The monoclinic crystal structure of coesite comprises four silicon dioxidetetrahedra in Si_4O_8 and Si_8O_{16} rings.[252] Table 3.12 compares the calculated properties and the charges of the oxygen and silicon atoms for coesite with experimental values. The results of the performed MD simulations using all three BOVC force fields accurately predict the properties of coesite.

The monoclinic cell of coesite is characterized as $a \neq b \neq c$ and $\beta \neq 90^o$. The β angle is shown experimentally to be 120.34°.[252] All three force fields predict this angle to within 1° of the experimental value. The MD simulation results of the coesite properties, with the COMB10, ReaxFF$^{H_2O}_{SiO}$, and ReaxFF$^{GSI}_{SiO}$ force fields, are within 1.7%, 2.2%, and 2.3% of the experimental values, respectively. Such good accuracy attests to the transferability of these force fields to the coesite bonding environment.

Table 3.12: Comparison of calculated properties (standard deviation shown in parenthesis) and atom charges for coesite, in MD simulations with the BOVC force fields, to experimental values.

Parameter	Exp.[252]	Force Fields		
		COMB10[221]	ReaxFF$^{H_2O}_{SiO}$[222]	ReaxFF$^{GSI}_{SiO}$[282]
a (Å)	7.136	7.04 (1e-2)	7.29 (2e-2)	7.20 (1e-2)
b (Å)	12.369	12.40 (2e-2)	12.33 (1e-2)	12.19 (2e-2)
c (Å)	7.174	7.22 (9e-3)	7.12 (7e-3)	7.01 (1e-2)
ρ (g/cm^3)	2.921	2.97 (6e-3)	2.88 (3e-3)	2.96 (4e-3)
β (°)	120.34	121.12 (1e-1)	119.75 (8e-2)	119.41 (1e-1)
q_{avg} (O)	-	-1.46 (2e-4)	-0.79 (3e-3)	-0.46 (1e-3)
q_{avg} (Si)	-	2.91 (4e-4)	1.59 (5e-3)	0.91 (2e-3)

q_{range} (O)	-	-1.37 to -1.54	-0.71 to -0.88	-0.41 to -0.50
q_{range} (Si)	-	2.89 – 2.93	1.48 – 1.76	0.87 – 0.95

3.1.2.2.5 Stishovite

The crystal structure of stishovite resembles that of rutile (TiO_2), with each of the octahedrally coordinated silicon atoms bound to six oxygen atoms.[289] Therefore, the transferability of the force fields can be critically evaluated based on their ability to change from a tetrahedra bonding environment (quartz, cristobalite, coesite) to an octahedra bonding environment (stishovite). Table 3.13 compares the calculated properties and charges of the oxygen and silicon atoms of stishovite in the MD simulations with the three BOVC force fields, with experimental values.

Table 3.13: Comparison of calculated properties (standard deviation shown in parenthesis) and atom charges for stishovite in MD simulations with BOVC force fields to experimental results.

Parameter	**Exp.**[289]	**Force Field**		
		COMB10[221]	**ReaxFF$^{H_2O}_{SiO}$**[222]	**ReaxFF$^{GSI}_{SiO}$**[282]
a (Å)	4.180	4.09 (7e-3)	4.56 (4e-3)	5.68 (4e-2)
c (Å)	2.666	2.97 (2e-3)	3.04 (2e-3)	2.54 (2e-2)
ρ (g/cm^3)	4.283	4.02 (4e-3)	3.16 (3e-3)	2.38 (2e-2)
q_{avg}(O)	-	-1.47 (1e-4)	-0.53 (2e-3)	-0.41 (3e-3)
q_{avg}(Si)	-	2.94 (3e-4)	1.07 (3e-3)	0.82 (6e-3)
q_{range}(O)	-	-1.43 to -1.51	-0.48 to -0.59	-0.23 to -0.51
q_{range}(Si)	-	2.93 – 2.96	1.02 – 1.11	0.60 – 0.96

The performed MD simulations with ReaxFF$^{H_2O}_{SiO}$ and ReaxFF$^{GSI}_{SiO}$ inaccurately predict the properties of the stishovite under equilibration in the NPT ensemble. The calculated properties are within ~26% and 44% of experimental results for the ReaxFF$^{H_2O}_{SiO}$ and ReaxFF$^{GSI}_{SiO}$, respectively. This could be because the density and the cohesive energies of various polymorphs were determined with single point energies at different densities, which is more of an evaluation than an optimization. Thus, despite the fact that MD simulations

with both $ReaxFF_{SiO}^{H_2O}$ and $ReaxFF_{SiO}^{GSI}$ accurately predict the properties of the other silica polymorphs, these force fields are not necessarily suitable for all phases of silica, and need to be optimized more effectively for stishovite. The MD simulation results with the COMB10 force field are accurate to within ~11% of the experimental values for the "c" lattice parameter, and ~2.2% for the "a" lattice parameter (Table 3.13). Thus, the COMB10 force field is a more appropriate choice for modeling stishovite.

3.1.2.3 **Highlights and Concluding Remarks**

The accuracy and transferability of the three BOVC force fields: COMB10, $ReaxFF_{SiO}^{H_2O}$, and $ReaxFF_{SiO}^{GSI}$, are investigated for modeling the four SiO_2 polymorphs, quartz, cristobalite, coesite, and stishovite. These force fields have been designed for modeling interfaces and complex chemical reactions. MD simulation results of the structural properties of crystalline silica, using these force fields, are compared to experimental values. In these simulations, the atom charges are updated each time step. The results with updating the atom charges every 10-time steps are inaccurate, since energy is not conserved.

The MD simulation results with the COMB10 force field accurately predict the properties of the quartz and coesite polymorphs at ambient conditions, to within 7.3% and 1.7% of the experimental values, respectively. The simulation results for the α-cristobalite and stishovite are not as accurate; they are within ~21% and 11% of the experimental values, respectively.

The simulation results with $ReaxFF_{SiO}^{H_2O}$ and $ReaxFF_{SiO}^{GSI}$, of the properties for quartz, cristobalite, and coesite at ambient conditions, except the BAD function, are accurate to within ~5% of the experimental values. The simulation results with $ReaxFF_{SiO}^{H_2O}$ of the BAD function for quartz are within 10% of the experimental values.

The simulation results with $ReaxFF_{SiO}^{H_2O}$ and $ReaxFF_{SiO}^{GSI}$ inaccurately predict the properties of the high-pressure stishovite polymorph; they are within ~26% and 44% of the experimental values, respectively. In addition, the results of the MD simulations with the COMB10 and the $ReaxFF_{SiO}^{H_2O}$ inaccurately model the α-β transition for quartz. The results of the cell volume expansion at the α-β transition are quite different from experimental values and do not predict the experimentally measured plateau, caused by the rotation of the SiO_4 tetrahedra.

The next section presents and discusses the accuracy and transferability of the Pedone potential to model all metal oxides of interest to this dissertation research. The accuracy and transferability are quantified in terms of various structural properties, as well as equations of state as a function of temperature and pressure.

3.2 Investigation of Pedone potential for SiO_2, Al_2O_3, Cr_2O_3, TiO_2, and MgO

The objectives of this study are to quantify the accuracy of the Pedone potential for modeling the structural properties of several metal oxides.

3.2.1 Methodology

LAMMPS is used to conduct the present MD simulations, with a system size of 4,320 atoms for Cr_2O_3 and Al_2O_3, 4,608 atoms for TiO_2 and SiO_2, and 4,096 atoms for MgO. These oxides [Cr_2O_3 (eskolite), Al_2O_3 (corundum), TiO_2 (rutile), SiO_2 (α-quartz), and MgO (periclase)], are all crystalline. The crystal structure is trigonal for SiO_2, Cr_2O_3, and Al_2O_3, tetragonal for TiO_2, and cubic for MgO (Fig. 3.26). The Pedone potential is expressed as:

$$E_{ij} = \frac{q_i q_j}{r_{ij}} + D_{ij}\left\{\left[1 - e^{-\alpha_{ij}(r_{ij}-r_o)}\right]^2 - 1\right\} + \frac{F_{ij}}{r_{ij}^{12}} \qquad \text{Eq. 3.8}$$

The right-most term in this expression is a strong repulsive term, which is useful in high-temperature and/or high-pressure simulations.

The performed MD simulations with the Pedone potential set the cutoff at 15 Å and the relative error of the particle-particle particle-mesh (PPPM) solver for the Coulomb interactions to $1x10^{-6}$. In addition, the simulations used the Polak-Ribiere version of the conjugate gradient (CG) algorithm to perform energy minimization of the atoms. The systems of atoms used are equilibrated in the NPT ensemble at 300 K and 1.0 atm for 20 ps. The data on the structural properties for the oxides is gathered over the second half of the equilibration period. In the final preparation before initiating the simulations, the systems of atoms for the different oxides are equilibrated in the NVE ensemble for 10 ps.

3.2.2 Results

An important aspect of ensuring the reliability and accuracy of the MD simulation results is to validate the potential used. The calculated lattice constants and cell volume of all oxides are compared to the reported experimental values (Tables 3.14 and 3.15). As these tables show, the differences between the calculated and the experimental values of the lattice

constants and cell volume are less than 2%, except that the calculated SiO_2 cell volume differs from the experimental value by 2.24% and the calculated MgO cell volume differs from the experimental value by 3.54%.

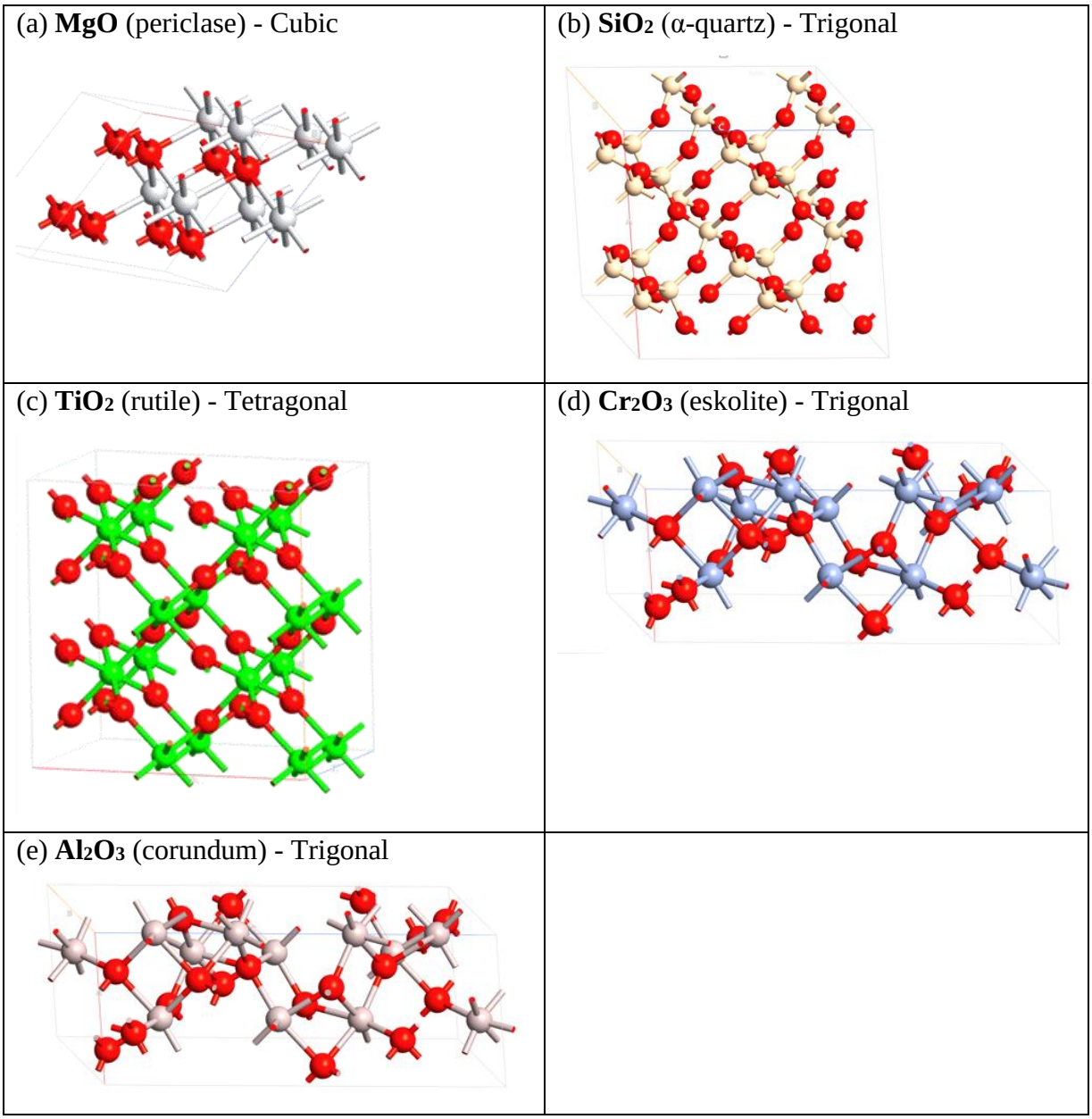

Figure 3.26: Crystal structures of the five oxides investigated (oxygen atoms in red and metal atoms in different colors).

The accuracy of the calculated elastic constants and bulk modulus using MD simulations is not the same for all oxides.[217] While the calculated values for most oxides are within ~10% of the experimental results, a few differ by more than 10%. The calculated C_{44} elastic

constant for Cr_2O_3, Al_2O_3, and MgO differ from the experimental values by 19.4%, 22.5%, and 32%, respectively. For Al_2O_3, other potentials may be more accurate than the Pedone potential for predicting some of the physical properties,[290] but they are either not parameterized for all oxides in this work, or not compatible with radiation damage simulations. The Pedone potential, however, is parameterized for all oxides of interest.

Table 3.14: A comparison of calculated properties of Cr_2O_3, Al_2O_3, and SiO_2, at 300 K and 1.0 atm, with reported experimental values

Property	Cr_2O_3		Al_2O_3		SiO_2	
	Calc. (Exp.)[291]	Diff. (%)	Calc. (Exp.)[292]	Diff. (%)	Calc. (Exp.)[153]	Diff. (%)
a (Å)	5.013 (4.97)	0.87	4.724 (4.7602)	0.76	4.949 (4.916)	0.66
b (Å)	5.013 (4.97)	0.87	4.724 (4.7602)	0.76	4.949 (4.916)	0.66
c (Å)	13.621 (13.6)	0.17	13.046 (12.9933)	0.41	5.454 (5.405)	0.91
Cell Vol ($Å^3$)	296.411 (290.8)	1.93	252.117 (254.98)	1.12	115.663 (113.131)	2.24
C_{11} (10^{10} Pa)[217]	39.32 (37.4)	5.13	48.82 (49.70)	1.77	8.68 (8.66)	0.23
C_{33} (10^{10} Pa)[217]	35.31 (36.2)	2.5	50.18 (50.10)	0.16	10.63 (10.61)	0.19
C_{44} (10^{10} Pa)[217]	12.82 (15.9)	19.4	11.38 (14.68)	22.5	4.95 (5.78)	5.78
C_{12} (10^{10} Pa)[217]	16.89 (14.8)	14.1	19.70 (16.20)	21.6	0.88 (0.67)	31.3
C_{13} (10^{10} Pa)[217]			15.00 (11.60)	29.3	1.18 (1.26)	6.4
C_{14} (10^{10} Pa)[217]					-1.78 (-1.78)	0.0
B (10^{10} Pa)[217]	23.73 (23.4)	1.41	27.45 (25.35)	8.3	3.79 (3.78)	0.26

To further determine the accuracy of the Pedone potential, the calculated equations of state for all five oxides, as functions of temperature and pressure, are compared with reported experimental results. Fig. 3.27 compares the calculated and experimental equation of states of a/a_0 and c/c_0 for SiO_2,[262] TiO_2,[293] Al_2O_3,[294] Cr_2O_3,[295] and MgO[296] as functions of temperature, confirming the accuracy of the Pedone potential. The Pedone potential is highly accurate for modeling a/a_0 and c/c_0 for Al_2O_3, Cr_2O_3, and TiO_2, with the calculated values close to the reported experimental values. For MgO, the calculated a/a_0 is slightly overestimated; it is 1.01 at 878 K, compared to the experimental value of 1.007. In SiO_2, a/a_0 is very accurate, while c/c_0 is slightly over-estimated at the α-β transition. More information about equations of state for SiO_2 can be found in the reviews by Cowen and El-Genk.[52,53]

Table 3.15: A comparison of calculated properties of TiO_2 and MgO, at 300 K and 1.0 atm, with reported experimental values

Property	TiO_2		MgO	
	Calc. (Exp.)[297]	Diff. (%)	Calc. (Exp.)[298]	Diff. (%)
a (Å)	4.583 (4.593)	0.22	4.260 (4.211)	1.15
b (Å)	4.583 (4.593)	0.24	4.261 (4.211)	1.18
c (Å)	3.014 (2.959)	1.87	4.260 (4.211)	1.17
Cell Vol($Å^3$)	63.311 (62.154)	1.86	77.318 (74.672)	3.54
C_{11} (10^{10} Pa)[217]	34.78 (26.9)	29.3	29.46 (29.40)	0.20
C_{33} (10^{10} Pa)[217]	45.64 (48.0)	4.9		
C_{44} (10^{10} Pa)[217]	13.48 (12.4)	8.71	10.53 (15.5)	32
C_{66} (10^{10} Pa)[217]	16.64 (19.20)	13.3		
C_{12} (10^{10} Pa)[217]	16.0 (17.7)	9.5	10.53 (9.30)	13
C_{13} (10^{10} Pa)[217]	14.48 (14.60)	0.82		
B (10^{10} Pa)[217]	22.56 (21.55)	4.7	16.84 (16.0)	5.3

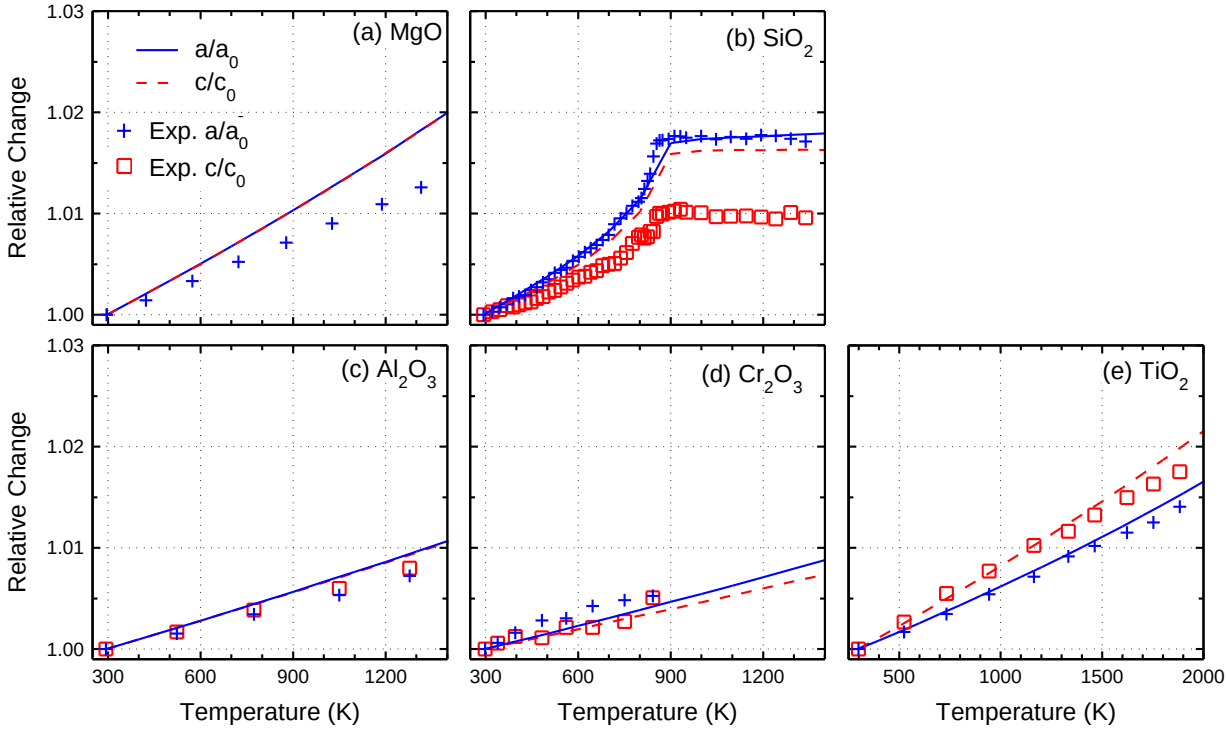

Figure 3.27: Comparison of lattice constants as a function of temperature for MgO, SiO_2, Al_2O_3, Cr_2O_3, and TiO_2, with experimental results.

Fig. 3.28 compares the calculated and experimental equations of state of a/a_0 and c/c_0 for SiO_2,[269] TiO_2,[299] Al_2O_3,[300] Cr_2O_3,[295] and MgO[301] as functions of pressure. These results confirm that the Pedone potential is accurate in calculating a/a_0 and c/c_0 for MgO, Al_2O_3, SiO_2, and TiO_2; the calculated values are close to the experimental results, except for c/c_0 in Cr_2O_3. At 20 GPa, the calculated c/c_0 for TiO_2 is 0.97, compared to an experimental value of 0.99. This should not affect the accuracy of the present MD simulations, which equilibrated the pressure at 1 atm.

3.2.3 Highlights and Concluding Remarks

The equations of state and other structural properties are modeled fairly accurately for the materials of interest. While there are some differences of up to ≈30%, the Pedone potential is unique in the fact that it is parameterized for all oxides. The next section discusses the determined TDEs for the oxides and carbides of interest, as modeled using the

BKS and Pedone potentials for the metal oxides, and the Tersoff potential for crystalline and amorphous SiC.

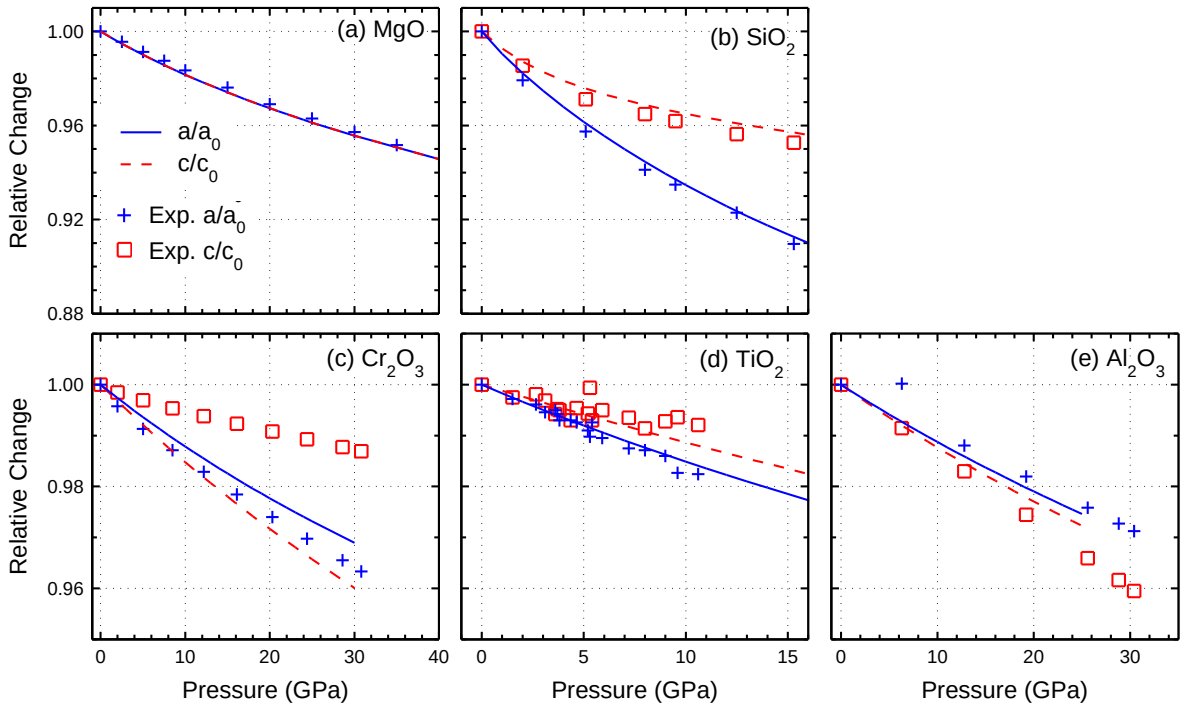

Figure 3.28: Comparison of lattice constants as a function of pressure for MgO, SiO_2, Al_2O_3, Cr_2O_3, and TiO_2, with experimental results.

4 THRESHOLD DISPLACEMENT ENERGIES

This section first presents and discusses PKA displacement using both the BKS and Pedone potentials for SiO_2. The subsequent section presents an extensive analysis of the TDE for all oxides of interest using just the Pedone potential. The last section presents the determined TDEs for 3C-SiC and amorphous (a-SiC).

4.1 Comparison of BKS and Pedone Potentials for PKA Displacement in SiO_2

The objectives of this study are to use MD simulations to investigate the effect of the potential cutoffs on the probability distribution of the TDEs for oxygen and silicon atoms in α-quartz, and to investigate the effect of the interatomic potential used. The simulations use a smoothly splined BKS-ZBL and Pedone potentials, and compares the calculated TDEs with experimental and theoretical values, when available. The results of this work provide invaluable input to radiation damage estimates of silica-based materials and additives to ATFs under development.

4.1.1 Methodology

The performed MD simulations used LAMMPS, a system of 4,068 atoms, an equilibration time step of 1.0 fs, and the particle-particle particle-mesh (PPPM)[90] solver with a relative error of 1.0e-6. They also used the splined BKS+ZBL potential with short (5.5 Å and Coulomb 10 Å), and long (15 Å and Coulomb 15 Å) cutoffs, and the Pedone with long cutoff (15 Å and Coulomb 15Å). The BKS potential is of the Buckingham form[207], whereas the Pedone is a Morse-stretch potential[217]. In the performed MD simulations, the system of atoms is first equilibrated, by integrating the Nose-Hoover style, non-Hamiltonian equations of motion, and sampling from the NPT ensemble for 20 ps, with damping parameters, T_{damp} and P_{damp}, of 100x and 1000x the time step, respectively. Subsequently, the system is relaxed in the micro-canonical ensemble (NVE) for 10 ps. The NVE ensemble precludes the unphysical damping of the atoms.

A randomly chosen PKA is given an initial velocity corresponding to an energy up to 150 eV. The simulations used different time steps of 0.5, 0.2, 0.1, and 0.05 fs, and varied the total simulation time from 1-5 ps. The results are used to determine the probability-based statistical averages of the TDEs for the oxygen and silicon atoms in α-quartz.

The BKS potential, which is accurate and transferable for MD simulations of crystalline silica[53], is expressed as:

$$E_{ij} = \frac{1}{4\pi\epsilon_0}\frac{q_i q_j}{r_{ij}} + A_{ij}\exp\left(-\frac{r_{ij}}{\rho_{ij}}\right) - \frac{C_{ij}}{r_{ij}^6}, \quad \text{Eq. 4.1}$$

where E_{ij} is the energy between the i_{th} and j_{th} particles, q_i and q_j are the atom charges, r_{ij} is the distance between atoms, and A_{ij}, ρ_{ij}, and C_{ij} are additional parameters defined in the original paper[207]. The BKS potential cannot model high-energy particles because it diverges at small interatomic distances (Fig. 4.1). To remedy this, the present MD simulations used the ZBL potential at short interatomic distances. This potential is expressed as:

$$E_{ij}^{ZBL} = \frac{1}{4\pi\epsilon_0}\frac{Z_i Z_j e^2}{r_{ij}}\phi\left(\frac{r_{ij}}{a}\right) + S(r_{ij}), \quad \text{Eq. 4.2}$$

where ϵ_0 is the vacuum permittivity, e is the electron charge, S is a switching function, Z_i and Z_j are the nuclear charges of the atoms, and $\phi\left(\frac{r_{ij}}{a}\right)$ is an exponential function. In this work, the BKS potential is smoothly splined to the ZBL potential for the purposes of calculating the TDEs for the oxygen and silicon atoms in α-quartz. The developed exponential spline (Fig. 4.1), with defined attachment and detachment points (DPs), is expressed as:

$$E_{ij} = \exp\left(B_0 + B_1 r_{ij} + B_2 r_{ij}^2 + B_3 r_{ij}^3 + B_4 r_{ij}^4 + B_5 r_{ij}^5\right), \quad \text{Eq. 4.3}$$

where the B's are the spline coefficients. The expression in Eq. (4.3) allows the BKS potential to smoothly transition into the ZBL potential at small interatomic distances, expected at high temperatures and pressures. It also maintains the high accuracy of the BKS potential at ambient conditions.

The Pedone[217] potential, developed to model oxides, while keeping a constant O-O term, is expressed as:

$$E_{ij} = \frac{q_i q_j e^2}{r_{ij}} + D_{ij}\left\{\left[1 - e^{-\alpha_{ij}\left(r_{ij} - r_{ij}^0\right)}\right]^2 - 1\right\} + \frac{F_{ij}}{r_{ij}^{12}} \quad \text{Eq. 4.4}$$

where D_{ij}, α_{ij}, r_{ij}^0, and F_{ij} are parameters. Unlike the BKS potential, the Pedone potential already includes a repulsive core (Eq. (4.4) and Fig. 4.2). Fig. 4.2a and 4.2b figure compares the potential energy as a function of interatomic distance for both the BKS-ZBL and Pedone potentials.

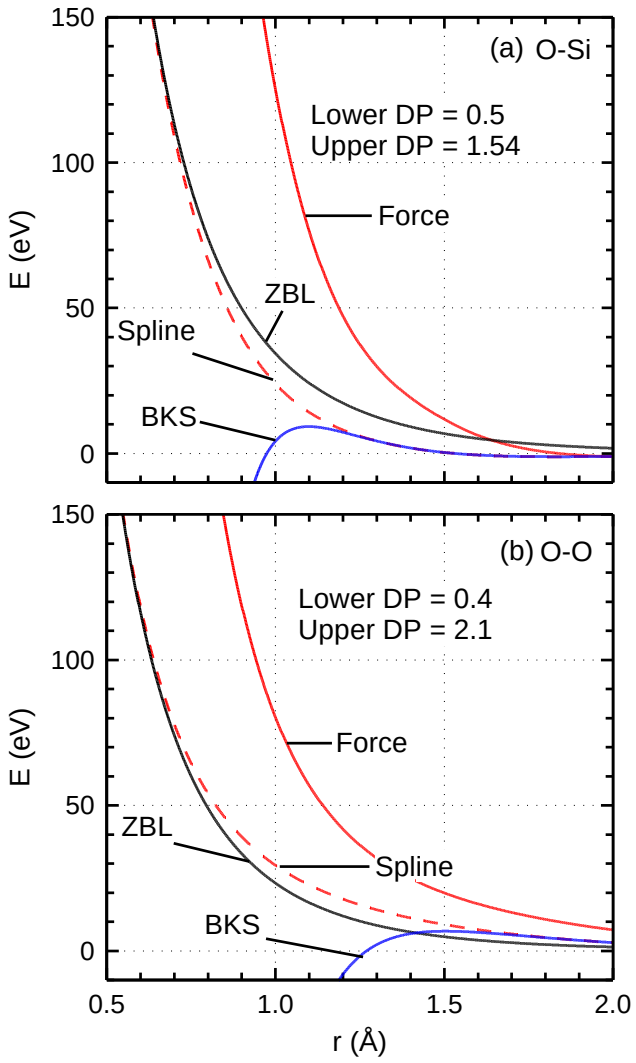

Figure 4.1: The splined BKS-ZBL potential and force curves for O-Si and O-O pairs.

The TDEs for the oxygen and silicon atoms in α-quartz are determined by incrementally increasing the energy given to a random PKA until it is permanently displaced from its original lattice site. The PKA energy increased in increments of 1.0 eV up to 150 eV. A very large number of MD simulations are performed to account for the anisotropy of the various directions and locations of the atoms within the crystal lattice. Each of the three perpendicular planes (XY, XZ, and YZ) are divided into 24 evenly spaced directions.

Owing to the orthogonal nature of these planes, six of these directions are duplicates. Thus, 66 directions are examined for each random PKA. A total of six oxygen and three silicon atoms are investigated (one representing each atom in the α-quartz primitive cell),

yielding 89,100 MD simulations for each potential investigated. Fig. 4.3 indicates the unique positions of the atoms. The following section presents the probability-based statistical averages of the calculated TDEs (Figs. 4.4-4.11).

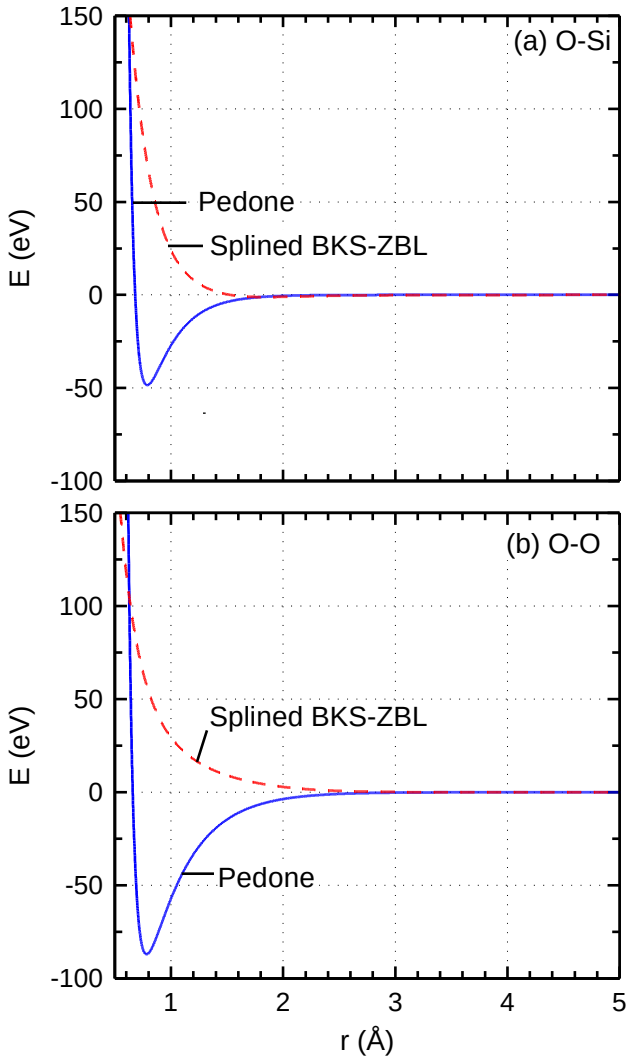

Figure 4.2: Comparison of potential energies for the BKS-ZBL and Pedone potentials.

4.1.2 Results

Presented in this section are the results of the effects of the simulation time and time step, as well as the potential cutoffs, on the probability-based statistical averages of the TDEs for the oxygen and silicon atoms in α-quartz.

4.1.2.1 **Effects of time step and simulation time**

Figs. 4.4 and 4.5 plot the obtained probability distributions of the TDE of a silicon atom using different total simulation times and time steps. Results show that using a simulation time > 1.0 ps and a time step < 0.2 fs negligibly affects the TDE probability values. The results for a 0.5 fs time step are not shown in Fig. 4.5 because it is too large, causing the atoms to become too close to one another. Based on the results in Figs. 4.4 and 4.5, the performed MD simulations in the remainder of this section use a 0.2 fs time step and a total simulation time of 1 ps. Using a variable time step algorithm is also an option, but for such short simulations and low PKA energies (≤ 150 eV), using a fixed time step suffices.

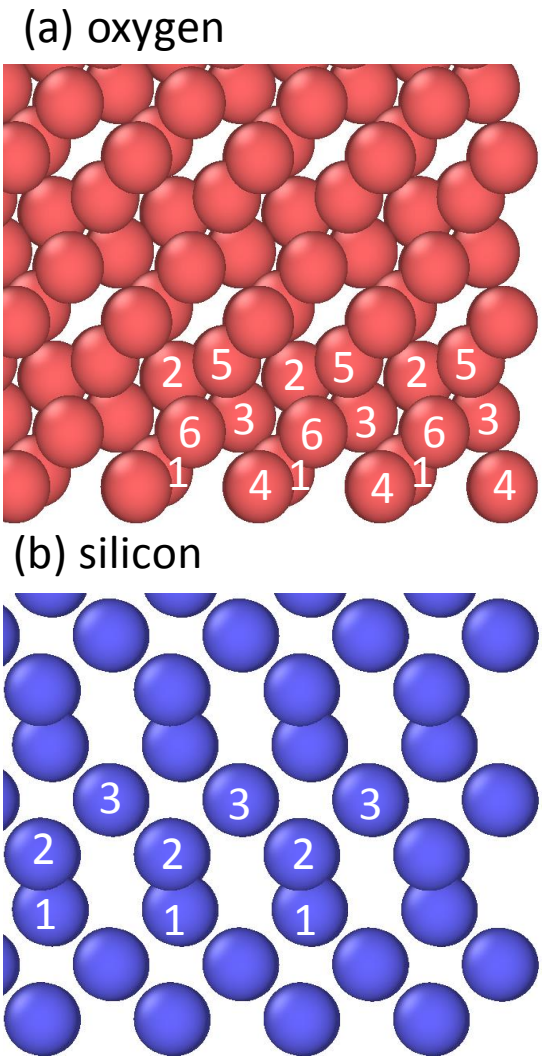

Figure 4.3: Crystal structure of sub-lattices in α-quartz.

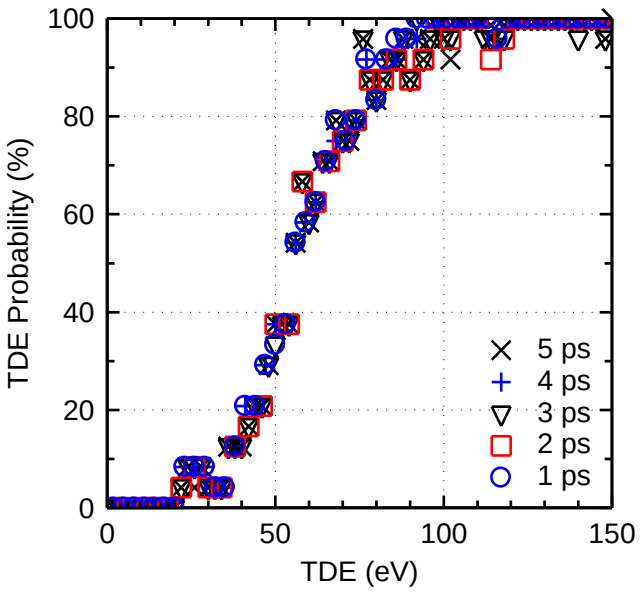

Figure 4.4: Effect of simulation time on the TDE probability distribution of a silicon atom in α-quartz.

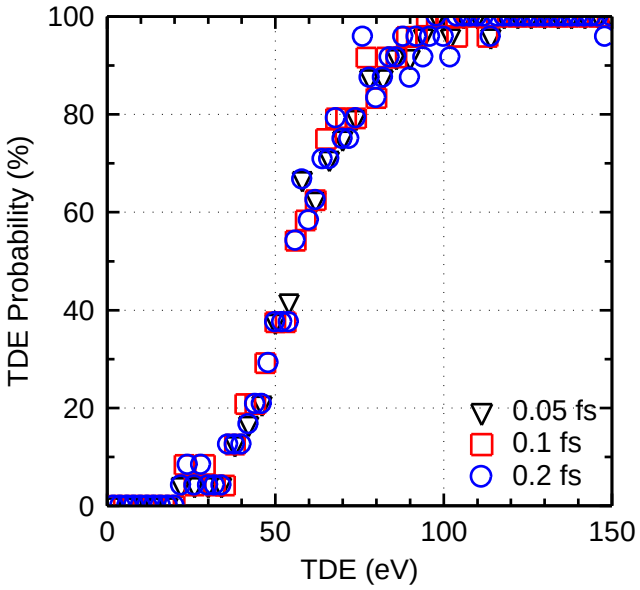

Figure 4.5: Effect of time step on the TDE probability distribution of a silicon atom in α-quartz.

4.1.2.2 **Effects of atom locations on the TDE**

Crystalline materials exhibit anisotropic properties, resulting in various TDEs, depending on the location of the atom within the crystal lattice. As shown in Fig. 4.3, the primitive cell

of α-quartz contains nine atoms (6 oxygen and 3 silicon). All other atoms are just replications of the primitive cell. Fig. 4.6 compares the calculated TDE probabilities for all atoms within the primitive cell using the BKS and Pedone Long potentials. The most notable difference is the first oxygen atom investigated at PKA energy of 41 eV. For the same TDE, the probabilities between the two potentials differ by 47.5%.

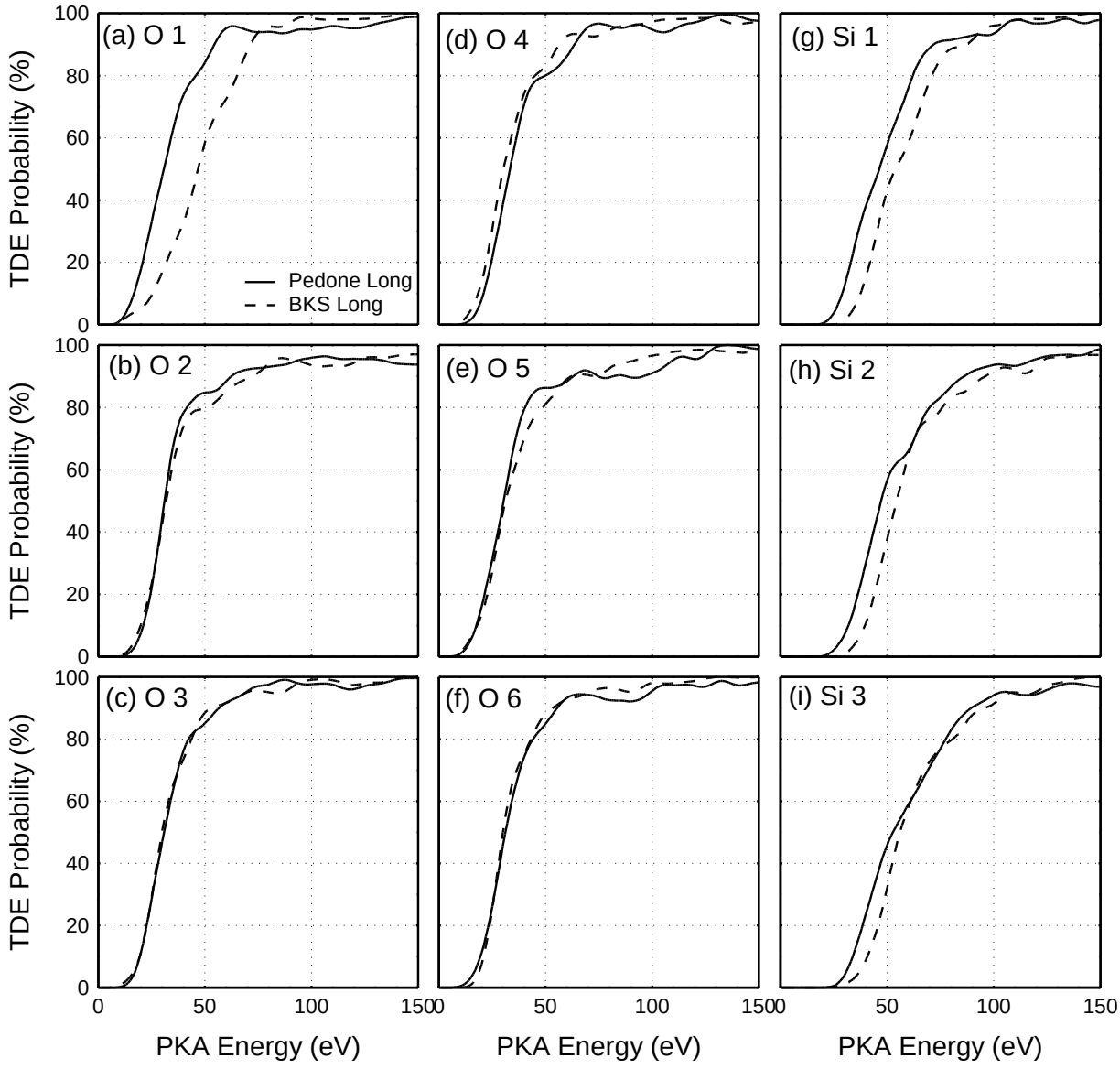

Figure 4.6: Dependence of TDE probability on various atom locations within a crystal lattice of α-quartz.

To identify the effect on the results, Fig. 4.7 plots the oxygen TDEs using the BKS and Pedone Long potentials, based on averaging those of the last five oxygen atoms (5), and all

six oxygen atoms (6). There is a difference between the values with the BKS Long (5) and BKS Long (6), but not between the Pedone Long (5) and Pedone Long (6). The results with the BKS (5) compare well with both the Pedone (5) and Pedone (6). For consistency, the remainder of the paper used all atoms when calculating the TDEs average probability distributions.

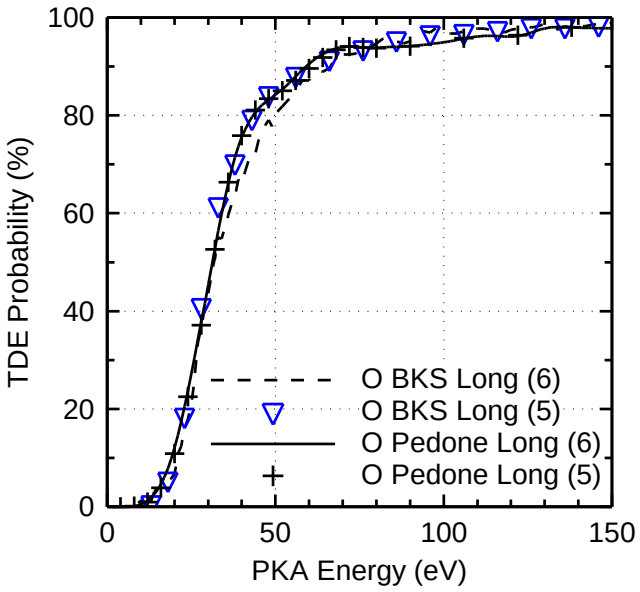

Figure 4.7: Effect of using 5 and 6 oxygen atoms for averaging the calculated TDEs for the oxygen atoms with the BKS Long and Pedone Long potentials in α-quartz.

4.1.2.3 **TDE probability-based statistical averages**

Fig. 4.8 compares the calculated distributions of the probability-based statistical averages of the TDEs for both the oxygen and silicon atoms, using the BKS Short and Long potentials. Results show that the choice of the potential cutoffs with the BKS-ZBL potential affects the TDE averages by as much as ~30% and by ~20% for the oxygen and silicon atoms, respectively. Fig. 4.9 compares the calculated combined TDE probabilities for the oxygen and the silicon atoms with the BKS Short and Long potentials. The combined probability is the weighted average for the oxygen and silicon atoms, considering that there are two oxygen atoms for every silicon atom. The results in Fig. 4.9 show a difference in the TDE values in the 15-60 eV range for the BKS potential with the short and long cutoffs. At lower energies, the short cutoff gives a ~20% higher TDE probability for a PKA permanent displacement, than the longer cutoff. The TDE probability curves for the individual oxygen and silicon

atoms, when combined for determining the total TDE probability, tend to overlap at the low and high energies (Fig. 4.9).

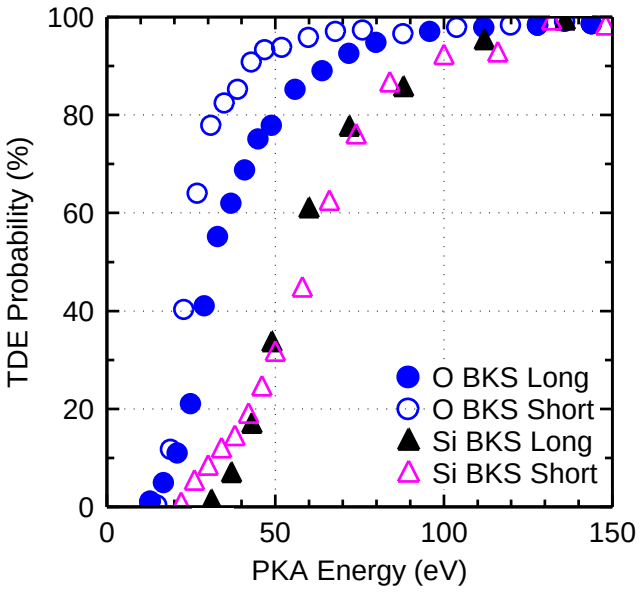

Figure 4.8: Effect of the BKS potentials on the calculated TDE probability-based statistical averages for the 6 oxygen and 3 silicon atoms in α-quartz.

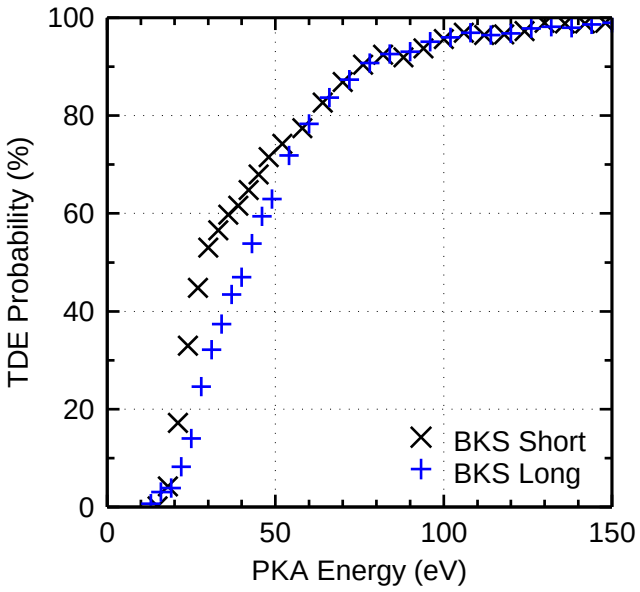

Figure 4.9: Effect of the BKS cutoff on the TDE weighted probability curves for both the 6 oxygen and 3 silicon atoms in α-quartz.

4.1.2.4 **Comparison of the BKS and Pedone potentials**

This section presents the MD simulation results with the BKS and Pedone Long potentials. Fig. 4.10 compares the calculated TDE probability curves for both oxygen and silicon atoms, using the Pedone and the BKS Long potentials. The TDE probability averages with the Pedone Long potential nearly match those with the BKS Long potential, predicting slightly higher values for both the oxygen and silicon atoms throughout most of the investigated energy range.

Table 4.1 compares the calculated TDEs associated with the various probabilities. The TDE values with all three potentials are in good agreement for the oxygen atoms at 1% probability (10.8-12.3 eV), which may be considered the minimum TDE. The TDE for the silicon atoms at this probability varies, depending on the potential used. For instance, the TDE values with the BKS Long and Short potentials differ, with the latter predicting a TDE of 20.5 eV and the former predicting 29.6 eV. The BKS Short potential predicts lower TDE values for the oxygen atoms, and higher values for the silicon atoms, throughout the entire energy range in Table 4.1, except at 1% probability.

Table 4.1: Comparison of the calculated TDEs for oxygen and silicon atoms in α-quartz at different probabilities, using various potentials.

Potential	Calculated Probability-Based TDEs (eV)											
	1%		33%		50%		67%		80%		90%	
	O	Si	O	Si	O	Si	O	Si	O	Si	O	Si
BKS Short	12.3	20.5	21.9	51.0	24.9	60.8	28.6	70.2	33.9	78.1	43.9	98.5
BKS Long	10.8	29.6	27.4	48.4	32.4	54.9	40.2	63.4	50.2	74.5	65.7	91.9
Pedone Long	11.5	22.8	26.7	40.8	31.2	47.7	36.3	58.9	43.3	68.7	59.1	83.8

At the high probability of 80%, the calculated TDE values for the silicon atoms using all three potentials are generally in good agreement (74.5–78.1 eV). However, the results are more divergent for the oxygen atoms, with TDE values of 33.9, 50.2, and 43.3 eV using the BKS Short, BKS Long, and Pedone Long potentials, respectively. The calculated value of 50.2 eV at 80% probability using the BKS Long potential, corresponds well to the reported

experimental value for the oxygen atoms (50 eV)[104]. As shown in Fig. 4.11, at higher energies, the TDE probabilities approach 100% for both atom types.

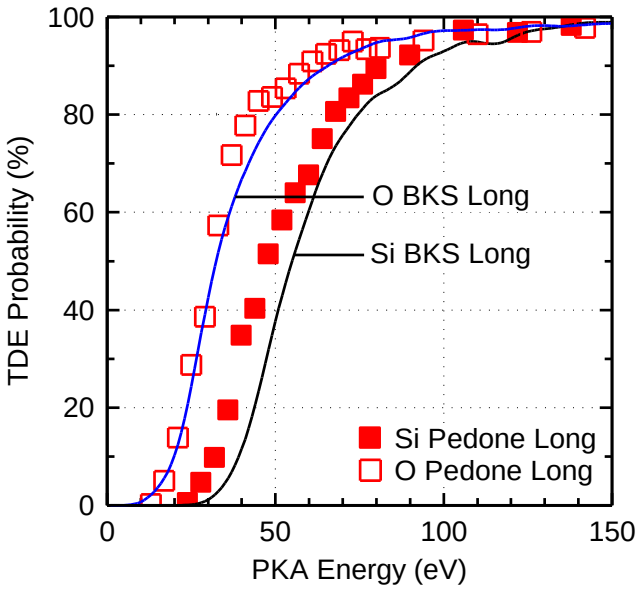

Figure 4.10: Comparison of the calculated TDE probability curves with the BKS Long and Pedone Long potentials, for the 6 oxygen and 3 silicon atoms in α-quartz.

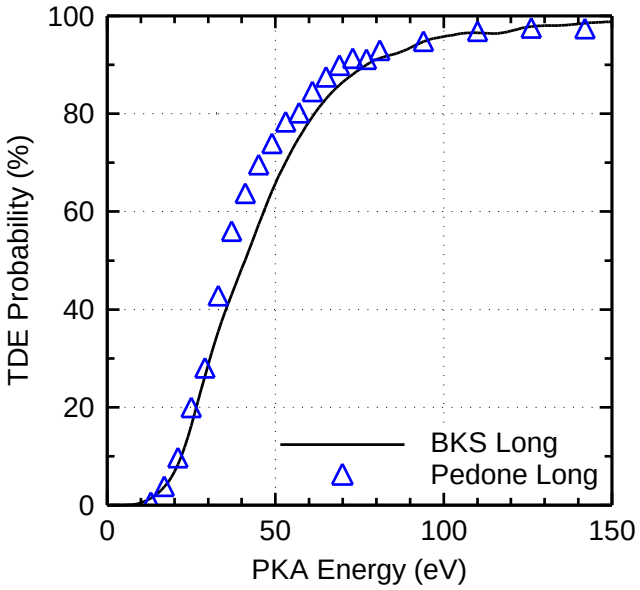

Figure 4.11: Comparison of the TDE weighted probability curves, with the BKS Long and Pedone Long potentials, in α-quartz.

The calculated TDE values for the oxygen atoms at 50% probability with the BKS Short, BKS Long, and the Pedone Long potentials are 24.9, 32.4, and 31.2 eV, respectively. Mota et

al.[302] found that a stable defect was produced in fused silica (ODC) at 30 eV, which corresponds to a probability of 50%. Thus, the present TDEs in α-quartz are comparable to the energy required to produce a stable defect in fused silica. At 50% probability, the TDE values calculated using the BKS Short, BKS Long, and Pedone Long potentials for the silicon atoms are 60.8, 54.9, and 47.7 eV, respectively. The values corresponding to a 67% probability with the BKS Short potential (28.6 and 70.2 eV) compare almost perfectly with the single values reported by Wang et al.[51] (28.9 and 70.5 eV), which are shown in Table 4.2. The experimental results by Arnold[104] showed that the TDE for the oxygen atoms in quartz is 50 eV, which based on the present results (Table 4.1), has an 80% probability with the BKS Long potential. Table 4.2 compares the present TDEs with 50% and 90% probabilities, with theoretical and experimental results obtained elsewhere. The calculated probability distributions of the TDEs would be more useful than a single TDE value, and often a better option for predicting the radiation damage in the bulk material.

Table 4.2: Comparison of calculated TDEs for oxygen and silicon atoms in α-quartz with probabilities of 50% and 90%, to prior theoretical and experimental values.

		Calculated Probability-Based TDEs						
		Wang et al.[51]	This Work					
		BKS Short	BKS Short Probability		BKS Long Probability		Pedone Long Probability	
PKA	**Exp.[104]**		50%	90%	50%	90%	50%	90%
Oxygen	50 eV	28.9 eV	24.9 eV	43.9 eV	32.4 eV	65.7 eV	31.2 eV	59.2 eV
Silicon	-	70.5 eV	60.8 eV	98.5 eV	54.9 eV	91.9 eV	51.9 eV	87.6 eV

4.1.3 Highlights and Concluding Remarks

MD simulations are performed to determine the TDEs for oxygen and silicon atoms in α-quartz using a smoothly splined BKS-ZBL potential and the Pedone potential, a system of 4,068 atoms, a time step of 0.2 fs, and 1.0 ps total simulation time. The simulations increased

the PKA energy in increments of 1.0 eV up to 150 eV. Investigated are the effects of the potential cutoffs on the probability-based statistical averages of the TDEs.

Results show that total simulation time > 1.0 ps and a time step < 0.2 fs insignificantly alters the TDE probability-based statistical averages. The simulations with all three potentials (BKS Long and Short and Pedone Long) predict a similar TDE value (10.8-12.3 eV) at the 1% probability for the oxygen atoms, but not for the silicon atoms. The TDE values for the silicon atoms at 1% probability are 20.5, 29.6, and 22.8 eV, for the BKS Short, BKS Long, and Pedone Long potentials, respectively. The reason for the large discrepancies among the BKS potential with the short and long cutoffs are most likely due to the change in structural properties that are directly associated with the cutoff chosen.

The values of the TDE at 50% probability for the oxygen atoms are 24.9, 32.4, and 31.2 eV for the BKS Short, BKS Long, and Pedone potentials, respectively. These energies are comparable to that of Mota el. al,[302] reporting a 50% probability for an oxygen atom to create a stable defect in fused silica at 30 eV. For the silicon atoms at 50% probability, the calculated TDEs are 60.8, 54.9, and 51.9 eV, with the BKS Short, BKS Long, and Pedone Long potentials, respectively. Typically, a single TDE is used in the input to radiation damage codes to predict defects in bulk materials. However, the probability-based TDEs (Figs. 4.1-4.11) would give results that are more realistic. Thus, the present results are valuable input to future investigations of the effect of irradiation on the silica-based additives in ATFs. In order to compare the TDE with that of other oxides of interest, the next section uses the Pedone potential to investigate the TDE in SiO_2, TiO_2, Al_2O3, Cr_2O_3, and MgO.

4.2 TDE Probability Distributions and Directional Dependence in SiO_2, TiO_2, Al_2O_3, Cr_2O_3, and MgO

The objectives of this study are to conduct MD simulations in 66 crystallographic directions using adequate system sizes and the Pedone interatomic potential to determine the directional dependence of the TDEs in Cr_2O_3, Al_2O_3, TiO_2, SiO_2, and MgO, and track defect formation on both cation and anion sublattices. The use of the Pedone potential in the MD simulations of the five oxides of interest is validated by comparing the calculated material properties and equation of states with experimental results. Also investigated are the probability distributions for the displacement of the PKA and any atom in the lattice, as well as the average number of Frenkel pairs produced, based on the results is all 66

crystallographic directions. The calculated TDEs are compared with experimental results and those reported by others using MD simulations, when available.

4.2.1 Methodology

LAMMPS[249] is used to conduct the present MD simulations, with a system size of 4,320 atoms for Cr_2O_3 and Al_2O_3, 4,608 atoms for TiO_2 and SiO_2, and 4,096 atoms for MgO. These oxides [Cr_2O_3 (eskolite), Al_2O_3 (corundum), TiO_2 (rutile), SiO_2 (α-quartz), and MgO (periclase)], are all crystalline. The crystal structure is trigonal for SiO_2, Cr_2O_3, and Al_2O_3, tetragonal for TiO_2, and cubic for MgO. The Pedone potential is expressed as:

$$E_{ij} = \frac{q_i q_j}{r_{ij}} + D_{ij}\left\{\left[1 - e^{-\alpha_{ij}(r_{ij}-r_o)}\right]^2 - 1\right\} + \frac{F_{ij}}{r_{ij}^{12}} \qquad \text{Eq. 4.5}$$

The right-most term in this expression is a strong repulsive term, which is useful in high-temperature and/or high-pressure simulations. Prior work has shown that Pedone and BKS+ZBL potentials produced similar TDE probability distributions in SiO_2.[54] The Pedone and ZBL potentials are compared at short interatomic distances in Fig. 4.12.

The performed MD simulations with the Pedone potential set the cutoff at 15 Å and the relative error of the particle-particle particle-mesh (PPPM) solver for the Coulomb interactions to $1x10^{-6}$. In addition, the simulations used the Polak-Ribiere version of the conjugate gradient (CG) algorithm to perform energy minimization of the atoms. The systems of atoms used are equilibrated in an NPT ensemble at 300 K and 1.0 atm for 20 ps. The data on the structural properties for the oxides is gathered over the second half of the equilibration period. In the final preparation before initiating the simulations, the systems of atoms for the different oxides are equilibrated in the NVE ensemble for 10 ps. The radiation damage cascades are also carried out in the NVE ensemble.

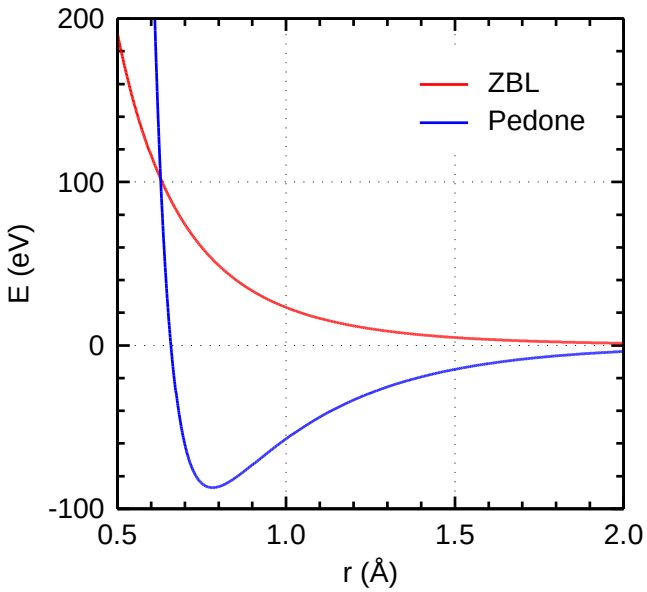

Figure 4.12: Comparison of the ZBL and Pedone potentials at short interatomic distances.

A time step of 0.2 fs and a total simulation time of 1 ps are found adequate for the low-energy PKAs;[54] as the produced defects typically anneal within 1 ps for low PKA energies. Simulations were also run for up to 10 ps for 24 crystallographic directions in Al_2O_3 to determine the sensitivity of the results to the total simulation time. Fig. 4.13a shows that the average number of Frenkel pairs produced with PKA energies < 150 eV does not change when the total simulation time is varied from 1-3 ps. Above this energy, there are slight differences; however, the average number of defects produced does not vary by more than 0.1-0.2 defects for simulation times of 2-3 ps. Fig. 4.13b show that the average number of displaced atoms does not change significantly for simulation times up to 10 ps. At PKA energies above 200 eV, the average number of displaced atoms changes by less than 0.2-0.3 displaced atoms for simulation times up to 10 ps. Thus, it is worth acknowledging that the average number of defects produced varies with simulation time, but the differences are small and will not significantly affect the results. In order to run such an extensive set of simulations as outlined previously, the simulation time is thus kept at 1 ps.

The present MD simulations varied the energies of the oxygen PKAs from 1.0 to 400 eV in increments of 1 eV and those of the metal PKAs in increments of 1 eV, for energies from 1.0 to 50 eV, and 10 eV above that, up to 350 eV. For each oxide, the MD simulations investigated 3 oxygen and 3 metal PKAs, except for SiO_2, the simulations used six oxygen

PKAs. The PKA angles changed in increments of 15° in three separate planes (XY, XZ, and YZ), for a total of 360°, and 24 directions in each plane. However, 6 of these directions are duplicates from one plane to another, leaving 66 unique PKA directions for calculating the TDEs. Therefore, the oxygen PKAs each undergoes a total of 26,400 simulations, and each metal PKA undergoes a total of 5,280 simulations, in which the energy and direction are varied. In addition, the TDE probability distribution curves for the oxygen PKAs represents 79,200 simulations, and those for the metal PKAs represents 15,840 simulations. Each probability curve is generated by averaging the probabilities of causing displacements over all 66 crystallographic directions and all 3 PKAs at a given energy.

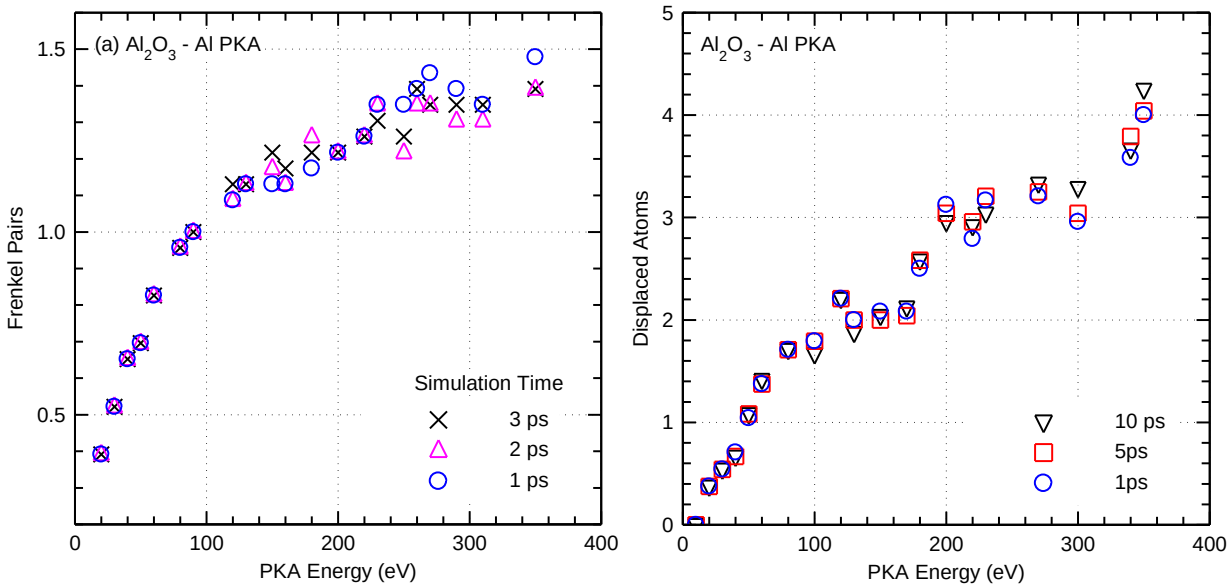

Figure 4.13: Comparison of the average (a) number of Frenkel pairs and (b) displaced atoms in 24 crystallographic directions, with Al PKAs in Al_2O_3, for different simulation times.

4.2.2 Results

The first section presents the TDE directional dependence for the different oxides with regards to PKA displacement and Frenkel pair formation. The second and third sections summarize the extensive data presented in the first section. The fourth section presents and discusses the TDE averages, including displacement probabilities, Frenkel pair formation, and total number of displaced atoms. The results are then compared to prior MD and experimental results, when available. Lastly, key findings from this work are presented and summarized.

4.2.2.1 **Directional Dependence**

This section presents and discusses the results of the directional dependence of the TDEs for the formation of stable oxygen and metal atom Frenkel pairs, with oxygen and metal PKAs, as well as the results for the displacement of the oxygen and metal PKAs. For each oxide investigated, the MD simulation results are presented in two sets of three polar plots. The polar plots are of the crystallographic directions corresponding to the (a) XY (b) XZ, and (c) YZ planes. The crystallographic directions in MgO and TiO_2 are represented using 3-index notation, whereas those in SiO_2, Cr_2O_3, and Al_2O_3, use 4-index notation. The directions using 4-index notation can be converted to 3-index notations corresponding to the XY, XZ, and YZ planes.

The first set of the polar plots is of PKA displacement (E_d) for the oxygen and metal PKAs. In each crystallographic direction investigated there are 6 E_d values, representing the 3 metal and 3 oxygen PKAs (note that for SiO_2, there are up to 6 oxygen PKAs). The absence of an E_d value indicates that the PKA, with all the energies investigated, is not displaced in that direction. The second set of polar plots is of Frenkel pair formation (E_{FP}) for the oxygen and metal sublattices with oxygen and metal PKAs. The individual sets of polar plots for E_d and E_{FP} of the oxygen and metal PKAs in the different oxides are presented and discussed sequentially.

4.2.2.1.1 MgO

Fig. 4.14 and Fig. 4.15 present the calculated E_d and E_{FP} values in 66 directions on both anion and cation sublattices in MgO. These planes are identical since MgO has a cubic lattice, which is not the case for the other oxides. Fig. 4.14 shows a high level of symmetry of E_d in MgO, amongst the low- and high-index directions, for both the oxygen and Mg PKAs. For instance, along the low-index directions of [100], [010], and [001] (identical in cubic materials), there is no oxygen PKA displaced for the energies investigated (≤400 eV), confirming the formation of a stable Frenkel pair is always associated with a PKA displacement. Results in Figs. 4.14 and 4.15 show that although oxygen PKAs with energies as low as ~57 eV are not displaced, they produce Mg Frenkel pairs.

For the 400 eV oxygen PKAs in the [100] direction, Fig. 4.16 shows the manner in which the PKA in MgO recoils back to its original lattice site, while still creating stable Frenkel pairs. In this case, the magnesium atom, knocked away from its lattice site (t = 4 fs), anneals

to a new site on a different plane (t = 500 fs). In this example, the oxygen PKA actually creates a line defect (t = 100 fs), which can be seen in the top plane in Fig. 4.16, and is highlighted in Fig. 4.17.

The E_d values for the Mg PKAs do not follow the same trend as those of the oxygen PKAs. In the low-index directions of [100], [010], and [001], the Mg PKAs are typically displaced at ~30 eV. Thus, while the oxygen PKAs are more likely to recoil off the nearest neighboring Mg atoms and return to their original lattice sites, the Mg PKAs are more likely to become displaced. Along the [110], [101], and [011] directions, and even in the directions inclined by 15°, the energy for a displacement of the Mg PKA is higher, ~100 eV, and sometimes as high as ~250 eV. The higher E_d values of the Mg PKAs in these directions are because the secondary knock-on atoms (SKAs) are Mg atoms.

Result show that the Mg atom Frenkel pairs are likely formed by Mg PKAs. The energy required to form stable Mg atom Frenkel pairs with Mg PKAs is higher along the low-index directions, and lower along the high-index directions (Fig. 4.15). A similar pattern is shown for the formation of oxygen atom Frenkel pairs by oxygen PKAs, but at higher energies. However, the directional dependence and the symmetry of the formation of Mg and oxygen atom Frenkel pairs are different (Fig. 4.15a-c).

In the cubic MgO with oxygen and metal atom sublattices, for an oxygen atom to create an Mg atom Frenkel pair in low-index directions, it needs sufficient energy to displace the Mg atom that is directly next to it. However, it needs more energy in the high-index directions because the next closest Mg atom is significantly further away. Additionally, the PKA that travels in high-index directions is likely to slow down by the Coulomb interaction with the surrounding atoms, thus by the time it reaches an Mg atom, it will have insufficient energy to displace it.

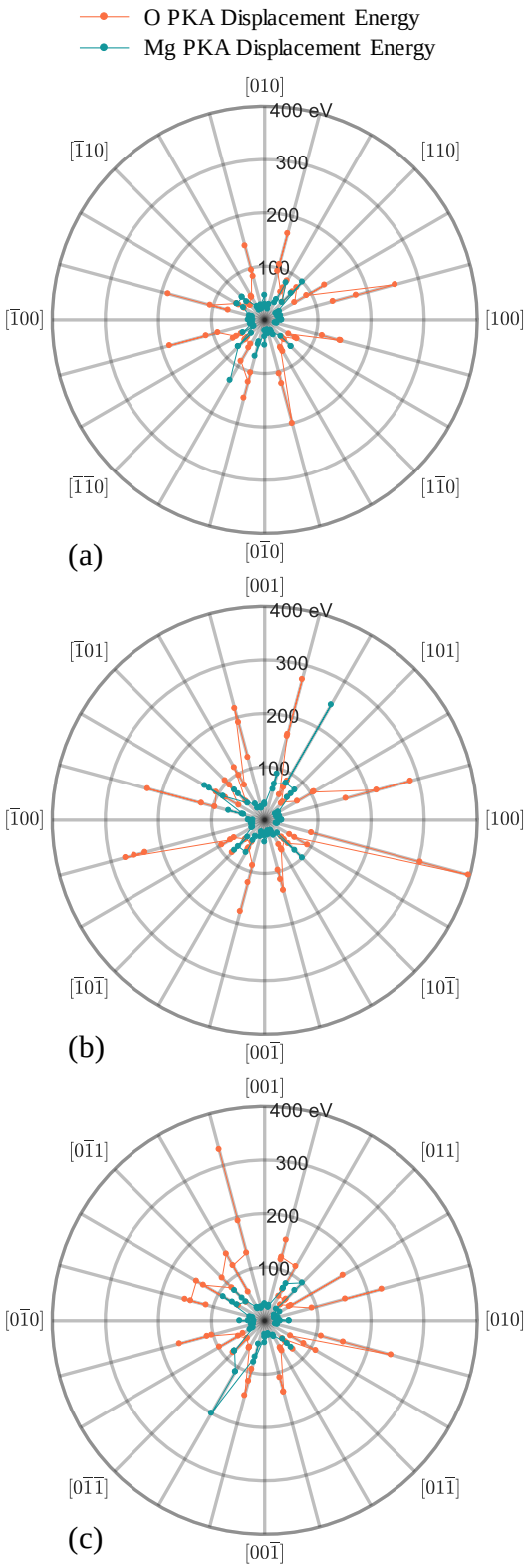

Figure 4.14: The calculated TDEs for the displacement (E_d) of the oxygen and Mg PKAs in MgO.

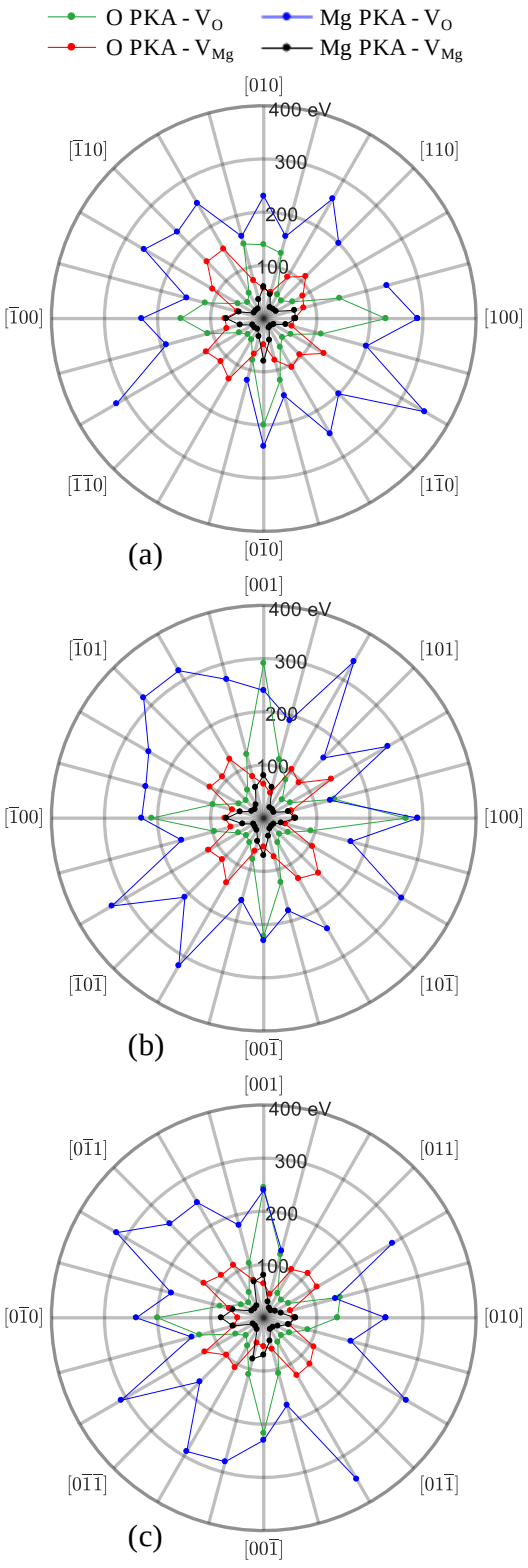

Figure 4.15: The calculated TDEs for the formation of a stable Frenkel pair (E_{FP}) with oxygen and Mg PKAs, on both the anion and cation sublattices in MgO.

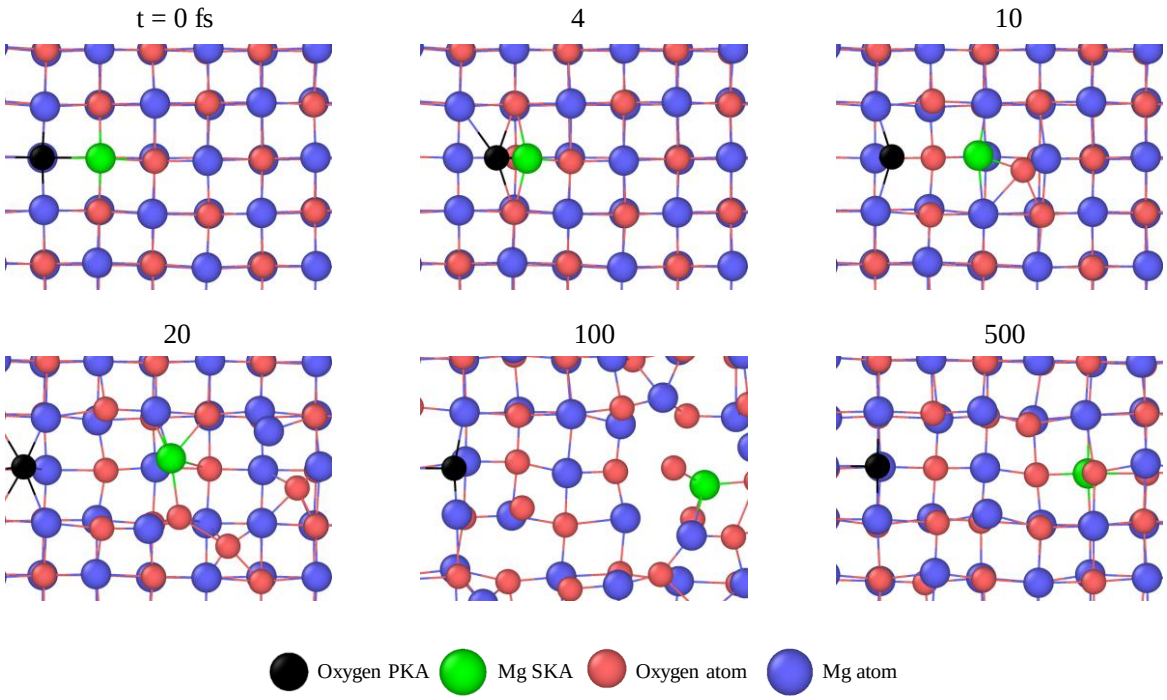

Figure 4.16: The timeline of a 400 eV oxygen PKA along the [100] direction in MgO.

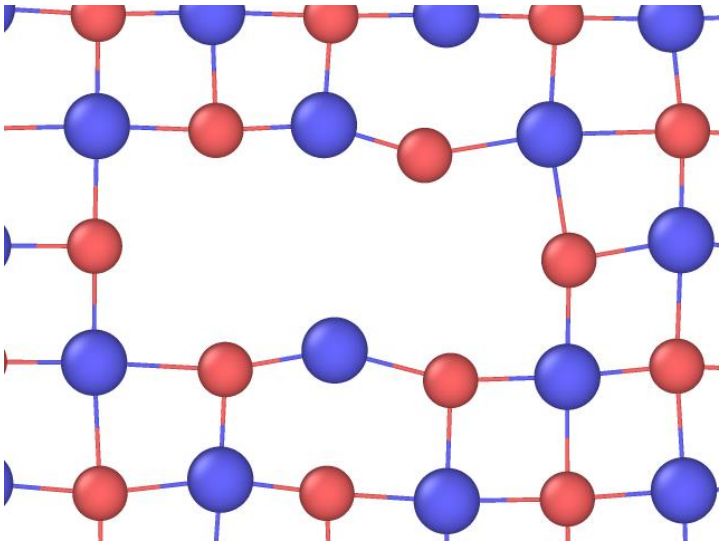

Figure 4.17: A line defect created by a 400 eV oxygen PKA in the [100] direction in MgO.

4.2.2.1.2 TiO_2

Fig. 4.18 and Fig. 4.19 present the E_d and E_{FP} values in 66 directions on both anion and cation sublattices in TiO_2. Fig. 4.18a shows that E_d for Ti PKAs is ~100–150 eV, with little variance amongst the directions. On the other hand, Figs. 4.18b,c show large variances in the

E_d values amongst the XZ and YZ planes. The energy for the displacement of Ti PKAs is largest in the [001] direction, ~200 eV, compared to ~100 eV for most other crystallographic directions in the plane. At 15° inclination from the [001] direction, E_d is ~150 eV. The high PKA displacement energies in the [001] crystal direction is due to the direct collision with the same atom type.

The Ti atoms are octahedrally coordinated to 6 oxygen atoms, thus a direct collision of a Ti PKA with a Ti atom directly above it, often causes the Ti PKA to recoil to its original lattice site. The oxygen PKAs are also more likely to recoil in this direction compared to the other directions, but are displaced in the [001] direction at lower energies than the Ti PKAs.

The E_d values for the oxygen PKAs in TiO_2 are typically ~50–100 eV, but higher along the [001] and [110] directions (Fig. 4.18). In the [001] direction, the displacement energy of the oxygen PKA is slightly above 100 eV, and in limited cases in the [110] direction is much higher, >300 eV. However, it is important to note that in many cases in this direction, E_d values for the oxygen PKAs are significantly lower, ~40 eV.

Fig. 4.19 shows that the least likely defects to form in TiO_2 are titanium atom Frenkel pairs by oxygen PKAs. Because a Ti atom has ~3 times the mass of an oxygen atom, the latter is likely to recoil off of the Ti atom and return to its original lattice site. Conversely, the most likely defects to form in TiO_2 are oxygen atom Frenkel pairs with oxygen PKAs. Fig. 4.19a shows that for all 24 directions investigated, the energy for forming Ti atom Frenkel pairs with Ti PKAs is ~100 eV, but slightly more variable in the other directions in Figs. 4.19b,c. This could correspond to the variance in the Ti E_d values in those directions. It is worth mentioning that oxygen atom Frenkel pairs form in TiO_2 at lower energies with Ti PKAs than the Ti atom Frenkel pairs with oxygen PKAs. For the latter, the E_{FP} values in some crystallographic directions exceed 400 eV (Fig. 4.19). Fig. 4.20 shows a cross-sectional view of the TiO_2 lattice in the plane corresponding to Fig. 18b. The symmetry of the Ti PKA displacement energies in Fig. 18b,c is due to the location of the Ti atoms with respect to the Ti PKA. The larger E_d in [100], [001], etc., is because the Ti PKA directly recoils off the Ti SKA, marked with arrows in Fig. 4.20.

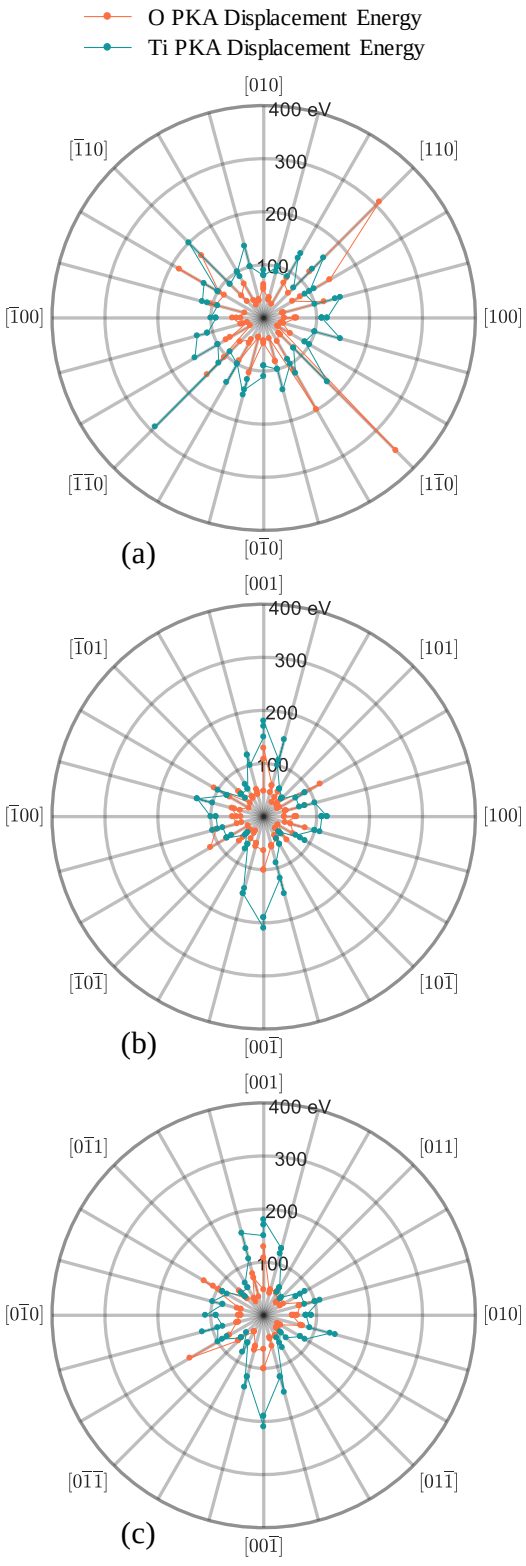

Figure 4.18: The calculated TDEs for the displacement (E_d) of the oxygen and Ti PKAs in TiO_2.

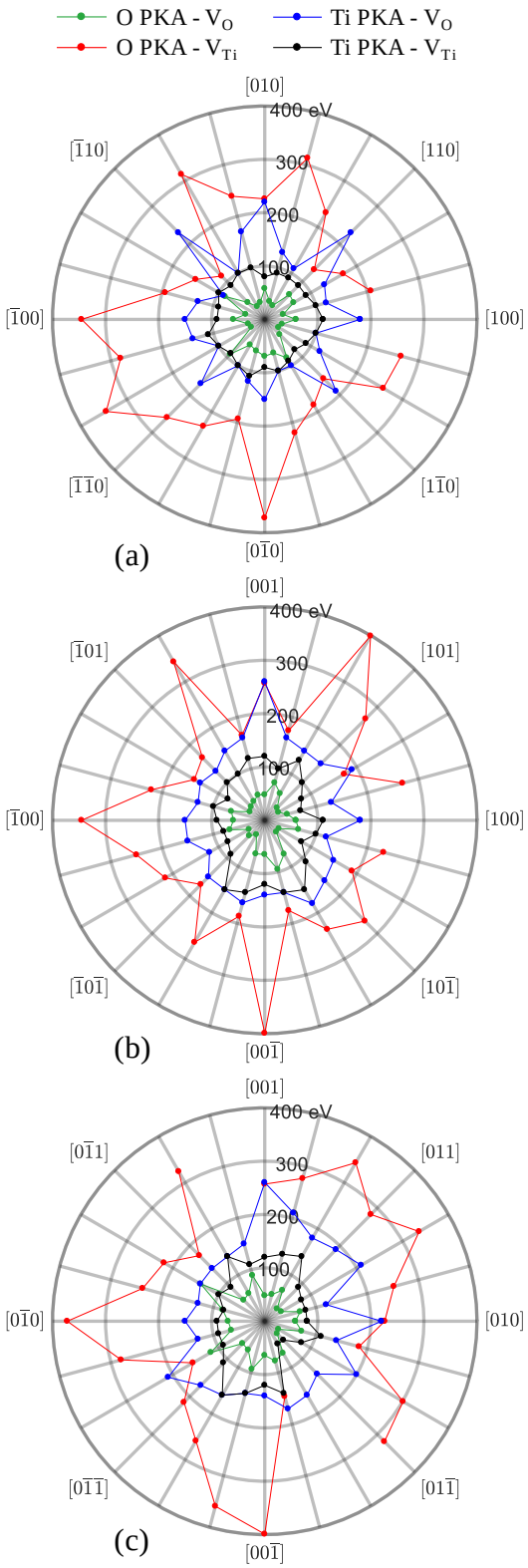

Figure 4.19: The calculated TDEs for the formation of a stable Frenkel pair (E_{FP}) with oxygen and Ti PKAs, on both the anion and cation sublattices in TiO_2.

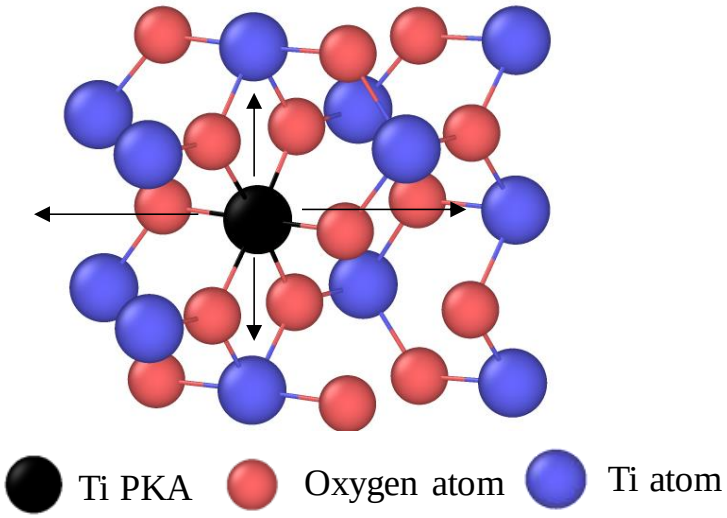

Figure 4.20: Cross-sectional view of the TiO_2 lattice in the plane corresponding to Fig. 10b.

For the results of the remaining oxides, discussed in the following subsections, the 3-index system is converted to 4-index, which is customarily used when representing crystallographic directions in hexagonal crystals. The trigonal crystals are part of the hexagonal crystal family and thus the results are presented using the 4-index system.

4.2.2.1.3 Cr_2O_3

Fig. 4.21 and Fig. 4.22 present the calculated E_d and E_{FP} values in 66 directions on both the anion and cation sublattices in Cr_2O_3. The E_d values for the Cr PKAs in Cr_2O_3 show an interesting symmetrical pattern (Fig. 4.21a). In the crystal directions $[11\bar{2}0]$, $[\bar{1}100]$, and $[1\bar{2}10]$, and those inclined from those directions by 15–30°, the E_d values for the Cr PKAs are ~60–90 eV, but as little as 12-40 eV in other directions. Along the $[2\bar{1}\bar{1}0]$ direction, the E_d values of the Cr PKAs are ~14 eV, but as high as ~80 eV within ±15° of the [0001] direction (Fig. 4.21b). Fig. 4.21c shows less variance amongst the displacement energies of the Cr PKAs, most are between 30–80 eV. Fig. 4.21a shows sporadic E_d values for the oxygen PKAs in Cr_2O_3, ranging from ~42–160 eV, with little symmetry. In the other planes in Figs. 4.21b,c, the oxygen E_d values in a few of the crystallographic directions are up to ~300 eV. The Cr PKAs with $E_d < 100$ eV create Frenkel pair defects, thus their displacement energies are much higher than those to create a stable Frenkel pair.

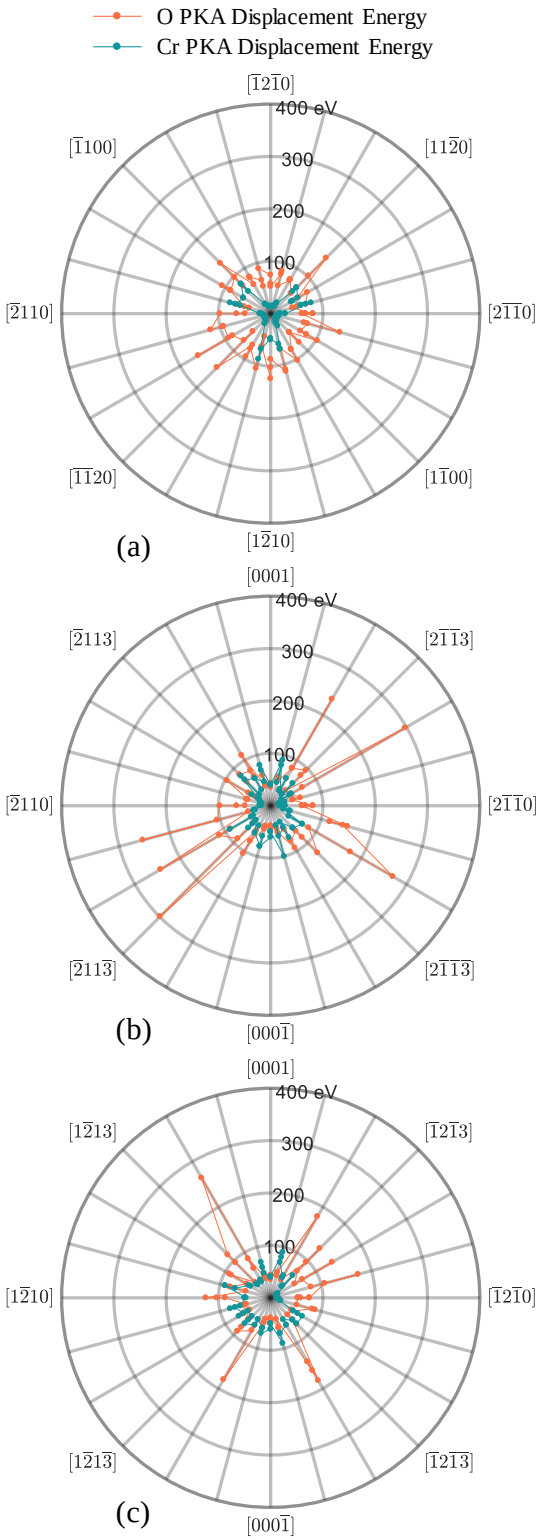

Figure 4.21: The calculated TDEs for the displacement (E_d) of the oxygen and Cr PKAs in Cr_2O_3.

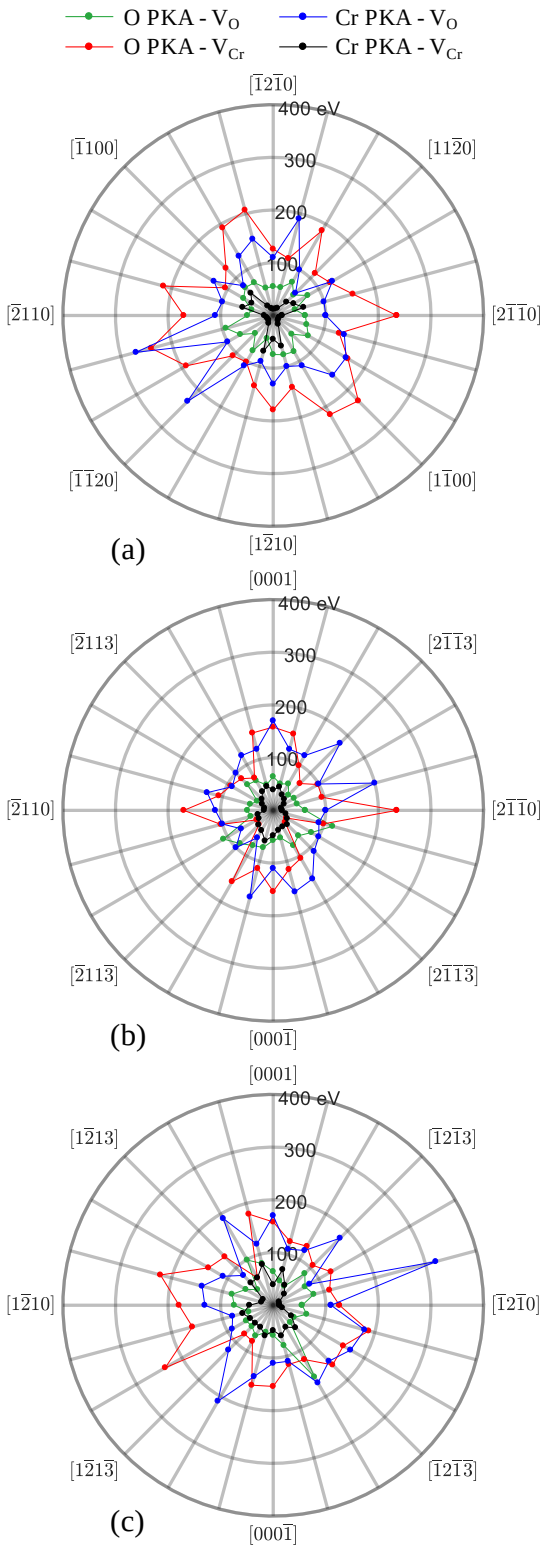

Figure 4.22: The calculated TDEs for the formation of a stable Frenkel pair (E_{FP}) with oxygen and Cr PKAs, on both the anion and cation sublattices in Cr_2O_3.

In Cr_2O_3, Cr atom Frenkel pairs are formed by Cr PKAs at relatively low energies (Fig. 4.22). However, the E_{FP} value is strongly dependent on the PKA direction. In many of the directions investigated, the E_{FP} values vary from ~11–22 eV (Fig. 4.22a). However, in several directions, such as $[11\bar{2}0]$, $[\bar{1}100]$, and $[1\bar{2}10]$ and angles slightly inclined from these directions, the E_{FP} values are larger, ranging from ~31–80 eV. These directions are those corresponding to angles in which the Cr PKA immediately collides with a nearby Cr atom. In the high-index directions, the Cr PKA easily escapes its original lattice site to become an interstitial, creating a Cr atom Frenkel pair. The formation of oxygen vacancies by the oxygen PKAs are the second-most likely point defect to form in Cr_2O_3 (Fig. 4.22). The PKAs that form point defects on a different sublattice are only those with energies >100 eV (Fig. 4.22a-c).

Fig. 4.23 shows a single XY plane of Cr_2O_3 atoms, which help identify the reasons for the symmetrical pattern of the E_d values in Fig. 4.21a. Results in Fig. 4.21a and 4.23 suggest that when a Cr PKA is displaced in the direction of another Cr atom, it is more likely to return to its original lattice site. The Cr PKAs displaced in the direction of the three voided areas in Fig. 4.23 are on a plane below that of the other Cr atoms, thus do not recoil to their original lattice site. The same scenario applies for Al_2O_3, discussed next.

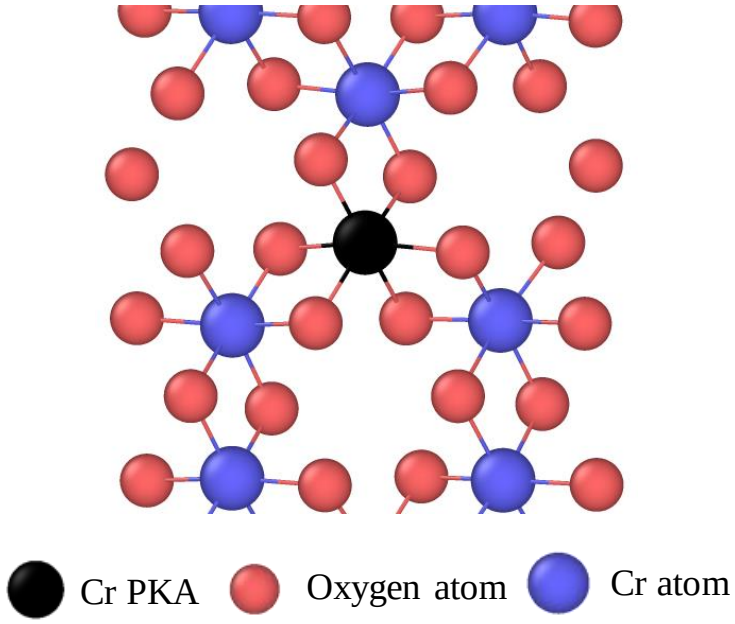

Figure 4.23: A single plane of Cr_2O_3 atoms highlighting the Cr PKA displacement kinetics.

4.2.2.1.4 Al_2O_3

Fig. 4.24 and Fig. 4.25 present the calculated E_d and E_{FP} values in Al_2O_3. The Al_2O_3, in 66 directions on both the anion and cation sublattices, exhibit similar characteristics to those in Cr_2O_3. This is expected since both oxides have the same crystal structure. Despite the difference in the metal atom size and mass (Al vs. Cr), the E_d values for the two oxides are virtually identical (Figs. 4.21, 4.24). The symmetry of the defects in Fig. 4.24a in Al_2O_3 is for the same reason explained earlier for Cr_2O_3. However, there are distinguishable differences in the E_{FP} (Fig. 4.25). The formation of oxygen atom Frenkel pairs with Al PKAs in Al_2O_3 occurs at higher energies than the formation of oxygen atom Frenkel pairs with Cr PKAs. This is likely because an Al atoms has ~½ the mass of a Cr atom.

4.2.2.1.5 SiO_2

Figs. 4.26 and Fig. 4.27 present the calculated values of E_d and E_{FP} in SiO_2, in 66 directions on both the anion and cation sublattices. Note that these values are much lower than for the other oxides investigated in this work. The E_d for the oxygen PKAs in SiO_2 appears to be independent of direction (Fig. 4.26). Many of the oxygen PKAs are displaced with E_d ~25 eV, and a few with higher E_d values, up to ~50 eV. The silicon PKAs are displaced with E_d values of ~25–75 eV.

The formation of stable Frenkel pairs in SiO_2 also occurs at very low PKA energies (Fig. 4.27). The oxygen atom Frenkel pairs form with oxygen PKAs energies of ~25 eV, which is roughly the same as the E_d of the oxygen PKAs. The formation of the silicon atom Frenkel pairs by oxygen and silicon PKAs, as well as the formation of silicon atom Frenkel pairs by oxygen PKAs, are equally likely with energies ranging from ~25 to 50 eV. The results also show that because the values of E_d and E_{FP} are similar, a PKA displacement is a good indication of the formation of a stable Frenkel pair in SiO_2.

4.2.2.2 **PKA Displacement Energies**

Based on the MD simulation results and the examination of many images in the five oxides investigated, the following observations can be made regarding the dependence of PKA displacement energy on the PKA type, crystal structure, and crystallographic direction (Table 4.3):

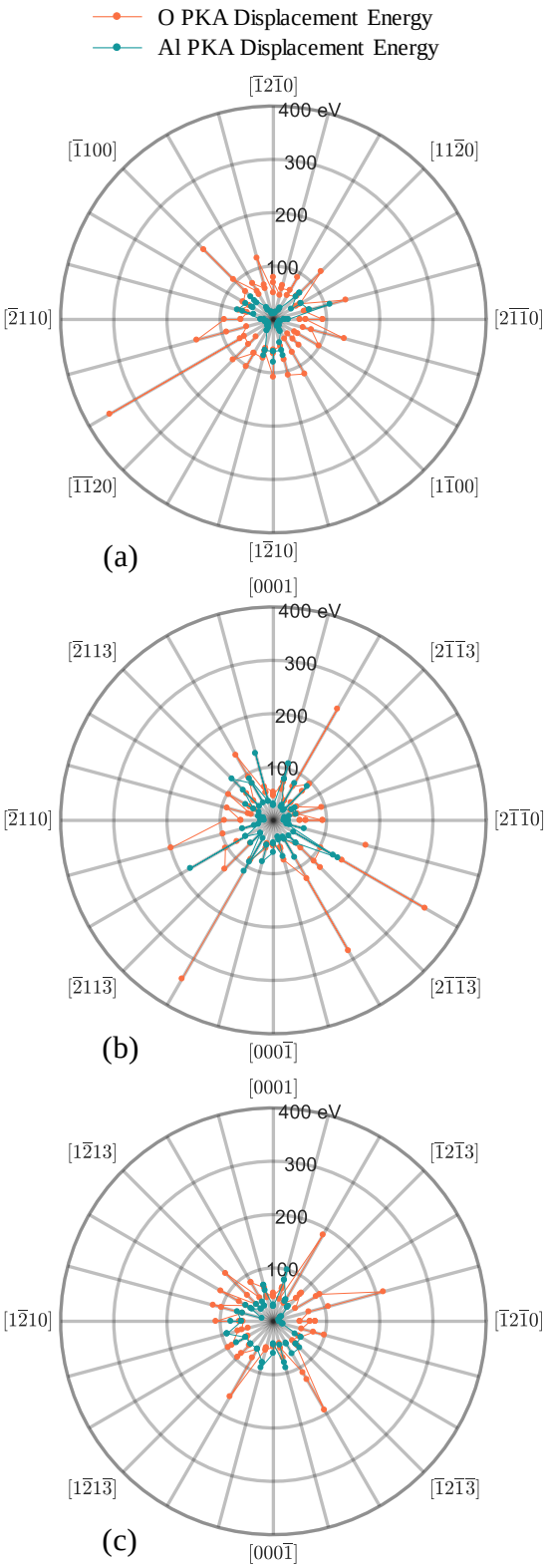

Figure 4.24: Calculated TDEs for displacement (E_d) of the oxygen and Al PKAs in Al_2O_3.

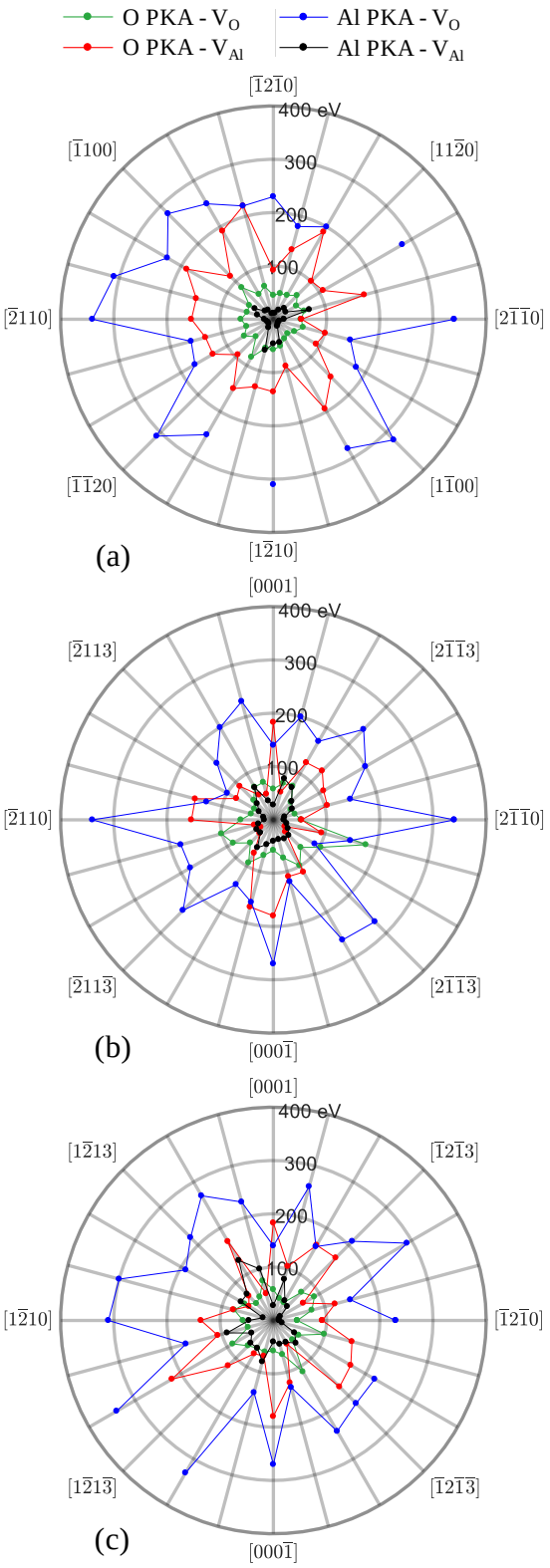

Figure 4.25: The calculated TDEs for the formation of a stable Frenkel pair (E_{FP}) with oxygen and Al PKAs, on both the anion and cation sublattices in Al_2O_3.

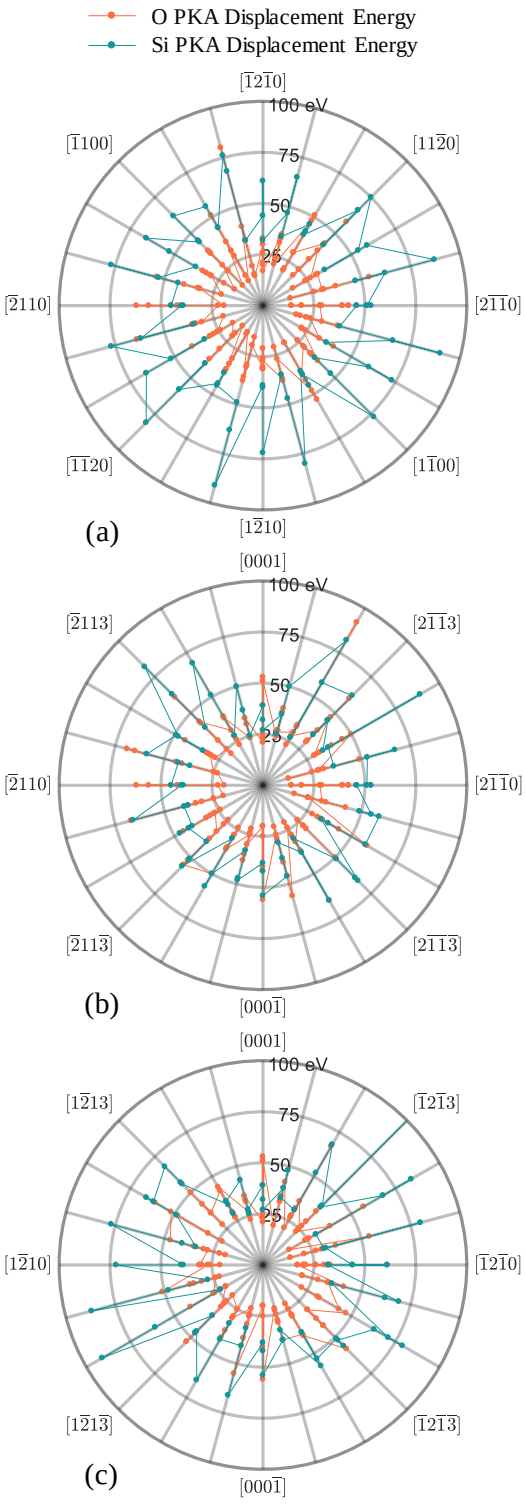

Figure 4.26: The calculated TDEs for the displacement (E_d) of the oxygen and Si PKAs in SiO_2.

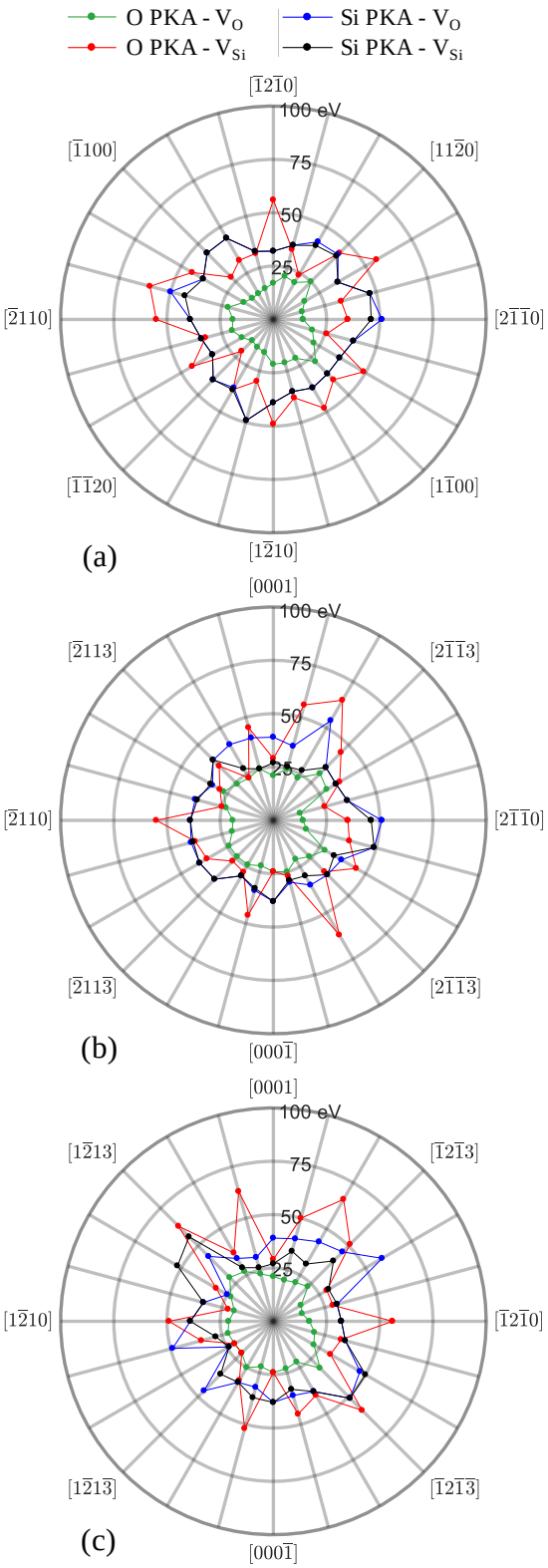

Figure 4.27: The calculated TDEs for the formation of a stable Frenkel pair (E_{FP}) with oxygen and Si PKAs, on both the anion and cation sublattices in SiO_2.

(1) In all the 66 directions investigated, the Mg PKAs in MgO are displaced at low energies (25-46 eV) (Table 4.3). However, the oxygen PKAs with energies up to 400 eV, are not displaced in the low-index directions of [100], [010], and [001]. In these directions, the oxygen PKAs collide with Mg atoms, recoiling back to their original lattice sites. In the other directions of [110], [101], and [011], the oxygen PKAs, with energies comparable to those of the Mg PKAs, are displaced. In these directions, the Mg PKAs may scatter off other Mg atoms, and the oxygen PKAs may scatter off other oxygen atoms.

(2) In TiO_2, the metal and oxygen PKA displacement energies in the [001] direction, in which the nearest neighbor is 3.014 Å, are higher than in the [100] and [010] directions, in which the nearest neighbor is further, 4.583 Å. In the low-index directions of [100] and [010], the Ti PKAs with energies of 110-120 eV are displaced and cause replacement collisions with another Ti atom. The replacement collision sequence in the [001] direction occurs at much higher energies (150-180 eV). Similar replacement collision sequences are experienced by the oxygen PKAs in the [100], [010], and [001] directions, but at lower energies. In the [110] direction, there are a wide range of energies for the displacement of the oxygen and titanium PKAs, depending on the type of the adjacent atoms in the lattice (Table 4.3). In the [101] and [011] directions, the oxygen and titanium PKAs with moderate energies undergo scattering collisions with other atoms and are displaced at low energies.

(3) In Cr_2O_3 and Al_2O_3, which have the same crystal structure, the energies to displace the oxygen and metal PKAs are nearly identical, despite the fact that the Cr atom has about twice the mass of the Al atom. This suggests that the atom mass is of a minor role for the displacement of the oxygen and metal PKAs in these oxides. In both oxides, the metal PKAs in the [010] direction engage in a glancing or scattering collision with another metal atom. In the [100] and [001] directions, the metal PKAs collide with metal atoms, recoiling back to their original sites in the lattice, requiring high energies for displacement (Table 4.3).

(4) The energies for displacing the oxygen PKAs in SiO_2 in the [001] direction are higher than in the [100] and [010] directions; however, the opposite is true for the Si PKAs. The higher displacement energies of the Si PKAs are because they are more likely to engage in replacement collisions than the oxygen PKAs. These observations are in agreement with results by Wang et al.[51] Furthermore, the present MD simulation results show that the oxygen PKAs in SiO_2 are more likely to become interstitials than to replace oxygen SKAs.

(5) In all crystallographic directions (Table 4.3), the oxygen PKAs in Cr_2O_3 and Al_2O_3 are displaced at much higher energies than the metal PKAs. However, the opposite is true in SiO_2 and TiO_2. This may be attributed to the fact that there are more metal atoms in Cr_2O_3 and Al_2O_3 than in TiO_2 and SiO_2. Also, it is possible that in Cr_2O_3 and Al_2O_3 the metal atoms adjacent to the oxygen PKAs make their displacement difficult, unless at high energies (Table 4.3).

Table 4.3: PKA energy for the displacement of the oxygen and metal PKAs in five oxides.

Oxide	**PKA Type**	**PKA Energy for Displacement (eV)**					
		[100]	[010]	[001]	[110]	[101]	[011]
SiO_2 (α-quartz) Trigonal	O Si	19-39 46-53	17-33 32-61	31-60 27-39	14-31 42-75	13-49 35-62	21-54 40-103
Cr_2O_3 (eskolite) Trigonal	O Cr	60-81 17-28	52-74 12-14	35-43 39-41	55-150 60-70	41-95 30-60	72-133 30-60
Al_2O_3 – (corundum) Trigonal	O Al	50-93 20-28	50-79 11-12	46-53 28-31	62-127 60-70	47-96 26-90	61-75 37-40
MgO (periclase) Cubic	O Mg	- 27-32	- 25-46	- 29-32	47-85 46-100	44-61 60-80	42-57 31-100
TiO_2 (rutile) Tetragonal	O Ti	39-62 110-120	54-63 80-90	48-129 150-180	66-309 80-160	33-47 47-50	33-36 44-48

4.2.2.3 **PKA Energies for the formation of stable Frenkel pairs**

Based on the results and examination of the many images of the five oxides investigated, the following observations can be made regarding the dependence of stable Frenkel pair formation on the PKA energy, crystal structure, and crystallographic direction (Table 4.4):

(1) Although oxygen PKAs in MgO are not displaced in the [100], [010], and [001] directions (Table 4.3), they create stable Frenkel pairs on both anion and cation sublattices (Table 4.4). The oxygen PKAs in these directions, with energies of 57-64 eV, create Mg vacancies. The oxygen PKAs create oxygen vacancies in the [110], [101], and [011] directions at lower energies. Since the SKAs are oxygen atoms, the primary oxygen PKAs do not recoil back to their original lattice sites upon collision. In the [110], [101], and [011] directions, the Mg PKAs are displaced at relatively low energy (19-25 eV), creating vacancies and becoming interstitials.

(2) Not only does the PKA type, crystallographic direction and the crystal structure affect the PKA energy for creating a stable Frenkel pair, but also the atom mass. The energy of the metal PKA to create a stable oxygen atom Frenkel pair in Al_2O_3 is higher than in Cr_2O_3, which could be because the Cr atom mass is ~3.2 times that of the oxygen atom, while that of the Al atom is only ~1.7 times that of the oxygen atom. Therefore, an oxygen atom Frenkel pair is likely to form by the more massive Cr PKAs in Cr_2O_3 at lower energies, than by Al PKAs in Al_2O_3 (Table 4.4).

(3) The energies for the oxygen and the metal PKAs to create stable oxygen and metal atom Frenkel pairs in SiO_2 are the lowest (Table 4.4). The energies required to create Frenkel pairs in all directions in SiO_2 vary from 14-56 eV, compared to 12-235, 11-340, 19-291, and 33-283 eV in Cr_2O_3 Al_2O_3, MgO, and TiO_2, respectively.

(4) Note that the energies of the metal PKAs to create metal atoms Frenkel pairs are the lowest in Cr_2O_3 and Al_2O_3, 12 and 11 eV, respectively. The reasons are the same as those discussed earlier for the low PKA energies for displacement (Tables 4.3 and 4.4). The results in Table 4.4 show that the different types of point defects in various directions in SiO_2 form at approximately the same energy. The exception is the oxygen vacancies form with oxygen PKAs at energies as low as 14-31 eV. For all other oxides investigated, the type of Frenkel pairs strongly depends on the direction and PKA type. These results confirm that SiO_2 would be the most susceptible to irradiation damage.

4.2.2.4 **TDE Averages**

The following sub-sections present and discuss the calculated PKA displacement and an atom displacement probabilities, as well as the number of Frenkel pairs, averaged over all 66 crystallographic directions. The displacement probability curves are generated by calculating

the probability of displacement for 66 crystallographic directions and averaging them at each PKA energy.

Table 4.4: PKA energy for forming stable Frenkel pairs on both the anion and cation sublattices, with oxygen and metal PKAs in five oxides.

Oxide	**PKA Type**	**Defect Type**	**PKA Energy for Frenkel Pair Formation (eV)**					
			[100]	[010]	[001]	[110]	[101]	[011]
SiO_2 (α-quartz) Trigonal	O	V_O	14	17	21	25	31	23
		V_{Si}	35	56	29	44	45	51
	Si	V_O	51	32	39	43	35	46
		V_{Si}	46	32	27	42	35	40
Cr_2O_3 (eskolite) Trigonal	O	V_O	61	55	64	55	41	85
		V_{Cr}	235	126	158	113	72	107
	Cr	V_O	100	110	170	60	180	180
		V_{Cr}	17	12	39	36	30	30
Al_2O_3 – (corundum) Trigonal	O	V_O	52	45	58	63	47	75
		V_{Al}	53	92	183	101	130	166
	Al	V_O	340	230	140	-	240	210
		V_{Al}	20	11	28	29	49	37
MgO (periclase) Cubic	O	V_O	230	139	291	47	49	47
		V_{Mg}	58	57	64	112	94	118
	Mg	V_O	290	230	240	200	150	190
		V_{Mg}	60	60	80	25	23	19
TiO_2 (rutile) Tetragonal	O	V_O	59	58	48	66	33	33
		V_{Ti}	-	226	257	132	269	283
	Ti	V_O	180	220	260	230	150	190
		V_{Ti}	110	80	120	90	100	90

4.2.2.4.1 Displacement Probability

Figs. 4.28a,b compare the calculated probability distributions of E_d for the oxygen and metal PKAs in the five oxides investigated. The E_d for the oxygen PKAs in SiO_2 is the lowest, followed by TiO_2 (Fig. 4.28a), suggesting that these oxides are the least resistant to the displacement of the oxygen PKAs. The E_d in MgO is the highest, making it the most resistant to the displacement of oxygen PKAs. The E_d values in Al_2O_3 and Cr_2O_3, which have the same crystal structure, are identical. For the metal PKAs, the E_d probability distributions are the highest for TiO_2 (Fig. 4.28b), making it the most resistant to the displacement of the metal PKAs. For instance, an E_d of 100 eV corresponds to 57.9% probability for displacing the titanium PKAs, compared to 87.5%, 90.0%, 95.8%, and 93.7%, for displacing the metal PKAs in MgO, Al_2O_3, Cr_2O_3, and SiO_2, respectively. The E_d values at displacement probabilities of 10% and 50% are listed in Table 4.5.

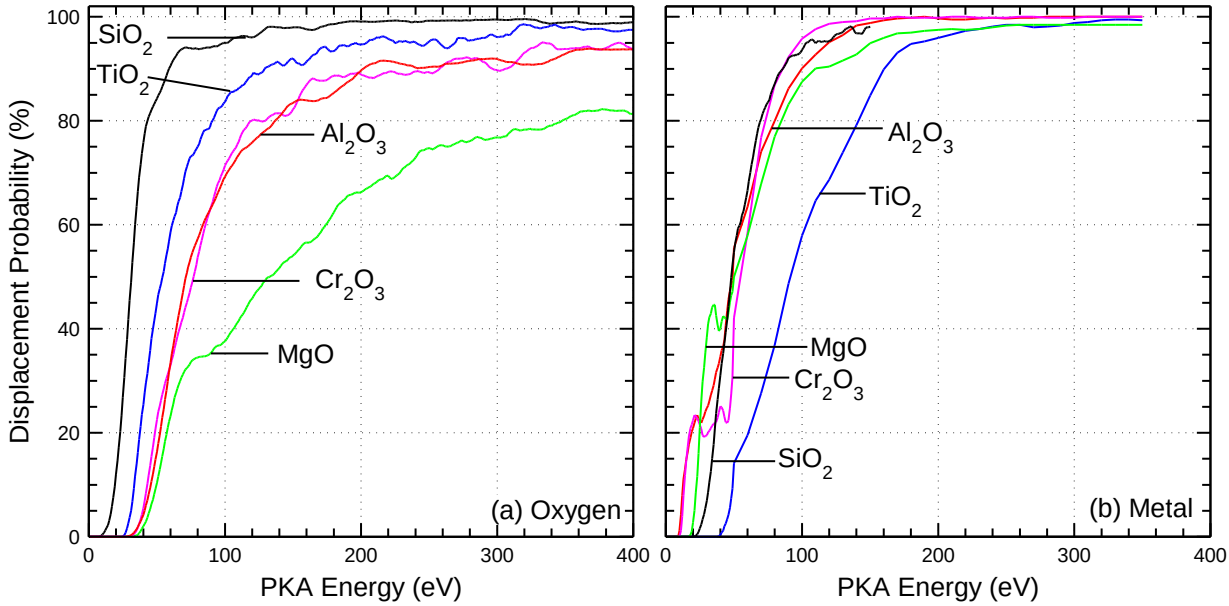

Fig. 4.28: Comparisons of the calculated TDE probability distributions for displacement of oxygen and metal PKAs in the various oxides.

Figs. 4.29-4.30 show the comparison of the displacement probabilities of oxygen and metal PKAs, compared to the displacement probability of an atom in the lattice. Naturally, the displacement probability for an atom will also be greater than or equal to the PKA displacement probability since the displacement of an atom can include the PKA. Results in Fig. 4.29 show that for oxygen PKAs, the displacement probability of an atom in the lattice is

almost identical to the PKA for SiO_2 and TiO_2. There are only slight deviations at probabilities ≥80%. The probabilities are not as similar for Al_2O_3 and Cr_2O_3, especially at PKA energies > 100 eV, where the differences between the displacement of the PKA and an atom approach ~15%.

Table 4.5: Comparison of TDEs with 10% and 50% probabilities for displacement of oxygen and metal PKAs in various oxides

Oxide	TDE (eV)			
	PKA Displacement Probability, 10%		PKA Displacement Probability, 50%	
	O PKA	Metal PKA	O PKA	Metal PKA
SiO_2	19.2	31.7	31.7	48.0
TiO_2	33.3	49.3	54.2	91.5
Cr_2O_3	43.0	13.5	71.4	54.9
Al_2O_3	45.5	12.7	77.0	49.2
MgO	49.7	22.5	132.9	50.0

In MgO, the difference in these displacement probabilities can reach as high as 40% (Fig. 4.29). These differences indicate that Frenkel pairs in the oxides are sometimes caused by SKAs, while the PKA returns to its original lattice site. For metal PKAs, the displacement probabilities are almost identical to the displacement probability of an atom in the lattice for all PKA energies and all oxides (Fig. 4.30). The reason that the metal PKA probability distribution matches that for any atom in the lattice could be due to the fact that the more massive metal atoms are unlikely to recoil to their original position.

4.2.2.4.2 Frenkel Pair Formation

Figs. 4.31a-d present the average number of stable Frenkel pairs produced by the oxygen and metal PKAs, on both the anion and cation sublattices in the five oxides investigated. Error bars are shown which represent the uncertainties in the 3 planes investigated for the 3 PKAs in each oxide. In all oxides, the number of metal atom Frenkel pairs created by the metal PKAs is higher than that of the oxygen atom Frenkel pairs (Figs. 4.31a,b). Although the metal atoms are more likely to recoil off other metal atoms, they are unlikely to return to their original lattice sites when the SKA is an oxygen atom. In TiO_2, Cr_2O_3, and Al_2O_3, the

formation of oxygen atom Frenkel pairs is more likely by oxygen PKAs, than metal atom Frenkel pairs (Figs. 4.31c,d). In MgO, and SiO_2, metal atom Frenkel pairs are more likely to form at higher energies (Figs. 4.31c,d)

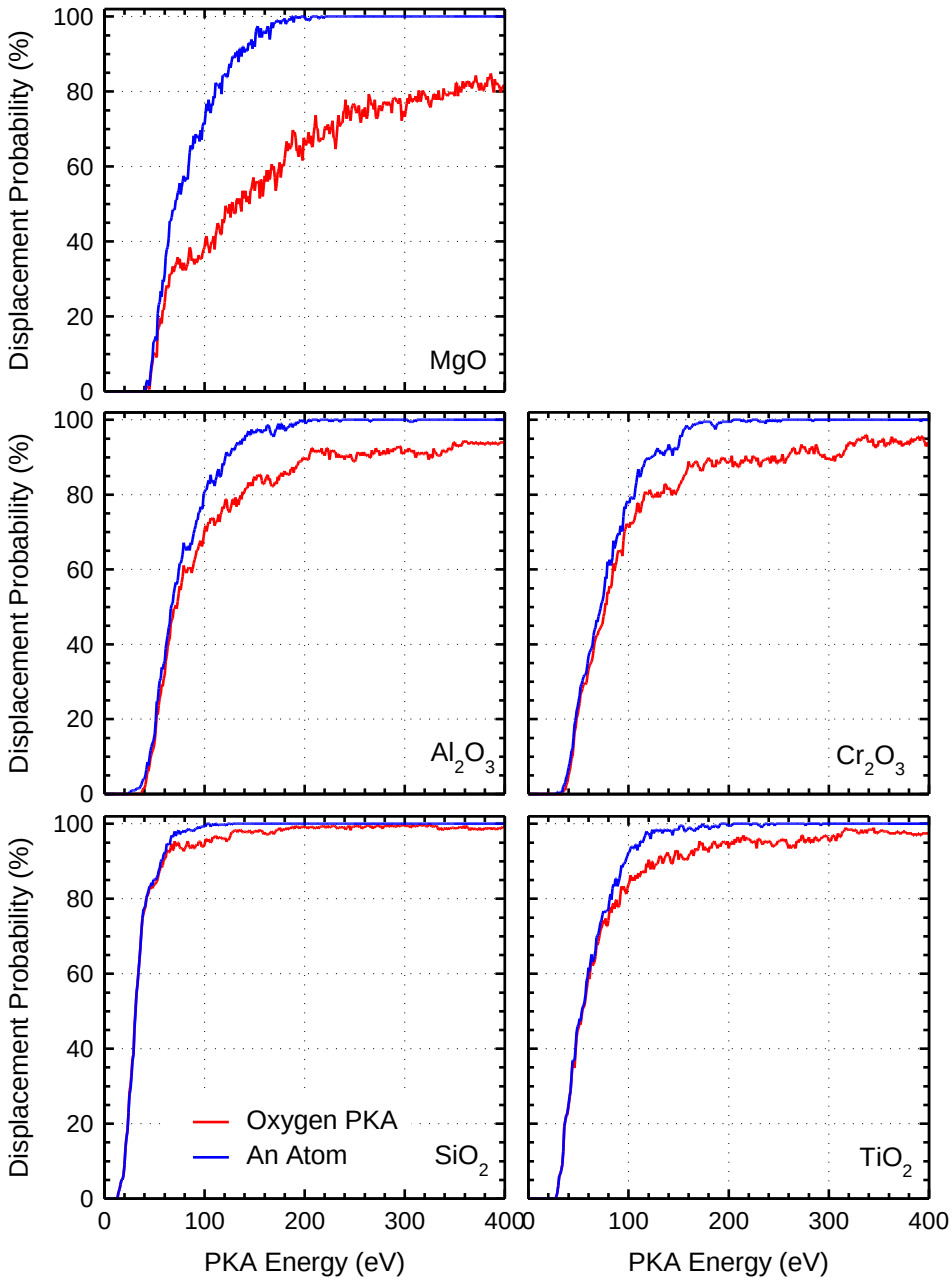

Figure 4.29: Displacement probabilities of an oxygen PKA and of an atom in various oxides versus the oxygen PKA energy.

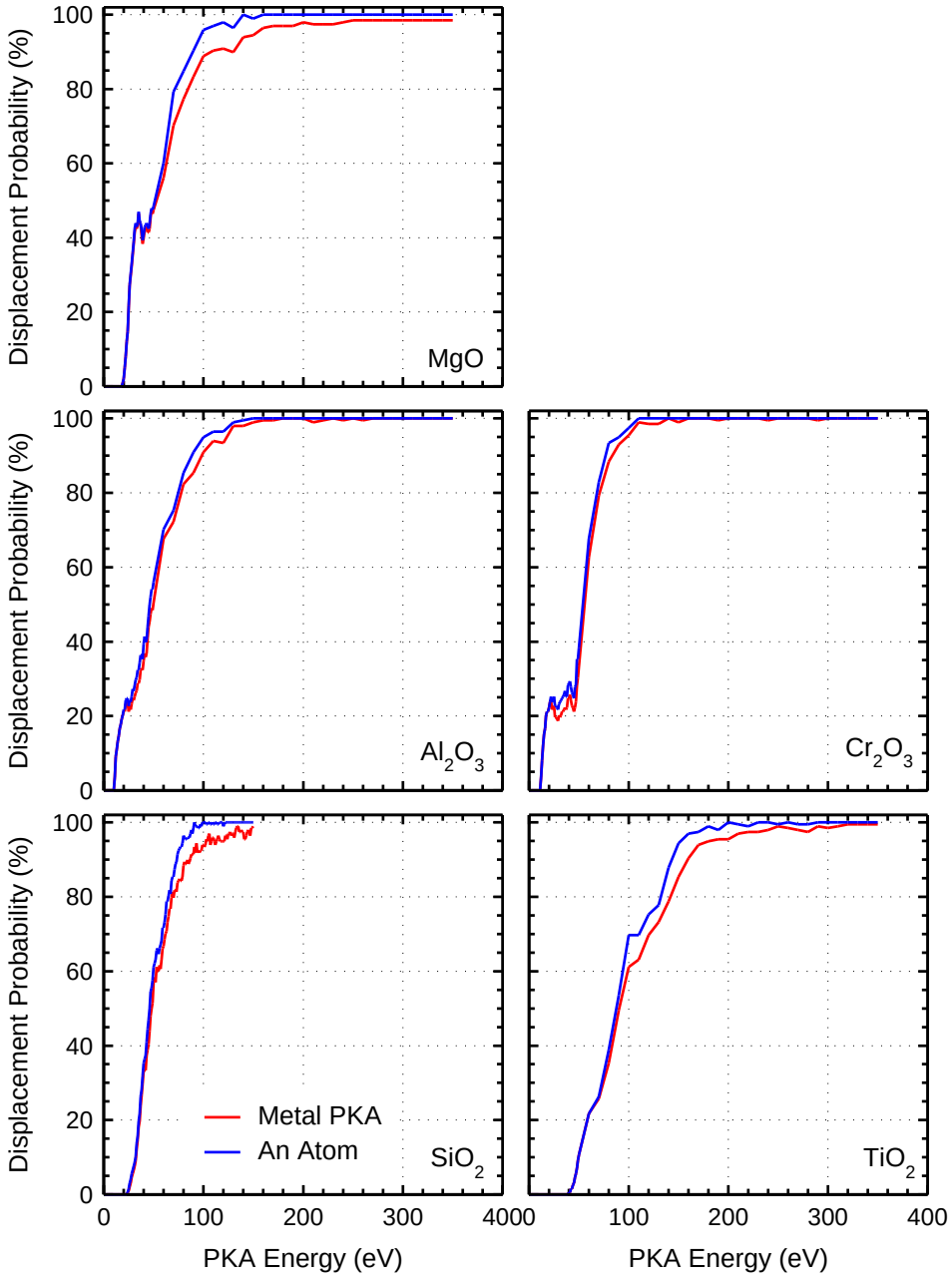

Figure 4.30: Displacement probabilities of a metal PKA and of an atom in various oxides versus the metal PKA energy.

In all oxides, oxygen atom Frenkel pairs form with oxygen PKAs at similar energies, except SiO_2, in which Frenkel pairs form more readily at lower energies. The production of metal atom Frenkel pairs with oxygen PKAs depends on the metal oxide. The number of titanium atom Frenkel pairs created by oxygen PKAs in TiO_2, averaged over all crystallographic directions, is only 0.26 by a PKA energy of 400 eV. This suggests that in

most of the crystallographic directions in TiO_2, stable Ti atom Frenkel pairs do not form with oxygen PKAs. Fig. 4.31c shows that the average number of metal atom Frenkel pairs created in Cr_2O_3, Al_2O_3, and MgO with 400 eV oxygen PKAs, is 0.92, 1.08 and 2.01, respectively. For the oxygen PKAs in Al_2O_3 and Cr_2O_3, the number of metal atom Frenkel pairs produced are similar (Fig. 4.31c), since they are of the same crystal structure.

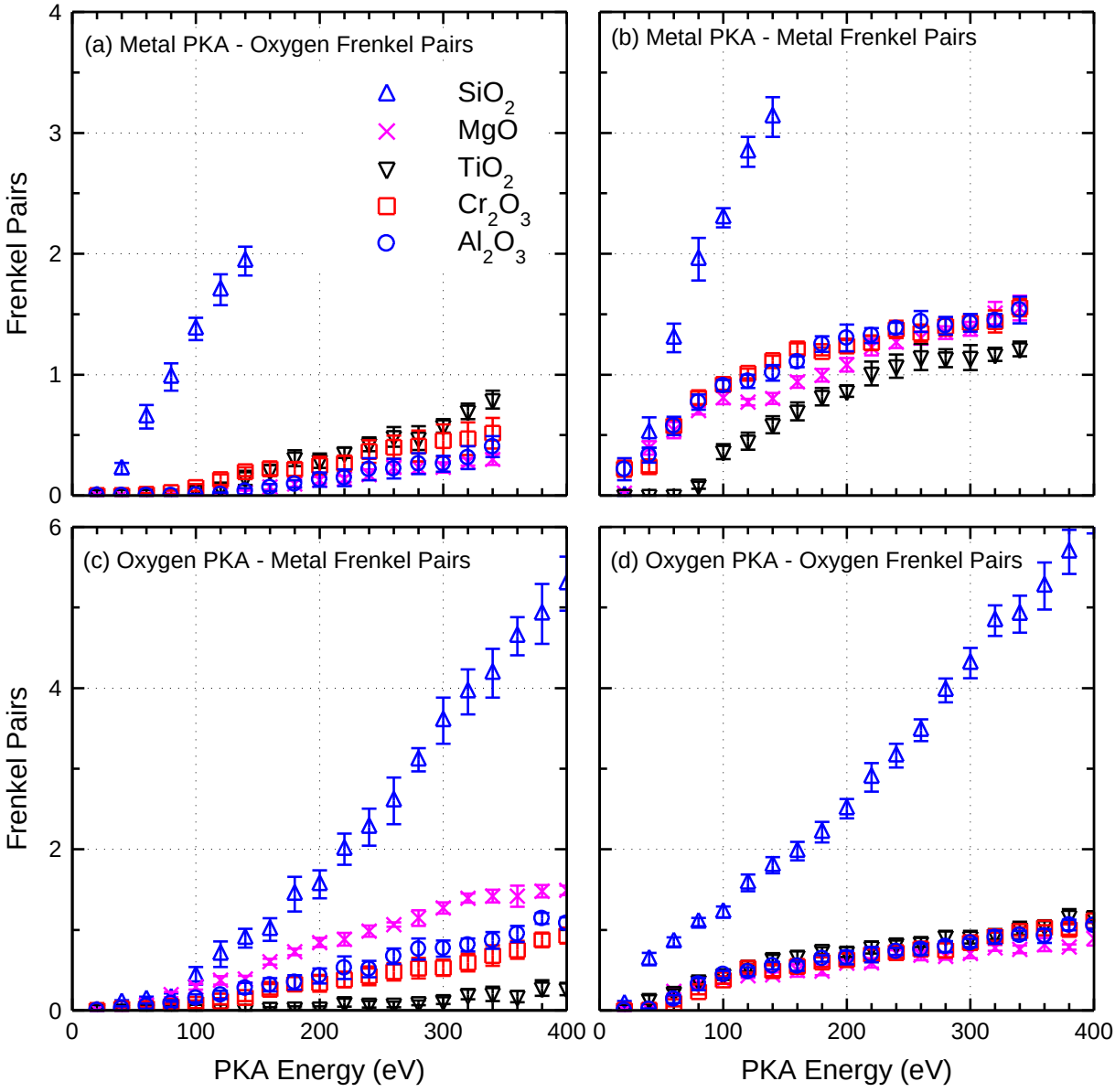

Figure 4.31: Comparisons of the calculated average number of Frenkel pairs produced with both oxygen and metal PKAs in various oxides, on both the anion and cation sublattices.

4.2.2.4.3 Displaced Atoms

Fig. 4.32 compares the total number of displaced atoms for all oxides with both oxygen and metal PKAs. For both PKA types, SiO_2 has the highest number of displaced atoms at all PKA energies, followed by MgO, TiO_2, Cr_2O_3, and Al_2O_3. Despite the large number of displacements, most of these displaced atoms anneal. Fig. 4.33 compares the average number of displaced atoms and the corresponding number of stable Frenkel pairs produced.

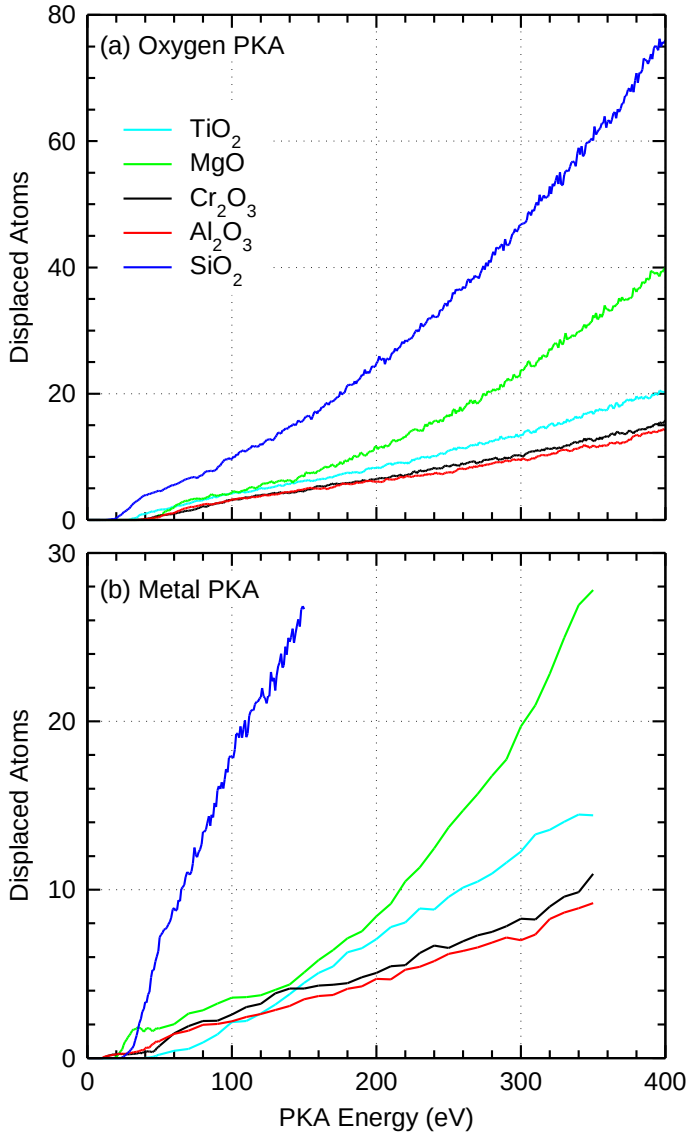

Figure 4.32: The number of displaced atoms in various oxides versus the energy of the oxygen and metal PKAs.

The results show that SiO_2 is more prone to the formation of stable Frenkel pairs because more atoms are displaced, not because the annealing efficiency is lower than in other oxides.

In fact, for the same number of displaced atoms, the number of stable Frenkel pairs produced in SiO_2 is among the lowest of all the oxides with metal PKAs. The number of displaced atoms per stable Frenkel pairs is highest for both MgO and TiO_2 (Fig. 4.33). This indicates that while it may take more energy to cause displaced atoms in MgO and TiO_2, the displaced atoms are more likely to anneal.

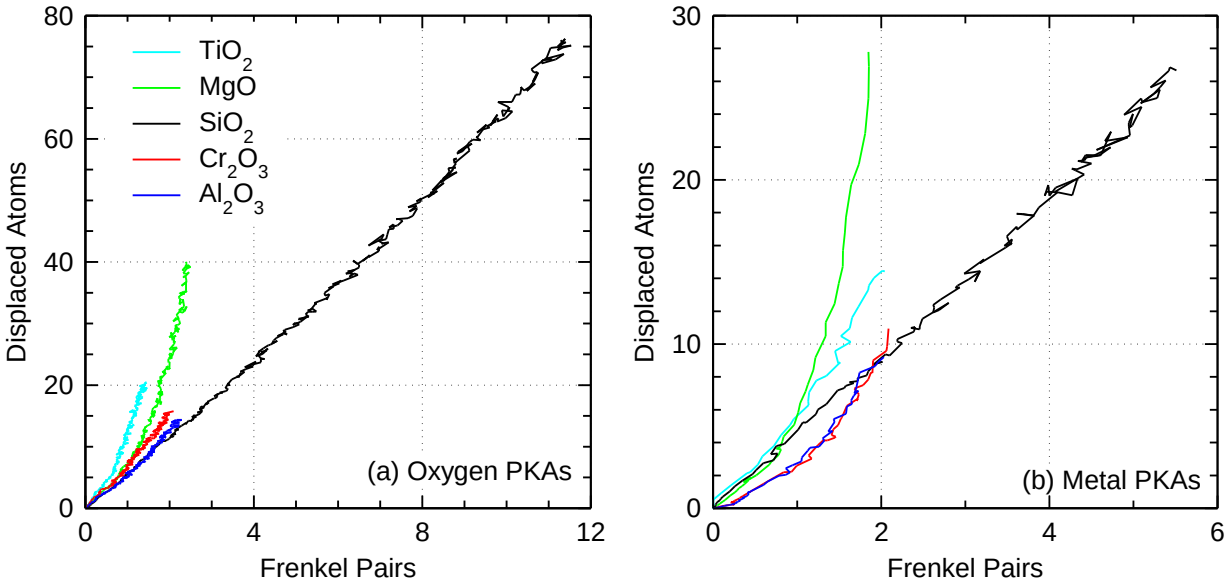

Figure 4.33: Comparison of the number of displaced atoms versus the number of Frenkel Pairs produced in various oxides with oxygen and metal PKAs.

4.2.3 Comparison with Reported Experimental and MD Results

The polar plots presented in the previous sections for certain oxides are shown again in Figs. 4.34-4.36, to compare the calculated TDEs with the reported experimental values. The experimental TDEs are represented in these figures by solid symbols, and located in the direction they were measured. Note that for the experimental TDEs, the type of the PKA was not reported. The experimental TDEs in MgO[110] match well with the calculated values. The experimental E_{FP} values for Mg PKAs in the [001] direction are almost identical to those calculated in the present MD simulations. The calculated E_{FP} for the oxygen PKAs to produce oxygen atom Frenkel pairs is much higher than the experimental value; however, the calculated E_{FP} for oxygen PKAs to produce metal atom Frenkel pairs is much closer to the experimental value (Fig. 4.34 and Table 4.4). In their MD simulations, Sonoda et al.[105] also reported higher PKA energy of 160 eV for forming oxygen atom Frenkel pairs in the [001] direction. The large difference between MD simulations and the experimental TDE values

could be attributed to the uncertainties in determining the precise direction in experiments. If the direction is even slightly offset from the [001] direction, which would be difficult to measure, the oxygen atoms may have a glancing interaction with the Mg atoms and become an interstitial, rather than recoil to their original lattice site. As indicated in Fig. 4.34, a small deviation from the [001] direction results in a lower PKA energy to form an oxygen atom Frenkel pair.

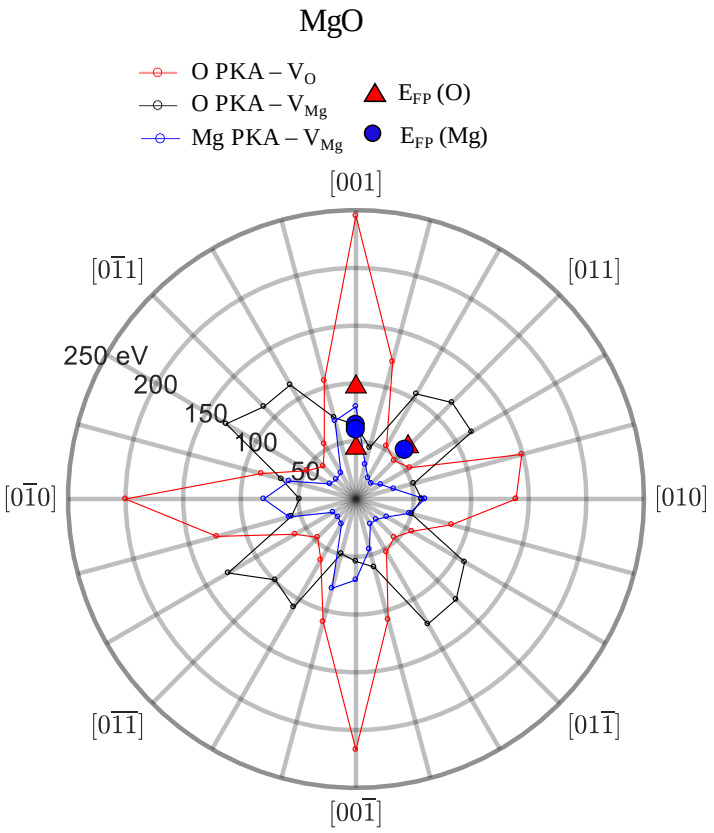

Figure 4.34: Comparison of the calculated TDEs with experimental results for MgO.

Fig. 4.35 compares the experimental TDE values for the TiO_2 rutile to those calculated in this work. The calculated TDEs at 300 K are significantly different from the experimental values at higher temperatures (673-773 K).[121] Thomas et al.[60] have carried out MD simulations of rutile and found that the E_{FP} for Ti PKAs at 50% probability in the [001] and [100] directions, is 80 eV and 115 eV, respectively, which is much closer to the present results of 120 and 110 eV.

Fig. 4.36 show some differences between the reported experimental TDEs in Al_2O_3,[114-118] and those calculated herein. In the [11$\bar{2}$0] direction, the experimental TDE for oxygen atoms to produce oxygen atom Frenkel pairs is 41 eV, while the calculated is 63 eV. In the [0001] direction, the calculated E_{FP} for the oxygen PKAs to produce oxygen atom Frenkel pairs is close to the experimental value (Fig. 4.36b). The calculated E_{FP} for the Al PKAs to create Al atom Frenkel pairs are only slightly below the experimental value. The differences between the experimental and calculated TDEs in Al_2O_3 could be partially attributed to the difficulties of measuring the TDE experimentally in the precise direction, and the dependence of the PKA type, which had not been specified.

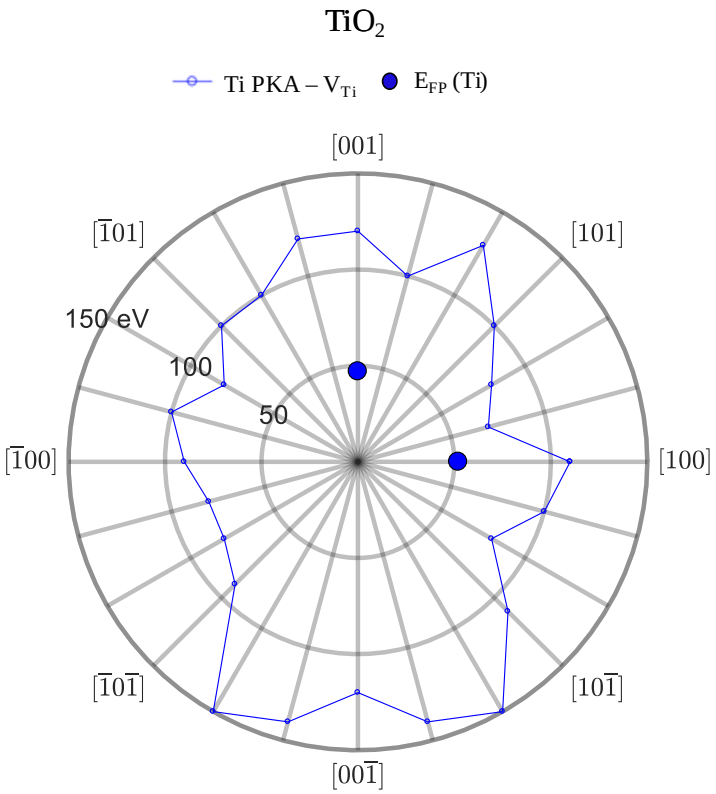

Figure 4.35: Comparison of the calculated TDEs with experimental results for TiO_2.

Fig. 4.37 compares the calculated PKA displacement probability distributions in TiO_2, with energies of 25- 400 eV, to those reported by Robinson et al.[55] for PKA energies of 25-200 eV. Their MD simulations used the Matsui-Akaogi pair potential in conjunction with the Ziegler-Biersack-Littmark (ZBL) pair potential, to account for close-range interactions. The

comparison in Fig. 4.37 shows good agreements of the E_d probability distributions for both the oxygen and the Ti PKAs.

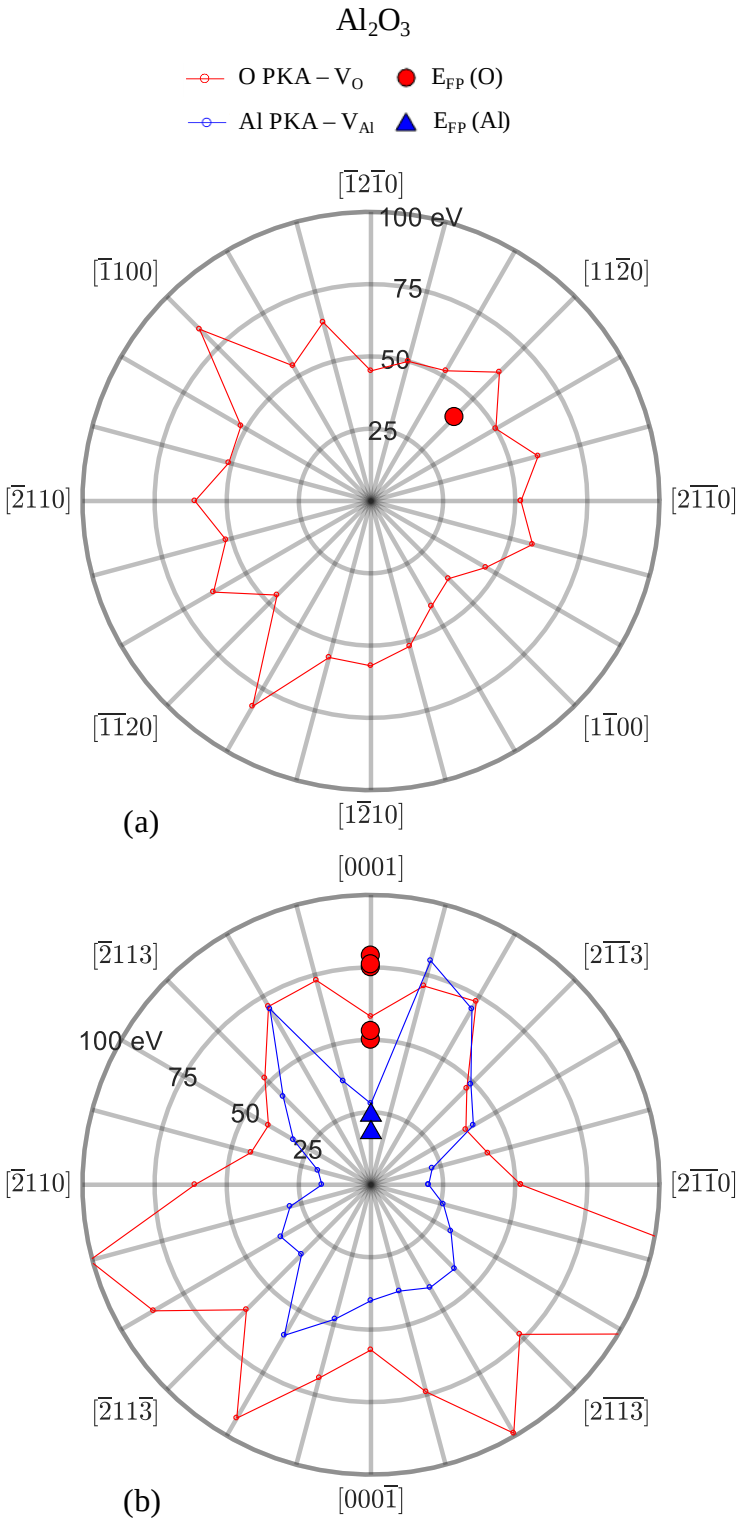

Figure 4.36: Comparison of the calculated TDEs with experimental results for Al_2O_3.

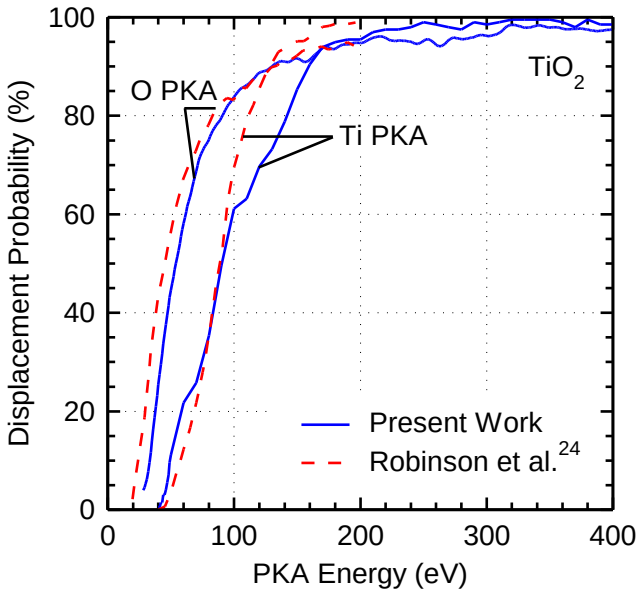

Figure 4.37: Comparison of present TDE probability distributions for the displacement of the metal and oxygen PKAs in TiO_2, to those reported by Robinson et al.[55]

4.2.4 Highlights and Concluding Remarks

The calculated TDEs for the displacement of metal and oxygen PKAs and the formation of stable Frenkel pairs in Cr_2O_3, Al_2O_3, TiO_2, SiO_2, and MgO are strongly dependent on the crystal structure and crystallographic direction. The results for the metal PKA with energies up to 350 eV and the oxygen PKA with energies up to 400 eV clearly show that the formation of stable Frenkel pairs is not always associated with the PKAs displacement, and vice-versa. Oxygen PKAs are likely to recoil to their original lattice site after colliding with metal atoms, but may result in the formation of a stable Frenkel pair.

The TDEs for the displacement of oxygen PKAs in MgO are lower in the high-index directions than in the low-index directions. Conversely, in the low-index directions, the TDEs for the oxygen PKAs to produce stable Mg Frenkel pairs are lower than in the high-index directions. The PKA displacement and Frenkel pair formation energies for Al_2O_3 and Cr_2O_3 are the same for each of the 66 crystallographic directions, except that the formation of oxygen atom Frenkel pairs with Al PKAs occurs at higher energies than with Cr PKAs. This suggests that the PKA type affects the number and formation energies of the Frenkel pairs. In SiO_2, the TDEs for forming stable Frenkel pairs with both oxygen and metal PKAs are

typically <50 eV in all directions, and on both anion and cation sublattices, compared to >100 eV in other oxides, in some crystallographic directions.

The SiO_2 has the highest probability for displacing the oxygen PKAs and one of the highest probabilities for the displacement of the metal PKAs. The TiO_2 has the second highest probability for the displacement of the oxygen PKAs, but the lowest probability for the displacement of metal PKAs. The MgO has the lowest probability for the displacement of the oxygen PKAs, while that for the displacement of the metal PKAs is one of the highest. In Al_2O_3 and Cr_2O_3, the probabilities for the displacements of both the oxygen and metal PKAs are similar.

Metal PKA displacement probabilities are similar to the probabilities to displace an atom in the lattice, indicating they are unlikely to recoil to their original lattice site once a Frenkel pair forms. Oxygen PKA displacement probabilities in MgO, Cr_2O_3, and Al_2O_3 are not as similar to the displacement probabilities of an atom in the lattice, indicating that SKAs are sometimes responsible for Frenkel pair formation, while the PKA returns to its original lattice site. The total number of displaced atoms is higher in SiO_2 than the other oxides across the energy range investigated. Since atoms are more readily displaced in SiO_2, more Frenkel pairs are produced compared to the other oxides. However, for the same number of displaced atoms with metal PKAs, Al_2O_3 and Cr_2O_3 yield the highest number of Frenkel pairs, indicating displaced atoms in these oxides are less likely to anneal.

In conclusion, given the stochastic nature of the radiation interactions with materials and the demonstrated strong directional dependence of the TDEs in the SiO_2, TiO_2, Cr_2O_3, Al_2O_3, and MgO, the current values calculated in 66 crystallographic directions would be a more representative input to the radiation damage models, instead of single values calculated from TDEs in one or a few crystallographic directions. Additionally, the calculated average number of Frenkel pairs produced on both the anion and cation sublattices in these oxides would help the full assessment of the extent and type of radiation damage in each oxide, thus a useful input to the radiation damage models. These models can serve to determine the relationship between atomic-scale defects and changes in bulk material properties, which is of practical importance.

This section has exhaustively reported on TDEs in metal oxides, including directional dependence and TDE averages. However, SiC is also one of the materials of interest for next-

generation nuclear reactor designs as well as in the blankets of fusion reactors. Therefore, the next section presents and discusses the calculated TDE values in 3C-SiC and a-SiC.

4.3 TDE Probability Distributions and Directional Dependence in crystalline and amorphous SiC

The objectives of this study are to conduct MD simulations using the Tersoff+ZBL potential to determine the values and investigate the directional dependence of the TDEs for defects production by carbon and silicon PKAs with energies up to 400 eV in 3C-SiC and amorphous (a-SiC). Additionally, the TDE probability distributions for displacing a PKA and an atom in 3C-SiC and a-SiC are calculated and compared. The determined TDEs are compared to experimental values and those reported by others using MD simulations, when available.

4.3.1 Methodology

The present MD simulations are carried out using LAMMPS[249] and a system size of 8,000 atoms. The atom-atom interactions are modeled using the Tersoff potential and equilibration time-step size of 0.2 fs. To account for the short interatomic distances during radiation damage cascades, the Tersoff[64] potential is splined to the commonly used ZBL potential. The simulations use the velocity-Verlet integrator and minimize energy using the Polak-Ribiere[287] version of the conjugate gradient algorithm, before the equilibration of the system of atoms in an isothermal-isobaric ensemble (NPT) at 300 K for 20 ps. Subsequently, 3C-SiC is equilibrated for 10 ps in the microcanonical ensemble (NVE), before carrying out the MD simulations of radiation damage. The a-SiC is prepared in a similar manner as described by Devanathan et al.[303]

In the present MD simulations of 3C-SiC, a Si or a C PKA is given energy in a crystallographic direction in the NVE ensemble, with a time step of 0.1 fs. For each PKA type, the energy for the MD simulations increased from 1.0 to 400 eV, in increments of 1 eV, to help attain high resolution of the calculated TDEs. The TDEs for the displacements of a PKA and an atom, and the PKA energies for the formation of Frenkel pairs are determined at the end of 3 ps of simulation time. Beyond this time, the number of defects produced no longer changes with increasing simulation time (Fig. 4.38).

Wigner-Seitz (WS) defect analysis is used to quantify the production of Frenkel pairs and antisites in 3C-SiC, on both the C and Si sublattices. Displacements in 3C-SiC and a-SiC are determined based on the detected changes in coordination for each atom in the system after irradiation. The Open Visualization Tool (OVITO)[304] with its customized python scripting interface is used to carry out these analyses.

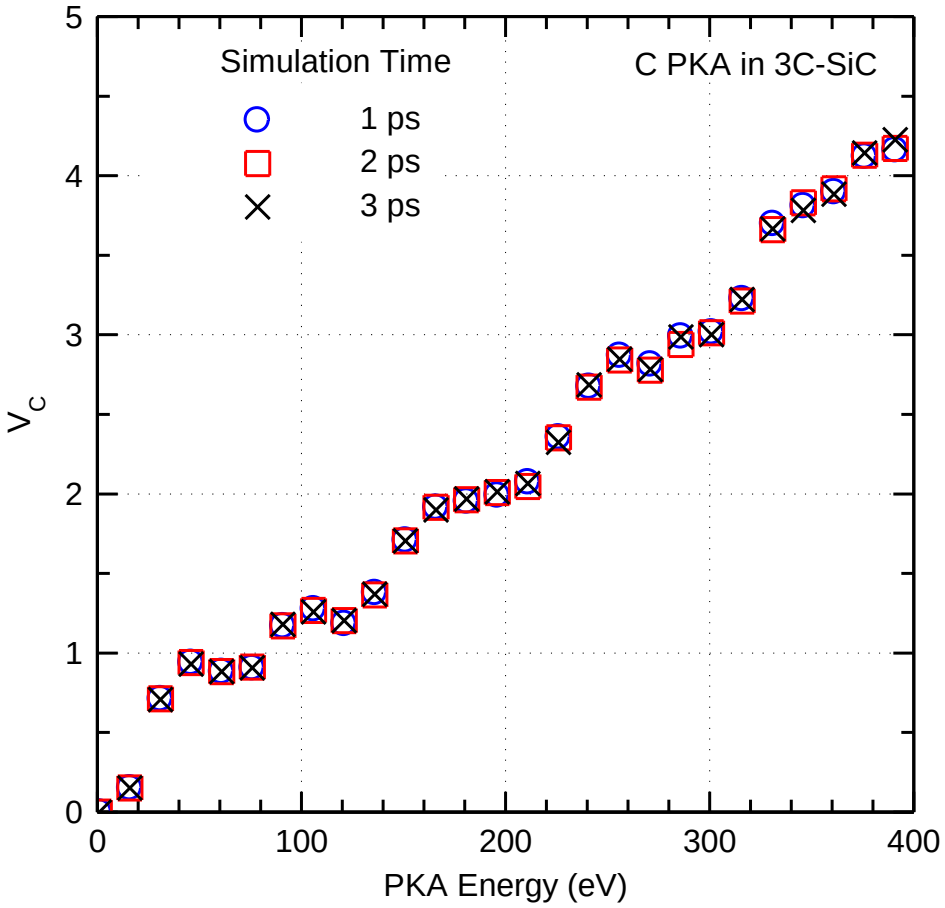

Figure 4.38: Effect of simulation time on the calculated total number of V_C produced by C PKAs.

The performed MD simulations investigated 9 C and 9 Si PKAs, each in 24 evenly spaced directions within the XY plane, for a total of 86,400 simulations for each PKA type. In 3C-SiC, these planes are identical, and many of the angles within each plane are symmetric. In addition, the [111] and [$\bar{1}$ $\bar{1}$ $\bar{1}$] directions are also investigated with 9 C and 9 Si PKAs (additional 7,200 simulations), for completeness and comparing results to prior work. The weighted probability distributions are calculated by taking into account the

multiplicity of the four low-index crystallographic directions [100], [110], [111], and [$\bar{1}\ \bar{1}\ \bar{1}$], of 6, 4, 12, and 4, respectively.

4.3.2 Results

This section presents and discusses TDE estimates for the production of a Frenkel pair and for the displacement of a PKA and an atom in 3C-SiC and a-SiC. The calculated TDE probability distributions and the number of defects produced as a function of PKA energy up to 400 V are also provided and discussed.

4.3.2.1 **Threshold Displacement Energies**

Fig. 4.39 presents polar plots of the range of the TDEs for producing C vacancies (V_C) and Si vacancies (V_{Si}) in 3C-SiC for a total of 9 PKAs. The width of the band of the TDEs in this figure reflects the spread of the values for the Si PKAs and C PKAs investigated. The large band of the TDEs indicates the variance in the TDE estimates, even in the same crystallographic direction. This could partially explain the discrepancies in the reported TDEs in the literature. The present results benefit from the statistics of compiling the TDE estimates of the different PKAs in the same crystallographic direction. The calculated ranges of the TDEs to produce a vacancy or antisite in the four low-index crystallographic directions of [100], [110], [111], and [$\bar{1}\ \bar{1}\ \bar{1}$] in 3C-SiC are listed in Table 4.6.

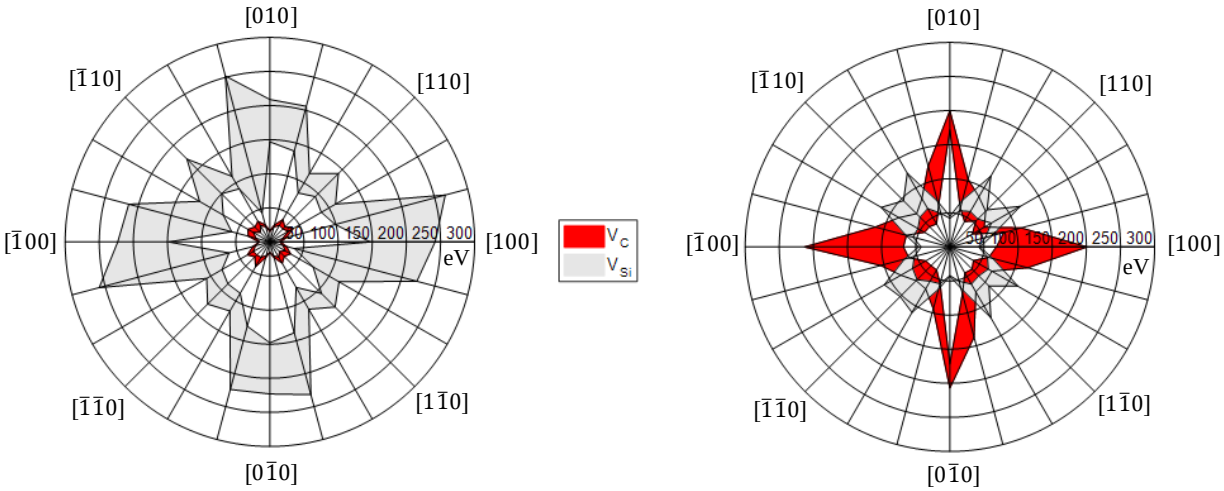

(a) C PKA (a) Si PKA

Figure 4.39: Comparison of the calculated TDEs for the formation of V_C and V_{Si} with C and Si PKAs in 3C-SiC.

Table 4.6 shows that the energy required for a C PKA to produce a V_C is in general agreement with the *ab initio* results by Gao et al.[305] Table 4.6 also reports the TDEs for the production of a V_{Si} and carbon and silicon antisites (C_{Si} and Si_C) with C PKAs, which are typically unreported in prior studies. Table 4.6 also lists the present TDEs for the production of vacancies and antisites on both sublattices in 3C-SiC with Si PKAs. Note that the C PKA energies to produce a V_{Si} is much higher than for the Si PKAs because it is difficult for the lighter C atoms to displace the more massive Si atoms. While the production of antisites is less common, it is still possible with C PKA energies as low as 47 eV. The present TDEs for the Si PKAs are also in general agreement with Gao et al,.[305] but the produced defects are not always V_{Si}. For example, in the [110] and [111] directions, the calculated TDE to produce a V_C is lower than that needed for a V_{Si}. In the [111] direction, a Si PKA at energies as low as 21 eV would produce a V_C, compared to 90 eV for producing a V_{Si}. This is because a Si PKA frequently displaces a C SKA, and returns to its original lattice site.

Table 4.6: Estimates of the TDEs for defect production with both C and Si PKAs.

PKA Type	**Defect Type**	**[100]**	**[110]**	**[111]**	**[$\bar{1}\bar{1}\bar{1}$]**
C	V_C	14-17	20-31	20-23	45-57
	V_{Si}	147-242	87-172	63-229	59-72
	C_{Si}	47-113	120-184	51-100	109-168
	Si_C	120-183	48-113	51-100	72-99
Si	V_C	68-213	39-74	21-24	37-99
	V_{Si}	42-46	58-103	90-184	42-46
	C_{Si}	202-370	69-191	56-78	86-102
	Si_C	62-222	58-103	59-78	44-61

Fig. 4.40a-d shows the calculated defect production surfaces on both C and Si sublattices with PKA energies up to 400 eV. Note that each surface is an average of the results of 9 PKAs of each type. The line between the white region and the yellow region in these figures represents the polar TDE surface, and is of the minimum energy needed to produce a defect. The average number of V_C produced with C PKAs up to 400 eV is fairly isotropic,

considering that the minimum TDEs in Fig. 4.40a are somewhat similar in all directions. The results in Figs. 4.40b-d show strong directional dependence of defect production in this plane. Fig. 4.40b shows that the average number of V_C produced with Si PKAs is strongly anisotropic at PKA energies <300 eV, but diminishes at higher PKA energies up to 400 eV. Defect production becomes more isotropic as the PKA energy increases, since the direction of the initial recoil will become less important.

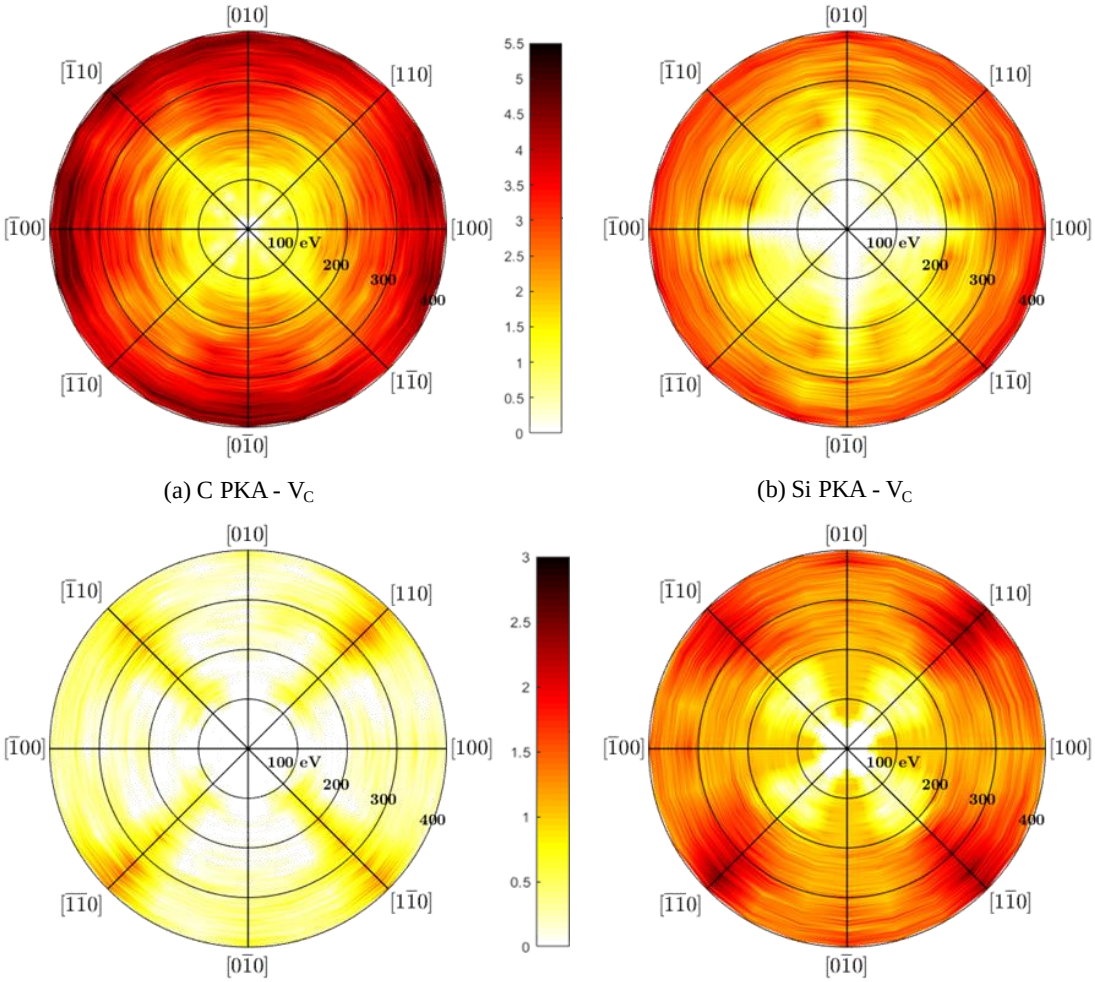

(a) C PKA - V_C (b) Si PKA - V_C

(c) C PKA - V_{Si} (d) Si PKA - V_{Si}

Figure 4.40: Comparison of the calculated average number of V_C and V_{Si} produced in 3C-SiC, as a function of the C and Si PKA energy.

Fig. 4.40c shows that V_{Si} are not easily produced with C PKAs, even at energies of 400 eV. The [110] crystallographic direction is the only direction on this plane in which C PKAs readily produce a V_{Si} at energies as low as 100 eV. Fig. 4.40d indicates strong anisotropy of

the V_{Si} produced with Si PKAs. In the [110] direction, in which the Si PKA recoils with its Si second neighbor, the energy required to produce a V_{Si} can be as high as ~150 eV. Typically, the Si PKAs recoil to their initial positions, but at ~150 eV and through a replacement collision sequence, the Si secondary knock-on atom (SKA) becomes an interstitial. This is in general agreement with prior work,[155] but the actual energies differ due to the different interatomic potential used.

Frenkel pair production is one of the most useful metrics for investigating radiation damage in materials. However, some binary collision approximation codes estimate the number of displaced atoms using the reported or measured TDEs. The number of displaced atoms is not necessarily indicative of the residual damage in the crystal, but can provide information on the extent of the radiation damage cascade. Thus, calculating the total number of displaced atoms is useful for comparing with higher-level models. Fig. 4.41a,b presents polar contours of the average number of displaced atoms produced in 3C-SiC with C and Si PKAs. For both PKA types, the number of displaced atoms is anisotropic and the figure shows that it is more difficult to cause displaced atoms in the crystallographic direction offset from the [110] plane by 15° than in the other directions investigated. In this direction, the PKAs engage in glancing interactions with both C and Si atoms, and do not easily displace either of them at low energies.

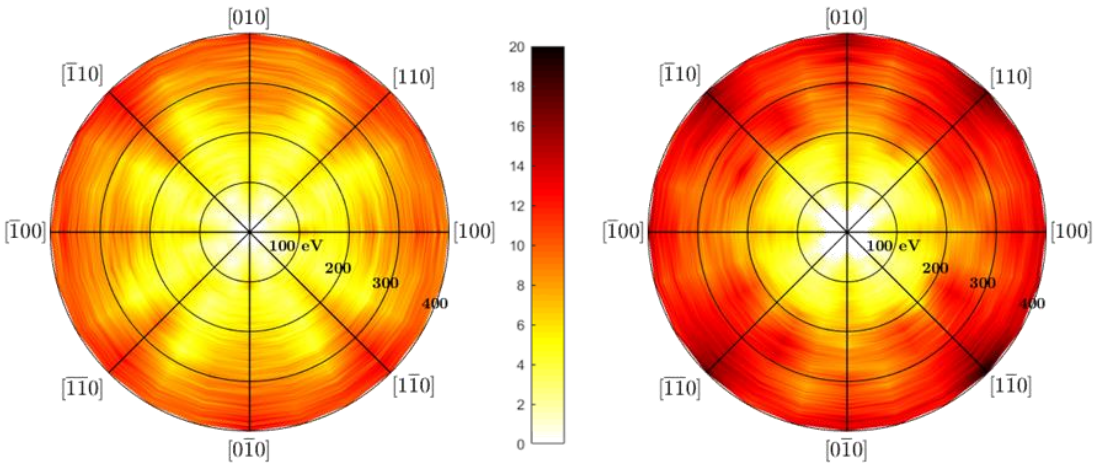

(a) C PKA (b) Si PKA

Figure 4.41: Comparison of the calculated average number of displaced atoms in 3C-SiC, as a function of the C and Si PKA energy.

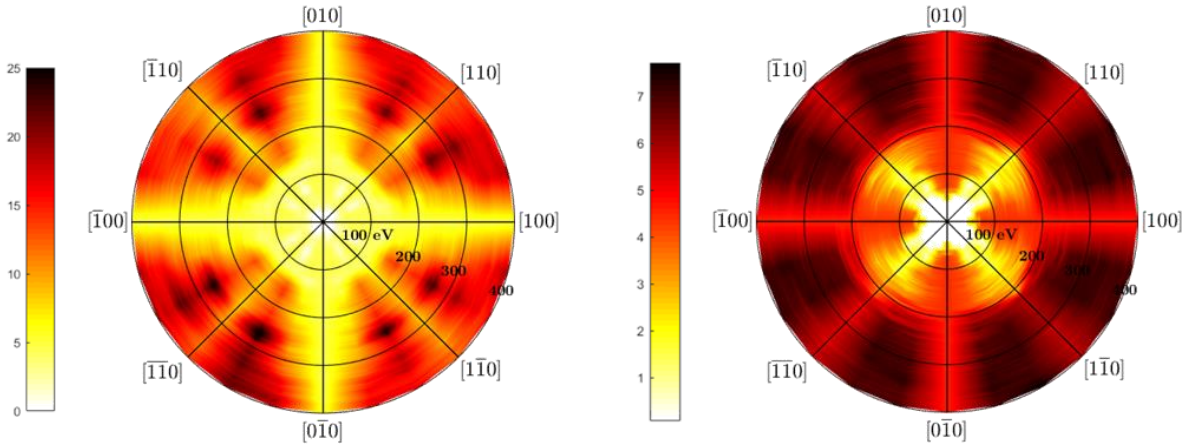

(a) C PKA Displacement Distance (Å) (b) Si PKA Displacement Distance (Å)

Figure 4.42: Comparison of the calculated average displacement distance (Å) of C and Si PKAs in 3C-SiC, as a function of PKA energy.

The obtained polar contours of the C and Si PKA displacement distances, with energies up to 400 eV are presented in Fig. 4.42a,b. Although the production of vacancies by a 400 eV C PKA shows little directional dependence, the displacement distance of the C PKA at this energy is very much directional dependent (Fig. 4.42a). In the [100] directions, the C PKA is only displaced approximately by the lattice parameter and sometimes creates a replacement collision with the nearest C SKA. In the [110] directions, the C PKA is only displaced ~7-15 Å compared to as much as 24-25 Å in the high-index directions in which it has glancing collisions with both C and Si atoms. The Si PKAs are not displaced from their original lattice site as far as the C PKAs. With energies up to 200 eV, the Si PKAs are displaced by as little as 2 Å in the [110] directions. At high energies up to 400 eV, the Si PKAs are displaced ~5 Å in the [100] and [110] directions, and ~7 Å in the high-index directions. Like defect formation energies, the predictions of displacement distance depends on the PKA types and are somewhat potential-dependent due to the variances in the recombination barriers and diffusion of the atoms. Thus, selected potentials need to be in agreement with prior first principles calculations.

4.3.2.2 **TDE Probability Distributions**

This section presents and discusses the calculated TDE probability distributions for the displacements of PKAs and an atom in 3C-SiC and a-SiC. The energy for displacing a PKA

is not necessarily the same as that for the displacement of an atom. This is generally true for different materials, including SiC investigated in the present work. Sometimes, a PKA recoils back to its original lattice site, while an SKA is displaced. Fig. 4.43 presents the calculated TDE probability distributions for C and Si PKAs to displace an atom in the four low-index directions of [100], [110], [111], and [$\bar{1}\ \bar{1}\ \bar{1}$].

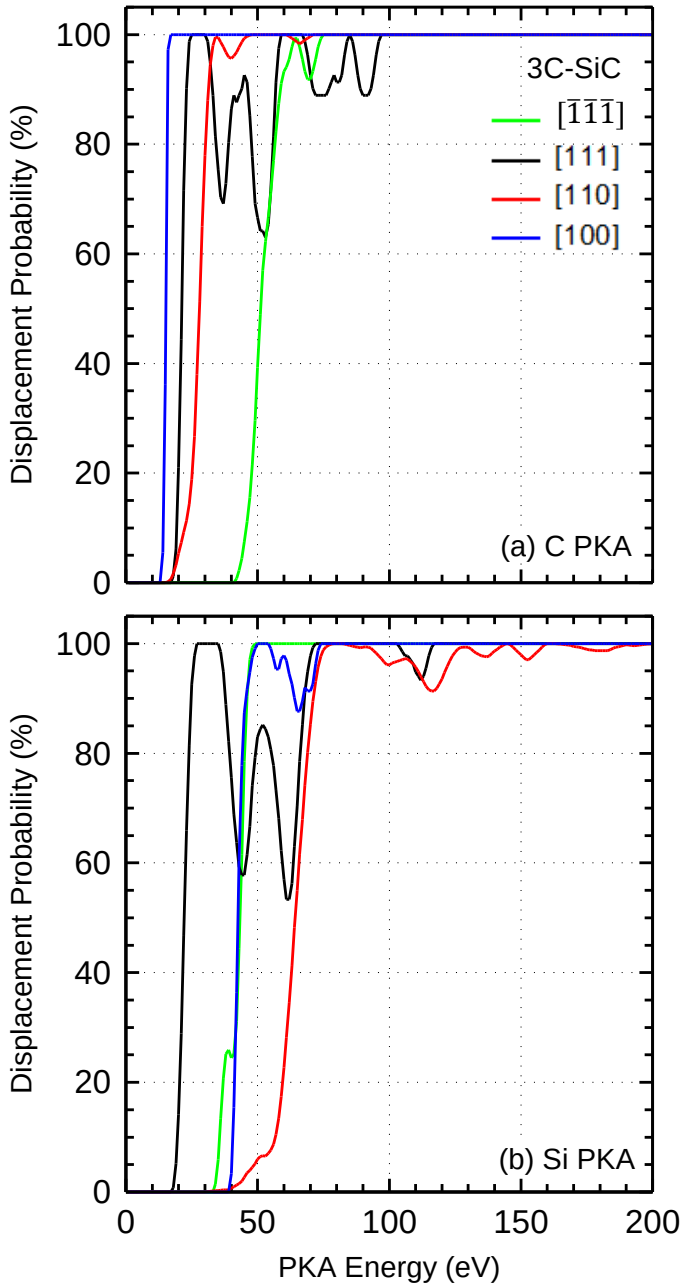

Figure 4.43: Probability distributions of displacing an atom in 4 low-index crystallographic directions with C and Si PKAs in 3C-SiC

In the [100] direction, the C PKA recoils off the C SKA and forms a C atom Frenkel pair if its energy is above a certain threshold or TDE. Results show that the C PKAs with energies of 14.1 eV and 15.9 eV in the [100] direction have a 10% and 90% probability, respectively, to displace an atom, indicating that the TDE for a displacement in that direction is ~14-16 eV. The calculated displacement probabilities in that direction resemble a step function and rapidly go to 100% probability once the PKA energy reaches a certain threshold. In the other directions, there is more variance in the values of the PKA threshold energy for displacing an atom. For instance, Si PKAs with energies of 56.7 eV and 71.1 eV in the [110] direction have 10% and 90% probability to displace an atom. The large spread in the calculated TDEs in that direction is due to the different types of interaction sequences taking place, including replacement collisions and Frenkel pair formation. This is supported by a prior work using a different interatomic potential.[155] Table 4.7 lists the determined TDEs for C and Si PKAs and the corresponding probabilities for displacing an atom in 3C-SiC.

Table 4.7: Calculated TDEs and corresponding probabilities for displacing an atom with C and Si PKAs in 3C-SiC.

TDEs for displacing an atom

Direction	**[100]**			**[110]**			**[111]**			**[$\bar{1}\bar{1}\bar{1}$]**		
Probability	10 %	50 %	90 %	10 %	50 %	90 %	10 %	50 %	90 %	10 %	50 %	90 %
C PKA, TDE (eV)	14.1	15.2	15.9	22.3	27.9	31.3	19.3	21.2	23.0	45.7	51.1	58.7
Si PKA, TDE (eV)	40.5	42.6	45.7	56.7	64.3	71.1	19.5	22.1	24.8	35.5	43.3	45.9

Results indicate that atoms are least likely to be displaced by C PKAs in the [$\bar{1}$ $\bar{1}$ $\bar{1}$] direction and by Si PKAs in the [110] direction (Fig. 4.43). A C PKA in the [$\bar{1}$ $\bar{1}$ $\bar{1}$] direction transfers most of its kinetic energy to the nearest Si neighbor. Results show that when the energy of a C PKA is ≤40 eV, the PKA fails to displace a Si SKA, and recoils back to its

original lattice site. The C PKAs with energies as low as 14-22 eV in the [100], [110], and [111] directions are likely displaced, producing a C vacancy/interstitial pair or a Frenkel pair. In the [111] direction, the Si PKAs have the lowest TDE and a steep rise in the probability for displacing an atom in 3C-SiC. This is because the Si PKAs at energies as low as ~19 eV easily displace their first C neighbors and recoil back to their original lattice sites (Fig. 4.43).

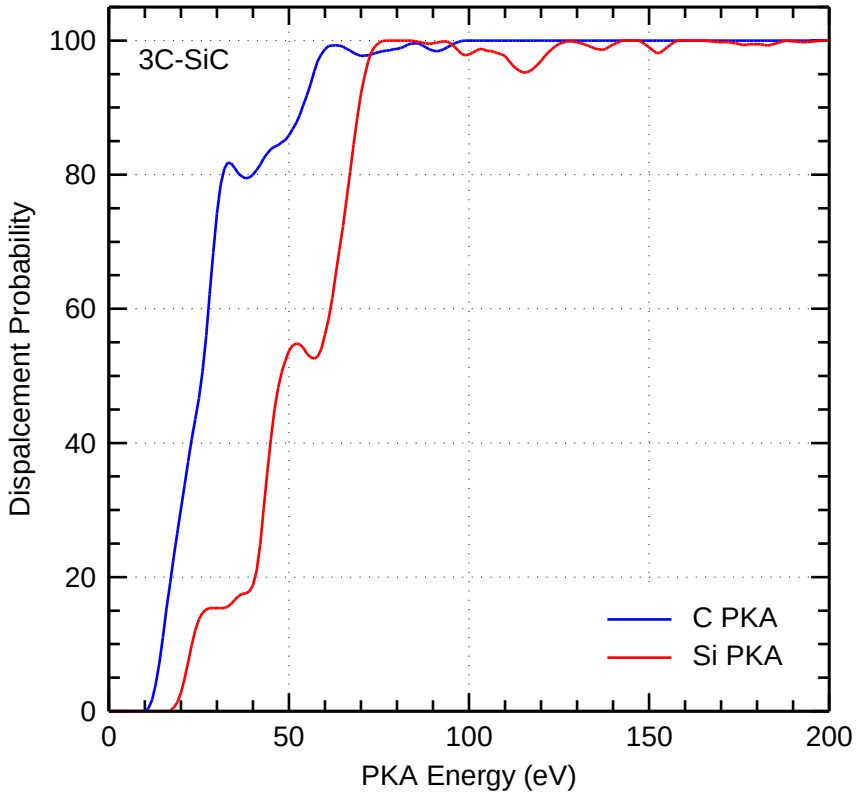

Figure 4.44: Comparison of weighted TDE probability distributions for C and Si PKAs to displace an atom in 3C-SiC.

The TDE probability distributions in the 4 low-index directions are used to develop a weighted probability distribution based on the multiplicity of each direction.[155] Fig. 4.44 compares the weighted TDE probability distributions for displacing an atom with C and Si PKAs in 3C-SiC. The TDE for a C PKA to displace an atom is lower than for a Si PKA. For instance, a C PKA with energy of 26 eV has a 50% probability to displace an atom compared to 48 eV for a Si PKA. Fig. 4.45a shows that the TDE weighted probability distributions for displacing the PKA and an atom in 3C-SiC are identical for C PKAs up to ~50 eV, but then diverge with increased PKA energy. For instance, the probability to displace a C PKA of 149

eV is ~85%, compared to 100% for displacing an atom. For the Si PKAs, the TDEs and the corresponding probabilities for displacing a PKA and an atom are different. At Si PKA energy of 136 eV, the calculated displacement probabilities are 66% and 100%, respectively (Fig. 4.45b). The difference is because in the [110], [111], [$\bar{1}\ \bar{1}\ \bar{1}$] directions, the lighter C SKAs are easily displaced by Si PKAs, which recoil back to their original lattice sites.

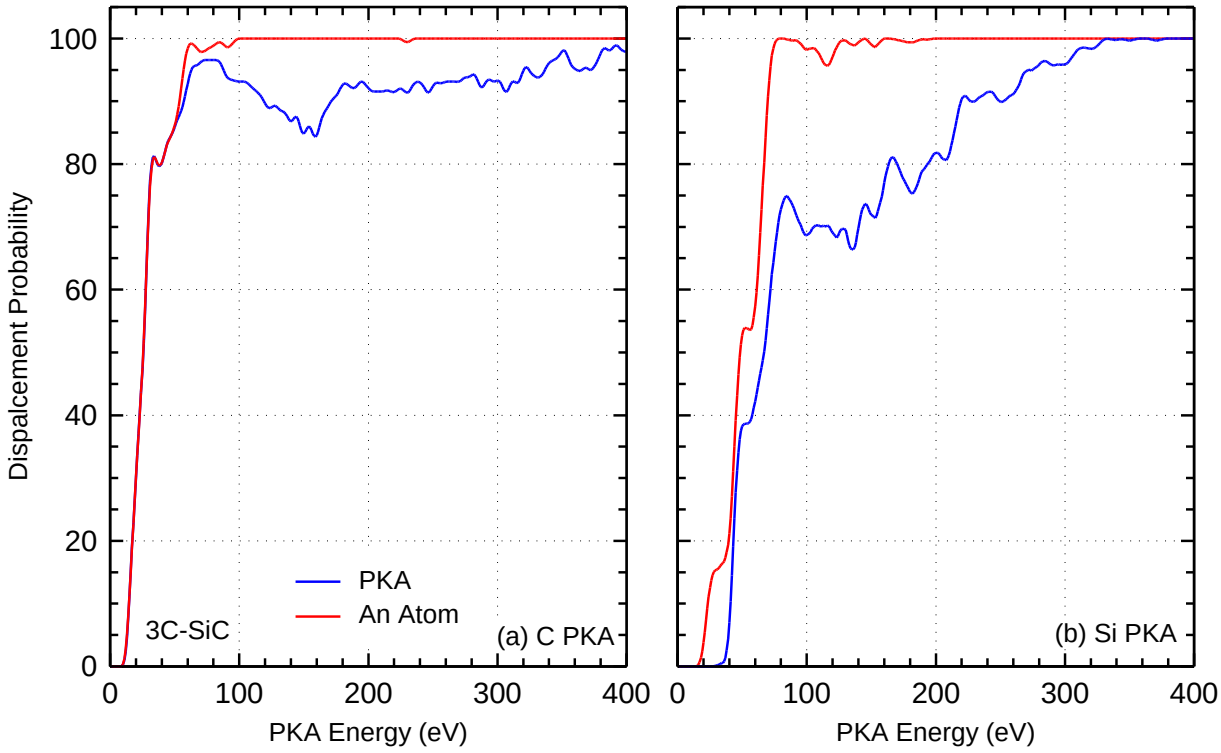

Figure 4.45: Comparison of TDEs weighted probability distributions for displacing a PKA and an atom in 3C-SiC.

In a-SiC, the calculated TDE probability distributions for displacing a C PKA and an atom are almost identical (Fig. 4.46), indicating that these TDE definitions could be used interchangeably. The Si PKAs are likely to displace the less-massive C PKAs at lower energies than required to displace the Si PKA. For instance, a Si PKAs of 50 eV has an 80% probability to be displaced, compared to 95% probability to displace an atom. The Si PKA can cause an avalanche of defects on the carbon sublattice before it is displaced in the [110], [111], [$\bar{1}\ \bar{1}\ \bar{1}$] directions. However, the probability of this happening in a-SiC is somewhat lower than in 3C-SiC (Fig. 4.46b). This figure shows that a Si PKA with 36 eV has 50%

probability to be displaced in a-SiC, compared to 27 eV to displace an atom with the same probability.

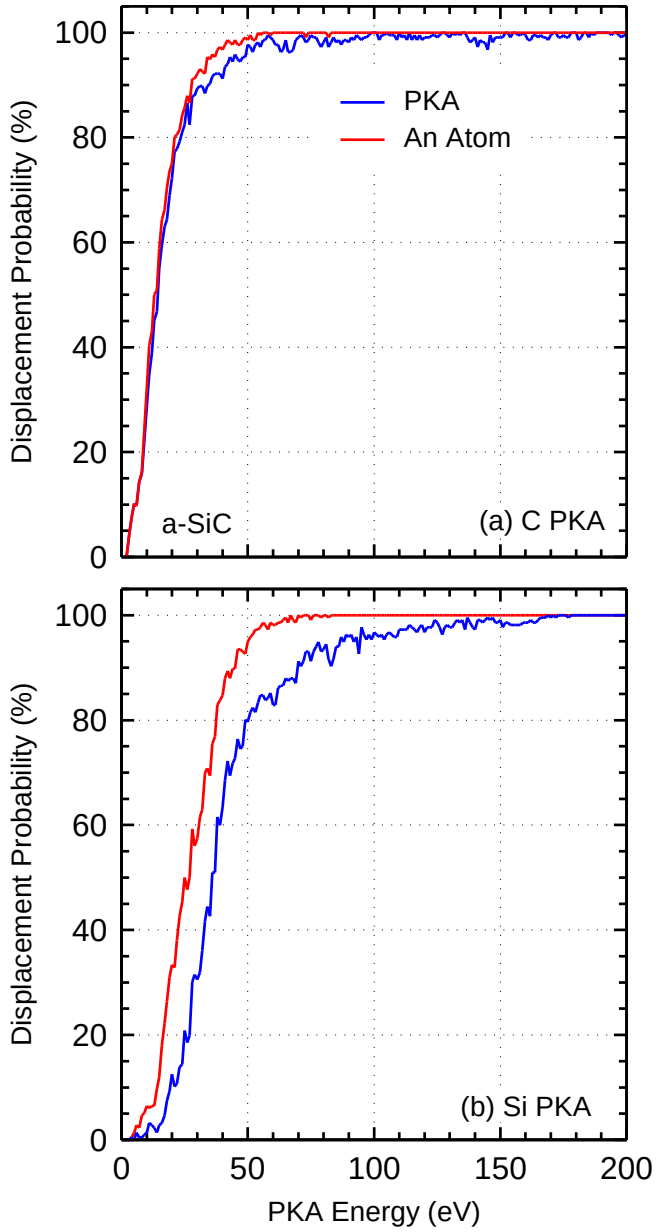

Figure 4.46: Comparison of the probabilities to displace the PKA and an atom in a-SiC.

Fig. 4.47 compares the calculated probability distributions for the displacement of an atom in 3C-SiC and a-SiC. The higher probability for a displacement in a-SiC suggests that atoms are more readily displaced than in 3C-SiC due to the lack of crystal order to cage them in. Furthermore, the produced interstitials in 3C-SiC tend to annihilate with vacancies,

reducing tensile and compressive stresses in the material. Such annihilation process occurs more readily because it is not driven by random-walk diffusion and the strain caused by vacancies and interstitials facilitates annihilation.

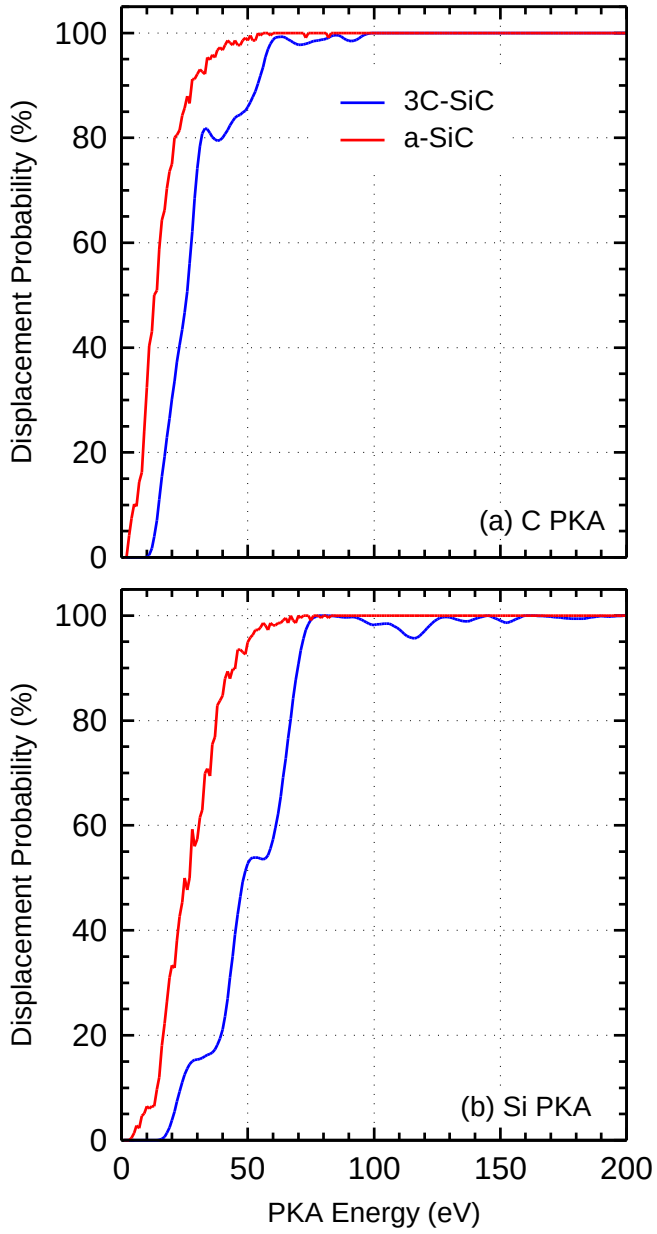

Figure 4.47: Comparison of the probabilities to displace an atom with C and Si PKAs in 3C-SiC and a-SiC.

The activation barrier for an interstitial to jump into the volume around a vacancy and annihilate is not the same as the activation barrier for diffusion.[306] The difference in the

displacement probabilities in 3C-SiC and a-SiC by Si PKAs is relatively larger by C PKAs (Fig. 4.47). For instance, the C PKA energy for a 50% probability to displace an atom in a-SiC and 3C-SiC is 13 eV and 26 eV, respectively. However, for Si PKAs, the corresponding energies are much higher, 27 eV and 48 eV, respectively. It is worth noting that both C and Si PKAs are displaced in a-SiC at roughly half the energies in 3C-SiC.

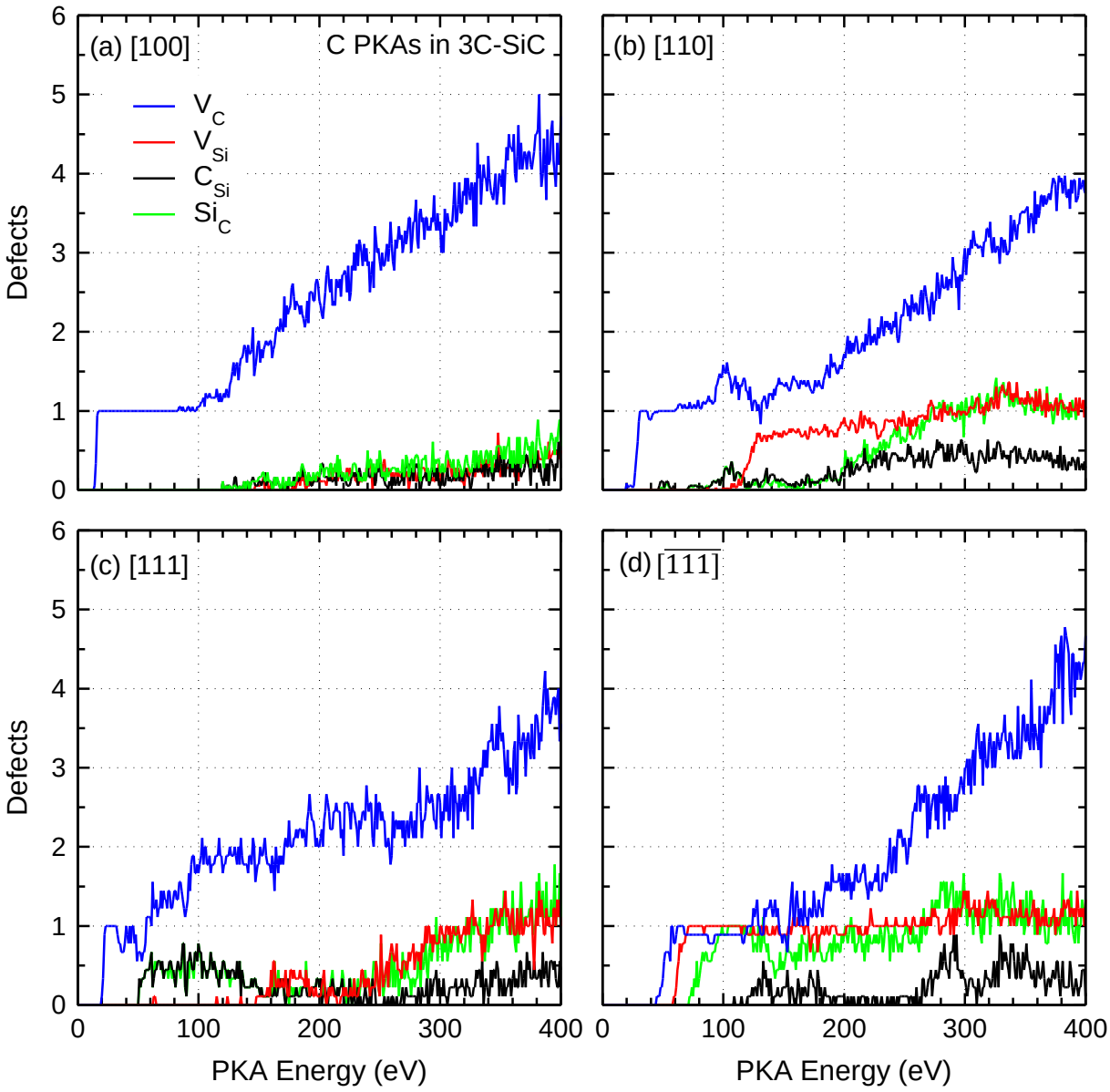

Figure 4.48: Average number of vacancies and antisites produced with C PKAs in 3C-SiC.

4.3.2.3 **Defect Production**

Fig. 4.48 shows the calculated average number of vacancies and antisites produced with C PKAs in 3C-SiC. While V_C are produced at low PKA energies, V_{Si} are produced at much

higher energies, except in the [$\bar{1}$ $\bar{1}$ $\bar{1}$] direction. In that direction, the C PKAs recoil off Si first neighbors, losing a large fraction of their kinetic energy. While the energy needed for a C PKA to displace a Si SKA could be as low as 57 eV; often times, such energy is not enough to force a Si SKA to leave its lattice site. However, a 72 eV C PKA produces a V_{Si} in the [$\bar{1}$ $\bar{1}$ $\bar{1}$] direction 100% of the time (Fig. 4.48).

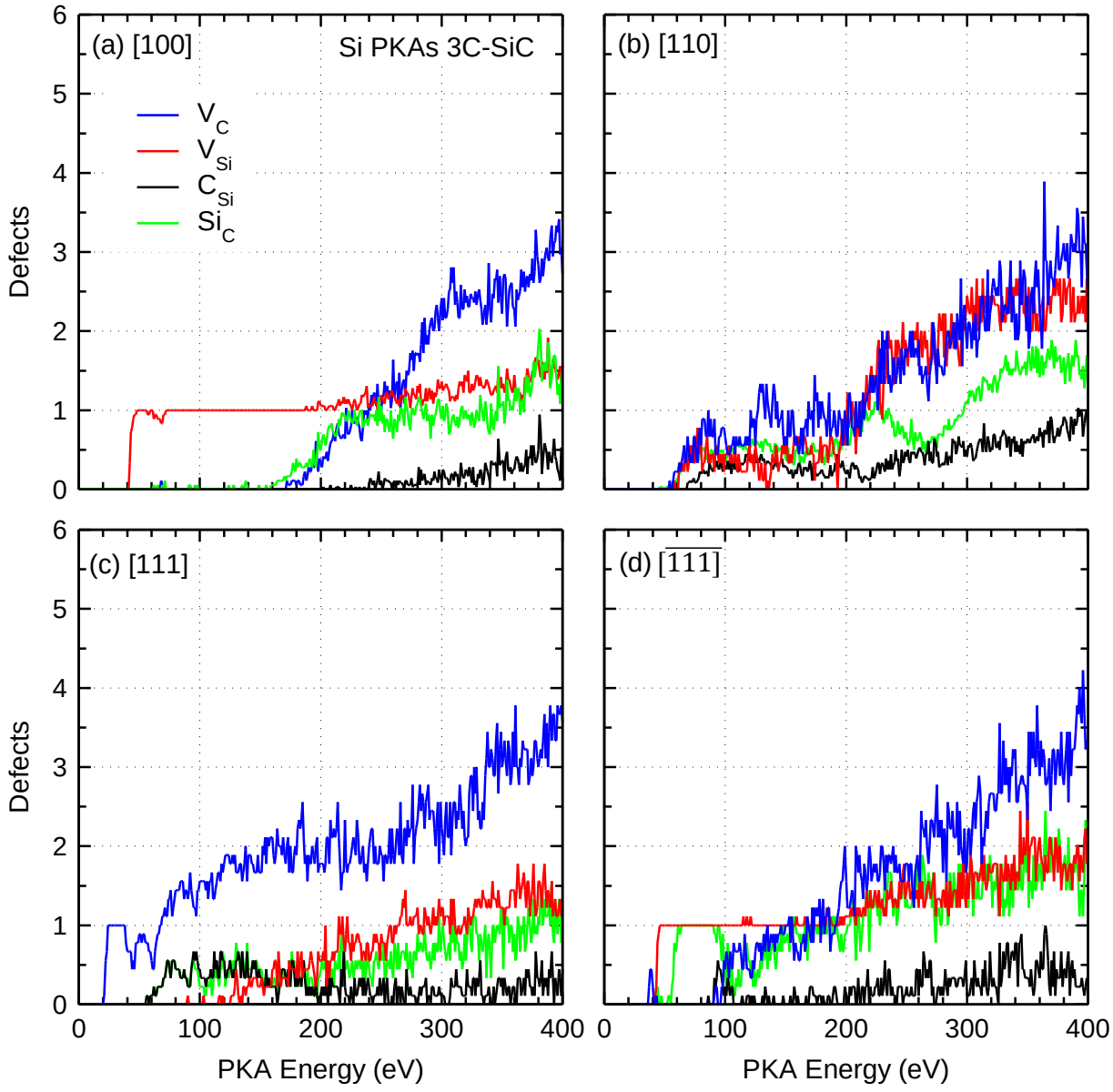

Figure 4.49: Average number of vacancies and antisites produced with Si PKAs in 3C-SiC.

The production of both C_{Si} and Si_C with C PKAs is fairly minimal, and typically occurs at energies of several hundred eV In the [100] direction the 400 eV C PKAs recoil off their C nearest neighbors, producing <1 antisite on average. This is because in that direction a C

PKA is not likely to displace a Si atom and produce an antisite. In the [110] and [111] directions, C PKAs produce similar number and types of defects. The C PKAs in the [110] direction collide with their nearest Si atoms, causing them to deviate to the [111] direction, instead of causing a replacement collision.[155] In these and the $[\bar{1}\,\bar{1}\,\bar{1}]$ direction a 400 eV C PKA produces on average ~4 V_C and 1 V_{Si}.

Fig. 4.49 compares the calculated number of vacancies and antisites produced with Si PKAs in 3C-SiC versus the PKA energy. On average, Si PKAs with energies of 46 and 48 eV produce one V_{Si} in the [100] and the $[\bar{1}\,\bar{1}\,\bar{1}]$ directions. In the [111] direction, the carbon vacancies are produced at lower energies than the silicon vacancies, because Si PKAs displace their nearest C neighbors and recoil off, returning to their original sites. In the [111] direction, the Si PKA with 400 eV produces ~1 V_{Si} and 4 V_C. Over the entire energy range investigated carbon vacancies (V_C) are formed preferentially in this direction. In the [100] direction, Si PKAs produce a V_{Si} at ~42 eV, and additional V_{Si} are not likely to form even for PKA energies of 400 eV (Fig. 4.49). Instead, the Si PKA and SKA produce an avalanche of defects on the C sublattice. For example, the 400 eV Si PKAs are predicted to produce more V_C than V_{Si} in all four low-index crystallographic directions (Fig. 4.49). While direction-specific defect production is important for assessing radiation damage, weighted defect production versus PKA energy could be a useful input for higher-level, coarse-grained models.

Fig. 4.50 compares the average number of vacancies and antisites produced on both sublattices versus the PKA energy, by accounting for the multiplicity of the four low-index crystallographic directions of [100], [110], [111], and $[\bar{1}\,\bar{1}\,\bar{1}]$. For 400 eV C PKAs, only ~4 V_C and ~1 V_{Si} are produced, compared to ~3.3 V_C and ~1.9 V_{Si} produced with Si PKAs for the same energy. Thus, the V_C produced with C PKAs are 4x the V_{Si}, compared to 1.75x with Si PKAs. Results also show that silicon antisites are more likely to form than carbon antisites with both C and Si PKAs. In fact, the number of silicon antisites produced with C PKAs is approximately the same as the number of V_{Si} produced. This suggests that many of the displaced Si atoms cause replacement collision sequences with C atoms, rather than becoming interstitials. The carbon antisites are less likely to form because displaced C atoms do not readily cause a replacement collision sequence with a Si atom. This is because the mass of the latter is ~2.34x that of C atom. Models that use the TDE as an input for radiation

damage codes may use the defect production results in Fig. 4.50 to ensure that the predicted defects production matches that from the present MD simulations for C and Si PKA energies up to 400 eV.

Fig. 4.51 plots the number of displaced atoms with C and Si PKAs versus energy up to 400 eV. The results display a linear increase in displaced atoms with increased PKA energy of both types, with a somewhat steeper slope for Si PKAs. These linear trends (ignoring the results below 100 eV in order to avoid near-threshold energies) of the number of displaced atoms, N_{disp}, with C and Si PKAs, are correlated (Fig. 51), as:

$$N_{disp}(\text{C PKA}) = 0.042296(E_{PKA}) - 1.4771, \quad E_{PKA} > 100 \text{ eV} \qquad \text{Eq. 4.6}$$

and,

$$N_{disp}(\text{Si PKA}) = 0.027088(E_{PKA}) + 1.4058, \quad E_{PKA} > 100 \text{ eV} \qquad \text{Eq. 4.7}$$

The larger mass Si PKAs are likely to displace more atoms than the C PKAs.

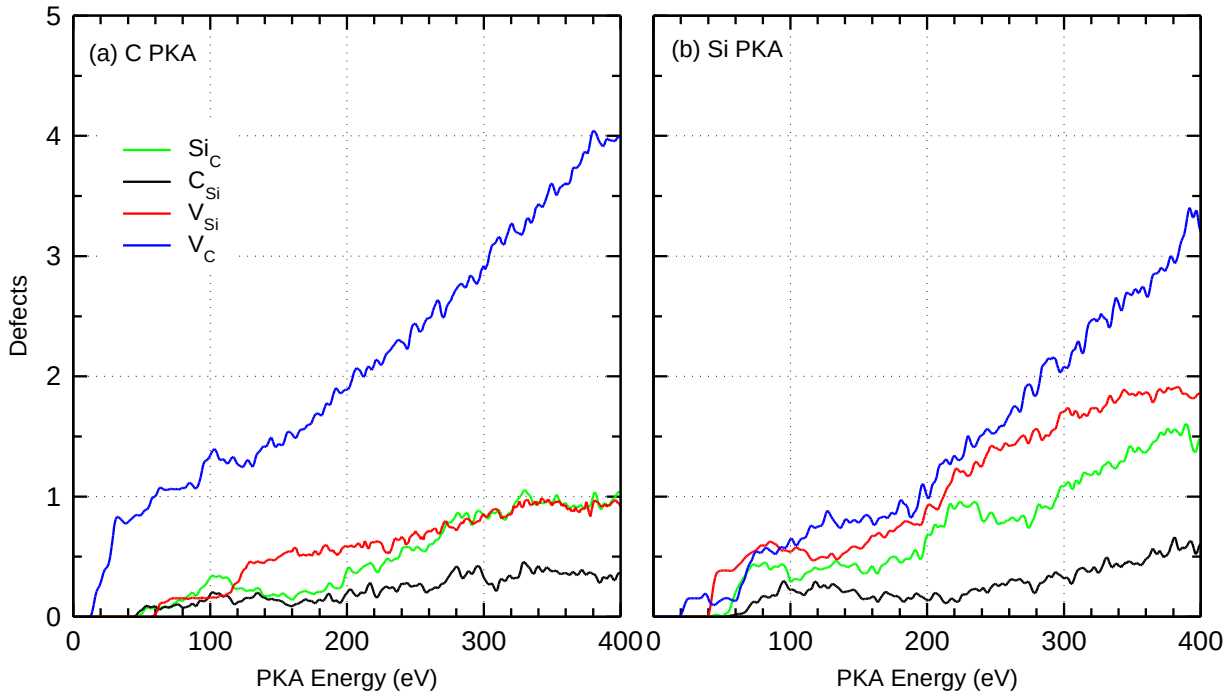

Figure 4.50: Comparison of the weighted Frenkel pair production curves with C and Si PKAs in 3C-SiC.

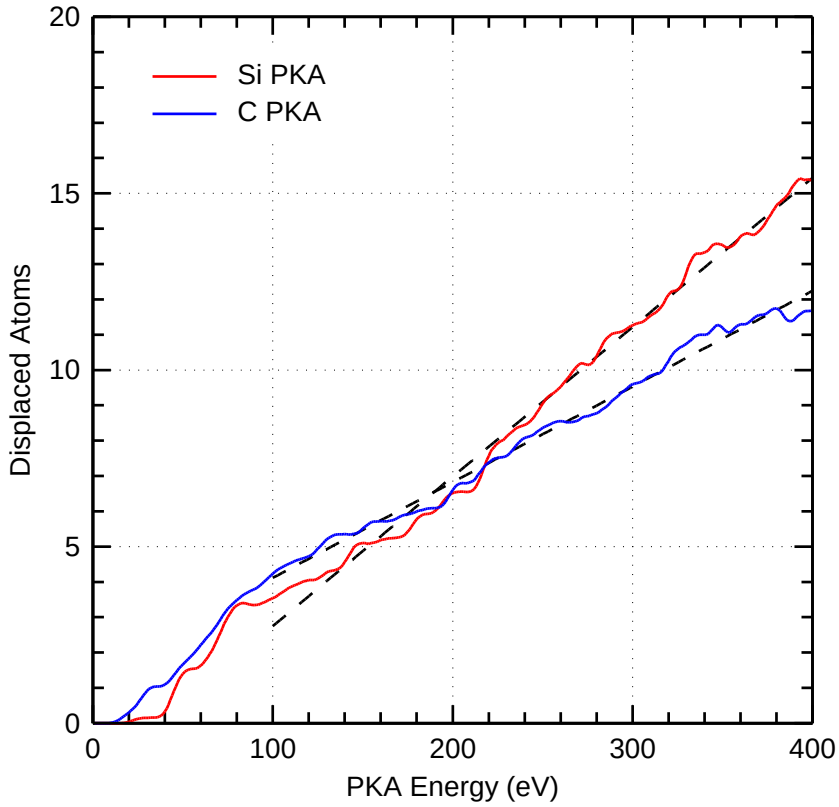

Figure 4.51: Comparison of the number of displaced atoms as a function of C and Si PKA energy in 3C-SiC.

4.3.3 Highlights and Concluding Remarks

The present MD simulations investigated TDEs and the directional dependence of defect production in 3C-SiC and a-SiC by C and Si PKAs of energies up to 400 eV. Results demonstrated that TDEs for the displacement of PKAs and of an atom, and the formation of Frenkel pairs are different and cannot be used interchangeably. The obtained polar contours of defect production on both sublattices show strong anisotropy on both sublattices. The lowest TDE for a C PKA to produce a carbon vacancy in any crystallographic direction is 14-16 eV for C PKAs and 38-58 eV for the Si PKAs. The lowest TDEs for the C and Si PKAs to produce a Si vacancy are 59-71 eV and 42-46 eV, respectively. These results are in good agreement with prior *ab initio* simulations. The number of displaced atoms with either C or Si PKAs increase linearly with increased energies above the determined TDEs.

The weighted probability distributions for displacements of a PKA and an atom in the four low-index crystallographic directions of [100], [110], [111], and $[\bar{1}\,\bar{1}\,\bar{1}]$ are identical for the C PKAs with energies below 50 eV, but diverge at higher energies. The carbon vacancies

are the most common defect produced with both C and Si PKAs. The number of C vacancies produced by a C PKA and a Si PKA of 400 eV are 4x and 1.75x the silicon vacancies produced, respectively. While the production of antisites is not as common as Frenkel pairs, PKAs with energies of a few hundred eV could generate at least one antisite on average. Additionally, Si antisites are more likely to form than C antisites since C atoms are less likely to displace the more massive Si atoms and cause a replacement collision sequence.

The calculated probability distributions for the displacements of a C PKA and an atom in a-SiC are nearly identical, indicating that respective TDEs could be used interchangeably. However, the Si PKAs are likely to displace C SKAs at lower energies than for displacing the Si PKAs. This is similar to interaction sequences in some directions in 3C-SiC. For the same PKA energy, atoms are more likely to be displaced in a-SiC than in 3C-SiC. The energy for C PKAs to cause displacements 50% of the time in 3C-SiC is 26 eV, compared to 13 eV in a-SiC. For Si PKAs, the corresponding energies are 48 eV and 27 eV, respectively. The crystal order in 3C-SiC can often cause the PKA to be caged in, making it difficult to escape its lattice site, unless it has enough energy to displace its neighbor.

The present results would be useful to higher level, coarse-grained, mesoscale models for predicting the rates of defect production in bulk materials, and of interest to industrial applications of 3C-SiC structures and of a-SiC coatings for protecting against harsh environments of high temperature, corrosive gasses, and irradiation in nuclear reactors. These materials are currently being investigated as part of the DOE campaign for developing accident tolerant fuel systems for enhancing operation and safety of existing and future advanced light water reactors.

This chapter has extensively presented results regarding the TDE; however, this does not allow for the observation of large-scale defect cascades, which would occur inside nuclear reactors. The next section presents MD simulation results of bulk radiation damage in SiO_2 (0.25 – 2 keV PKAs) and TiO_2 (1 – 10 keV PKAs). The following chapter presents bulk-radiation effects in TiO_2 (46 keV projectile), SiC (10 – 100 keV PKAs), and MgO (1 – 50 keV, multiple ions) and compares the results to *in situ* TEM ion beam irradiation.

5 MD SIMULATIONS OF BULK RADIATION DAMAGE

This section presents the effects of high-energy PKAs in SiO_2 (quartz) and TiO_2 (rutile). PKA energies of up to 2 keV are investigated in SiO_2, and up to 10 keV in TiO_2.

5.1 SiO_2

This study performed MD simulations to investigate the production of point defects in crystalline SiO_2, or α-quartz, by oxygen and silicon PKAs having energies of 0.25, 0.5, 1.0, and 2 keV. The simulations used the BKS-ZBL force field, a universal cutoff of 15 Å, and a variable time step algorithm. The results are analyzed for the defect production using both the WS and coordination analysis methods. The amount and types of the defects produced at the end of the ballistic phase (peak defects) are compared to those of the residual defects after annealing to determine the annealing efficiencies of the different types of point defects. In addition, the present results of the produced defects at PKA energies up to 2 keV are compared to those of Wang et al.[51]

5.1.1 Methodology

LAMMPS[249] is used to conduct the present MD simulations of the point defects production using oxygen and silicon PKAs with energies $\leq$ 2 keV. The oxygen and silicon PKAs of the different energies are investigated in three crystalline directions, namely; [100], [110], and [111]. These directions are converted to the 4-index system, since quartz is part of the hexagonal crystal family. The corresponding three 4-index directions are $[2\bar{1}\bar{1}0]$, $[11\bar{2}0]$, and $[11\bar{2}3]$. To ensure statistically sound results, for each PKA type (oxygen and silicon) and energy (0.25 – 1.0 keV), the results of 24 simulations in each of the three directions are averaged, with ± one standard deviation. Only the results for the 2.0 keV PKAs, are averaged in a single direction ($[2\bar{1}\bar{1}0]$).

The number of system atoms used varies with the PKA energy. For instance, 36,864 atoms are used for the 0.25 and 0.5 keV PKAs, while 72,000 and 243,000 atoms are used for the 1.0 keV and the 2.0 keV PKAs, respectively.

The spline connecting the BKS and ZBL force fields, used in the present MD simulations, is expressed as:

$$E_{ij} = \exp\left(B_0 + B_1 r_{ij} + B_2 r_{ij}^2 + B_3 r_{ij}^3 + B_4 r_{ij}^4 + B_5 r_{ij}^5\right). \quad (5.1)$$

It has detachments points of 0.5 and 1.54 Å for the O-Si interactions, and 0.4 and 2.1 Å for the O-O interactions.[54]This splined BKS and ZBL potential has been used successfully in

earlier MD simulations of crystalline silica[54] for determining the TDE probability distributions for the oxygen and silicon PKAs in α-quartz. In this potential, Coulomb interactions are simulated using the particle-particle particle-mesh (PPPM) solver, with a relative error of 1.0e-6. The implemented variable time-step algorithm in the present MD simulations ensures high accuracy and computational efficiency. The input to the algorithm is the maximum distance the atoms are allowed to move in a given time step (r_{max}). In the present MD simulations, r_{max} decreased gradually from 0.1 to 0.001 Å, when a further decrease no longer affected the results.

In the implemented simulation methodology, to relax the structure, the system of atoms is first equilibrated for 20 ps in an NPT ensemble at 300 K and 1.0 atm. The system is then equilibrated in an NVE ensemble with a thermostatic boundary layer (NVT ensemble), maintained at 300 K for 10 ps, as done by Dholakia et al.[307] Many studies involving radiation damage have implemented this boundary layer, typically a few lattice units thick, to dissipate the heat produced in the course of interactions in the system of atoms used in the MD simulations.[47,308,309] In reported simulations, the thickness of this layer varied from ~3 to 10 Å.[47,309] The thermostatic boundary layer and the temperature damping parameter used in the present MD simulations is 6 Å and 0.1 ps, respectively. Finally, either an oxygen or silicon PKA with an energy ranging from 0.25 – 2 keV is invoked and the evolution of the induced damage cascade is followed for 10 ps, including the ballistic and annealing phases of interaction. In the present MD simulations, if a cascade hits the thermostatic boundary layer, the case is discarded and the results omitted from consideration. This only occurred in a couple out of 480 simulations.

In the ballistic phase of interaction, the PKA and associated secondary knock-on atoms (SKAs) have energies much higher than the TDE. In the annealing phase, over the next several ps of simulation, thermal recombination allows many of the displaced atoms to anneal to appropriate lattice sites. Thus, the residual defects at the end of the annealing phase are much lower than the peak defects in the ballistic phase, but the difference depends on the PKA energy. To estimate the annealing efficiency, the number of the peak defects is compared to that of the residual defects during the last 2 ps of the simulation time. The annealing efficiency is the percentage of peak defects recombining before the end of the annealing phase in the analysis. Post-processing of the MD simulation results is carried out

using both the WS and coordination defect analysis methods. These methods, implemented by OVITO,[304] characterize and quantify the various types of point defects. The WS analysis method determines the antisite defects by comparing the sites of the different atom types in the crystal before and after irradiation. All point defects investigated are shown in Fig. 5.1.

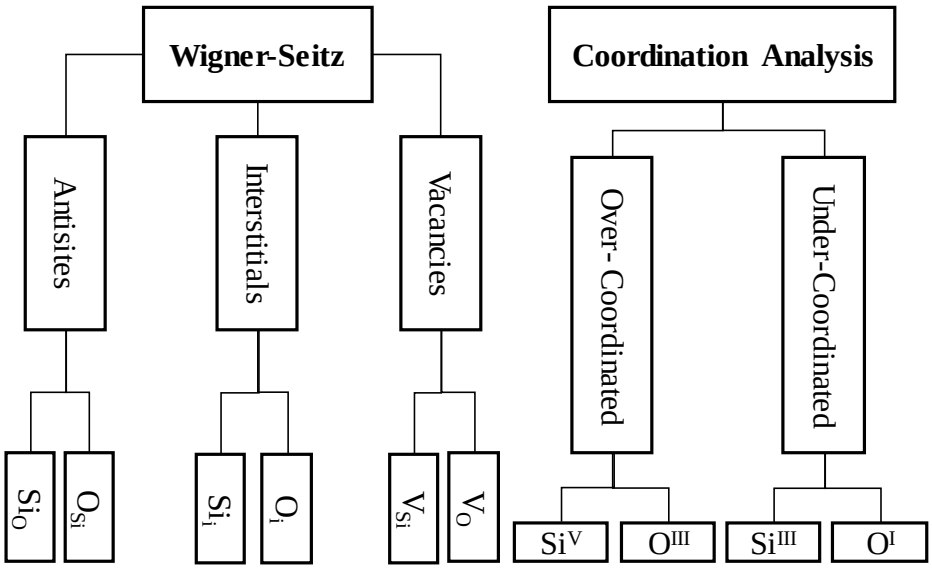

Figure 5.1: Defects investigated with the Wigner-Seitz and coordination analysis methods.

5.1.2 Results

This section presents the MD simulation results of the production of point defects in α-quartz by oxygen and silicon PKAs with energies of 0.25, 0.5, 1.0, and 2.0 keV, in 3 crystallographic directions of $[2\bar{1}\bar{1}0]$, $[11\bar{2}0]$, and $[11\bar{2}3]$. The performed MD simulations investigated the effects of the time step size and the implemented variable time step on the results convergence, and the estimates of various types of defects production. This is accomplished using the WS defect analysis and coordination analysis. Annealing efficiencies for the different defect types are also calculated and compared. In addition, the present results of defects production for PKA energies up to 2 keV are compared to those of Wang et al.[51]

5.1.2.1 Effect of the variable time step

Determining the appropriate time step size for simulating the irradiation effect in α-quartz is an involved task, as the dynamics of the atom-atom interactions continuously change throughout the simulation. The initial ballistic phase requires using a very small time step in

order to accurately capture the defects peak production. However, as multiple secondary cascades of defects are produced, the energy imparted to the atoms through elastic collisions decreases with simulation time. After a few ps, the PKAs and the produced defects no longer move quickly through the lattice, attempting to anneal (or recombine) to release local tensile and compressive loads. One method to capture the details of the interactions of the PKA with the atoms in the system and track the defects production is to start with a small time step, and gradually increase it after a specified simulation time, as it has been done by Dholakia[307] in studying cascades in yttria. Another method is to use a variable time step algorithm that varies the time step size, based on a user specified maximum distance allowable for any given atom to move during that time step (r_{max}).

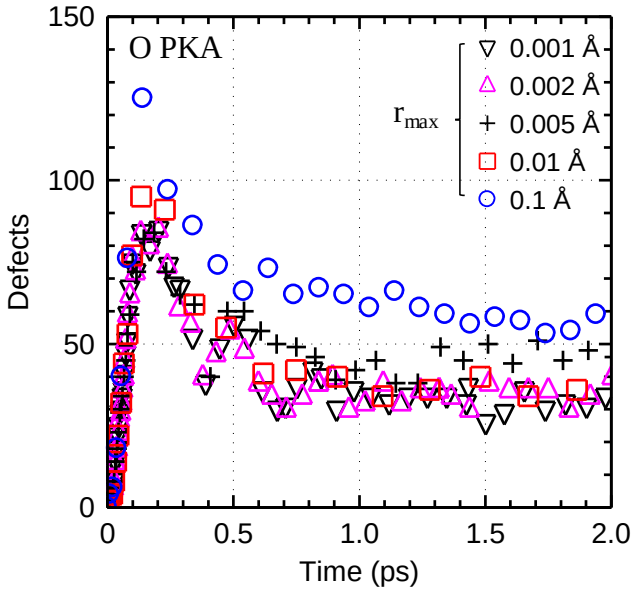

Figure 5.2: Effect of r_{max} on point defects production in α-quartz with 1.0 keV oxygen PKA.

In the present MD simulations, the smallest time step size with a variable time step in the simulation depends on the PKA energy. This time step is subsequently adjusted every 100 steps so as to reduce the computational resources required, but maintain the accuracy of the results. The distance an atom can move during a single time step, r_{max}, in the present MD simulations, is decreased incrementally, until it no longer affects the convergence and the results. The results presented in Fig. 5.2, for oxygen PKA energy of 1.0 keV, show the effect of varying r_{max}, and thus the time step size on the point defects production during the simulation time. The convergence is conservatively reached using r_{max} of 0.001 Å. Larger

values result in higher peak and residual defects. An r_{max} of 0.1 Å gives the largest peak and residual point defects. Thus, the results presented in the remainder of this section, for oxygen and silicon PKA energies of 0.25 – 2.0 keV, are with r_{max} of 0.001 Å. For oxygen PKA energies of 0.25 keV, the time step size varied from $2x10^{-3}$ to 0.05 fs, from $9x10^{-4}$ to 0.05 fs for 1.0 keV, and from $6x10^{-4}$ to 0.05 fs for 2.0 keV. The corresponding values for the silicon PKAs are $2.4x10^{-3}$ to 0.05 fs, $1.0x10^{-3}$ to 0.05 fs, and $9x10^{-4}$ to 0.05 fs, respectively. The smaller initial time steps for the oxygen PKAs is because for the same energy, they travel faster than the silicon PKAs.

5.1.2.2 **Wigner-Seitz Defect Analysis**

In this section, the results of the peak and residual defects produced in α-quartz with oxygen and silicon PKAs of energies up to 2 keV, are analyzed using the WS method. The produced defects peak near the end of the ballistic phase, < 0.3 ps into the simulations, then partially anneal thereafter. Both the peak and residual defects increase with increased PKA energy (Fig. 5.3). In this figure, the peak defects are marked by open symbols, while the residual defects are taken as the average of those remaining during the last 2 ps of the simulation time (10 ps). A large fraction of the produced defects during the ballistic phase anneal, by diffusing to appropriate lattice sites, within 2 ps from the start of the simulation and remain basically unchanged to the end (10 ps) (Fig. 5.3).

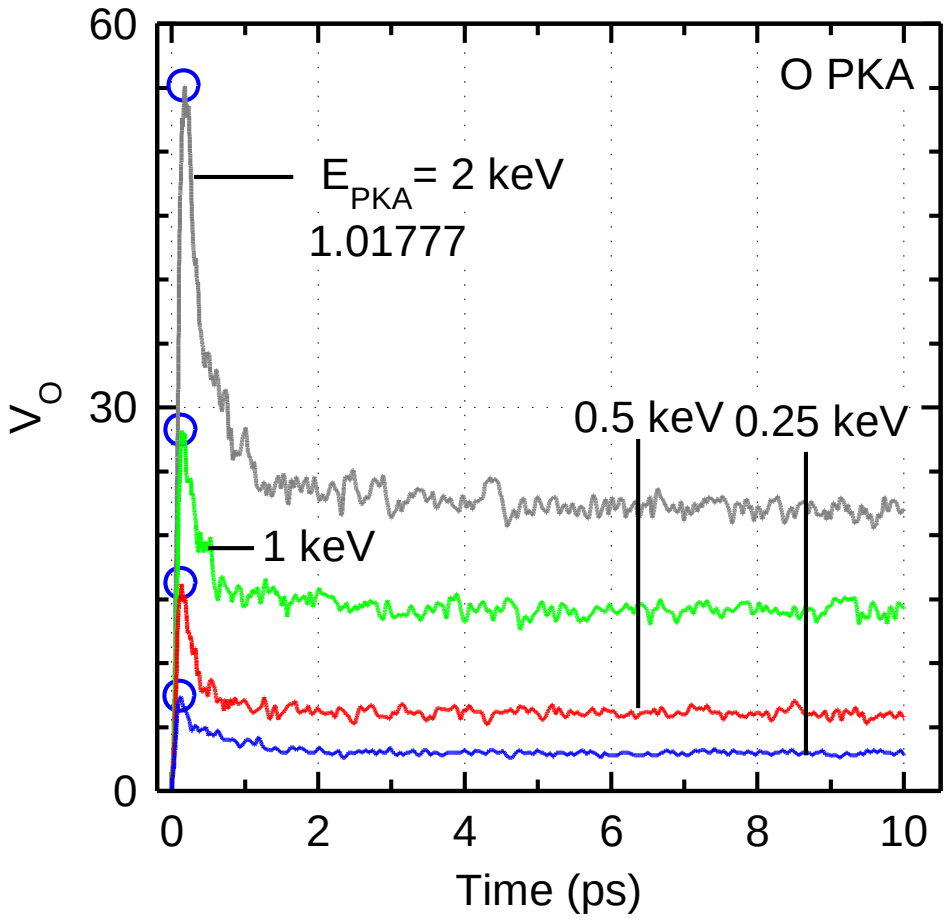

Figure 5.3: Comparison of the produced oxygen vacancies with increasing energy of the oxygen PKAs (0.25 – 2 keV).

Increasing the oxygen PKA energy from 0.25 to 0.5, 1.0, and 2.0 keV increases the number of the peak vacancies production from 9 to 17, 33, and 59, respectively. The corresponding residual vacancies increase from 4 to 7, 14, and 26, respectively. Note that the heating during the ballistic phase of interaction, depending on the PKA energy (E_{PKA}), could tender the material in the interaction zone amorphous. Nonetheless, the number and type of the residual defects are indicative of the amount of the radiation damage in the target material.

Fig. 5.4 compares the peak and residual vacancies, interstitials, and antisites for both the O and Si PKAs in the three directions investigated ([$2\bar{1}\bar{1}0$], [$11\bar{2}0$], [$11\bar{2}3$]). The results show that the number of vacancies is independent of the PKA direction, thus the results in all

3 directions, which are statistically the same, are averaged in subsequent figures. The produced peak and residual vacancies, interstitials, and antisites, by the oxygen and silicon PKAs, are presented and compared in Figs. 5.5a-d and Table 5.1, versus E_{PKA} up to 2.0 keV. To help quantify the differences in the defects production by the oxygen and silicon PKAs, the datasets for each type of defects in Figs. 5a -d are fitted as:

$$N_d = A\, E_{PKA}^{m}. \qquad \text{Eq. 5.2}$$

In this equation, E_{PKA} is in keV, N_d is the number of defects produced, and "A" and "m" are the least square fitting coefficient and exponent. The values of "A" and "m" for the fitted results (Fig. 5.4) are listed in Table 5.2, and could be used for interpolation. The value of the coefficient is indicative of the defect production with low PKA energy, and the value of the exponent is indicative of the increase in the defects production with increased E_{PKA}. The obtained values for the peak and residual defects of different types produced by the oxygen and silicon PKAs are listed in Table 5.1. This table shows that at 2 keV, the oxygen PKAs produce 61.5 ± 6.8 oxygen interstitials and 59.4 ± 6.2 oxygen vacancies at the peak of the ballistic phase, compared to 61.1 ± 10.3, and 58.2 ± 10.2 by the Si PKAs, respectively. These results are statistically the same for both PKA types.

Table 5.1 also shows that PKA type does not influence defects production for all the energies investigated. The primary defects produced during the ballistic phase are oxygen vacancies and interstitials and slightly less silicon vacancies and interstitials. Because the silicon atoms need to break twice as many bonds as the oxygen atoms, they are more difficult to remove from their lattice sites. However, the number of annealed oxygen vacancies and interstitials are statistically the same as the number of the annealed silicon vacancies and interstitials.

The antisites production, which requires the presence of a sufficient number of oxygen and silicon vacancies and interstitials, forms during the ballistic phase. However, antisites are much harder to form than vacancies and interstitials, as shown in Fig. 5.5 and Table 5.1. While results on the energies of the Si and O PKAs to form vacancies and interstitials are easily found in the literature, the values for the formation of antisites in quartz are scarce or nonexistent.

Once the ballistic phase of lower energy PKAs is over (0.25 and 0.5 keV), all oxygen and silicon antisites produced would anneal. However, at higher PKA energy (≥1.0 keV), some of the antisites produced in the ballistic phase remains in the material after annealing. For instance, the 2.0 keV O PKAs produce on average, 10.1 ± 3.6 silicon antisites and ~7.3 ± 2.1 oxygen antisites during the ballistic phase. These defects anneal to 2.0 ± 1.3 oxygen and 2.7 ± 1.4 silicon antisites, respectively. Since there are more oxygen than silicon vacancies produced, the number of the silicon antisites is higher than the oxygen antisites, and the difference and the number increases with increasing the PKA energy. Silicon atoms are also more likely to cause replacement collisions than oxygen atoms, as indicated by Wang et al.[51]

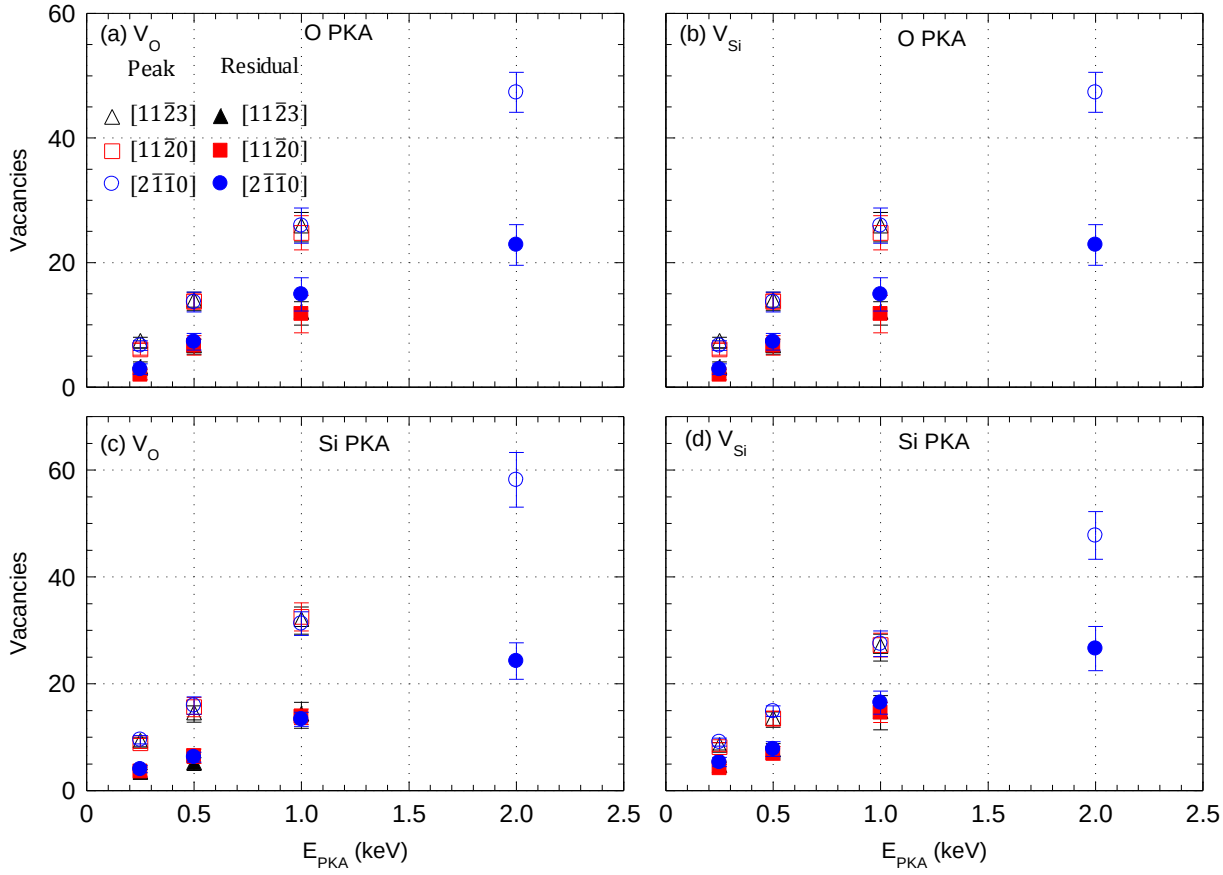

Figure 5.4: Comparison of the numbers of peak and annealed oxygen and silicon vacancies produced in three different crystallographic directions.

Table 5.1: Tabulated values of the peak and residual vacancies, interstitials, and antisites, using both oxygen and silicon PKAs at energies from 0.25 – 2 keV.

Type of Point Defects, N_d	PKA Energy (keV)	Peak Average Defects (#)		Residual Average Defects (#)	
		O PKA	Si PKA	O PKA	Si PKA
Vacancies:					
	0.25	8.9 ± 2.1	9.1 ± 1.7	3.5 ± 1.6	3.6 ± 1.6
V_O	0.5	17.2 ± 3.1	15.3 ± 3.3	7.1 ± 2.3	5.9 ± 2.4
	1.0	32.7 ± 5.2	31.7 ± 4.9	14.0 ± 4.1	13.8 ± 3.6
	2.0	59.4 ± 6.2	58.2 ± 10.2	25.5 ± 5.8	24.3 ± 6.8
	0.25	6.6 ± 1.8	8.5 ± 1.5	2.6 ± 1.9	4.7 ± 1.7
V_{Si}	0.5	13.8 ± 2.8	13.9 ± 2.6	6.9 ± 2.7	7.4 ± 2.7
	1.0	25.7 ± 5.3	27.1 ± 4.7	12.8 ± 5.3	15.2 ± 5.0
	2.0	47.3 ± 6.4	47.8 ± 9.0	22.8 ± 6.5	26.6 ± 8.3
Interstitials					
	0.25	9.3 ± 2.2	9.2 ± 1.8	3.6 ± 1.6	3.8 ± 1.6
O_i	0.5	17.8 ± 3.3	15.8 ± 3.2	7.4 ± 2.2	6.3 ± 2.4
	1.0	33.6 ± 5.5	32.6 ± 5.1	14.7 ± 4.1	14.1 ± 3.7
	2.0	61.5 ± 6.8	61.1 ± 10.3	26.2 ± 5.8	25.2 ± 7.2
	0.25	6.4 ± 1.7	8.4 ± 1.6	2.5 ± 1.9	4.4 ± 1.7
Si_i	0.5	13.5 ± 2.7	13.5 ± 2.6	6.6 ± 2.7	7.0 ± 2.6
	1.0	25.0 ± 5.4	26.2 ± 4.5	12.1 ± 5.2	14.5 ± 4.7
	2.0	45.8 ± 5.7	45.9 ± 9.0	22.1 ± 6.6	25.0 ± 8.7
Antisites					
	0.25	1.7 ± 0.8	2.0 ± 0.9	0.2 ± 0.4	0.3 ± 0.6
O_{Si}	0.5	3.1 ± 1.3	3.0 ± 1.4	0.7 ± 0.7	0.6 ± 0.6
	1.0	4.8 ± 1.9	5.3 ± 1.9	1.0 ± 1.1	1.1 ± 1.0
	2.0	7.3 ± 2.1	7.5 ± 2.1	2.0 ± 1.3	1.9 ± 1.2
	0.25	2.1 ± 1.0	2.3 ± 1.0	0.3 ± 0.5	0.5 ± 0.9
Si_O	0.5	3.8 ± 1.2	3.6 ± 1.2	1.0 ± 0.8	0.9 ± 0.8
	1.0	6.0 ± 1.8	6.4 ± 1.8	1.7 ± 1.2	1.6 ± 1.3
	2.0	10.1 ± 3.6	10.3 ± 2.6	2.7 ± 1.4	3.2 ± 1.3

In order to verify the accuracy of the present results, two sets of 24 simulations are carried out with oxygen PKA energy of 50 eV in the $[2\bar{1}\bar{1}0]$ and $[11\bar{2}0]$ directions, and the number of the residual oxygen vacancies are compared to the experimental value by Arnold[104] at the same energy. The calculated value varied from 1.05 – 1.22, compared to a single oxygen vacancy in the experiments.[104]

Table 5.2: Fitting parameters for the production of vacancies, interstitials, and antisites, with O and Si PKAs of energies of 0.25 – 2 keV.

Type of Point Defects, N_d	Peak				Residual			
	O PKA		Si PKA		O PKA		Si PKA	
	A	m	A	m	A	m	A	m
Vacancies:								
V_O	32.13	0.891	30.99	0.906	13.50	0.938	12.83	0.957
V_{Si}	25.40	0.902	26.46	0.843	12.09	0.964	14.61	0.863
Interstitials								
O_i	33.21	0.892	32.05	0.925	14.01	0.934	13.33	0.943
Si_i	24.66	0.896	25.62	0.834	11.62	0.967	13.85	0.860
Antisites								
O_{Si}	4.687	0.651	4.895	0.655	1.01	0.983	1.056	0.869
Si_O	6.061	0.731	6.231	0.730	1.493	0.928	1.707	0.882

Figs. 5.6a and 5.6b compare the estimates of the annealing efficiency of the different types of defects produced by the oxygen and silicon PKAs of different energies, respectively. The annealing efficiency is the percentage of the peak defects produced near the end of the ballistic phase that recombine "or anneal" by the end of the simulation time (10 ps). For both the O and Si PKAs, the highest annealing efficiencies are those of the oxygen and silicon antisites (73% to 92% depending on PKA energy) (Fig. 5.6). The oxygen vacancies and interstitials anneal at lower efficiencies of ~55-60%, while the silicon vacancies and interstitials typically anneal at efficiencies of ~40-55%, depending on the energy and the type of the PKAs. The decrease in the annealing efficiency with increased PKA energy could be attributed to the high degree of disorder in the defect cascades at the higher PKA energies.

The local crystal structure in the cascade region may permanently change. This makes it difficult to perform WS analysis, because the lattice sites after irradiation would not correspond to those in the perfect crystal before irradiation.

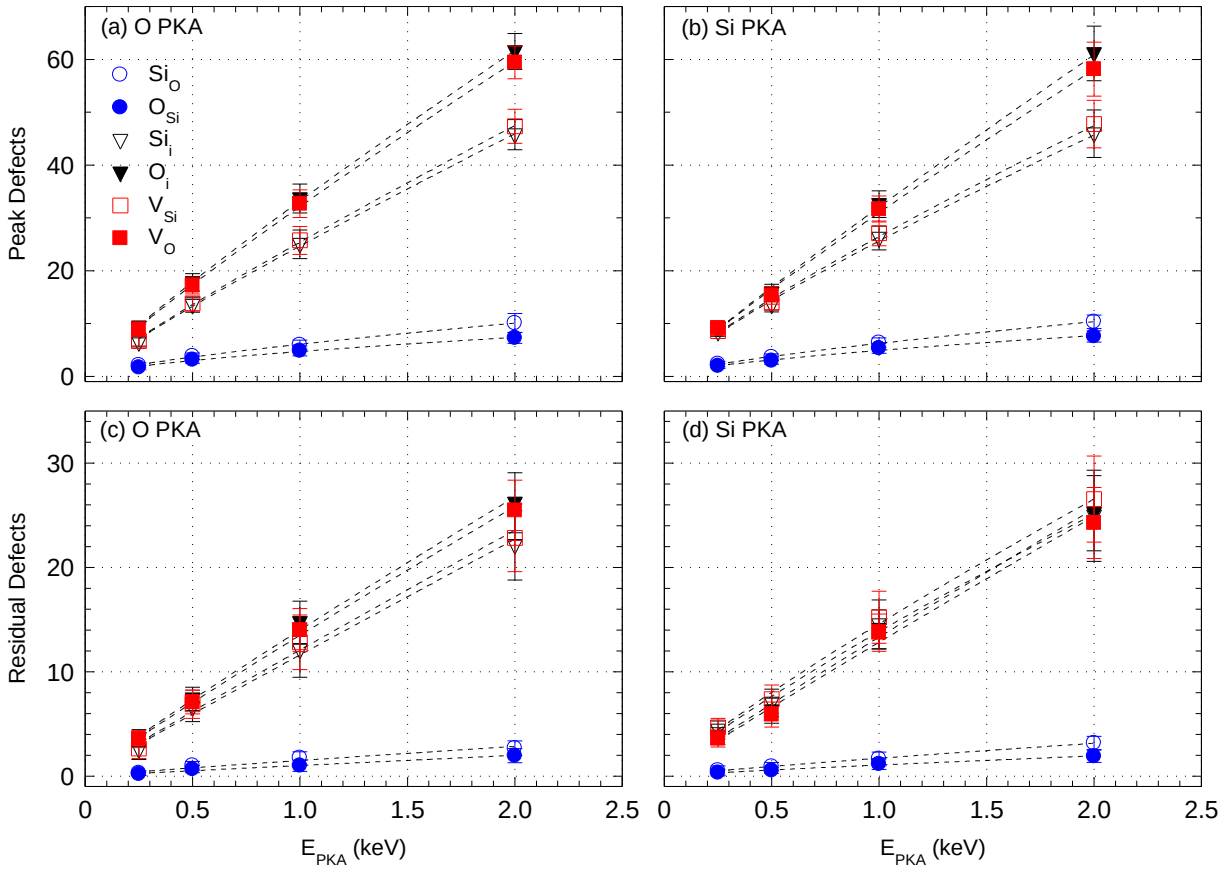

Figure 5.5: Comparison of the numbers of peak and residual vacancies, interstitials, and antisites produced by oxygen and silicon PKAs.

The results of the WS defect analysis detailed in Figs. 5.5 and 5.6 indicate that oxygen vacancies, responsible for forming E' centers, are in fact the primary type of defects produced. However, since the WS defect analysis assumes that the material is largely crystalline, it does not account for the possible formation of amorphous pockets in areas bombarded with the oxygen and silicon PKAs. In order to account for this effect, the coordination analysis of the present MD simulation results is carried out. The aim is to determine the number of the under- and over-coordinated defects and investigate the local changes in the lattice structure to accommodate these defects.

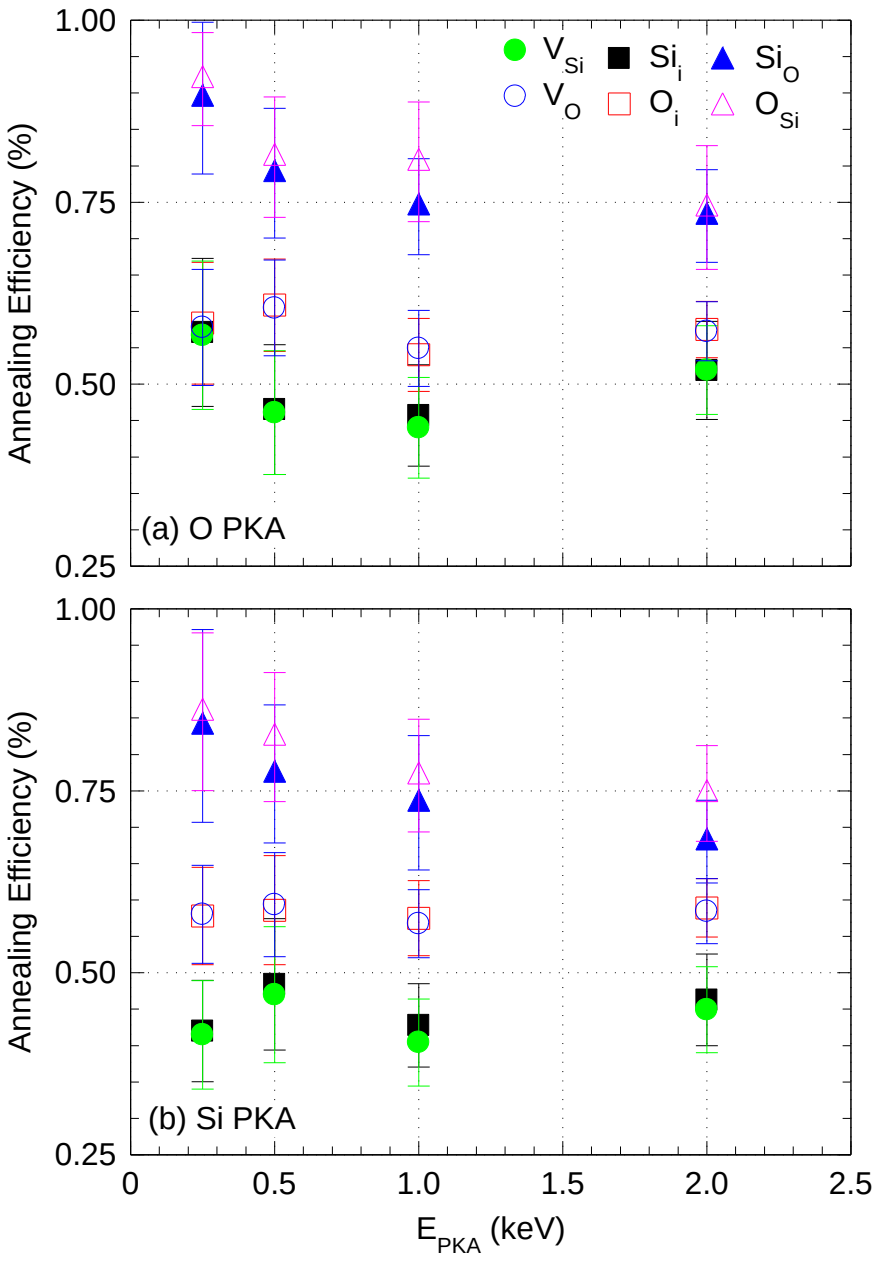

Figure 5.6: Estimates of the annealing efficiency for vacancies, interstitials, and antisites produced by the O and Si PKAs of different energies.

5.1.2.3 **Coordination Analysis**

In highly disordered materials that lack crystallinity, coordination analysis can provide unique information on the point defects production. It is often the case that a crystalline structure locally relaxes to a different configuration in order to accommodate the disorder brought up by irradiation-induced vacancies and interstitials. For instance, once an oxygen

atom is displaced, two Si^{III} (under-coordinated silicon atom) defects are formed. While an under-coordinated oxygen defect, O^{I}, forms in the presence of a local silicon vacancy, an over-coordinated oxygen defect, O^{III}, forms when an interstitial oxygen or silicon atom is wedged into the local crystal lattice. Similarly, silicon under-coordinated defects, Si^{III}, form in the presence of oxygen vacancies, while silicon over-coordinated defects, Si^{V}, form due to local interstitial atoms.

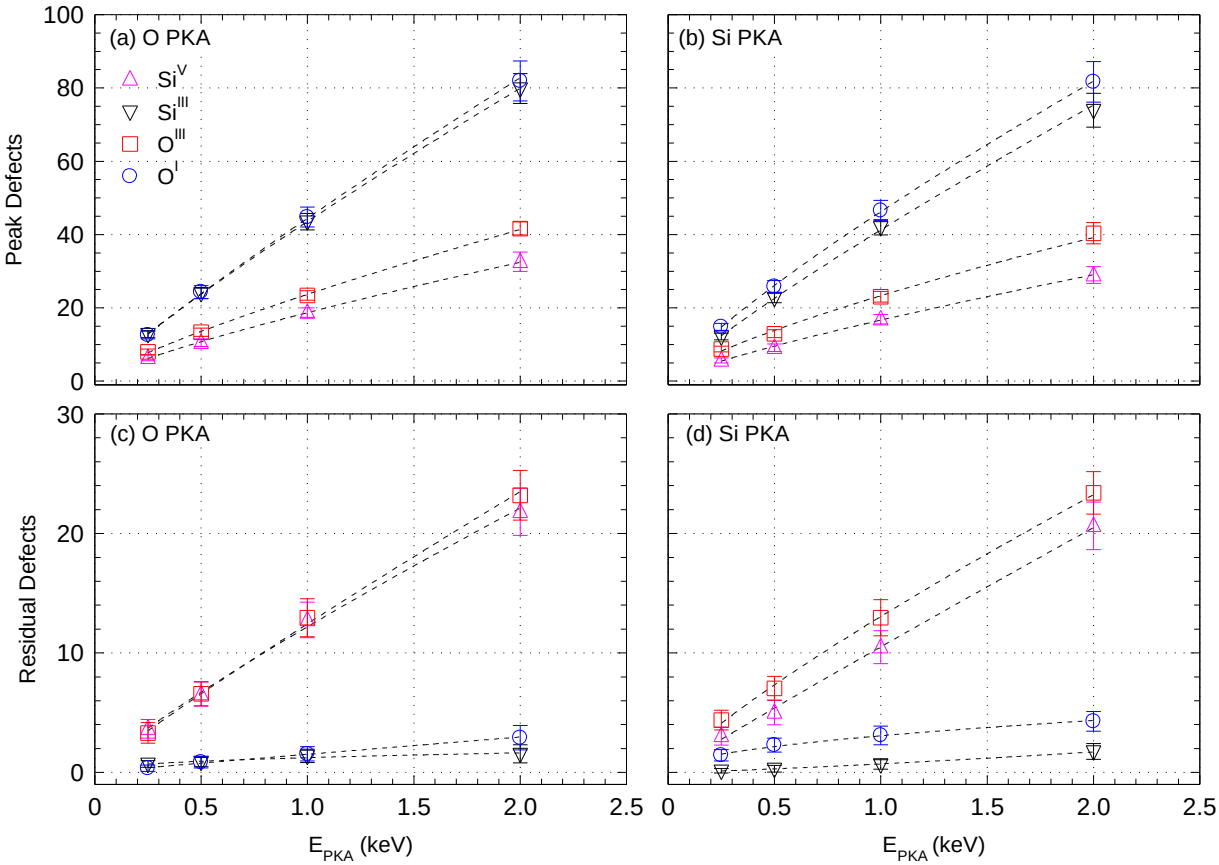

Figure 5.7: Comparison of the numbers of peak and residual under- and over-coordinated defects produced by oxygen and silicon PKAs.

Table 5.3: Comparison of the obtained values of the under- and over-coordinated defects with O and Si PKAs of different energies, up to 2.0 keV.

Type of Point Defects, N_d	PKA Energy (keV)	Peak Average Defects (#)		Residual Average Defects (#)	
		O PKA	Si PKA	O PKA	Si PKA
1. Under-Coordinated					
	0.25	12.6 ± 2.1	14.8 ± 1.9	0.4 ± 0.5	1.4 ± 1.0
O^{I}	0.5	24.3 ± 3.5	25.8 ± 3.3	0.9 ± 0.9	2.3 ± 1.2
	1.0	44.8 ± 5.4	46.6 ± 5.5	1.6 ± 1.2	3.1 ± 1.6
	2.0	82.0 ± 10.9	81.7 ± 11.1	2.9 ± 2.0	4.3 ± 1.7
	0.25	12.8 ± 1.9	12.2 ± 1.8	0.7 ± 0.5	0.1 ± 0.3
Si^{III}	0.5	24.0 ± 2.8	22.7 ± 2.6	0.9 ± 0.8	0.3 ± 0.5
	1.0	43.5 ± 4.5	42.0 ± 4.2	1.4 ± 1.1	0.7 ± 0.8
	2.0	79.8 ± 8.1	74.0 ± 9.3	1.6 ± 1.5	1.8 ± 1.3
2. Over-Coordinated					
	0.25	8.0 ± 1.6	8.8 ± 1.6	3.3 ± 1.7	4.4 ± 1.6
O^{III}	0.5	13.3 ± 2.2	13.0 ± 2.2	6.6 ± 2.0	7.0 ± 2.0
	1.0	23.4 ± 2.6	23.0 ± 3.0	13.0 ± 3.2	13.0 ± 3.0
	2.0	41.7 ± 3.5	40.4 ± 5.9	23.2 ± 4.1	23.4 ± 3.6
	0.25	6.4 ± 1.6	5.6 ± 1.4	3.7 ± 1.6	3.0 ± 1.5
Si^{V}	0.5	10.5 ± 2.1	9.1 ± 2.1	6.6 ± 2.0	5.0 ± 2.0
	1.0	18.7 ± 2.6	16.9 ± 2.6	12.8 ± 3.0	10.5 ± 2.8
	2.0	32.6 ± 5.3	29.0 ± 4.6	21.8 ± 4.0	20.6 ± 4.0

Figs. 5.7a and 5.7b compare the peak and Figs. 5.7c and 5.7d compare the residual defects produced by the oxygen and silicon PKAs, respectively. These figures show that the oxygen and silicon under-coordinated defects (O^{I} and Si^{III}) form at a much higher rate with

increased E_{PKA} than the over-coordinated defects (O^{III} and Si^{V}). For 2 keV PKAs, 82.0 ± 10.9 O^{I} and 79.8 ± 8.1 Si^{III} defects are produced by O PKAs during the ballistic phase, compared to 81.7 ± 11.1 O^{I} and 74.0 ± 9.3 S^{III} defects by Si PKAs. As with WS analysis, the number of defects produced by both PKA types are statistically the same. A total of 41.7 ± 3.5 O^{III} and 32.6 ± 5.3 Si^{V} peak defects are produced with 2.0 keV O PKAs, while 40.4 ± 5.9 O^{III} and 29.0 ± 4.6 Si^{V} are produced by Si PKAs of the same energy. Many of the under-coordinated defects anneal after the ballistic phase, whereas over-coordinated defects are much more resistant to annealing (Figs. 5.7c and 5.7d). The numbers of the residual over-coordinated defects (Figs 5.7c and 5.7d) are several times higher that of the under-coordinated defects. The obtained values of the peak and annealed under- and over-coordinated defects are compared in Table 5.3.

The values of the coefficient "B" and the exponent "n" for the peak and residual over- and under-coordinated defects, N_{ou}, produced by the oxygen and silicon PKAs are listed in Table 5.4. The coefficient "B" is indicative of the number of defects produced, while the exponent "n" in indicative of the increase of the produced defects with increased energy of the PKAs.

The defects production datasets in Figs. 5.7a – 5.7d are fitted to a function of the form:

$$N_{ou} = B\ E_{PKA}^{n}. \qquad \text{Eq. 5.3}$$

The parameters listed in Table 5.4 confirm that: (a) the peak oxygen and silicon under-coordinated defects in the ballistic phase are more than twice and increase more with increased E_{PKA} than the over-coordinated defects; and (b) the residual oxygen and silicon under-coordinated defects are significantly less than the over-coordinated defects. The over-coordinated defects of O^{III} and Si^{V} do not anneal readily, and their annealing efficiencies, which are much lower than for the under-coordinated defects, decrease with increased energy of the PKAs (Fig. 5.8a). For example, for Si PKA energies of 0.25 keV, the annealing efficiencies of the over-coordinated oxygen, O^{III}, and silicon, Si^{V}, are ~52% and 55%, respectively. They decrease to ~42% and 28%, respectively, with increased PKA energy to 2.0 keV (Fig. 5.8a). Similarly, the annealing efficiencies of the over-coordinated oxygen and

silicon defects produced by 0.25 keV O PKAs are ~63% and 47%, respectively, and decrease to ~44% and 33%, respectively, for the 2.0 keV O PKA (Fig. 5.8a).

Fig. 5.8b shows that for all PKA energies investigated, the Si^{III} defects produced by Si PKAs anneal and form edge-shared tetrahedra at efficiencies $\geq$ 97%. The Si^{III} defects produced by 0.25 keV oxygen PKAs have an annealing efficiency of ~94%, which increases to ~98% at 2 keV. For all PKA energies investigated, the annealing efficiency of the under-coordinated oxygen defects produced by O PKAs is ~96-97%. However, the annealing efficiency of the defects produced by Si PKAs is ~89% at 0.25 keV, and increases to ~95% at 2keV.

Table 5.4: Fitting parameters for the production of under and over-coordinated defects, with O and Si PKAs of energies of 0.25 – 2 keV.

Type of Point Defects, N_{ou}	Peak				Residual			
	O PKA		Si PKA		O PKA		Si PKA	
	B	n	B	n	B	n	B	n
Under-Coordinated								
O^{I}	44.47	0.897	46.25	0.824	1.522	0.964	3.068	0.502
Si^{III}	43.58	0.875	41.27	0.868	1.238	0.402	0.717	1.258
Over-Coordinated								
O^{III}	23.70	0.804	23.31	0.751	12.44	0.918	13.06	0.832
Si^{V}	18.69	0.796	16.65	0.802	12.20	0.859	10.52	0.962

There are several possible processes for annealing of the Si^{III} defects, namely: (a) annihilation with an interstitial atom, (b) when three member Si-O rings and three-fold coordinated oxygen atoms form, they locally accommodate oxygen vacancies and thus affect the annealing of the Si^{III} defects, as explained by Wang et al,.[51] and (c) for the same energy, the higher momentum of the Si PKAs influence the radiation damage cascade, and hence the annealing efficiency and the residual Si^{III} defects.

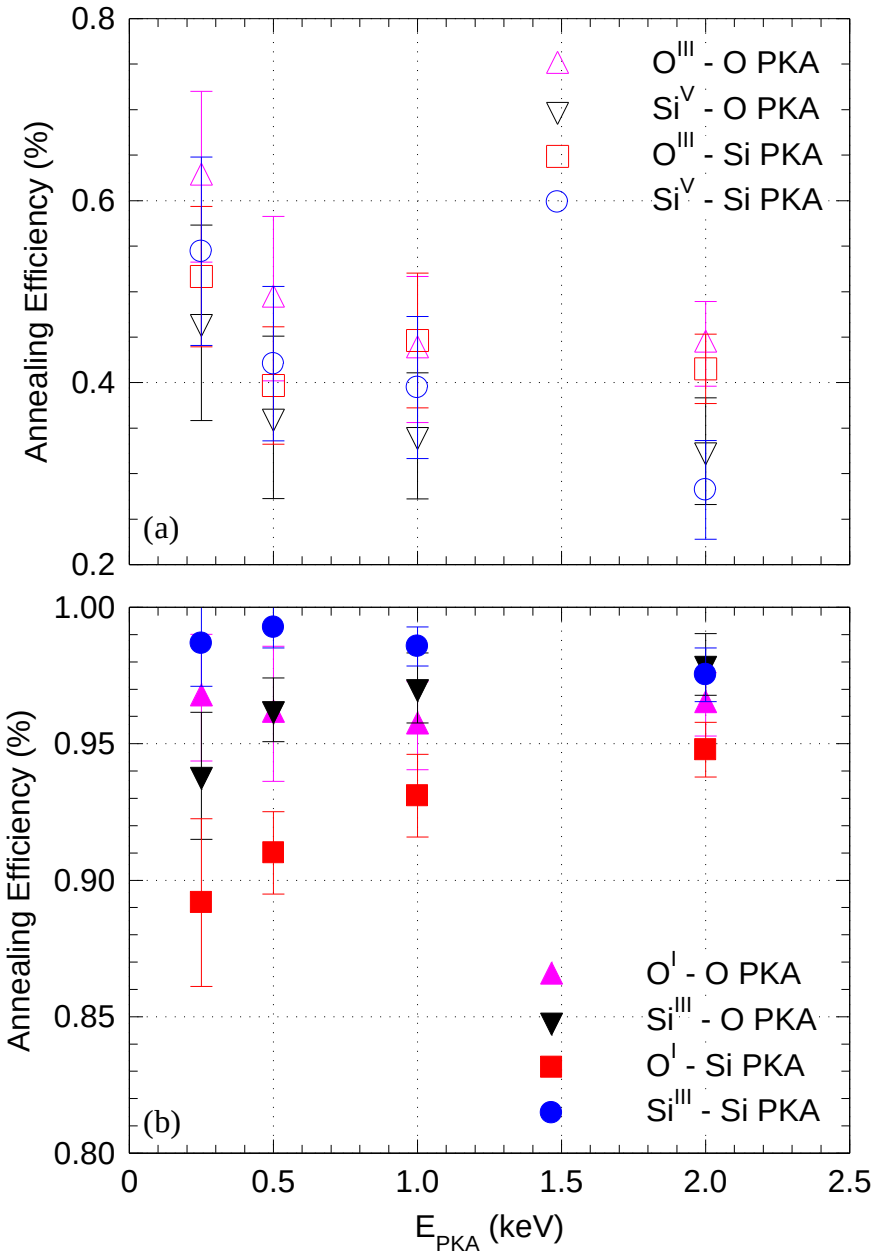

Figure 5.8: Estimates of the annealing efficiencies for the under- and over-coordinated defects produced by O and Si PKAs of different energies.

For instance, Si PKAs are more likely than O PKAs to produce replacement collisions.[51] This could reduce the number of Si^{III} defects, resulting in a higher annealing efficiency of the under-coordinated Si^{III} defects than of those produced by the O PKAs (Fig. 5.8b). At higher PKA energies, the produced defects anneal more efficiently due to the increase in the local

temperature. The high temperature increases the mobility of the atoms around the vacant sites to preferably form over-coordinated defects. Thus, the increased annealing of the under-coordinated defects at higher PKA energies increases the residual over-coordinated defects.

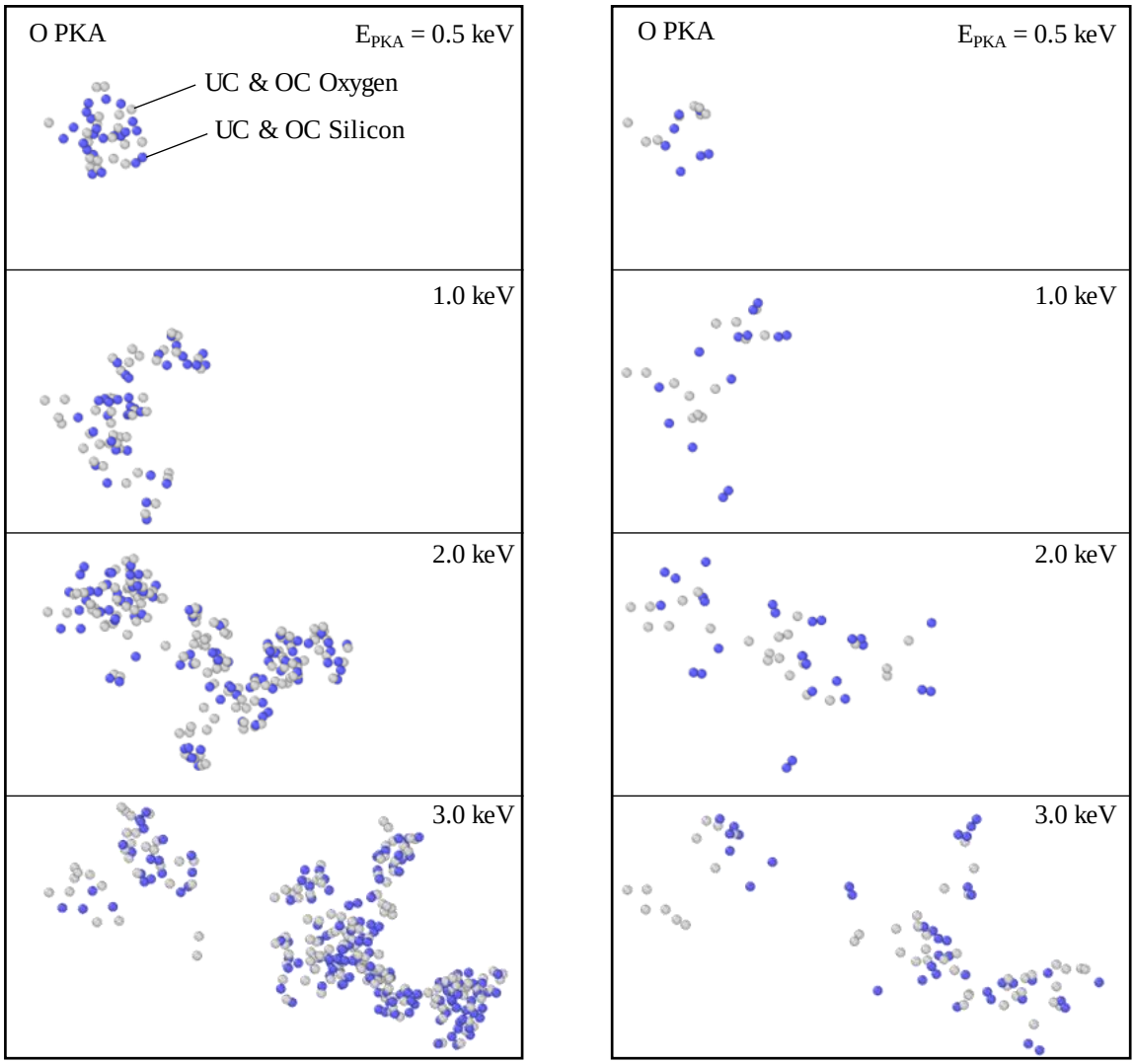

(a) Peak Point Defects (b) Residual Point Defects

Figure 5.9: Comparison of the numbers of the peak and annealed under- and over-coordinated defects produced by oxygen PKAs of various energies.

Figs. 5.9a and 5.9b present images generated based on the coordination analysis of the present MD simulations results of the peak and residual under- and over-coordinated defects produced in in α-quartz by oxygen PKAs of different energies. These images clearly show the increase in the intensity and volumes of the peak (Figs. 5.9a) and residual (Fig. 5.9b)

cascades of the point defects produced with increased PKA energy from 0.5 to 3.0 keV. It is worth noting that at PKA energy $\geq$ 2.0 keV, channeling is likely to occur, causing the produced clusters of displaced atoms to be much more widely spaced within the lattice (Figs. 5.9a and 5.9b).

5.1.2.4 **Comparison with Prior Work**

The estimates of the residual over and under-coordinated defects in α-quartz are compared to those reported by Wang et al.[51] (Fig. 5.10) for PKA energies 0.3 - 0.9 keV. The MD simulations by Wang et al.[51] used a BKS-ZBL potential, a variable time step with a maximum size of 1.0 fs, a short cutoff, and systems of only 4,536, 9,720, and 21,060 atoms for the 0.3, 0.6, and 0.9 keV PKAs, respectively. However, they did not explicitly disclose the PKA types (O or Si) for their final fits to the number of residual defects. Conversely, the present MD simulations with a splined BKS and ZBL potential, a variable time step and a long cutoff, used are large system sizes of 36,864 to 243,000 atoms, depending on the PKA energy. These simulations also investigated defect production with silicon and oxygen PKAs of energies up to 2.0 keV. The present results of the residual over- and under-coordinated defects produced by Si PKAs (Fig. 5.10a) are in closer agreement with those of Wang et al.[51] than those by O PKAs (Fig. 5.10b). Despite the differences in the simulation methodologies, the present results are generally consistent with those reported by Wang et al.[51] (Fig. 5.10). The specific contributions of the present work are:

(1) The results of the effect of using a variable time step algorithm, and the time step size on the point defects production.

(2) The results of the WS defect analysis for determining the formation and estimating the number of the produced vacancies, interstitials, and antisites on the cation and anion sublattices.

(3) Estimates of the defects production and annealing efficiencies for both O and Si PKAs of energies up to 2 keV.

(4) Estimates of the number of vacancies, interstitials, antisites, under-coordinated, and over-coordinated defects produced by both O and Si PKAs.

(5) Estimates of the peak and residual defects production by O and Si PKAs, and of the annealing efficiency of the defects produced during the ballistic phase of interaction by O and Si PKAs in α-quartz.

(6) Results of the directional dependence of defects production with O and Si PKAs of different energies.

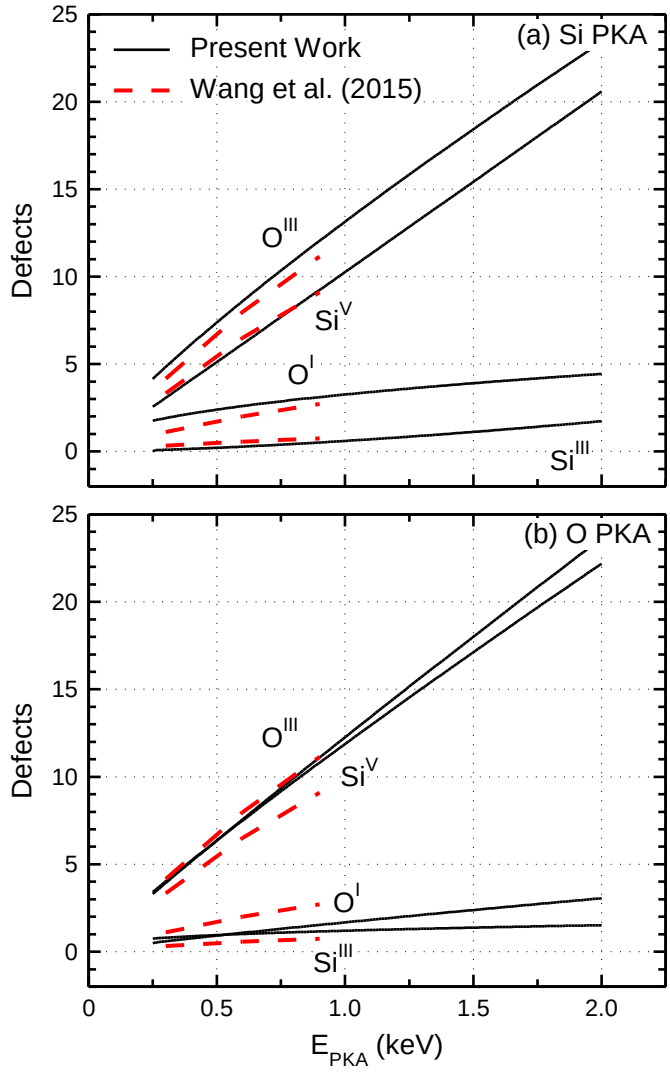

Figure 5.10: Comparison of present results of the production of over- and under-coordinated defects by oxygen and silicon PKAs, with those of Wang et al.[36]

5.1.3 Highlights and Concluding Remarks

This study used MD simulations to investigate the production of point defects in α-quartz by oxygen and silicon PKAs of energies from 0.25 to 2.0 keV. These simulations with a splined BKS-ZBL potential, a long cutoff of 15 Å, a variable time step, and r_{max}, of 0.001 Å, investigated the production of defects by oxygen and silicon PKAs of different energies in three directions ($[2\bar{1}\bar{1}0]$, $[11\bar{2}0]$, $[11\bar{2}3]$) to ensure statistically sound results. For each PKA type (oxygen and silicon) and energy, a total of 24 simulations are carried out in all three

directions. The system size used increased from 36,864 to 243,000 atoms with increased PKA energy from 0.25 to 2.0 keV PKAs, respectively.

The smallest size time steps in the simulations, which depend on the PKA energy, are adjusted every 100 steps to reduce the computational resources required, but maintain the accuracy of the results. For oxygen PKAs with an energy of 0.25 keV, the time step size varied from $2x10^{-3}$ to 0.05 fs, from $9x10^{-4}$ to 0.05 fs for 1.0 keV, and from $6x10^{-4}$ to 0.05 fs for 2.0 keV. The corresponding values for the silicon PKAs are $2.4x10^{-3}$ to 0.05 fs, $1.0x10^{-3}$ to 0.05 fs, and $9x10^{-4}$ to 0.05 fs, respectively.

The results of the present MD simulations demonstrated the importance of using both the WS and coordination analysis methods to fully identify and quantify the various types of point defects produced. The oxygen and silicon vacancies are the primary defects during the ballistic and annealing phases of the simulations. The WS analysis shows that despite the annihilation during the annealing phase, some vacancies remain at the end of that phase. The coordination analysis shows that most of the defects produced are locally accommodated through the formation of interstitial sites. Thus, the affected regions would contain amorphous pockets and incur permanent structural changes.

The defects at the end of the ballistic phase and the residual defects, after annealing, increase with increased PKA energy, and are statistically the same for the oxygen and silicon PKAs. The WS defect analysis shows that the numbers of the oxygen vacancies and interstitials (V_O, O_i) at the end of the ballistic phase are the highest, followed closely by those of the silicon vacancies and interstitials ($V_{Si,}$ Si_i). Furthermore, the number of the residual oxygen and silicon vacancies and interstitials are statistically similar. In addition, the under-coordinated O^I and Si^{III} are the primary defects produced during the ballistic phase, and have high annealing efficiencies $\geq$ 89%. The over-coordinated defects of O^{III} and Si^V, which are not nearly as abundant in the ballistic phase, have lower annealing efficiencies (< 63%) that decrease with increased PKA energy.

In conclusion, the results of the present investigations of the point defects production provide welcome input to predicting radiation damage in bulk α-quartz. The results demonstrate the importance of using both the WS analysis and the coordination analysis to fully characterize and quantify the defects peak production and the residual defects, as functions of the energy and direction of the Si and O PKAs.

5.2 TiO_2

The objectives of this study are to conduct MD simulations, for wide ranges of temperatures and PKA energies, to investigate irradiation effects in rutile TiO_2 and determine defects production on the oxygen and titanium sublattices. The energies of the oxygen and titanium PKAs are 1, 5, and 10 keV and the simulations are carried out at 300, 600, and 900 K. In addition to tracking the defects production and clustering, potential amorphization is investigated using simulated selected area electron diffraction (SAED) patterns and radial distribution functions (RDFs). The present work also determines the amount of stored energy in residual defects, as a function of PKA type and system temperature.

5.2.1 Methodology

The Large-scale Atomic/Molecular Massively Parallel Simulator (LAMMPS)[249] is used to carry out the present MD simulations. The simulations employ a fitted Pedone[217] interatomic potential to a repulsive term to account for the short interatomic distances of the atoms during irradiation. This potential gives displacement probability distributions that are nearly identical to those reported using a splined Buckingham – ZBL potential.[164] The accuracy of this potential is investigated in prior work[164,217] which shows that the lattice and elastic constants, density, equations of state as a function of temperature and pressure, and defect formation energies are in good agreement with experimental results**.** A shortcomings of ionic potentials, such as one used in this present work, is that they overestimate the melting point, which is relatively well-known. Still, these potentials are the most viable for simulating radiation effects due to their accuracy and modest computational requirements. The Coulomb interactions in the present simulations are calculated using the particle-particle particle-mesh (PPPM) solver, with a relative error of 10^{-6}. The periodic systems of atoms for the MD simulations are first equilibrated in the isothermal-isobaric (NPT) ensemble at the desired temperature (300, 600, or 900 K) and 0 atm for 20 ps. Subsequently, these systems are equilibrated for 10 ps using a microcanonical ensemble (NVE). A thermostatic boundary layer, using the canonical ensemble (NVT), is 6 Å thick, and is applied to emulate the physical dissipation of heat to the bulk. The radiation events are also carried out using the NVE ensemble, with a NVT thermostatic boundary layer.

In the present MD simulations, the defect cascades are generated using O and Ti PKAs with energies of 1, 5, and 10 keV. A total of 165,888 atoms are used for the simulations with

1 keV PKAs, and 884,736 atoms are used for the simulations with the 5 and 10 keV PKAs. The system dimensions are 36x64x64, in order to allow for channeling of the PKAs. In order to ensure statistically sound results, simulations using 24 oxygen (O) and 24 titanium (Ti) PKAs are carried out at each temperature and PKA energy, yielding a total of 432 defect cascades. The simulations use a variable time-step algorithm for the thermal spike and ballistic phases of interaction to ensure that no atom moves more than 0.005 Å in a given time step.

During the ballistic phase, PKAs produce avalanches of defects whose total number "peaks" before the annealing phase of the defects ensues. Using a variable time step is suspended and a fixed time step of 1.0 fs is used after 10 ps into the simulations of the 1.0 keV PKAs, and after 20 ps of the 5 and 10 keV PKAs. The systems of atoms are allowed to anneal until the change in the number of residual defects becomes negligibly small. The duration of the annealing phase of interaction ranges from 80 to 240 ps, depending on the temperature and PKA type and energy. Note that if a cascade reaches the thermostatic boundary layer, the case is discarded, which happened only 10 times out of a total of 432 simulated cascades.

The Wigner Seitz (WS) defect analysis is used to characterize and quantify the types of the point defects (vacancies, interstitials, and antisites), and cluster analysis is used to identify clusters of vacancies. The lattice parameter of TiO_2 is used as the cutoff for identifying the defects in each cluster, permitting adjacent lattice sites to be part of the same cluster. These methods are used within the framework of the Open Visualization Tool (OVITO), and its customizable python scripting interface.[304]

Selected area electron diffraction (SAED) patterns are generated of the unirradiated crystal and the irradiation damaged region of TiO_2 at peak defect production and after annealing, for the [001], [100], [110], and [111] zone axes. SAED patterns are presented for a case in which a single defect production core is formed, and a case in which several subcascades formed in different regions of the material. The electron diffraction intensity is calculated on a mesh of reciprocal lattice nodes[310] and the visualization of the SAED patterns is carried out in Paraview[311] by taking the logarithm of the diffraction intensity.

5.2.2 Results

The present work tracked each of the 432 simulated cascades with attosecond resolution in order to determine the number and types of peak defects forming during the ballistic phase, and those of the residual defects after annealing. Radiation damage cascades consist of an avalanche of defect production during the ballistic phase of interaction, followed by an annealing phase, leaving residual defects. The total number of defects produced reaches a "peak" near the end of the ballistic phase, before the annealing phase commences. The number of peak defects produced are indicated by closed blue and red circles in Fig. 5.11. The average simulation time to reach peak defect production is ≈0.10, 0.20, and 0.38 ps, for the 1, 5 and 10 keV O PKAs, respectively. The numbers of peak defects produced by the Ti PKAs are very similar but reached at slightly longer times. The jagged section after ≈1 ps of simulation time is due to higher temporal resolution taken in this regime.

5.2.2.1 **Point Defects Production**

For instance, at 300 K, the number of residual Ti vacancies produced by 10 keV O and Ti PKAs is 47.5 ± 32.5 and 37.1 ± 33.4, compared to 9.37 ± 2.98 and 10.6 ± 2.83 residual O vacancies produced with the same PKAs, respectively. The abundance of residual O vacant sites makes it easier for the O interstitials to diffuse to vacant O lattice sites. The high number of residual Ti vacancies could be due to several reasons, namely:

(a) O atoms are lighter and more mobile than Ti atoms, enabling O interstitials to travel through the lattice and annihilate with O vacancies more readily than Ti atoms.

(b) Ti atoms are octahedrally coordinated to 6 oxygen atoms in rutile, making it difficult for Ti atoms to reach appropriate lattice sites, which might be surrounded by 6 other O atoms.

(c) With the same PKA energy, Ti atoms are typically displaced further away from their original lattice sites than O atoms. For instance, in the [010] crystallographic direction, present simulations show that O PKAs are displaced ≈1 nm, compared to ≈10 nm for Ti PKAs. Since the displacement distance for an O interstitial is an order of magnitude less, the probability that it diffuses to its lattice site is much greater than that for a Ti interstitial.

Table 5.5: Comparisons of the average number of peak vacancies, interstitials, and antisites, produced with O and Ti PKAs, at 300, 600, and 900 K.

Defects Type	PKA Energy (keV)	Average number of Peak Defects Produced (#)					
		O PKA			Ti PKA		
		300 K	600 K	900 K	300 K	600 K	900 K
1. Vacancies							
	1	19.6 ± 3.26	22.0 ± 3.73	23.7 ± 3.51	18.7 ± 4.7	21.2 ± 4.45	25.0 ± 5.15
V_O	5	119 ± 26.2	125 ± 30.3	166 ± 59.1	118 ± 40.2	114 ± 33.5	164 ± 67.9
	10	404 ± 178	406 ± 153	549 ± 301	339 ± 187	419 ± 162	455 ± 269
	1	13.2 ± 3.1	15.4 ± 3.94	17.8 ± 4.46	15.8 ± 4	18.2 ± 3.51	19.4 ± 4.22
V_{Ti}	5	95.2 ± 23.4	103 ± 23.3	130 ± 33.5	91.1 ± 28.6	93.6 ± 26.7	127 ± 36
	10	293 ± 94.8	306 ± 74.5	379 ± 160	240 ± 100	294 ± 79.7	317 ± 128
2. Interstitials							
	1	17.4 ± 3.6	20.8 ± 3.19	21.5 ± 3.22	17.6 ± 3.92	20.0 ± 4.81	23.0 ± 4.7
O_i	5	106 ± 22.3	113 ± 23.1	144 ± 42.4	105 ± 28.1	105 ± 27.4	140 ± 46.2
	10	313 ± 111	322 ± 101	418 ± 187	265 ± 113	325 ± 101	353 ± 156
	1	14.5 ± 3.36	17.0 ± 4.23	18.8 ± 4.64	17.3 ± 4.44	20.0 ± 3.71	21.5 ± 4.80
Ti_i	5	108 ± 28.8	114 ± 29.4	151 ± 50.6	104 ± 38.6	106 ± 34.8	152 ± 55.8
	10	387 ± 160	391 ± 126	510 ± 276	316 ± 176	388 ± 140	420 ± 237
3. Antisites							
	1	3.08 ± 1.64	4.71 ± 1.68	5.42 ± 2.55	4.25 ± 2.11	5.38 ± 1.86	7.17 ± 2.70
O_{Ti}	5	39.1 ± 19.7	40.0 ± 20.0	61.8 ± 36.1	38.0 ± 25.6	38.7 ± 23.0	65.6 ± 40.9
	10	213 ± 141	191 ± 91.6	288 ± 225	164 ± 145	200 ± 109	224 ± 190
	1	2.17 ± 1.79	3.21 ± 1.29	3.79 ± 1.87	2.75 ± 1.42	3.83 ± 1.58	4.80 ± 2.06
Ti_O	5	25.6 ± 15.5	26.9 ± 12.4	40.6 ± 21.7	24.6 ± 14.2	26.8 ± 14.6	38.8 ± 20.4
	10	117 ± 71.8	104 ± 43.1	156 ± 112	88.8 ± 69.0	106 ± 51.2	120 ± 76.1

Results in Fig. 5.12c,f show that although both O and Ti antisites are produced during the ballistic phase, almost 100% of the antisites anneal, indicating that they are not as stable as the vacancies and interstitials (Table 5.6). Results listed in this table also show that there are fewer residual defects produced at higher temperatures due to the higher mobility of the atoms. However, more Ti vacancies and interstitials anneal at higher temperatures. For example, the percentage of the peak titanium defects that anneal is 83-87% at 300 K, 87-91% at 600 K, and 96-97% at 900 K. Conversely, the percentage of the peak oxygen defects that anneal varies in a very narrow range (96-99%) and is independent of temperature. Thus, at lower temperatures, more Ti Frenkel pairs form in TiO_2, increasing local stresses to store energy in the crystal. It is important to note that these simulations are limited to time scales achievable with MD (several hundred picoseconds). Over experimental time scales of

days/weeks/years, more diffusion would likely occur, and thus the defect concentrations would decrease.

Table 5.6: Comparisons of the average number of residual vacancies, interstitials, and antisites, produced with O and Ti PKAs, at 300, 600, and 900 K.

Defects Type*	PKA Energy (keV)	Average number of Residual Defects Produced(#)					
		O PKA			**Ti PKA**		
		300 K	**600 K**	**900 K**	**300 K**	**600 K**	**900 K**
1. Vacancies							
	1	1.68 ± 0.89	1.08 ± 0.83	<1	1.58 ± 0.93	1.35 ± 1.15	1.21 ± 0.66
V_O	5	5.46 ± 1.74	4.33 ± 1.88	3.33 ± 1.40	5.50 ± 2.09	3.83 ± 1.17	3.42 ± 1.84
	10	9.37 ± 2.98	8.21 ± 3.08	7.08 ± 2.72	10.6 ± 2.83	9.00 ± 2.72	6.38 ± 2.55
	1	<1	<1	<1	2.00 ± 1.14	1.63 ± 0.83	1.25 ± 0.897
V_{Ti}	5	10.7 ± 10.2	4.67 ± 4.03	2.80 ± 2	10.4 ± 9.34	5.79 ± 4.78	5.63 ± 8.42
	10	47.5 ± 32.5	28.3 ± 22.4	12.0 ± 12.4	37.1 ± 33.4	37.4 ± 29.7	11.5 ± 11.5
2. Interstitials							
	1	1.65 ± 0.92	1.04 ± 0.86	<1	1.33 ± 1.05	1.06 ± 1.04	0.708 ± 0.55
O_i	5	5.17 ± 1.90	3.83 ± 1.97	2.88 ± 1.68	4.71 ± 1.85	3.33 ± 1.49	2.33 ± 1.74
	10	8.33 ± 2.53	6.79 ± 2.83	5.88 ± 2.62	9.08 ± 2.67	6.92 ± 2.59	5.21 ± 2.48
	1	<1	<1	<1	2.25 ± 1.22	1.92 ± 0.98	1.75 ± 1.11
Ti_i	5	11.0 ± 10.1	5.17 ± 4.18	3.25 ± 2.01	11.2 ± 9.89	6.29 ± 4.7	6.71 ± 8.53
	10	48.5 ± 32.7	29.7 ± 23.1	13.1 ± 12.5	38.6 ± 34.2	39.5 ± 30	12.7 ± 15.3
3. Antisites							
	1	<1	<1	0.00 ± 0.00	<1	<1	<1
O_{Ti}	5	<1	0.708 ± 0.55	<1	<1	<1	1.17 ± 1.01
	10	1.75 ± 2.15	1.50 ± 1.53	1.75 ±1.15	1.88 ± 1.88	2.58 ± 1.44	1.54 ± 1.22
	1	<1	0.00 ± 0.00	0.00 ± 0.00	<1	<1	<1
Ti_O	5	<1	<1	<1	0	<1	<1
	10	<1	<1	<1	<1	<1	<1

*V_O = oxygen vacancy; V_{Ti} = titanium vacancy; O_i = oxygen interstitial; Ti_i = titanium interstitial; O_{Ti} = oxygen antisite; Ti_O=titanium antisite

The standard deviations of the average number of residual titanium vacancies and interstitials (Fig. 5.12d,e and Table 5.6) are caused by the variances in the results of the 24 simulations performed for each PKA type, at three different PKA energies and temperatures. The simulated cascades show various modes of interaction. In some simulations, various regions of defect production form, and the highly energetic atoms are displaced by 10-20 nm. In these cases, most titanium vacancies and interstitials annihilate resulting in a few or no

residual defects. In other simulations, a single cluster is produced, with mostly vacancies primarily in the core region, and mostly interstitials at the periphery of the cluster. In these simulations, the clustered interstitials are more stable than the individual interstitials spread out through the lattice.

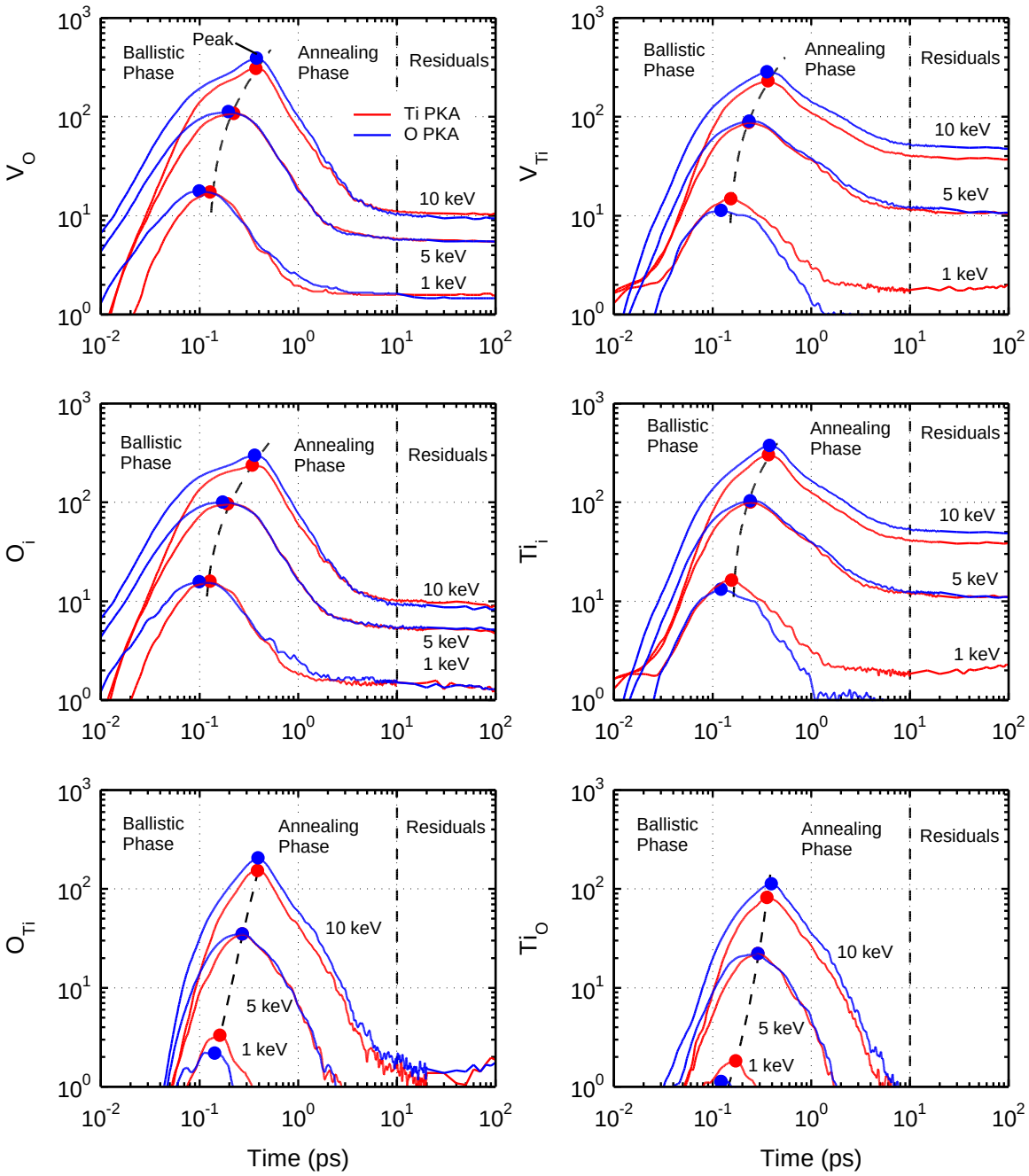

Figure 5.11: Comparison of the number of oxygen and titanium vacancies, interstitials, and antisites produced as a function of time, with O and Ti PKAs of 1, 5 and 10 keV.

Fig. 5.13 compares the number of oxygen vacancies produced by oxygen PKAs at 300 K, and compares the results to those obtained at near-threshold energies in prior work.[164] A power law fit to the data shows that the results from both studies are in general agreement. The equation of the fitted curve is:

$$V_O = 1.78E_{PKA}^{0.72} \quad \text{Eq. 5.4}$$

In prior work, an average of one oxygen vacancy is produced in TiO_2 with oxygen PKAs of energies of ~400 eV. The power law fit shown in Fig. 3 predicts that on average, one oxygen vacancy forms at PKA energies between 400-450 eV.

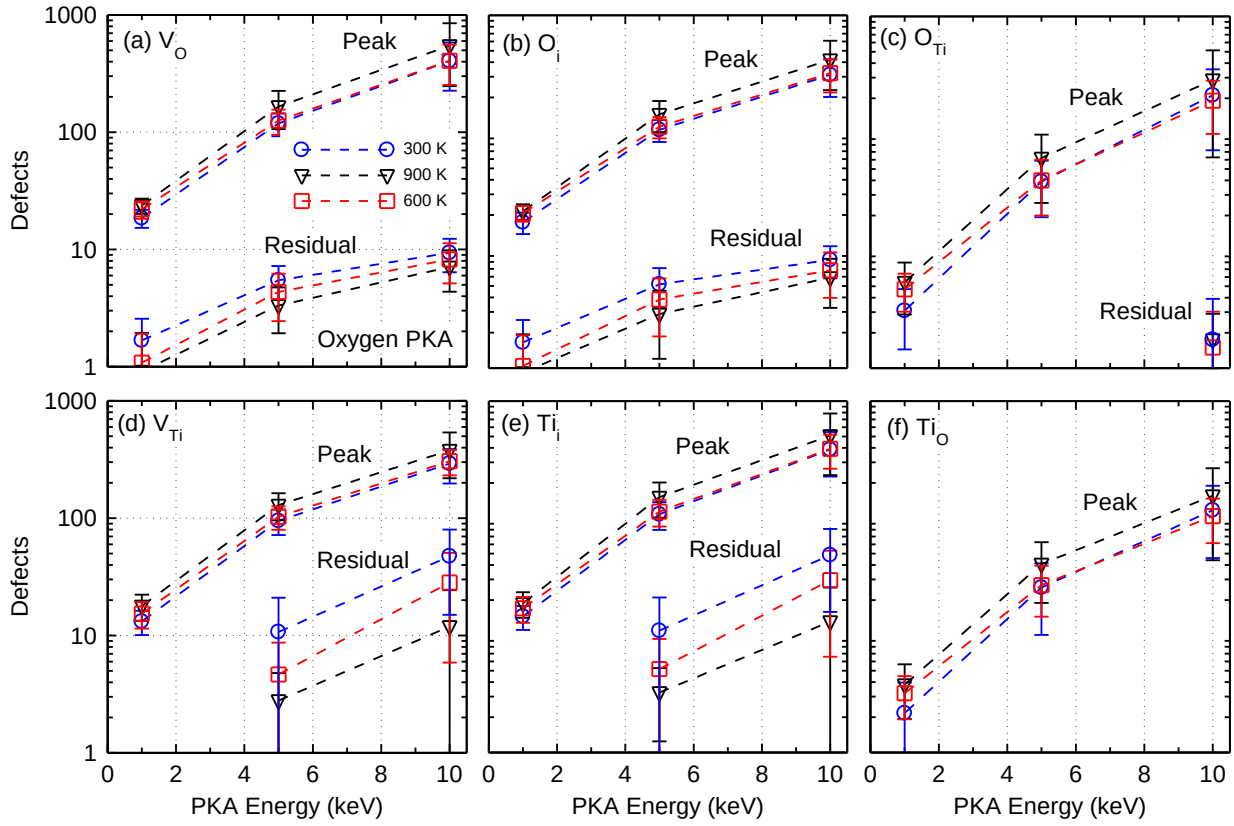

Figure 5.12: Average number of peak and residual vacancies, interstitials, and antisites produced by O PKAs of 1, 5, and 10 keV.

5.2.2.2 **Cascade Morphology**

The images in Figs. 5.14A,B are those produced by a 10 keV Ti PKA in TiO_2 at 300 K. The images in Fig. 5.14A show the Ti PKA displaced by 18.5 nm before coming to rest, and those in Fig. 5.14B show the production of a defect cascade in which the Ti PKA is only

displaced 4.6 nm, and there are no significant displacements of the secondary knock-on atoms (SKAs). Despite the identical conditions for the MD simulations for the results in Fig. 5.14A and 5.14B, these images demonstrate different damage cascades, because different atomic lattice vibrations occur in different regions of the TiO_2 system. Thus, a slight change in the position of an atom relative to the PKA can cause significant changes in the produced damage cascade.

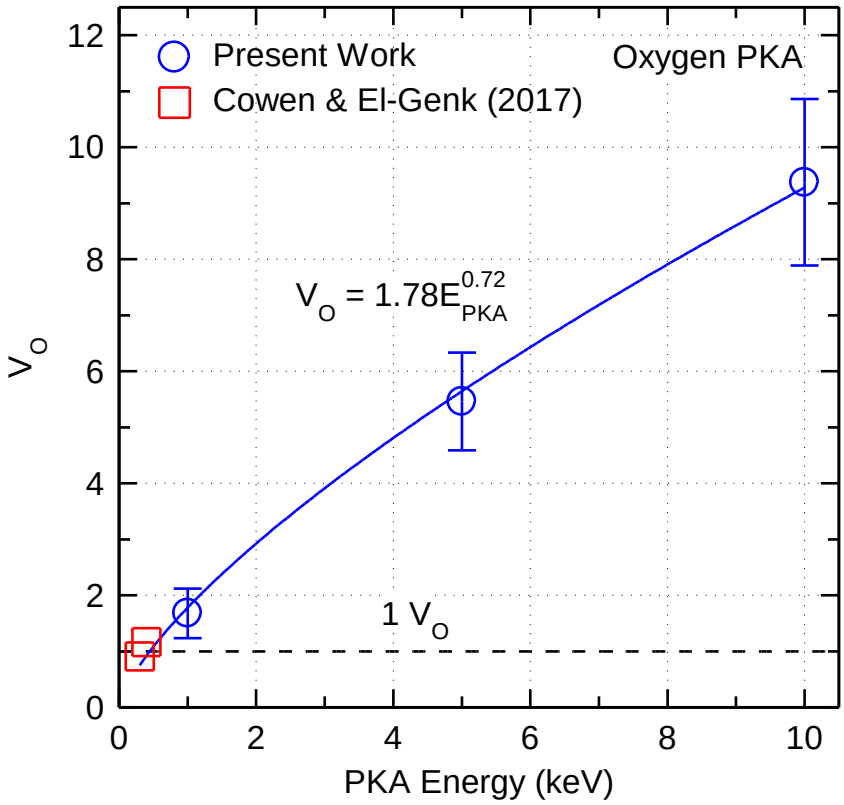

Figure 5.13: Comparison of oxygen vacancy production in the present work with prior work near the threshold displacement energy.

The images in Fig. 5.14A show that the produced defect cascade is spread out through the crystal lattice, and no single defect production core is formed. At peak defect production in the ballistic phase of interaction, only 171 oxygen and 105 titanium vacancies form, compared to 14 and 2 remaining after 100 ps. The images in Fig. 4B show that when none of the atoms are displaced by more than a few nm, a different mode of interaction occurs in which the produced defects form in a single core region. The produced peak defects include 721 oxygen and 446 titanium vacancies, compared to 8 and 86 residual defects after 100 ps.

For all cascades, the number of oxygen defects is similar, while the number of titanium defects varies significantly, depending on the extent of clustering defects (Tables 1 and 2).

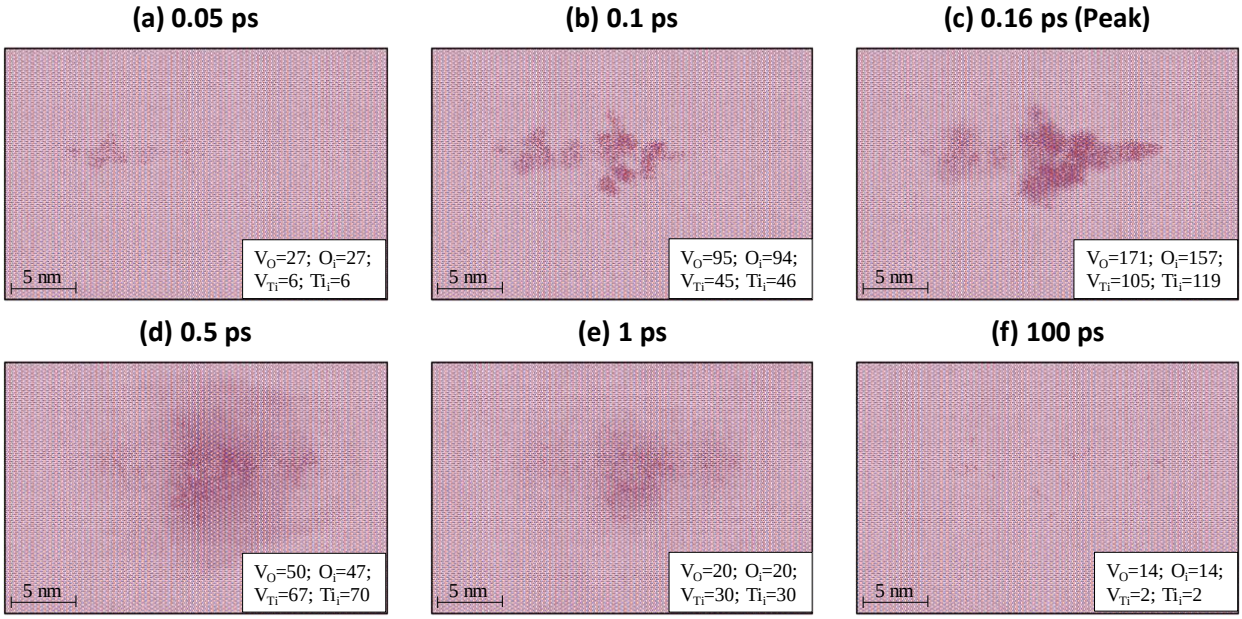

(A) Cascade resulting in no defects clusters

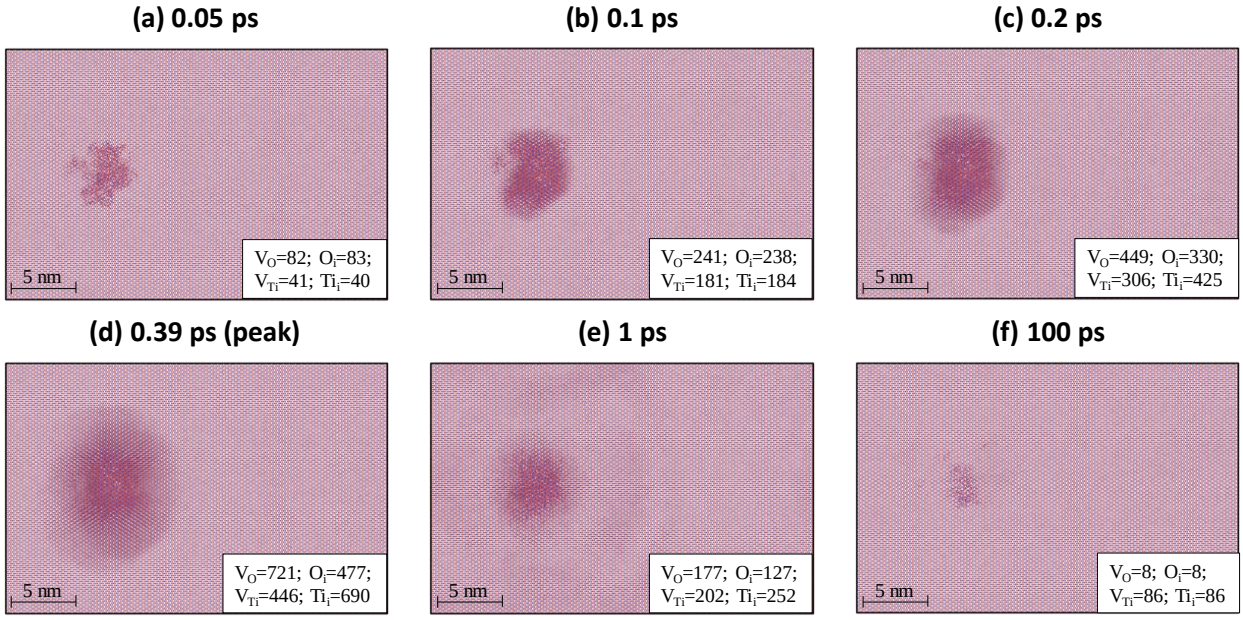

(B) Cascade resulting in defects cluster

Figure 5.14: Evolution of the produced defects clustering in crystalline TiO_2 by Ti PKA of 10 keV at 300 K.

Fig. 5.15a,b shows two configurations of the produced oxygen and titanium vacancies within the crystal lattice. When no defect cluster forms (Fig. 5.15a), most of the defects

anneal, and there are a few remaining residual point defects, mostly oxygen vacancies (shown by solid red symbols in Fig. 5.15a), spread out through the crystal lattice. When a single defect cluster forms at peak defect production, it is a vacancy cluster of mostly oxygen vacancies and fewer Ti vacancies (Fig. 5.15b). Conversely, the residual vacancy cluster is made up of mostly Ti vacancies (shown by solid blue symbols in Fig. 5.15b). *In the online version of the article, there are supplementary video-files, which are developed using WS analysis. They show the sequential events of the formation and annealing of the vacancies produced in Figs. 5.15a and 5.15b. The supercell boundaries are excluded in order to obtain a high resolution video of the region in which the cascade occurs.*

Since different modes of interaction occur during irradiation, it is useful to determine how different defect cascades affect the crystallinity of the material. This is attempted next using simulated SAED patterns of the two cases of 10 keV Ti PKAs presented in Figs. 5.14 and 5.15. The results are presented in Fig. 5.16.

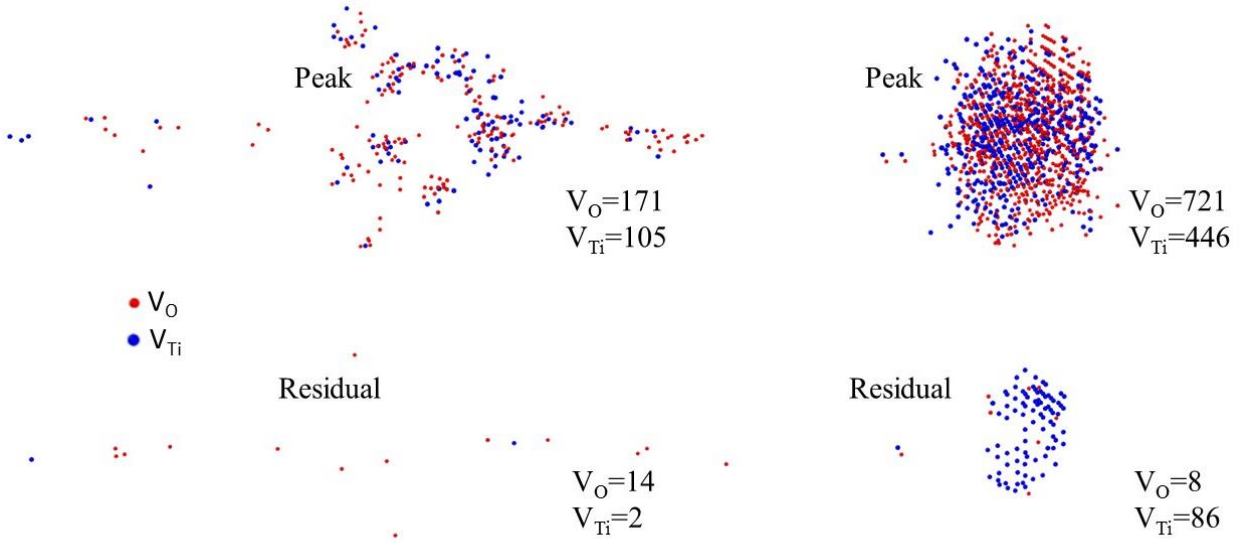

Figure 5.15: Images of the defects cascades forming in crystalline TiO_2, by 10 keV Ti PKAs at 300 K, at the peak production and after annealing.

5.2.2.3 **Simulated Selected Area Electron Diffraction Patterns**

The SAED patterns for the unirradiated TiO_2 rutile in Fig. 5.16 are for four zone axes ([001], [100], [110], and [111]), and are averaged over 10 ps. The sharp diffraction peaks in the SAED patterns confirm the crystallinity of the TiO_2 rutile. The SAED pattern of the irradiated TiO_2 is calculated over the irradiated region only. The lines connecting the

diffraction peaks are because the SAED pattern is for a single snapshot in time (Fig. 5.16a,b), unlike that of the unirradiated crystal which is averaged over 10 ps.

The SAED patterns in Fig. 5.16a is for a 10 keV Ti PKA displaced by 18.5 nm, resulting in little disruption of the lattice at the peak defect production (Fig. 5.14A). After annealing, the SAED patterns for all four zone axes mostly recovers. The SAED pattern in Fig. 5.16b is of a 10 keV Ti PKA displaced by only 4.5 nm, producing a single core of defects (Fig. 5.14B). The results in Fig. 5.16b show some crystalline order throughout the irradiated region at peak defect production, even if the diffraction peaks are not as readily defined. Although the TiO_2 is does not experience bulk amorphization in the irradiated region, there is a significant amount of induced damage and amorphous pockets that form. The diffraction peaks for all zone axes investigated are more pronounced after annealing. However, some disorder is shown by the annealed SAED patterns (Fig. 5.16b). The SAED patterns of the irradiated TiO_2 at 600 K and 900 K are similar to that at 300 K, but show slightly less damage since the number of residual defects decreases with increased temperature.

5.2.2.4 **Radial Distribution Functions**

The obtained RDFs of TiO_2 rutile at peak defect production and of the residual defects, for the cases presented in Fig. 5.14A,B, are compared in Fig. 5.17a,b. Fig. 5.17a is of the RDFs for the MD simulation in which no defect cluster forms, and Fig. 5.17b shows the RDFs for when a defect cluster forms. The RDFs in Fig. 5.17a shows no statistical difference between the irradiated and unirradiated TiO_2. The produced damage is spread out through the lattice (Fig. 5.14A), in which individual point defects do not locally affect the crystallinity of the TiO_2. On the other hand, the RDFs in Fig. 5.17b show that the long-range order is lost at peak defect production, as $g(r) \rightarrow 1$ at $\approx$5 Å.

Although some of this order returns after annealing, there is clearly still damage to the crystal lattice, in agreement with the SAED patterns in Fig. 5.16b. The likelihood for the irradiated TiO_2 to amorphize at 300 K would depend on the total energy deposited, extent of the damage region, and the nature of defect clustering, as demonstrated experimentally.[101,188,312] The present results suggest that the titanium defects in larger clusters are more stable, causing some disorder in the crystal lattice, as demonstrated by the SAED patterns in Fig. 5.16a,b. Therefore, the results of the 432 cascades simulated in this work are analyzed to quantify the extent of defect clustering.

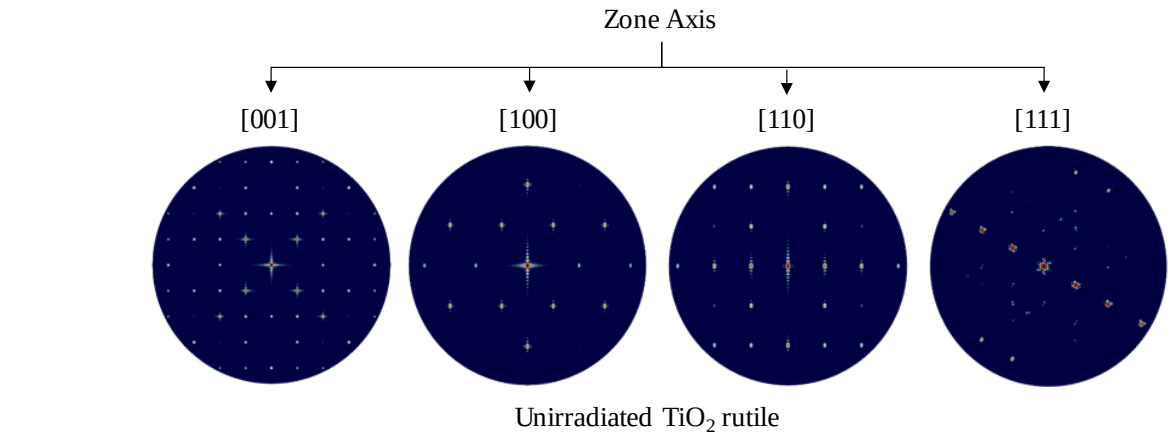

Unirradiated TiO_2 rutile

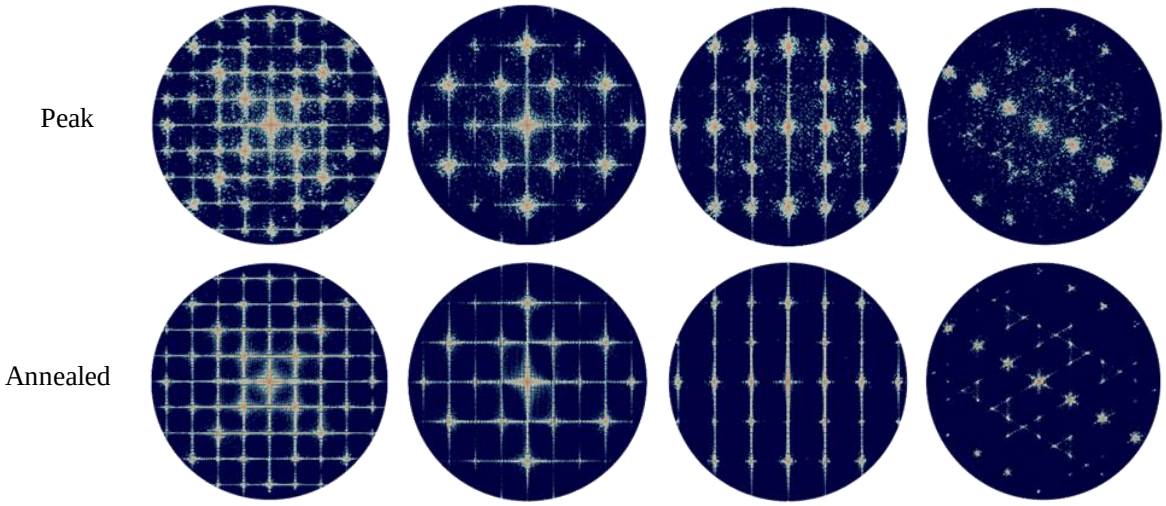

(a) 10 keV Ti PKA – Cascade resulting in no defects clusters

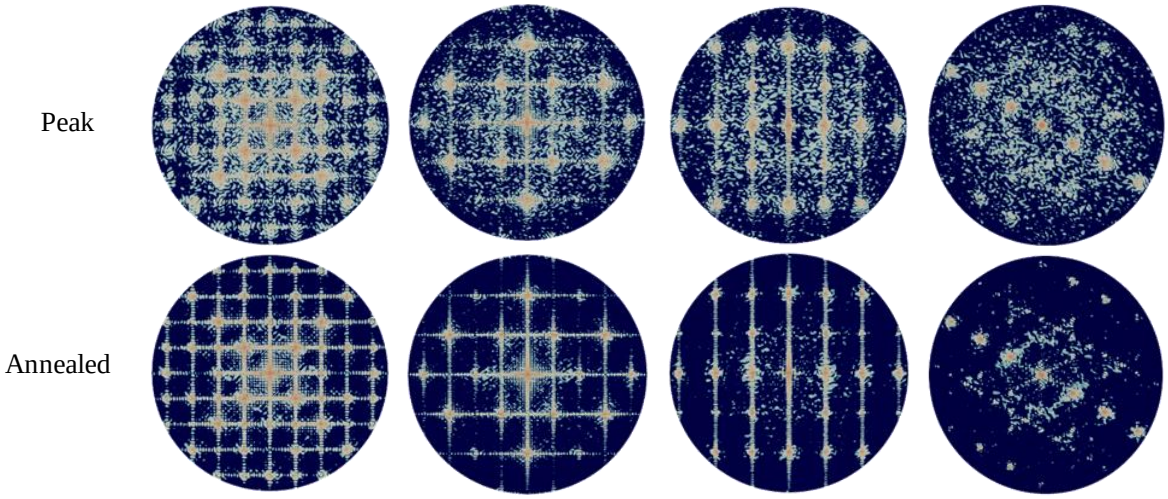

(b) 10 keV Ti PKA – Cascade resulting in defects cluster

Figure 5.16: Comparison of simulated SAED patterns of unirradiated and irradiated TiO_2 at the defects peak production and after annealing.

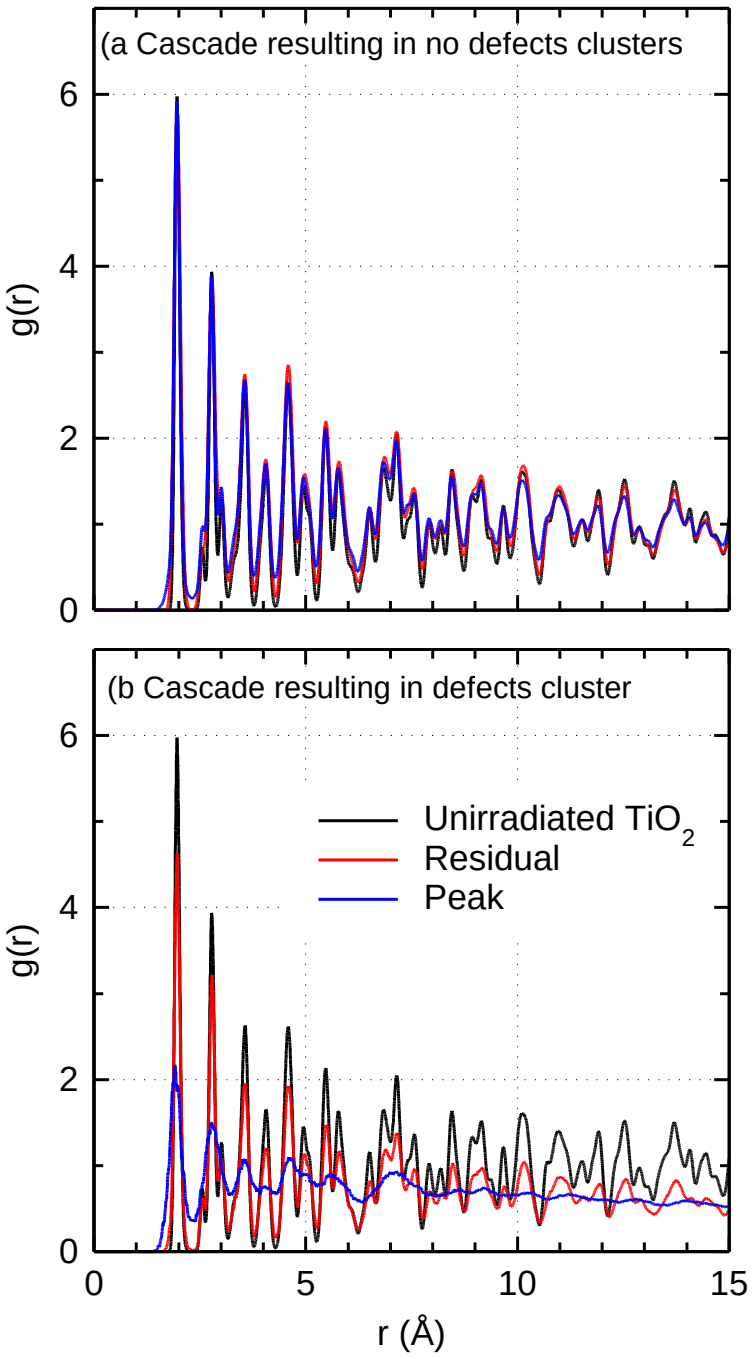

Figure 5.17: Comparison of the radial distribution functions (RDFs) of unirradiated and irradiated TiO_2 rutile at the defects peak production and after annealing.

5.2.2.5 **Defect Clustering**

Fig. 5.18 show the range of the number of vacancies in the clusters produced at peak defect production and after annealing, as functions of PKA energy, PKA type, and system temperature; *these clusters are those of 2 or more vacancies*. Results indicate defect

clustering is independent of the PKA type, but strongly dependent on the PKA energy and system temperature. For instance, at 300 K, the largest vacancy clusters forming at peak defect production using 1, 5, and 10 keV O PKAs contain 14-45, 42-311, and 180–1174 vacancies, respectively. After annealing, these clusters shrink significantly to only contain <5, <40, and <104 vacancies, respectively. Some of the vacancy clusters that formed by the interactions of 1 and 5 keV O PKAs completely disappear during the annealing phase of interaction.

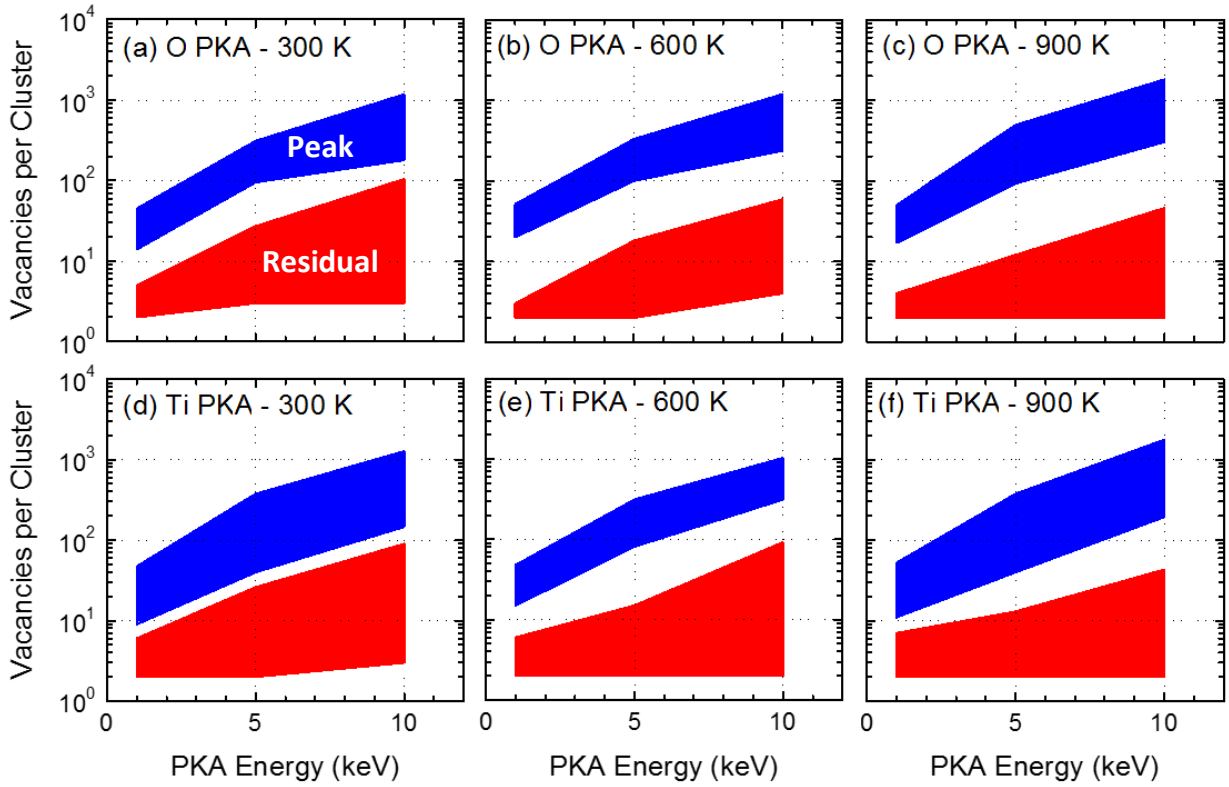

Figure 5.18: Range of the largest cluster of vacancies produced in all simulated cascades, as a function of temperature, and PKA type and energy.

For all PKA energies investigated in this work, on average the forming vacancy clusters during the ballistic phase of interaction shrink in size by 1-2 orders of magnitude during the annealing phase. The vacancy cluster at the peak defect production is weakly dependent on system temperature, however, temperature affects the shrinkage of the cluster during the annealing phase. For instance, the residual vacancy clusters produced by 5 keV O PKAs at

300, 600, and 900 K, contain <40, <18, and <12 vacancies, respectively. The increased atom mobility at higher temperatures fosters the diffusion and recombination of residual vacancies and interstitials. Similar results are obtained for the other O and Ti PKAs investigated in this work.

5.2.2.6 **Potential Energy**

In addition to tracking defect production and examining the effect on crystallinity, prior work[173] has shown that defect cascades cause energy storage in the lattice. Fig. 5.19 shows the change in kinetic and potential energy, and the system temperature (mean kinetic energy =3/2kT), as a function of simulation time, for a case involving a 10 keV Ti PKA. The temperature increases to ≈388 K upon the initiation of the Ti PKA and slowly subsides to 300 K over 100 ps. While the change in kinetic energy drops to 0 once the energy has dissipated at the thermostatic boundary layer, the potential energy does not return to its initial value. This is due to the residual defects remaining in the material, which eventually could recombine and release the stored energy.

Fig. 5.20 compares the current estimates of the stored energy in the TiO_2 lattice, by the residual defects produced by 10 keV O PKAs at different system temperatures. The stored energy decreases with increased temperature, as more defects anneal. At 300 K, the residual defects produced by 10 keV O PKAs results in the storage of ≈150-260 eV in the irradiated crystal. The stored energies at 600 and 900 K are estimated at ≈70-200 eV and ≈20-180 eV, respectively. Increasing temperature fosters more diffusion, and thus more recombination of defects, releasing some of the stored energy. The systems with the most stored energy are the ones with more than 90% Ti Frenkel pair defects.

The energy storage also occurs through defect production in crystalline TiO_2 with Ti PKAs (Fig. 5.21). This figure compares the estimates of stored energy due to the residual defects produced by 10 keV Ti PKAs, at different system temperatures. At 300 K, ≈140-310 eV is stored in the produced defects, compared to ≈100-250 eV and ≈5-180 eV at 600 K and 900 K, respectively. Once again, the cascades of the residual defects of > 90% Ti Frenkel pairs result in the largest amount of stored energy. These results suggest that TiO_2 effectively stores energy in the point defects produced by irradiation at low temperatures.

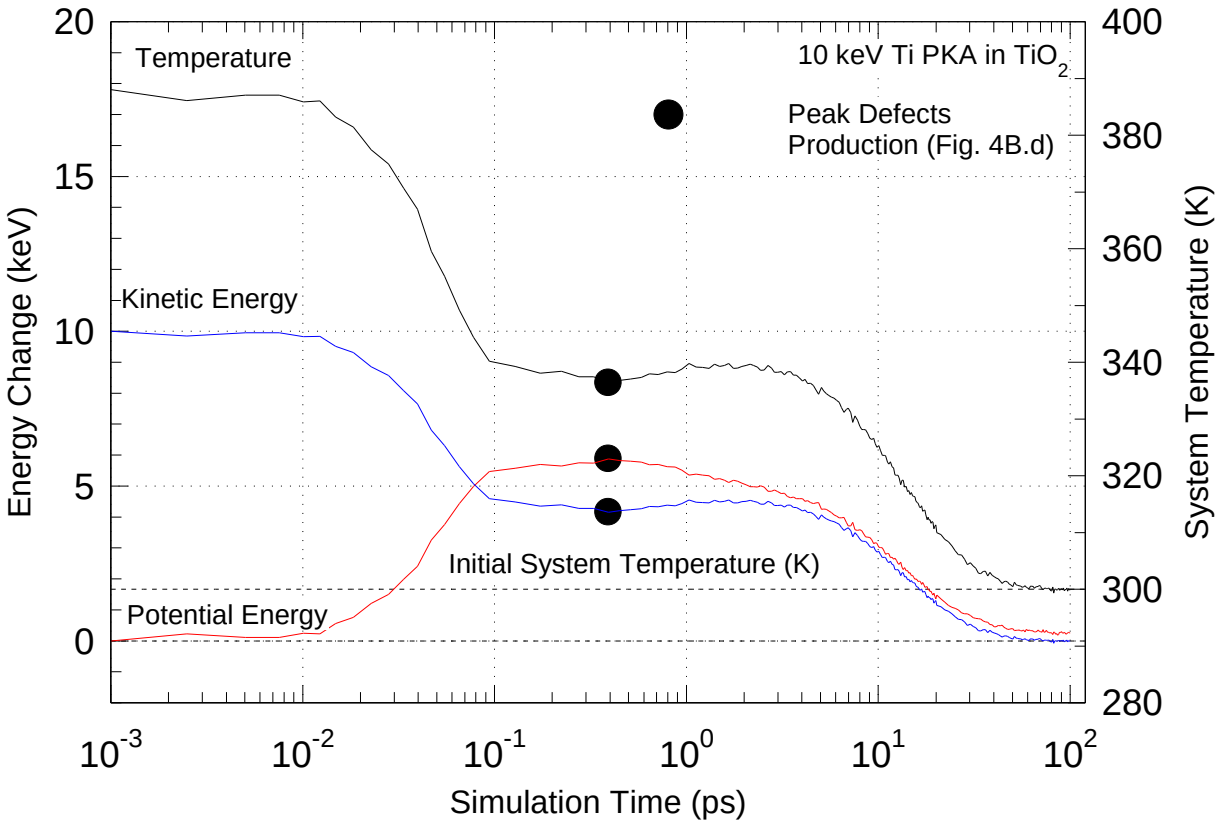

Figure 5.19: Change in the system temperature, kinetic energy, and potential energy, during the MD simulation with a 10 keV Ti PKA in TiO_2.

5.2.3 Highlights and Concluding Remarks

MD simulations are performed, which investigated the production of point defects and defect clusters in TiO_2 rutile by O and Ti PKAs of energies of 1, 5, and 10 keV, at system temperatures of 300, 600, and 900 K. Defect production depends on the PKA energy, but not the type, and the system temperature. In the present MD simulations, the defect cascades are generated using O and Ti PKAs with energies of 1, 5, and 10 keV. A system size of 165,888 atoms is used in the simulations with 1.0 keV PKAs, and of 884,736 atoms in the simulations with 5 and 10 keV PKAs.

In order to ensure statistically sound results, simulations are carried out for 24 oxygen (O) and 24 titanium (Ti) PKAs, at each temperature and PKA energy, yielding a total of 432 defects cascades. The simulations use a variable time-step algorithm for the thermal-spike and ballistic phases of interaction to ensure that no atom moves more than 0.005 Å in a given time step. The obtained defect cascades are analyzed for the formation and stability of the

defect clusters after annealing. In addition to tracking defect production and clustering, potential amorphization is investigated using SAED patterns and RDFs, and the amount of stored energy in residual defects, as a function of PKA type and system temperature, are determined and compared.

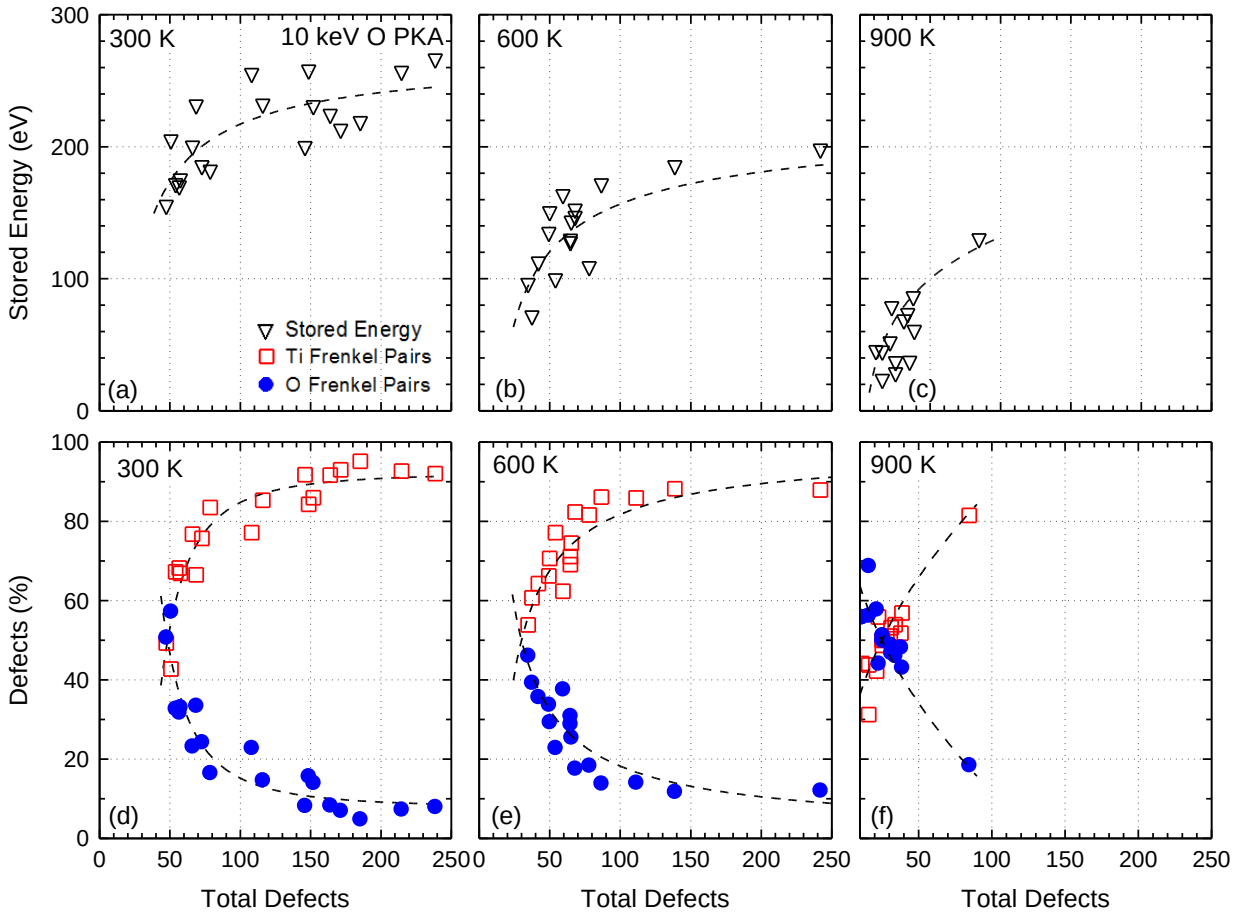

Figure 5.20: Estimates of the stored energy in TiO_2 crystal after irradiation with O PKAs of 10 keV at 300, 600, and 900 K.

The SAED patterns and RDFs confirmed the retention of TiO_2 crystallinity during peak defect production and after annealing for the cases in which dispersed subcascades formed. However, in the cases of forming a single defect production core, long-range order is lost at peak defect production since $g(r) \rightarrow 1$ at ≈ 5 Å. At the peak of the ballistic phase of interaction, more oxygen than titanium defects form. Conversely, the residuals after annealing are primarily Ti defects. The percentage of peak Ti defects that anneal increase

with increased temperature, however that of the residual O defects is higher and independent of temperature.

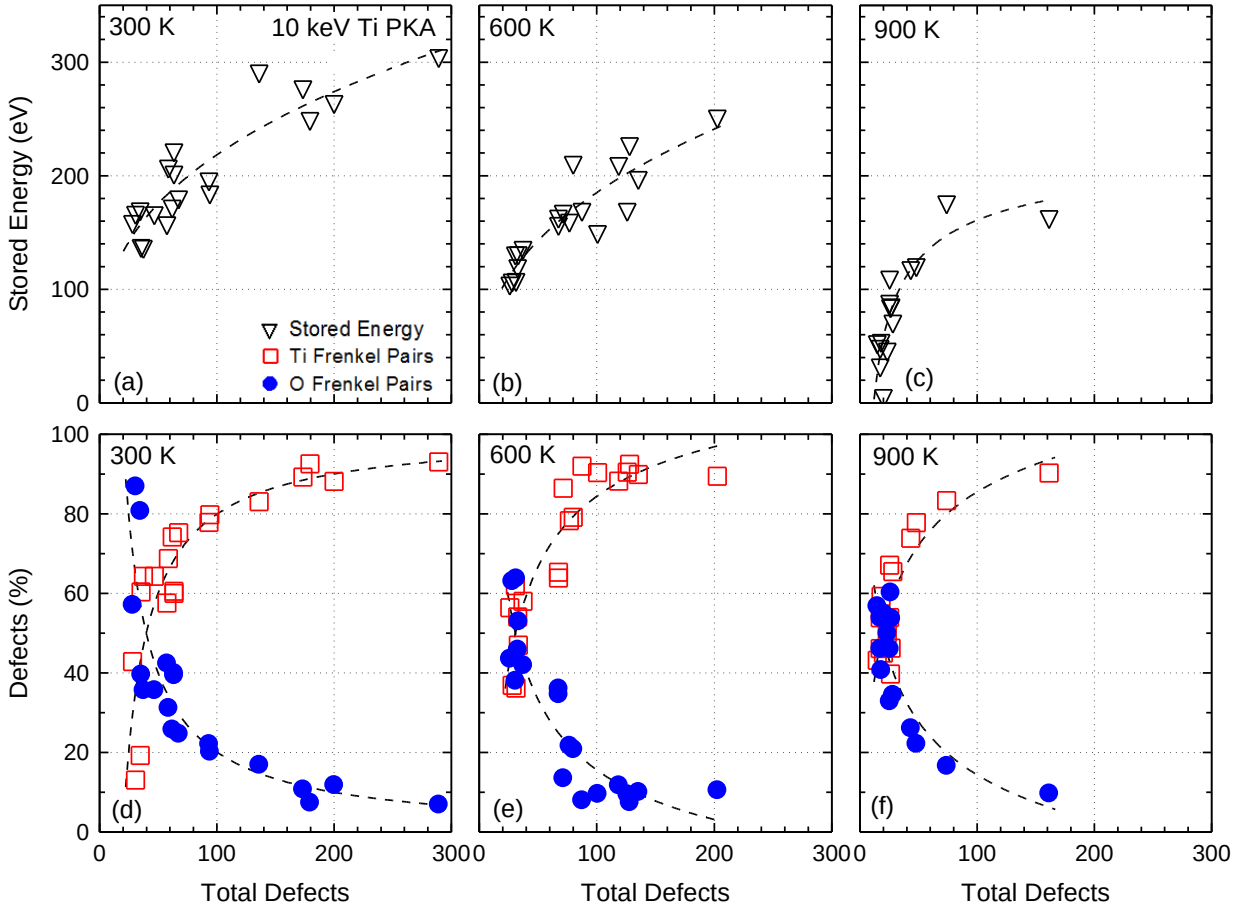

Figure 5.21: Estimates of the stored energy in the TiO_2 crystal after irradiation with Ti PKAs of 10 keV at 300, 600, and 900 K.

The sizes of the defect clusters forming at the peak of the ballistic phase, significantly shrink after annealing due to the recombination of the Ti vacancies and interstitials. When a single core of defects is formed, the titanium vacancies cluster in the central region, with the produced interstitials at the periphery. The size of the produced vacancy cluster at peak defect production decreases by 1-2 orders of magnitude after annealing, and could contain a few to 10s of residual vacancies that are mostly titanium. The size of the residual vacancy cluster also decreases with increased temperature. This might explain why amorphization of TiO_2 has been reported in ion beam irradiation experiments at 300 K, but not at higher temperatures.

Results also show that the produced residual point defects cause local stresses which store energy in the crystal lattice. The estimates of the stored energy decrease with increased system temperature due to the increased mobility and recombination of defects. The energy stored estimates of ≈140 - 310 eV at 300 K, decrease to ≈ 5 - 180 eV at 900 K.

This chapter has investigated defect production in SiO_2 and TiO_2, up to 2 and 10 keV, respectively. These energies are relatively low for comparison to ion beam irradiation, since defect production would likely be undetectable with several nanometer resolution. Therefore, the next chapter presents and discusses the results of MD simulations with PKAs/projectiles up to 100 keV, and compares the results to *in situ* TEM ion beam irradiation.

6 COMPARING RADIATION DAMAGE USING MD SIMULATIONS AND *IN SITU* TEM ION BEAM IRRADIATION

Understanding radiation damage in crystalline systems at the atomic scale is essential for the development of multi-scale predictive models for advancing nuclear science and engineering applications. State-of-the-art techniques used for investigating irradiation effects include molecular dynamics (MD) simulations, which can provide attosecond resolution of damage cascades over picosecond time scales, and *in situ* transmission electron microscopy (TEM), which can provide millisecond resolution in real-time. While neither provide a full-account or radiation effects, together they are an effective tool-set for understanding and characterizing the effect of radiation in materials and the resulting changes in microstructure and properties.

6.1 TiO_2

The objectives of this study are to perform molecular dynamics (MD) simulation and *in situ* TEM ion beam irradiation of TiO_2 rutile with 46 keV Ti^- ions to investigate the effects on defects production and clustering and qualitatively compare results. The MD simulation of radiation damage in TiO_2 with a 46 keV Ti projectile tracks defect production, including Frenkel pairs, clustering of vacancies and interstitials of TiO_2 rutile on a picosecond time-scale with attosecond resolution. On the other hand, the performed *in situ* TEM ion beam irradiation of TiO_2 with a 46 keV Ti^{1-} at a fluence of $6.96x10^{14}$ ions/cm^2 could provide a real-time account of ion strikes with 200 millisecond resolution.

6.1.1 Methodology

This section presents the methods the thin film deposition of the TiO_2 on a-SiN, the *in situ* TEM ion beam irradiation of the TiO^2 thin film with a 46 keV Ti^- beam, and MD simulations of a 46 keV Ti PKA in TiO_2 rutile.

6.1.1.1 Sample Preparation and In Situ TEM

For the *in situ* TEM ion beam irradiation experiments, the TiO_2 samples are prepared on a DuraSiN™ TEM grid[313] from a 99.9% pure TiO_2 sputtering target.[314] The deposition of TiO_2 onto the α-SiN TEM grid is carried out using Radio Frequency (RF) ATC 1800 Magnetron Sputtering System in the Center for Integrated Nanotechnologies at Los Alamos National Laboratory. The base pressure in the sputtering chamber is $5.0x10^{-8}$ Torr, while keeping the

working pressure at $3x10^{-3}$ Torr. During deposition, the partial pressures of the Ar and O_2 in the sputtering chamber are kept at 30 and 20 sccm, respectively. The temperature of the substrate during deposition is kept at 900 °C in order to form crystalline TiO_2. The RF power is kept at 300 W and the distance between the target and substrate is ≈50 cm. At a deposition rate of ≈2 Å/s, the TiO_2 is deposited for 60 seconds to obtain a nominal film thickness of ≈12 nm.

The resulting TiO_2 specimen is irradiated in the JEOL 2100 TEM in the I^3TEM facility at Sandia National Laboratories.[76] The ion beam comes in at 60° relative to the sample normal. To best emulate the MD simulations, the TiO_2 islands were irradiated with a 46 keV Ti^{1-} ion beam for 15 minutes to an estimated total fluence of $6.96x10^{14}$ ions/cm^2 at an average flux of $7.73x10^{11}$ ions/cm^2-s. This corresponds to a nominal average damage dose of 0.27 dpa in the first 50 nm of the material, with a peak damage of 0.44 dpa. These values are calculated with SRIM using inputs based on the recommendations by Stoller *et al.*[315] and recently reported estimates of the TDEs (54 and 90 eV for the oxygen and titanium atoms, respectively) that correspond to 50% displacement probability.[164] With the TEM operating at 200 kV during irradiation, bright-field video of the data is recorded and SAED patterns are collected periodically.

6.1.1.2 **MD Simulations**

The present MD simulation of a 46 keV Ti projectile in TiO_2 rutile at an initial temperature of 300 K is carried out using the LAMMPS,[249] in conjunction with the Pedone[217] interatomic potential. At short interatomic distances, the Pedone potential is fitted to a repulsive term to accommodate the short-range interactions during a radiation damage cascade. The Coulomb interactions are modeled using the particle-particle particle-mesh (PPPM) solver, with a relative error of 1.0×10^{-6}. The calculated equation of state with the Pedone potential accurately models TiO_2 at various temperatures and pressures, and is in agreement with other MD simulation results of the energies for defect production in TiO_2.[55,164]

A system of 12 million atoms is used in the MD simulations with periodic x and y boundaries and a fixed boundary in the z-dimension. The system is equilibrated in an NPT ensemble for 210 ps at 300 K and 0 atm, with a time step of 1 fs. Subsequently, the atoms are equilibrated in a NVE ensemble for 10 ps, with a Nose-Hoover canonical (NVT) thermostatic

boundary layer, set to emulate the effect of phonon-assisted energy dissipation. Following equilibration, a 46 keV Ti PKA is introduced 1 nm above the surface of the crystal with velocity components; V_x=747.7849 Å/ps, V_y=0 Å/ps, and V_z=-4240.9 Å/ps. The small V_x helps avoid channeling through the crystal. The angle of incidence of the Ti projectile relative to the normal of the surface is 10°. The normal to all faces of the TiO_2 crystal is a <100> family direction. A variable time step algorithm is used for the radiation events, such that no atom can move more than 0.005 Å per time step. The time between frames during the ballistic phase varies from 0.6 – 60 fs, and from 60 – 200 fs during the annealing phase. After the number of residual defects is no longer changing (≈20 ps), the time between frames is 1 ps.

The Wigner Seitz (WS) defect analysis is used to characterize and quantify the vacancies, interstitials, and antisites produced, while cluster analysis is used to identify the produced clusters of vacancies (voids) and interstitials. Defect production is tracked during both the ballistic and annealing phases. The term "annealing" in this context refers to damage recovery immediately following the radiation event. Atoms are highly mobile due to their increase in kinetic energy they received either directly or indirectly from the Ti projectile. For this reason, many of the produced interstitials and vacancies recombine. This definition of annealing should not be confused with slow cooling as it is used in metals and alloys processing. The TiO_2 lattice parameter is used as the cutoff to identify the defects in the same cluster and allow adjacent lattice sites to be part of the same cluster. These methods are used within the framework of OVITO and its customizable python scripting interface.[304] It is important to note that since radiation damage is stochastic in nature, a cascade produced by another 46 keV Ti PKA may produce somewhat different results. However, computational resources set limitations to a single cascade in the 12 million atom system. Simulated SAED patterns are generated of the perfect TiO_2 crystal and of the irradiated damage region of the crystal with a 46 keV Ti PKA cascade by calculating the electron diffraction intensity on a mesh of reciprocal lattice nodes.[310] The visualization of the SAED patterns is carried out by taking the logarithm of the diffraction intensity in Paraview.[311]

6.1.2 Results

This section presents and discusses the results of the deposition of a thin film of TiO_2, the *in situ* TEM ion beam irradiation with 46-keV Ti^- ions, and the performed MD simulation of

defect production in TiO_2 with a 46 keV Ti projectile. The results of the *in-situ* TEM irradiation include bright field images of the deposited TiO_2 thin film, and a comparison of the SAED patterns of TiO_2, before and after irradiation. The MD simulation results are of the number of defects produced at the peak of the ballistic phase and the residual defects after annealing, defects clustering, radial distribution functions (RDFs), and simulated SAED patterns. Discussed are the attributes of using MD simulation and *in-situ* TEM experiments methods of contrasting irradiation effects in TiO_2.

6.1.2.1 *In Situ* TEM Ion Beam Irradiation Results

During the deposition of the TiO_2 thin film onto the α-SiN TEM grids, many islands of TiO_2 have formed (Fig. 6.1a). The inset SAED pattern prior to irradiation shows bright spots, corresponding to the different crystalline islands shown in the bright-field image. The SAED patterns of the unirradiated crystal inset in Fig. 6.1a confirm that the structure of the TiO_2 islands is crystalline. The diffuse amorphous rings in the SAED patterns are due to the α-SiN substrate.

During irradiation, bright field video showed contrast changes in the TiO_2 islands. However, most of the contrast changes are likely due to bending or deflection of the substrate during irradiation, making it difficult to identify the induced material damage by single ion strikes. The deflection by the substrate confirms the incidence of the ion beam on the specimen even though no traceable radiation damage occurred. No amorphization on a large-scale is observed either, as the SAED patterns taken from the TEM show crystalline regions before and after irradiation (Fig. 6.1a,b). Note that the differences in the TEM SAED spots are likely due to changes in orientation, rather than changes in crystal structure.

The retention of crystallinity after irradiation of the present TiO_2 sample at a fluence of 6.96×10^{14} 46 keV Ti ions/cm^2, corresponding to a dose of only 0.44 dpa, is consistent with prior studies[188,198] indicating that a fluence on the order of 10^{15} ions/cm^2 is needed to amorphize TiO_2 rutile at 300 K.[101,188,198] Li *et al.*[198] have shown that radiation damage accumulation in TiO_2 does not cause it to amorphize below approximately 10 dpa at a depth corresponding to the peak damage. However, these prior studies show that radiation-induced defects in TiO_2 can accumulate at room temperature, and will eventually cause amorphization of the thin film, once a critical fluence is reached. Thus, ion strikes in TiO_2 at room temperature seem to produce stable defects, but a cascade from a single ion strike

would not render the material amorphous. Since amorphization can occur at 300 K, investigating defect production from a single ion strike would provide valuable information in terms of understanding the process of amorphization in TiO_2. The next section presents the MD simulation results of a single 46 keV Ti projectile ion strike in TiO_2 rutile.

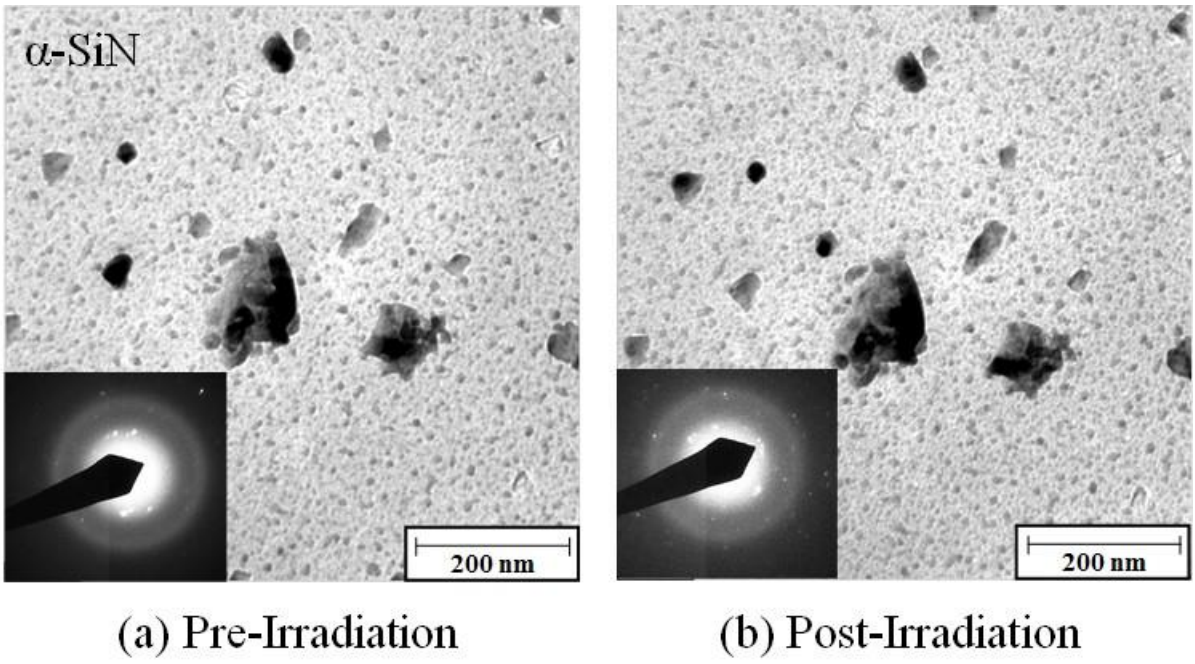

Figure 6.1: Comparison of bright field images of TiO_2 nanoparticles on α-SiN with inset SAED pattern before and after irradiation.

6.1.2.2 **Molecular Dynamics Simulation Results**

Fig. 6.2a compares the produced point defects of oxygen and titanium vacancies, interstitials, and antisites, and Fig. 6.2b,c compares the size of the three largest defect clusters of vacancies and interstitials, respectively, with a 46 keV Ti projectile in TiO_2 rutile as a function of time. The ballistic phase of interaction extends to the peak defects production, followed by the annealing phase of interaction that ends with plateaus indicating the residual defects and defect clusters (Fig. 6.2a-c). It is important to note that the temporal resolution of the residual defects in the MD simulation is several orders of magnitude away from the real-time images of irradiation with *in situ* TEM. Table 6.1 lists the numbers of the various types of the peak and residual defects produced in the simulations. The 9,249 oxygen and 4,339

titanium vacancies produced at the peak of the ballistic phase are mostly annealed except for 232 residual oxygen and 650 titanium vacancies.

Table 6.1: Number of oxygen and titanium vacancies, interstitials, and antisites at the peak of radiation damage, and residuals after annealing.

Defect Type	Defects		
	Peak	**Residual**	**Annealed (%)**
Oxygen Vacancies (V_O)	9,249	232	97.5
Titanium Vacancies (V_{Ti})	4,339	655	84.9
Oxygen Interstitials (O_i)	3,179	107	96.6
Titanium Interstitials (Ti_i)	9,827	741	92.5
Oxygen Antisites (O_{Ti})	9,759	178	98.2
Titanium Antisites (Ti_O)	4,220	107	97.5

The production of vacancies occurs primarily in the core region of the defects cluster, where the accumulated vacancies forms a void. In the core of the defect cluster, atoms are knocked out from the center to the outer edges, before many diffuse into appropriate lattice sites. Fig. 6.2b compares the sizes of the three largest voids forming as a function of simulation time. The three largest voids/clusters forming during the peak phase of irradiation are smaller after annealing, but still the largest. The largest forming void at the peak of the ballistic phase comprises >10,000 O and Ti vacancies, decreasing due to thermal recombination to only 795 after annealing. The two second largest voids are significantly smaller comprising only 44 and 15 vacancies after annealing.

The results in Fig. 6.2c compare the changes in the sizes of the three largest clusters of the interstitials forming during the peak and annealing phases of the MD simulation. These clusters become much smaller after annealing but retain the same size order as at the peak of the ballistic phase. At the peak of the ballistic phase of interaction, the largest cluster formed comprises >10,000 interstitials, similar to the number of vacancies in the largest formed void (Fig. 6.2b). After annealing, the three largest clusters in Fig. 6.2c contain only 752, 33, and 22 interstitials. While clustering of the produced vacancies occurs in the core region of the cascade that of the interstitials is dominant at the periphery of the core region. This type of

defect production causes density inhomogeneity that can provide fast diffusion pathways, which have been previously observed in zirconium silicate, using MD simulations and X-ray scattering.[316,317]

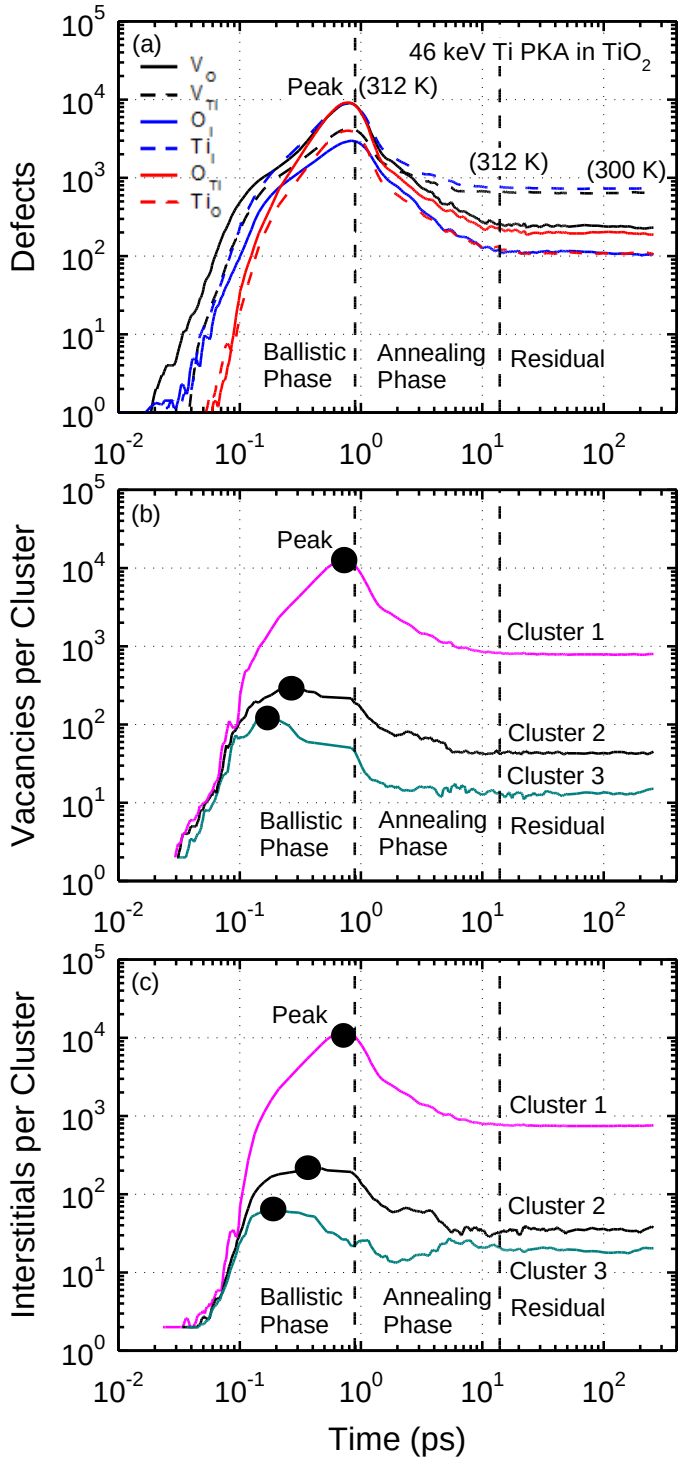

Figure 6.2: Comparison of the number of the different types of defects and three largest vacancy and interstitial clusters in the MD simulation with a 46 keV Ti PKA in TiO_2 during the ballistic and annealing phases of interaction, and the residuals.

In the present simulations, a second Ti projectile is injected into the TiO_2 system to potentially observe the effects of overlapping cascades. Instead, the projectile channeled through the entire system, and only produced point defects, suggesting that defects production by different projectiles, even of the same energy and incidence angle, would tend to interact differently, and thus produce different results. The defects production depends not only on the type and energy of the projectiles, but also on the target material. The inhomogeneous defects production would cause density inhomogeneity in some materials and none in others.[75,165,167]

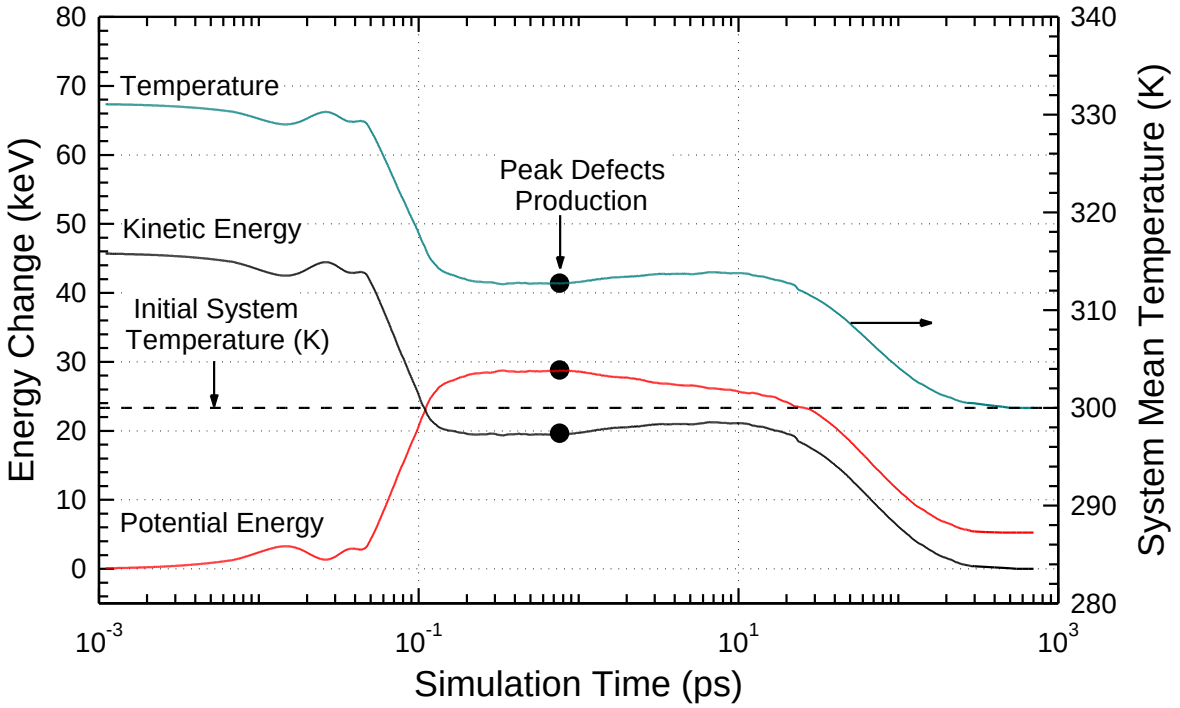

Figure 6.3: Changes in the system temperature, kinetic energy, and potential energy during the MD simulation with a 46 keV Ti projectile in TiO_2.

Fig. 6.3 shows the changes in the atom system temperature, T, kinetic energy, (mean kinetic energy per atom = 3/2 kT, where k is Boltzmann's constant = 8.61747x10-8 keV/K) and potential energy with simulation time, including the ballistic and annealing phases of interaction. When the Ti projectile is injected into the system, adding 46 keV, the average system temperature spikes to ≈331 K. Immediately following the spike in the system temperature, an elastic wave propagates radially, spreading the projectile energy to a larger

volume. The added kinetic energy to the system is partially converted into potential energy, which is associated with the increase in the number of produced defects. The system's mean temperature drops from ≈331 K, at the start of the simulation, to ≈312 K at the peak defects production in the ballistic phase of interaction (Figs. 6.2a and 6.3). The system temperature continues to drop slowly due to the energy dissipation at the thermostatic boundary. It eventually drops to zero when the system mean temperature reaches the same value prior to the simulation (300 K). At such time, the change in the kinetic energy diminishes, while that in the potential energy reaches an asymptotic value of ~5 keV due to the residual defects (Figs. 6.2a and 6.3). This potential energy is ~ 10.87% of the Ti projectile energy in the simulation.

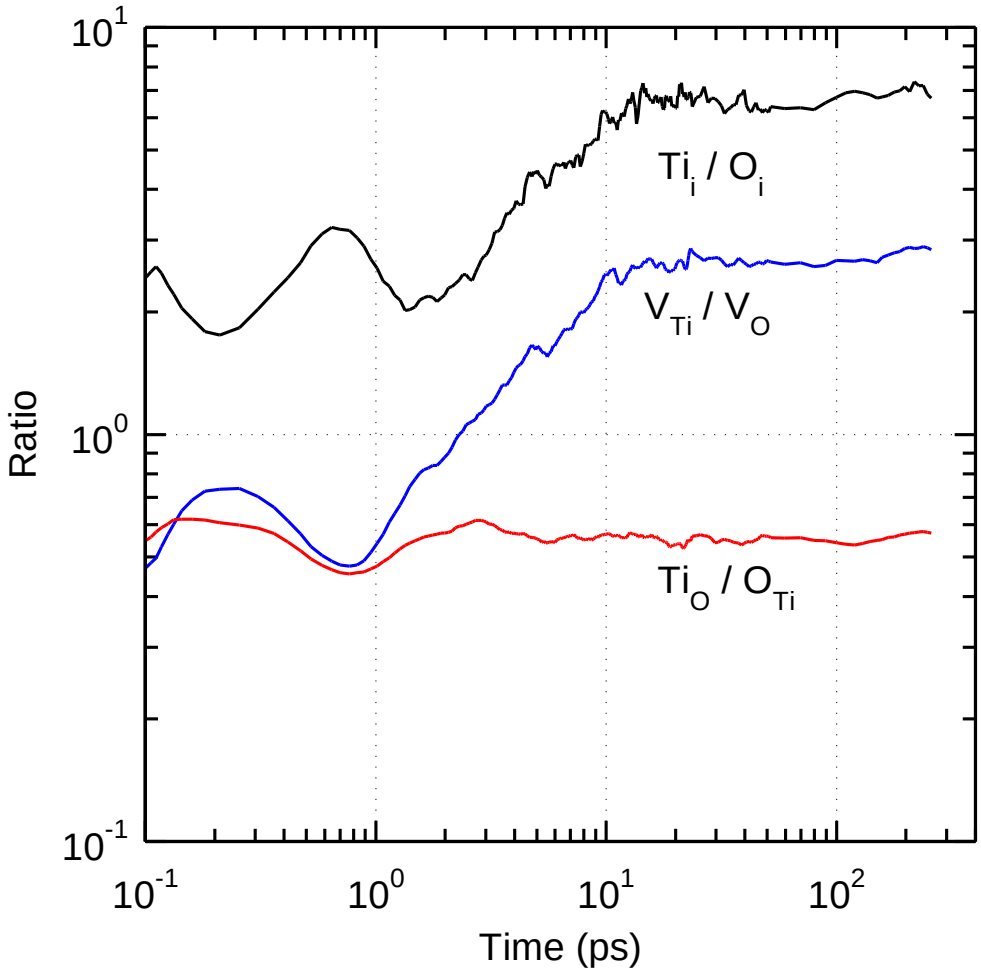

Figure 6.4: Comparison of the ratios of titanium to oxygen vacancies, interstitials, and antisites as a function of time.

After annealing, the produced clusters are primarily made up of titanium defects. Fig. 6.4 shows the evolution of the titanium to oxygen defect ratios for vacancies, interstitials, and antisites, as a function of simulation time. The V_{Ti}/V_O and Ti_i/O_i ratios increase during the ballistic and annealing phases but plateau at ≈20 ps with ratios of 2.6 and 6.2, respectively. The ratio of the titanium to the oxygen antisites throughout the entire simulation is ≈0.5.

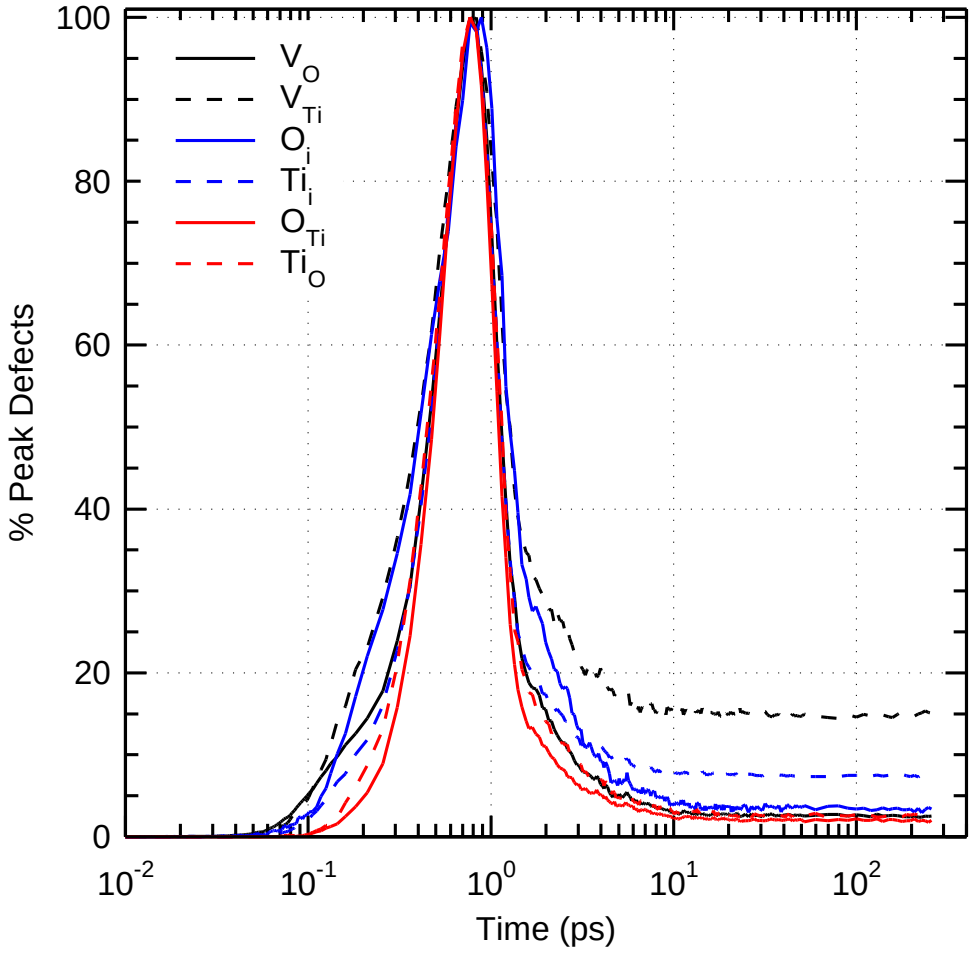

Figure 6.5: Comparison of the percentages of peak defects as a function of simulation time.

Fig. 6.5 shows the percentage of peak defects for oxygen and titanium vacancies, interstitials, and antisites, as a function of simulation time. During the ballistic phase, the peak production of the different types of defects rises to 100%, and then decreases during the annealing phase. Most of the defects present after 10 ps of simulation are also present after 50 ps. The defects with the lowest annealing efficiencies are the titanium interstitials and vacancies. For instance, ≈15% of the peak titanium vacancies and 7.3% of the peak titanium

interstitials remains after annealing, compared to 2.5% and 3.9% for the oxygen vacancies and interstitials, respectively. In TiO_2 rutile, Ti atoms are octahedrally coordinated to 6 oxygen atoms each, thus it is difficult for the Ti interstitials to diffuse to the vacant Ti sites, compared to the oxygen interstitials that readily diffuse to vacant oxygen lattice sites. Moreover, the more massive Ti atoms are less mobile than the lighter oxygen atoms.

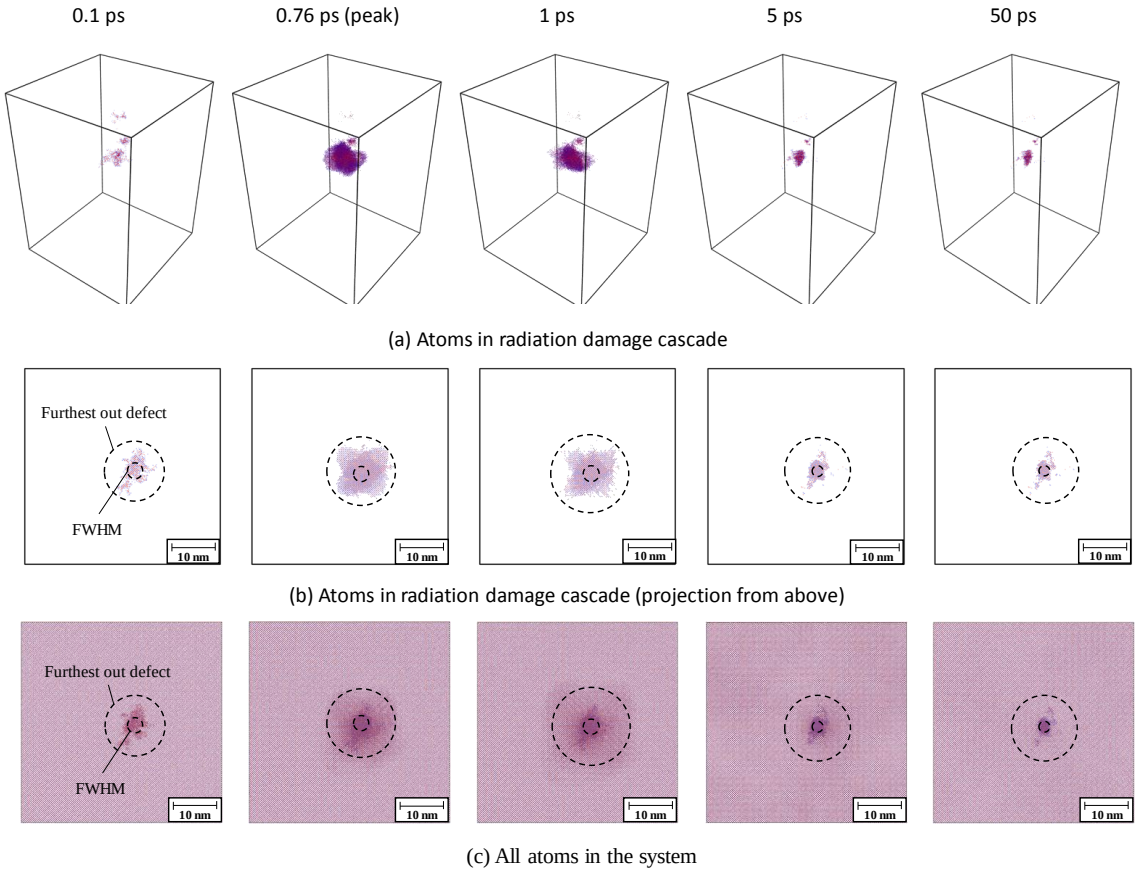

Figure 6.6: Calculated radiation damage cascade in TiO_2 with a 46 keV Ti PKA. The inner circle is the full-width half maximum of the defect density distribution and the outer circle is the furthest out defect from the central core region.

The atoms contributing to the produced defects are identified using Wigner-Seitz defect analysis and the results are shown in Fig. 6.6a,b. Its shows a central core of defects that is almost spherical (with some periphery defects not part of the core cascade) with a radius of 5.8 nm and total volume of approximately 817 nm^3. This core shrinks as the simulation time increases. After 50 ps, there is a small but still distinct core of defects measuring approximately 40 nm^3. The inner dashed circles in Fig. 6.6a,b is of the full-width half-

maximum of the defect density distribution and the outer circle is the furthest defect from the central core region. The radius of the FWHM circle reaches ≈3 nm at peak defect production, before decreasing to ≈2 nm after annealing.

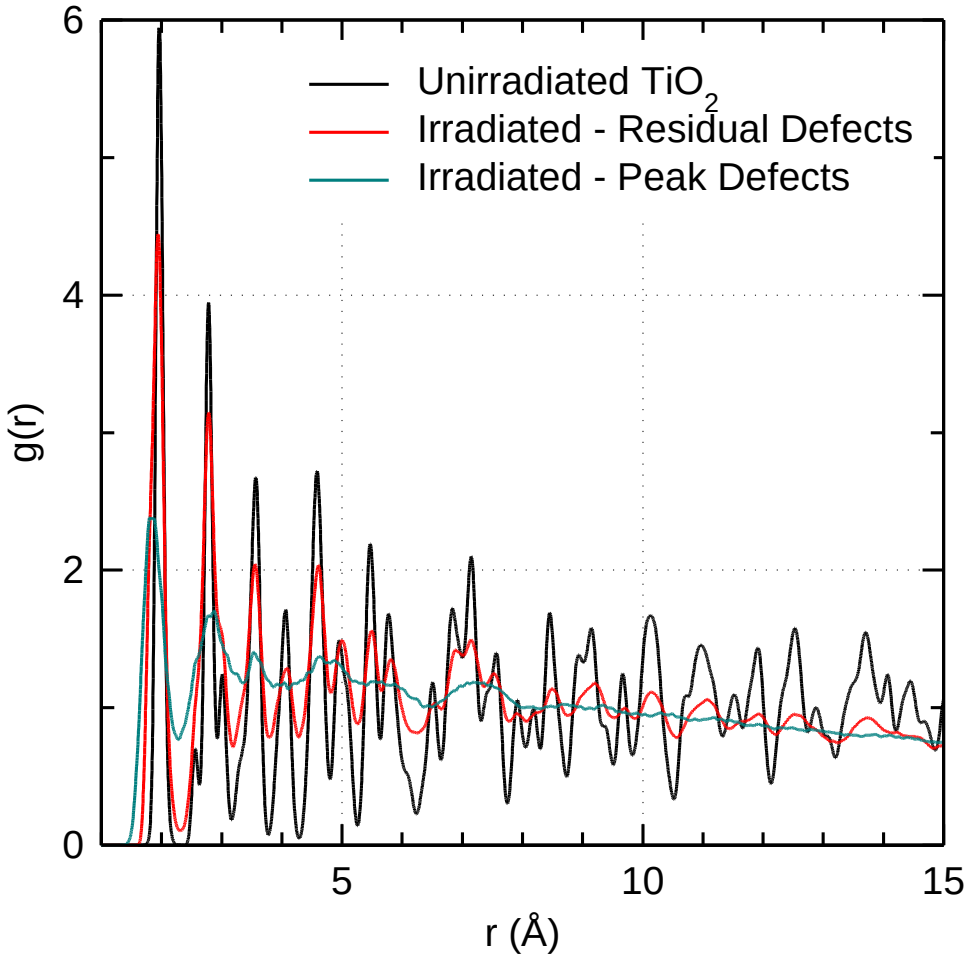

Figure 6.7: Comparison of the radial distribution functions (RDFs) for TiO_2 before irradiation, at peak defects production, and of the residuals.

The differences in numbers of vacancies and interstitials of each atom type are due to the antisite defects, in which an oxygen atom occupies a titanium lattice site or vice versa. Many of the antisites produced during the ballistic phase are affiliated with the elastic deformation of the crystal, as opposed to actual crystalline disorder.[68] The formation of many of the antisites are due to translations of the atoms due to elastic deformation and the possibility of shifting the oxygen atoms over the titanium atom lattice sites. Antisites forming by crystalline disorder are due to replacement collision sequences between different atom types.

This is evident by the elastic wave commencing by the impact of the Ti projectile and travelling through the system.

The accumulation of vacancies and interstitials can affect the crystallinity of the material in the irradiated region and hence the local material properties. The RDFs over the irradiated region are used to investigate the crystallinity in the irradiated region, since the peaks in the RDF represent local order from a repeating crystal structure (Fig. 6.7). Each RDF peak indicates the probability of finding another atom at a given distance within the crystal. During the ballistic phase of irradiation, only 0.34% of the atoms are defects, compared to 0.017% after annealing. Thus, a RDF calculated over the whole system does not capture the irradiation effects in the core region of defects production.

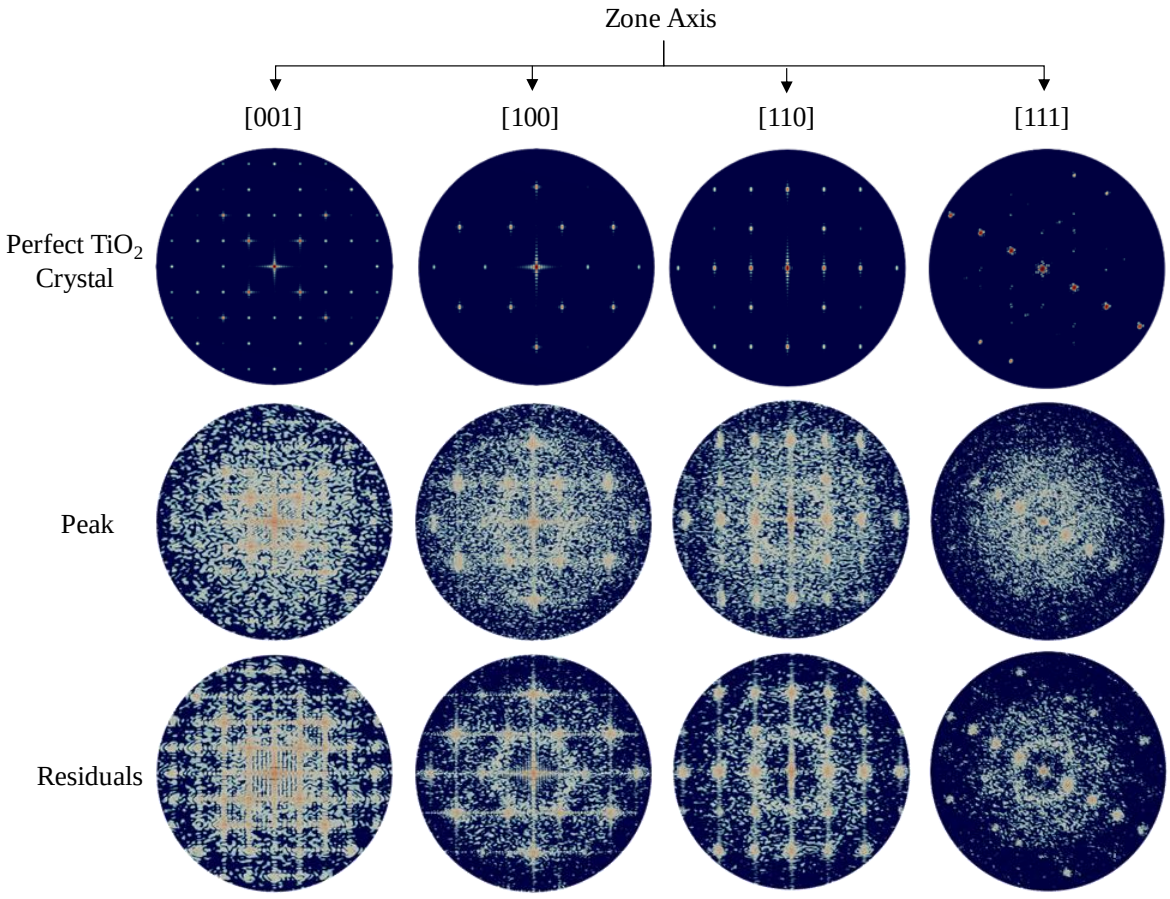

Figure 6.8: Comparison of selected area electron diffraction (SAED) patterns of the perfect and irradiated TiO_2 crystal, at peak defects production and of the residuals.

The results in Fig. 6.7 compare the RDFs of the unirradiated and irradiated TiO_2 rutile crystal at the peak of the ballistic phase and of the residual defects after annealing. As a material becomes disordered, the peaks are not as well-defined, and $g(r) \rightarrow 1$ for amorphous materials. In the RDF, g(r) represents the probability of finding a particle at a given distance from a particle at r = 0. Fig. 6.7 shows that during peak defect production, the material is highly disordered in the core of the produced defects, since $g(r) \rightarrow 1$ at approximately 5 Å. Beyond 5 Å, no RDF peaks are noticeable during the peak defects production, indicating the absence of long-range order. Conversely, some short- and medium-range order exits even at the peak of the ballistic phase. After annealing, although the lattice mostly recovers, as >90% of the produced defects recombine, the RDF still shows some disorder in the defect production core, and peaks are not as defined as for the unirradiated crystal. There are clearly short- and medium-range and some long-range order (Fig. 6.7).

SAED patterns are commonly obtained with TEM experiments to determine crystallinity and the phase of a given material. The present work applies the simulated SAED calculation[310] with LAMMPS over the defects production region using MD simulation with a 46 keV Ti PKA in TiO_2, and results are shown in Fig. 6.8. This figure compares the SAED patterns of the perfect TiO_2 rutile crystal to those during the peak of the ballistic phase of defects production and the residuals. Four zone axes are investigated, namely: [001], [100], [110], and [111] to observe, from different perspectives, the induced damage. During the peak phase of defects production, some disorder is produced in the defects production region, but the diffraction peaks corresponding to the perfect TiO_2 crystal are still noticeable for all zone axes examined. If the crystal had fully amorphized in the irradiated region, the SAED pattern would show a diffuse ring, as opposed to faint diffraction peaks. Thus, it is clear that some order still exists in the irradiated crystal at the peak phase of defect production, even if the diffraction peaks are not as readily defined as in the unirradiated TiO_2 crystal. After annealing the crystal shows significant recovery with more pronounced diffraction peaks, compared to the peak defect production. However, the lattice is not fully recovered because of the residual Frenkel pairs and defect clusters in the system (Fig. 6.8).

6.1.2.3 **Discussion**

This section discusses the results of the *in situ* TEM ion beam irradiation experiments and of the MD simulation of 46 keV Ti projectile in crystalline TiO_2. Also discussed is the

potential use of these complementary methods for investigating irradiation effects. While the MD simulation results provide attosecond resolution over picosecond time scales, the results of the *in situ* TEM ion irradiation experiments provide millisecond resolution in real-time. Although the differences in the temporal resolutions of the two methods makes a quantitative comparison of the results impossible, a qualitative comparison of the results would be useful to better understanding irradiation effects and develop multi-scale predictive models.

Despite the orders of magnitude difference in the temporal resolution, there are similarities in the obtained results of the irradiation effects in TiO_2 using both methods. For instance, neither methods show amorphization of TiO_2 with either single ion strike in MD simulation or Ti ion beam in the experiments to 0.44 dpa. This is in agreement with prior work[198] which indicated that a significantly larger dose of 10 dpa is needed to amorphize TiO_2 rutile at 300 K. The retention of crystallinity after annealing is confirmed by the SAED patterns from the *in situ* TEM experiments and the simulated SAED patterns and RDF from the MD simulation. The MD simulation show that at the peak ballistic defect production, long-range order in the irradiated region is lost, since $g(r) \rightarrow 1$ at approximately 5 Å. Nonetheless, this order reemerges after annealing.

Investigation of point defects production from individual ion strikes with *in situ* TEM is prohibitive. However, an MD simulation of an identical setup can provide the atomic-level resolution needed to characterize induced defects by single ion strikes, and potentially improve models for predicting irradiation damage. In addition to showing retention of crystallinity, the MD simulation provides details of the defects production and annealing during the very short simulation time (up to 250 ps). These include the number of residual defects and those produced at the peak of the ballistic phase, and the formation of both clusters of interstitials and void of vacancies. The present results of the MD simulation indicate that reversible elastic and irreversible inelastic deformation take place during the ballistic phase of interaction. The accumulation of irreversible inelastic deformation from many ion strikes might cause localized amorphization in the crystalline TiO_2.

These detailed results at the atomic scale using MD simulation at a time scale of picoseconds are not traceable in the ion beam irradiation test with a relatively larger time resolution of 200 milliseconds. While the MD simulations results on irradiation-induced defects at the atomistic scale could not substitute for those of the ion beam irradiation results

at the macroscale, together they can enhance the broad understanding of radiation effects in materials.

6.1.3 Highlights and Concluding Remarks

MD simulations at the atomistic scale and ion beam irradiation tests at the nanoscale would enhance the broad understanding of radiation effects in materials. The performed MD simulation and *in-situ* TEM irradiation investigated the interaction of a 46 keV Ti projectile into islands of crystalline TiO_2. The MD simulation results provide detailed information of the individual types of defects produced and retained with picosecond resolution. This combination of length and time scale cannot be matched by any current experimental facility, but the irradiation experiments with a 46 keV Ti ion beam confirmed the presence of a post-annealing crystalline phase, as expected due to the low irradiation dose of 0.44 dpa at 300 K.

MD simulation results show that despite much more oxygen than titanium vacancies are produced during the peak of the ballistic phase, the residual vacancies after annealing are mostly titanium. Some of the defects identified by WS analysis during the ballistic phase of interaction are a result of elastic deformation from the ion strike rather than changes in the crystal structure. Cluster analysis identified up to approximately 10,000 vacancies in the core of the cascade during the ballistic phase of interaction, which decreased in size to <1,000 vacancies after annealing. After annealing, the volume of the defects cascade is ≈40 nm^3. The diameter of the irradiated region at FWHM of the defect density distribution is ≈3 nm at the defects peak production, decreasing to ≈2 nm after annealing. Clusters of interstitials, approximately the same sizes as the vacancy clusters, form mostly at the periphery of the core region. The RDFs and simulated SAED patterns of irradiated region at the peak of the ballistic phase show short- and medium-, but no long-range order. After annealing, however, some long-range order returns, which is validated by the *in situ* TEM ion irradiation experiments. The MD simulation and the complementary in *situ* TEM ion beam irradiation experiment are an effective tool-set for understanding and characterizing the effect of radiation in materials and the resulting changes in microstructure and properties.

6.2 SiC

In this study, extensive MD simulations with high energy PKAs are performed to investigate radiation damage in 3C-SiC and amorphous (a-SiC) with 10, 20, 30, 40, 50, 60, and 100 keV Si PKAs in 3C-SiC and 10 and 30 keV Si PKAs in a-SiC. In addition, *in situ*

TEM ion beam irradiation experiments of 3C-SiC and a-SiC thin samples are performed using 1.7 MeV Au^{3+} ions. The obtained MD simulations and experimental results are compared and the SAED patterns from both are examined for any changes in morphology and apparent radiation damage. The present MD simulations results of defects production and clustering in 3C-SiC are compared to those reported by earlier investigators[75,165,167] with PKAs energies up to 50 keV. The stored energies in the irradiated 3C-SiC and a-SiC are calculated and used to assess the radiation resistance of 3C-SiC and a-SiC.

6.2.1 Methodology

The following section presents the MD simulations methods, and the subsequent section presents the manner in which the thin films were deposited and irradiated.

6.2.1.1 Molecular Dynamics Simulations

The present MD simulations for investigating radiation damage in 3C-SiC and a-SiC with Si PKAs of different energies (10-100 keV) are carried out using LAMMPS,[249] in conjunction with the Tersoff+ZBL[64] potential. Performing MD simulations to emulate radiation damage by the 1.7 MeV Au^{3+} in the performed *in situ* TEM experiments would be prohibitive, likely requiring a system of tens of billions of atoms. Instead, Si PKAs with energies up to 100 keV are used in the present MD simulations. Because these simulations neglect the energy loss due to electronic stopping, the experimental PKA energies they represent would likely be much higher.[165,167]

To ensure that the produced defect cascades in the present MD simulations, by channeling high-energy PKAs and secondary knock-on atoms (SKAs), do not reach the periodic boundaries,[167] the present MD simulations employed significantly large system sizes. The simulations increased system size with increased PKA energy. A system of 64 million atoms is used in the simulations with 10, 20, 30, 40, 50, and 60 keV Si PKAs, and a system of 512 million atoms is used in the simulations with the 100 keV Si PKA. As shown in Table 6.2, the number of atoms in the present MD simulation of a 100 keV Si PKA is more than an order of magnitude higher than previously used in MD simulations with 50 keV PKAs.[75,160,165] For PKA energies of 10 - 60 keV, 3-4 simulation cascades are performed to improve the statistics of the results. However, for the 100 keV Si PKA, only a single simulation is carried out due to computational limitations.

Table 6.2: Listing of the PKA energies and system sizes used in prior MD studies, compared to the present work.

Reference	PKA Energies (keV)	Atoms Used	System Dimensions1 (Lattice unit)
Gao *et al.*[160]	0.25 - 50	8,000 - 6,040,000	10x10x10 - 60x60x210
Liu *et al.*[165]	0.01 - 50	101,376 - 16,252,928	24x24x22 - 128x128x124
Samolyuk *et al.*[75]	10, 50	409,600 - 22,070,021	80x80x80 - 150x150x150
Present Work	10 - 60	64,000,000	200 x 200 x 200
Present Work	100	512,000,000	400 x 400 x 400

In the simulations of radiation damage in 3C-SiC, the system of atoms is first equilibrated in an NPT ensemble at 300 K and 0 atm for 20 ps. Subsequently, it is equilibrated for 20 ps in a NVE ensemble. A thermostatic boundary layer is applied at the boundaries of the system to readily dissipate the heat deposited by the radiation events. The a-SiC is prepared in the same manner, as discussed in prior work.[303] The performed MD simulations for 3C-SiC and a-SiC used a variable time step, with no atom moving more than 0.005 Å in a single time step.

This work used Wigner-Seitz (WS) defect analysis to determine the number of vacancies, interstitials, and antisites and cluster analysis to identify the clusters of vacancies (voids) and interstitials in 3C-SiC[75]. The lattice parameter is used to determine which defects belong to the same cluster. Simulated SAED patterns of the unirradiated 3C-SiC crystal and of the radiation damaged region are generated by calculating the electron diffraction intensity on a mesh of reciprocal lattice nodes.[310] The visualization of the SAED patterns was possible using the logarithm of the diffraction intensity in Paraview.[311]

6.2.1.2 **Ion beam irradiation experiments**

For the *in situ* TEM irradiation experiments, a-SiC and 3C-SiC samples are deposited onto single crystal pure Si TEM windows using a 99.5% pure SiC sputtering target and the Direct Current (DC) ATC 1800 Magnetron Sputtering System at the Center for Integrated Nanotechnologies at Los Alamos National Laboratory. The base pressure in the sputtering chamber was 5.0×10^{-8} Torr (~ 6.67×10^{-10} Pa), while the working pressure was 3×10^{-3} Torr (2.25×10^{-5} Pa). During deposition, the partial pressure of the inert Argon gas in the

sputtering chamber was 30 sccm, the substrate temperature was 700 °C, the DC Power was 300 W, and the distance between the target and substrate was ≈50 cm. At a deposition rate of 0.93 Å/s, the SiC was deposited for 430 seconds to obtain a nominal film thickness of ≈40 nm. SAED patterns showed that these samples are amorphous SiC.

Following deposition, some of the a-SiC specimens were annealed for four hours at 1200 °C in a vacuum furnace at Sandia National Laboratories, to form 3C-SiC, before being irradiated with a 1.7 MeV Au^{3+} ion beam in the JEOL 2100 TEM for 15 minutes in the *in-situ* ion irradiation TEM (I^3TEM) facility at Sandia National Laboratories.[76] The total fluence at an average flux of $3.18x10^{11}$ ions/cm^2-s was $2.87x10^{14}$ ions/cm^2, which corresponds to an average dose of 0.55 dpa in the top 40 nm of the 3C-SiC specimen and 0.995 dpa in the top 40 nm of the a-SiC specimen. These dose values are calculated with SRIM using inputs based on the recommendations by Stoller *et al.*[315] and recommend estimates of the TDEs[67] (26 and 48 eV for carbon and silicon atoms in 3C-SiC, and 13 and 27 eV in a-SiC, respectively). These TDEs correspond to a 50% displacement probability.[164] During the irradiation experiments, TEM was operated at 200 kV, while bright-field video data was recorded and SAED patterns collected periodically.

6.2.2 Results

This section presents the results of the performed MD simulations of the defect production in 3C-SiC and a-SiC by Si-PKAs with energies up to 100 keV. The deposition of thin films of 3C-SiC and a-SiC, and the results of the *in situ* TEM ion beam irradiation with 1.7 MeV Au^{3+} ions are also presented. In addition, the results of the MD simulations and the *in situ* TEM ion beam irradiation are compared and discussed. The MD simulation results include the number and types of residual defects produced, defect clustering, extent of defect cascade, simulated SAED patterns, and estimates of the stored energy due to residual defects. The *in situ* TEM ion beam irradiation results include bright field images of the SiC specimens, and SAED patterns of the 3C-SiC specimen before and after irradiation.

6.2.2.1 **Molecular Dynamic Simulation Results**

Fig. 6.9 compares the numbers of the different types of residual defects produced in 3C-SiC in the present MD simulations using Si PKAs with energies from 10 – 100 keV. The primary residual defects are carbon interstitials and vacancies, followed sequentially by the carbon antisites, and the silicon vacancies, antisites, and interstitials. The order of the

residual defects in 3C-SiC is consistent with that reported previously for PKAs with energies up to 50 keV.[75] The number of the residual defects produced in the present MD simulations increased linearly with increased PKA energy, as:

$$N_d = a + m\, E_{PKA}(keV). \qquad \text{Eq. 6.1}$$

In this equation, "a" is the number of defects produced by the lowest energy PKA of 10 keV and "m" is the residual defects rate of increase with increased PKA energy, E_{PKA}. As shown in Fig. 6.9 and listed in Table 6.3, the values of "a" and "m" depends on the type of the residual defects produced in the present MD simulations.

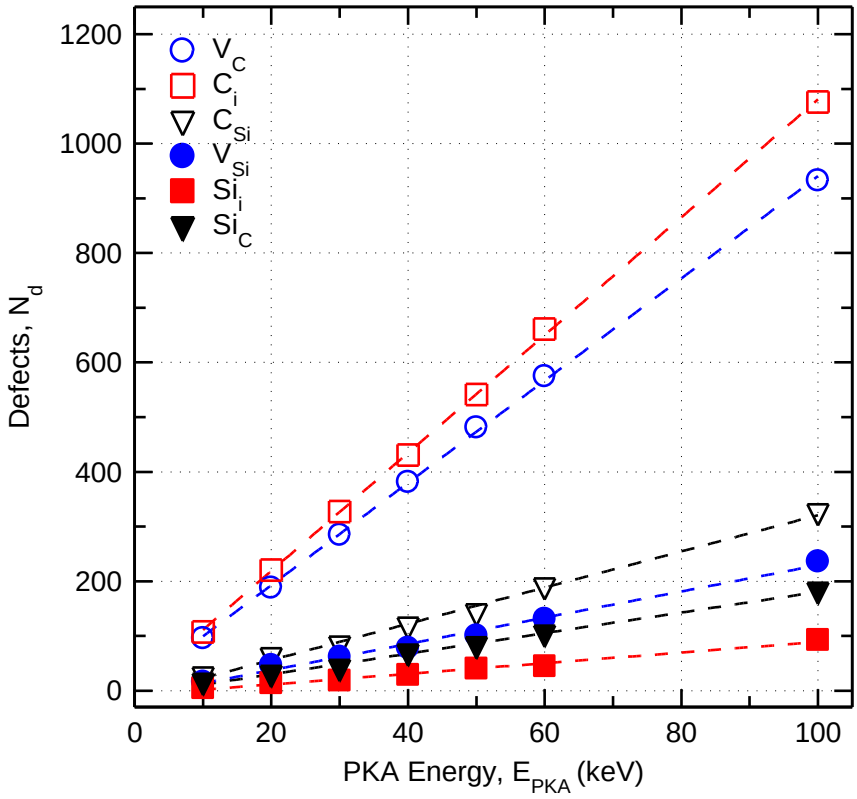

Figure 6.9: Comparison of the residual number and types of defects produced in 3C-SiC with Si PKAs ranging from 10 – 100 keV.

Fig. 6.10 compares the calculated ratios of the residual carbon to silicon interstitials, vacancies, and antisites in the present MD simulations as a function of the Si PKA energy. For the 10 keV Si PKAs, the number of the residual carbon interstitials is about 23 times that of silicon and decreases to about 10 times that of silicon with 100 keV Si PKAs. The higher carbon interstitial population is due to the high carbon interstitial migration barrier modeled

with the Tersoff+ZBL potential, which is higher than density functional theory (DFT) calculations.[75,161] The high migration barrier suppresses recombination of the carbon interstitials that are only one lattice parameter away from a carbon vacancy.[75] With higher PKA energies of 100 keV, more carbon interstitials recombine due to the increase in the localized heating in and around the defect regions, due to the higher energy deposition by the PKA. The ratios of carbon to silicon vacancies and antisites, much lower and independent of the Si PKA, are ≈4-6x and ≈1-2x, respectively.

Table 6.3: Fitting parameters for the production of residual vacancies, interstitials, and antisites, with Si PKAs of energies of 10 – 100 keV in 3C-SiC.

Defect	a	m
C_i	10.8	3.57
V_C	9.35	5.96
C_{Si}	3.31	-10.2
V_{Si}	2.40	-10.5
Si_C	1.88	-7.79
Si_i	0.97	-8.13

Figs. 6.11 and 6.12 show images of the residual defect cascades produced in 3C-SiC by Si PKAs incident in the [100] direction, with energies ranging from 10-30 and 40-100 keV, respectively. These images show that the produced defect cascade forms several smaller cascades, and the produced defects are not concentrated in a single region. Similar results have been shown in prior work, but for PKA energies up to 50 keV.[75,160,165] The images of the residual defect cascades in Figs. 6.11 and 6.12 show the clustering of vacancies and interstitials is not dominant in 3C-SiC, which is also in agreement with prior work by others.[75,103,167] The present images of the residual defects produced by Si PKAs with energies up to 100 keV, show that defect cascades branch off to several smaller cascades along the trail of the induced radiation damage. Conversely, defects produced in metals[129,318] have been shown to form a single core.

Figs. 6.13a and 6.13b compares the average number of produced residual clusters of vacancies and interstitials, averaged over all cascades simulated, at different Si PKA

energies. As shown in Table 6.4, the size of the largest vacancy cluster produced is ≈2 to 3 times that of the largest interstitial cluster produced, for all cascades investigated in the present MD simulations. The number of the clusters produced, particularly the small ones, increases with increased Si PKA energy. Increasing the Si PKA energy would increase the extent of the cascade, which increases the number of the small defect clusters produced. However, the average size of the very few large clusters produced is weakly dependent on the PKA energy (Table 6.3), due to the formation of many smaller cascades, rather than increasing the number of defects in the forming clusters. The average size of the largest residual vacancy and interstitial clusters produced increases from 10.3 ± 2.1 to 30.3 ± 13.1 and from 4.0 ± 1.4 to 12.0 ± 4.4, as the Si PKA energy increases from 10 to 40 keV, respectively. Above 40 keV, there is no clear trend observed.

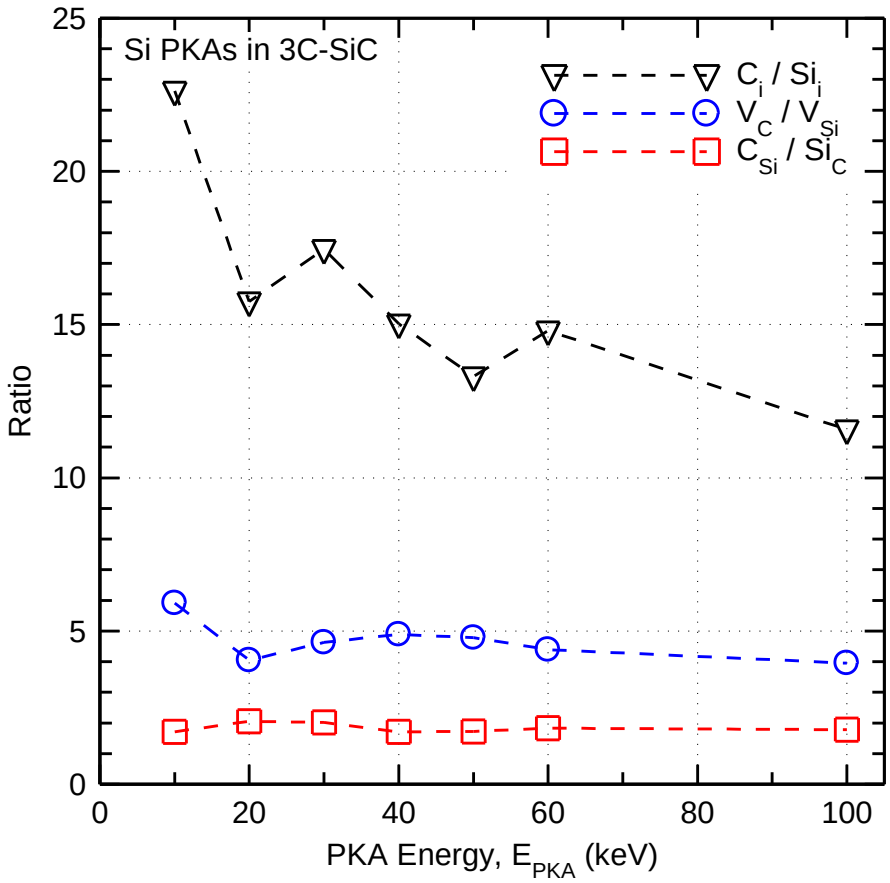

Figure 6.10: Comparison of the ratios of carbon to silicon vacancies, interstitials, and antisites as a function of Si PKA energy.

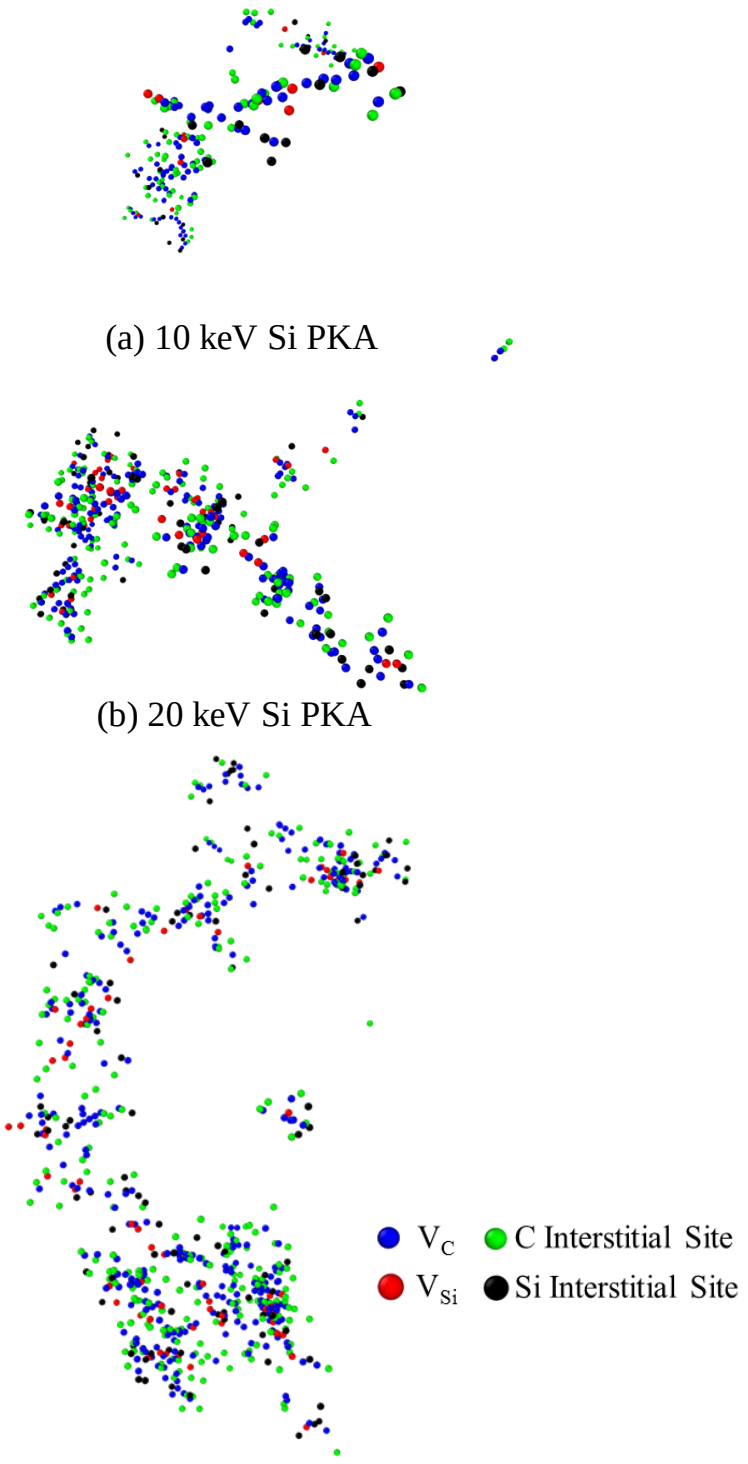

Figure 6.11: Comparison of the extent of the radiation damage cascades produced in 3C-SiC by Si PKAs incident in the [100] direction, of 10, 20, and 30 keV.

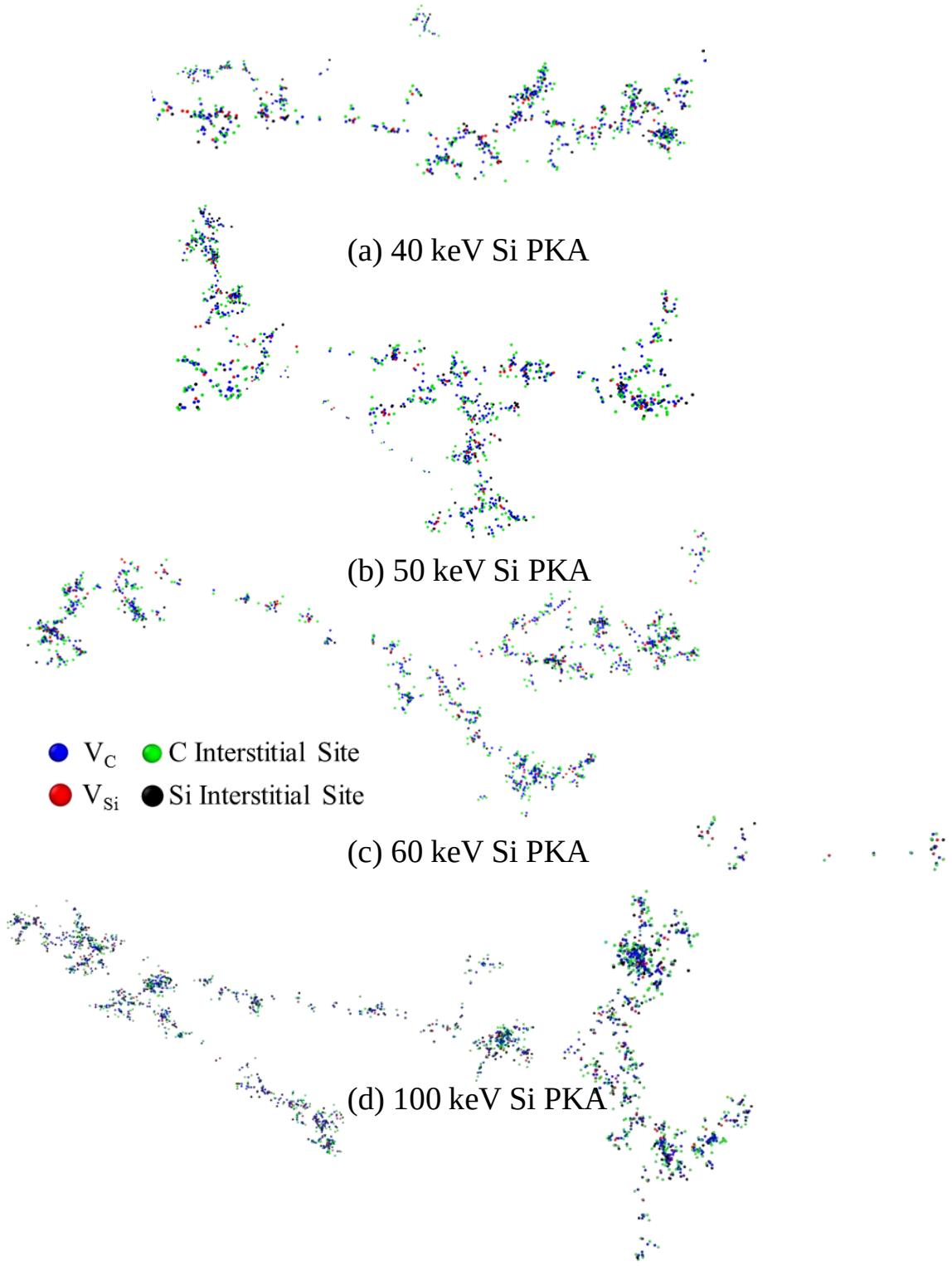

Figure 6.12: Comparison of the extent of the radiation damage cascades produced in 3C-SiC by Si PKAs incident in the [100] direction, of 40, 50, 60 keV, and 100 keV.

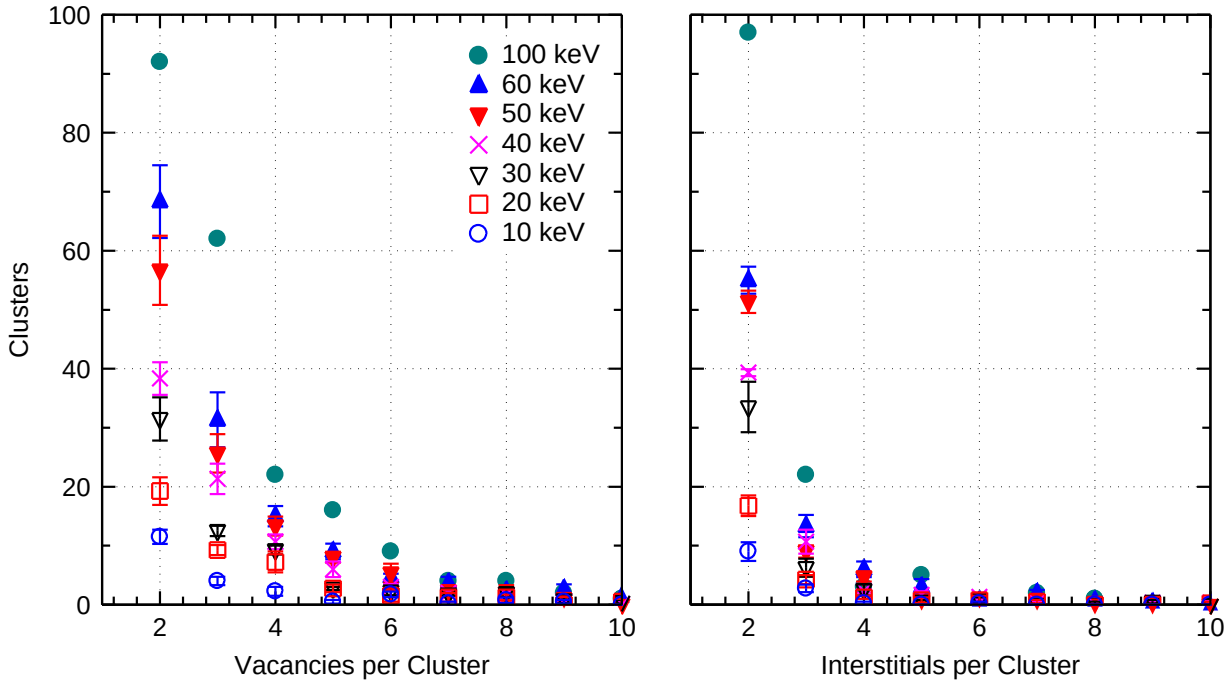

Figure 6.13: Comparison of the average number and size of vacancy and interstitial clusters produced with Si PKAs of energies ranging from 10 – 100 keV in 3C-SiC.

Table 6.4: Comparison of the largest residual vacancy and interstitial clusters produced with Si PKAs ranging from 10 – 100 keV in 3C-SiC.-

PKA Energy (keV)	Average size of Largest Cluster	
	Vacancies	Interstitials
10	10.3 ± 2.1	4.0 ± 1.4
20	14.3 ± 7.3	6.5 ± 2.6
30	21.8 ± 4.0	11.5 ± 2.9
40	30.3 ± 13.1	12.0 ± 4.4
50	16.0 ± 3.0	8.0 ± 3.4
60	20.0 ± 2.0	8.0 ± 1.0
100	34.0	17.0

The clustered fraction of the interstitials produced, f_{cl}^{i}, which is the ratio of residual interstitials in clusters of size two or more, to the total number of the residual interstitials produced, is a good measure of cluster formation. For 50 keV Si PKAs in 3C-SiC, Gao *et*

al.[167] reported an $f_{cl}^{i} = 0.28$, which is in agreement with the present work in which f_{cl}^{i} averages to be between 0.26 and 0.33 for all cascades investigated with different Si PKA energies. The calculated f_{cl}^{i} in the present work is almost constant for Si PKA energies from 10 to 100 keV. The calculated clustered fraction of vacancies, f_{cl}^{v}, in the present work, is much higher and increases slightly from 0.67 to 0.70, as the Si PKA energy increases from 10 to 100 keV.

Fig. 6.14 shows images of the extent of the residual defect cascades produced in the present MD simulations with 10 - 60 keV Si PKAs. While Figs. 6.11-6.12 show magnified images of the damage cascade and the types of defects being produced, Fig. 6.14 shows the extent of the defect cascade within the simulation domain. The extent of the defect cascade is defined as the distance of the furthest defect atom from the initial lattice plane of the PKA. The images in Fig. 6.14 show that using 64 million atoms in the simulations is more than adequate to accommodate the extent of the produced cascades. The calculated average extent of the defect cascades, X (nm), is plotted in Fig. 6.15 versus the Si PKA energy, E_{PKA}, from 10 – 60 keV, and correlated, as:

$$\mathrm{X\,(nm)} = 18.1 + 4.84\, E_{PKA}^{2.78} \qquad \text{Eq. 6.2}$$

The calculated total volume of defect production regions for the Si PKAs with energies from 10 – 60 keV vary from a few to several hundreds of nm^3. The extent of the defect cascade produced with the 100 keV Si PKA is not shown in Fig. 6.15, or included in the correlation in Eq. (2), since only a single cascade is simulated, due to the limitation on time and computation requirement to run several cascades. Fig. 6.16 presents images of the residual cascade produced in the present simulation with the 100 keV Si PKA. There are regions, each of several defect clusters. The areas of these regions range from several to 76 nm^2 (Fig. 6.16), and the volume ranges from tens to several hundreds of nm^3. Note that this is not the size of a single defect cluster, but the size of several defect clusters in close proximity, which would likely be indistinguishable using *in sit*u TEM. These regions do not represent the full extent of the residual defect cascade produced. The total size of these regions, if stable over a millisecond (ms) time scale, could be compared to those appearing in TEM bright field images.

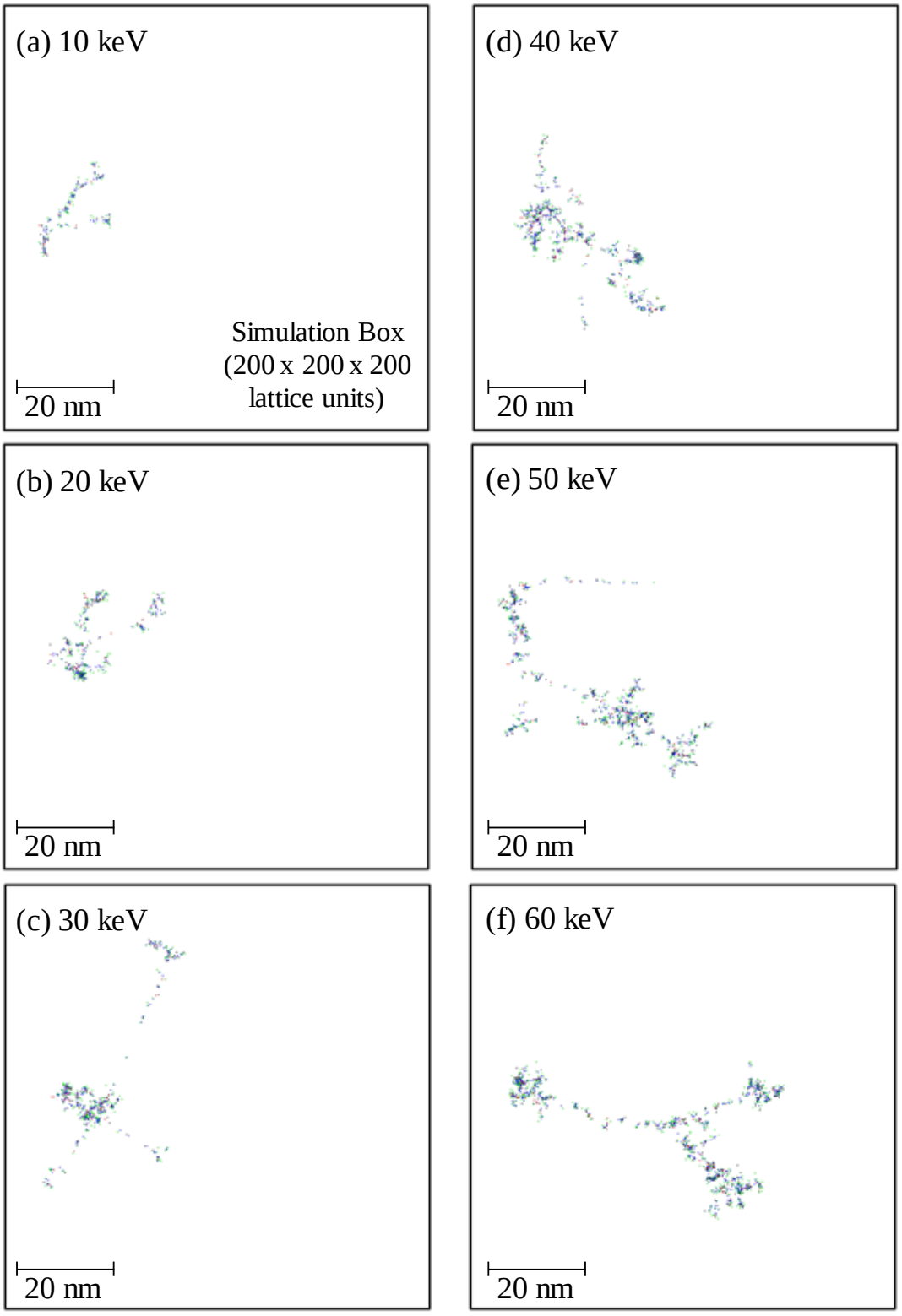

Figure 6.14: Comparison of cascade penetration depth produced by Si PKAs with energies from 10 – 60 keV.

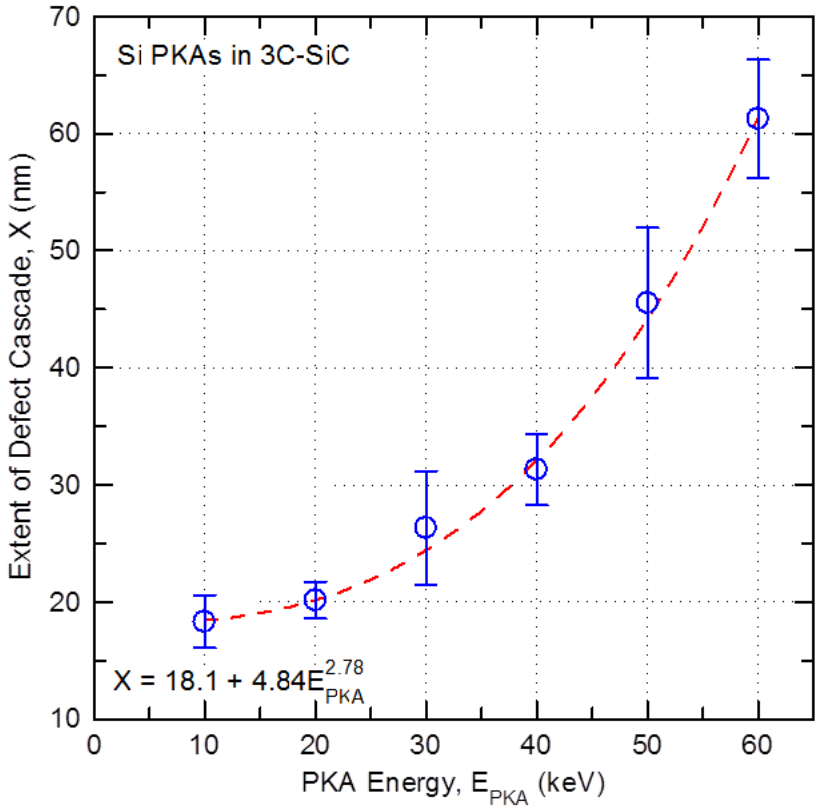

Figure 6.15: Comparison of average cascade penetration depth with Si PKAs ranging from 10 – 60 keV in 3C-SiC.

The absence of large defect clusters in 3C-SiC with the 100 keV Si PKA, suggests that amorphous regions are unlikely to form using only a single Si PKA, and that amorphization is likely due to overlapping cascades from several ion strikes. To confirm the retention of crystallinity in the region of the defect cascade produced by the 100 keV Si PKA, the simulated SAED patterns are obtained for four zone axes ([100],[110], [111], and $[\bar{1}\bar{1}\bar{1}]$), and compared to the those of unirradiated 3C-SiC (Fig. 6.17). It is important to note that the SAED patterns for the irradiated 3C-SiC is taken over the irradiated region, and not the entire simulation domain. The SAED pattern taken over the entire 512 million atom system used in the simulations filters out the residual defects produced as just noise.

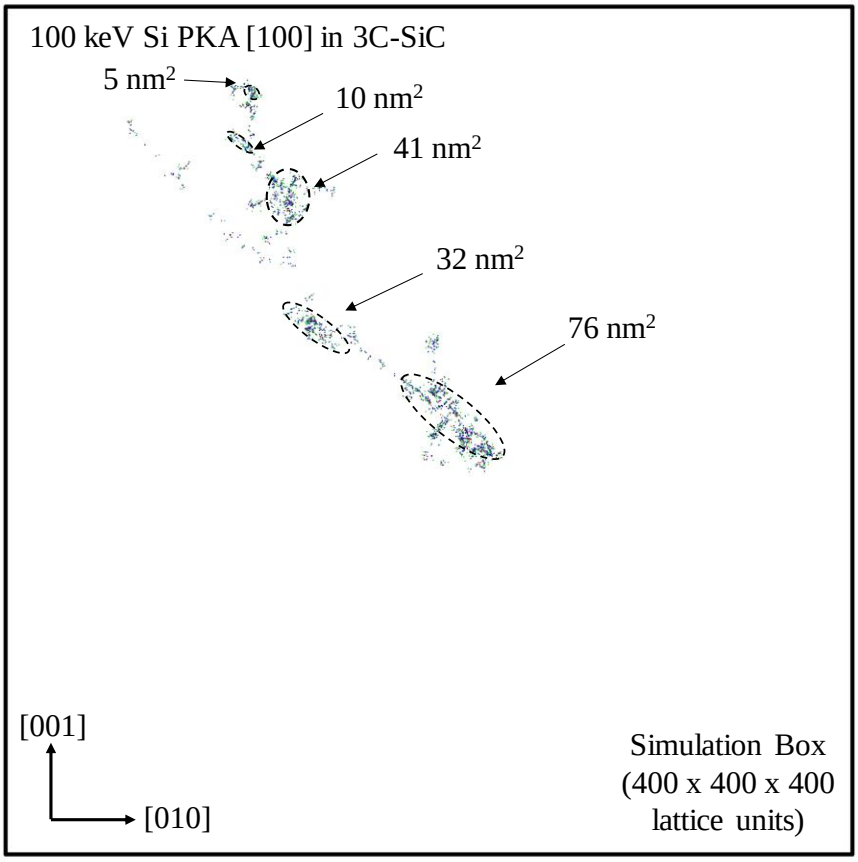

Figure 6.16: Cross-sectional view of the radiation damage cascade produced by a 100 keV Si PKA in 3C-SiC.

The simulated SAED patterns over the irradiated region confirms that crystallinity is retained in 3C-SiC for a 100 keV Si PKA in the present MD simulations (Fig. 6.17). Simulated SAED patterns at lower Si PKA (10 – 60 keV) energies show similar results. The stronger diffraction peaks for the unirradiated 3C-SiC are because the results are averaged over 10 ps, whereas the ones for the irradiated crystal are just a single snapshot in time. SAED patterns of the unirradiated and irradiated a-SiC, with a 30 keV Si PKA (Fig. 6.17) show no crystallization in the irradiated region, or significant change in the short-range order. This is also confirmed with the radial distribution function of the irradiated a-SiC with a 30 keV Si PKA (Fig. 6.19). The RDF after irradiation is identical to before irradiation, which is why only one curve is shown in the figure. Thus, the results confirm that both 3C-SiC and a-SiC are unlikely to experience significant structural changes with a single Si PKA up to 100

keV, and up to 30 keV for a-SiC. Despite the absence of significant structural changes, energy of the PKA can be partially stored in the produced defects in the material.[173]

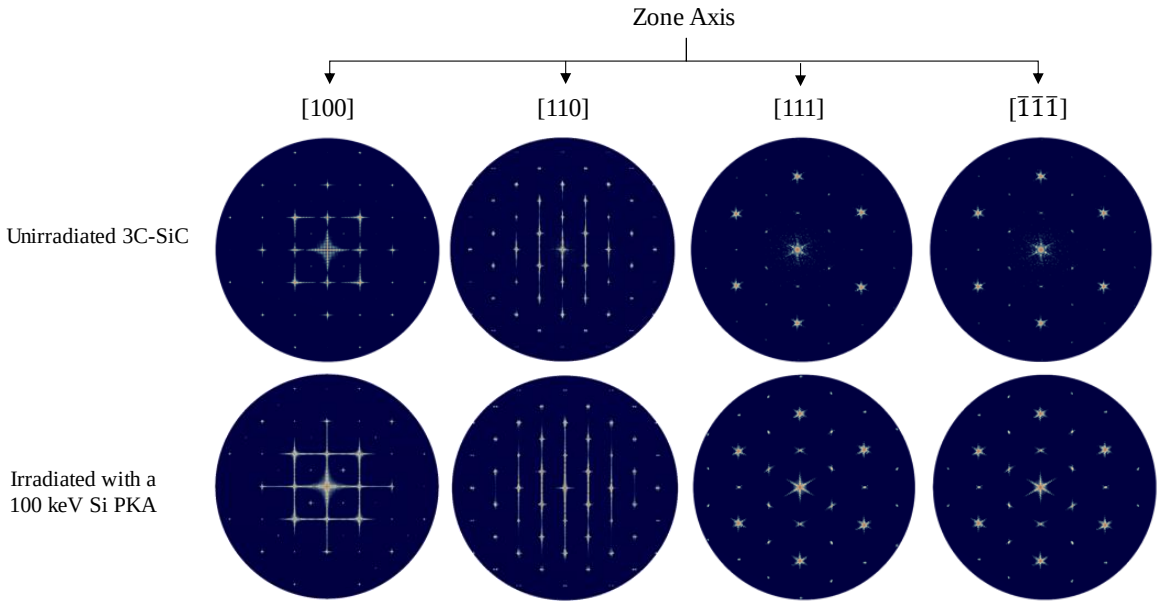

Figure 6.17: Comparison of simulated SAED patterns for four zone axes of the unirradiated 3C-SiC, to the region irradiated with a 100 keV Si PKA.

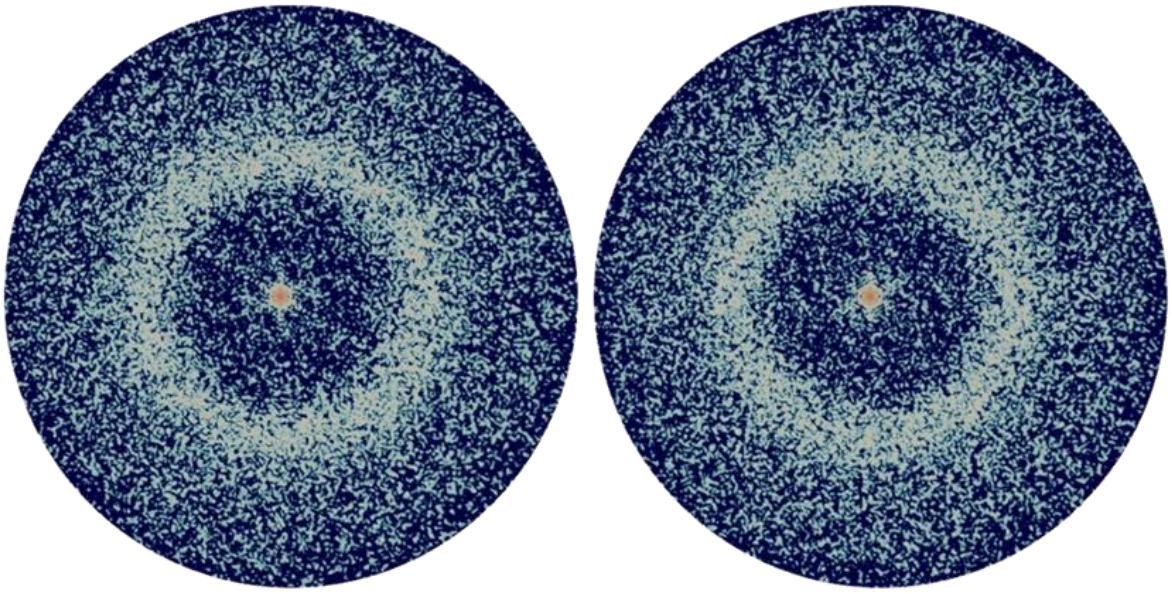

(a) Unirradiated a-SiC (b) 30 keV Si PKA in a-SiC

Figure 6.18: Comparison of simulated SAED patterns of unirradited a-SiC and a region of the a-SiC irradiated with a 30 keV Si PKA.

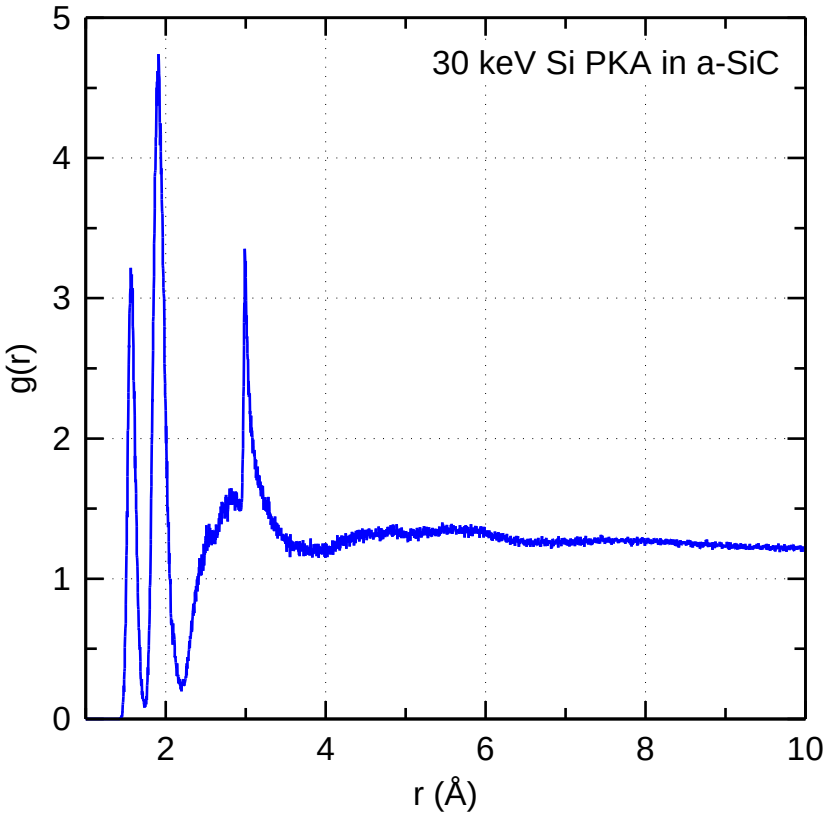

Figure 6.19: Radial distribution function of a-SiC before and after irradiation with a 30 keV Si PKA (identical RDFs).

Before irradiation, and once the system of atoms is fully equilibrated at 300 K, the potential energy of the entire system is calculated. After irradiation, and once the system temperature drops down to its initial value of 300 K, the potential energy is once again calculated. The difference between the values of the potential energy before and after irradiation represents the amount of stored energy due to the produced point defects and small defect clusters. They cause local stresses in the 3C-SiC, commensurate with the stored energy. In the present MD simulations at 300 K, since the produced vacancies are not mobile, they are to remain in the material until self-interstitial atoms and clusters annihilate with these vacancies. The fraction of the PKA energy that remains stored in the crystal lattice as defects is 10% for all PKA energies investigated. Unlike crystalline SiC, none of the PKA energy is stored in irradiated a-SiC. The PKA energy dissipates to the bulk material at the thermostatic boundary, suggesting that no change in morphology occurs. While atoms are

more likely to be displaced in irradiated a-SiC, no measurable damage occurred in the present MD simulations with Si PKAs up to 30 keV. This suggests that a-SiC is more radiation tolerant than 3C-SiC, in agreement with prior work that has shown than amorphous SiOC alloys were promising for their ability to provide superior radiation tolerance.[319]

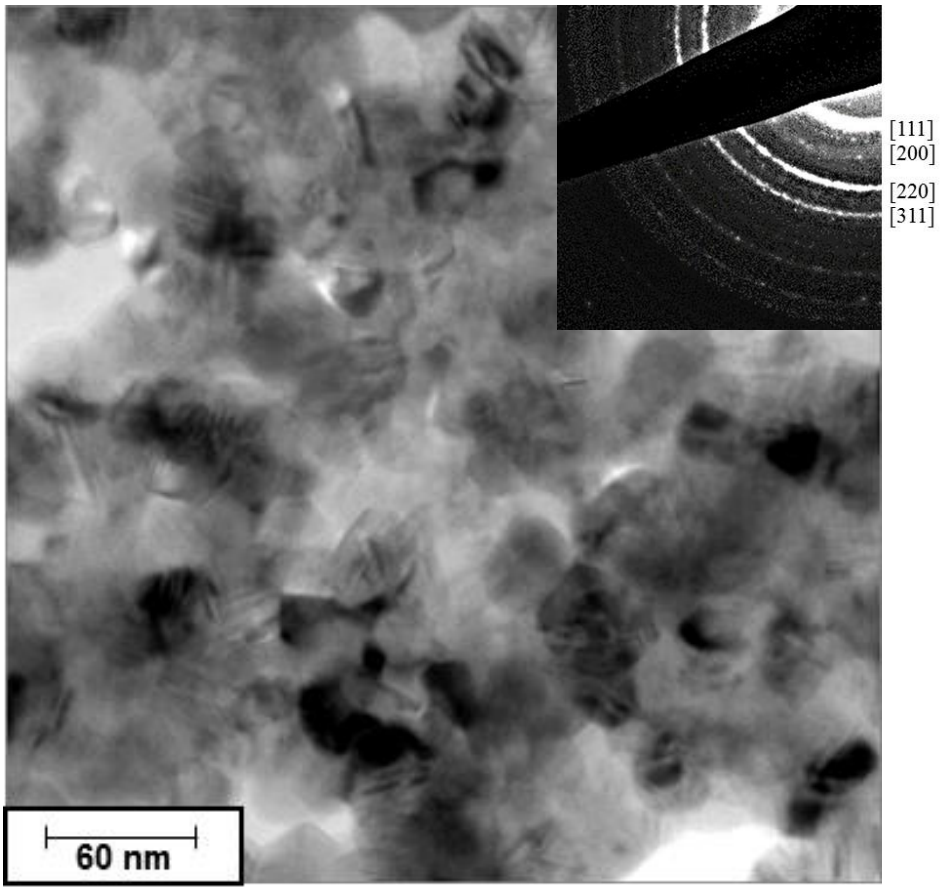

Figure 6.20: Bright field image and SAED pattern of unirradiated 3C-SiC.

6.2.2.2 **In Situ TEM Ion Beam Irradiation Results**

In order to provide complementary experimental results to those of the present MD simulations, *in situ* ion irradiation experiments are performed at the I^{3}TEM facility[76] using 1.7 MeV Au^{3+} ions. Despite the significantly longer time scale, compared to that of the MD simulations, the experiments provide real time observation of the ions strikes, and potential radiation damage information. The high energy of the ions in the irradiation experiments is selected to produce high cascade damage in the tilted (30^o) thin film specimens, without affecting composition since the vast majority of ions pass through the thin specimens. The

ion flux and TEM imaging conditions are optimized to facilitate direct real-time observation of single strikes. A limitation of the TEM is the low spatial and temporal resolutions, for identifying point defects and small defect clusters. The spatial resolution (a few nanometers), and the temporal resolution of milliseconds (ms), are much higher than in MD simulations (angstroms and several hundred picoseconds).

The bright field image and inset SAED pattern in Fig. 6.20 confirms that the thin film specimen used in the experiment is crystalline 3C-SiC. The still images in Fig. 6.21a,b are taken from recorded sequential frames, separated by 200 ms, during the *in situ* TEM irradiation experiment. The image in Fig. 6.21c highlights an observable contrast change measuring 30 nm^2 (5 nm x 6 nm). Similar changes observed during the experiment that had areas ranging from 9.1 to 83.5 nm^2. The variance in the area of the changing contrast regions is likely due to different amounts of energy transfer from the incident Au^{3+} ions to the lattice atoms in the SiC specimen (referred to as PKA in the MD simulations). The SAED pattern of the specimen after irradiation is unchanged from that taken of the pre-irradiated specimen.

A bright field image and inset SAED pattern for the deposited a-SiC specimen, are shown in Fig. 6.22. The SAED pattern confirms that indeed the specimen was a-SiC, since no ring structure and/or sharp diffraction peaks can be detected. During irradiation of the a-SiC with 1.7 MeV ions of Au^{3+}, no contrast changes are observed, suggesting little to no structural changes.

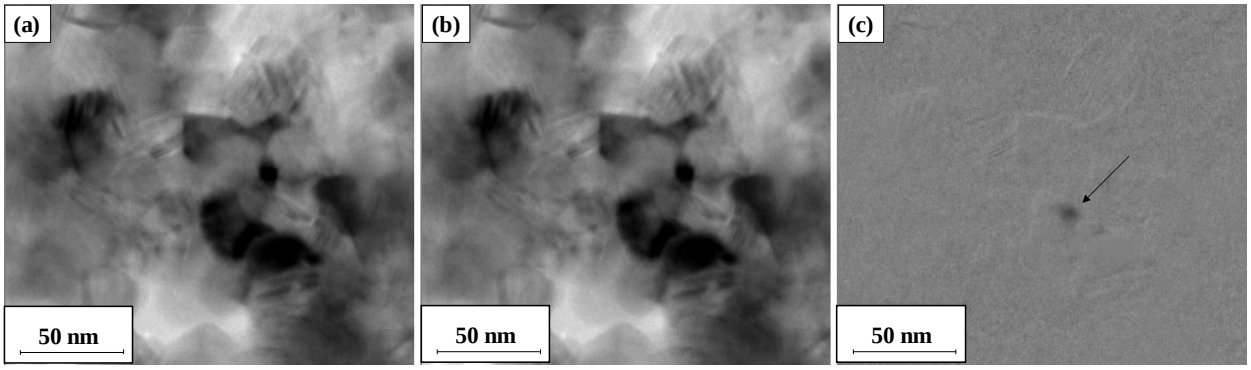

Figure 6.21: Bright field micrograph of sputter deposited, porous, nanocrystalline SiC collected during *in situ* TEM ion irradiation with 1.7 MeV Au^{3+}. (b) Still frame after a single observable ion strike taken from the same video, 200 milliseconds after micrograph shown in (a). c) Difference image comparing figures (a) and (b) to highlight the contrast changes resulting from the single ion strike (arrowed).

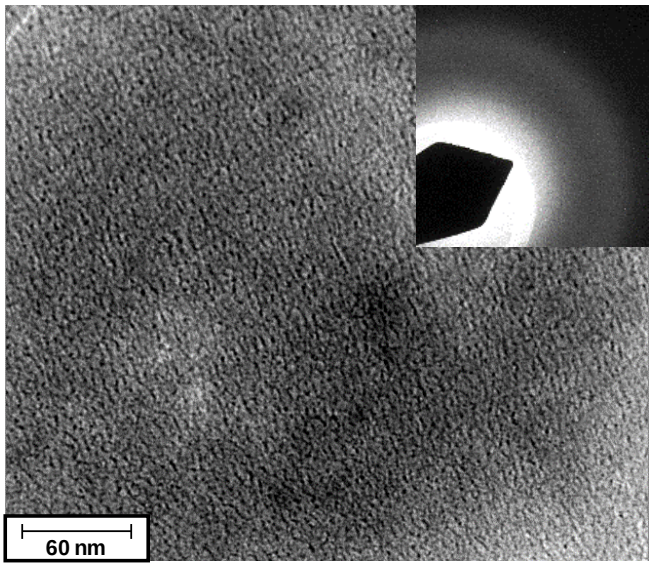

Figure 6.22: Bright field image and SAED pattern of unirradiated a-SiC.

6.2.2.3 **Discussion**

Several observations are made in contrasting the results of present MD simulations with Si PKAs with energies ranging from 10 – 100 keV in 3C-SiC, and 10 and 30 keV in a-SiC, to those of the *in situ* TEM irradiation with 1.7 MeV Au^{3+} ions. Defect production in 3C-SiC is confirmed in the MD simulations and the ion beam irradiation experiments, and the observed areas of contrast change in the 3C-SiC in the experiments might be correlated to the calculated defect cluster area in the MD simulations. The results of the MD simulation with 100 keV Si PKAs show several defect cascades that vary in area from 5 – 76 nm^2 (Fig. 6.16) regions, and volumes varying from tens to several hundreds of nanometers. The regions of defect production from an ion strike in the experiments can range from 9.1 nm^2 to 83.5 nm^2, which qualitatively is in good agreement with the MD simulation results. Since the observed area of defect production using both MD simulations and *in situ* TEM are in agreement, this suggests that the volumes of defect production in the MD simulations could be used to estimate the volumes of the defect cascades observed with *in situ* TEM. The contrast regions from the ion beam irradiation experiment likely vary in size due to the different amounts of energy being deposited by the incident ions to a specific region of the thin film 3C-SiC specimen, which partially depend on the incident angle of the Au^{3+} ions. In the MD

simulations, the extent and the area of the defect cascades directly correlate to the energy of the Si PKA.

While TEM ion irradiation experimental results show defect regions that are tens of nm^2 in cross-sectional area, the contrast changes from individual point defects and smaller defect clusters, cannot be detected. The MD simulations determine the number and types of all defects produced, the size of defect clusters, and the average number of interstitials and vacancies per cluster, which is not possible to detect with *in situ* TEM irradiation. However, predicting irradiation effects in bulk materials requires multi-scale approach that incorporate MD simulations and *in situ* irradiation results. Computational tools such as MD simulations determine fundamental changes to the crystal lattice at the atomic level within picosecond time scales, while *in situ* TEM irradiation can be used to observe radiation effects within millisecond time scale. The evolution of radiation damage cascades in 3C-SiC beyond a nanosecond and extending to a millisecond are still not well understood, and is the subject of extensive investigation at the present time.[103,165,320] Developing better interatomic potentials could improve MD simulation results to be in better agreement with the gold-standard of density functional theory, and thus improve the multi-scale predictive models.

The present results of the MD simulations and *in situ* TEM irradiation confirmed the absence of observable radiation damage in a-SiC. No defect clusters such as void formation occurred in a-SiC. In addition, the total potential energy of the system in the MD simulations of a-SiC changes significantly less than kT, thus any changes are lost in the thermal noise. The *in situ* TEM results show no contrast changes at any time during irradiation, suggesting no morphological changes. These results confirm that, despite the lower TDE for displacements in a-SiC than in 3C-SiC,[67] a-SiC appears to be more radiation tolerant.

6.2.3 Highlights and Concluding Remarks

MD simulations and complementary *in situ* TEM Au^{3+} ion beam irradiation are performed to assess radiation effects in 3C-SiC and a-SiC. The MD simulations with Si PKAs of energies ranging from 10-100 keV, investigated the production of residual point defects and defect clusters. Sequential bright field images of ion beam irradiation helped identify contrast changes in the irradiated regions, and SAED patterns helped detect the changes in the microstructure before and after irradiation. Due to the difference in the time

scale for the MD simulations and the *in situ* TEM irradiation, different, but complementary information is obtained.

MD simulation results confirm that carbon vacancies and interstitials are the primary residual point defects in 3C-SiC, while the clustering and the extent of the defect cascades depend on the Si PKA energy. The largest clusters increase in size from 10.3 ± 2.1 to 30.3 ± 13.1 vacancies and from 4.0 ± 1.4 to 12.0 ± 4.4 interstitials, respectively, as the Si PKA energy increases from 10 to 40 keV. Beyond 40 keV, the formation of clusters is more random and extends over a large region of the simulation domain. Generally, the size of the largest vacancy cluster is ≈2 to 3 times that of the largest interstitial cluster, for all Si PKA energies investigated. The retention of 3C-SiC crystallinity is confirmed by the simulated SAED patterns before and after irradiation for the MD simulations and *in situ* TEM irradiation. These patterns also confirmed the lack of changes in a-SiC after irradiation.

The stored energy in the irradiated 3C-SiC, due to point defects and defect clusters is estimated, to be ≈10% of all energies of the Si PKAs. In contrast, the lack of stored energy in irradiated a-SiC, suggests that it is more radiation tolerant than 3C-SiC. The retention of the amorphous phase is also confirmed by simulated SAED patterns for MD simulations and those obtained for sequential images recorded during the *in situ* TEM irradiation using Au^{3+} ions. In conclusion, the combined contribution of the MD simulations and the *in situ* TEM experiments provide valuable information on the effect of irradiation in crystalline and amorphous SiC. This information would help future consideration of using these materials in developing radiation tolerant fuel systems for the present fleet of light water reactors and next-generation reactors. The radiation hardness of a-SiC, combined with the absence of grain boundaries, makes it a suitable protective coating for ceramic and metallic substrates or structures in harsh environments combining high temperature and radiation.

6.3 MgO

The objectives of this study are to conduct MD simulations to determine the TDE directional dependence for interatomic potential validation, and TDE probability distributions for displacements. The displacement energy at 50% probability is used as input into SRIM to estimate the dose in the *in-situ* TEM ion beam irradiation experiments of 1.7 MeV Au^{3+} projectiles in MgO. Single Au projectiles with energies of 5, 10, 20, and 50 keV are simulated using MD simulations, and the number and types of point defects, and defects

clustering is determined. Simultaneous multiple ion strikes of 5 and 10 ions, with energies of 5, 10, and 20 keV are also investigated in order to investigate the production of larger-defect clusters not previously observed. The morphology of the cascades are followed during the ballistic and annealing phases, and amorphicity in the defects clusters regions are investigated using radial RDFs and SAED patterns. The produced defect clusters are compared to contrast changes of single ion strikes observed using *in-situ* TEM ion beam irradiation experiments with Au^{3+} ions.

6.3.1 Methodology

The following sections presents the methods for carrying out the MD simulations of multi-ion projectiles, thin film depositions of MgO, and *in situ* TEM ion beam irradiation with 1.7 MeV Au^{3+}.

6.3.1.1 Molecular Dynamics Simulations

LAMMPS is used to carry out the MD simulations of radiation damage in MgO. The interatomic potential used to model atom-atom interactions is a Buckingham potential, also used by Uberuagu *et al.*[45] to model radiation damage in MgO, and based off the parameterizations of Lewis and Catlow.[321] The Buckingham potential form is expressed as:

$$E_{ij} = \frac{1}{4\pi\epsilon_0}\frac{q_i q_j}{r_{ij}} + A_{ij}\exp\left(-\frac{r_{ij}}{\rho_{ij}}\right) - \frac{C_{ij}}{r_{ij}^6}, \qquad \text{Eq. 6.3}$$

where E_{ij} is the energy between the i_{th} and j_{th} particles, q_i and q_j are the atom charges, r_{ij} is the distance between atoms, and A_{ij}, ρ_{ij}, and C_{ij} are fitted parameters. In order to account for the short-range interactions encountered with radiation damage simulations, the Buckingham potential is smoothly splined to the ZBL potential at short interatomic distances. The ZBL potential is expressed as:

$$E_{ij}^{ZBL} = \frac{1}{4\pi\epsilon_0}\frac{Z_i Z_j e^2}{r_{ij}}\phi\left(\frac{r_{ij}}{a}\right) + S(r_{ij}), \qquad \text{Eq. 6.4}$$

where e is the electron charge, S is a switching function, Z_i and Z_j are the nuclear charges of the atoms, ϵ_0 is the vacuum permittivity, and $\phi\left(\frac{r_{ij}}{a}\right)$ is an exponential function. The exponential spline to smoothly transition the Buckingham potential to the ZBL potential at short interatomic distances is expressed as:

$$E_{ij} = \exp\left(B_0 + B_1 r_{ij} + B_2 r_{ij}^2 + B_3 r_{ij}^3 + B_4 r_{ij}^4 + B_5 r_{ij}^5\right), \qquad \text{Eq. 6.5}$$

The splined Buckingham+ZBL potential for O-O and O-Mg interactions is shown in Fig. 6.23. Both the first and second derivatives are smooth and continuous. Note that Mg-Mg interactions are excluded since A_{ij}, ρ_{ij}, and C_{ij} are 0 and the Buckingham interactions are ignored. All Coulomb interactions are modeled using the particle-particle particle-mesh (PPPM) solver, with a relative error of 1.0 $x10^{-6}$.

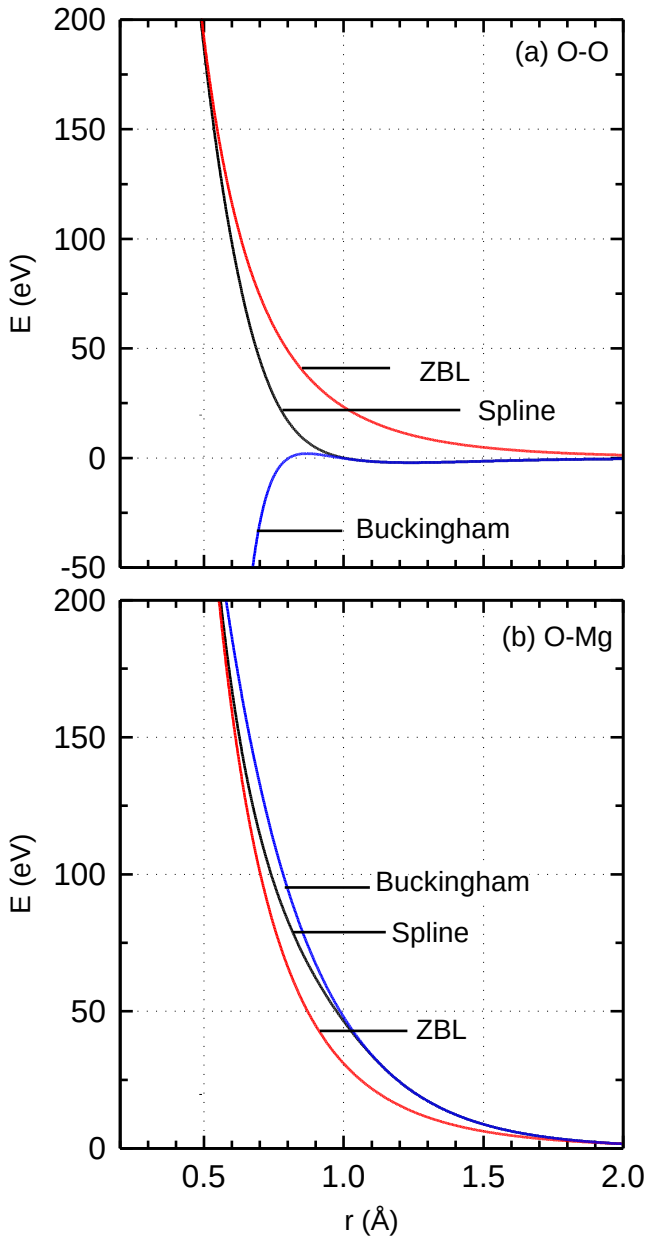

Figure 6.23: The splined Buckingham+ZBL potential for O-O and O-Mg pairs.

In order to estimate the directional dependence and probability distributions of the TDE, the 21,952 atom system first used the Polak-Ribiere version of the conjugate gradient algorithm to perform energy minimization of the atoms. The system of atoms is subsequently equilibrated in an NPT ensemble for 100 ps, before being equilibrated in a NVE ensemble for 100 ps, with a thermostatic boundary layer. The thermostatic boundary layer allows for the physical dissipation of the heat induced by the PKA to the bulk. A total of 5 O and 5 Mg PKAs are investigated in 23 crystallographic directions from 1.0 to 400 eV, in increments of 1 eV. Thus, the total number of simulations carried out for estimating the TDE is 92,000. A variable time step algorithm is used in such that no atom moves more than 0.005 Å per time step. The TDE probability distribution for displacements is averaged over all crystallographic directions and PKAs for each type. The system is allowed to evolve for 10 ps before determining the effects of the PKA on the crystal lattice.

The bulk MgO system is comprised of 27,648,000 atoms, and is periodic in the x and y dimensions, but fixed in the z dimension to allow for external projectiles. The system of atoms also used the Polak-Ribiere version of the conjugate gradient algorithm to perform energy minimization of the atoms. The system is then equilibrated using an NPT ensemble for 500 ps, then equilibrated using an NVE ensemble for 30 ps, before the irradiation events. A thermostatic boundary later is applied at the periodic boundaries that is 10 Å thick, and the same variable time step algorithm as used in the TDE simulations is used in the bulk radiation simulations.

In order to best emulate the *in situ* TEM conditions, Au^{3+} projectiles are used, with energies ranging from 5 to 50 keV. The direction of the projectile is $[00\bar{1}]$ which is normal to all faces of the MgO crystal, which is a <100> family direction. Additional simulations are carried out for the same projectile energies, but instead of using a single Au^{3+} projectile, cases of 5 and 10 projectiles are investigated. Note that the Au^{3+} projectiles essentially enter the system simultaneously, which would be unphysical when using an actual ion beam. However, the reason for this is to investigate the effects of multiple cascades on amorphicity in the crystal lattice, and to investigate the production and evolution of large defect clusters that would not form with low-energy single ions. The incident area of the ions is kept constant for all simulations at 5 ions/nm^2.

Wigner-Seitz (WS) defect analysis is used to determine the number and type of produced vacancies, interstitials, and antisites during the peak of the ballistic phase and after annealing. Note that annealing refers to the immediate recombination of displaced atoms, rather than the slow-cooling definition used for metals. Cluster analysis is used to determine clusters of vacancies and interstitials. The cutoff for determining defects of the same cluster is the lattice parameter. These methods are carried out using OVITO,[304] and its customizable python scripting interface. RDFs and simulated selected area electron diffraction (SAED) patterns are used to investigate changes to the crystal lattice. The simulated SAED patterns are obtained by calculating the electron diffraction intensity on a mesh of reciprocal lattice nodes,[310] and the visualization is carried out by taking the logarithm of the diffraction intensity in Paraview.[311]

6.3.1.2 **Sample preparation and in situ TEM ion beam irradiation**

Two MgO samples were prepared on two different substrates: (a) a-SiN TEM grid (b) bulk NaCl. The deposition of both samples were prepared using a 99.95% pure MgO sputtering target, from the Kurt J. Lesker Company,[314] using the Radio Frequency (RF) ATC 1800 Magnetron Sputtering System in the Center of Integrated Nanotechnologies at Los Alamos National Laboratory. The base pressure in the sputtering chamber was 5.0×10^{-8} Torr, while the working pressure was kept at 3×10^{-3} Torr. The RF power was kept at 300 W and the distance between the target and the substrate was ≈50 cm.

For the deposition of MgO onto NaCl, a partial pressure of 6 standard cubic centimeters per minute (sccm) Ar was provided in the sputtering chamber. The temperature of the substrate during deposition was held at 300 °C. At a deposition rate 0.0015 Å/s the MgO was deposited for 74 minutes to obtain a nominal film thickness of 40 nm. The NaCl was dissolved in deionized water and the MgO thin film was placed onto a TEM grid.

For the direct deposition of MgO onto 100-nm-thick a-SiN TEM grid, partial pressures of 30 sccm Ar and 6 sccm O_2 were provided in the sputtering chamber. The temperature of the substrate during deposition was held at 600 °C. At a deposition rate of 0.09 Å /s, the MgO was deposited for 185.25 minutes to obtain a nominal film thickness of 100 nm. The sample was then annealed at 900 °C in a vacuum furnace for 1 hour.

Following deposition, the thin films were irradiated with a 1.7 MeV Au^{3+} ion beam in the JEOL 2100 TEM for 15 minutes in the I^3TEM facility at Sandia National Laboratories,[76]

for an estimated total fluence of $2.87x10^{14}$ ions/cm^2 at an average flux of $3.18x10^{11}$ ions/cm^2-s. This corresponds to a nominal average damage dose of 0.228 dpa displacements per atom (dpa) in the first 40 nm of the MgO, and 0.245 dpa in the first 100 nm. These values are calculated with SRIM using inputs based on the recommendations by Stoller *et al.*[315] Estimates of the TDEs calculated in the present work that correspond to a 50% displacement probability are 94 eV for oxygen atoms and 91 eV for magnesium atoms.[164] The TEM was operated at 200 kV during irradiation and bright-field video with intermediate SAED patterns were collected.

6.3.2 Results

This section presents and discusses the results of the MD simulations of defect production using 1, 5, and 10 Au projectiles, with energies up to 20 keV, in addition to a single 50 keV Au projectile, in crystalline MgO. The deposition of thin films of MgO on NaCl and a-SiN, and subsequent *in-situ* TEM ion beam irradiation with 1.7 MeV Au^{3+} ions are also presented. The present results of the MD simulations and the *in-situ* TEM ion beam irradiation are compared and discussed. The MD simulation results include the number and type of point defects produced at the peak of the ballistic phase and the residuals, defect clustering, the extent of the damage cascades, and simulated SAED patterns and RDFs to determine changes in crystallinity. The *in-situ* TEM ion beam irradiation results include bright field images and SAED patterns of both MgO specimens, and difference images from single ion strikes.

6.3.2.1 Molecular Dynamics Simulations

The MD simulation results are broken up into two sections: (2) directional dependence of the TDE and TDE probability distributions, and (2) Au ion strikes. The TDE probability distributions are used to determine an appropriate TDE for SRIM dose estimates of the ion beam irradiation experiments. The cascades produced by the Au ion strikes are later compared to the *in-situ* TEM Au^{3+} ion beam irradiation results.

6.3.2.1.1 Threshold Displacement Energy

It is important to specify the definition used when reporting the TDE, since this could lead to fewer discrepancies in the literature. Still, this energy is difficult to obtain for each definition because radiation damage is stochastic in nature, and atomic lattice vibrations can yield different TDEs for the same crystallographic direction. The minimum energy required

to create vacancies on both sublattices using both O and Mg PKAs for several different crystallographic directions is presented in Table 6.5. Note that the TDEs correspond to the lowest energy required to create the indicated defect out of all 5 PKAs investigated of each PKA type. The results show that defect production at near-threshold energies are primarily limited to the sublattice of the PKA for most directions investigated, which is in agreement with prior work.[58] However, this is not always the case for all crystallographic directions. For instance, in the [100] direction, the energy required for an O PKA to form an oxygen vacancy is 159 eV, compared to 86 eV for a magnesium vacancy.

Table 6.5: TDE surface for the production of oxygen and magnesium vacancies with both oxygen and magnesium PKAs in MgO.

	Threshold Displacement Energy (eV)			
	O PKA		Mg PKA	
	V_O	V_{Mg}	V_O	V_{Mg}
[100]	159	86	167	88
[110]	44	265	-	49
[111]	145	120	135	105
[123]	55	226	210	51
[135]	49	293	-	47
[015]	99	109	124	74
[025]	61	172	155	74
[012]	54	159	-	77
[035]	51	148	155	52
[045]	47	170	-	44
[188]	68	152	-	60
[144]	64	177	-	77
[133]	66	169	158	85
[122]	75	212	208	87
[233]	84	186	197	79
[566]	119	98	113	113

The reason for this is due to the fact that in the [100] direction, the O PKA collides directly with an Mg secondary knock-on atom (SKA) and recoils to its initial lattice site. At high enough energy (86 eV), the Mg SKA is displaced and becomes an interstitial. Once the O PKA has enough energy to become permanently displaced, it causes a replacement collision sequence with the Mg SKA.

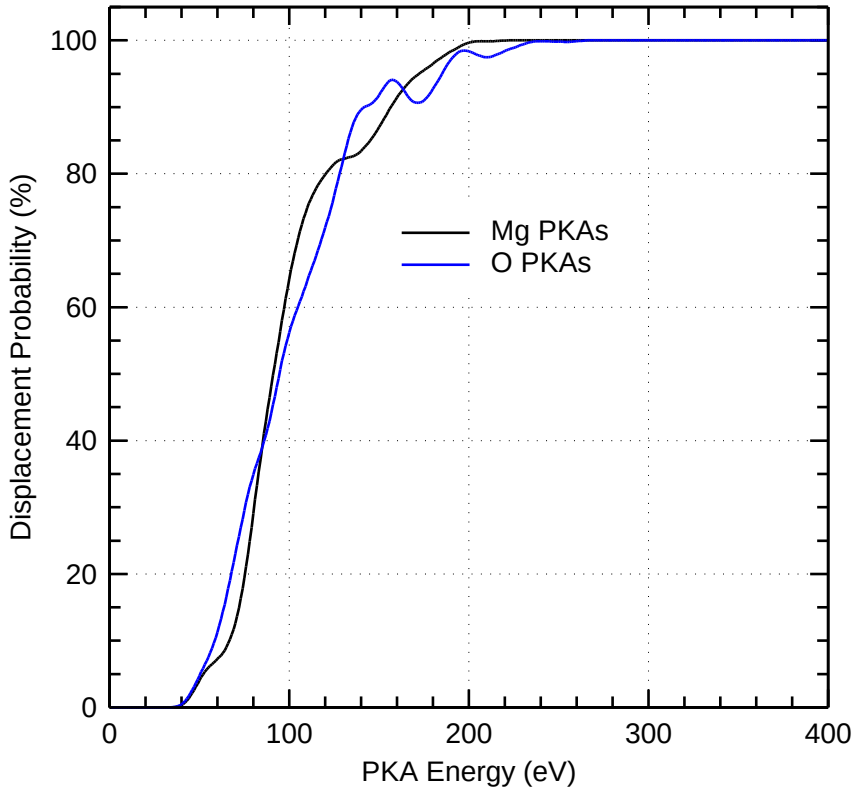

Figure 6.24: Comparison of the TDE probability distributions for displacing an atom with O and Mg PKAs in crystalline MgO.

These values are in better agreement with experiments[109,110] than prior work[58] that investigated the directional-dependence of the TDE in MgO. Park et al.[58] found that the minimum energy to cause a stable Frenkel pair with Mg PKAs out of the many directions that they investigated was 90±2 eV, despite the fact that experiments report TDEs as low as 60 eV. The MD simulations that employ the interatomic potential used in this work estimates the minimum energy to cause a stable Mg Frenkel pair with Mg PKAs, if averaged over all directions, to be 73 eV. For O PKAs to form O Frenkel pairs, the averaged minimum energy is 77 eV. However, since radiation damage is stochastic in nature, the minimum TDE should

not necessarily be used as input into binary collision approximations. Instead, a probability distribution to account for the stochastic processes would be more representative of the nature of defect production.

TDE probability displacements for a displacement are presented in Fig. 6.24. Fig. 6.24 shows the energy required to displace an atom using both O and Mg PKAs in MgO. The results show that the displacement probability distributions are nearly identical for PKA types. At 50% displacement probability, the TDE for O and Mg atoms, respectively, is 94 and 91 eV. These TDEs are used as input into SRIM to obtain the dose estimate of the 1.7 MeV^{3+} ion beam irradiation.

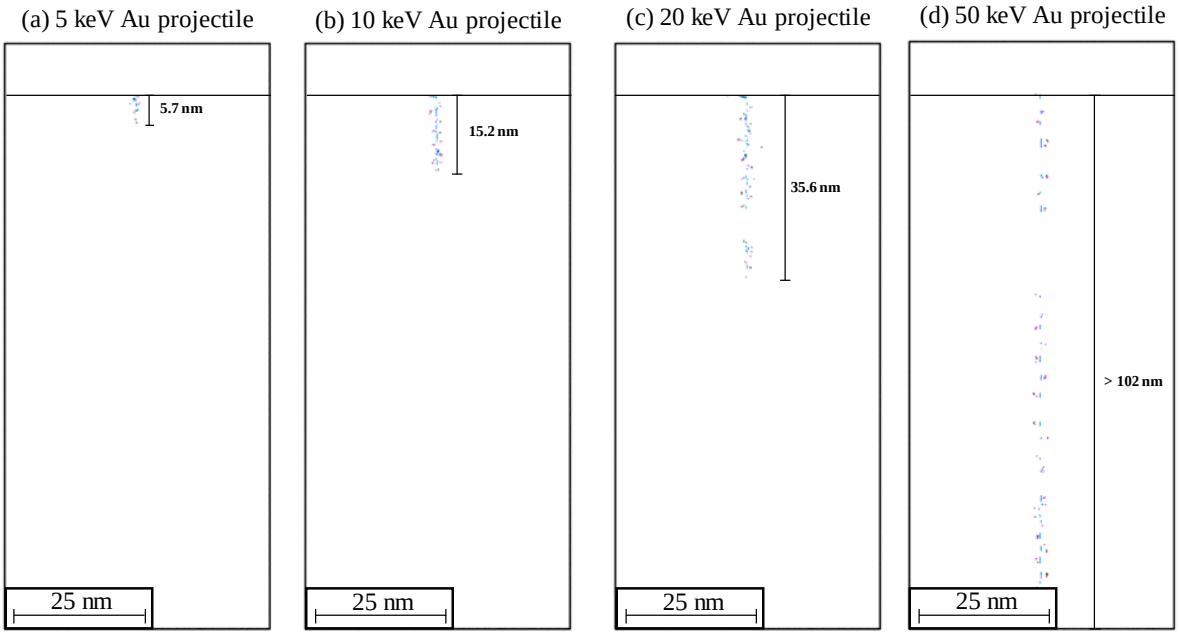

Figure 6.25: Comparison of the extent of the damage cascades caused by single Au projectiles with energies of 5, 10, 20, and 50 keV.

6.3.2.1.2 Au Ion Irradiation

Presented in Fig. 6.25 is the extent of the radiation damage cascade for single Au projectiles with energies of 5, 10, 20, and 50 keV. The MD simulation results show that the extent of the cascade increases with projectile energy, from 5.7 nm to 35.6 nm, as the Au projectile energy increases from 5 to 20 keV. The cascades are contained within the simulation box, except the 50 keV Au^{3+} projectile, which channels through the entire simulation domain, due to its high energy, and the fact that the angle of incidence is $[00\bar{1}]$, a high-channeling direction. While

most studies avoid investigating directions which are more prone to channeling, this study focuses on them since they would also be indicative of radiation effects in MgO. The 50 keV Au projectile loses 64% of its energy as it channels through the 100 nm of the MgO, but the primary defects that form are just point defects, such as vacancies and interstitials. Since the defect production cascade is spread out throughout the entire simulation domain, defect clustering does not occur in any significance in this case. There is some sputtering out of the back-end of the simulation box due to the Au projectile exiting the system.

Fig. 6.26 shows the number and types of point defects produced as a function of PKA energy and number of Au projectiles, during the ballistic and annealing phases. The figure shows that the number of interstitials, vacancies, and antisites produced are similar on both sublattices, which is in agreement with the TDEs calculated which showed nearly identical values for both PKA types. The figure also indicates that for the same total energy deposited, increasing the number of projectiles causes more damage that increasing the energy of each ion. For example, 2,000 residual oxygen vacancies are produced in the simulation of 10 10-keV Au projectiles, compared to 160 oxygen vacancies produced in the simulation of 5 20-keV Au projectiles. Despite the fact that a total of 100 keV of energy is introduced into the system in both cases, the increase in number of interacting damage cascades causes more stable defects to form. This same phenomenon is observed for all Au projectile energies and number of ions investigated. The number of residual point defects always increases as the number of ions increases, regardless of the projectile energy. The increase in the damage cascades causes more disruption in the crystal lattice, and makes it difficult for the surviving defects to rebuild the crystal lattice on the 50 ps time scale investigated.

The large number of antisites produced during the ballistic phase of interaction is partially due to elastic deformation of the crystal lattice, rather than irreversible inelastic damage. An elastic wave of deformation (Fig. 6.27) propagates away from the impact region to the thermostatic boundary layer. Fig. 6.27 shows a view of the top of the crystal lattice where the projectiles are inserted, and compares the surface damage of the 1, 5, and 10 20-keV Au projectiles during the peak of the ballistic phase and the residuals. During the peak of the ballistic phase, the surface damage area is 1.95 nm^2, 8.64 nm^2, and 65.9 nm^2 for the 1, 5, and 10 20-keV Au projectiles, respectively. The damage area decreases after annealing to 0.94 nm^2, 5.9 nm^2, and 44.0 nm^2, respectively. The increase in damage area is partially related to

keeping the striking particle density constant at 5 particles/nm^2. Thus, the area over which the 10 projectiles hit is larger than for 5 projectiles.

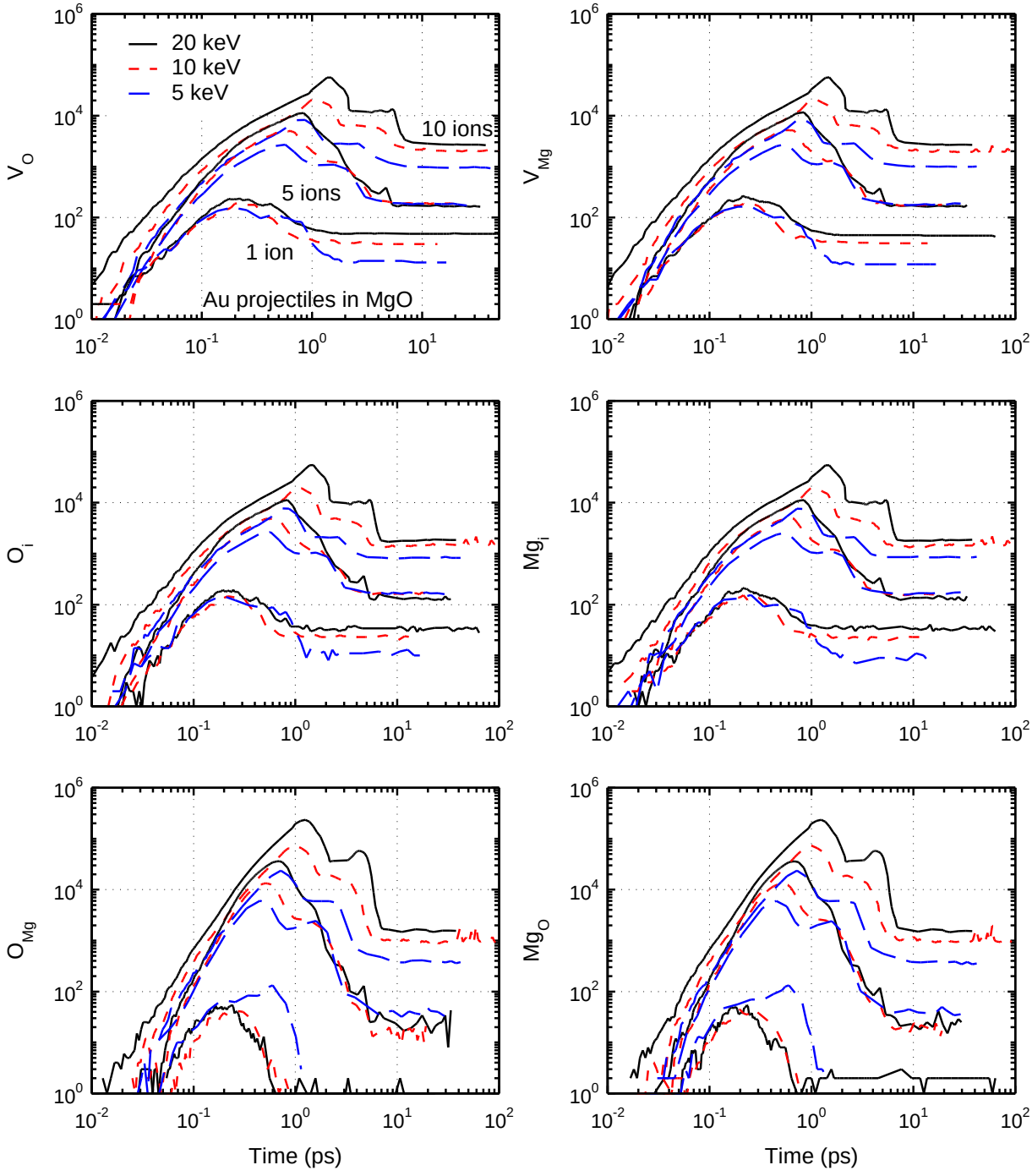

Figure 6.26: Comparison of the number and types of point defects produced as a function of PKA energy and number of Au projectiles, during the ballistic and annealing phases.

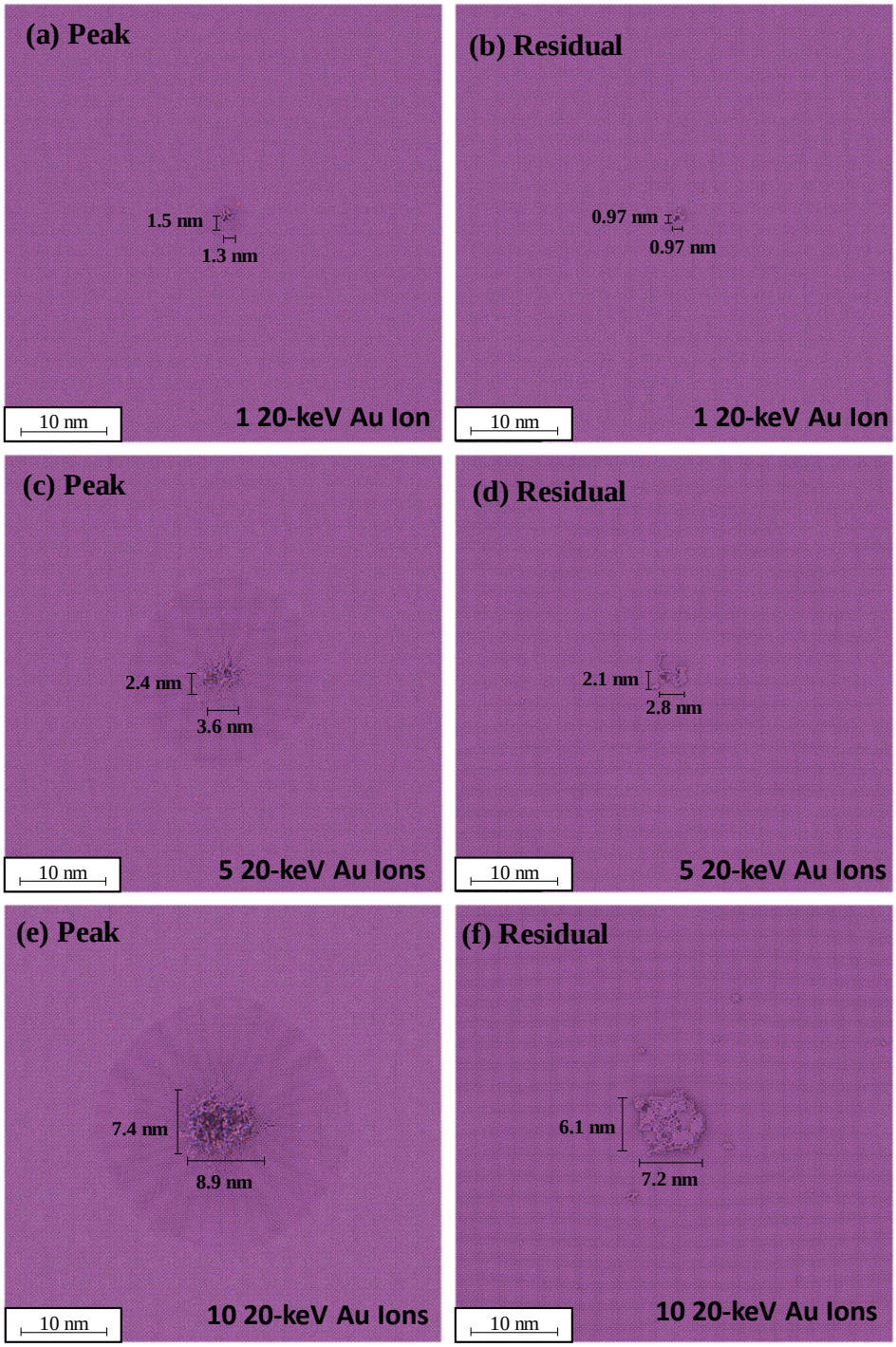

Figure 6.27: Comparison of the damage as observed from above the surface for 1, 5, and 10 Au projectiles with energies of 20 keV, during the peak of the ballistic phase and after annealing.

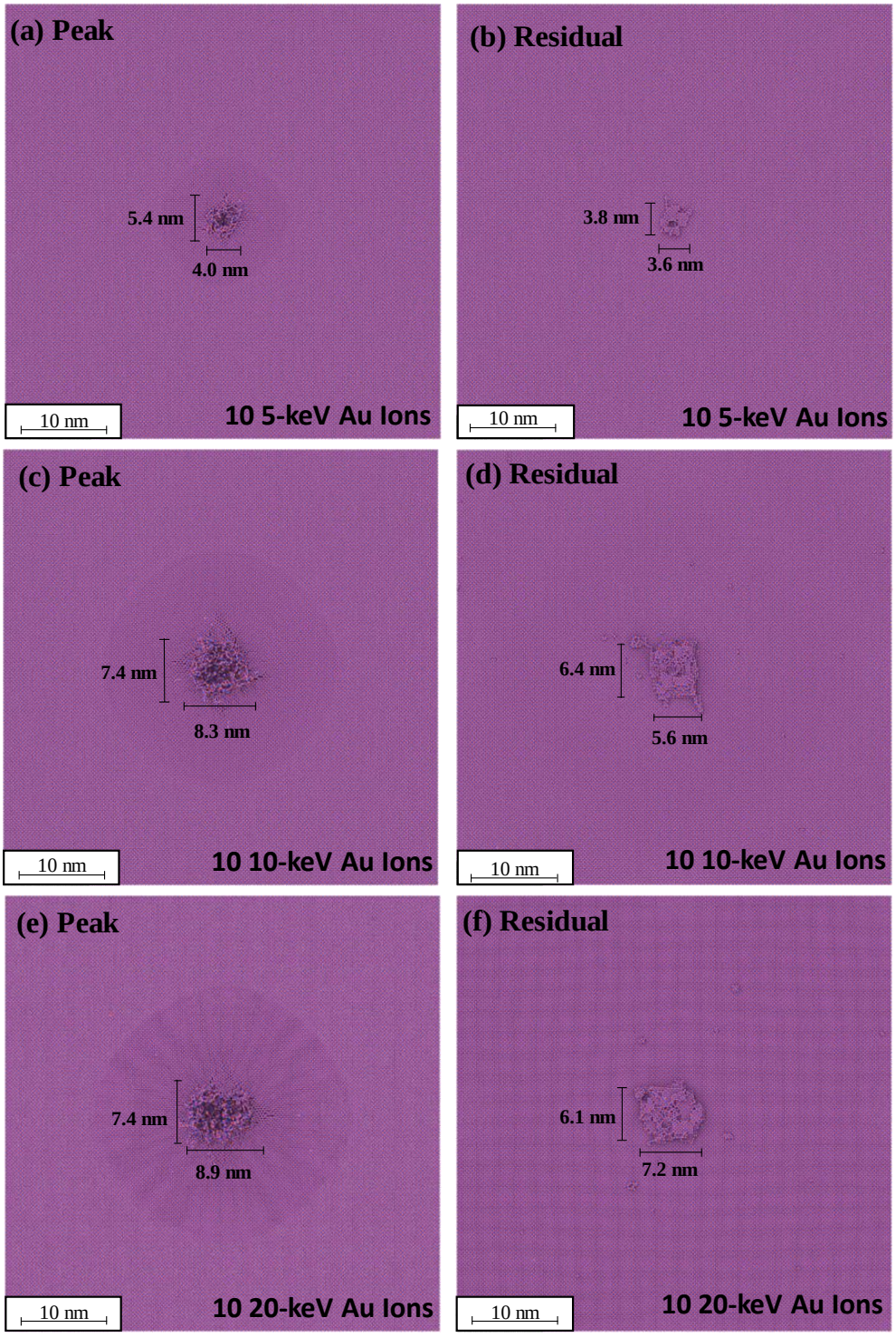

Figure 6.28: Comparison of the damage as observed from above the surface for 10 Au projectiles with energies of 5, 10, and 20 keV, during the peak of the ballistic phase and after annealing.

Fig. 6.28 shows that the energy of the ions can also impact the surface damage area. The figure shows the surface damage from 10 ions, with energies ranging from 5, 10, and 20 keV. The surface damage area is 21.6 nm^2, 61.4 nm^2, and 65.9 nm^2 for projectile energies (10 ions) of 5, 10, and 20 keV, respectively. This surface damage area decreases to 13.7 nm^2, 35.8 nm^2, and 43.9 nm^2, respectively, after annealing. Fig. 6.29 shows a close-up view of the surface damage caused by the 10 20-keV Au projectiles at the peak of the ballistic phase. The figure shows a lot of sputtering and upswelling at the surface. In fact, a total of 169 atoms were sputtered off of the surface due to the impacts by the 10 20-keV Au ions, compared to 171 atoms by the 10 10-keV Au ions, and 40 by the 10 5-keV Au ions. The changes in surface morphology from the 10 10-keV Au projectiles are similar to that by the 20 10-keV Au projectiles. However, the extent of the damage cascade induced by the projectiles is dependent on the energy of the projectiles, and extends further as the energy of the Au projectiles increases.

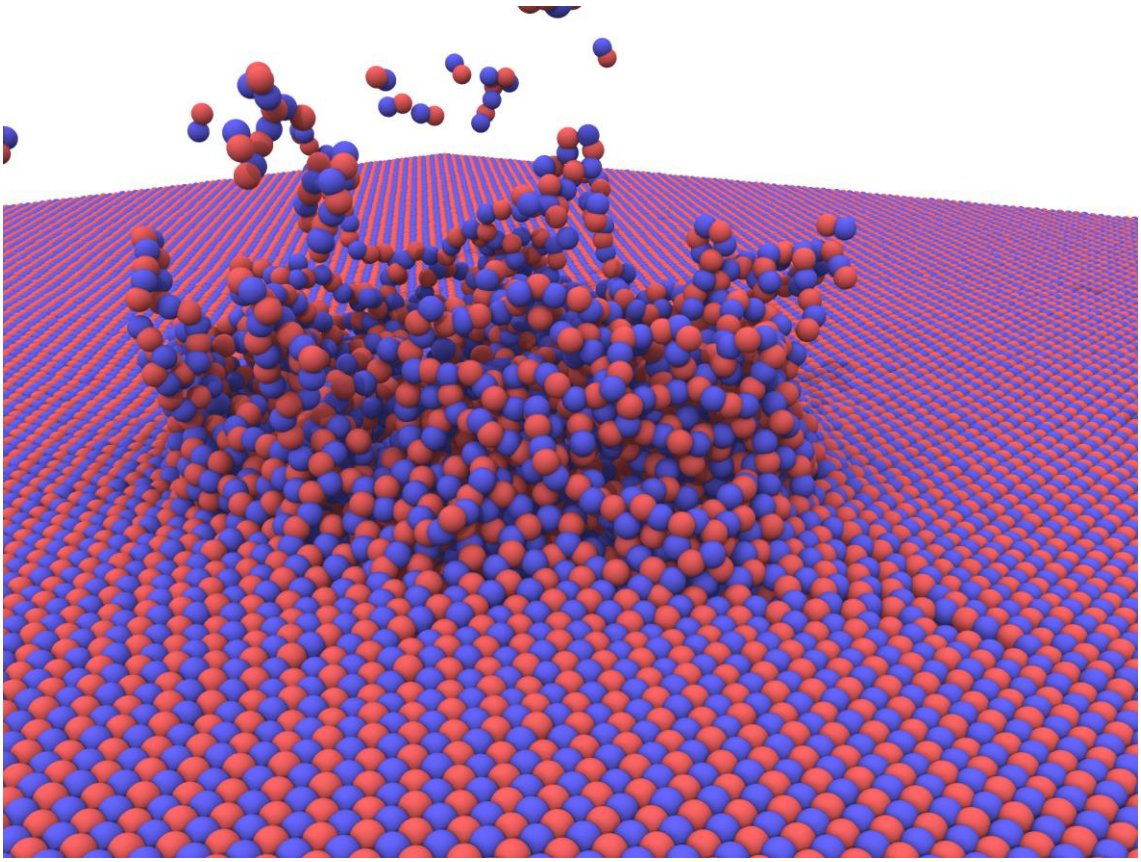

Figure 6.29: Lattice disruption and upwelling at the surface of MgO from 10 20-keV Au projectiles.

Fig. 6.30 shows the produced vacancies and interstitial sites as identified using WS defect analysis for cases involving 5 Au projectiles, with energies of 5, 10, and 20 keV. The defects are shown for both the peak of the ballistic phase and after annealing. The figure shows that significant damage below the surface occurs, and that the damage increases with projectile energy. During the peak of the ballistic phase, atoms are knocked out of a central core region, leading to the production of a void that increases in size with projectile energy.

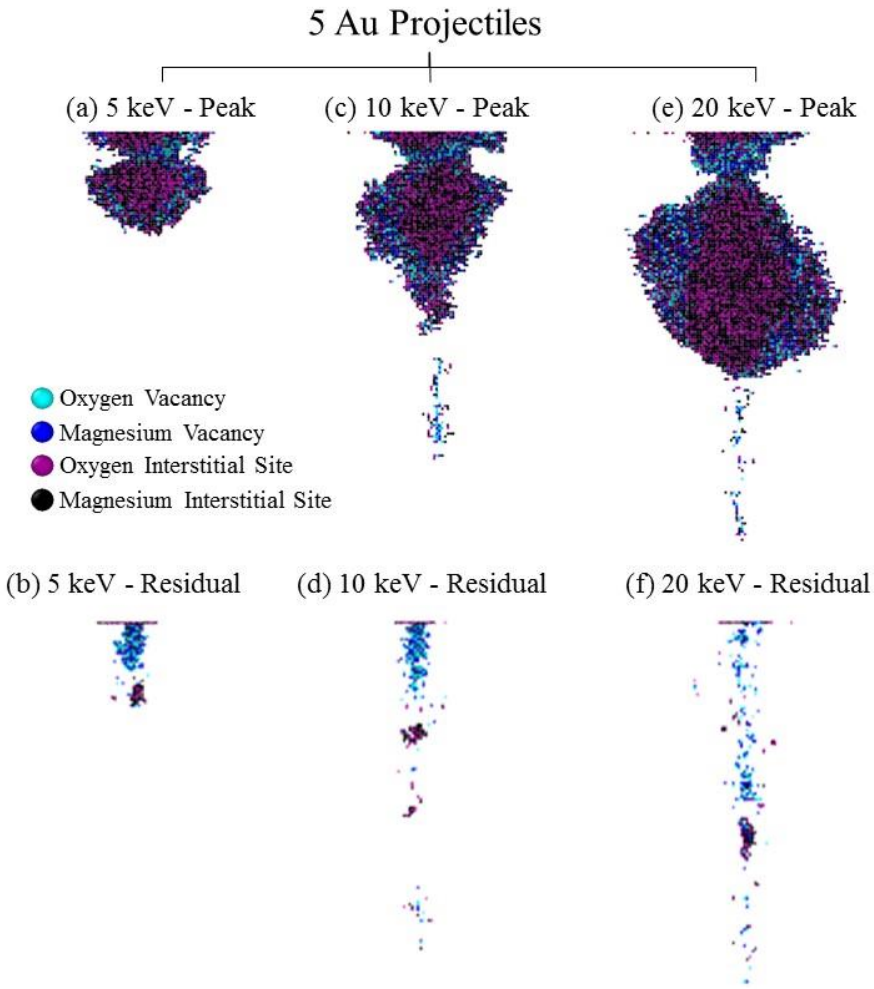

Figure 6.30: Comparison of the produced vacancies and interstitials at the peak of the ballistic phase and after annealing, for 10 Au projectiles of 5, 10, and 20 keV.

On the outer-edge of the void, interstitials form, and are highly mobile during the cascade event. Immediately following the ballistic phase, a significant number of the defects anneal, but some residual point defects and defect clusters remain. In fact, voids can be quickly

visually identified by localized light and dark blue atoms (oxygen and magnesium vacancies) in Fig. 6.30. Note that the entire defect production region for the 5 20-keV Au projectiles is not shown in the figure. The reason for this is because one of the projectiles caused damage as far as ≈74 nm from the surface, while the other 4 ions only caused defect production cascades that extended ≈20 nm.

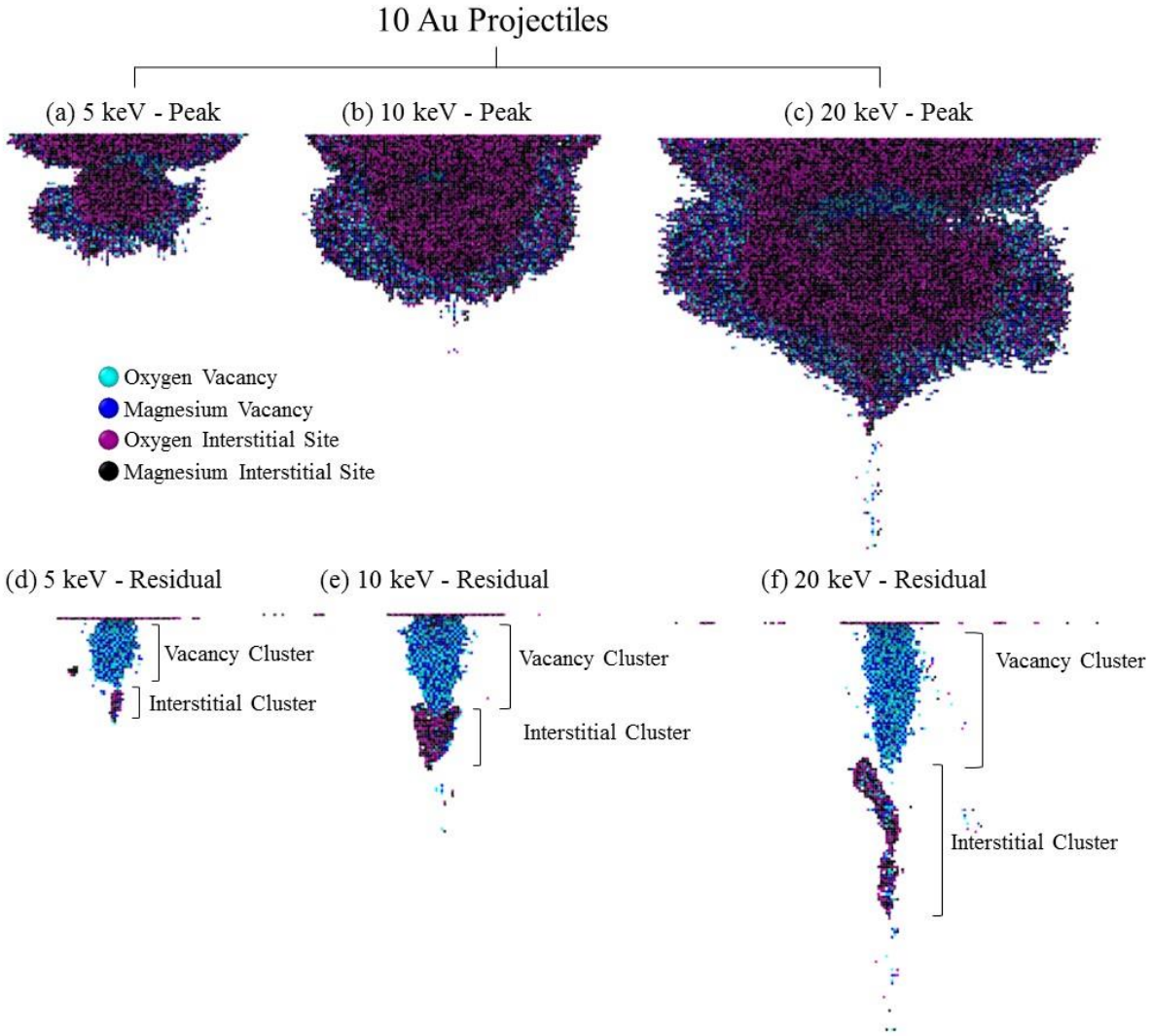

Figure 6.31: Comparison of the produced vacancies and interstitials at the peak of the ballistic phase and after annealing, for 10 Au projectiles of 5, 10, and 20 keV.

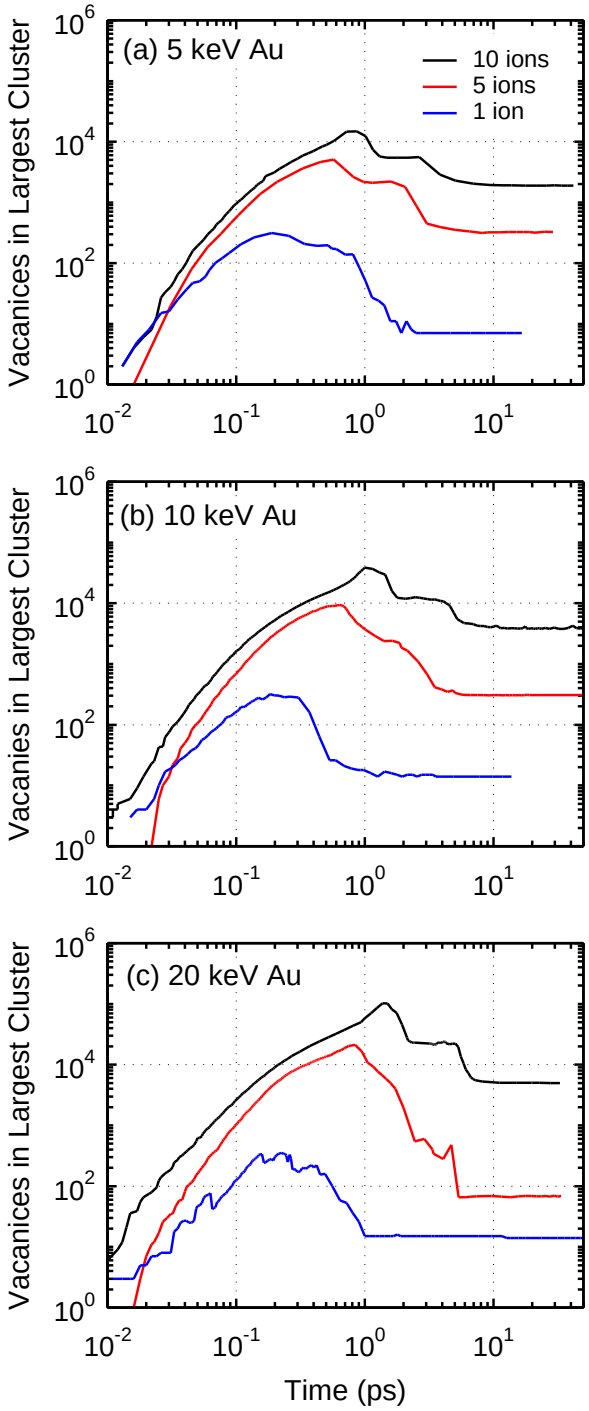

Figure 6.32: Comparison of the largest vacancy cluster produced with 1, 5, and 10 Au projectiles of 5, 10, and 20 keV.

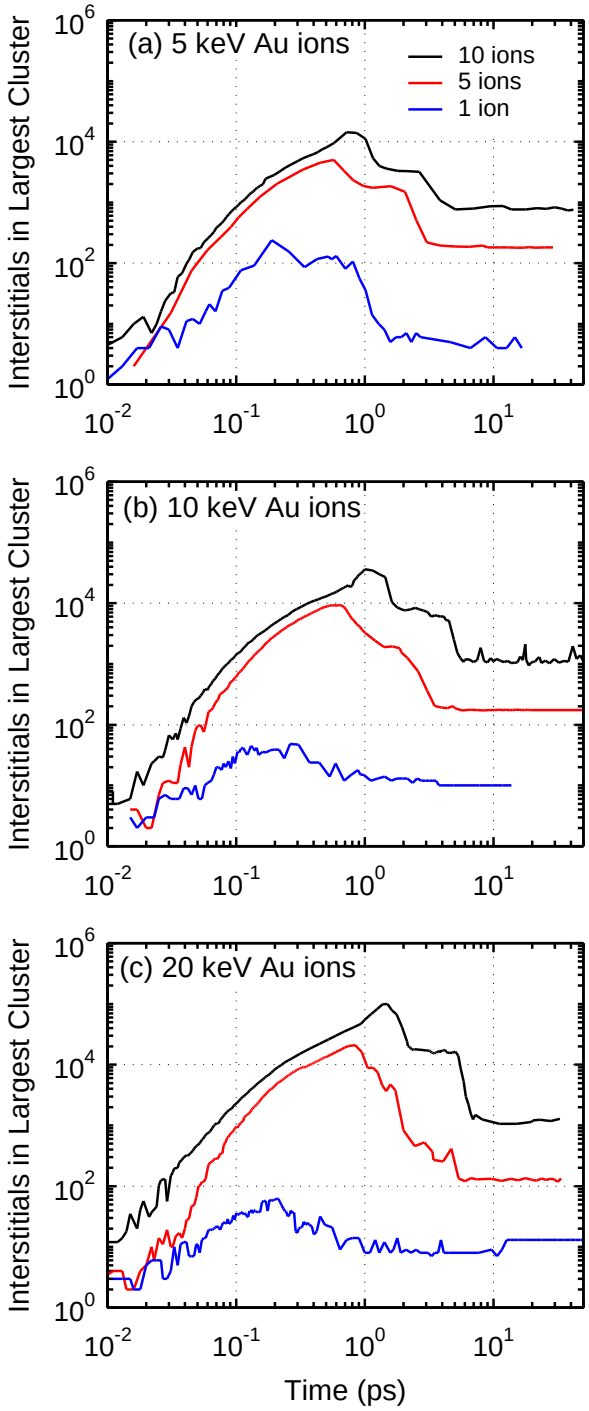

Figure 6.33: Comparison of the largest interstitial cluster produced with 1, 5, and 10 Au projectiles of 5, 10, and 20 keV.

Fig. 6.31 shows the produced vacancies and interstitial sites as identified using WS defect analysis for cases involving 10 Au projectiles, with energies of 5, 10, and 20 keV. It is interesting to note that for these cases, and the ones presented in Fig. 6.30, necking of the

defect production cascade occurs several nanometers below the surface. Thus, there appears to be some surface effects, causing the damage to spread outward, while the bulk of the projectile energy is deposited below the necking region. Following annealing, residual vacancy clusters and interstitial clusters remain in the material. However, for each case, there is a cluster of vacancies (void) and interstitials that are significantly larger than the rest. Fig. 6.31 shows the residual void, identified by the light blue and dark blue atoms, as well as a large nearby interstitial cluster. The void region starts at the surface and extends just beyond the necking region, and a cluster of interstitials is directly below it. Thus, while most of the defects anneal, the formation of a large and stable interstitial cluster, precludes thermal recombination with the region rich in vacancies.

Fig. 6.32 shows the largest void that forms during the peak of the ballistic phase, and after annealing, for the 5, 10, and 20 keV ions for the cases involving 1, 5, and 10 Au projectiles. The results show a clear dependence of the void size on the number of ions. The size of the void is also dependent on the energy of the projectiles, but only if more than one projectile is used. For instance, the size of the largest void formed during the peak of the ballistic phase is 313, 319, and 354, for single Au ions with energies of 5, 10 and 20 keV, respectively. The void reduces by more than an order of magnitude to 7, 14, and 14 vacancies, respectively, after annealing. The size of the largest forming void increases significantly when more Au projectiles are inserted into the MgO system. For example, the size of the largest void formed at the peak of the ballistic phase is comprised of 14,800, 38,400, and 102,500 vacancies for 10 Au projectiles of 5, 10, and 20 keV, respectively. The size reduces to 1,900, 4,000, and 5,000 vacancies, respectively, after annealing.

These results shows a clear dependence of void size on the Au projectile energy when 5 and 10 projectiles are used, and a dependence on the number of ions. The overlapping cascades tend to foster higher stability amongst the defects, and thus can have a greater impact on the morphology of the system under irradiation. Fig. 6.33 shows the largest interstitial cluster that forms during the peak of the ballistic phase, and after annealing, for the 5, 10, and 20 keV ions for the cases involving 1, 5, and 10 Au projectiles. The results are similar to that presented in Fig. 6.32 for the largest void formation, but slightly less. The largest interstitial cluster is smaller for two reasons: (1) Some of the formed vacancies are a result of sputtering induced by the Au projectiles. Thus, there will be more vacant sites than

interstitials to fill them. (2) The WS defect analysis identifies interstitial sites, and cluster analysis groups these sites. This does not account for the fact that there could be more than one interstitial at a given site. Since defect clustering is a dominant form of defect production in MgO, investigating changes in crystallinity would provide valuable information regarding the changes in morphology of the system.

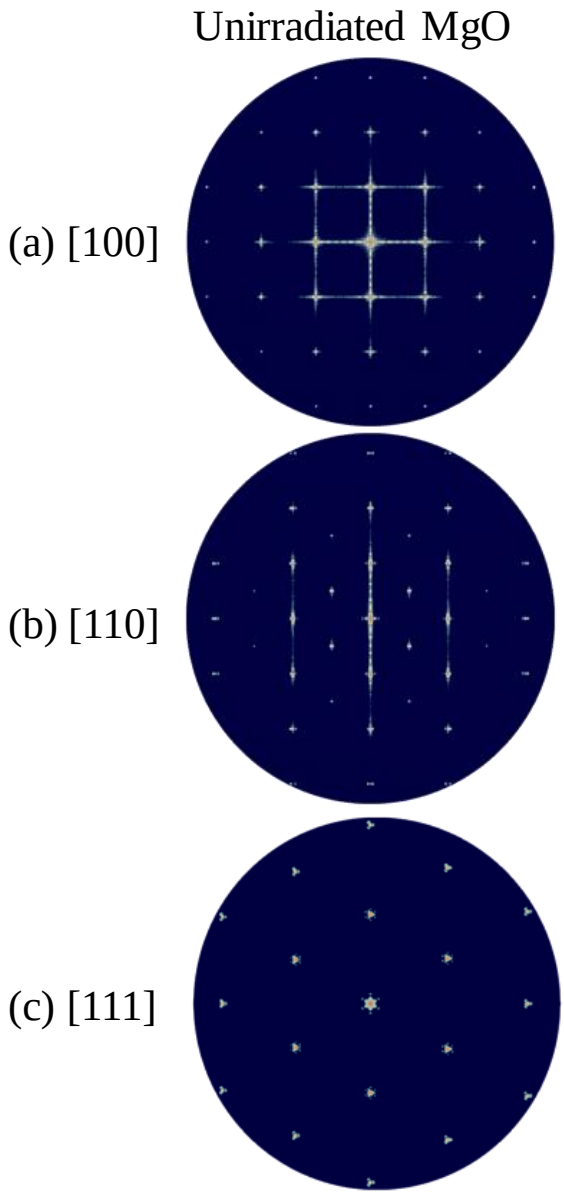

Figure 6.34: Comparison of simulated SAED patterns of unirradiated MgO for 3 zone axes ([100], [110], [111]).

Fig. 6.34 shows the unirradiated SAED patterns for MgO (periclase) in the zone axes of [100], [110], and [111] and shows clear diffraction peaks of the monocrystalline MgO. The unirradiated SAED patterns can be compared to the SAED patterns after irradiation in Figs. 6.35-6.37, which are at the peak of the ballistic phase and after annealing for 5, 10, and 20 keV ions, for the cases involving 1, 5, and 10 Au projectiles. Note that for the irradiated cases, only the [111] zone axis is shown. The area sampled for the SAED pattern is 40 nm^3 in the area of insertion of the projectiles. The investigated region size was chosen to be 40 nm^3 so as to be small enough to not cover the unirradiated region, but also large enough to avoid finite size effects in the simulated SAED pattern. The figures show that amorphicity does not occur in any noticeable form when only 1 Au projectile was used, regardless of the Au projectile energy. However, there is clearly some observed damage from the SAED pattern, most noticeably for the 5 keV Au projectile case at the peak of the ballistic phase. The reason that the lower energy projectile shows more local damage is because the defects produced from the 10 and 20 keV projectiles are more spread out, and the crystallinity between defect regions tends to filter out the small amount of produced defects. For the 5 keV case, the defects are more localized to a single region, since the Au projectile did not travel far from the surface. However, after annealing, crystallinity is fully retained for all single ion strikes, as demonstrated by the simulated SAED patterns in Fig. 6.35b,d,f.

Fig. 6.36 shows the simulations that used 5 projectiles with varying energy, and there is some loss of crystallinity during the peak of the ballistic phase. This is demonstrated by the SAED patterns in Fig. 6.36,a,c,d which show disorder in the midst of the diffraction peaks. After annealing, crystallinity is fully retained and amorphization does not occur on a scale measurable with the simulated SAED patterns. Fig. 6.37 shows the simulations that used 10 projectiles with varying energy, and shows complete amorphization at the peak of the ballistic phase. The diffraction peaks corresponding to the unirradiated crystal are only faintly visible with 10 5-keV Au projectiles, and unnoticeable with 10 10-keV and 10 20-keV Au projectiles. This is in agreement with WS defect analysis and cluster analysis which showed a large radiation damage cascade disrupting the entire crystal lattice near the path of the Au ions. While the diffraction peaks are visible after annealing for all energies involving 10 Au projectiles, there is still measurable disorder, which shows that increasing the number of ions, rather than the energy of the ions, is what leads to amorphization in MgO.

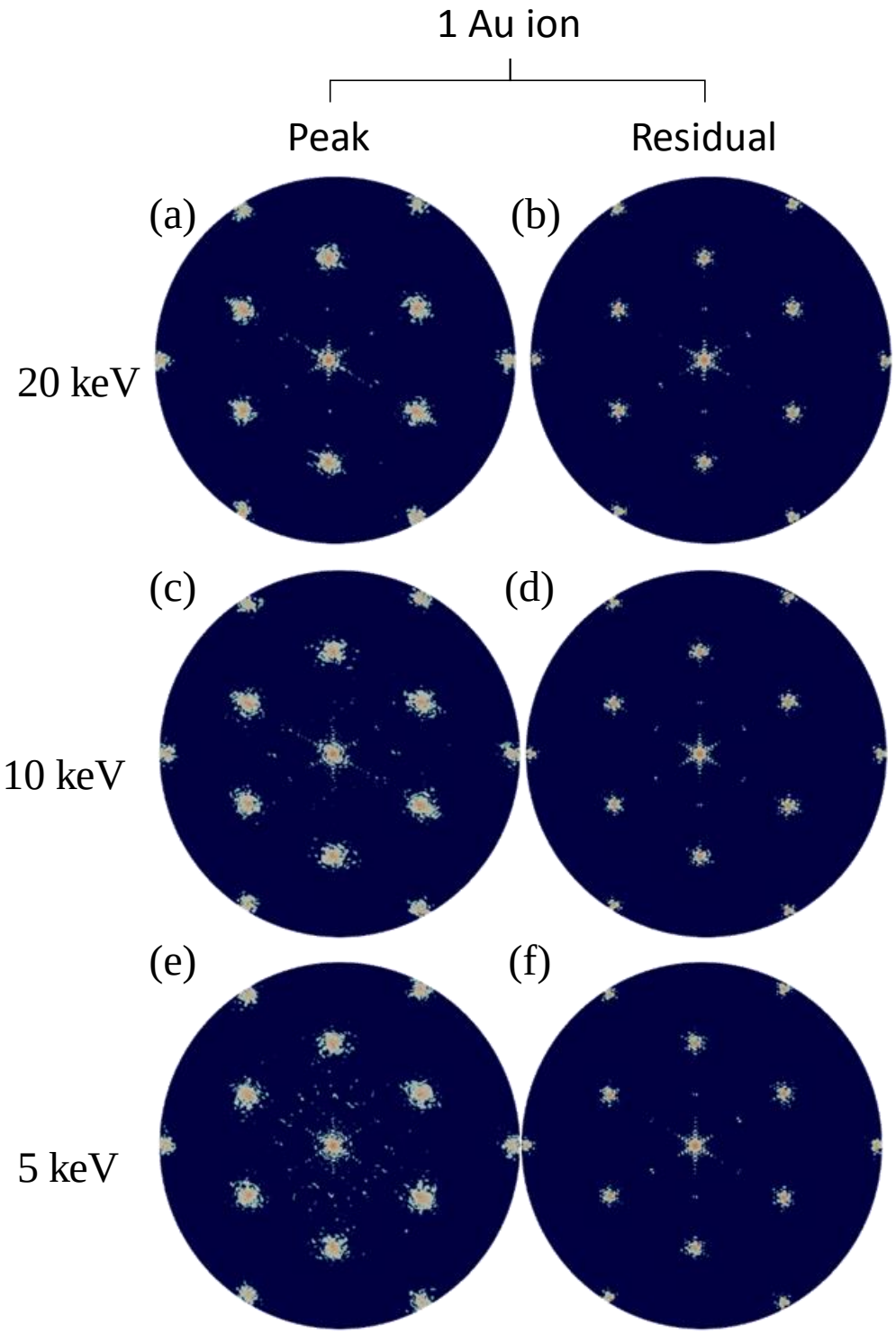

Figure 6.35: Comparison of simulated SAED [111] patterns of peak defect production and of the residuals from a single Au projectile, at energies of 5, 10, and 20 keV, in crystalline MgO.

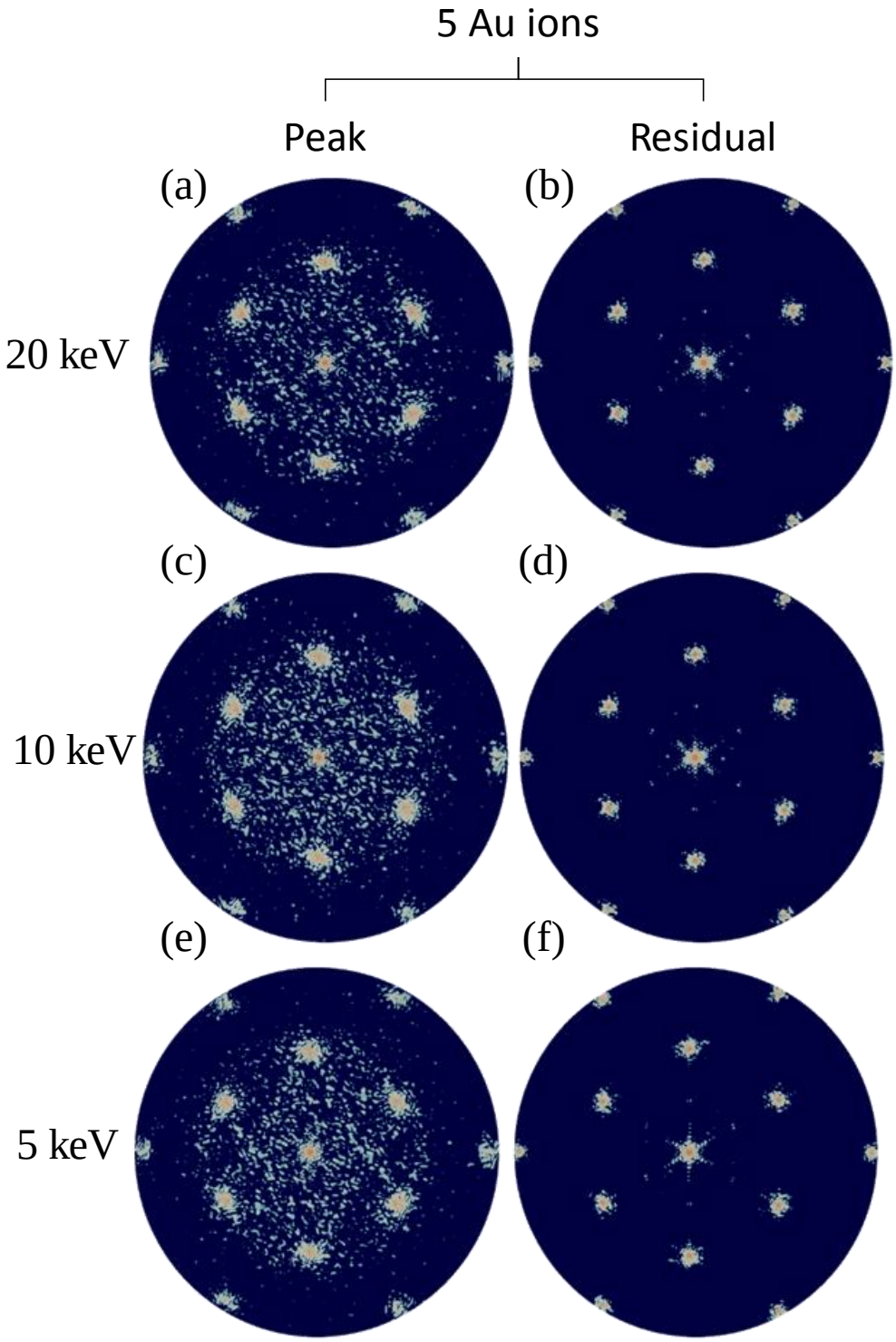

Figure 6.36: Comparison of simulated SAED [111] patterns of peak defect production and of the residuals from 5 Au projectiles, at energies of 5, 10, and 20 keV, in crystalline MgO.

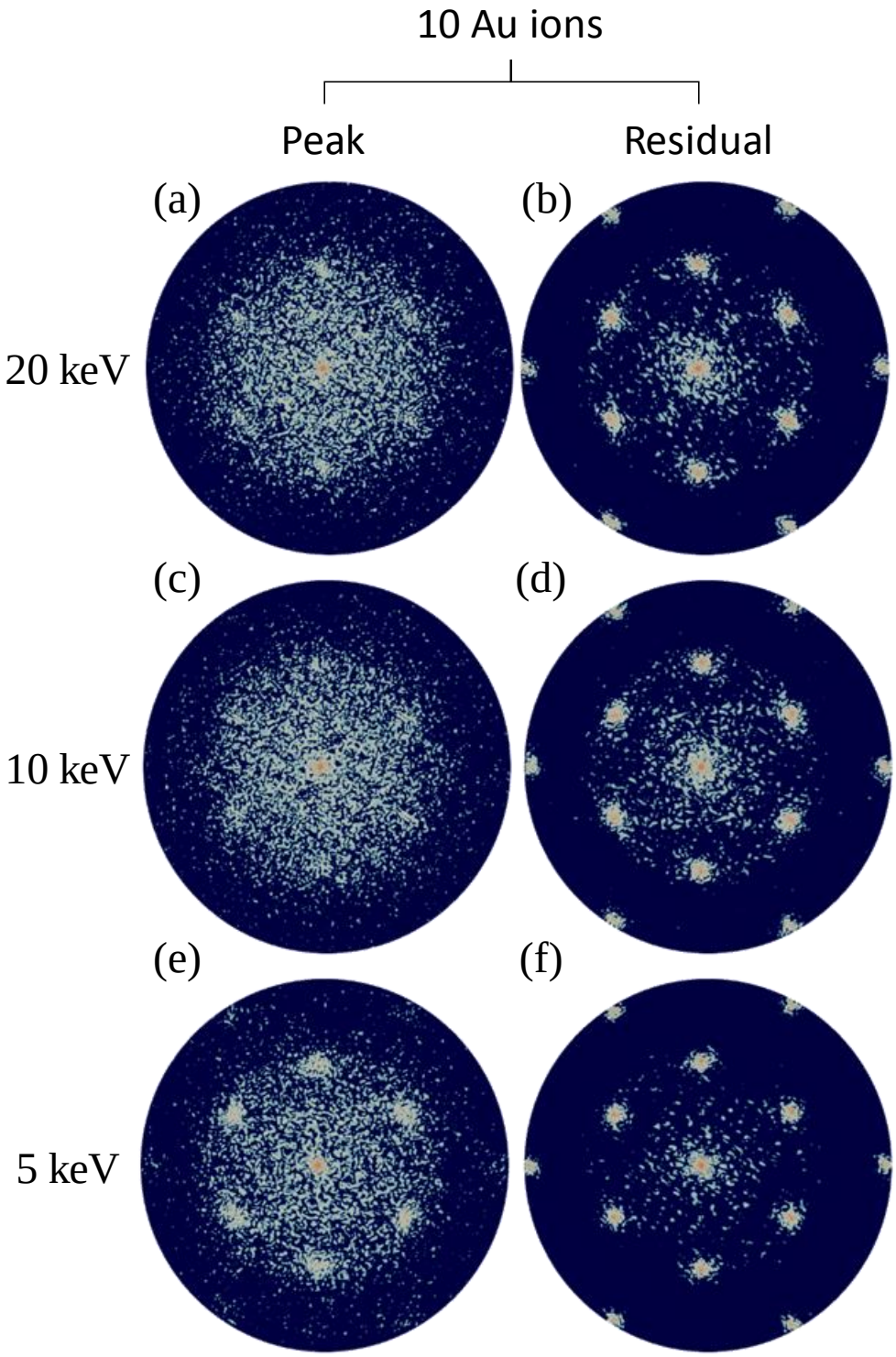

Figure 6.37: Comparison of simulated SAED [111] patterns of peak defect production and of the residuals from 10 Au projectiles, at energies of 5, 10, and 20 keV, in crystalline MgO.

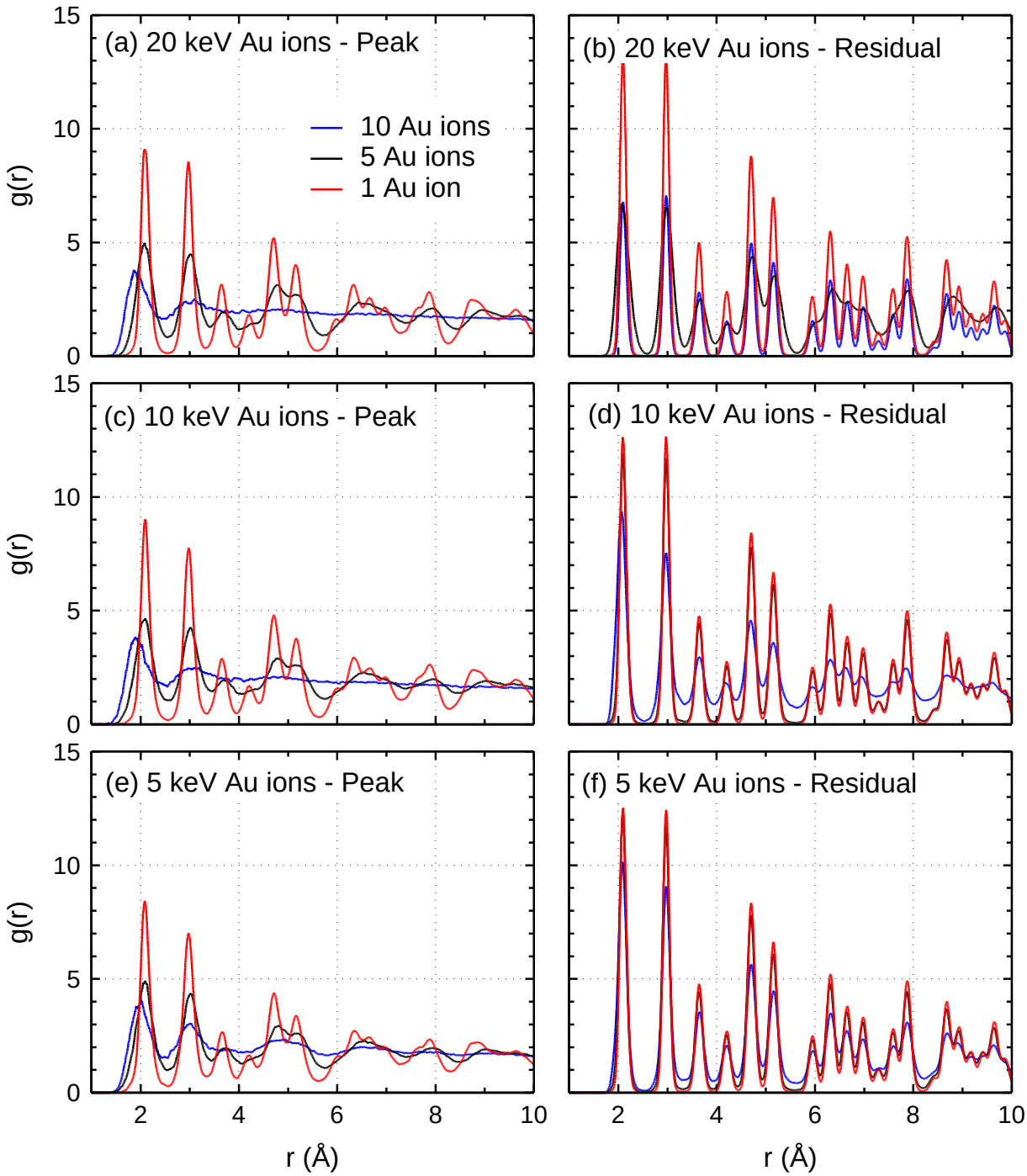

Figure 6.38: Comparison of RDFs of the irradiated region for Au projectiles of 5, 10, and 20 keV, at peak defect production and of the residuals.

All of the results from the simulated SAED patterns are supported by the RDFs of the irradiated region (Fig. 6.38). At the peak of the ballistic phase for the case involving 10 20-

keV Au projectiles, g(r) → 1 at ≈3 Å, confirming the complete loss of crystal order. After annealing, the peaks in the RDF are observable for all cases investigated, but the peaks are not as sharp. For the case involving 20 keV Au projectiles, the full-width half-maximum is 0.2, 0.4, and 0.61 for 1, 5, and 10 ions, respectively at the peak of the ballistic phase. Thus, the amount of disorder increases as the number of projectiles increases, in agreement with the results of the simulated SAED patterns.

6.3.2.2 **In Situ TEM Ion Beam Irradiation Results**

Complementary *in-situ* ion beam irradiation experiments experimental results, carried out at the I^{3}TEM facility[76] using 1.7 MeV Au^{3+} ions, are useful for comparing to those of the present MD simulations. The *in-situ* experiments are capable of real time observation (200 milliseconds) of the ions strikes, which exceeds the temporal resolution of MD simulations by several orders of magnitude. This allows for determining whether defect production at picosecond time scales using MD simulations is at all reflected in contrast changes of the experiments with millisecond and nanometer resolution. The energy of the Au ions in the irradiation experiments is 1.7 MeV in order to produce high cascade damage in the tilted (30^o) thin film specimens. The ion flux and TEM imaging conditions are optimized to facilitate direct real-time observation of single ion strikes.

The bright field image and inset SAED pattern in Fig. 6.39 are of the deposited thin film on NaCl. The SAED pattern shows rings which confirms that the thin film specimen used in the experiment is crystalline MgO. The still images in Fig. 6.40a,b are taken from recorded sequential frames, separated by 200 ms, during the *in situ* TEM irradiation experiment. The image in Fig. 6.40c highlights an observable contrast change measuring 80.96 nm^2 (8.8 nm x 9.2 nm). Similar changes observed during the experiment had contrast change regions of 12 nm^2 (3 nm x 4 nm), 24.75 nm^2 (4.5 nm x 5.5 nm), and 45 nm^2 (5 nm x 9 nm). The difference in the area of the changing contrast regions could be a result of differing angles of incidence, or due to the stochastic processes that cause different types of defect production and clustering at the same conditions. It is important to note that bulk amorphization did not occur, as the SAED pattern after irradiation has not changed. However, it is unclear if local amorphization in the ion strike regions occurs.

The bright field image and inset SAED pattern in Fig. 6.41 are of the deposited MgO on the a-SiN. The few diffraction peaks in the SAED pattern inset in Fig. 6.41 confirms that the

spherical nanoparticles are crystalline MgO. The reason that the rings are not as clearly defined is because the spherical nanoparticles only take up a fraction of the a-SiN grid, thus the amorphous nature of the TEM grid will affect the produced SAED pattern. Additionally, the amount of material that the SAED pattern is taken over is less than that than was deposited on NaCl, so there will not be as much diffraction.

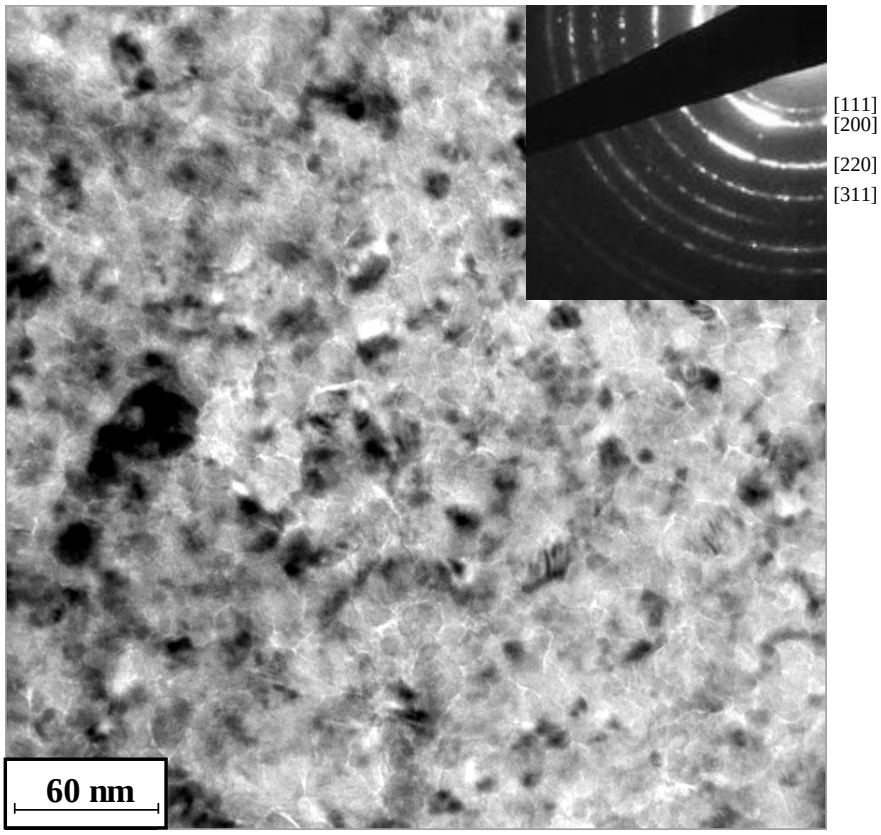

Figure 6.39: Bright field image and SAED pattern of unirradiated MgO, deposited onto NaCl.

The still images in Fig. 6.42a,b are taken from recorded sequential frames, separated by 200 ms, during the *in-situ* TEM irradiation experiment. The image in Fig. 6.42c highlights an observable contrast change measuring 77.6 nm^2 (9.7 nm x 8 nm). Similar changes observed during the experiment had contrast changes varying from 20 nm^2 (4 nm x 5 nm) to 88 nm^2 (8 nm x 11 nm). Like with the previous sample, bulk amorphization is not observed, as diffraction peaks remain in the SAED patterns after annealing. The next section discusses and compares the MD simulation results with those of the *in-situ* TEM ion beam irradiation experiment.

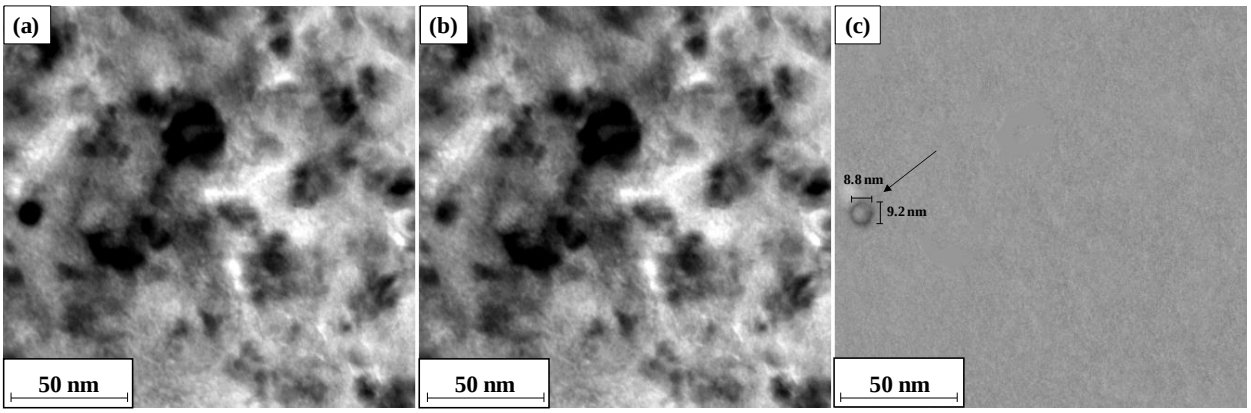

Figure 6.40: Bright field micrograph of sputter deposited, porous, nanocrystalline MgO collected during *in-situ* TEM ion irradiation with 1.7 MeV Au^{3+}. (b) Still frame after a single observable ion strike taken from the same video, 200 milliseconds after micrograph shown in (a). c) Difference image comparing figures (a) and (b) to highlight the contrast changes resulting from the single ion strike (arrowed).

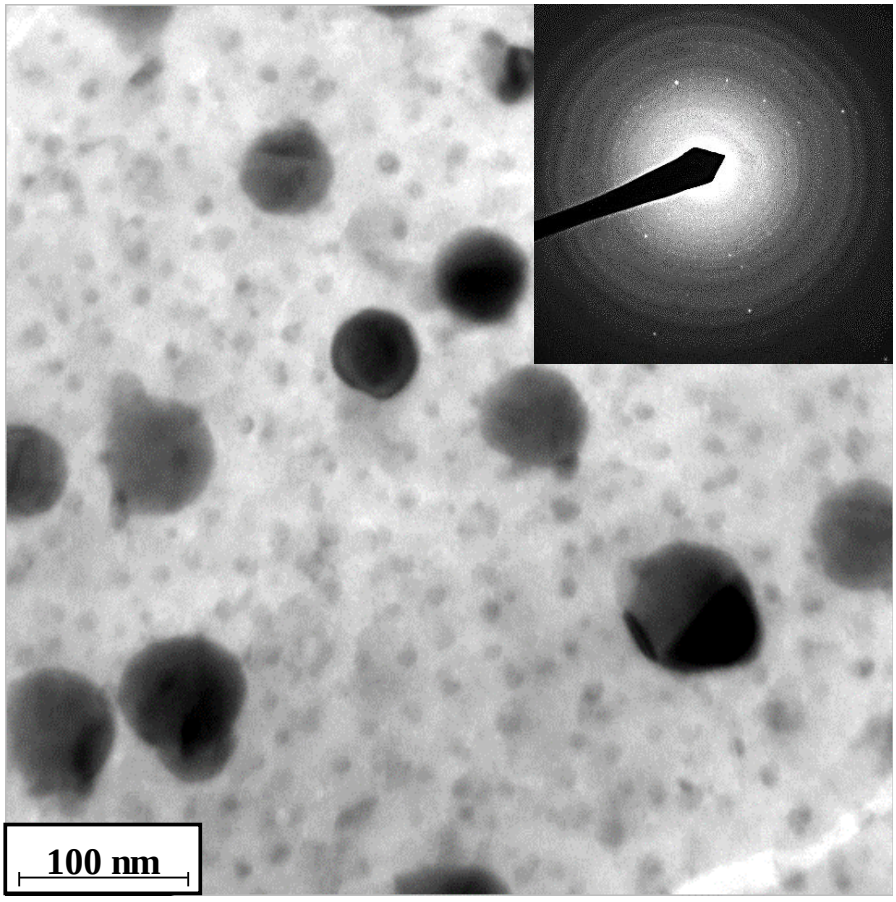

Figure 6.41: Bright field image and SAED pattern of unirradiated MgO, deposited onto a-SiN.

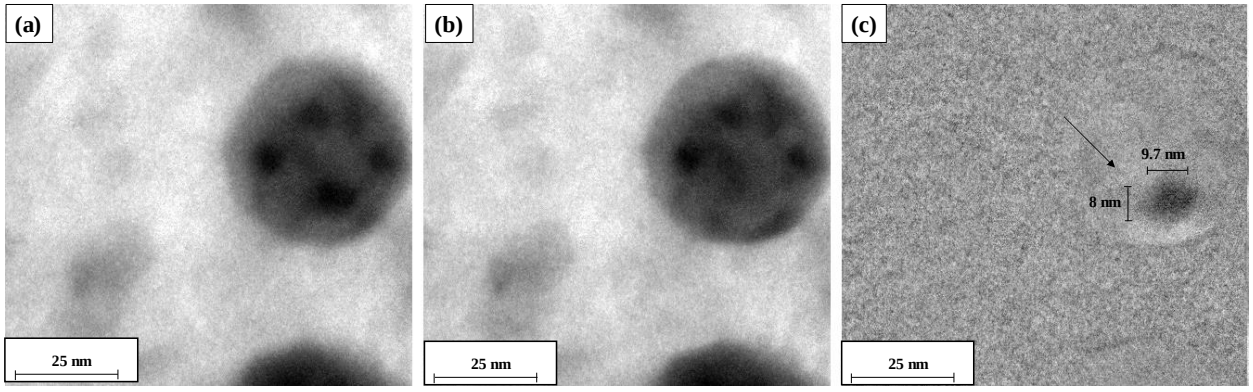

Figure 6.42: Bright field micrograph of sputter deposited, porous, nanoparticles of MgO collected during *in-situ* TEM ion irradiation with 1.7 MeV Au^{3+}. (b) Still frame after a single observable ion strike taken from the same video, 200 milliseconds after micrograph shown in (a). c) Difference image comparing figures (a) and (b) to highlight the contrast changes resulting from the single ion strike (arrowed).

6.3.2.3 **Discussion**

The development of multi-scale models is essential for accurately predicting irradiation effects in materials. The mechanistic insight gained from MD simulations is needed to predict the long-term evolution of defect clusters using computational tools such as cluster dynamics. Irradiation effects are observed in MgO using both MD simulations and *in situ* TEM ion beam irradiation. Defect production using single Au ions up to 50 keV does not compare well with observable contrast changes observed in the difference images of ion strikes produced by 1.7 MeV Au^{3+} ions. For instance, the observable damage as observed from above the surface from a 20 keV Au projectile is 1.95 nm^2 (1.5 nm x 1.3 nm) at the peak of the ballistic phase, reducing to 0.94 nm^2 (0.97 nm x 0.97 nm) after annealing. The observable contrast changes of the *in-situ* TEM ion beam irradiation using 1.7 MeV Au^{3+} ranges from 12 nm^2 to 88 nm^2. The large differences are likely due to the difference in energy of the incoming Au projectiles (50 keV in the MD simulations, compared to 1.7 MeV in the *in situ* TEM ion beam irradiation experiments). Additionally, there are likely some produced defect clusters using *in situ* TEM ion beam irradiation, but size resolution precludes the

observations of these defects.[103] Regardless, defect production regions that extend tens of nanometers outwards at the surface are not observed with single ions strikes. However, modeling 1.7 MeV Au projectiles using MD simulations is prohibitive due to computational limitations. Therefore, a new means of emulating radiation damage is presented, in which simultaneous impact of several projectiles causes large-scale defect clusters which are in better agreement with experimental observations.

MD simulations that modeled the injection of 5 and 10 Au projectiles into the MgO system simultaneously are carried out, with projectile energies of 5, 10 and 20 keV. The observable damage from above the surface using 5 20-keV Au ions is 8.64 nm^2 (2.4 nm x 3.6 nm) and 5.88 nm^2 (2.1 nm x 2.8) at the peak of the ballistic phase, and after annealing, respectively. This area increases for 10 20-keV Au projectiles, with the damage region to 65.9 nm^2 (7.4 nm x 8.9 nm) at the peak of the ballistic phase, and reducing to 43.9 nm^2 (6.1 nm x 7.2 nm) after annealing. Thus, the observable defect region is in excellent agreement with that seen using *in situ* TEM ion beam irradiation. While the simultaneous injection of multiple projectiles is unphysical, it allows for modeling larger defect clusters, to gain mechanistic insight into their evolution.

While the *in situ* TEM ion beam irradiation experiment cannot be used to identify individual point defects, and the exact size of defect clusters, MD simulations can provide this level of detail. The MD simulations show that a necking region occurs in the produced defect cascade, with the bulk of the projectile energy deposited below the necking region. The necking is likely a surface effect, which causes the damage to spread outward, primarily due to reversible elastic deformation, but also some irreversible inelastic deformation. The WS defect analysis, in conjunction with cluster analysis, shows that the size of the forming void at the peak of the ballistic phase is comprised of 14,800, 38,400, and 102,500 vacancies for 10 Au projectiles of 5, 10, and 20 keV, respectively. The size reduces to 1,900, 4,000, and 5,000 vacancies, respectively, after annealing. The results shows a clear dependence of void size on the Au projectile energy when 5 and 10 projectiles are used, and a strong dependence on the number of ions. The overlapping cascades tend to foster higher stability amongst the defects, and thus can have a greater impact on the morphology of the system under irradiation. The results show that vacancy clusters and interstitial clusters formed during the peak of the ballistic phase will reduce by more than an order of magnitude during annealing,

but that as much as 5,000 vacancies can form a stable residual void. A similar size interstitial cluster is produced in these cases, which lies below the void, due to tens of thousands of atoms being displaced further into the crystal. While it is possible that diffusion of the interstitial cluster could annihilate with the void, and further reduce its size, the complementary *in-situ* TEM ion beam irradiation shows contrast changes observable over several minutes. This suggests that the produced defect clusters are stable.

The MgO specimens, irradiated for 15 minutes to a total dose of 0.228 in the first 40 nm of the material, and 0.245 dpa in the first 100 nm, did not show bulk amorphization. The SAED patterns obtained with TEM do not show any changes in crystallinity, but this could be partially due to the difficulty in only sampling regions that were damaged by Au projectiles. Additionally, the temporal resolution of *in situ* TEM is not high enough to capture SAED patterns of the peak of the ballistic phase. MD simulations can be used to investigate changes in crystallinity in the irradiated region, using simulated SAED patterns and RDFs. The results show that the irradiated region fully amorphizes at the peak of the ballistic phase when 10 10-keV and 20-keV Au projectiles are used. While some of the crystal order returns after the annealing phase, there is still clear damage, and small amorphous pockets. The accumulation of these pockets of radiation damage if irradiated further, would likely lead to bulk amorphization.

6.3.3 Highlights and Concluding Remarks

This work has investigated irradiation effects in crystalline MgO using both MD simulations and complementary *in situ* TEM ion beam irradiation with 1.7 MeV Au^{3+}. The MD simulations are used to determine the TDE directional dependence and TDE probability distributions. The TDEs corresponding to 50% probability are used as input into SRIM to estimate the dose of the ion beam irradiation experiments. Irradiation effects of single Au ions with 5, 10, 20, and 50 keV of energy are investigated, as well as the effects of 5 and 10 ions with energies of 5, 10, and 20 keV. Defect production, clustering, amorphization, and recombination are investigated during the peak of the ballistic phase and after annealing, and compared to the *in-situ* TEM ion beam irradiation results.

The MD simulation results show a clear dependence of defect production, clustering, and amorphization on the energy of the Au projectiles and number of ions inserted. Single Au projectiles of up to 50 keV do not compare well with *in situ* TEM ion beam irradiation with

1.7 MeV Au^{3+}, due to such large differences in the energy of the projectiles. For instance, the observable damage as observed from above the surface from a 20 keV Au projectile is 1.95 nm^2 (1.5 nm x 1.3 nm) at the peak of the ballistic phase, reducing to 0.94 nm^2 (0.97 nm x 0.97 nm) after annealing. The observable contrast change does not compare well with that of the *in-situ* TEM ion beam irradiation using 1.7 MeV Au^{3+}, which ranges from 12 nm^2 to 88 nm^2. On the other hand, the observable damage from above the surface using 5 20-keV Au ions is 8.64 nm^2 (2.4 nm x 3.6 nm) and 5.88 nm^2 (2.1 nm x 2.8) at the peak of the ballistic phase, and after annealing, respectively. This area increases for 10 20-keV Au projectiles, with the damage region to 65.9 nm^2 (7.4 nm x 8.9 nm) at the peak of the ballistic phase, and reducing to 43.9 nm^2 (6.1 nm x 7.2 nm) after annealing. These observable defect regions are in excellent agreement with that seen using *in-situ* TEM ion beam irradiation.

The MD simulation results can be used to understand the evolution of large-defect clusters that would likely form during the *in situ* TEM ion beam irradiation. Results show that the size of residual void can be comprised by as much as 102,500 vacancies during the ballistic phase, reducing to 5,000 after annealing. While the size of the void reduces by ≈20 times during the annealing phase, a significant size void remains which would affect the crystallinity and local material properties. SAED patterns and RDFs show complete amorphization in the irradiated region during the peak of the ballistic phase, and only some of this order returns after annealing. These defect clusters appear to be stable over longer time-scales, since contrast changes using *in situ* TEM are observed after 200 milliseconds.

This work has carried out large-scale MD simulations with a system size of over 27 million atoms to model the injection of single and multiple high-energy projectiles, for direct comparison with experimental results. By using both tools in a complementary way, better multi-scale models can be developed for predicting irradiation effects, which is of timely importance for the development of next-generation nuclear reactor designs.

The next chapter of this dissertation summarizes the key findings from each study presented, and discusses potential implications of the results. Additionally, recommendations for future work related to this dissertation is provided.

7 SUMMARY AND CONCLUSIONS

This dissertation research has investigated irradiation effects in metal oxides and carbides using extensive MD simulations and complementary *in situ* TEM ion beam irradiation. The results of this research show that MD simulations are an effective tool for investigating and characterizing irradiation effects in ceramics, as long as proper vetting of interatomic potentials is carried out to ensure accuracy, transferability, and computational efficiency. An extensive literature review of interatomic potentials returned dozens of possible options, developed over the last several decades. Out of all the possible choices, 8 of the most widely used potentials are chosen for intensive investigation of accuracy, transferability, and computational cost. Out of the 8 potentials investigated, one of them is a many-body potential which ignores Coulomb interactions (Munetoh), 4 are pair potentials which assign fixed-charges to the atoms (BKS, Pedone, TTAM, CHIK), and 3 are bond-order variable charge potentials (COMB10, $\mathrm{ReaxFF}_{\mathrm{SiO}}^{\mathrm{H_2O}}$, $\mathrm{ReaxFF}_{\mathrm{SiO}}^{\mathrm{GSI}}$), which can accommodate for a rapidly changing bonding environment.

The review of these 8 interatomic potentials for modeling SiO_2 shows that neglecting Coulomb interactions to save on computational cost is not justified, since the material being modeled would not be representative of the actual material. This is supported by the fact that the contributions of the electronegativity are an order of magnitude higher than those of the short-range forces, such as bond-angles. [202] [202] [197] [197] [197] Therefore, it is imperative that the potentials for MD simulations include the Coulomb forces in order to provide an accurate description of the ceramic being modeled. While the bond-order variable-charge potentials are the most computationally expensive, they were primarily developed for modeling complex interfaces, and do not model some of the equations of state of various SiO_2 polymorphs accurately. For example, none of them accurately predict the experimentally measured plateau (α-β transition in quartz), caused by the rotation of the SiO_4 tetrahedra. The results suggest that these potentials should primarily be used for modeling interfaces such as Si/SiO_2, especially since the computational cost is an order of magnitude larger than the more accurate, pair potentials.

The most promising potentials of the ones investigated are the BKS and Pedone potentials, for their accuracy, transferability, and reasonable computational requirements. The BKS potential (Buckingham form) is the most accurate for modeling the structural

properties, phase transitions, and equations of state to within 2% for most polymorphs. The Pedone potential (Morse-stretch form), while not as accurate as BKS, models the other metal oxides of interest reasonably well. Most of the calculated lattice and elastic constants, density, and equations of state as a function of temperature and pressure, compared to experimental results, are accurate to within a few percent. Due to the accuracy, transferability, and computational efficiency of both the BKS and Pedone interatomic potentials, they were both used to investigate threshold energies for PKA displacement in crystalline SiO_2.

The MD simulation results of PKA displacement in SiO_2 show that a total simulation time > 1.0 ps and a time step < 0.2 fs insignificantly alters the TDE probability-based statistical averages. The simulations with the BKS long cutoff (15 Å), short cutoff (5.5 Å) and Pedone potentials predict the TDE corresponding to 1% of oxygen PKA displacement value of 10.8-12.3 eV, compared to 20.5 - 29.6 eV for silicon PKA displacement. The TDE at 50% probability for the oxygen atoms range from 24.9 - 32.4 eV, which are comparable to that of Mota el. al,[302] reporting a 50% probability for an oxygen atom to create a stable defect in fused silica at 30 eV. For the silicon atoms at 50% probability, the calculated TDEs vary from 51.9 – 60.8 eV. Typically, a single TDE is used as the input to radiation damage codes to predict defects in bulk materials, and is sometimes takes as the minimum energy needed to cause a displacement. However, the probability-based TDEs give results that are more realistic, and show that the minimum energy to potentially cause a displacement may only occur 1% of the time, depending on the crystallographic direction. Thus, the PKA displacement probability distributions provide valuable input to future investigations of the effect of irradiation on the silica-based additives in ATFs. In order to compare the TDE with that of other oxides of interest, and to expand on the definition of the TDE to be inclusive of what most studies used throughout the literature, the Pedone potential is used to investigate PKA displacement, an atom displacement, and stable Frenkel pair formation in crystalline SiO_2, TiO_2, Al_2O3, Cr_2O_3, and MgO.

The calculated TDEs for the displacement of metal and oxygen PKAs, the displacement of an atom in the crystal, and the formation of stable Frenkel pairs in Cr_2O_3, Al_2O_3, TiO_2, SiO_2, and MgO are strongly dependent on the crystal structure and crystallographic direction. The results for the metal PKA with energies up to 350 eV and the oxygen PKA with energies

up to 400 eV clearly show that the formation of stable Frenkel pairs is not always associated with PKA displacement, and vice-versa. Oxygen PKAs are likely to recoil to their original lattice site after colliding with metal atoms, but may result in the formation of a stable Frenkel pair.

The TDEs for the displacement of oxygen PKAs in MgO are lower in the high-index directions than in the low-index directions. Conversely, in the low-index directions, the TDEs for the oxygen PKAs to produce stable Mg Frenkel pairs are lower than in the high-index directions. The PKA displacement and Frenkel pair formation energies for Al_2O_3 and Cr_2O_3 are the same for each of the 66 crystallographic directions, except that the formation of oxygen atom Frenkel pairs with Al PKAs occurs at higher energies than with Cr PKAs. This suggests that the PKA type affects the number and formation energies of the Frenkel pairs. In SiO_2, the TDEs for forming stable Frenkel pairs with both oxygen and metal PKAs are typically <50 eV in all directions, and on both anion and cation sublattices, compared to >100 eV in other oxides, in some crystallographic directions.

Metal PKA displacement probabilities are similar to the probabilities to displace an atom in the lattice, indicating they are unlikely to recoil to their original lattice site once a Frenkel pair forms. Oxygen PKA displacement probabilities in MgO, Cr_2O_3, and Al_2O_3 are not as similar to the displacement probabilities of an atom in the lattice, indicating that SKAs are sometimes responsible for Frenkel pair formation, while the PKA returns to its original lattice site. The total number of displaced atoms is higher in SiO_2 than the other oxides across the energy range investigated. Since atoms are more readily displaced in SiO_2, more Frenkel pairs are produced compared to the other oxides. However, for the same number of displaced atoms with metal PKAs, Al_2O_3 and Cr_2O_3 yield the highest number of Frenkel pairs, indicating displaced atoms in these oxides are less likely to anneal.

Given the stochastic nature of the radiation interactions with materials and the demonstrated strong directional dependence of the TDEs in the SiO_2, TiO_2, Cr_2O_3, Al_2O_3, and MgO, the current values calculated in 66 crystallographic directions would be a more representative input to the radiation damage models, instead of single values calculated from TDEs in one or a few crystallographic directions. Additionally, the calculated average number of Frenkel pairs produced on both the anion and cation sublattices in these oxides would help the full assessment of the extent and type of radiation damage in each oxide, thus

a useful input to the radiation damage models. These models can serve to determine the relationship between atomic-scale defects and changes in bulk material properties, which is of practical importance.

An investigation into the TDE in 3C-SiC by C and Si PKAs of energies up to 400 eV, showed that the TDEs for the displacement of PKAs and of an atom, and the formation of Frenkel pairs are also different and cannot be used interchangeably. The obtained polar contours of defect production on both sublattices show strong anisotropy on both sublattices. The lowest TDE for a C PKA to produce a carbon vacancy in any crystallographic direction is 14-16 eV for C PKAs and 38-58 eV for the Si PKAs. The lowest TDEs for the C and Si PKAs to produce a Si vacancy are 59-71 eV and 42-46 eV, respectively. These results are in good agreement with prior *ab initio* simulations. The number of displaced atoms with either C or Si PKAs increase linearly with increased energies above the determined TDEs.

The weighted probability distributions for displacements of a PKA and an atom in the four low-index crystallographic directions of [100], [110], [111], and $[\bar{1}\,\bar{1}\,\bar{1}]$ are identical for the C PKAs with energies below 50 eV, but diverge at higher energies. The carbon vacancies are the most common defect produced with both C and Si PKAs. The number of C vacancies produced by a C PKA and a Si PKA of 400 eV are 4x and 1.75x the silicon vacancies produced, respectively. While the production of antisites is not as common as Frenkel pairs, PKAs with energies of a few hundred eV could generate at least one antisite on average. Additionally, Si antisites are more likely to form than C antisites since C atoms are less likely to displace the more massive Si atoms and cause a replacement collision sequence.

The calculated probability distributions for the displacements of a C PKA and an atom in amorphous (a-SiC) are nearly identical, indicating that their respective TDEs could be used interchangeably. However, the Si PKAs are likely to displace C SKAs at lower energies than for displacing the Si PKAs. This is similar to interaction sequences in some directions in 3C-SiC. For the same PKA energy, atoms are more likely to be displaced in a-SiC than in 3C-SiC. The energy for C PKAs to cause displacements 50% of the time in 3C-SiC is 26 eV, compared to 13 eV in a-SiC. For Si PKAs, the corresponding energies are 48 eV and 27 eV, respectively. The crystal order in 3C-SiC can often cause the PKA to be caged in, making it difficult to escape its lattice site, unless it has enough energy to displace its neighbor.

All of the work on TDEs has provided an extensive database of near-threshold irradiation effects in the metal oxides and carbides of interest. However, it is also necessary to investigate bulk radiation at much higher energies, in order to investigate radiation damage cascades, defect clustering, and changes in crystallinity. In order to do this, MD simulations are carried out to investigate the production of point defects in α-quartz by oxygen and silicon PKAs of energies from 0.25 to 2.0 keV. The results of the MD simulations demonstrate the importance of using both the Wigner-Seitz (WS) and coordination analysis methods to fully identify and quantify the various types of point defects produced. The oxygen and silicon vacancies are the primary defects during the ballistic and annealing phases of the simulations. WS analysis shows that despite the annihilation during the annealing phase, some vacancies remain at the end of that phase. Coordination analysis shows that most of the defects produced are locally accommodated through the formation of interstitial sites. Thus, the affected regions would contain amorphous pockets and incur permanent structural changes.

The defects at the end of the ballistic phase and the residual defects, after annealing, increase with increased PKA energy, and are statistically the same for the oxygen and silicon PKAs. The WS defect analysis shows that the numbers of the oxygen vacancies and interstitials (V_O, O_i) at the end of the ballistic phase are the highest, followed closely by those of the silicon vacancies and interstitials ($V_{Si,}$ Si_i). Furthermore, the number of the residual oxygen and silicon vacancies and interstitials are statistically similar. In addition, the under-coordinated O^I and Si^{III} are the primary defects produced during the ballistic phase, and have high annealing efficiencies $\geq$ 89%. The over-coordinated defects of O^{III} and Si^V, which are not nearly as abundant in the ballistic phase, have lower annealing efficiencies (< 63%) that decrease with increased PKA energy. These results of point defects production provide welcome input to predicting radiation damage in bulk α-quartz. The results demonstrate the importance of using both the WS analysis and the coordination analysis to fully characterize and quantify the defects peak production and the residual defects, as functions of the energy and direction of the Si and O PKAs. Since SiO_2 is more likely to experience radiation-induced displacements, it would also be prudent to investigate a material that is more radiation-resistant. For this reason, MD simulations of irradiation effects in TiO_2 are carried out up to 10 keV.

The MD simulations investigated the production of point defects and defect clusters in rutile TiO_2 by O and Ti PKAs of energies of 1, 5, and 10 keV, at system temperatures of 300, 600, and 900 K. The results show that defect production depends on the PKA energy and system temperature, but not PKA type. The simulated SAED patterns and RDFs confirmed the retention of TiO_2 crystallinity during peak defects production and after annealing. However, in the cases of forming a single defect production core, long-range order is lost at peak defect production since $g(r) \rightarrow 1$ at $\approx$ 5 Å. At the peak of the ballistic phase of interaction, more oxygen than titanium defects form. Conversely, the residuals after annealing are primarily Ti defects. The percentage of peak Ti defects that anneal increase with increased temperature, however that of the residual O defects is higher and independent of temperature.

The sizes of the defect clusters forming at the peak of the ballistic phase, significantly shrink after annealing due to the recombination of the Ti vacancies and interstitials. When a single core of defects is formed, the titanium vacancies cluster to form a void, with the produced interstitials at the periphery. The size of the produced void at the defects peak production, decreases by 1-2 orders of magnitude after annealing, and could contain a few to tens of residual vacancies that are mostly titanium. The size of the residual void also decreases with increased temperature. This might explain why amorphization of TiO_2 has been reported in ion beam irradiation experiments at 300 K, but not at higher temperatures. Results also show that the produced residual point defects store energy in the TiO_2 crystal due to local stresses from changes in the crystal lattice. The stored energy decreases with increased system temperature due to increased mobility and recombination of defects. The energy stored estimates of $\approx$140 - 310 eV at 300 K, decrease to $\approx$5 - 180 eV at 900 K.

While the results from these MD simulations of radiation damage are useful, comparing to experimental results of bulk radiation damage would enhance the broad understanding of radiation effects in materials. In order to do this, the computational limitations must be pushed to accommodate high energy PKAs and/or projectiles that emulate observable ion strikes using *in si*tu TEM ion beam irradiation. Therefore, an MD simulation and *in-situ* TEM ion beam irradiation investigated the interaction of a 46 keV Ti projectile into crystalline TiO_2. The MD simulation results provide detailed information of the individual types of defects produced and retained with attosecond resolution. This combination of

length and time scale cannot be matched by any current experimental facility, but the irradiation experiments with a 46 keV Ti ion beam confirmed the presence of a post-annealing crystalline phase, as expected due to the low irradiation dose of 0.44 dpa at 300 K. SRIM is used to estimate the dose of the ion beam irradiation experiment using the 50% displacement probability determined in this dissertation.

The MD simulation results show that despite much more oxygen than titanium vacancies are produced during the peak of the ballistic phase, the residual vacancies after annealing are mostly titanium, in agreement with the MD simulations carried out up to 10 keV in TiO_2. Some of the defects identified by WS analysis during the ballistic phase of interaction are a result of elastic deformation from the ion strike rather than changes in the crystal structure. Cluster analysis identified up to approximately 10,000 vacancies in the core of the cascade during the ballistic phase of interaction, which decreased in size to <1,000 vacancies after annealing. After annealing, the volume of the defects cascade is ≈40 nm^3. The diameter of the irradiated region at FWHM of the defect density distribution is ≈3 nm at the defects peak production, decreasing to ≈2 nm after annealing. Clusters of interstitials, approximately the same sizes as the vacancy clusters, form mostly at the periphery of the core region. The RDFs and simulated SAED patterns of the irradiated region at the peak of the ballistic phase show short- and medium-, but no long-range order. After annealing, however, some long-range order returns, which is validated by the *in situ* TEM ion irradiation experiments.

MD simulations and complementary *in situ* TEM Au^{3+} ion beam irradiation are also performed to assess radiation effects in 3C-SiC and a-SiC. The MD simulations with Si PKAs of energies ranging from 10-100 keV, investigated the production of residual point defects and defect clusters. Sequential bright field images of ion beam irradiation helped identify contrast changes in the irradiated regions from single ion strikes, and SAED patterns helped detect the changes in the microstructure before and after irradiation. Due to the differences in temporal resolution of the MD simulations and the *in situ* TEM ion beam irradiation, different, but complementary information is obtained.

MD simulation results confirm that carbon vacancies and interstitials are the primary residual point defects in 3C-SiC, while the clustering and the extent of the defect cascades depend on the Si PKA energy. The largest clusters increase in size from 10.3 ± 2.1 to 30.3 ± 13.1 vacancies and from 4.0 ± 1.4 to 12.0 ± 4.4 interstitials, respectively, as the Si PKA

energy increases from 10 to 40 keV. Beyond 40 keV, the formation of clusters is more random and extends over a large region of the simulation domain. Generally, the size of the largest vacancy cluster is ≈2 to 3 times that of the largest interstitial cluster, for all Si PKA energies investigated. The retention of 3C-SiC crystallinity is confirmed by the simulated SAED patterns before and after irradiation for the MD simulations and *in situ* TEM irradiation. These patterns also confirmed the lack of structural changes in a-SiC after irradiation.

The stored energy in the irradiated 3C-SiC, due to point defects and defect clusters is estimated to be ≈10% of all energies of the Si PKAs. In contrast, the lack of stored energy that is distinguishable from the thermal noise in irradiated a-SiC, suggests that it is more radiation tolerant than 3C-SiC. The retention of the amorphous phase is also confirmed by simulated SAED patterns for MD simulations and those obtained for sequential images recorded during the *in situ* TEM irradiation using Au^{3+} ions. These results of the combined contribution of the MD simulations and the *in situ* TEM experiments provide valuable information on the effect of irradiation in crystalline and amorphous SiC. This information would help future consideration of using these materials in developing radiation tolerant fuel systems for the present fleet of light water reactors and next-generation reactors. The radiation hardness of a-SiC, combined with the absence of grain boundaries, makes it a suitable protective coating for ceramic and metallic substrates or structures in harsh environments combining high temperature and radiation.

In order to investigate effects from overlapping damage cascades, MD simulations are used to investigate irradiation effects of single Au ions with 5, 10, 20, and 50 keV of, as well as the effects of 5 and 10 ions with energies of 5, 10, and 20 keV. Defect production, clustering, amorphization, and recombination are investigated during the peak of the ballistic phase and after annealing, and compared to the *in situ* TEM ion beam irradiation results.

The MD simulation results show a clear dependence of defect production, clustering, and amorphization on the energy of the Au projectiles and number of ions inserted. Single Au projectiles of up to 50 keV do not compare well with *in situ* TEM ion beam irradiation with 1.7 MeV Au^{3+}, due to such large differences in the energy of the projectiles. For instance, the observable damage as observed from above the surface from a 20 keV Au projectile is 1.95 nm^2 (1.5 nm x 1.3 nm) at the peak of the ballistic phase, reducing to 0.94

nm^2 (0.97 nm x 0.97 nm) after annealing. The observable contrast change does not compare well with that of the *in situ* TEM ion beam irradiation using 1.7 MeV Au^{3+} ions, which ranges from 12 nm^2 to 88 nm^2. On the other hand, the observable damage from above the surface using 5 20-keV Au ions is 8.64 nm^2 (2.4 nm x 3.6 nm) and 5.88 nm^2 (2.1 nm x 2.8) at the peak of the ballistic phase, and after annealing, respectively. This area increases for 10 20-keV Au projectiles, with the damage region to 65.9 nm^2 (7.4 nm x 8.9 nm) at the peak of the ballistic phase, and reducing to 43.9 nm^2 (6.1 nm x 7.2 nm) after annealing. These observable defect regions are in excellent agreement with that observed using *in-situ* TEM ion beam irradiation.

The MD simulation results can be used to understand the evolution of large-defect clusters that would likely form during the *in situ* TEM ion beam irradiation. Results show that the size of residual void can be comprised by as much as 102,500 vacancies during the ballistic phase, reducing to 5,000 after annealing. While the size of the void reduces by ≈20 times during the annealing phase, a significant size void remains which would affect the crystallinity and local material properties. SAED patterns and RDFs show complete amorphization in the irradiated region during the peak of the ballistic phase, and only some of this order returns after annealing. These defect clusters appear to be stable over longer time-scales, since contrast changes using *in situ* TEM are observed after 200 milliseconds.

To summarize the key contributions of this dissertation research, the extensive review and investigation of several interatomic potentials showed that the most appropriate interatomic potentials to use for investigating irradiation effects in metal oxides are fixed-charge, pair potentials for their high accuracy and transferability for modeling various structural properties, equations of state, phase transitions, and defect formation energies, as well as modest computational requirements. MD simulations using these potentials demonstrate that averaging the MD simulation results of the TDE over several crystallographic directions is appropriate due to the varying nature of collisions, including oxygen-oxygen, metal-metal, and oxygen-metal collisions, and accounting for low- and high-index directions. Results show that the PKA or projectile energy in MD simulations increases the extent of the damage cascade, and depending on the crystal structure, can either increase the number of small defect clusters rather than increasing the size of any individual cluster (e.g. SiC), or increase the size of a single defect production core and/or the number of small

defect clusters (e.g. TiO_2). This dissertation research has shown that defect production is directly correlated with the change in system potential energy in the MD simulations, both during the ballistic and annealing phases of interaction. Additionally, despite the large temporal differences between MD simulations and *in situ* TEM ion beam irradiation, the use of high enough PKA or projectile energies using MD simulations qualitatively represents observed changes from single ion strikes. The results also indicate that simulations of radiation damage with multiple ions gives more realistic results than attainable with single projectiles that could be related to potential applications. To conclude, this dissertation research shows that MD simulations is an effective tool for investigating irradiation effects in metal oxides and carbides. By using both MD simulations and *in situ* TEM ion beam irradiation in a complementary way, better multi-scale models can be developed for predicting radiation effects, which is of timely importance for the development of next-generation nuclear reactor designs.

7.1 Recommendations for Further Research

Continued study of irradiation effects in materials for the DOE's ATFs campaign and advanced ADOPT fuel would benefit from improved interatomic potentials, based off of density functional theory (DFT) results. DFT is considered to be the gold-standard, but many potentials used predict defect formation energies that are not in full agreement with DFT. Improving the potentials could include better fits to known properties, accounting for charge-transfer, which would occur when local bonding environments change due to irradiation, and improved algorithms to reduce the computational resources required for investigating bulk radiation. Additionally, using acceleration methods such as parallel-replica dynamics would foster the ability to observe changes in defect structures, cluster interactions, diffusion, and annihilation, at longer time-scales. This could facilitate the ability to develop rate equations for input into cluster dynamics models, for predicting radiation effect at the mesoscale.

Further comparisons of MD simulation results with that of *in situ* TEM would also improve the current understanding of irradiation effects in metal oxides and carbides. Multi-ion MD simulations could show changes in crystallinity from subsequent ions injected into the system once the lattice has had time to relax from each radiation event. Simulated SAED patterns and RDFs of the irradiated damaged region could then be compared to *in situ* TEM ion beam irradiation at higher doses, when bulk amorphization occurs. The MD simulations

would provide mechanistic insight into defect formation, clustering, annihilation, and diffusion, and would emulate the experiments of subsequent radiation-induced cascades in regions already damaged. This endeavor would be computationally expensive, since subsequent projectiles injected into a simulation domain would likely cause damage cascades in various regions of the material. However, such an exercise could prove invaluable for developing multi-scale predictive models of irradiation effects in ceramics.

Publications Associated with this Dissertation Research

Journal Papers

Cowen, B. J., & El-Genk, M. S. (2015). On force fields for molecular dynamics simulations of crystalline silica. *Computational Materials Science*, *107*, 88-101.[53]

Cowen, B.J., & El-Genk, M. S. (2016). Bond-order reactive force fields for molecular dynamics simulations of crystalline silica. *Computational Materials Science*, *111*, 269-276.[52]

Cowen, B.J., & El-Genk, M. S. (2016). Probability-based threshold displacement energies for oxygen and silicon atoms in α-quartz silica. *Computational Materials Science*, *117*, 164-171.[54]

Cowen, B.J., & El-Genk, M. S. (2017). Estimates of point defect production in α-quartz using molecular dynamics simulations. *Modelling and Simulation in Materials Science and Engineering*, *25*(5), 055001.[44]

Cowen, B.J., & El-Genk, M. S. (2017). Directional dependence of the threshold displacement energies in metal oxides. *Modelling and Simulation in Materials Science and Engineering*, *25*(8), 085009.[164]

Cowen, B.J., & El-Genk, M. S. (2018). Point defects production and energy thresholds for displacements in crystalline and amorphous SiC. *Computational Materials Science*, *151*, 73-83.[67]

El-Genk, M.S., Talaat, K., & Cowen, B.J. (2018). Thermal conductivity of silicon using reverse non-equilibrium molecular dynamics. *Journal of Applied Physics*, *123*(20), 205104.[322]

Cowen, B.J., El-Genk, M.S., Hattar, K., & Briggs, S.A., (2018). A study of irradiation effects in TiO_2 using molecular dynamics simulation and complementary *in situ* transmission electron microscopy. *Journal of Applied Physics*, Accepted, In Press

Journal Papers under Review

Cowen, B.J., El-Genk, M.S. (2018). Characterization of radiation damage in TiO_2 using molecular dynamics simulations. *Modelling and Simulation in Materials Science and Engineering*

Cowen, B.J., El-Genk, M.S., Hattar, K., & Briggs, S.A. (2018). Irradiation effects in crystalline and amorphous SiC using molecular dynamics simulations and complementary *in situ* transmission electron microscopy.

Journal Papers in Preparation

Cowen, B.J., El-Genk, M.S., Hattar, K., & Briggs, S.A. (2018). Irradiation effects in MgO using molecular dynamics simulations and complementary *in situ* transmission electron microscopy.

Cowen, B.J., El-Genk, M.S. (2018). Multi-ion molecular dynamics simulations of radiation damage in MgO.

Appendices

A Accident-Tolerant Claddings

In efforts to mitigate the disastrous hydrogen buildup that dissolves in the cladding material, new materials are being studied as candidates for accident-tolerant cladding materials in existing and future LWRs. Some of the cladding materials being investigated include Zircaloy claddings with protective coatings to reduce oxygen diffusion, SiC/SiC composites, and stainless steels with high chromia and alumina additives.[4,7,323,324] These accident-tolerant claddings will be reviewed in the following sections.

A.1 Zircaloy Cladding with Coatings

The simplest approach in the development of accident-tolerant cladding materials would be to continue making modifications to the existing Zircaloy claddings; however, optimization of Zircaloy claddings has taken place over the last several decades, making further attempts unlikely to enhance the accident tolerance of the fuel system. Still, efforts are underway to further reduce the high temperature oxidation rate of Zircaloy claddings which govern the oxidation of core materials during LOCA scenarios.[5]

One method is to continue to modify the solute additives to the Zircaloy; however, this path would most likely prove ineffective for achieving the desired oxidation rates.[5,325] An alternative to this approach is to develop protective oxidation-resistant coatings.[1,326] Oxidation-resistant coatings being considered would need to undergo extensive testing to determine their thermal stability at high temperatures, resistance to radiation damage, and its ability to adhere to the Zircaloy cladding. One coating that has been investigated is that of TiAlN, as it forms a dense layer of Al_2O_3 at the surface of the Zircaloy. The layer of Al_2O_3 reduces oxygen diffusion by orders of magnitude compared to the zirconium oxide layer formed in current systems.[327,328] Additionally, TiAlN, with a monolayer of TiN, has been shown to adhere to the ZIRLO^{TM} cladding.[1,329] Further investigations into the thickness of the layers have been carried out.[329]

Another study investigated a FeAlCr coating which inhibited the formation of zirconia, and in its place, Al_2O_3 formed at the surface. Alat et al.,[1,329] showed that this oxide layer reduced the mobility of oxygen at the surface.[330] Several other studies have been carried out which investigate the coatings of Ti,[331] Cr,[332,333] Ni,[334] Ti_2AlC,[335] CrN,[336] YSZ,[26] Cr_3Cr_2-

NiCr,[337] polycrystalline diamond,[338] multilayer Ti/TiN,[339] and multilayered Cr-Zr/Cr/Cr-N.[340] Many of these materials (Fe, Cr, and Ni) have been investigated as Zircaloy coatings for their alternative use as alloying elements to improve the corrosion resistance at high temperatures and their low absorption cross sections for thermal neutrons. The use of amorphous SiC as a coating is of special interest since it's a glass and thus has no grain boundaries. This means that corrosion at grain boundaries observed in crystalline oxide coatings, is non-existent in amorphous SiC.

Many of these studies suggested that these coatings be implemented into nuclear power plants, despite the fact that little has been done to investigate the thermal conductivity, mechanical properties, and neutron economies under degradation induced by irradiation.[341] Additionally, the thermal expansion coefficients of the oxide layer would need to match that of the Zircaloy in order to minimize interfacial stresses.[5]

A.2 SiC and SiC Composites

SiC is being considered as an alternative cladding material to replace Zircaloy due to its high thermal conductivity, strength, and melting temperature, as well as improved oxidation resistance, low chemical activity, and low neutron absorption cross section. It also retains its strength at high temperatures (<2000 °C), unlike Zircaloy claddings. Early testing indicates that these materials could increase the safety margins of current nuclear reactors and reduce the complications that come with nuclear-related accidents such as reactivity-initiated accidents (RIAs), loss-of-coolant accidents (LOCAs), partial-cooling mismatches (PCMs), and hydrogen generation.[11,342-345] However, it can be challenging to manufacture at high densities due to the strong covalent bonding. Several techniques have been developed in order to make the SiC matrix more theoretically dense. Sintering of hot SiC with additives leaves the material very porous with reduced thermal conductivity and oxidation resistance at high temperatures. A popular form of SiC is obtained from a process known as Nano Infiltration Transient Eutectic Phase, which uses nano SiC powder with sintering additives such as alumina, yttria, and silica, to form the liquid phase under the sintering process. This allows for the creation of a densified SiC matrix.[346]

Another common form of SiC is from the chemical vapor deposition (CVD) process which produces a very pure material that provides hardness and increased thermal conductivity.[347] When sintering is used on hot SiC, various additives make the matrix less

dense. Porous SiC does not have the heightened oxidation resistance at high temperatures when compared to CVD SiC.[348]

The Massachusetts Institute of Technology is investigating a SiC-based fuel cladding with an inner monolith of high-density SiC, a continuous SiC fiber-reinforced SiC matrix, and an environmental barrier coating. The study of this material showed that corrosion rates and swelling were acceptable under irradiation, but that the strength and thermal diffusivities decreased.[349,350]

Several other studies have investigated SiC and SiC-based composites to determine its feasibility to replace Zircaloy claddings. Kawaharada et al.[351] tested CVD SiC in high-temperature steam environments and found that the corrosion rate of SiC was 1/1000th of Zr-2. They found that corrosion behavior is highly dependent on the fabrication process, and found that ions were ineffective at affecting the corrosion rate.[351] Yueh et al.[352] found that SiC was highly susceptible to irradiation-induced swelling, but was resistant to fragmentation. Lorrette et al.[353] investigated CVD in steam environments and found that the integrity of SiC/SiC composite were not affected after oxidation at high temperature water and steam environments, but fractures were observed at temperatures of 1400 °C. Despite the low thermal conductivity of irradiated SiC, its high oxidation and radiation resistance, and low absorption cross sections for thermal neutrons, makes it a good candidate for accident tolerant claddings.[5,354]

A.3 Fe Alloys and Stainless Steels

Various ferritic alloys and stainless steels with oxide additives have been investigated as candidates for accident-tolerant cladding materials. Stainless steels such as 310SS provide oxidation resistance two orders of magnitude better than Zircaloy claddings due to the formation of Cr_2O_3 in steam. However, the neutronic penalty associated with Ni in 310SS presents challenges that must be overcome before it can be used as an accident-tolerant cladding material.[324]

Ferritic alloys have also been investigated but showed that the content of Cr required would lead to accelerated embrittlement, which is undesirable for accident scenarios. Despite the advantages associated with the formation of the thin Cr_2O_3 layer which reduces oxidation, both ferritic alloys and 310SS are not considered primary candidates for accident-tolerant claddings.[324] Other studies have found significant challenges that must be overcome.

For instance, George et al.[354] found that in order to match lifetime requirements of the UO_2 fuel, the thickness of FeCrAl and 310SS would have to be reduced by half. The other option would require increasing the enrichment by 1-1.5%, which would exceed current licensed limits. The study also showed that FeCrAl and 310SS have higher neutron absorption cross sections than Zr alloys, and yielded a harder neutron spectrum.[354]

Brown et al.[355] found that FeCrAl alloys had higher thermal expansion rates than Zr and SiC claddings, resulting in PCI sooner. Another study showed that monolithic FeCrAl cladding would increase fission gas release and fuel temperature; however, they argued that the higher strength, enhanced corrosion resistance, and improved embrittlement properties, which allow for the fabrication of the cladding with thinner walls, should make Cr_2O_3 forming alloys a candidate for accident-tolerant claddings.[356]

Another class of materials being considered are referred to as oxide-dispersion strengthened (ODS) steels. ODS steels are well known for their resistance to radiation damage and their stability at high temperatures, thereby making them good candidates for fusion reactors and the next generation of fission reactors.[357,358]

While FeCrAl alloys are primarily being considered for their oxidation resistance and desirable mechanical properties, ODS FeCrAl alloys have higher strength as well as improved radiation tolerance. Like the regular FeCrAl alloy, ODS FeCrAl alloys are designed with enough Cr and Al to form a protective Al_2O_3 layer, and reduce oxidation.[359] Common constituents of ODS steels include fine yttria particles due to their high temperature creep strength, high thermal conductivity, and high thermodynamically stability,[25,307,358] as well as chromia, yttrium titanate, and alumina.[357]

B Accident Tolerant Fuels

Two different ATFs are discussed in this section; namely the U-Mo metal fuel, and microencapsulated fuel pellets. Both concepts are briefly reviewed in the following sections.

B.1 U-Mo

Under development at PNNL, U-Mo offers the possibility of using a metal fuel, which would provide higher power densities, burnups, and linear heating rates. This ATF concept also incorporates innovative accident-tolerant claddings that are also being developed. Included in the design is a triple co-extruded fuel system consisting of an annular U-Mo fuel slug, surrounded by a layer such as niobium to reduce corrosion, and an accident-tolerant cladding, such as FeCrAl alloy.[360] The central void is used to help contain fission gas release and swelling. A schematic of the ATF design is shown in Fig. B.1.

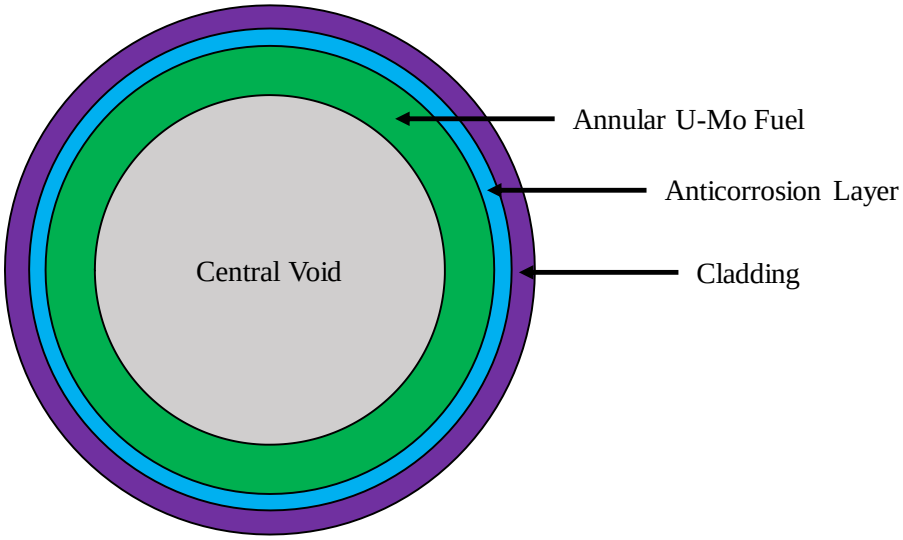

Figure B.1: Cross-section of the annular U-Mo metal fuel ATF design.

Other advantages of the U-Mo fuel concept include high thermal conductivity and uranium atom density, and low heat capacity. Design requirements regarding the fuel rods and assembly are met with this fuel, while providing enhanced mechanical performance during normal operating conditions. Due to the better thermal properties of this fuel compared to UO_2, the reduced stored energy may reduce the temperature of the core below 500-600°C during the initial phase of a LOCA.[361]

B.2 Microencapsulated Fuel Pellet

The fully ceramic micro-encapsulated (FCM) matrix with TRISO fuel particles is another ATF under consideration for future nuclear reactors.[18] A schematic of the TRISO fuel particle is shown in Fig. B.2. The focus of the FCM is to use the outer shell of the TRISO fuel particle, comprised of SiC, to act as a barrier to fission products. In addition to this barrier, the particles are contained within a dense SiC matric that provides high thermal conductivity, structural stability, and heat capacity, which allows the reactor to operate at a much lower temperature compared to the standard UO_2-Zircaloy system.[18,23]

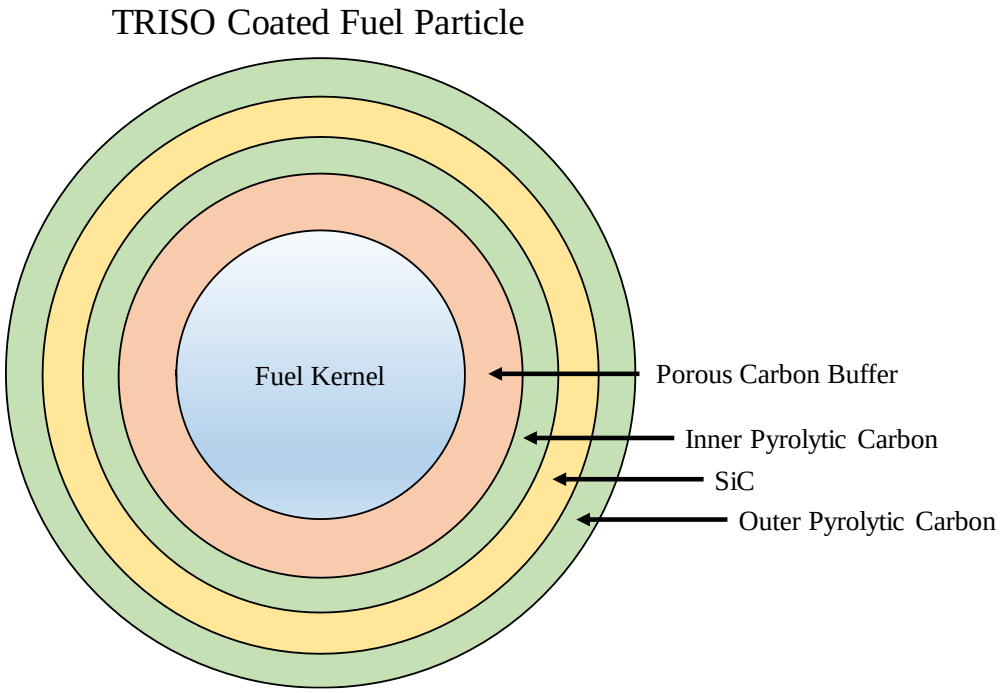

Figure B.2: Cross-section of a TRISO coated fuel particle.

Due to the containment of fission products, there should be a large reduction in fuel swelling which would reduce or eliminate the need for a gap between the fuel and cladding. The FCM design also reduces the chances for hydrogen explosions resulting from the oxidation of the zirconium cladding, as seen in the Fukushima Daiichi accident. Not only does this design improve thermo-mechanical properties, but it reduces the generation of hydrogen and improves reaction kinetics with steam.[23]

Snead et al.[24] showed that the FCM also has decreased irradiation-induced swelling, compared to UO_2 fuel, but that one of the challenges that arises is that the enrichment of the

^{235}U would need to be increased, to account for the ^{235}U mass reduction. Additionally, in order for this concept to ever be used inside a reactor, a wealth of knowledge would need to be provided in order to ensure it provides sufficient reliability and safety under design-basis accident scenarios.

C Advanced Doped Pellet Technology (ADOPT) Fuel

Large grains of UO_2 have been considered as a method to reduce fission gas release and intergranular bubble swelling at high burnups due to the longer distances the fission gases must travel to reach the grain boundary.[19] Another advantage includes the ability of the oxide nanoparticles to pin dislocations and trap radiation-induced defects, to improve the fuel's mechanical strength, creep resistance and radiation tolerance.

After the benefits of Cr_2O_3 and Al_2O_3 nanoparticles were discovered, many other oxide nanoparticles have also been investigated. The addition of Al_2O_3-SiO_2 nanoparticles (0.1 – 0.2 wt. %) to the UO_2 fuel have had similar effects, and SiO_2 and TiO_2 have been shown to reduce Zircaloy cladding strain during reactor operation.[12,19,362,363]

The effects of the Cr_2O_3, Al_2O_3, SiO_2, and MgO nanoparticles on increasing the retention of fission gases in nuclear fuel matrices have been investigated.[14] The SiO_2 nanoparticles yield an order of magnitude smaller diffusion coefficient for Xenon than in the un-doped UO_2 fuel over a range of temperatures. On the other hand, MgO and Al_2O_3 had no effect on the diffusion coefficient of the fission gases.[14] The BeO additive has been shown to enhance the thermal conductivity of UO_2, which reduces the temperature, and hence increases the retention of fission gasses.[364]

Another study investigated the effect of some of these oxide nanoparticles on the deformation of the UO_2 fuel. Koo et al.[12] have shown that UO_2 pellets with SiO_2-TiO_2 and SiO_2-TiO_2-Al_2O_3 additives deform relatively easier, potentially decreasing the cladding strain during the reactor operation. Une et al.[19] have shown that small amounts (0.025 – 0.25 wt.%) of aluminum-silicate nanoparticles with 60 wt.% SiO_2 and 40 wt.% Al_2O_3, make it possible to use large grain with higher density, without compromising the structure strength of the UO_2 fuel. This occurs during sintering because the alumino-silicate segregates at the grain boundaries, forming a liquid phase, which leads to enhanced grain growth. In addition, Matsunaga et al.[365] have suggested that Al-Si-O additives could chemically trap Cs fission products by forming stable cesium silicate. Thus, the chemically stable oxides of MgO, BeO, SiO_2, TiO_2, Al_2O_3, and Cr_2O_3 are all promising additives to the UO_2 fuel matrix for future LWRs.

D Molecular Dynamics

Both *ab initio* and classic MD can be used to model atom-atom interactions. A brief history of the development of each is provided.

D.1 Ab Initio Molecular Dynamics

The AIMD simulation method models atom-atom interactions by performing "on-the-fly" electronic structure calculations to determine the forces acting on the nuclei and calculates the trajectories for all atoms. The electronic structure calculations originate from the TDSE, which, except for the simplest of systems, cannot be solved analytically.[83] This has led to the development of several approximations to facilitate integrating the electronic degrees of freedom. These approximations are those proposed by Ehrenfest,[366] Born-Oppenheimer,[367] and Car-Parrinello.[368] The Ehrenfest approximation was the first to be introduced to solve the TDSE by treating the nuclei as classical particles and the electrons quantum mechanically.[366] A self-consistent optimization of the initial wave function at the start of the simulation and propagation of the minimized wave function results in a smoothly evolving electron subsystem. However, with explicit electron dynamics, the selected time step in the simulations needs to be small enough to provide accurate results. Later, Born and Oppenheimer postulated that since electrons move much faster than their nuclei, they could be assumed to react instantaneously to the motion of the nuclei.[367] The assumption effectively disregards the electronic dynamics with respect to the motion of the nuclei, thus a much larger time step can be used in the simulation. Unfortunately, this approach requires solving the static electronic structure for the fixed nuclei at each time step, which slows down the simulation significantly. Car-Parrinello[368] combined the advantages of Ehrenfest and Born-Oppenheimer MD into a unified approach. This approach has generated the most interest and has been widely used in AIMD simulations.

The history of AIMD provides an exhaustive list of reported applications, including modeling surfaces, interfaces, adsorbates, glasses, and materials at extreme temperatures and pressures. Marx and Jürg have recently published a thorough review of the subject.[369] The primary limitations of AIMD are the system sizes. Even with the most advanced supercomputers, it is difficult to find studies that have investigated atomic configurations with AIMD for more than a few hundred atoms. For this reason, the only properties that AIMD can currently model must have time scales smaller than that of current AIMD

limitations, and characteristic lengths that are within the system sizes that are reasonable to model. This precludes the observation of radiation damage cascades, as they often require hundreds of thousands to billions of atoms, depending on the PKA energy. An alternative to AIMD is classical MD, reviewed next.

D.2 Classical Molecular Dynamics

MD simulations generate trajectories by numerically integrating Newton's equations of motion. The atom-atom interactions are characterized by interatomic "potentials" (also known as force fields). These potentials are typically fitted to experimental data or high-level AIMD simulation results. Alder and Wainwright, pioneers in the field of MD, have studied the interaction of hard spheres in the late 1950s.[84,85] However, it was not until 1964 that the first potential to produce realistic and accurate results was used to model liquid argon.[86] Still, the first credible and realistic simulation to accurately reproduce the water properties did not take place until 1974.[87]

These early successes with MD simulation have inspired the development of an exhaustive list of potentials. They are classified as pair and many-body potentials, with terms that account for the various interactions such as van der Waals, Coulomb, bond, bend, and dihedral angle.[88] The many different ways proposed for expressing these interactions resulted in a diverse list of potentials. For instance, incorporating Coulomb interactions with fixed charges is typically associated with solvers such as EWALD[89] or particle-particle particle-mesh (PPPM).[90] However, some authors use dynamics charges, which often incorporate the electronegativity equilibration (QEq) scheme (or a derivative) developed by Rappé & Goddard,[91] and allow for calculating the self-charges on the atoms. Still, some authors elected to neglect the Coulomb interactions altogether in simulations that do not require them or in order to reduce the computation time of the simulation. The inclusion of other terms, often expressed in various ways, further complicates the selection process of a potential. Choosing between a pair-potential and a many-body potential, or the manner in which Coulomb interactions are handled, is often a compromise between accuracy, transferability, and computational cost.

MD simulations also have their own shortcomings. An example is the limited transferability to various regions of the phase diagram. This is because the selected potential in the simulation was not fitted to experimental data in these regions. In addition, the changes

in the chemical bonding are not accurately modeled because of neglecting the effects of quantum chemical electronic polarization. When the materials undergo transformations to other polymorphs, the empirically derived potentials do not perform well because the parameters do not fit the new material. The QEq[91] empirical scheme attempts to mitigate this concern, but it does not express transformations as accurately as AIMD. Another concern with MD arises when several materials are incorporated into a single model or when many-body effects are included. Both cases increase the computational cost, in terms of computation time and hardware requirements, and could impede the chance to obtain acceptable results in a reasonable timeframe.

Notwithstanding the aforementioned limitations, MD simulations are renowned in their ability to effectively describe atom-atom interactions. Successful applications have been reported to all sorts of materials, including carbon nanotubes, biomolecules, hydrocarbons, and metallic oxides to name a few. For this reason, MD simulations have been used extensively to investigate the radiation damage cascades in materials, and to determine the number and types of defects produced.

D.2.1 Interatomic Potentials

While the extensive review of interatomic potentials discussed in this section was inspired for modeling SiO_2, all of these potentials have been fitted for modeling countless materials. Understanding the physics incorporated into each potential helps assess which ones would be appropriate for modeling radiation effects.

In order to assess the ability of a given potential to model silica, it is essential to understand the underlying physics of the terms they include. Some of the potentials do not incorporate the necessary physics to model certain properties. Potentials generally take the form of one-body, two-body, or three-body, etc. contributions, as follows:

$$E(1,\dots,N) = \sum_{i} v_1(i) + \sum_{\substack{i,j \\ i<j}} v_2(i,j) + \sum_{\substack{i,j,k \\ i<j<k}} v_3(i,j,k) + \cdots + v_N(1,\dots,N) \qquad \text{Eq. D.1}$$

Many potentials neglect the first order term that describes external forces, such as from a container wall. However, a choice is based on whether to use a simple two-body potential (pair-potential) or to include many-body effects, which can affect the results and

computational time. The inclusion or exclusion of terms is generally a compromise between accuracy, transferability, and computational time.

D.2.1.1 Pair Potentials

Pair potentials construct the potential energy surface of the additive contributions from pairs of atoms. These types of potentials, which comprise two components: short-range (E_s) and long-range (E_l) interactions, are expressed as:

$$E(r) = E_s + E_l \qquad \text{Eq. D.2}$$

One of the most simple and commonly used pair potentials is Lennard-Jones (LJ or 12-6),[230] expressed as:

$$E(r) = 4\epsilon\left[\left(\frac{\sigma}{r_{ij}}\right)^{12} - \left(\frac{\sigma}{r_{ij}}\right)^{6}\right] \qquad \text{Eq. D.3}$$

In this expression, r^{-12} in the first term describes the repulsive forces due to overlapping orbits of electrons and the r^{-6} in the second term describes the attractive short-range van der Waals forces. Limitations of the LJ potential include divergence as the atoms approach each other, and the absence of bond directionality. Despite these limitations, the LJ potential has been widely used in MD. It has inspired other potential forms. One commonly used potential is that of Born and Mayer,[233] often referred to as the Born-Mayer potential. This potential, with a simple exponential term for short-range repulsion was used when ions have small polarizabilities. It is expressed as:

$$E_{ij} = A_{ij}\exp(-b_{ij}r_{ij}) \qquad \text{Eq. D.4a}$$

It is alternatively expressed as:

$$E_{ij} = A_{ij}\exp\left(\frac{-r_{ij}}{\rho_{ij}}\right) \qquad \text{Eq. D.4b}$$

In 1938, the popular Buckingham potential,[233] a modification of the Lennard-Jones potential, had been introduced. It added an attractive dispersion term to account for the van der Waals short-range interactions. This potential allows parameters to be fitted to three physical properties, instead of two, and is expressed as:

$$E_{ij} = A_{ij}\exp\left(\frac{-r_{ij}}{\rho_{ij}}\right) - \frac{C_{ij}}{r_{ij}^{6}} \qquad \text{Eq. D.5}$$

The Buckingham potential is limited at close interatomic distances, where the power term overrides the exponential term, leading to unphysical fusion of atoms at high temperature

and/or pressure. This eventually gave rise to the Born-Mayer-Huggins (BHM) potential by Fumi and Tosi,[370,371] expressed as:

$$E_{ij} = A_{ij} \exp\left(\frac{\sigma - r_{ij}}{\rho_{ij}}\right) - \frac{C_{ij}}{r_{ij}^6} + \frac{J_{ij}}{r_{ij}^8} \qquad \text{Eq. D.6}$$

This potential reduces to that of the Buckingham potential, when σ and J_{ij} are both zero. Additionally, when C_{ij} is also zero, this potential reduces even further to the Born-Mayer form. Therefore, the Buckingham and Born-Mayer potentials are subsets of the BMH potential. The added repulsive term in the BMH potential has been modified by others in order to model silica at high temperature and/or pressure, and can take on slightly different forms.[152,372]

Woodcock et al.[204] have used a Born-Mayer potential with fixed point charges to create a suitable force field or potential for silica. Full charge of +4 and -2 were assigned to the silicon and oxygen atoms, respectively. While this potential paved the way to developing future BMH-type potentials, it is not in itself very accurate. Lasaga and Gibbs[205] have fitted a potential to ab initio data derived through the Hartree-Fock calculations. Tsuneyuki et al.[206] also used the ab initio Hartree-Fock calculations to empirically fit a potential for modeling four of the silica polymorphs. The potential used by Tsuneyuki et al.,[206] is expressed as:

$$E_{ij} = U_{ij}^{Coul}(r_{ij}) + f_0(b_i + b_j) * \exp\left[\frac{a_i + a_j - r_{ij}}{b_i + b_j}\right] - \frac{C_{ij}^0}{r_{ij}^6} \qquad \text{Eq. D.7}$$

Note that form for $U_{ij}^{Coul}(r)$ can be found in the original paper.[206] As seen in Equation (14), this potential includes a more complex exponential term that replaces the r^{-12} term in the LJ potential. This has led to one of the most widely used potentials for silica, often referred to as the BKS potential.[207] They noted that prior attempts[205,206] to fit a potential to AIMD calculations failed to accurately describe quartz when compared to strict fitting to experimental data.

The ab initio calculations of small clusters could not simulate long times because the electronic structure theory is computationally expensive. Hence, van Beest et al.[207] have argued that experimental results need to be included in the fitting of the potential parameters. They performed ab initio calculations on small clusters of atoms coupled with experimental data to empirically obtain the potential parameters that are so widely used today. The BKS[207]

potential takes on the Buckingham form in Equation (8), with an additional first term to account for the Coulomb interactions, as shown below:

$$E_{ij} = \frac{q_i q_j}{r_{ij}} + A_{ij}\exp\left(\frac{-r_{ij}}{\rho_{ij}}\right) - \frac{C_{ij}}{r_{ij}^6} \qquad \text{Eq. D.8}$$

The Morse potential,[229] historically used to model covalently bonded systems, is expressed as:

$$E_{ij} = D_{ij}\left[1 - e^{-\alpha_{ij}(r_{ij}-r_0)}\right]^2 \qquad \text{Eq. D.9}$$

Another common potential form is known as the Morse-stretch potential. The difference between Morse and Morse-stretch potential is that the latter subtracts the D_{ij} term. Pedone et al.[217] have used the Morse-stretch potential to model several metallic oxides, while keeping the oxygen-oxygen interaction term constant. They coupled these parameters with a Columbic term for increased accuracy and a repulsive term for enhanced transferability. The repulsive term is needed in simulations involving high temperature and/or pressure. In general, the parameters in the Morse potential have physical meanings. For instance, the D_{ij}, α_{ij}, and r_0 terms represent the bond dissociation energy, a function of the slope of the potential energy well, and equilibrium bond length, respectively. However, by fitting the additional two terms within the Morse-stretch potential to existing experimental data, the physical meaning of the aforementioned Morse terms is irrelevant, and they can be now thought of as parameters. With the additional two terms, the Morse-stretch potential becomes:

$$E_{ij} = \frac{q_i q_j}{r_{ij}} + D_0\left\{\left[1 - e^{-\alpha_{ij}(r_{ij}-r_0)}\right]^2 - 1\right\} + \frac{F_{ij}}{r_{ij}^{12}} \qquad \text{Eq. D.10}$$

Demiralp et al.[211] have coupled the QEq[15] scheme with a Morse-stretch potential to model the quartz-stishovite phase transition and silica glass. Fluctuating charges promise better transferability by allowing individual atom charges to adjust to the local environment. They expressed their potential form as:

$$E_{ij} = D_1\left[e^{\gamma\left(1-\frac{r_{ij}}{r_0}\right)} - 2e^{\frac{\gamma}{2}\left(1-\frac{r_{ij}}{r_0}\right)}\right] \qquad \text{Eq. D.11}$$

Tangney and Scandolo[212] have modeled silica and also used the Morse-stretch form, but rather than using the QEq[91] method, they used the approach by Rowley et al.[235] to model dipole moments caused by the electrostatic and short-range repulsive forces.

The aforementioned potentials neglect the third order and higher terms, in order to reduce the computational time for a simulation. However, several potentials developed for modeling silica find higher order terms essential in modeling the properties of interest. These many-body potentials are reviewed next.

D.2.1.2 Many-Body Potentials

Tersoff[228] inspired the introduction of refined potentials for MD simulations of silica. He developed a potential that incorporates the dependence of bond order but does not account for Coulomb interactions. Instead, it describes covalent systems by means of the coordination number. Silicon has a varying degree of coordination, depending on the structure modeled. Increasing the coordination number of an atom nearly cancels the increase in the number of bonds. The Tersoff potential that describes the universal bonding behavior, is expressed as:

$$E_{ij} = \frac{1}{2}\{f_{ij}^{c}(r_{ij})[f_{ij}^{R}(r_{ij}) + b_{ij}f_{ij}^{A}(r_{ij})]\} \qquad \text{Eq. D.12}$$

where,

$$f_{ij}^{R}(r_{ij}) = G_{ij}\exp(-\lambda_{ij}r_{ij}), \qquad \text{Eq. D.2}$$

and,

$$f_{ij}^{A}(r_{ij}) = -H_{ij}\exp(-\mu_{ij}r_{ij}). \qquad \text{Eq. D.3}$$

This cutoff function is defined as:

$$f_{ij}^{c}(r_{ij}) = \begin{cases} 1, & \text{for} \quad r_{ij} < R_{ij} \\ \frac{1}{2} + \frac{1}{2}\cos\left(\pi\frac{r_{ij} - R_{ij}}{S_{ij} - R_{ij}}\right), & \text{for} \quad R_{ij} < r_{ij} < S_{ij} \\ 0, & \text{for} \quad r_{ij} > S_{ij} \end{cases} \qquad \text{Eq. D.4}$$

At first glance, this potential is similar to ones already discussed. The novelty is in the b_{ij} term, which incorporates the effects of bond order, and is expressed as:

$$b_{ij} = \chi_{ij}(1 + \beta_{i}^{n_i}\zeta_{ijk}^{n_i})^{\frac{-1}{2n_i}}, \qquad \text{Eq. D.16}$$

where, the symmetry function, ζ_{ijk}, is given as:

$$\zeta_{ijk} = \sum_{k\neq i,j} f^{c}(r_{ik})g(\theta_{ijk})\, e_{ijk}, \qquad \text{Eq. D.5}$$

e_{ijk} is expressed as:

$$e_{ijk} = \begin{cases} \exp\left[\lambda_3^3(r_{ij} - r_{ik})^3\right], & \text{For pure Si} \\ 1, & \text{For mixed Systems} \end{cases} \qquad \text{Eq. D.18}$$

and the angular function $g(\theta_{ijk})$ is expressed as:

$$g(\theta_{ijk}) = 1 + \frac{c_i^2}{d_i^2} - \frac{c_i^2}{d_i^2 + (h_i - \cos\theta_{ijk})^2} \qquad \text{Eq. D.19}$$

Although Tersoff's[228] work is parameterized only for silicon, it paved the way for a new approach for modeling atom-atom interactions. Yasukawa[209] noted that limitations of most potentials are in neglecting the bond order and charge transfer in ionic systems.

Recognizing that Tersoff[228] had taken the effects of the coordination number for silicon into account, Yasukawa[209] included parameters for oxygen and hydrogen as well. However, in modelling silica, Yasukawa found it essential to include the effects of charge transfer, and added some terms to account for these effects. Later, Yasukawa[214] modified these parameters to give better results. The final potential developed by Yasukawa is given as:

$$E_{ij} = \sum_i \left[E_i^S + \frac{1}{2} \sum_{j \neq i} V_{ij}(r_{ij}, q_i, q_j) \right] \qquad \text{Eq. D.20}$$

where E_i^S, the self-energy term, includes the effect of charge equilibration, similar to the QEq method developed by Rappé and Goddard.[91] This self-energy term represents the different charge states for an atom, and is expressed as:

$$E_i^S(q_i) = \chi_i q_i + \frac{1}{2} J_i q_i^2 \qquad \text{Eq. D.6}$$

The second term on the right hand side of Equation (28), consists of four separate contributions: repulsive energy, short-range attraction energy, ionic bond energy, and van der Waals energy. These terms are noted as:

$$V_{ij}(r_{ij}, q_i, q_j) = f_{ij}^R(r_{ij}) + f_{ij}^A(r_{ij}, q_i, q_j) + f_{ij}^I(r_{ij}, q_i, q_j) + f_{ij}^V(r_{ij}) \qquad \text{Eq. D.22}$$

where,

$$f_{ij}^R(r_{ij}) = f_{s_{ij}} Q_{ij} e^{\left(-\lambda_{ij}^0 r_{ij}\right)}, \qquad \text{Eq. D.23}$$

$$f_{ij}^A(r_{ij}, q_i, q_j) = -f_{s_{ij}} z_{ij} T_{ij} e^{\left(-\mu_{ij} r_{ij}\right)}, \qquad \text{Eq. D.24}$$

$$f_{ij}^I(r_{ij}, q_i, q_j) = \frac{f_{L_{ij}} \eta_i \eta_j q_i q_j}{4\pi\varepsilon_0 r_{ij}}, \qquad \text{Eq. D.25}$$

and

$$f_{ij}^{V}(r_{ij}) = \frac{f_{L_{ij}}\sqrt{C_{VDW_i}C_{VDW_j}}}{r_{ij}^{6}} \quad \text{Eq. D.26}$$

asukawa modified the exponential term in the original Tersoff potential),[228] to be expressed as:

$$e_{ijk}^{IJ} = \exp\left[\lambda_{ij}^{m_I}(r_{ij} - r_{ik})^{m_I}\right] \quad \text{Eq. D.27}$$

The additional parameter, m, is set to the original value of 3 for silicon, and 1 for elements other than silicon.

Yasukawa's work[209,214] inspired Yu et al.[220] to develop a charge-optimized many-body (COMB) potential (commonly referred to as COMB07) for Si/SiO_2 systems. They have found that some of the shortcomings of Yasukawa's potential was its inability to model charge neutrality as the lowest energy states for Si and SiO_2. Additionally, they found that Yasukawa's potential had difficulty modeling silica polymorphs and could not model a unimodal distribution for the bond length of Si-O. To alleviate these issues, Yu et al.[220] modified the Yasukawa[214] potential to be expressed as:

$$E = \sum_i \left[E_i^S + \frac{1}{2}\sum_{j\neq i} V_{ij}(r_{ij}, q_i, q_j) + E_i^{BB}\right] \quad \text{Eq. D.28}$$

The self-energy term (E_i^S) is modified, while keeping the effects of the modification on bulk silicon and silica to a minimum, as:

$$E_i^S(q_i) = \chi_i(q_i - q_o) + \frac{1}{2}J_i(q_i - q_o)^2 + J_{3\_i}(q_i - q_o)^3 + J_{4\_i}(q_i - q_o)^4 \quad \text{Eq. D.29}$$

Additionally, the COMB07[220] potential incorporated Si-O-Si and O-Si-O bond bending terms (E_i^{BB}) to accurately model silica polymorphs. These terms are expressed as:

$$E_{OSiO}^{BB} = \sum_i \sum_{j\neq i} \sum_{k\neq i,j} f_{c_{ij}} f_{c_{ik}} K_{OSiO}(\cos\theta_{OSiO} - \cos\theta_{OSiO}^0)^2 \quad \text{Eq. D.30}$$

$$E_{SiOSi}^{BB} = \sum_i \sum_{j\neq i} \sum_{k\neq i,j} f_{c_{ij}} f_{c_{ik}} K_{SiOSi}(\cos\theta_{SiOSi} - \cos\theta_{SiOSi}^0)^2 \quad \text{Eq. D.31}$$

Without these additional energy terms, α-cristobalite, instead of α-quartz, is predicted to be the most stable phase, which is unphysical.

The final modification that Yu et al.[220] made is the addition of a repulsion term to adjust the lattice constants and the cohesive energy so that they would line up more accurately with the experimental data. The added term is in the square brackets in the expression below:

$$f_{ij}^{R}(r_{ij}, q_i, q_j) = f_{s_{ij}} Q_{ij} e^{(-\lambda_{ij} r_{ij})} \left[1 + K_r \left(1 - \frac{r_{ij}}{r_{ij}^{0\prime}}\right)^2\right] \quad \text{Eq. D.32}$$

Shan et al.[221] have recently modified the COMB07 potential and named the new potential COMB10. The general form is the same as that for COMB07, but with some adjustments. For instance, they represented the ionic bond energy by a Coulomb integral over 1s-type Slater orbitals as:

$$f_{ij}^{I}(r_{ij}, q_i', q_j') = J_{ij}(r_{ij}) q_i' q_j', \quad \text{Eq. D.33}$$

where

$$J_{ij}(r_{ij}) = \int d^3 r_i \int d^3 r_j \rho_i(r_i, q_i') \rho_j(r_j, q_j')/r_{ij}, \quad \text{Eq. D.34}$$

and

$$\rho_i(r_i, q_i) = q_i \frac{\xi_i^3}{\pi} \exp(-2\xi_i |r_{ij} - r_i|) \quad \text{Eq. D.35}$$

To account for the changing ionic lattice field, they added a penalty function to the $E_i^S(q_i)$ term in Equation (37), expressed as:

$$V_i^S(r, q_j) = \frac{1}{4\pi\varepsilon_0} \sum_{j \neq i}^{NN} \left(\frac{\rho_1 q_j^2}{r_{ij}^5} - \frac{\rho_2 q_j}{r_{ij}^5}\right) \quad \text{Eq. D.36}$$

In addition, Shan et al.[221] have modified the bond bending functions by weakening the strength of the K_{OSiO} and K_{SiOSi} terms and neglecting the added repulsive term shown in the square brackets in equation 39. Ultimately, the COMB07[220] and COMB10[221] potential comprised of the following terms:

$$E_T = E^{self} + E^{Coul} + E^{vdW} + E^{bond} + E^{others} \quad \text{Eq. D.37}$$

A potential that has similar characteristics is the ReaxFF for Si/SiO_2 systems. It has been developed by van Duin et al.[232] and incorporates very similar physics to that of the COMB07 and COMB10 potentials. The ReaxFF potential is expressed as:

$$E_T = E^{self} + E^{Coul} + E^{vdW} + E^{bond} + E^{angle} + E^{torsion} + E^{conjugation} \quad \text{Eq. D.38}$$
$$+ E^{H-bond} + E^{lone-pair} + E^{over} + E^{under} + E^{others}$$

The first four terms (E^{self}, E^{Coul}, E^{vdW}, E^{bond}) in this potential are fundamentally the same as in the COMB07[220] and COMB10,[221] and incorporate the same physics. The terms: $E^{angle}, E^{torsion}, E^{over}, E^{under}, E^{conjugation}$ are incorporated implicitly in the E^{bond} term in the COMB07 and COMB10 potentials, while the ReaxFF potential includes them explicitly. The ReaxFF potential, as originally designed, does not use the QEq[91] method, but instead uses the electronegativity equalization method (EEM) developed by Mortier et al.[373] Since ReaxFF has such an exhaustive list of terms, each deals with several mathematical functions, these authors opt to point the reader to the original papers for details.[215,232] Later, Fogarty et al.[222] parameterized the ReaxFF potential for the silica-water interface, with the introduced modifications detailed in the original paper. Considering all of the terms included, it is fair to say that the ReaxFF potential intricately describes the various types of bonding but at a high computational cost.

Another branch off from the original Tersoff[228] potential is the potential introduced by Munetoh et al.[219] for SiO_2 systems. It has the same functional form as the Tersoff potential, but unlike other potentials based on Tersoff,[209,214,220,221] it does not take into account the Coulomb interactions. The authors stipulate that Coulomb interactions are too computationally expensive for large systems. All but two Si-Si parameters are the same as those used by Tersoff.[228] The other parameters that take oxygen interactions into account were fitted to experimental data, to reproduce the properties of Si_2OH_6, $Si_4O_4H_8$, $Si_2O_2H_2$, and $Si_6O_6H_{12}$ molecules. Umeno et al.[213] have used the Tersoff potential to model the Si/SiO_2 interface by fitting their potential to ab initio calculations. They noted that the rules of combination for parameters of different types of atoms performed poorly and thus they optimized each pair of atoms independently.

Billeter et al.[218] have derived an augmented Tersoff potential and made different modifications other than those of Yasukawa.[209,214] They noted that the e_{ijk} term did not produce accurate coordination numbers for systems that were not pure silicon. They mitigated this effect by using the characteristic length of different types of atoms and measuring the interatomic distance. They expressed the exponential in Eq. (25) as:

$$e_{ijk}^{IJK} = \exp\left[\left(\lambda_{ij} r_{ij} - \lambda_{ik} r_{ik}\right)^{m_I}\right] \qquad \text{Eq. D.39}$$

Billeter et al.[218] followed the efforts of Umeno et al.[213] in independently optimizing each pair of atoms to avoid poor parameterization due to differential bonding. In addition, since this

potential was designed to be highly transferable to a wide range of systems, the original energy expression in the Tersoff potential has been augmented, as follows:

$$E_{ij} = \frac{1}{2}\sum_{i\neq j}\{f_{ij}^{c}(r_{ij})[f_{ij}^{R}(r_{ij}) + b_{ij}f_{ij}^{A}(r_{ij})]\} + N_I \sum_I E_I^0, \quad \text{Eq. D.40}$$

where E_I^0 is the core energies and N_I is the number of atoms of the i^{th} element. Finally, in an attempt to reproduce the interface between silicon and its oxides, special consideration is given to addressing the over-coordination and under-coordination effects. These effects tend to create defects at interfaces due to the lack of symmetry. Therefore, Billeter et al.[218] added an additional penalty function, expressed as:

$$E_i^C = C_{I,1}\Delta z_i + C_{I,2}\Delta z_i^2, \quad \text{Eq. D.41}$$

where Δz_i is the difference between the expected and the actual coordination number.

A number of potentials for MD simulation of silica branches off the Stillinger-Weber (SW)[231] potential. As in the LJ potential, the energy and length units are assigned to ϵ and σ, respectively, however, the formulation of the SW potential is different and takes into account many-body interactions. The SW[231] potential is expressed as:

$$E_{ij} = \sum_i \sum_{j>i} \epsilon\, v_2(i,j) + \sum_i \sum_{j>i} \sum_{k>j} \epsilon v_3(i,j,k), \quad \text{Eq. D.42}$$

where the first term that accounts for the two-body interactions is expressed as:

$$v_2(r) = \begin{cases} W_{ij}\left(Y_{ij}r_{ij}^{-\rho_{ij}^0} - r_{ij}^{-q_{ij}^0}\right)\exp\left[\left(r_{ij}-a_0\right)^{-1}\right], r < a \\ 0, r \geq a \end{cases}, \quad \text{Eq. D.43}$$

The second term on the right hand side of Eq. (49) that accounts for many-body interactions is expressed as:

$$v_3(r_i, r_j, r_k) = h(r_{ij}, r_{ik}, \theta_{jik}) + h(r_{ji}, r_{jk}, \theta_{ijk}) + h(r_{ki}, r_{kj}, \theta_{ikj}) \quad \text{Eq. D.44}$$

In this expression, without loss of generality, h is expressed as:

$$h(r_{ij}, r_{ik}, \theta_{jik}) = \lambda^0 \exp\left[\gamma^0\left(r_{ij}-a_0\right)^{-1} + \gamma(r_{ik}-a_0)^{-1}\right] * \left(\cos\theta_{ijk} + \frac{1}{3}\right)^2 \quad \text{Eq. D.45}$$

The original SW[231] potential, parameterized for silicon, does not account for the Coulomb interactions, a distinct advantage for decreasing the computation time. In order to use this potential for modeling silica, it needs to be re-parameterized to include the oxygen (O) interactions.

Watanabe et al.[210] extended the SW potential for mixed Si and O systems, but neglected the charge effects as in the original paper by Stillinger & Weber.[231] Watanabe et al.[210] used their form of the SW potential to reproduce orders of stability for five silica polymorphs. Additionally, they claimed to be the first to describe the Si-SiO_2 interaction, essential due to the technological importance of the Si-SiO_2 interface. The two-body and three-body terms are the same except for the addition of a pre-factor, g_{ij}:

$$v_2(r) = \begin{cases} g_{ij}A(Br^{-\rho} - r^{-q})\exp\left[\left(r_{ij} - a_{ij}\right)^{-1}\right], & \text{for } (r < a) \\ 0, & \text{for } (r \geq a) \end{cases} \quad \text{Eq. D.46}$$

However, this newly defined pre-factor that only affects Si-O pairs, is given as:

$$g_{ij} = \begin{cases} g(z_i), & i = 0 \text{ and } j = Si \\ g(z_j), & i = Si \text{ and } j = 0 \\ 1, & \text{otherwise} \end{cases},$$

where,

$$g(z) = \frac{m_1}{\exp[(m_2 - z)/m_3] + 1}\exp[m_4(z - m_5)^2], \quad \text{Eq. D.47}$$

and,

$$z_i = \sum_{j=Si} f_{ij}^{c}. \quad \text{Eq. D.48}$$

In this expression, the cutoff function, f_c, forms bonds between Si and O, depending on the inter-atomic distance between them. Later, Watanabe et. al.[216] revised their original potential, as it poorly described silica structures that were compressively constrained. Also, their original potential showed an unphysical peak in the pair correlation function for amorphous silica.

Jiang and Brown[208] have developed a hybrid potential, a combination of the BKS[207] and SW[231] potentials, and fitted it to AIMD calculations. This potential is expressed as:

$$E_{ij} = \sum_i e_i(q_i') + \sum_i \sum_{j>i}\left[\epsilon v_2(i,j) + E_{ij}^{BKS}\right] + \sum_i \sum_{j>i} \sum_{k>j} \epsilon v_3(i,j,k), \quad \text{Eq. D.49}$$

where E_{ij}^{BKS} is the potential form used by van Beest et al.[207] in Equation (15) and $e_i(q_i)$ is the ionization energy contribution from each atom. Further details of modifications and an updated parameter list can be found.[208]

As indicated in this review, silica has been modeled with pair-potentials and many-body potentials. Each potential must determine how to account for Coulomb interactions. It is common to see no-charge, fixed-charge, and dynamic-charge potentials representing Coulomb interactions. Table D.2.1.1 presents the potentials for MD simulation of crystalline

silica, grouped as pair-potentials, many-body potentials, and according to how they handle Coulomb interactions. This Table helps identify which potential might take longer computation time, based on the physics it includes.

This section has thoroughly reviewed the underlying physics for the different potentials with the goal of giving an understanding of the nature of different terms for modeling atom-atom interactions. There are five essential root potentials that led to the potentials reviewed in this paper for modeling crystalline silica, each with different terms and atom-atom characterizations. The influence of the root potentials are briefly summarized below.

The Tersoff[228] root potential, a three-body potential, models atom-atom interactions by characterizing the strength of bonds given the coordination number of the atoms. It was originally parameterized for silicon, but has inspired many bond-order, variable charge potentials[209,214,220,221] as well as other non-charge potentials that were all used to model silica.[213,218,219]

The Stillinger-Weber[231] root potential characterizes atom energies from the sum of two-body and three-body interactions. The two-body term is solely a function of distance, and the three-body term incorporates the rotational and translational symmetry. Like Tersoff,[228] this root potential was originally designed for modeling silicon. However, Watanabe et al.[210,216] made slight modifications and parameterized the SW potential for silica.

The Morse[229] root potential led to the widely transferable and fixed-charge Morse-stretch potential by Pedone et al.[217] that can model several metallic oxides, while keeping the oxygen-oxygen term constant. This root potential has inspired other Morse-stretch potentials by Demiralp et al.[211] and Tangney & Scandolo[212] that used the approaches by Rappé & Goddard[91] and Rowley et al.[235] respectively, to model the effects of charge-transfer.

The Lennard-Jones[230] root potential is similar to the Morse root potential in that they both express atom-atom interactions with pair-potentials, albeit with different terms. However, this root potential has led to the development of the fixed-charge, BMH potentials such as the ones by Tsuneyuki et al.[206] and van Beest et al.[207] that are widely used today. A hybrid potential by Jiang & Brown[208] utilized the potential forms of van Beest et al.,[207] as well as of Stillinger & Weber.[231]

The ReaxFF root potential,[232] a bond-order, reactive potential (similar to COMB) allows atoms to determine their self-charge and local bonding environments. Both the ReaxFF and

COMB potentials have striking similarities and are powerful for modeling complex chemical behavior. A notable difference is that the ReaxFF models silica as a primarily covalent material, while COMB describes silica in terms of ionic charges. It is likely that at some point, these two potentials could merge into an even more powerful and transferable potential, paving the way for the next generation of bond-order potentials.[236] Going forward, the specific ReaxFF parameterization used in this paper is the one by Fogarty et al.,[222] used to model the silica-water interface. Its easy implementation is due to the work of Aktulga et al.[286]

Table D.2.1.1.1: This presents the potentials by arranging them according to whether they incorporate two-body or many-body terms, and according to how they each deal with Coulomb interactions.

Treatment of Coulomb Interactions	**Two-Body Potentials**	**Many-Body Potentials**
No Charge	N/A	Watanabe et al.[39] Umeno et al.[42] Watanabe et al.[45] Munetoh et al.[48]
Fixed Charge	Woodcock et al.[31] Lasaga & Gibbs[33] Tsuneyuki et al.[34] van Beest et al.[36] Pedone et al.[46]	Jiang & Brown[37]
Dynamic Charge	Demiralp et al.[40] Tangney & Scandolo[41]	Yasukawa[38] Yasukawa[43] van Duin et al.[44] Yu et al.[49] Shan et al.[50] Fogarty et al.[51]

Solely understanding the physics and some of the previously reported applications of each potential is not in itself adequate enough in determining the most appropriate potential for a given simulation. The accuracy, transferability, and computational cost are also essential in selecting the proper interatomic potential for the system of interest. An extensive review of these are discussed in this dissertation research.

E Experimental Techniques for Detecting and Measuring Radiation Damage

This section discusses various experimental techniques used to determine the irradiation effects of materials, including optical spectroscopy, EPR, and TEM.

E.1 Optical Spectroscopy

Optical Spectroscopy is one of the primary methods of detecting radiation damage in ceramics. The mechanisms behind this technique rely on the large band-gap of semiconductors. The general principle behind this technique involves transferring energy from a photon to an electron in the valence band. If the photon energy exceeds that of the bandgap energy, E_g, it moves to the conduction band. During this process, the photon is absorbed, resulting in the creation of an electron-hole pair. On the other hand, photons with energies smaller than E_g are not absorbed, and are transparent to light for wavelengths longer than $\frac{hc_o}{E_g}$.[94]

E.2 EPR

EPR, a technique which detects atoms that have unpaired electrons, is used to track free radicals in materials. The mechanism behind EPR is to detect radiation by paramagnetic systems, in the presence of an applied magnetic field. Its main applications are in biological systems, for measuring free radicals to determine biodosimetric assessments.[374] However, it has also been used to track Frenkel pairs in irradiated ZnSe.[96] Paramagnetic neutral anion vacancies with a trapped electron have been investigated in oxides like MgO and Al_2O_3, with both EPR and OA techniques.[375] However, similar to OA, if displacement damage does not occur on both sublattices, it can be challenging to observe any damage. A different technique that does not rely on paramagnetic defects to identify radiation damage is transmission electron microscopy (TEM), which is briefly reviewed next.

E.3 TEM

Of all of the experimental techniques used for observing radiation damage in materials, TEM is proving itself to be the gold standard by providing comprehensive data on the different types of defects in the material. Contrast mechanisms are utilized such as bright-field and dark-field images, which take advantage of the changes in diffraction due to the local defect strain field.[102] This type of method can help identify the extent of damage, and even identify types of defects, such as dislocation loops, stacking fault tetrahedra, cavities, voids, and bubbles.

English[376] used contrast techniques in the TEM to observe the effects of neutron irradiation at various temperatures in Cu, Mo, α-Fe, and Cu-Ge alloys. They found that there was a large degree of spatial variation of damaged regions, and that the extent of the damage was highly dependent on the material, temperature, and dose. Results showed that at high temperatures in copper, the primary mechanisms behind radiation damage was the formation of vacancies, which were dependent on the formation of stacking fault tetrahedra and voids.

Contrast mechanisms can typically give resolution that allows for identifying defects in the range of 1 nm. However, full characterization of defects is hard to achieve once the defects are smaller than 5 nm. The I^3TEM at Sandia National Laboratories, with state-of-the-art equipment, has managed to develop resolution that pushes these limits. For instance, Bufford et al.[377] investigated the changes in the microstructure of molybdenum under helium irradiation with the I^3TEM and were able to observe the formation of cavities that were 0.5 nm in diameter at a fluence of $1.7x10^{15}$ helium cm^{-2}. However, they found that these cavities did not continue to grow, despite increasing the fluence two orders of magnitude, and allowing for room temperature aging. Tougou et al.[378] investigated the effects of irradiation hardening due to cavity formation in BCC metals with in situ TEM. They found that screw dislocations formed and interacted with the cavities in molybdenum approximately 16-18% of the time.

While using TEM can provide unique insight into irradiation, there are limitations. For instance, the thin films used might not represent bulk material properties accurately, since the surface area to volume ratio is much higher in thin films. Additionally, with TEM, it is challenging to identify point defects, as resolution is usually on the order of nanometers. One recurring theme among experimental results is the inability to obtain resolution on the scale of the angstrom.

References

[1] E. Alat, A. T. Motta, R. J. Comstock, J. M. Partezana, and D. E. Wolfe, (2015) Surface and Coatings Technology **281** 133.

[2] D. Peng, X. Bai, F. Pan, H. Sun, and B. Chen, (2006) Vacuum **80** 530.

[3] C. Lemaignan and A. T. Motta, (1994) Materials science and technology.

[4] T. Cheng, J. R. Keiser, M. P. Brady, K. A. Terrani, and B. A. Pint, (2012) J Nucl Mater **427** 396.

[5] S. J. Zinkle, K. A. Terrani, J. C. Gehin, L. J. Ott, and L. L. Snead, (2014) J Nucl Mater **448** 374.

[6] H.-G. Kim, J.-H. Yang, W.-J. Kim, and Y.-H. Koo, (2016) Nuclear Engineering and Technology **48** 1.

[7] K. A. Terrani, S. J. Zinkle, and L. L. Snead, (2014) J Nucl Mater **448** 420.

[8] S. J. Zinkle and C. Kinoshita, (1997) J Nucl Mater **251** 200.

[9] B. A. Pint, K. A. Terrani, Y. Yamamoto, and L. L. Snead, (2015) Metall Mater Trans E **2** 190.

[10] Y. Yamamoto, B. A. Pint, K. A. Terrani, K. G. Field, Y. Yang, and L. L. Snead, (2015) J Nucl Mater **467** 703.

[11] L. L. Snead, K. A. Terrani, Y. Katoh, C. Silva, K. J. Leonard, and A. G. Perez-Bergquist, (2014) J Nucl Mater **448** 389.

[12] Y. H. Koo, J. H. Yang, J. Y. Park, K. S. Kim, H. G. Kim, D. J. Kim, Y. I. Jung, and K. W. Song, (2014) Nucl Technol **186** 295.

[13] J. Arborelius, K. Backman, L. Hallstadius, M. Limback, J. Nilsson, B. Rebensdorff, G. Zhou, K. Kitano, R. Lofstrom, and G. Ronnberg, (2006) J Nucl Sci Technol **43** 967.

[14] S. Kashibe and K. Une, (1998) J Nucl Mater **254** 234.

[15] K. Backman, L. Hallstadius, and G. Rönnberg, (2010) Advanced Fuel Pellet Materials and Fuel Rod Design for Water Cooled Reactors 117.

[16] H. Matzke, (1966) J Nucl Mater **20** 328.

[17] A. Stohl, P. Seibert, D. Wotawa, D. Arnold, J. F. Burkhart, S. Eckhardt, C. Tapia, A. Vargas, and T. J. Yasunari, (2012) Atmospheric Chemistry and Physics **12** 2313.

[18] L. J. Ott, K. R. Robb, and D. Wang, (2014) J Nucl Mater **448** 520.

[19] K. Une, M. Hirai, K. Nogita, T. Hosokawa, Y. Suzawa, S. Shimizu, and Y. Etoh, (2000) J Nucl Mater **278** 54.

[20] P. Yvon, Woodhead Publishing (2016).

[21] Y. Katoh, K. Ozawa, C. Shih, T. Nozawa, R. J. Shinavski, A. Hasegawa, and L. L. Snead, (2014) J Nucl Mater **448** 448.

[22] Y. Katoh, L. L. Snead, I. Szlufarska, and W. J. Weber, (2012) Curr Opin Solid St M **16** 143.

[23] J. J. Powers, W. J. Lee, F. Venneri, L. L. Snead, C. Jo, D. Hwang, J. Chun, Y. Kim, and K. A. Terrani, (2013) ORNL/TM-2013173 and KAERI/TR-5136/2013, Oak Ridge National Laboratory and Korea Atomic Energy Research Institute.

[24] L. Snead, K. Terrani, J. Kiggans, B. Pint, and Y. Katoh, Fully ceramic microencapsulated fuel design and irradiation testing. OECD/NEA Workshop on Accident Tolerant Fuels for LWRs, NEA Headquarters, Issy-les-Moulineaux, France, 2012.

[25] X. Xie, R. Kumar, J. Sun, and L. Henson, (2010) Journal of Power Sources **195** 5660.

[26] S. Rezaee, G. R. Rashed, and M. Golozar, (2013) International Journal of Corrosion **2013**.

[27] S. J. Park, J. P. Lee, J. S. Jang, H. Rhu, H. Yu, B. Y. You, C. S. Kim, K. J. Kim, Y. J. Cho, S. Baik, and W. Lee, (2013) Nanotechnology **24**.

[28] M. Schulz, (1999) Nature **399** 729.

[29] C. J. Cochrane and P. M. Lenahan, (2013) Appl Phys Lett **103** 053506.

[30] M. A. Hines, (2003) Annu Rev Phys Chem **54** 29.

[31] A. Rahnamoun and A. C. T. van Duin, (2014) J Phys Chem A **118** 2780.

[32] H. Q. Cao, X. Q. Qiu, L. A. Yu, M. J. Zhao, and Q. M. Zhu, (2006) Appl Phys Lett **88**.

[33] A. Chaudhari, R. D. Vispute, and H. Efstathiadis, (2014) Mater Lett **121** 47.

[34] R. A. Coward, C. R. Winkler, W. A. Hanson, M. L. Jablonski, and M. L. Taheri, (2015) J Nucl Mater **457** 298.

[35] K. Murty and I. Charit, (2008) J Nucl Mater **383** 189.

[36] L. B. B. Aji, J. B. Wallace, and S. O. Kucheyev, (2017) Scientific Reports **7**.

[37] A. Fissel, (2003) Phys Rep **379** 149.

[38] A. Ivekovic, S. Novak, G. Drazic, D. Blagoeva, and S. G. de Vicente, (2013) J Eur Ceram Soc **33** 1577.

[39] Y. H. Yun, Y. H. Park, M. Y. Ahn, and S. Cho, (2014) Ceram Int **40** 879.

[40] Y. Ma, X. L. Wang, Y. S. Jia, X. B. Chen, H. X. Han, and C. Li, (2014) Chem Rev **114** 9987.

[41] O. L. Bratus, A. A. Eytukh, O. S. Lytvyn, M. V. Voitovych, and V. O. Yukhymchuk, (2011) Semiconductor Physics, Quantum Electronics & Optoelectronics **14** 247.

[42] S. McKeever and M. Akselrod, (1999) Radiation protection dosimetry **84** 317.

[43] J. F. Ziegler and J. P. Biersack, Springer (1985).

[44] B. J. Cowen and M. S. El-Genk, (2017) Model Simul Mater Sc **25** 055001.

[45] B. Uberuaga, R. Smith, A. Cleave, G. Henkelman, R. Grimes, A. Voter, and K. Sickafus, (2005) Phys Rev B **71** 104102.

[46] B. Uberuaga, R. Smith, A. Cleave, F. Montalenti, G. Henkelman, R. Grimes, A. Voter, and K. Sickafus, (2004) Physical review letters **92** 115505.

[47] C. Zhang, W. Zhou, Y. Li, Z. Zeng, and X. Ju, (2015) J Nucl Mater **458** 138.

[48] K. Trachenko, E. Zarkadoula, I. Todorov, M. Dove, D. Dunstan, and K. Nordlund, (2012) Nuclear Instruments and Methods in Physics Research Section B: Beam Interactions with Materials and Atoms **277** 6.

[49] X. M. Bai and B. P. Uberuaga, (2012) Philos Mag **92** 1469.

[50] J. M. Delaye, S. Peuget, G. Bureau, and G. Calas, (2011) J Non-Cryst Solids **357** 2763.

[51] B. Wang, Y. T. Yu, I. Pignatelli, G. Sant, and M. Bauchy, (2015) J Chem Phys **143** 024505.

[52] B. J. Cowen and M. S. El-Genk, (2016) Comp Mater Sci **111** 269.

[53] B. J. Cowen and M. S. El-Genk, (2015) Comp Mater Sci **107** 88.

[54] B. J. Cowen and M. S. El-Genk, (2016) Comp Mater Sci **117** 164.

[55] M. Robinson, N. A. Marks, K. R. Whittle, and G. R. Lumpkin, (2012) Phys Rev B **85** 104105.

[56] M. Robinson, N. A. Marks, and G. R. Lumpkin, (2014) Mater Chem Phys **147** 311.

[57] L. A. Miller, D. K. Brice, A. K. Prinja, and S. T. Picraux, (1990) Defects in Materials **209** 171.

[58] B. Park, W. J. Weber, and L. R. Corrales, (2000) Nucl Instrum Meth B **166** 357.

[59] F. Mota, M. J. Caturla, J. M. Perlado, E. Dominguez, and A. Kubota, (2005) Fusion Eng Des **75-79** 1027.

[60] B. S. Thomas, N. A. Marks, L. R. Corrales, and R. Devanathan, (2005) Nucl Instrum Meth B **239** 191.

[61] A. El-Azab and N. M. Ghoniem, (1992) J Nucl Mater **191** 1110.

[62] F. Gao and D. J. Bacon, (1993) Philos Mag A **67** 289.

[63] F. Gao and D. J. Bacon, (1993) Philos Mag A **67** 275.

[64] R. Devanathan, T. D. de la Rubia, and W. J. Weber, (1998) J Nucl Mater **253** 47.

[65] R. Devanathan and W. J. Weber, (2000) J Nucl Mater **278** 258.

[66] W. Windl, T. J. Lenosky, J. D. Kress, and A. F. Voter, (1998) Nucl Instrum Meth B **141** 61.

[67] B. J. Cowen and M. S. El-Genk, (2018) Comp Mater Sci **151** 73.

[68] K. Trachenko, M. T. Dove, E. Artacho, I. T. Todorov, and W. Smith, (2006) Phys Rev B **73** 174207.

[69] D. J. Bacon and T. D. Delarubia, (1994) J Nucl Mater **216** 275.

[70] C. S. Becquart, C. Domain, A. Legris, and J. C. Van Duysen, (2000) J Nucl Mater **280** 73.

[71] C. L. Phillips, R. J. Magyar, and P. S. Crozier, (2010) J Chem Phys **133**.

[72] A. Dunn, R. Dingreville, E. Martínez, and L. Capolungo, (2016) Comp Mater Sci **120** 43.

[73] A. Dunn, B. Muntifering, R. Dingreville, K. Hattar, and L. Capolungo, (2016) J Nucl Mater **480** 129.

[74] G. D. Samolyuk, S. I. Golubov, Y. N. Osetsky, and R. E. Stoller, (2011) J Nucl Mater **418** 174.

[75] G. D. Samolyuk, Y. N. Osetsky, and R. E. Stoller, (2015) J Nucl Mater **465** 83.

[76] K. Hattar, D. C. Bufford, and D. L. Buller, (2014) Nucl Instrum Meth B **338** 56.

[77] G. Srinivas, D. E. Discher, and M. L. Klein, (2004) Nature materials **3** 638.

[78] M. L. Klein and W. Shinoda, (2008) Science **321** 798.

[79] M. S. Friedrichs, P. Eastman, V. Vaidyanathan, M. Houston, S. Legrand, A. L. Beberg, D. L. Ensign, C. M. Bruns, and V. S. Pande, (2009) Journal of computational chemistry **30** 864.

[80] W. Jiang, J. C. Phillips, L. Huang, M. Fajer, Y. Meng, J. C. Gumbart, Y. Luo, K. Schulten, and B. Roux, (2014) Comput Phys Commun **185** 908.

[81] I. Buch, T. Giorgino, and G. De Fabritiis, (2011) Proc Natl Acad Sci U S A **108** 10184.

[82] T. D. de la Rubia, H. M. Zbib, T. A. Khraishi, B. D. Wirth, M. Victoria, and M. J. Caturla, (2000) Nature **406** 871.

[83] T. Helgaker, P. Jorgensen, and J. Olsen, Wiley, New York, USA (2000).

[84] B. J. Alder and T. E. Wainright, (1957) J Chem Phys **27** 1208.

[85] B. J. Alder and T. E. Wainright, (1959) J Chem Phys **31** 459.

[86] A. Rahman, (1964) Phys Rev **136**.

[87] F. H. Stillinger and A. Rahman, (1974) J Chem Phys **60** 1545.

[88] M. E. Tuckerman, (2002) J Phys-Condens Mat **14** R1297.

[89] P. Ewald, (1921) Ann Phys **369** 253.

[90] R. W. Hockney, McGraw-Hill, New York, USA (1981).

[91] A. K. Rappé and W. A. Goddard, (1991) J Phys Chem-Us **95** 3358.

[92] P. D. Townsend, (1961) PhD Thesis, University of Reading.

[93] G. W. Arnold, (1965) Phys Rev **139** 1234.

[94] H. Zimmermann, (2010) Springer Ser Opt Sci **148** 1.

[95] Y. M. Abdulraheem, S. Ghoraishi, L. Arockia-Thai, S. K. Zachariah, and M. Ghannam, (2013) Adv Mater Sci Eng.

[96] G. D. Watkins, (1974) Physical review letters **33** 223.

[97] H. Von Bardeleben and J. Cantin, (1997) Brazilian Journal of Physics **27** 314.

[98] G. R. Piercy and J. L. Whitton, (1962) J I Met **90** 386.

[99] B. Hudson and B. E. Sheldon, (1973) J Microsc-Oxford **97** 113.

[100] L. W. Hobbs, (1979) Journal of the American Ceramic Society **62** 267.

[101] T. Hartmann, L. M. Wang, W. J. Weber, N. Yu, K. E. Sickafus, J. N. Mitchell, C. J. Wetteland, M. A. Nastasi, M. G. Hollander, N. P. Baker, C. R. Evans, J. R. Tesmer, and C. J. Maggiore, (1998) Nucl Instrum Meth B **141** 398.

[102] M. L. Jenkins, (1994) J Nucl Mater **216** 124.

[103] C. Liu, L. He, Y. Zhai, B. Tyburska-Püschel, P. Voyles, K. Sridharan, D. Morgan, and I. Szlufarska, (2017) Acta Mater **125** 377.

[104] G. W. Arnold, (1965) Phys Rev **140** A176.

[105] T. Sonoda, C. Kinoshita, and Y. Isobe, (1995) Ann Phys-Paris **20** 33.

[106] L. Kittiratanawasin, R. Smith, B. P. Uberuaga, and K. Sickafus, (2010) Nucl Instrum Meth B **268** 2901.

[107] K. J. Caulfield, R. Cooper, and J. F. Boas, (1995) Journal of the American Ceramic Society **78** 1054.

[108] J. L. Grant, R. Cooper, P. Zeglinski, and J. F. Boas, (1989) J Chem Phys **90** 807.

[109] J. Sharp and D. Rumsby, (1973) Radiation Effects **17** 65.

[110] G. P. Pells, (1982) Radiat Eff Defect S **64** 71.

[111] Y. Satoh, C. Kinoshita, and K. Nakai, (1991) J Nucl Mater **179** 399.

[112] Y. Chen, Truebloo.Dl, O. E. Schow, and H. T. Tohver, (1970) J Phys Part C Solid **3** 2501.

[113] D. Simeone, J. M. Costantini, L. Luneville, L. Desgranges, P. Trocellier, and P. Garcia, (2015) J Mater Res **30** 1495.

[114] R. S. Barnard, (1977) PhD Thesis, Case Western University.

[115] G. Das, (1983) J Mater Sci Lett **2** 453.

[116] P. Agnew, (1992) Philos Mag A **65** 355.

[117] G. P. Pells and D. C. Phillips, (1979) J Nucl Mater **80** 215.

[118] G. P. Pells and A. Y. Stathopoulos, (1983) Radiat Eff Defect S **74** 181.

[119] W. D. Compton and G. W. Arnold, (1961) Discuss Faraday Soc 130.

[120] R. E. Williford, R. Devanathan, and W. J. Weber, (1998) Nucl Instrum Meth B **141** 94.

[121] E. C. Buck, (1995) Radiat Eff Defect S **133** 141.

[122] M. S. Daw and M. I. Baskes, (1984) Phys Rev B **29** 6443.

[123] S. M. Foiles, M. I. Baskes, and M. S. Daw, (1986) Phys Rev B **33** 7983.

[124] M. Baskes, (1992) Phys Rev B **46** 2727.

[125] B.-J. Lee, M. Baskes, H. Kim, and Y. K. Cho, (2001) Phys Rev B **64** 184102.

[126] B.-J. Lee, J.-H. Shim, and M. Baskes, (2003) Phys Rev B **68** 144112.

[127] B. Jelinek, J. Houze, S. Kim, M. Horstemeyer, M. Baskes, and S.-G. Kim, (2007) Phys Rev B **75** 054106.

[128] A. Sand, S. Dudarev, and K. Nordlund, (2013) EPL (Europhysics Letters) **103** 46003.

[129] D. Bacon, F. Gao, and Y. N. Osetsky, (2000) J Nucl Mater **276** 1.

[130] M. Caturla, N. Soneda, E. Alonso, B. Wirth, T. D. de la Rubia, and J. Perlado, (2000) J Nucl Mater **276** 13.

[131] L. Malerba, (2006) J Nucl Mater **351** 28.

[132] J.-P. Crocombette and D. Ghaleb, (2001) J Nucl Mater **295** 167.

[133] M. G. Campbell, Q. Liu, A. Sanders, J. S. Evans, and I. I. Smalyukh, (2014) Materials **7** 3021.

[134] D. P. Yu, Q. L. Hang, Y. Ding, H. Z. Zhang, Z. G. Bai, J. J. Wang, Y. H. Zou, W. Qian, G. C. Xiong, and S. Q. Feng, (1998) Appl Phys Lett **73** 3076.

[135] L. Y. Jiang, H. Wu, W. Jia, and X. Y. Li, (2012) J Appl Phys **111** 023508.

[136] A. Steinfeld, (2005) Solar energy **78** 603.

[137] G. Zhang, W. Kataphinan, R. Teye-Mensah, P. Katta, L. Khatri, E. A. Evans, G. G. Chase, R. D. Ramsier, and D. H. Reneker, (2005) Mat Sci Eng B-Solid **116** 353.

[138] K. G. Field, I. Remec, and Y. Le Pape, (2015) Nuclear Engineering and Design **282** 126.

[139] Y. Le Pape, K. G. Field, and I. Remec, (2015) Nuclear Engineering and Design **282** 144.

[140] G. J. Youinou and R. S. Sen, (2014) Nucl Technol **188** 123.

[141] Z. Li and Y. Pan, Quartz: Deposits, Mineralogy and Analytics, First-principles calculations of the E′ 1 center in quartz: structural models, 29Si hyperfine parameters and association with Al impurity, Springer 161 (2012).

[142] R. Weeks, (1956) J Appl Phys **27** 1376.

[143] G. Pacchioni, L. Skuja, and D. Griscom, Springer Science & Business Media (2012) Ch. 3.

[144] R. I. Mashkovtsev and Y. M. Pan, (2011) Phys Chem Miner **38** 647.

[145] R. Devine, (1983) Appl Phys Lett **43** 1056.

[146] R. Devine and A. Golanski, (1984) J Appl Phys **55** 2738.

[147] R. Mashkovtsev and Y. Pan, (2016) EPL (Europhysics Letters) **113** 64004.

[148] R. I. Mashkovtsev and Y. Pan, in: B. Novack, P. Marek (Eds.), Nova Science Publishers, New York (2013) 65.

[149] A. Alessi, in: A. Lund, M. Shiotani (Eds.), Springer International Publishing, Cham (2014) 255.

[150] B. Wang, Y. Yu, Y. J. Lee, and M. Bauchy, (2015) Frontiers in Materials **2** 11.

[151] F. Yuan and L. Huang, (2014) Scientific reports **4** 5035.

[152] K. Vollmayr, W. Kob, and K. Binder, (1996) Phys Rev B **54** 15808.

[153] L. Levien, C. T. Prewitt, and D. J. Weidner, (1980) Am Mineral **65** 920.

[154] J. M. Perlado, L. Malerba, A. Sanchez-Rubio, and T. D. de la Rubia, (2000) J Nucl Mater **276** 235.

[155] L. Malerba and J. M. Perlado, (2002) Phys Rev B **65** 045202.

[156] J. M. Perlado, (1997) J Nucl Mater **251** 98.

[157] G. Lucas and L. Pizzagalli, (2005) Nucl Instrum Meth B **229** 359.

[158] A. A. Demkov, J. Ortega, O. F. Sankey, and M. P. Grumbach, (1995) Phys Rev B **52** 1618.

[159] F. Gao, E. J. Bylaska, W. J. Weber, and L. R. Corrales, (2001) Phys Rev B **64** 245208.

[160] F. Gao and W. J. Weber, (2000) Phys Rev B **63** 054101.

[161] F. Gao and W. J. Weber, (2002) Nucl Instrum Meth B **191** 504.

[162] R. Devanathan, W. Weber, and T. D. de La Rubia, (1998) Nuclear Instruments and Methods in Physics Research Section B: Beam Interactions with Materials and Atoms **141** 118.

[163] D. E. Farrell, N. Bernstein, and W. K. Liu, (2009) J Nucl Mater **385** 572.

[164] B. J. Cowen and M. S. El-Genk, (2017) Model Simul Mater Sc **25** 085009.

[165] C. Liu and I. Szlufarska, (2018) J Nucl Mater.

[166] N. Swaminathan, P. J. Kamenski, D. Morgan, and I. Szlufarska, (2010) Acta Mater **58** 2843.

[167] F. Gao, W. J. Weber, and R. Devanathan, (2001) Nuclear Instruments and Methods in Physics Research Section B: Beam Interactions with Materials and Atoms **180** 176.

[168] F. Gao, W. J. Weber, and W. Jiang, (2001) Phys Rev B **63**.

[169] R. Devanathan, W. J. Weber, and F. Gao, (2001) J Appl Phys **90** 2303.

[170] F. Gao and W. J. Weber, (2002) Phys Rev B **66**.

[171] L. Jamison, M.-J. Zheng, S. Shannon, T. Allen, D. Morgan, and I. Szlufarska, (2014) J Nucl Mater **445** 181.

[172] L. Jamison, K. Sridharan, S. Shannon, and I. Szlufarska, (2014) J Mater Res **29** 2871.

[173] I. T. Lu and M. Bernardi, (2017) Scientific Reports **7**.

[174] D. S. Aidhy, P. C. Millett, D. Wolf, S. R. Phillpot, and H. Huang, (2009) Scripta Materialia **60** 691.

[175] Y. J. Yin, N. Guo, C. X. Wang, and Q. Q. Rao, (2014) Ind Eng Chem Res **53** 14322.

[176] M. E. Taheri, A. Petala, Z. Frontistis, D. Mantzavinos, and D. I. Kondarides, (2017) Catal Today **280** 99.

[177] A. Petala, Z. Frontistis, M. Antonopoulou, I. Konstantinou, D. I. Kondarides, and D. Mantzavinos, (2015) Water Res **81** 157.

[178] W. Zhao, W. H. Ma, C. C. Chen, J. C. Zhao, and Z. G. Shuai, (2004) J Am Chem Soc **126** 4782.

[179] L. Zhao, M. Han, and H. Lian, (2008) Thin Solid Films **516** 3394.

[180] Y. G. Zhang, L. L. Ma, J. L. Li, and Y. Yu, (2007) Environ Sci Technol **41** 6264.

[181] H. Kawamura, E. Ishitsuka, K. Tsuchiya, M. Nakamichi, M. Uchida, H. Yamada, K. Nakamura, H. Ito, T. Nakazawa, H. Takahashi, S. Tanaka, N. Yoshida, S. Kato, and Y. Ito, (2003) Nuclear Fusion **43** 675.

[182] D. Mandal, M. R. K. Shenoi, and S. K. Ghosh, (2010) Fusion Eng Des **85** 819.

[183] D. Mandal, D. Sathiyamoorthy, and V. G. Rao, (2012) Fusion Eng Des **87** 7.

[184] G. Vitins, G. Kizane, A. Lusis, and J. Tiliks, (2002) J Solid State Electr **6** 311.

[185] J. Lian, L. M. Wang, K. Sun, and R. C. Ewing, (2009) Microsc Res Techniq **72** 165.

[186] Y. Chen, N. Li, D. C. Bufford, J. Li, K. Hattar, H. Wang, and X. Zhang, (2016) J Nucl Mater **475** 274.

[187] O. El-Atwani, A. Suslova, T. J. Novakowski, K. Hattar, M. Efe, S. S. Harilal, and A. Hassanein, (2015) Mater Charact **99** 68.

[188] J. M. Zhang, J. Lian, F. Namavar, J. W. Wang, H. Haider, K. Garvin, and R. C. Ewing, (2011) J Phys Chem C **115** 22755.

[189] J. Lian, J. Chen, L. M. Wang, R. C. Ewing, J. M. Farmer, L. A. Boatner, and K. B. Helean, (2003) Phys Rev B **68**.

[190] W. Jiang, H. Wang, I. Kim, Y. Zhang, and W. J. Weber, (2010) J Mater Res **25** 2341.

[191] W. Jiang, H. Wang, I. Kim, I. T. Bae, G. Li, P. Nachimuthu, Z. Zhu, Y. Zhang, and W. J. Weber, (2009) Phys Rev B **80**.

[192] L. Jamison, P. Xu, K. Sridharan, and T. Allen, Radiation resistance of nanocrystalline silicon carbide, Advances in Materials Science for Environmental and Nuclear Technology II-Materials Science and Technology 2010 Conference and Exhibition, MS and T'10, 2011, p. 161.

[193] H. Inui, H. Mori, and H. Fujita, (1990) Philosophical Magazine B **61** 107.

[194] H. Inui, H. Mori, A. Suzuki, and H. Fujita, (1992) Philosophical Magazine B **65** 1.

[195] Y. Zhang, M. Ishimaru, T. Varga, T. Oda, C. Hardiman, H. Xue, Y. Katoh, S. Shannon, and W. J. Weber, (2012) Phys Chem Chem Phys **14** 13429.

[196] Y. Katoh, L. Snead, and S. Golubov, (2008) Ceram Eng Sci Proc **28** 297.

[197] W. E. Carlos, N. Y. Garces, E. R. Glaser, and M. A. Fanton, (2006) Phys Rev B **74**.

[198] F. X. Li, M. Ishimaru, P. Lu, I. V. Afanasyev-Charkin, and K. E. Sickafus, (2000) Nucl Instrum Meth B **166** 314.

[199] W. J. Weber, R. C. Ewing, C. R. A. Catlow, T. D. de la Rubia, L. W. Hobbs, C. Kinoshita, H. Matzke, A. T. Motta, M. Nastasi, E. K. H. Salje, E. R. Vance, and S. J. Zinkle, (1998) J Mater Res **13** 1434.

[200] S. J. Zinkle and L. L. Snead, (1996) Nucl Instrum Meth B **116** 92.

[201] F. W. Clinard, G. F. Hurley, and L. W. Hobbs, (1982) J Nucl Mater **108** 655.

[202] J. D. Gale, (1996) Philos Mag B **73** 3.

[203] M. Schaible, (1999) Crit Rev Solid State **24** 265.

[204] L. V. Woodcock, (1976) J Chem Phys **65** 1565.

[205] A. C. Lasaga and G. V. Gibbs, (1987) Phys Chem Miner **14** 107.

[206] S. Tsuneyuki, M. Tsukada, H. Aoki, and Y. Matsui, (1988) Physical review letters **61** 869.

[207] B. W. van Beest, G. J. Kramer, and R. A. van Santen, (1990) Physical review letters **64** 1955.

[208] Z. Jiang and R. A. Brown, (1994) Chem Eng Sci **49** 2991.

[209] A. Yasukawa, (1996) Jsme Int J a-Mech M **39** 313.

[210] T. Watanabe, H. Fujiwara, H. Noguchi, T. Hoshino, and I. Ohdomari, (1999) Jpn J Appl Phys 2 **38** L366.

[211] E. Demiralp, T. Cagin, and W. A. Goddard, (1999) Physical review letters **82** 1708.

[212] P. Tangney and S. Scandolo, (2002) J Chem Phys **117** 8898.

[213] Y. Umeno, T. Kitamura, K. Date, M. Hayashi, and T. Iwasaki, (2002) Comp Mater Sci **25** 447.

[214] A. Yasukawa, (2003) JSME Int **71**.

[215] A. C. T. van Duin, A. Strachan, S. Stewman, Q. S. Zhang, X. Xu, and W. A. Goddard, (2003) J Phys Chem A **107** 3803.

[216] T. Watanabe, D. Yamasaki, K. Tatsumura, and I. Ohdomari, (2004) Appl Surf Sci **234** 207.

[217] A. Pedone, G. Malavasi, M. C. Menziani, A. N. Cormack, and U. Segre, (2006) J Phys Chem B **110** 11780.

[218] S. R. Billeter, A. Curioni, D. Fischer, and W. Andreoni, (2006) Phys Rev B **73**.

[219] S. Munetoh, T. Motooka, K. Moriguchi, and A. Shintani, (2007) Comp Mater Sci **39** 334.

[220] J. G. Yu, S. B. Sinnott, and S. R. Phillpot, (2007) Phys Rev B **75** 085311.

[221] T. R. Shan, B. D. Devine, J. M. Hawkins, A. Asthagiri, S. R. Phillpot, and S. B. Sinnott, (2010) Phys Rev B **82** 255.

[222] J. C. Fogarty, H. M. Aktulga, A. Y. Grama, A. C. T. van Duin, and S. A. Pandit, (2010) J Chem Phys **132** 174704.

[223] A. Carre, J. Horbach, S. Ispas, and W. Kob, (2008) Epl-Europhys Lett **82**.

[224] B. P. Feuston and S. H. Garofalini, (1988) J Chem Phys **89** 5818.

[225] J. G. Yu, S. R. Phillpot, and S. B. Sinnott, (2007) Phys Rev B **75**.

[226] A. Takada, P. Richet, C. R. A. Catlow, and G. D. Price, (2004) J Non-Cryst Solids **345** 224.

[227] K. P. Schroder and J. Sauer, (1996) J Phys Chem-Us **100** 11043.

[228] J. Tersoff, (1988) Phys Rev B **37** 6991.

[229] P. M. Morse, (1929) Phys Rev **34** 57.

[230] J. E. Jones, (1924) P R Soc Lond a-Conta **106** 463.

[231] F. H. Stillinger and T. A. Weber, (1985) Phys Rev B **31** 5262.

[232] A. C. T. van Duin, S. Dasgupta, F. Lorant, and W. A. Goddard, (2001) J Phys Chem A **105** 9396.

[233] M. Born and J. E. Mayer, (1932) Zeitschrift für Physik **75** 1.

[234] R. A. Buckingham, (1938) Proc R Soc Lon Ser-A **168** 264.

[235] A. J. Rowley, P. Jemmer, M. Wilson, and P. A. Madden, (1998) J Chem Phys **108** 10209.

[236] Y. K. Shin, T. R. Shan, T. Liang, M. J. Noordhoek, S. B. Sinnott, A. C. T. van Duin, and S. R. Phillpot, (2012) Mrs Bull **37** 504.

[237] P. Y. Huang, S. Kurasch, J. S. Alden, A. Shekhawat, A. A. Alemi, P. L. McEuen, J. P. Sethna, U. Kaiser, and D. A. Muller, (2013) Science **342** 224.

[238] Z. Y. Ong and E. Pop, (2010) Phys Rev B **81**.

[239] Z. Y. Ong, E. Pop, and J. Shiomi, (2011) Phys Rev B **84** 165418.

[240] S. Tsuneyuki, H. Aoki, M. Tsukada, and Y. Matsui, (1990) Physical review letters **64** 776.

[241] D. Herzbach, K. Binder, and M. H. Müser, (2005) J Chem Phys **123** 124711.

[242] D. J. Lacks and R. G. Gordon, (1993) J Geophys Res-Sol Ea **98** 22147.

[243] R. G. Gordon and Y. S. Kim, (1972) J Chem Phys **56** 3122.

[244] C. Muhlhausen and R. G. Gordon, (1981) Phys. Rev. B, Condens. Matter **23** 900.

[245] C. Muhlhausen and R. G. Gordon, (1981) Phys. Rev. B, Condens. Matter **24** 2147.

[246] T. F. Soules, G. H. Gilmer, M. J. Matthews, J. S. Stolken, and M. D. Feit, (2011) J Non-Cryst Solids **357** 1564.

[247] T. F. Soules, (1990) J Non-Cryst Solids **123** 48.

[248] J. S. Tse and D. D. Klug, (1991) J Chem Phys **95** 9176.

[249] S. Plimpton, (1995) J Comput Phys **117** 1.

[250] E. L. Pollock and J. Glosli, (1996) Comput Phys Commun **95** 93.

[251] D. R. Peacor, (1973) Z Kristallogr **138** 274.

[252] L. Levien and C. T. Prewitt, (1981) Am Mineral **66** 324.

[253] L. G. Liu, W. A. Bassett, and Takahash.T, (1974) J Geophys Res **79** 1160.

[254] E. Polak and G. Ribiere, (1969) ESAIM: Mathematical Modelling and Numerical Analysis-Modélisation Mathématique et Analyse Numérique **3** 35.

[255] E. Polak, Academic press (1971).

[256] E. G. Gamaly, (2011) Phys Rep **508** 91.

[257] S. E. Swanson and P. M. Fenn, (1986) Am Mineral **71** 331.

[258] H. E. Maclellan and L. T. Trembath, (1991) Am Mineral **76** 1291.

[259] I. Tajima, O. Asami, and E. Sugiura, (1998) Anal Chim Acta **365** 147.

[260] J. Fontanel, C. Andeen, and D. Schuele, (1974) J Appl Phys **45** 2852.

[261] E. K. Chang, M. Rohlfing, and S. G. Louie, (2000) Physical review letters **85** 2613.

[262] M. A. Carpenter, E. K. H. Salje, A. Graeme-Barber, B. Wruck, M. T. Dove, and K. S. Knight, (1998) Am Miner **83** 2.

[263] M. H. Müser and K. Binder, (2001) Phys Chem Miner **28** 746.

[264] Y. H. Cheng, N. D. Luo, X. J. Xie, M. Li, L. L. Jiang, and S. J. Yu, (2009) Icpadm 2009: Proceedings of the 9th International Conference on Properties and Applications of Dielectric Materials **1-3** 378.

[265] X. J. Xie, Y. H. Cheng, K. Wu, and B. Xiao, (2012) J Appl Phys **111** 104116.

[266] N. Binggeli and J. R. Chelikowsky, (1991) Nature **353** 344.

[267] C. Campana, M. H. Muser, J. S. Tse, D. Herzbach, and P. Schoffel, (2004) Phys Rev B **70**.

[268] J. Badro, J. L. Barrat, and P. Gillet, (1996) Physical review letters **76** 772.

[269] R. M. Hazen, L. W. Finger, R. J. Hemley, and H. K. Mao, (1989) Solid State Commun **72** 507.

[270] K. J. Kingma, R. J. Hemley, H. K. Mao, and D. R. Veblen, (1993) Physical review letters **70** 3927.

[271] J. Badro, D. M. Teter, R. T. Downs, P. Gillet, R. J. Hemley, and J. L. Barrat, (1997) Phys Rev B **56** 5797.

[272] I. P. Swainson and M. T. Dove, (1995) J Phys-Condens Mat **7** 1771.

[273] I. P. Swainson, M. T. Dove, and D. C. Palmer, (2003) Phys Chem Miner **30** 353.

[274] W. W. Schmahl, I. P. Swainson, M. T. Dove, and A. Graemebarber, (1992) Z Kristallogr **201** 125.

[275] H. Kimizuka, S. Ogata, and J. Li, (2008) J Appl Phys **103**.

[276] L. Coes, (1953) Science **118** 131.

[277] E. C. T. Chao, E. M. Shoemaker, and B. M. Madsen, (1960) Science **132** 220.

[278] E. C. T. Chao, J. J. Fahey, J. Littler, and D. J. Milton, (1962) Journal of Geophysical Research **67** 419.

[279] R. G. McQeen, J. N. Fritz, and S. P. Marsh, (1963) Journal of Geophysical Research **68** 2319.

[280] Y. Tsuchida and T. Yagi, (1989) Nature **340** 217.

[281] N. L. Ross, J. F. Shu, R. M. Hazen, and T. Gasparik, (1990) Am Mineral **75** 739.

[282] A. D. Kulkarni, D. G. Truhlar, S. G. Srinivasan, A. C. T. van Duin, P. Norman, and T. E. Schwartzentruber, (2013) J Phys Chem C **117** 258.

[283] S. Grazulis, D. Chateigner, R. T. Downs, A. F. T. Yokochi, M. Quiros, L. Lutterotti, E. Manakova, J. Butkus, P. Moeck, and A. Le Bail, (2009) J Appl Crystallogr **42** 726.

[284] S. Grazulis, A. Daskevic, A. Merkys, D. Chateigner, L. Lutterotti, M. Quiros, N. R. Serebryanaya, P. Moeck, R. T. Downs, and A. Le Bail, (2012) Nucleic Acids Res **40** D420.

[285] R. T. Downs and M. Hall-Wallace, (2003) Am Mineral **88** 247.

[286] H. M. Aktulga, J. C. Fogarty, S. A. Pandit, and A. Y. Grama, (2012) Parallel Comput **38** 245.

[287] E. Polak and G. Ribiere, (1969) Rev Fr Inform Rech O **3** 35.

[288] Y. H. Kim, M. S. Hwang, H. J. Kim, J. Y. Kim, and Y. Lee, (2001) J Appl Phys **90** 3367.

[289] L. G. Liu, W. A. Bassett, and T. Takahashi, (1974) Journal of Geophysical Research **79** 1160.

[290] K. Choudhary, T. Liang, A. Chernatynskiy, S. R. Phillpot, and S. B. Sinnott, (2015) J Phys-Condens Mat **27**.

[291] A. M. Logvinova, R. Wirth, N. V. Sobolev, Y. V. Seryotkin, E. S. Yefimova, C. Floss, and L. A. Taylor, (2008) Am Mineral **93** 685.

[292] J. Lewis, D. Schwarzenbach, and H. D. Flack, (1982) Acta Crystallogr A **38** 733.

[293] K. Sugiyama and Y. Takeuchi, (1991) Z Kristallogr **194** 305.

[294] H. Chikh, F. S. I. Ahmed, A. Afir, and A. Pialoux, (2016) J Alloy Compd **654** 509.

[295] A. Dymshits, P. Dorogokupets, I. Sharygin, K. Litasov, A. Shatskiy, S. Rashchenko, E. Ohtani, A. Suzuki, and Y. Higo, (2016) Phys Chem Miner **43** 447.

[296] R. M. Hazen, (1976) Am Mineral **61** 266.

[297] E. P. Meagher and G. A. Lager, (1979) Can Mineral **17** 77.

[298] R. M. HnzBnr, (1976) Am Mineral **61** 266.

[299] L. C. Ming and M. H. Manghnani, (1979) J Geophys Res **84** 4777.

[300] H. Hart and H. Drickamer, (1965) The Journal of Chemical Physics **43** 2265.

[301] E. A. Perez-Albuerne and H. G. Drickamer, (1965) J Chem Phys **43** 1381.

[302] F. Mota, M. J. Caturla, J. M. Perlado, E. Dominguez, and A. Kubota, (2004) J Nucl Mater **329** 1190.

[303] R. Devanathan, F. Gao, and W. J. Weber, (2007) Nucl Instrum Meth B **255** 130.

[304] A. Stukowski, (2010) Model Simul Mater Sc **18** 015012.

[305] F. Gao, H. Y. Xiao, and W. J. Weber, (2011) Nucl Instrum Meth B **269** 1693.

[306] J. F. Prins, (2000) Diam Relat Mater **9** 1835.

[307] M. Dholakia, G. Kaur, and M. C. Valsakumar, (2013) Solid State Physics, Vol 57 **1512** 1288.

[308] Y. Xiao, F. Fang, Z. Xu, and X. Hu, (2015) Appl Surf Sci **343** 56.

[309] E. Zarkadoula, S. Daraszewicz, D. Duffy, M. Seaton, I. Todorov, K. Nordlund, M. Dove, and K. Trachenko, (2013) Journal of Physics: Condensed Matter **25** 125402.

[310] S. P. Coleman, D. E. Spearot, and L. Capolungo, (2013) Model Simul Mater Sc **21**.

[311] U. Ayachit, The paraview guide: a parallel visualization application, 2015.

[312] F. X. Li, P. Lu, K. E. Sickafus, C. R. Evans, and M. Nastasi, (1999) Microstructural Processes in Irradiated Materials **540** 311.

[313] Electron Microscopy Sciences **https://www.emsdiasum.com/microscopy/products/films/silicone_nitride.aspx#DTF**.

[314] Kurt J. Lesker Company **http://www.lesker.com/newweb/deposition_materials/depositionmaterials_sputtertargets_1.cfm?pgid=ti4&highlight=EJTTIO2302A2**.

[315] R. E. Stoller, M. B. Toloczko, G. S. Was, A. G. Certain, S. Dwaraknath, and F. A. Garner, (2013) Nucl Instrum Meth B **310** 75.

[316] T. Geisler, K. Trachenko, S. Rios, M. T. Dove, and E. K. H. Salje, (2003) J Phys-Condens Mat **15** L597.

[317] K. Trachenko, M. T. Dove, and E. K. H. Salje, (2003) J Phys-Condens Mat **15** L1.

[318] S. J. Zinkle and B. N. Singh, (1993) J Nucl Mater **199** 173.

[319] M. Nastasi, Q. Su, L. Price, J. A. C. Santana, T. Y. Chen, R. Balerio, and L. Shao, (2015) J Nucl Mater **461** 200.

[320] H. Jiang, C. Jiang, D. Morgan, and I. Szlufarska, (2014) Comp Mater Sci **89** 182.

[321] G. V. Lewis and C. R. A. Catlow, (1985) J Phys C Solid State **18** 1149.

[322] M. S. El-Genk, K. Talaat, and B. J. Cowen, (2018) J Appl Phys **123**.

[323] E. D. Herderick, K. Cooper, and N. Ames, (2012) Advanced Materials & Processes **170** 24.

[324] B. A. Pint, K. A. Terrani, M. P. Brady, T. Cheng, and J. R. Keiser, (2013) J Nucl Mater **440** 420.

[325] K. Barrett, S. Bragg-Sitton, and D. Galicki, (2012) Light Water Reactor Sustainability Program, US Department of Energy. Idaho Falls, ID: Idaho National Laboratory.

[326] J. P. Mazzoccoli, P. Xu, S. Ray, C. J. Long, and G. L. Eddy, Deposition of a protective coating including metal-containing and chromium-containing layers on zirconium alloy for nuclear power applications. Google Patents, 2015.

[327] S. PalDey and S. Deevi, (2003) Materials Science and Engineering: A **342** 58.

[328] W. D. Münz, (1986) Journal of Vacuum Science & Technology A: Vacuum, Surfaces, and Films **4** 2717.

[329] E. Alat, A. T. Motta, R. J. Comstock, J. M. Partezana, and D. E. Wolfe, (2016) J Nucl Mater **478** 236.

[330] W. Zhong, P. A. Mouche, X. Han, B. J. Heuser, K. K. Mandapaka, and G. S. Was, (2016) J Nucl Mater **470** 327.

[331] J. R. Baczynski, University of Illinois at Urbana-Champaign, 2014.

[332] H.-G. Kim, I.-H. Kim, Y.-I. Jung, D.-J. Park, J.-Y. Park, and Y.-H. Koo, (2015) J Nucl Mater **465** 531.

[333] J. Brachet, M. Le Saux, M. Le Flem, S. Urvoy, E. Rouesne, T. Guilbert, C. Cobac, F. Lahogue, J. Rousselot, and M. Tupin, On-going studies at CEA on chromium coated zirconium based nuclear fuel claddings for enhanced Accident Tolerant LWRs Fuel, TopFuel 2015, Zurich, Switzerland.

[334] A. K. Valeeva, I. S. Valeev, O. Valiakhmetov, D. Zhemchuzhnikova, M. Markushev, and R. Mulyukov, (2012) Inorganic Materials: Applied Research **3** 226.

[335] B. R. Maier, B. L. Garcia-Diaz, B. Hauch, L. C. Olson, R. L. Sindelar, and K. Sridharan, (2015) J Nucl Mater **466** 712.

[336] K. Daub, R. Van Nieuwenhove, and H. Nordin, (2015) J Nucl Mater **467** 260.

[337] D. Jin, F. Yang, Z. Zou, L. Gu, X. Zhao, F. Guo, and P. Xiao, (2016) Surface and Coatings Technology **287** 55.

[338] P. Ashcheulov, R. Škoda, J. Škarohlíd, A. Taylor, L. Fekete, F. Fendrych, R. Vega, L. Shao, L. Kalvoda, and S. Vratislav, (2015) Appl Surf Sci **359** 621.

[339] U. Wiklund, P. Hedenqvist, S. Hogmark, B. Stridh, and M. Arbell, (1996) Surface and Coatings Technology **86** 530.

[340] A. Kuprin, V. Belous, V. Voyevodin, V. Bryk, R. Vasilenko, V. Ovcharenko, E. Reshetnyak, G. Tolmachova, and P. V'yugov, (2015) J Nucl Mater **465** 400.

[341] Z. Duan, H. Yang, Y. Satoh, K. Murakami, S. Kano, Z. Zhao, J. Shen, and H. Abe, (2017) Nuclear Engineering and Design **316** 131.

[342] I. Younker and M. Fratoni, (2016) Prog Nucl Energ **88** 10.

[343] C. P. Deck, G. M. Jacobsen, J. Sheeder, O. Gutierrez, J. Zhang, J. Stone, H. E. Khalifa, and C. A. Back, (2015) J Nucl Mater **466** 667.

[344] G. L. Harris, Iet (1995).

[345] J. A. Powell, (1983).

[346] H. K. Yoon, Y. J. Lee, H. J. Cho, and T. G. Kim, (2010) International Journal of Modern Physics B **24** 2928.

[347] A. Ellison, J. Zhang, J. Peterson, A. Henry, Q. Wahab, J. Bergman, Y. N. Makarov, A. Vorob'ev, A. Vehanen, and E. Janzén, (1999) Materials Science and Engineering: B **61** 113.

[348] M. Mynbaeva, S. Saddow, G. Melnychuk, I. Nikitina, M. Scheglov, A. Sitnikova, N. Kuznetsov, K. Mynbaev, and V. Dmitriev, (2001) Appl Phys Lett **78** 117.

[349] D. M. Carpenter, Massachusetts Institute of Technology, 2010.

[350] J. D. Stempien, D. M. Carpenter, G. Kohse, and M. S. Kazimi, (2013) Nucl Technol **183** 13.

[351] Y. Kawaharada, F. Kano, Y. Tsuchiya, K. Kakiuchi, K. Okonogi, S. Higuchi, T. Hinoki, N. Hashimoto, and S. Ohnuki, (2014).

[352] K. Yueh, K. Edsinger, G. Griffith, J. Garnier, E. Pilat, P. Cantonwine, H. Feinroth, and R. Shinavski, Silicon carbide composite for BWR channel application, LWR Fuel Performance (TOPFUEL12) Conference, ENS/ANS, 2012.

[353] C. Lorrette, C. Sauder, P. Billaud, C. Hossepied, G. Loupias, A. Michaux, E. Torres, F. Rebillat, J. Bischoff, and A. Ambard, SiC/SiC composite behavior in LWR conditions and under high temperature steam environment, Proc. of TOP FUEL meeting, 2015.

[354] N. M. George, K. Terrani, J. Powers, A. Worrall, and I. Maldonado, (2015) Ann Nucl Energy **75** 703.

[355] N. R. Brown, A. J. Wysocki, K. A. Terrani, K. G. Xu, and D. M. Wachs, (2017) Ann Nucl Energy **99** 353.

[356] X. Wu, T. Kozlowski, and J. D. Hales, (2015) Ann Nucl Energy **85** 763.

[357] C. A. Williams, P. Unifantowicz, N. Baluc, G. D. Smith, and E. A. Marquis, (2013) Acta Mater **61** 2219.

[358] Y. Z. Shen, T. T. Zou, S. Zhang, and L. Z. Sheng, (2013) ISIJ international **53** 304.

[359] S. N. Dryepondt, K. A. Unocic, D. T. Hoelzer, and B. A. Pint, Advanced ODS FeCrAl alloys for accident-tolerant fuel cladding. Oak Ridge National Laboratory (ORNL), 2014.

[360] S. Bragg-Sitton, (2014) Nuclear News **57** 83.

[361] W. D. Bennett, A. L. Doherty, C. H. Henager, C. A. Lavender, R. O. Montgomery, R. P. Omberg, M. T. Smith, and R. A. Webster, FY16 Status Report for the Uranium-Molybdenum Fuel Concept. Pacific Northwest National Lab.(PNNL), Richland, WA (United States), 2016.

[362] G. d. Assis, W. B. Ferraz, and E. B. Tambourgi, Aspects of Sintering and grain growth in pure and Al_2O_3-SiO_2 doped UO_2 pellets, International Nuclear Atlantic Conference, Rio de Janeiro, Brazil, 2009.

[363] C. Delafoy, P. Blanpain, S. Lansiart, P. Dehaudt, G. Chiarelli, and R. Castelli, (2004) Advanced fuel pellet materials and designs for water cooled reactors 163.

[364] D. S. Li, H. Garmestani, and J. Schwartz, (2009) J Nucl Mater **392** 22.

[365] J. Matsunaga, Y. Takagawa, K. Kusagaya, K. Une, R. Yuda, and M. Hirai, Fundamentals of GNF Al-Si-O additive fuel, Proc. Top Fuel 2009, Paris, France, 2009.

[366] P. Ehrenfest, (1927) Zeitschrift für Physik **45** 455.

[367] M. Born and J. R. Oppenheimer, (1927) Ann. Physik **84** 458.

[368] R. Car and M. Parrinello, (1985) Physical review letters **55** 2471.

[369] D. Marx and J. Hutter, Cambridge University Press (2009).

[370] F. G. Fumi and M. P. Tosi, (1964) J Phys Chem Solids **25** 31.

[371] M. P. Tosi and F. G. Fumi, (1964) J Phys Chem Solids **25** 45.

[372] A. Winkler, J. Horbach, W. Kob, and K. Binder, (2004) J Chem Phys **120** 384.

[373] W. J. Mortier, S. K. Ghosh, and S. Shankar, (1986) J Am Chem Soc **108** 4315.

[374] S. Rana, R. Chawla, R. Kumar, S. Singh, A. Zheleva, Y. Dimitrova, V. Gadjeva, R. Arora, S. Sultana, and R. K. Sharma, (2010) Journal of Pharmacy And Bioallied Sciences **2** 80.

[375] B. Henderson and J. E. Wertz, Taylor, London.

[376] C. A. English, (1982) J Nucl Mater **108** 104.

[377] D. Bufford, C. Snow, and K. Hattar, (2017) Fusion Sci Technol 1.

[378] K. Tougou, A. Shikata, U. Kawase, T. Onitsuka, and K. Fukumoto, (2015) J Nucl Mater **465** 843.